INFORMATION TO USERS

This manuscript has been reproduced from the microfilm master. UMI films the text directly from the original or copy submitted. Thus, some thesis and dissertation copies are in typewriter face, while others may be from any type of computer printer.

The quality of this reproduction is dependent upon the quality of the copy submitted. Broken or indistinct print, colored or poor quality illustrations and photographs, print bleedthrough, substandard margins, and improper alignment can adversely affect reproduction.

In the unlikely event that the author did not send UMI a complete manuscript and there are missing pages, these will be noted. Also, if unauthorized copyright material had to be removed, a note will indicate the deletion.

Oversize materials (e.g., maps, drawings, charts) are reproduced by sectioning the original, beginning at the upper left-hand corner and continuing from left to right in equal sections with small overlaps.

ProQuest Information and Learning
300 North Zeeb Road, Ann Arbor, MI 48106-1346 USA
800-521-0600



Experimental and Field Investigations of Serpentinization and Rodingitization.

Charles Normand

January, 2001

A thesis submitted to the Faculty of Graduate Studies and Research in partial fulfillment of the requirements of the degree of Doctor of Philosophy

Department of Earth and Planetary Sciences,
McGill University,
Montréal, Québec, Canada

© Charles Normand, 2001

National Library of Canada
Acquisitions and Bibliographic Services
395 Wellington Street
Ottawa ON K1A 0N4
Canada

Bibliothèque nationale du Canada
Acquisitions et services bibliographiques
395, rue Wellington
Ottawa ON K1A 0N4
Canada

Your file Votre référence

Our file Notre référence

The author has granted a non-exclusive licence allowing the National Library of Canada to reproduce, loan, distribute or sell copies of this thesis in microform, paper or electronic formats.

L'auteur a accordé une licence non exclusive permettant à la Bibliothèque nationale du Canada de reproduire, prêter, distribuer ou vendre des copies de cette thèse sous la forme de microfiche/film, de reproduction sur papier ou sur format électronique.

The author retains ownership of the copyright in this thesis. Neither the thesis nor substantial extracts from it may be printed or otherwise reproduced without the author's permission.

L'auteur conserve la propriété du droit d'auteur qui protège cette thèse. Ni la thèse ni des extraits substantiels de celle-ci ne doivent être imprimés ou autrement reproduits sans son autorisation.

0-612-70115-8

Canada

ABSTRACT

The chemical evolution of peridotites and felsic rocks included in or adjacent to them, and fluids during the hydrothermal alteration of these rocks is the subject of this study. Experiments using a flow-through hydrothermal apparatus, and studies of natural samples from the JM Asbestos chrysotile deposit in the Asbestos ophiolite, Québec, were the means by which the various topics of this thesis were investigated. Open-system fluid-rock interaction was studied by flowing deionized water or a 0.1 *m* $CaCl_2$ solution through olivine (Fo_{91}) and lherzolite at a temperature of 300°C and a pressure of 300 bars. During these experiments, the original minerals (olivine, orthopyroxene and clinopyroxene) were altered to an assemblage, which consisted of serpentine-group minerals (conical, polygonal, and cylindrical fibers, and plates), brucite and magnetite. Although we could not determine precisely which of the serpentine-group minerals was the most stable, the textural relationships among them is consistent with lizardite forming metastably over a wider range of pressure and temperature conditions than is generally reported in the literature. Reaction of lherzolite with deionized water and thermodynamic modelling indicate that the highest pH and calcium concentration are attained when pyroxenes are present in the unaltered rock, and that these parameters are at maximum in the presence of the buffering assemblage serpentine + brucite + diopside. Alteration of olivine by 0.1 *m* $CaCl_2$ aqueous solution does not lead to the formation of secondary calcium phases. These results, supported by thermodynamic calculations, suggest that calcium-rich fluids can circulate through forsteritic olivine-rich lithologies without inducing calcium metasomatism. Calculations clearly indicate that nephrites and rodingites, which are calcium-rich rocks formed metasomatically from serpentinites and adjacent, more Si-Al-rich lithologies, develop primarily in response to strongly decreasing μSiO_2° and, to a lesser extent, sharp increases in pH gradients away from the Si-rich lithologies. Efforts aimed at identifying a single source for the calcium responsible for metasomatism are futile. Most hydrothermal fluids that have equilibrated with crustal rocks, and are likely to access peridotites, contain appreciable Ca, and during serpentinization undergo negligible enrichment in Ca relative to the original

concentration of this element in the fluid. Furthermore, calculations indicate that the differences in Ca concentration between a serpentinization-derived fluid and the same fluid equilibrated with rodingite mineral assemblages after reaction with a Si-Al-rich protolith are also small.

In the JM Asbestos mine, these Si-Al lithologies are largely felsic dykes, which, based on geological relationships, are interpreted to have been emplaced after serpentinization of the host peridotites began, but before obduction of the Asbestos ophiolite onto the Laurentian continental margin. Slates underlying and in thrust contact with serpentinite are also locally rodingitized. Mass balance calculations suggest that the calcium responsible for the rodingitization of the slates may have been derived locally, whereas the calcium responsible for the rodingitization of the felsic dykes was most probably derived from a source remote from the dykes. The strong dilution in rodingites and nephrites of the low-solubility minor and traces elements P, Cr and Zr suggests that very large amounts of fluids were involved in calc-silicate metasomatism of the felsic dykes and adjacent serpentinites. Investigation of fluid inclusions in the rodingites indicates that at least three types of fluids were involved in two episodes of rodingitization. Earlier, moderately to highly saline fluids of mixed origin, involving metamorphic fluids and/or formational waters and/or modified seawater and/or evolved meteoric waters, caused rodingitization of diorite, granite and slate at a pressure of approximately 2500 bars and at temperatures between 300 and 350°C. Moderately saline fluids, possibly involving a strong meteoric component, were involved in the later stages of alteration, and in the formation of low temperature (< 200°C), low pressure (< 1 kilobar) vesuvianite-rich "veins".

The absence of CO_2 and presence of hydrocarbons (alkanes from methane to pentane) in the fluid inclusions of both episodes is an indication that the fluids responsible for calc-silicate alteration were derived from the serpentinites. A new interpretation of the origin of hydrocarbons in serpentinites is proposed based on the equilibration of a carbon-rich fluid with a metastable mineral assemblage comprising magnetite, awaruite and cohenite.

RÉSUMÉ

Cette thèse porte sur l'étude des phénomènes reliés à l'altération hydrothermale des roches ultramafiques et des roches riches en Si et Al situées dans ou à proximité de celles-ci. Les sujets traités dans cette thèse ont été étudiés par l'entremise d'expériences hydrothermales conduites avec l'aide d'un autoclave à circulation continue ainsi que par l'examen minéralogique et géochimique d'échantillons provenant de la mine de chrysotile JM Asbestos, située dans l'ophiolite d'Asbestos au Québec. Les effets produits par l'interaction fluide/roche en système ouvert ont été étudiés au cours d'expériences impliquant la circulation d'eau déionizée ou d'une solution de 0.1 *m* $CaCl_2$ à travers de l'olivine (Fo_{91}) et de la lherzolite. Durant ces expériences, les minéraux originels (olivine, orthopyroxene et clinopyroxene) ont été altérés en minéraux du groupe de la serpentine (fibres coniques, polygonales et cylindriques, et plaquettes), en brucite et en magnétite. Malgré que nous n'ayons pu déterminer avec certitude lequel des minéraux du groupe de la serpentine était le plus stable, les relations texturales entre ces derniers suggèrent du moins que la lizardite se forme de façon métastable sous un plus large éventail de pressions et de températures qu'il ne l'est généralement admis dans la littérature. La réaction de la lherzolite avec l'eau déionizée et les modèles thermodynamiques indiquent que les valeurs de pH et les concentrations en calcium les plus élevées sont atteintes dans les fluides quand un pyroxene est initialement présent dans la roche, et que ces paramètres sont à leurs valeurs maximales en présence de l'assemblage serpentine + brucite + diopside. L'altération de l'olivine par une solution de 0.1 *m* $CaCl_2$ ne produit pas de minéraux secondaires contenant du calcium. Ces résultats, supportés par des calculs thermodynamiques, suggèrent que des fluides riches en calcium peuvent circuler au travers de roches riches en olivine sans causer une métasomatose du calcium. Les calculs indiquent clairement que la néphrite et la rodingite, qui sont des roches riches en calcium formées par la métasomatose des serpentinites et des lithologies adjacentes riches en Si et Al, se forment principalement en réponse à un fort gradient décroissant de μSiO_2° et, à un moindre degré, à un accroissement abrupt du pH dans la serpentinite en s'éloignant du contact avec les roches riches en Si et Al. Il est impossible de déterminer

une source unique pour l'origine du calcium dans les rodingites. La pluspart des fluides hydrothermaux équilibrés avec les roches qui composent la croûte terrestre, et sont susceptibles d'interagir avec les péridotites, contiennent des quantités appréciables de Ca, et, durant la serpentinization, ne sont enrichis en Ca que de façon négligeable par rapport au contenu initial du fluide en cet élément. De plus, des calculs basés sur les équilibres thermodynamiques indiquent que la différence de concentration en Ca entre un fluide issu de la serpentization et un fluide équilibré avec une rodingite est mineure.

Dans la mine JM Asbestos, les lithologies riches en Si et Al sont représentées principalement par des dykes felsiques (diorite et granite), qui, sur la base des relations de terrain et des observations faites en laboratoire, sont interprétés comme ayant été mis en place après le début de la serpentinization des péridotites hôtes, mais avant l'obduction de l'ophiolite d'Asbestos sur la marge continentale Laurentienne. Des schistes argileux sous le contact chevauchant avec les serpentinites sont aussi localement rodingitizés. Des calculs de bilan de masse suggèrent que le calcium impliqué dans la rodingitization des schistes argileux pourrait être d'origine locale, tandis que le calcium impliqué dans la rodingitization des dykes felsiques est probablement dérivé d'une source éloignée des dykes. La dilution importante de P, Cr et Zr dans les roches calco-silicatées suggère que de très importantes quantités de fluides ont été nécéssaires à la métasomatose du calcium dans les dykes felsiques et les serpentinites adjacentes. L'étude des inclusions fluides dans les rodingites indique qu'il y a eu au moins trois types de fluides impliqués dans deux épisodes de rodingitization. Durant le premier épisode, des fluides à salinité élevée à moyenne d'origine mixte (fluide métamorphique et/ou eau de formation et/ou eau de mer modifiée et/ou eau météorique évoluée) ont causé la rodingitization des diorites, des granites et des schistes argileux à une pression d'environ 2500 bars et à des températures variant entre 300 et 350°C. Un fluide modérément salin, possiblement à forte composante météorique, a été impliqué durant les stades tardifs de l'altération et dans la formation de filons riches en vésuvianite à basse température (< 200°C) et faible pression (< 1 kbar). L'absence de CO_2 et la présence d'hydrocarbures (alkanes, de méthane à pentane) dans les inclusions fluides associées aux deux épisodes de rodingitization indiquent que les fluides responsables des altérations à minéraux calco-silicatés ont préalablement réagi

avec les serpentinites. Une nouvelle interprétation de l'origine des hydrocarbures dans les serpentinites est proposée, basée sur l'équilibration d'un fluide riche en carbone avec un assemblage minéral comprenant la magnétite, l'awaruite et la cohénite.

ACKNOWLEDGEMENTS

This work could not have been completed without the aid of J. Potter and B. Mountain (in setting up the flow-through systems), P. Kranidiotis (who collected part of the fluid inclusion microthermometric data), G. Poirier (who provided technical assistance with the electron microprobe), G. Keating and S. Lalli (who aided in the atomic absorption spectroscopic and XRF analyses). The assistance of the following people is greatly appreciated: J. Clark, D. Palmer, and T. Mulja (technical assistance for scanning electron microscopy and electron microprobe analyses), and H. Vali for the transmission electron microscopic analyses. G. Poirier and M. Mlynarchyk carbon coated the samples used for electron microprobe analysis. R. Martin, G. Olivo, H. Vali, S. Shata and E. Sakoma performed the XRD analyses used in this thesis. The gas chromatographic analyses were performed with the technical assistance of S. Salvi, W. Halter and S. Archibald. Stimulating discussions on various portions of this thesis were had with A. Migdisov, C. Gammons, B. Mountain, Z. Xiao, A. Baronnet, R. Martin, A. Hynes, F. Wicks, D. Dolejs, P. Kranidiotis, T. Ahmedali, H. Vali, G. Olivo and E. Sakoma. I thank D. Dolejs for providing me with his least squares program to calculate mineral norms. S. McCauley was patient enough to answer my innumerable questions concerning computers and introduced me to the use of EQ3/6.

Financial support to the author was provided by postgraduate scholarships from the National Science and Engineering Research Council of Canada (NSERC), Fonds pour la Formation de Chercheurs et l'Aide à la Recherche (FCAR) and the Department of Earth and Planetary Sciences (William Henry Howard Award and Reinhardt Fellowship). Support for the research was provided by NSERC and FCAR grants to A. E. Williams-Jones. Additional support and access to the mine for the field portion of this study was provided by J.M. Asbestos Inc. The research formed part of a project designed to establish the distribution of tremolite and controls on its formation in the mine. Company geologists J. Millen, M. Arpin, and F. Spertini provided useful information on the local geology. Special thanks go to those involved in the Asbestos study for aid in the field work, laboratory separations, report preparation and geological mapping: J. Clark, S.

Smith, G. Olivo, E. Sakoma, M. Pueler, K. Skaret, J. Duggan, A. Olsen, and J. Roelofsen. Other members of the team involved in this research were: R. F. Martin, A. Dufresne and H. Vali.

The help provided by J. Roelofsen, M. Heiligmann and K. Ault in formatting and printing this thesis is greatly appreciated.

My sincere thanks go to my supervisor, Dr. A. E. Williams-Jones (Willy), for providing the encouragement and help (manuscript revisions) necessary to complete this work.

My family, Jeanette and friends were there for much needed moral support during work, but, most of all, to keep me grounded.

This thesis is dedicated to my parents.

PREFACE

This thesis has been produced with consideration of the following provisions:

Candidates have the option of including, as part of the thesis, the text of one or more papers submitted or to be submitted for publication, or the clearly-duplicated text of one or more published papers. These texts must be bound as an integral part of the thesis.

If this option is chosen, connecting texts that provide logical bridges between the different papers are mandatory. The thesis must be written in such a way that it is more than a mere collection of manuscripts; in other words, results of a series of papers must be integrated.

The thesis must still conform to all other requirements of the "Guidelines for Thesis Preparation". The thesis must include: A Table of Contents, and abstract in English and French, an introduction which clearly states the rationale and objectives of the study, a review of the literature, a final conclusion and summary, and a thorough bibliography or reference list.

Additional material must be provided where appropriate (e.g. in appendices) and in sufficient detail to allow a clear and precise judgement to be made of the importance and originality of the research reported in the thesis.

In the case of manuscripts co-authored by the candidate and others, the candidate is required to make an explicit statement in the thesis as to who contributed to such work and to what extent. Supervisors must attest to the accuracy of such statements at the doctoral oral defense. Since the task of the examiners is made more difficult in these cases, it is in the candidate's interest to make perfectly clear the responsibilities of all the authors of the co-authored papers.

TABLE OF CONTENTS

Abstract i

Résumé iii

Acknowledgements vi

Preface viii

Table of Contents ix

List of figures xiii

List of tables xviii

Chapter I: Introduction 1

PART I : EXPERIMENTAL INVESTIGATIONS OF SERPENTINIZATION AND APPLICATIONS TO RODINGITIZATION

Prologue 28

Introduction to Chapter II 29

Chapter II: Hydrothermal alteration of olivine in a flow-through autoclave: nucleation and growth of serpentine phases 30

Abstract 31

Introduction 32

Experimental and analytical methods 33

Results 36

Discussion 49

Conclusions 57

Acknowledgements 58

References 59

Introduction to Chapter III 62

Chapter III: Constraints on calc-silicate alteration associated with serpentinites: experimental and field evidence. 63

Abstract 64

Introduction 66
Hydrothermal experiments 68
Implications for rodingitization 110
Conclusions 122
Acknowledgements 124
References 125

PART II : FIELD AND LABORATORY STUDIES OF SERPENTINITES, FELSIC ROCKS AND THEIR PRODUCTS OF ALTERATION IN THE JM ASBESTOS MINE, ASBESTOS, QUEBEC

Prologue 133
Introduction to Chapter IV 134
Chapter IV: K-rich dioritic-monzodioritic, and granitic dyke intrusion in serpentinized peridotites of the JM Asbestos deposit, Quebec 135
Abstract 136
Introduction 137
Tectonic setting and metamorphism 137
Mine geology 144
Discussion 177
Conclusions 183
Acknowledgements 184
References 185
Introduction to Chapter V 192
Chapter V: Alteration of serpentinite, slate and felsic intrusive rocks from the JM Asbestos mine, Asbestos, Quebec: Constraints on rodingitization 193
Abstract 194
Introduction 195
Tectonic setting and metamorphism 196
The JM Asbestos deposit 198

Rodingite mineralogy 203
Chemical changes accompanying rodingitization 223
Discussion 249
Conclusions 266
Acknowledgements 267
References 268
Introduction to Chapter VI 274
Chapter VI: Fluid inclusions in rodingites from the JM Asbestos mine, Asbestos, Quebec 275
Abstract 276
Introduction 277
Geological setting 277
Rodingites 278
Fluid inclusions 280
Discussion 297
Conclusions 306
Acknowledgements 307
References 308
Introduction to Chapter VII 311
Chapter VII: Rodingites: Traps for Fischer-Tropsch-catalysed hydrocarbons in serpentinites? 312
Abstract 313
Introduction 314
Geology 316
Fluid inclusions 319
Discussion 325
Conclusions 339
Acknowledgements 340
References 341
Introduction to Chapter VIII 348

Chapter VIII: Controls of amphibole formation in chrysotile deposits: Evidence from the Jeffrey mine, Asbestos, Quebec 349

Abstract 350

Introduction 351

Geological setting 352

Nature and distribution of amphibole-group minerals 357

Types of amphibole 359

Distribution of amphibole-group minerals 362

Controls on the distribution of amphibole-group minerals 364

Approaches to identifying amphibole-rich zones 372

Conclusions 376

Acknowledgements 378

References 379

Chapter IX - Conclusions 382

General conclusions 383

Contributions to knowledge 386

Suggestions for further investigations 388

References 391

Appendices 419

Appendix I 419

Appendix II 434

Appendix III 522

Appendix IV 528

LIST OF FIGURES

Chapter II

Figure 1. Si, Mg, Ca, Ni, and Mn concentration variations during the reaction between water and San Carlos olivine. 39

Figure 2. TEM images of Pt/C replicas showing surface morphologies of unreacted olivine. 41

Figure 3. TEM Images of Pt/C replicas of fragments from the top of the reaction cell. 43

Figure 4. TEM images of Pt/C replicas of fragments from the center of the reaction cell. 44

Figure 5. SEM image of crystals of brucite. 45

Figure 6. TEM images of Pt/C replicas of fragments from the bottom part of the reaction cell. 48

Figure 7. Schematic representation of the steady state ion activity product profile with respect to lizardite and chrysotile. 56

Chapter III

Figure 1. pH-time and concentration-time profiles in water during reaction with olivine. 77

Figure 2. pH-time and concentration-time profiles in water during reaction with lherzolite. 80

Figure 3. pH-time and concentration-time profiles in the fluid during reaction of the 0.1 *M* $CaCl_2$ solution with olivine. 83

Figure 4. SEM photograph of secondary serpentine on olivine from near the inlet. 85

Figure 5. Al versus Fe concentration in serpentine grown on olivine, orthopyroxene and clinopyroxene. 87

Figure 6. pH versus log ($M\Sigma Ca/M\Sigma Mg$) relationship of the fluid chemistry 98

during reaction of water with olivine and lherzolite.

Figure 7. Log $M\Sigma$Si versus log ($M\Sigma$Ca/$M\Sigma$Mg) relationship of the fluid chemistry during reaction of olivine with the 0.1 *M* $CaCl_2$ solution. 100

Figure 8. Dissolution rate-time profile during reaction of water with San Carlos olivine. 102

Figure 9. Log $M\Sigma$Si versus log ($M\Sigma$Ca/$M\Sigma$Mg) relationship of the fluid chemistry during the olivine-water and lherzolite-water experiments. 105

Figure 10. Log $M\Sigma$Si versus log ($M\Sigma$Ca/$M\Sigma$Mg) diagram in the system Ca-Mg-Si-O-H-Cl (0.2 *M*). 113

Figure 11. Ca and Mg concentrations of fluids in equilibrium with the assemblage antigorite + tremolite + talc with decreasing temperature. 115

Figure 12. Log $aSiO_2°$ versus log (aCa^{2+}/aMg^{2+}) equilibrium relationships among phases in the system Na-Ca-Mg-Al-Si-O-H. 117

Figure 13. Evolution of mineralogical and fluid compositions during closed-system reaction of plagiogranite with serpentinizing fluid. 120

Chapter IV

Figure 1. Geological map of ophiolitic rocks in southeastern Québec. 138

Figure 2. Geological map of the Jeffrey Mine. 145

Figure 3. Photographs of a diorite dyke and a dioritic-granitic dyke. 147

Figure 4. Stereographic projections illustrating the variation in orientation of the dykes, schistosity in the slate, veins, and shear zones. 148

Figure 5. Photomicrographs of thin sections. 155

Figure 6. Triangular diagram showing the relative proportions of minerals in the dioritic-monzodioritic rocks. 159

Figure 7. Binary diagrams showing the relationship between concentrations of various oxides in the dioritic-monzodioritic rocks. 170

Figure 8. Spider diagram distribution of minor and trace elements in the dioritic-monzodioritic and the granodioritic-granitic rocks. 173

Figure 9. A/NK versus A/CNK diagrams of granodioritic and granitic 176

rocks.

Figure 10. Binary plots of oxides among dioritic-monzodioritic and granodioritic-granitic intrusive rocks. 178

Chapter V

Figure 1. Geological map of the JM Asbestos chrysotile mine. 199

Figure 2. Section through a sample of rodingitized slate. 207

Figure 3. Backscatter SEM image of oscillatory zoning in diopside. 212

Figure 4. Location of slate samples relative to the serpentinite and slate contact and associated relative mass changes. 229

Figure 5. Location of granite samples relative to the serpentinite and granite contact and associated relative mass changes. 240

Figure 6. Location of calc-silicate-altered serpentinite samples relative to the serpentinite and rodingitized dyke and associated relative mass changes. 248

Figure 7. pH versus log $a\mathrm{Na}^{+}$ equilibrium relationships at 325°C and 2 kbars. 253

Figure 8. Variation of Zr concentration in a diorite dyke near a serpentinite. 257

Figure 9. Binary trace element relationships among the least and most affected diorite, granite, slate, and serpentinite. 258

Figure 10. Solubility of OH-apatite as a function of pH and Ca concentration. 260

Figure 11. Sections through blackwall-rimmed rodingitized diorite and diorite dykes. 265

Chapter VI

Figure 1. Histogram of homogenization temperatures of type 1 fluid inclusions. 286

Figure 2. Histograms of homogenization temperatures in bubble of type 2 fluid inclusions. 287

Figure 3. Histograms of the initial ice melting temperatures of type 2 fluid inclusions. 289

Figure 4. Histograms of the final ice melting temperatures of type 2 fluid inclusions. 290

Figure 5. Histograms showing the distribution of the final clathrate melting temperatures of type 2 fluid inclusions. 291

Figure 6. Relationship between the melting temperature of the clathrate and the salinity of type 2 fluid inclusions. 293

Figure 7. Histograms of the calculated molar fractions of CH_4 in type 2 fluid inclusions. 295

Figure 8. Histograms of the temperatures of total homogenization of type 2 fluid inclusions. 296

Figure 9. Triangular diagram of CH_4, C_{2+} hydrocarbons and the unidentified species. 298

Figure 10. Pressure and temperature conditions under which the fluid inclusions were trapped and the mineral assemblages formed. 300

Chapter VII

Figure 1. Proportions of C_1-C_5 alkanes in rodingite-hosted fluid inclusions as a function of the carbon number. 330

Figure 2. Log fO_2 versus logfCO_2 diagram for the system Mg-Fe-Si-C-O-H. 333

Figure 3. Proportions of ethane in gaseous hydrocarbon mixtures coexisting with metastable mineral assemblages. 334

Figure 4. Variations in the proportion of secondary minerals and in fluid composition as a function of the fluid/rock ratio from reaction of H_2O-CO_2 fluid with peridotite. 335

Figure 5. Distribution of alkanes calculated for fluids in the presence of various minerals and measured in fluid inclusions. 338

Chapter VIII

Figure 1. Geological map of ophiolites in southern Québec. 353

Figure 2. Detailed geological map of the Jeffrey mine area. 354

Figure 3. Plan of the Jeffrey open pit. 356

Figure 4. Photograph of a lensoid fragment of a dismembered felsic dyke. 358

Figure 5. X-ray diffractograms of digested and untreated samples of serpentine and tremolite. 360

Figure 6. Electron backscatter images of amphibole textures. 361

Figure 7. Photograph of a nephrite block detached from a monzodiorite dyke. 363

Figure 8. Pressure-temperature diagram showing stability relationships among minerals in the system CaO-MgO-SiO_2-H_2O. 366

Figure 9. Log $a{SiO^0}_2$ versus log aCa^{2+}/aMg^{2+} diagrams for the system CaO-MgO-SiO_2-H_2O. 368

Figure 10. Triangular projection diagram for the system CaO-MgO-SiO_2-H_2O. 370

Figure 11. Binary plots showing the distribution of amphibole-bearing and amphibole-free samples. 374

LIST OF TABLES

Chapter II

Table 1. Composition of the air-saturated water reacted with olivine. 37

Chapter III

Table 1. Characteristics of the materials before and after reaction. 70

Table 2. Average of electron microprobe analyses. 71

Table 3. Composition of the air-saturated water reacted with olivine. 75

Table 4. Composition of the air-saturated water reacted with lherzolite. 79

Table 5. Composition of the 0.1 *M* $CaCl_2$ solution reacted with olivine. 82

Table 6. SEM-EDS analyses of secondary minerals formed after reaction of San Carlos olivine with water. 84

Table 7. SEM-EDS analyses of serpentine grown during reaction of lherzolite with water. 88

Table 8. SEM-EDS analyses of secondary minerals formed after reaction of olivine with the 0.1 *M* $CaCl_2$ solution. 96

Chapter IV

Table 1. Electron microprobe analyses of minerals from dioritic-monzodioritic rocks. 152

Table 2. Normative and modal composition of dioritic-monzodioritic rocks. 157

Table 3. Normative and modal composition of granodioritic-granitic rocks. 161

Table 4. Chemical analyses of dioritic-monzodioritic rocks. 165

Table 5. Chemical analyses of granodioritic-granitic rocks. 174

Chapter V

Table 1. X-ray fluorescence analyses of garnet from rodingitized diorites. 205

Table 2. Electron microprobe analyses of rodingite minerals from UG-C. 209

Table 3. Electron microprobe analyses of rodingite minerals from UG-2. 210
Table 4. Electron microprobe analyses of minerals from rodingitized diorites. 214
Table 5. Electron microprobe analyses of minerals from rodingitized diorites. 217
Table 6. Electron microprobe analyses of minerals from rodingitized granite. 221
Table 7. Chemical analyses of slate, albitized slate and rodingitized slate. 226
Table 8. Mass changes resulting from alteration of slate. 227
Table 9. Chemical analyses of altered diorite samples across a thick dyke. 231
Table 10. Mass changes resulting from alteration of diorite. 235
Table 11. Chemical analyses of rodingitized, feldspar-pyribole-altered and least altered granite from a serpentinite-hosted dyke. 237
Table 12. Mass changes resulting from alteration of granite. 238
Table 13. Chemical composition of serpentinites, nephrites and diopsidites. 242
Table 14. Mass changes that resulted from alteration of serpentinite. 245
Table 15. Chemical composition of vesuvianite-rich "veins". 250
Table 16. Chemical composition of blackwall. 262

Chapter VI

Table 1. Microthermometric data. 283
Table 2. Activity of end-member components in minerals from rodingites. 302

Chapter VII

Table 1. Results of gas-chromatographic analyses of inclusion fluids in rodingites. 323

CHAPTER I

INTRODUCTION

Generalities

Ultramafic rocks make up the asthenosphere of our planet and a major part of its lithosphere. Under certain conditions, these ultramafic rocks are transported to the surface of the Earth, either through magmatic or tectonic processes, where they are generally subjected to prograde or retrograde alteration by hydrous fluids. Typical examples of lithotectonic settings where serpentinized peridotitic rocks occur include layered ultramafic intrusions in the continental crust (Anhaeusser, 1976), the basal part of many obducted ophiolite slivers (Coleman, 1966; Evans and Trommsdorff, 1970; Laurent, 1975), and oceanic ridge (Aumento and Loubat, 1971; Bideau et al., 1991; Mével and Stamoudi, 1996) and fore-arc (Fryer and Mottl, 1992) regions of the seafloor.

Pervasive replacement of olivine-rich peridotites (harzburgite, lherzolite and dunite), the most abundant types of ultramafic rock, by serpentine-group mineral-rich assemblages occurs at temperatures below 400°C at shallow levels of the Earth's crust (Johannes, 1968; Evans et al., 1976; Moody, 1976; Day et al., 1985). The serpentinization temperatures in subduction environments may exceed 500°C, where devolatilization of the down-going slab has been proposed as a source for fluids causing the serpentinization or partial melting of peridotites situated above (Sakai et al., 1990; Peacock, 1987, 1993; Ulmer and Trommsdorff, 1995). However, large scale, complete serpentinization of peridotites is a relatively low temperature retrograde process that takes place almost exclusively at shallow levels in the Earth's crust. Oxygen isotopic studies have shown that serpentinization of ultramafic rocks in extensional settings of the oceanic crust is caused by seawater (Wenner and Taylor, 1973). In the continental crust, ultramafic rocks can be serpentinized by interaction with fluids derived from adjacent intrusive rocks, metamorphic fluids produced by the devolatilization of hydrous rock units in orogenic zones, or meteoric fluids near the surface of the Earth.

Serpentinized peridotites are frequently cut by mafic or felsic intrusive bodies, which are altered to calc-silicate-rich mineral assemblages. Tectonic inclusions of mafic to felsic lithologies commonly display a halo of calc-silicate alteration at the contact with the host serpentinites in zones of deformation affecting ultramafic rocks. In ophiolite

complexes, the country rocks over which serpentinized peridotites were thrust are also commonly altered to calc-silicate mineral assemblages. Such calc-silicate-rich rocks are called rodingites, a name which was originally given by Bell et al. (1911) to lime-rich, coarse- to fine-grained, gabbro-like rocks composed primarily of grossular or prehnite that occur in the vicinity of the Roding River in the Dun Mountain ultramafic complex, New Zealand. Since this description of rodingites by Bell et al. (1911), these rocks have been studied by numerous authors in all the tectonic settings where serpentinized peridotites occur (Coleman, 1966, 1967; Honnorez and Kirst, 1975; Anhaeusser, 1979), with the exception of fore-arc serpentinite mounds.

The origin of rodingites has been attributed to magmatic differentiation (Bell et al., 1911), the digestion of limestone blocks during intrusion of ultamafic rocks (Finlayson, 1909), and the alteration by magmatic fluids associated with dyke intrusions (Graham, 1917; Benson, 1926; Grange, 1927; Turner, 1933; De, 1961, 1972) or by fluids derived from a source remote from the rodingite precursor (Bloxam, 1954; Tilley, 1957; Baker, 1958; Bilgrami and Howie, 1960; Coleman, 1966, 1967; Thayer, 1966; de Waal, 1969; O'Brien and Rodgers, 1973; Honnorez and Kirst, 1975; Capedri et al., 1978; Sarp and Deferne, 1978; Anhaeusser, 1979; Laurent, 1980; Wares and Martin, 1980a; Barriga and Fyfe, 1983; Katoh and Niida, 1983; Hall and Ahmed, 1984; Bøe, 1985; Muraoka, 1985; Sivell and Waterhouse, 1986; Kobayashi and Shoji, 1988; Schandl et al., 1989; O'Hanley et al., 1992).

Today, usage of the term rodingite is not restricted to gabbro-like, calc-silicate-rich rocks associated with serpentinites, but applies to any rock that contains calc-silicate-rich mineral assemblages and occurs in contact with serpentinite. This broader definition recognizes that rodingites have no genetic relationship to gabbros, but instead are metasomatic rocks, which may have precursors as varied as granites and slates (Coleman, 1966; Wares and Martin, 1980a; Katoh and Niida, 1983). This metasomatic origin of rodingites is evident in mineral replacement textures and sequences, bulk rock immobile element signatures, and the common occurrence of these calc-silicate rocks between serpentinites and, for example, unaltered or weakly altered metasedimentary country rocks or dykes. From the above definition of rodingite, this term should include calc-

silicate metasomatized serpentinites (e.g., diopsidized serpentinites, and nephrites, which are serpentinites transformed to a compact, generally fine-grained tremolite-rich rock).

Previous work on serpentine mineral stability

Serpentine derives its name from the Greek word *serpentinus*, meaning *serpent-rock* (Agricola, 1556), in allusion to the green-coloured, mottled, scaly appearance of serpentinite, a rock-type composed essentially of serpentine-group minerals. Serpentine-group minerals are trioctahedral, layered phyllosilicates composed of alternating sheets of tetrahedrally [T] and octahedrally [O] coordinated cations with the general formula $M_3Z_2O_5(OH)_4$, where M = Al, Fe^{2+}, Fe^{3+}, Mg, Mn, Ni, and Zn and Z = Al, Fe^{3+}, and Si. However, the Mg-rich varieties are by far the most commonly occurring serpentine-group minerals, and include the phases antigorite, ideally $Mg_{48}Si_{34}O_{85}(OH)_{62}$, with a modulated structure, chrysotile, ideally $Mg_3Si_2O_5(OH)_4$, with a cylindrical structure, and lizardite, also ideally with the composition $Mg_3Si_2O_5(OH)_4$, but with a flat-layered structure. The curled nature of ideal chrysotile has been attributed to the mismatch between the octahedral and tetrahedral sheets as a result of $b_{oct}>b_{tet}$. Chemical and structural analyses have demonstrated that this misfit is favoured by substitution of Mg by Fe^{2+} in the octahedral sites or by the redox-related exchange $^{VI}Fe^{2+}H^{+} = {}^{VI}Fe^{3+}$ (O'Hanley and Dyar, 1998; this causes a decrease in H-bonding between T and O sheets). On the other hand, substitution of the type $^{VI}(Mg,Fe^{2+})^{IV}Si = {}^{VI}Al(Fe^{3+})\,{}^{IV}Al(Fe^{3+})$ has been shown to release the misfit and favour a flat-layered structure (Wicks and Whittaker, 1975).

Antigorite and chrysotile of ideal composition have different fields of stability with respect to pressure and temperature, and the presence of one or the other of these minerals is widely used, in conjunction with textural observations, to infer the conditions under which serpentinization occurred. Although the stability relationships between chrysotile and antigorite are reasonably well known (Evans et al., 1976; Day et al., 1985; Berman et al., 1986), those with lizardite remain unknown (Chernosky, 1975; Caruso and Chernosky, 1979; O'Hanley et al., 1989; O'Hanley, 1991; O'Hanley and Wicks, 1995;

O'Hanley and Dyar, 1998; Grauby et al., 1998). Specifically, while it has been shown from examination of naturally occurring mineral parageneses and theoretical investigations (e.g., O'Hanley et al., 1989: O'Hanley and Wicks, 1995) that lizardite, like chrysotile, forms at lower temperature than antigorite, it is not known whether lizardite and chrysotile of ideal composition have separate fields of stability, or if lizardite or chrysotile is metastable under all conditions. If ideal lizardite and chrysotile have separate fields of stability with respect to pressure and temperature, the fact that their composition and crystal structure are very close suggest that very small differences in free energy would characterize these phases at temperatures above or below an hypothetical condition of equilibrium, and would allow for metastable coexistence of both phases under a very wide range of P-T conditions.

Serpentinites most commonly form as a result of the hydrothermal alteration of Mg-rich silicates, notably olivine, in ultramafic rocks such as dunites, harzburgites and lherzolites. They also develop in impure crystalline limestones, albeit less commonly. Variations in the bulk composition of the ultramafic rock influence the composition of the fluid phase that causes serpentinization, and, in turn, indirectly the mineral assemblages resulting from this alteration. The oxygen and hydrogen isotopic signature of serpentinized peridotite samples collected from the seafloor suggest that seawater is the main fluid responsible for the serpentinization of the upper mantle and lower crust ultramafic rocks in the oceanic environment (Wenner and Taylor, 1973). The effects of fluid-rock interaction between seawater-like fluids and peridotites were investigated experimentally by Seyfried and Dibble (1980), Hajash and Chandler (1981), Janecky and Seyfried (1986), Menzies et al. (1993), and Kholodkevich and Barinov (1995) at temperatures between 200 and 500°C and pressures between 400 and 1,000 bars. All these studies have demonstrated that, after prolonged fluid/rock interaction, the concentrations of Si and Mg in serpentinizing fluids (especially in those which are SO_4^{2-}- and CO_3^{2-}-poor) become very low and the pH alkaline, while the Ca concentration has a "general" tendency to increase.

Studies of naturally occurring serpentinization fluids

Fluids derived from the serpentinization of ultramafic rocks have been observed in low temperature seeps in ophiolites and on the seafloor, and in fluid inclusions in metamorphosed serpentinites. Low temperature seeps from ophiolites comprise: 1) high pH (11.3-12.1) Ca-OH-rich aqueous fluids, 2) high pH (12.1), low-Ca (< 1 ppm), low-Mg (< 1 ppm) fluids of seawater-like salinity, 3) moderately high pH (7.8-9) Mg-HCO_3^--rich aqueous fluids, and 4) H_2-rich, hydrocarbon-bearing gases. The Ca-OH-type seeps have been found only in partially serpentinized peridotites, and originate from the serpentinization of olivine and pyroxenes by evolved meteoric waters (Barnes et al., 1967, 1972, 1978; Barnes and O'Neil, 1969; Neal and Stanger, 1983). The Ca concentrations of these fluids vary between 35 and 120 ppm. Mg-HCO_3^--type aqueous fluids form from the weathering of serpentinite.

H_2-rich and hydrocarbon-bearing gas seeps have been reported from serpentinites in many ophiolite complexes (Thayer, 1966; Neal and Stanger, 1983; Abrajano et al., 1988, 1990; Fritz et al., 1992; Devirts et al., 1993). H_2 was interpreted to have originated from the oxidation of the ferrous iron contained in the primary mafic silicates during serpentinization (see also Frost, 1985) and CH_4 via reaction of this hydrogen with CO_2. The presence of short-chain alkanes in the gases has been attributed to Fischer-Tropsch-type synthesis, which involves the transformation of CO-H_2 or CO_2-H_2 mixtures into hydrocarbons and H_2O in the presence of a catalyst, generally considered to be represented by magnetite (Szatmari, 1986; Berndt et al., 1996; Charlou et al., 1998).

Mottl (1992) reported the occurrence of two types of high pH pore waters in serpentinite seamounts from the Mariana and Izu-Bonin fore-arcs. A CH_4-, ethane- and propane-enriched and Cl-depleted fluid (relative to seawater) was interpreted by him as having been derived from the dehydration of a subducted slab of oceanic crust, and a low-CH_4 fluid as having been derived from the interaction of seawater with harzburgite. The higher hydrocarbons were interpreted to have originated as a result of the thermal degradation of organic compounds contained in sediments entrained in the subduction zone.

Fluid inclusions in metamorphosed serpentinites provide clues on the composition of fluids causing recrystallization of serpentinites at elevated temperatures in subduction and obduction zones. Scambelluri et al. (1997) reported microthermometric and decrepitate analyses of high-salinity (39-50 wt. % eq. NaCl) fluid inclusions in secondary olivine, diopside and titanian clinohumite from subduction-related eclogite-facies metamorphosed serpentinites of the Erro-Tobio peridotite, western Italian Alps. Their analyses indicated that the main elements dissolved in the fluid involved in metamorphism were Mg, Fe and Cl. According to them, this fluid originated from the metamorphic dehydration of the serpentinites. The Cl-rich nature of the fluid was attributed to the presence of this element in the original serpentinites, having been adsorbed on the surface of the serpentine minerals during a preceding, low temperature oceanic serpentinization event. Moderately saline (~ 12 wt. % eq. NaCl) and H_2-rich fluid inclusions were described by Peretti et al. (1992) in diopside from the Malenco peridotite, Italy. These fluids were interpreted as having been derived from the de-serpentinization of the peridotite during an episode of prograde metamorphism that resulted from nappe emplacement.

Previous work on rodingitization

When the formation of a specific serpentinite paragenesis has been correlated temporally with a rodingitization event, rodingites have been used as indicators of the conditions under which serpentinization, or de-serpentinization, occurred (Frost, 1975; Schandl et al., 1990; O'Hanley et al., 1992). Rodingites contain a larger diversity of mineral assemblages than serpentinites, and this diversity allows for a larger number of potential geothermometers to be used. The minerals most commonly reported from rodingites include garnet-group minerals (generally grossular-rich), clinopyroxenes (diopside-rich), epidote-group minerals (epidote, zoisite, and clinozoisite), vesuvianite, prehnite, tremolite-actinolite, and chlorites, and less commonly wollastonite, Ca-rich zeolites, pumpellyite, pectolite, xonotlite, and margarite. Other minerals found very rarely

and exclusively in rodingites include vuagnatite, $CaAlSi_4(OH)$ (Sarp et al., 1976), chantalite, $CaAl_2SiO_4(OH)_4$ (Sarp et al., 1977), and partheite, $CaAl_2Si_2O_8 \cdot 2H_2O$ (Sarp et al., 1979).

Most studies of rodingites have been concerned with mineralogical, petrographic and chemical description. Very few have attempted to quantify the mass exchange of chemical components and the mobility of trace elements resulting from rodingitization (Bøe, 1985; Schandl et al., 1989; Dubinska, 1997), and determine the nature of the rodingitizing fluids at elevated temperatures and pressures (Schandl et al., 1989; Schandl et al., 1990; Mittwede and Schandl, 1992; O'Hanley et al., 1992; Compagnoni et al., 1998). Using the method of Gresens (1967) to calculate gains and losses of components, Schandl et al. (1989) showed that volume remained constant during rodingitization of a lamprophyre dyke, whereas Bøe's (1985) calculations revealed that TiO_2 and P_2O_5 were removed as a result of the rodingitization of amphibolite dykes. The limited amount of fluid inclusion data published from studies of rodingites (Schandl et al., 1989; Schandl et al., 1990; Mittwede and Schandl, 1992; O'Hanley et al., 1992; Compagnoni et al., 1998) indicates that rodingitizing fluids are brines with salinities varying between 0 to 12.8 wt. % equivalent NaCl, and that rodingitization takes place at temperatures of 270 to > 350°C and pressures of < 2.5 kilobars. Initial melting temperatures of the ice at > -26.4°C indicated that the predominant salt dissolved in the fluid inclusions is NaCl. Schandl et al. (1990) and Compagnoni et al. (1998) identified CH_4, C_2H_6, C_3H_6, and C_3H_8 in fluid inclusions from rodingites using gas chromatographic analysis, and noted that CO_2 was not detected. However, these authors did not provide an explanation for the presence of these hydrocarbons.

O/H stable isotope studies of minerals in rodingite provided useful information about the temperatures and the origin of the fluids involved in rodingitization. In a study of rodingite minerals from localities worldwide, Wenner (1979) showed that pectolite and xonotlite form at low, near-surface temperatures, and suggested that the fluid responsible for the formation of these minerals is meteoric water. He attributed a non-meteoric origin to the fluid responsible for the formation of vesuvianite-, prehnite- or garnet-rich rodingites. In a study of nephrites from the Fengtien deposit, Taiwan, Yui et al. (1988)

suggested that antigorite, nephrite and rodingite formed contemporaneously within a restricted range of temperatures during ophiolite obduction. The fluids involved in the alteration were seawater-dominated at 420°C and meteoric water-dominated at about 320°C. Agrinier et al. (1995) calculated temperatures of 170-280°C for the formation of prehnite in rodingitized gabbro from the Hess Deep near the Galapagos triple junction.

Experimental hydrothermal studies

Few experimental studies have been conducted to investigate the process of rodingitization. Barnes et al. (1972) and Yale (1983: see also Potter et al., 1985, and Ponader, 1989) performed flow-through experimental studies to evaluate the rodingitization potential of serpentinizing, Ca-OH-type fluids. Barnes et al. (1972) circulated a 100 mg/L Ca^{2+} solution through albite at a temperature of 280°C and pressures between 276 and 414 bars. Equilibrium was not achieved during the experiment. The metastable mineral assemblage that formed by reaction of the fluid with albite contained foshagite and xonotlite (stable below 200°C: Gustafson, 1974). Yale (1983) and Potter et al. (1985) tentatively identified faujasite and pectolite as the secondary minerals formed by interaction of a 0.005 *m* $Ca(OH)_2$ solution with gabbro at a temperature of 300°C and a pressure of 200 bars. The secondary minerals reported in these studies are atypical of most naturally occurring rodingites.

Plyusnina et al. (1993) reported results of flow-through as well as static-fluid experiments involving the reaction of water and 0.1 M $CaCl_2$ solutions with on-line dunite→gabbro→dunite and serpentinite→gabbro→serpentinite reactants at temperatures of 400, 500, 550 and 600°C and a pressure of 1 kbar. Vesuvianite, grossular, diopside, and epidote formed at 500°C with dunite→gabbro→dunite as reactants, whether water or 0.1 M $CaCl_2$ solutions were used, whereas typical rodingite minerals did not form when serpentinite→gabbro→serpentinite were the reactants.

Origin of the calcium

The aspect that has been the most extensively debated about the origin of rodingites concerns the source of the calcium responsible for metasomatism. It has been

proposed that the calcium was derived from the precursor of the rodingites (Grange, 1927; de Waal, 1969; Capedri et al., 1978; Hall and Ahmed, 1984), from the serpentinization of the ultramafic rocks hosting the rodingites (Bilgrami and Howie, 1960; Coleman, 1963, 1967; Barnes and O'Neil, 1969; Sarp and Deferne, 1978), or from a source distant from the serpentinized peridotites and their enclosed rodingites (Bloxam, 1954; Barriga and Fyfe, 1983; Hall and Ahmed, 1984; Bøe, 1985). The most popular hypothesis invoked in recent years for the origin of the calcium, however, has been its derivation, principally or wholly, from the serpentinization of pyroxenes contained in the ultramafic rocks (Laurent, 1980; Wares and Martin, 1980a; Katoh and Niida, 1983; Muraoka, 1985; Sivell and Waterhouse, 1986; Kobayashi and Shoji, 1988; O'Hanley et al., 1992). The latter hypothesis rests on the widespread observation, reported by virtually all investigators, that rodingites are almost invariably associated with peridotites that were at least partially serpentinized, never with fresh peridotites (a notable exception is reported by Capedri et al., 1978, from the Pindos ophiolite). Based on this, geologists have deduced that serpentinization is a prerequisite to rodingitization. According to Coleman (1967, 1977), the average peridotite and dunite contain 3.5 and 0.75 wt. % CaO, whereas serpentinites average 0.08 wt. % CaO. According to Coleman (1967) and Sarp and Deferne (1978), such calcium losses are more than sufficient for the serpentinites to represent the source of the calcium needed to form rodingites, given that the size of the latter are quite small relative to that of the serpentinized peridotite hosts. Barnes and O'Neil (1969) reported the presence of SiO_2-poor and strongly alkaline Ca-OH-type, evolved meteoric waters from present-day serpentinizing pyroxene-bearing peridotites, and suggested that fluids of this type can induce rodingitization, thereby supporting the hypothesis that peridotite is the source of the calcium. However, as indicated above, fluid inclusion studies have shown that fluids responsible for rodingitization at elevated temperatures are NaCl-rich, and, therefore, are not the Ca-OH-type waters observed in near-surface environments.

Rodingites from Québec Appalachian ophiolites

Rodingites in the Appalachians occur everywhere alpine-type serpentinites occur. They represent the replacement products of gabbro (Hébert, 1980), diorite and leucomonzodiorite (De, 1961, 1972; Hébert, 1980, Laurent, 1980), slate (De, 1968), granite (De, 1961, 1972; Wares and Martin, 1980a, b; Taner and Laurent, 1984; Laurent et al., 1984; P. A. Cousineau, personal communication, 1996), serpentinite (Wares and Martin, 1980a, b), anorthosite (Laird et al., 1993), and amphibolite (Whitehead et al. (1995).

Laurent and Hébert (1979) correlated the rodingitization of the diorites and monzonites spatially and temporally with two serpentinization events. They attributed the formation of lizardite serpentinites to low temperature alteration in the oceanic environment, and the formation of chrysotile and antigorite to a higher temperature episode of ophiolite transport. The diorites were believed to have formed contemporaneously with the ophiolites through which they intruded, and before serpentinization. The monzonites were interpreted to have intruded later, in serpentinized peridotites. Pseudomorphic replacement of primary minerals by clinozoisite, diopside and hydrogrossular during rodingitization of diorites was correlated with the first episode of rodingitization, whereas calc-silicate vein occurrences were correlated with the second episode of serpentinization. Later, Laurent et al. (1984) revised their interpretation of the origin of the later monzonites, and suggested that they were tectonic inclusions instead of intrusions. However, recent U/Pb geochronological work on zircon from these intrusive rocks has confirmed that they intruded the ultramafic rocks (Whitehead et al., 2000).

Calc-silicate layers in serpentinized ultramafic rocks from the Thetford Mines ophiolite, believed to represent rodingitized anorthosite, were studied by Laird et al. (1993), who suggested from geothermobarometric calculations that they formed at temperatures of 300 to 400°C and pressures between 3 and 5 kilobars. However, they did not provide an interpretation of the timing of alteration and the process by which it occurred.

Rodingites in the Asbestos ophiolite

The felsic intrusive rocks and their rodingitized equivalents in the JM Asbestos mine have been studied by Olsen (1961), De (1961, 1972) and Wares and Martin (1980a, 1980b). Olsen (1961) suggested that the more mafic, biotite-rich rocks in the mine were metasomatized gabbros (implying they are epidiorites), whereas De (1961, 1972) suggested they represent diorites. According to De (1961, 1972), the rodingitized dioritic and granitic rocks originated from magmatic fluids, whereas Wares and Martin (1980a, 1980b) interpreted the rodingitization as being linked to serpentinization. De (1968) also very briefly described in a one page summary the occurrence of rodingitized slates at the base of the Asbestos ophiolite, and suggested that they formed by metamorphic differentiation during contact metamorphism.

Objectives

Understanding the metasomatic processes by which rodingites form is the principal objective of this thesis. Because serpentinizing fluids are believed to play an important role in the formation of rodingites, hydrothermal experiments were conducted in order to gain further understanding of the process of serpentinization and of the parameters that control the concentration of calcium in fluids that circulate in serpentinites or in peridotites undergoing serpentinization. In one experiment, serpentinization was simulated with a flow-through hydrothermal apparatus by circulating water through olivine (Fo_{91}) at a temperature of 300°C and a pressure of 300 bars to clarify some critical aspects of the problems pertaining to the relative stability of lizardite and chrysotile. Transmission electron microscopy (TEM), scanning electron microscopy (SEM) and electron microprobe analyses (EMPA) were used to describe the solids, and flame atomic absorption spectroscopy (FAAS) was used for analyses of the fluids. Two flow-through experiments were also conducted to gain insights into the behaviour of calcium during serpentinization. These experiments involved circulating water through lherzolite and a 0.1 M $CaCl_2$ solution through olivine at a temperature of 300°C and a

pressure of 300 bars. SEM and EMPA were used to describe the solids and FAAS was used for analyses of the fluids.

Natural occurrences of rodingites were also studied to improve our understanding of the rodingitization process. Rodingites are abundant in the JM Asbestos mine and were formed by the replacement of diverse rock types, i.e., slate, granite, diorite, and serpentinite, which makes them particularly interesting for study. A large body of literature exists on a variety of subjects related to rodingites. However, surprisingly few detailed studies have been published on rodingites from the Québec Appalachians, and these have focused mainly on their mineralogy (Grice and Williams, 1979; Chamberlain, 1980; Taner and Laurent, 1984; Grice and Robinson, 1984). Very few detailed electron microprobe and bulk rock major- and trace-element geochemical analyses are available in the literature on the serpentinites, the slates, the intrusive rocks, or the altered equivalents of these rocks, and fluid inclusion studies of the rodingites are non-existent. Moreover, recently published U/Pb zircon crystallization ages for the felsic dykes intruded in the serpentinized peridotites of the Asbestos and other Appalachian ophiolites called for a revision of ideas concerning, in particular, the timing of intrusion of the dioritic dykes. There was therefore an opportunity to greatly improve our understanding of the evolution of the Asbestos ophiolite and of the process of rodingitization in general.

Accordingly, I set out to establish the origin and timing of intrusion of the felsic rocks in the serpentinites of the Asbestos ophiolite. This was essential in order to place the rodingitization events within the context of the formation, serpentinization and emplacement history of the Asbestos ophiolite onto the Laurentian continental margin during the Taconic orogeny. Detailed mineralogical, geochemical and fluid inclusion studies of the various types of rodingites were conducted to understand the physico-chemical controls of rodingitization and the nature of the fluids involved in this unique type of alteration. Optical microscopy, SEM and EMPA were used for the mineralogical investigations of slates, felsic intrusive rocks, serpentinites, and the altered equivalents of these lithologies. X-ray fluorescence spectroscopy was used for most of the bulk rock and some of the individual mineral geochemical analyses of the major and trace elements. A LECO induction furnace was used to determine the C and S concentrations in slate

samples, and ammonium metavanadate titration was used to determine the FeO content of two samples of garnet. The fluid inclusions were studied using optical microscopy, microthermometry and gas chromatographic analysis.

Organization of the thesis

The body of the thesis comprises seven chapters that are subdivided into two parts. The first part comprises studies of the hydrothermal alteration of ultramafic rocks through hydrothermal experiments (Chapters II and III). The second part reports the results of field and laboratory investigations of altered ultramafic and felsic rocks from the JM Asbestos chrysotile mine, located in Asbestos, Québec (Chapters IV to VIII). The chapters were written in the form of articles, which are ready for submission to scientific journals.

In Chapter II, I report experimental results that help clarify some critical aspects of the problem pertaining to the relative stability of lizardite and chrysotile. This chapter was submitted to "The American Mineralogist" and has been accepted for publication. In Chapter III, experimental results are presented that improve our understanding of the behaviour of Ca-rich fluids during serpentinization of peridotites. In Chapter IV, the origin and timing of intrusion of the felsic rocks in the serpentinites of the Asbestos ophiolite are discussed. The chemical controls of rodingitization of slate, diorite, granite, and serpentinite from the JM Asbestos mine, and the composition of the fluids are discussed in Chapters V, VI and VII. The results of an extensive study aimed at determining the distribution and controls on the formation of amphiboles in the JM Asbestos mine are presented in Chapter VIII. This chapter was submitted to "The Canadian Mineralogist" and has been accepted for publication. The conclusions of this study and suggestions for further study are presented in Chapter IX.

Contribution of co-authors

The author of this thesis was responsible for the development of all the scientific ideas and hypotheses advanced throughout the thesis. He designed and performed all of the hydrothermal experiments and analyzed a portion of the experimental fluids. Other analyses of the fluids were performed by personnel of the Geochemical Laboratories at McGill University. All SEM analyses and photographs are those of the candidate. He performed a large portion of the EMPA and collected part of the microthermometric fluid inclusion data. Data collected by people who are not co-authors in the papers were acquired under the guidance of the candidate. Their contributions are acknowledged near the end of the appropriate chapters.

The supervisor, Dr. Anthony E. Williams-Jones, is a co-author of all the papers included in this thesis. His contribution to the manuscripts consisted in helping with the interpretations of data and perfecting hypotheses, and in partial writing and editing of text, except for Chapter VIII, where he is first author. The contribution(s) of additional authors, in Chapters II and VIII were as follows:

Chapter II: Dr. H. Vali performed the transmission electron microscopic work and X-ray diffraction analyses of the run products, provided the transmission electron microscope photographs, and made critical comments on the manuscript. Dr. R. F. Martin performed the X-ray diffraction analysis of olivine and provided critical comments.

Chapter VIII: This chapter involved a multi-disciplinary group of researchers who contributed mineralogical, geochemical and occupational-epidemiological results to a study of the nature and distribution of amphibole-group minerals in the JM Asbestos mine. J. Clark performed electron microprobe analyses and contributed critical reviews. H. Vali performed X-ray diffraction analyses and dissolution experiments. R. F. Martin contributed

to editing. A. Dufresne provided the health-related material (references and data) and critical reviews.

References

Abrajano, T. A., Sturchio, N. C., Bohlke, J. K., Lyon, G. L., Poreda, R. J. and C. M. Stevens, 1988, Methane-hydrogen gas seeps, Zambales ophiolite, Philippines: Deep or shallow origin? Chemical Geology, v. 71, p. 211-222.

Abrajano, T. A., Sturchio, N. C., Kennedy, B. M., Lyon, G. L., Muehlenbachs, K. and J. K. Bohlke, 1990, Geochemistry of reduced gas related to serpentinization of the Zambales ophiolite, Philippines, Applied Geochemistry, v. 5, p. 625-630.

Agricola, G., 1556, De Re Metallica, Hoover, H. C. and C. H. Hoover, English translation, 1950, Dover Publications, New York, 630 p.

Agrinier, P., Hékinian, R., Bideau, D. and M. Javoy, 1995, O and H stable isotope compositions of oceanic crust and upper mantle rocks exposed in the Hess Deep near the Galapagos Triple Junction, Earth and Planetary Science Letters, v. 136, p. 183-196.

Anhaeusser, C. R., 1976, The nature of chrysotile asbestos occurrences in southern Africa: a review, Economic Geology, v. 71, p. 96-116.

Anhaeusser, C. R., 1979, Rodingite occurrences in some Archaean ultramafic complexes in the Barberton Mountain Land, South Africa, Precambrian Research, 8, p. 49-76.

Aumento, F. and H. Loubat, 1971, The Mid-Atlantic Ridge near 45° N. XVI. Serpentinized ultramafic intrusions, Canadian Journal of Earth Sciences, v. 8, p. 631-663.

Baker, G., 1958, Rodingite in nickeliferous serpentinite, near Beaconsfield, Northern Tasmania, Journal of the Geological Society of Australia, v. 6, p. 21-35.

Barnes, I. and J. R. O'Neil, 1969, The relationship between fluids in some fresh Alpine-type ultramafics and possible modern serpentinization, western United States, Geological Society of America Bulletin, v. 80, p. 1947-1960.

Barnes, I., LaMarche, V. C., Jr., and G. Himmelberg, 1967, Geochemical evidence of present-day serpentinization, Science, v. 156, p. 830-832.

Barnes, I., O'Neil, J. R. and J. J. Trescases, 1978, Present day serpentinization in New Caledonia, Oman and Yugoslavia, Geochimica et Cosmochimica Acta, v. 42, p. 144-145.

Barnes, I., Rapp, J. B., O'Neil, J. R., Sheppard, R. A. and A. J. Gude, III, 1972, Metamorphic assemblages and the direction of flow of metamorphic fluids in four instances of serpentinization, Contributions to Mineralogy and Petrology, v. 35, p. 263-276.

Barriga, F. and W. S. Fyfe, 1983, Development of rodingite in basaltic rocks in serpentinites, East Liguria, Italy, Contributions to Mineralogy and Petrology, v. 84, p. 146-151.

Bell, J. M., Clarke, E. de C. and P. Marshall, 1911, The geology of the Dun Mountain subdivision, Nelson, New Zealand Geological Survey, Bulletin 12, new series, 71 p.

Benson, W. N., 1926, The tectonic conditions accompanying the intrusion of basic and ultrabasic igneous rocks, Memoirs of the National Academy of Sciences, Washington, D.C., v. 19, p. 1-9.

Berman, R. G., Engi, M., Greenwood, H. J. and T. H. Brown, 1986, Derivation of internally-consistent thermodynamic data by the technique of mathematical programming: a review with application to the system MgO-SiO_2-H_2O, Journal of Petrology, v. 27, p. 1331-1364.

Berndt, M. E., Allen, D. E. and W. E. Seyfried, Jr., 1996, Reduction of CO_2 during serpentinization of olivine at 300° C and 500 bar, Geology, v. 24, p. 351-354.

Bideau, D., Hébert, R., Hekinian, R. and M. Cannat, 1991, Metamorphism of deep-seated rocks from the Garrett ultrafast transform (East Pacific Rise near 13°25'S), Journal of Geophysical Research, v. 96, p. 10,079-10,099.

Bilgrami, S. A. and R. A. Howie, 1960, The mineralogy and petrology of a rodingite dyke, Hindubagh, Pakistan, American Mineralogist, v. 45, p. 791-801.

Bloxam, T. W., 1954, Rodingite from the Girvan-Ballantrae complex, Ayrshire, Mineralogical Magazine, v. 30, p. 525-528.

Bøe, R., 1985, Rodingite from Lindås, western Norway, Norsk Geologisk Tidsskrift, v. 65, p. 301-320.

Capedri, S., Garuti, G. and A. Rossi, 1978, Rodingites from Pindos. Constraints on the "rodingite problem", Neues Jahrbuch für Mineralogie Abhandlungen, v. 133, p. 242-263.

Caruso, L. J. and J. V. Chernosky, Jr., 1979, The stability of lizardite, Canadian Mineralogist, v. 17, p. 757-769.

Chamberlain, S. C., 1980, Wollastonite, vesuvianite, native copper and diopside from the Jeffrey mine in Asbestos, Quebec, Canada, Rocks and Minerals, p. 188-191.

Charlou, J. L., Fouquet, Y., Bougault, H., Donval, J. P., Etoubleau, J., Jean-Baptiste, P., Dapoigny, A., Appriou, P. and P. A. Rona, 1998, Intense CH_4 plumes generated by serpentinization of ultramafic rocks at the intersection of the 15°20'N fracture zone and the Mid-Atlantic Ridge, Geochimica et Cosmochimica Acta, v. 62, p. 2323-2333.

Chernosky, J. V., Jr., 1975, Aggregate refractive indices and unit cell parameters of synthetic serpentine in the system MgO-Al_2O_3-SiO_2-H_2O, American Mineralogist, v. 60, p. 200-208.

Coleman, R. G., 1963, Serpentinites, rodingites and tectonic inclusions in Alpine-type mountain chains, Geological Society of America Special Paper 73.

Coleman, R. G., 1966, New Zealand serpentinites and associated metasomatic rocks, New Zealand Geological Survey, Bulletin No. 76, 102 p.

Coleman, R. G., 1967, Low-temperature reaction zones and alpine ultramafic rocks of California, Oregon and Washington, United States Geological Survey, Bulletin No. 1247, 49 p.

Coleman, R. G., 1977, Ophiolites: ancient oceanic lithosphere? Springer-Verlag, New York.

Compagnoni, A., Conte, R., Facchinelli, A., Orione, P., Rossetti, P. and C. Trossarelli, 1998, The rodingite of Bellecombe (Val D'Aosta, Italy): A petrographic and fluid inclusion study, 17th general meeting, International Mineralogical Association, August 9-14, Toronto, Canada, Program and Abstracts, p. A77L.

Day, H. W., Chernosky, J. V. and H. J. Kumin, 1985, Equilibria in the system MgO-SiO_2-H_2O: a thermodynamic analysis, American Mineralogist, v. 70, p. 237-248.

De, A., 1961, Petrology of dikes emplaced in the ultramafic rocks of southeastern Quebec, Ph. D. dissertation, Princeton University, Princeton, 201 p.

De, A., 1968, Post-ultramafic dykes and associated rocks in the asbestos mining areas in the Eastern Townships, Quebec, Geological Survey of Canada, Report of Activities, Paper 68-1, Part A, p. 71.

De, A., 1972, Petrology of dikes emplaced in the ultramafic rocks of southeastern Quebec and origin of the rodingite, Geological Society of America, Memoir 132, p. 489-501.

de Waal, S. A., 1969, On the origin of hydrogrossularite and other calcium silicates in serpentinites, Transactions of the Geological Society of South Africa, v. 72, p. 23-27.

Devirts, A. L., Gagauz, F. G., Grinenko, V. A., Lagutina, Y. P., Pereversov, V. V. and Y. A. Shukolyukov, 1993, Origin of hydrogen in Kempirsay-intrusion ultramafites, Geochemistry International, v. 30, p. 139-144.

Dubinska, E., 1997, Rodingites and amphibolites from the serpentinites surrounding Sowie Góry block (Lower Silesia, Poland): record of supra-subduction zone magmatism and serpentinization, Neues Jahrbuch für Mineralogie Abhandlungen, v. 171, p. 239-279.

Evans, B. W. and V. Trommsdorff, 1970, Regional metamorphism of ultramafic rocks in the Central Alps: Parageneses in the system CaO-MgO-SiO_2-H_2O, Schweizerische Mineralogische und Petrographische Mitteilungen, v. 50, p. 481-492.

Evans, B. W., Johannes, W., Oterdoom, H. and V. Trommsdorff, 1976, Stability of chrysotile and antigorite in the serpentinite multisystem, Schweizerische Mineralogische und Petrographische Mitteilungen, v. 56, p. 79-93.

Finlayson, A. M., 1909, The nephrite and magnesian rocks of the South Island of New Zealand, Quarterly Journal of the Geological Society of London, v. 65, p. 351-381.

Fritz, P., Clark, I. D., Fontes, J.-C., Whiticar, M. J. and E. Faber, 1992, Deuterium and ^{13}C evidence for low temperature production of hydrogen and methane in a highly alkaline groundwater environment in Oman, *in* Water-rock Interaction, Kharaka and Maest, editors, Balkema, Rotterdam, p. 793-796.

Frost, B. R., 1975, Contact metamorphism of serpentinite, chloritic blackwall and rodingite at Paddy-Go-Easy Pass, Central Cascades, Washington, Journal of Petrology, v. 16, p. 272-313.

Frost, B. R., 1985, On the stability of sulfides, oxides, and native metals in serpentinites, Journal of Petrology, v. 26, p. 31-63.

Fryer, P. and M. J. Mottl, 1992, Lithology, mineralogy, and origin of serpentine muds recovered from Conical and Torishima forearc seamounts: results of Leg 125 drilling, Proceedings of the Ocean Drilling Program, Scientific Results, v. 125, p. 343-362.

Graham, R. P. D., 1917, Origin of massive serpentine and chrysotile-asbestos, Black Lake-Thetford area, Quebec, Economic Geology, v. 12, p. 159-202.

Grange, L. I., 1927, On the "rodingite" of Nelson, Transactions of the New Zealand Institute, v. 58, p. 160-166.

Grauby, O., Baronnet, A. and B. Devouard, 1998, Chrysotile - to - polygonal serpentines - to - lizardite reaction produced from a MgO-SiO_2-H_2O (MSH) gel, 17th General Meeting of the International Mineralogical Association, August 9-14, Toronto, Canada, Abstracts and Program, p. A81.

Gresens, R. L., 1967, Composition-volume relationships of metasomatism, Chemical Geology, v. 2, p. 47-55.

Grice, J. D. and R. Williams, 1979, The Jeffrey mine, Asbestos, Québec, Mineralogical Record, March-April, p. 69-80.

Grice, J. D. and G. W. Robinson, 1984, Jeffreyite, $(Ca,Na)_2(Be,Al)Si_2(O,OH)_7$, a new mineral species and its relation to the melilite group, Canadian Mineralogist, v. 22, p. 443-446.

Gustafson, W. I., 1974, The stability of andradite, hedenbergite, and related minerals in the system Ca-Fe-Si-O-H, Journal of Petrology, v. 15, p. 455-496.

Hajash, A. and G. W. Chandler, 1981, An experimental investigation of high-temperature interactions between seawater and rhyolite, andesite, basalt and peridotite, Contributions to Mineralogy and Petrology, v. 78, p. 240-254.

Hall, A. and Z. Ahmed, 1984, Rare earth content and origin of rodingites, Chemie der Erde, v. 43, p. 45-56.

Hébert, R., 1980, Etude pétrologique des roches ophiolitiques d'Asbestos et du Mont Ham (Ham Sud), M. Sc. Thesis, Université Laval, Québec, 182 p.

Honnorez, J. and P. Kirst, 1975, Petrology of rodingites from the equatorial Mid-Atlantic fracture zones and their geotectonic significance, Contributions to Mineralogy and Petrology, v. 49, p. 233-257.

Janecky, D. R. and W. E. Seyfried, Jr., 1986, Hydrothermal serpentinization of peridotite within the oceanic crust: experimental investigations of mineralogy and major element chemistry, Geochimica et Cosmochimica Acta, v. 50, p. 1357-1378.

Johannes, W., 1968, An experimental investigation of the system $MgO-SiO_2-H_2O-CO_2$, American Journal of Science, v. 267, p. 1083-1104.

Katoh, T. and K. Niida, 1983, Rodingites from the Kamuikotan tectonic belt, Hokkaido, Journal of the Faculty of Science, Hokkaido University, Serie IV, v. 20, p. 151-169.

Kholodkevich, I. V. and N. N. Barinov, 1995, Some features of harzburgite-seawater interaction at increased P-T conditions, *in* Water-Rock Interaction, Kharaka, Y. K. and O. V. Chudaev, editors, Proceedings of the 8th international symposium on water-rock interaction – WRI-8, Vladivostok, Russia, 15-19 August 1995, A. A. Balkema, Rotterdam, p. 801-804.

Kobayashi, S. and T. Shoji, 1988, Metasomatic process in the formation of rodingite in Boso Peninsula, Chiba, Japan, Journal of the Japanese Association of Mineralogy, Petrology and Economic Geology, v. 83, p. 514-526.

Laird, J., Trzcienski, W. E., Jr. and W. A. Bothner, 1993, High-pressure, Taconian, and subsequent polymetamorphism of southern Quebec and northern Vermont, Geological Society of America Field Trip Guidebook for the Northeastern United States, v. 2, Department of Geology and Geography, University of Massachusetts, Contribution 67, p. O 1- O 32.

Laurent, R., 1975, Petrology of the alpine-type serpentinites of Asbestos and Thetford Mines, Quebec, Schweizerische Mineralogische und Petrographische Mitteilungen, v. 55, p. 431-455.

Laurent, R., 1980, Regimes of serpentinization and rodingitization in Quebec Appalachian ophiolites, Archives des Sciences de la Société de Physique et d'Histoire Naturelle de Genève, v. 33, p. 311-320.

Laurent, R. and Y. Hébert, 1979, Paragenesis of serpentine assemblages in harzburgite tectonite and dunite cumulate from the Quebec Appalachians, Canadian Mineralogist, v. 17, p. 857-869.

Laurent, R., Taner, M. V. and J. Bertrand, 1984, Mise en place et pétrologie du granite associé au complexe ophiolitique de Thetford Mines, Québec, Canadian Journal of Earth Sciences, v. 21, p. 1114-1125.

Menzies, M. A., Long, A., Ingram, G., Tatnell, M. and D. Janecky, 1993, MORB peridotite-sea water interaction: experimental constraints on the behaviour of trace elements, $^{87}Sr/^{86}Sr$ and $^{143}Nd/^{144}Nd$ ratios, *in* Magmatic Processes and Plate Tectonics, Prichard, H. M., Alabaster, T., Harris, N. B. W. and C. R. Neary, editors, Geological Society Special Publication No. 76, p. 309-332.

Mével, C. and C. Stamoudi, 1996, Hydrothermal alteration of the upper-mantle section at Hess Deep, Proceedings of the Ocean Drilling Program, Scientific Results, v. 147, p.p. 293-309.

Mittwede, S. K. and E. S. Schandl, 1992, Rodingites from the southern Appalachian Piedmont, South Carolina, USA, European Journal of Mineralogy, v. 4, p. 7-16.

Moody, J. B., 1976, An experimental study of the serpentinization of iron-bearing olivines, Canadian Mineralogist, v. 14, p. 462-478.

Mottl, M. J., 1992, Pore waters from serpentinite seamounts in the Mariana and Izu-Bonin forearcs, Leg 125: evidence for volatiles from the subducting slab, Proceedings of the Ocean Drilling Program, Scientific Results, v. 125, p. 373-385.

Muraoka, H., 1985, Serpentinization reaction responsible for rodingite formation of the Ashidashi ultramafic complex, southwest Japan, Journal of the Japanese Association of Mineralogy, Petrology and Economic Geology, v. 80, p. 413-428.

Neal, C. and G. Stanger, 1983, Hydrogen generation from mantle source rocks in Oman, Earth and Planetary Science Letters, v. 66, p. 315-320.

O'Brien, J. P. and K. A. Rodgers, 1973, Xonotlite and rodingites from Wairere, New Zealand, Mineralogical Magazine, v. 39, p. 233-240.

O'Hanley, D. S., 1991, Fault-related phenomena associated with hydration and serpentine recrystallization during serpentinization, Canadian Mineralogist, v. 29, p. 21-35.

O'Hanley, D. S., Chernosky, J. V., Jr. and F. J. Wicks, 1989, The stability of lizardite and chrysotile, Canadian Mineralogist, v. 27, p. 483-493.

O'Hanley, D. S. and F. J. Wicks, 1995, Conditions of formation of lizardite, chrysotile and antigorite, Cassiar, British Columbia, Canadian Mineralogist, v. 33, p. 753-773.

O'Hanley, D. S. and M. D. Dyar, 1998, The composition of chrysotile and its relationship with lizardite, Canadian Mineralogist, v. 36, p. 727-739.

O'Hanley, D. S., Schandl, E. S. and F. J. Wicks, 1992, The origin of rodingites from Cassiar, British Columbia, and their use to estimate T and $P(H_2O)$ during serpentinization, Geochimica et Cosmochimica Acta, v. 56, p. 97-108.

Olsen, E. J., 1961, High temperature acid rocks associated with serpentinite in eastern Quebec, American Journal of Science, v. 259, p. 329-347.

Peacock, S. M., 1987, Serpentinization and infiltration metasomatism in the Trinity peridotite, Klamath province, northern California: implications for subduction zones, Contributions to Mineralogy and Petrology, v.95, p. 55-70.

Peacock, S. M., 1993, Large-scale hydration of the lithosphere above subducting slabs, Chemical Geology, v. 108, p. 49-59.

Peretti, A., Dubessy, J., Mullis, J., Frost, B. R. and V. Trommsdorff, 1992, Highly reducing conditions during Alpine metamorphism of the Malenco peridotite (Sondrio, northern Italy) indicated by mineral paragenesis and H_2 in fluid inclusions, Contributions to Mineralogy and Petrology, v. 112, p. 329-340.

Plyusnina, L. P., Likhoidov, G. G. and G. P. Zaraisky, 1993, Physicochemical conditions of rodingite formation: experimental data, Petrology, v. 1, p. 492-502.

Ponader, H. B., 1989, Experimental hydrothermal dissolution of forsterite, enstatite, diopside, and labradorite, Ph. D. Thesis, Stanford University, California, 184 p.

Potter, J. M., Pohl, D. C., Guillemette, R. N., Ponader, H. B. and J. G. Liou, 1985, A system for flow through experimental studies at hydrothermal conditions, Neues Jahrbuch für Mineralogie Monatshefte, v. 7, p. 329-335.

Sakai, R., Kusakabe, M., Noto, M. and T. Ishii, 1990, Origin of waters responsible for serpentinization of the Izu-Ogasawara-Mariana forearc seamounts in view of hydrogen and oxygen isotope ratios, Earth and Planetary Science Letters, v. 100, p. 291-303.

Sarp, H. and J. Deferne, 1978, Le bilan chimique de la rodingitization et l'origine de l'excès de chaux dans les rodingites, Schweizerische Mineralogische und Petrographische Mitteilungen, v. 58, p. 315-328.

Sarp, H., Bertrand, J. and E. Mc Near, 1976, Vuagnatite, $CaAl(OH)SiO_4$, a new natural calcium aluminium nesosilicate, American Mineralogist, v. 61, p. 825-830.

Sarp, H., Deferne, J. and B. W. Liebich, 1977, La chantalite $CaAl_2SiO_4(OH)_4$, un nouveau silicate naturel d'aluminium et de calcium, Bulletin Suisse de Minéralogie et Pétrographie, v. 57, p. 149-156.

Sarp, H., Deferne, J., Bizouard, H. and B. W. Liebich, 1979, La parthéite, $CaAl_2Si_2O_8.2H_2O$, un nouveau silicate naturel d'aluminium et de calcium, Schweizerische Mineralogische und Petrographische Mitteilungen, v. 59, p. 5-13.

Scambelluri, M., Piccardo, G. B., Philippot, P., Robbiano, A. and L. Negretti, 1997, High salinity fluid inclusions formed from recycled seawater in deeply subducted alpine serpentinite, Earth and Planetary Science Letters, v. 148, p. 485-499.

Schandl, E. S., O'Hanley, D. S. and F. J. Wicks, 1989, Rodingites in serpentinized ultramafic rocks of the Abitibi greenstone belt, Ontario, Canadian Mineralogist, v. 27, p. 579-591.

Schandl, E. S., O'Hanley, D. S., Wicks, F. J. and T. K. Kyser, 1990, Fluid inclusions in rodingites: a geothermometer for serpentinization, Economic Geology, v. 85, p. 1273-1276.

Seyfried, W. E., Jr. and W. E. Dibble, Jr., 1980, Seawater-peridotite interaction at 300°C and 500 bars: implications for the origin of oceanic serpentinites, Geochimica et Cosmochimica Acta, v. 44, p. 309-321.

Sivell, W. J. and J. B. Waterhouse, 1986, The geochemistry, origin and tectonic significance of rodingites from the Dun Mountain ultramafics, D'Urville Island, New Zealand, New Zealand Journal of Geology and Geophysics, v. 29, p. 9-27.

Szatmari, P., 1986, Plate tectonic control of synthetic oil formation. Oil and Gas Journal, Sept. 1, 67-69.

Taner, M. F. and R. Laurent, 1984, Iron-rich amesite from the Lake Asbestos mine, Black Lake, Quebec, Canadian Mineralogist, v. 22, p. 437-442.

Thayer, T. P., 1966, Serpentinization considered as a constant volume metasomatic process, American Mineralogist, v. 51, p. 685-710.

Tilley, C. E., 1957, On the replacement of anorthosite by hydrogrossular in the Transvaal, Transactions of the Geological Society of South Africa, v. 60, p. 15-17.

Turner, F. J., 1933, The metamorphic and intrusive rocks of southern Westland, Transactions of the New Zealand Institute, v. 63, p. 269-276.

Ulmer, P. and V. Trommsdorff, 1995, Serpentine stability to mantle depths and subduction-related magmatism, Science, v. 268, p. 858-861.

Wares, R. P. and R. F. Martin, 1980a, Rodingitization of granite and serpentinite in the Jeffrey mine, Asbestos, Quebec, Canadian Mineralogist, v. 18, p. 231-240.

Wares, R. P. and R. F. Martin, 1980b, Rodingitization of dyke rocks and enclosing serpentinites in the Jeffrey mine, Quebec Appalachians, Archives des Sciences de la Société de Physique et d'Histoire Naturelle de Genève, v. 33, p. 301-310.

Wenner, D. B., 1979, Hydrogen, oxygen and carbon isotopic evidence for the origin of rodingites in serpentinized ultramafic rocks, Geochimica et Cosmochimica Acta, v. 43, p. 603-614.

Wenner, D. B. and H. P. Taylor, Jr., 1973, Oxygen and hydrogen isotopic studies of the serpentinization of ultramafic rocks in oceanic environments and continental ophiolite complexes, American Journal of Science, v. 273, p. 207-239.

Whitehead, J., Reynolds, P. H. and J. G. Spray, 1995, The sub-ophiolitic metamorphic rocks of the Québec Appalachians, Journal of Geodynamics, v. 19, p. 325-350.

Whitehead, J., Dunning, G. R. and J. G. Spray, 2000, U-Pb geochronology and origin of granitoid rocks in the Thetford Mines ophiolite, Canadian Appalachians, Geological Society of America Bulletin, v. 112, p. 915-928.

Wicks, F. J. and E. J. W. Whittaker, 1975, A reappraisal of the structures of the serpentine minerals, Canadian Mineralogist, v. 13, p. 227-243.

Yale, L. B., 1983, An investigation of serpentinization and rodingitization, M. Sc. Thesis, Stanford University, California, 113 p.

Yui, T.-F., Yeh, H.-W. and C. W. Lee, 1988, Stable isotope studies of nephrite deposits from Fengtien, Taiwan, Geochimica et Cosmochimica Acta, v. 52, p. 593-602.

PART I

EXPERIMENTAL INVESTIGATIONS OF SERPENTINIZATION AND APPLICATIONS TO RODINGITIZATION

§

PROLOGUE

Previous studies have established that serpentinization is a prerequisite to the rodingitization of mafic and felsic dykes, and country rocks in and at the contact with ultramafic rocks. In Chapter II, flow-through experimental and TEM data are presented that suggest that the type of serpentine-group mineral replacing olivine by reaction with water at a temperature of 300°C and a pressure of 300 bars is strongly dependent on the level of supersaturation of the fluid with respect to the aforementioned serpentine, and less so on the type of surface over which these serpentines grow. In Chapter III, data are presented from additional flow-through experiments, in which lherzolite was reacted with water and olivine was reacted with a 0.1 *M* $CaCl_2$ solution at a temperature of 300°C and a pressure of 300 bars. The data indicate that serpentinizing fluids reacting with olivine-rich and pyroxene-bearing peridotites quickly saturate with respect to diopside and that the concentration of Ca in Ca-rich brines is unchanged by reaction with olivine. Thermodynamic equilibrium modelling indicates that the Ca concentration in Ca-rich brines is not significantly increased by reaction with pyroxene-bearing peridotites.

INTRODUCTION TO CHAPTER II

This chapter represents the first of two directed at characterizing experimentally the effects of fluid/rock interaction on the changes in mineralogy and fluid composition that accompany the serpentinization of olivine and lherzolite by water and a 0.1 M $CaCl_2$ aqueous solution. Other aspects touched upon in these chapters involved the mobility of calcium in fluids that cause serpentinization and the factors responsible for rodingitization during the interaction of serpentinizing fluids with other rock types. The following chapter describes the factors that controlled the formation of different serpentine-group minerals in a flow-through experiment that involved reaction of water with olivine.

CHAPTER II

HYDROTHERMAL ALTERATION OF OLIVINE IN A FLOW-THROUGH AUTOCLAVE: NUCLEATION AND GROWTH OF SERPENTINE PHASES.

by

Charles Normand, Anthony E. Williams-Jones, Robert F. Martin and Hojatollah Vali

Department of Earth and Planetary Sciences, McGill University, 3450 University Street, Montreal (Qué), Canada, H3A 2A7.

Accepted for publication in The American Mineralogist.

ABSTRACT

A single-pass flow-through experiment was conducted to induce serpentinization, and to relate serpentine mineralogy to reaction progress during open-system alteration of San Carlos olivine by air-saturated water. The fluid flowed at 300°C and 300 bars for 1368 hours through crushed olivine contained in a tubular titanium reaction cell. Chemical analysis of the fluids indicated a steady-state composition with respect to Mg and pH after 550 hours, which was interpreted to reflect saturation with brucite and one or more serpentine-group mineral. These phases and magnetite were identified, and characterized by SEM and by high-resolution platinum/carbon replica techniques using TEM. After reaction, olivine fragments displayed clear signs of dissolution, and growth of neoformed phases. Brucite and magnetite are distributed uniformly through the reaction cell, although magnetite is more abundant. There is, however, a distinct banding in the distribution of the serpentine phases from the inlet to the outlet of the reaction cell. Lizardite is the predominant serpentine phase at the inlet, whereas fibrous serpentines are predominant near the outlet. Lizardite crystals are more numerous but smaller in the middle of the cell, and are topotactically aligned along a single preferential crystallographic orientation of the olivine. Cylindrical chrysotile formed only on the surface of lizardite or conical and polygonal serpentine. The morphology and sorting of the serpentine phases through the reaction cell suggest that the crystallization of lizardite was controlled by heterogeneous nucleation on olivine under supersaturated conditions, and crystallization of chrysotile by nucleation on lizardite at higher levels of supersaturation.

INTRODUCTION

Lizardite and chrysotile represent the two structural types of magnesium-rich serpentine-group minerals composed of uniformly superimposed TO sheets. The essential difference between the two minerals is that in lizardite the sheets are flat, whereas in chrysotile they are rolled. Although considerable research has been devoted to these minerals, we still do not know why in some cases lizardite crystallizes, in other cases the mineral formed is chrysotile, and in still other cases the two minerals co-precipitate. On the basis of experiments conducted in the system MgO-SiO_2-H_2O, in which lizardite and chrysotile formed at temperatures < 420°C and lizardite converted to chrysotile at higher temperature, Chernosky (1975) concluded that chrysotile is the stable serpentine at high temperature. O'Hanley and Wicks (1995) reached the same conclusion from field, paragenetic, stable isotope, and phase equilibrium relationships. However, these studies do not explain the wide temperature interval over which lizardite and chrysotile are known to co-crystallize.

The most likely explanation for co-precipitation of lizardite and chrysotile is that there are kinetic inhibitions to the nucleation and/or growth of one of the minerals. Indeed, this is suggested by recent synthesis experiments in which Grauby et al. (1998) found that the type of serpentine formed depended on the degree of supersaturation of the solution. The purpose of the present study is to investigate possible kinetic controls on serpentine crystallization using a flow-through autoclave. Such open-system flow-through experimental systems are well suited to the study of kinetic effects in water-rock interaction, as the steps towards equilibration are expressed by changes in mineralogy from the inlet to the outlet of the reaction column. These changes in mineralogy are related to reaction progress during the course of alteration. In the flow-through experiment discussed here, the mineralogical changes were expressed in the morphological characteristics of the neo-formed serpentine minerals, and by the formation of brucite and magnetite. High-resolution platinum/carbon replica techniques using TEM are employed to enhance resolution of the surface features of solid phases,

and to facilitate new understanding of the mechanisms of serpentine mineral nucleation and growth.

EXPERIMENTAL AND ANALYTICAL METHODS

Hydrothermal experiments

Apparatus

A single-pass, flow-through hydrothermal system was used to simulate serpentinization of olivine. The apparatus ("FT2-C" built by Coretest Systems, Inc) is designed specifically to study open-system water-rock interaction, and can operate at temperatures up to 500°C and pressures up to 500 bars (Williams-Jones et al., 1994). It consists of a pneumatic inlet pump, a double-piston metering pump, a reaction cell contained within a large volume externally heated pressure vessel, a flow controller, and a fluid sampling system. Fluid flow through the reaction cell is achieved by pumping the reaction fluid directly from the reservoir to the reaction cell. The reservoir fluid is contained in a Viton bladder, and is forced into the reaction cell by pumping fluid in the external part of the bladder separator. Fluid flow is maintained by the double-piston metering pump at a desired, fixed rate within the range 0.01 to 80 mL/hr. The rate is obtained by varying the speed of the pump according to the pressure in the system, which is measured by a transducer in a feedback loop with the metering pump. Fluid pressure is controlled by a diaphragm-type, back-pressure regulator connected to an external back-pressure reservoir, and the confining pressure by a compressed-air-driven diaphragm pump (Williams-Jones et al., 1994). The fluid is collected in a pre-weighed syringe, and selected portions are sampled for pH measurements and elemental analysis.

Starting materials

San Carlos olivine (Fo_{91}) was purchased from Ward's Scientific Inc. in the form of tumbled stones 5-6 mm in diameter. Only grains that showed a uniform, light green colour and were free of visible impurities under a binocular microscope were used in the

experiments. The selected grains were crushed in a Bico disk grinder, sieved, and the 250-500 μm size fraction retained for the experiments. The latter grains were cleaned six times in alcohol in an ultrasonic bath. A portion of the grains was retained to verify the purity of the sample, and the remainder stored for 12 months to allow relaxation of strain and healing of distorted sites produced during grinding (Eggleston et al., 1989). No phases other than olivine were detected by X-ray diffraction, examination by scanning electron microscopy (SEM) and electron microprobe analyses (EMPA). The average composition of the olivine, calculated from 20 electron microprobe analyses, is $Mg_{1.807}Fe_{0.184}Ni_{0.006}Ca_{0.002}Si_{0.998}O_4$ ($Fo_{90.4}$). A very similar composition ($Fo_{90.5}$) was determined from the regression equation of Schwab and Kastner (1977) ($X_{fa} = 7.522 - 14.9071\ [3.0199 - d_{130}]^{1/2}$) using the d_{130} value of 2.7717 Å collected from X-ray diffraction data. Before the start of the experiment, a N_2(30%)-He(70%) BET measurement was conducted on a portion of the stored grains and showed them to have a specific surface area of 0.034 m^2/g.

Experimental conditions

The flow-through experiment was conducted using air-CO_2-saturated deionized water. The sample (4.21 grams) was placed in a 10 cm long, titanium reaction cell (5 mm i.d.; capacity of 1.96 cm^3) and reacted with fluid for 1368 hours at a temperature of 300°C and a pressure of 300 bars. The flow rate was 12 mL/day and, at any given moment, the cell contained approximately 0.7 mL of fluid. A stoppage in the flow of fluid occurred after approximately 440 hours and lasted for about 19 hours, during which time the reservoir bladder had to be refilled.

Mountain (1992) studied the regime of fluid flow in reaction cells identical to those used in this study. By flowing a Li-spiked solution through granular quartz (size fraction 500-850 μm) at a rate of 1 mL/hr, he was able to show that the fluid flow was essentially laminar with limited mixing. The "residence time" for a given fluid aliquot in the reaction cell was thus only marginally greater than that for plug flow. A further advantage of this flow regime is that it promotes linear changes in fluid chemistry and

mineralogy through a predominance of dissolution near the inlet and precipitation near the outlet.

Analytical methods

Samples of fluid were collected at intervals of ~40 hours for pH measurement and flame atomic absorption (AA) analysis. The pH of 1 mL aliquots was measured using an ORION RESEARCH pH meter comprising a pH/millivoltmeter 811 and a KCl-filled electrode calibrated against 3 standards. Ten mL of fluid were acidified with 1 mL of 70 %, analytical grade HNO_3 for AA spectrophotometric analyses. Si, Mg, Fe, Ni, and Ca were analysed with a Perkin Elmer 3100 AA spectrometer. Mn was analysed with a Perkin Elmer Zeeman 5100 graphite furnace AA spectrometer.

Sample preparation for SEM and TEM investigations of the solid phases

Grains were selected for mineral identification of the secondary minerals, for examination of the surface features of the starting and reacted olivine, and those of the secondary minerals, and for investigation of the internal structure of the fibrous secondary minerals. Grain-mounts from the inlet, the center and the outlet of the reaction cell were coated with carbon for examination by scanning electron microscopy (SEM).

Unfortunately, the limit of resolution of the SEM does not permit detection of potentially important, fine-scale morphological features. The surface microtopography of fragments was therefore examined by TEM using high-resolution (1 nm) Pt/C replicas (Baronnet, 1972, 1973; Paquette et al., 1996). In the case of the reacted olivine, fragments were studied from three locations in the reaction cell (inlet, center, and outlet). For each location, ten to fifteen grains (200-300 μm) having different morphologies were selected with tweezers using a stereomicroscope. The replicas comprised a thin Pt/C-metal film, one to two nanometers thick, consisting of 95% platinum and 5% carbon, and a supporting carbon film 15-20 nm thick. Individual fragments were mounted on a flat substrate using double-stick tape with the surface of interest parallel to the substrate. The shadowing and replication of the specimens were performed in a freeze-etch unit (Balzer 300) at high vacuum (10^{-6} Torr) and room temperature. The replicas were cleaned by

dissolving the crystals adhering to them with 10% HF solution and rinsing with deionized water. They were then transferred onto a 200 mesh TEM grid.

The high resolution replicas were obtained from oblique evaporation of Pt/C (shadowing) onto "as-fractured", and "as-grown" surfaces of untreated and reacted olivine fragments, respectively. The underlying assumption in the use of "shadowing" techniques, is that the local thickness of the replica is a function of the rate of deposition of the evaporated metal. Thus, the enhanced contrast observed in TEM represents the surface profile of the specimen. In most cases, TEM images obtained from the replicas reveal both negative and positive features. A positive feature displays a black contrast in TEM images (deposition of Pt atoms) on the same side as the shadowing direction and is accompanied by a shadow (white area in TEM images) on the opposite side. In the case of negative features, the locations of Pt deposition and shadow are reversed with respect to the shadowing direction.

The internal structure of the precipitates on the surface of olivine fragments was studied in ultrathin sections (70 nm) prepared with an ultramicrotome. Individual fragments were embedded in a low-viscosity epoxy. The resin blocks were trimmed to a cutting-face size of 200 x 300 μm using a stereo microscope.

Imaging and chemical analyses with the SEM were performed with a JSM-840A instrument equipped with a Tracor Northern energy-dispersive X-ray spectrometer, operated at 10 kV and 20 mA. TEM imaging was performed with a JEOL 100 CX instrument equipped with an energy-dispersive X-ray detector (PGT IV; analyzable area, 100 nm^2) and operated at 100 kV with underfocus imaging conditions.

RESULTS

Fluid chemistry

The results from the chemical analysis of the reacted fluid are presented in Table 1 and Figure 1. The concentration-time profiles in Figure 1 show that Si, Ni and Mn concentrations ($3.1x10^{-4}$, $5.1x10^{-6}$ and $2.2x10^{-11}$ M, respectively) were highest in the first

Table 1. Composition of the air-saturated water reacted with olivine.

Time in hours	pH		Elemental concentrations									
	25°C	300°C	Si		Mg		Ni		Mn		Ca	
			mg/L	*M*	mg/L	*M*	mg/L	*M*	µg/L	*M*	mg/L	*M*
43.12	6.68	6.05	8.77	3.12E-04	0.11	4.57E-06	0.30	5.11E-06	12.33	2.24E-11	<D.L.	—
69.87	6.38	6.31	3.66	1.30E-04	0.02	9.13E-07	0.12	2.08E-06	1.10	2.00E-12	0.39	9.69E-06
97.95	6.23	6.16	2.41	8.58E-05	0.04	1.83E-06	0.16	2.65E-06	1.18	2.14E-12	0.20	4.99E-06
126.25	6.29	6.24	<D.L.	—	0.07	2.74E-06	0.16	2.65E-06	1.23	2.24E-12	0.22	5.54E-06
167.25	6.21	6.15	<D.L.	—	0.07	2.74E-06	0.16	2.65E-06	2.35	4.28E-12	0.14	3.60E-06
208.33	6.53	6.15	<D.L.	—	0.08	3.20E-06	0.12	2.08E-06	1.47	2.67E-12	0.12	3.05E-06
241.33	6.47	6.20	<D.L.	—	0.10	4.11E-06	0.10	1.70E-06	1.74	3.17E-12	0.12	3.05E-06
269.33	6.54	6.23	<D.L.	—	0.11	4.57E-06	0.10	1.70E-06	1.31	2.38E-12	0.12	3.05E-06
315.83	6.51	6.26	<D.L.	—	0.12	5.02E-06	0.09	1.51E-06	0.58	1.05E-12	0.13	3.32E-06
362.83			<D.L.	—	0.14	5.94E-06	<D.L.	—	<D.L.	—	0.13	3.32E-06
407.33	6.56	6.30	<D.L.	—	0.13	5.48E-06	<D.L.	—	<D.L.	—	0.14	3.60E-06
438.16	6.71	6.28	<D.L.	—	0.12	5.02E-06	<D.L.	—	<D.L.	—	0.14	3.60E-06
503.33	6.50	6.46	<D.L.	—	0.19	7.76E-06	0.13	2.27E-06	5.84	1.06E-11	0.26	6.37E-06
549.58	6.18	6.36	<D.L.	—	0.20	8.22E-06	0.13	2.27E-06	1.58	2.87E-12	0.09	2.22E-06
595.58	6.25	6.33	<D.L.	—	0.19	7.76E-06	0.12	2.08E-06	0.78	1.41E-12	0.08	1.94E-06
644.83	6.31	6.33	<D.L.	—	0.19	7.76E-06	0.10	1.70E-06	1.39	2.53E-12	0.08	1.94E-06
692.83	6.01	6.34	<D.L.	—	0.20	8.22E-06	<D.L.	—	<D.L.	—	0.07	1.66E-06
740.66	6.35	6.29	<D.L.	—	0.20	8.22E-06	<D.L.	—	0.79	1.43E-12	<D.L.	—
791.66	6.09	6.34	<D.L.	—	0.20	8.22E-06	<D.L.	—	<D.L.	—	0.07	1.66E-06
838.66	6.37	6.35	<D.L.	—	0.20	8.22E-06	<D.L.	—	<D.L.	—	0.07	1.66E-06
887.66	6.31	6.33	<D.L.	—	0.20	8.22E-06	<D.L.	—	<D.L.	—	<D.L.	—
935.66	6.44	6.33	n.a.	—	0.22	9.13E-06	n.a.	—	0.85	1.56E-12	n.a.	—
983.99	6.40	6.37	n.a.	—	0.24	1.00E-05	n.a.	—	<D.L.	—	n.a.	—
1033.99	6.50	6.35	n.a.	—	0.23	9.59E-06	n.a.	—	<D.L.	—	n.a.	—

<D.L.: Below detection limit; n.a.: Not analyzed.

Detection limits: Si=7.83×10^{-3} *M*, Mg=1.23×10^{-7} *M*, Ni=1.36×10^{-6} *M*, Mn=1.82×10^{-13} *M*, Ca=1.5×10^{-6} *M*.

Table 1. (continued).

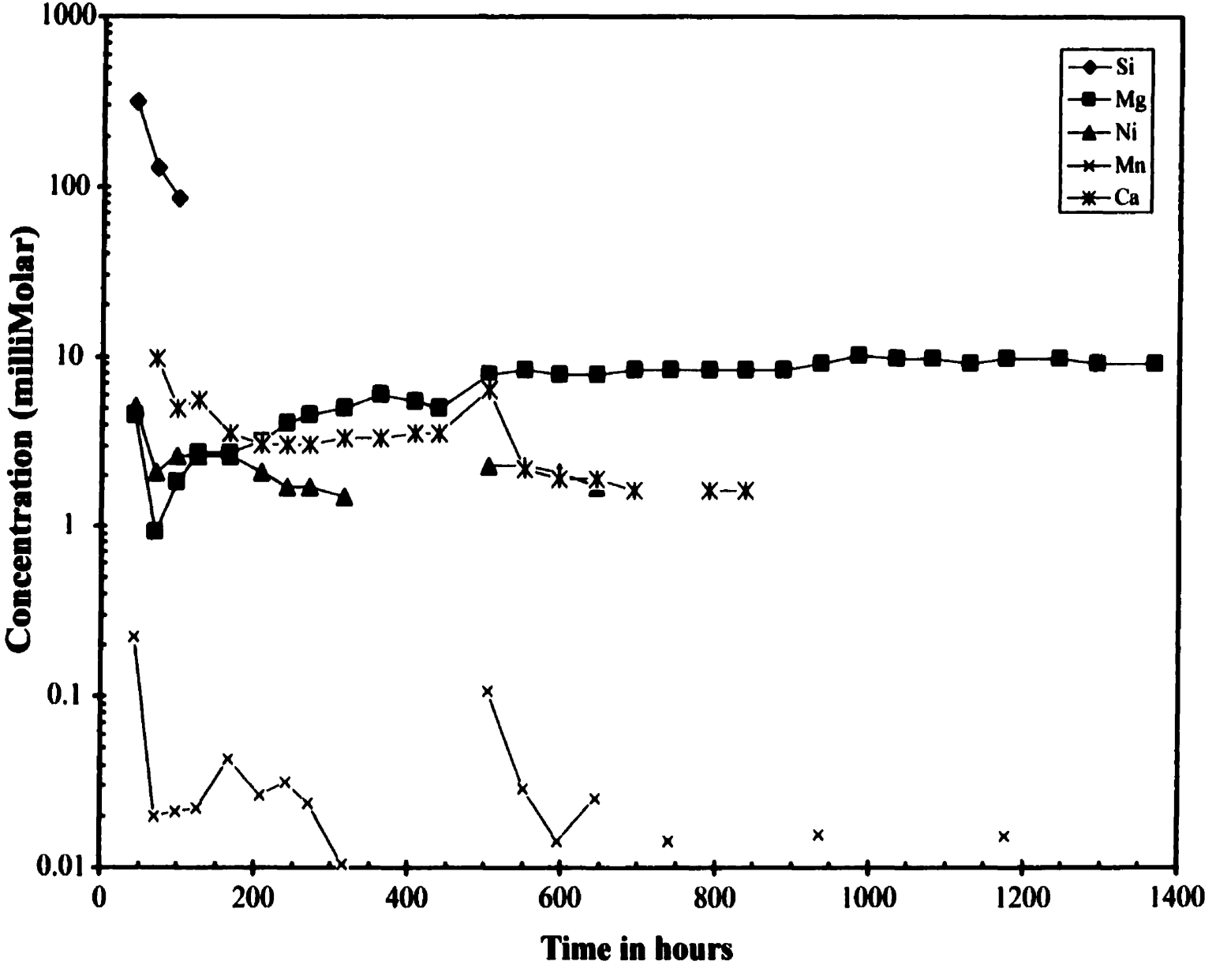
Time in hours	pH		Elemental concentrations									
	25°C	300°C	Si		Mg		Ni		Mn		Ca	
			mg/L	*M*	mg/L	*M*	mg/L	*M*	µg/L	*M*	mg/L	*M*
1080.07	6.56	6.35	n.a.	—	0.23	9.59E-06	n.a.	—	<D.L.	—	n.a.	—
1130.15	6.61	6.33	n.a.	—	0.22	9.13E-06	n.a.	—	<D.L.	—	n.a.	—
1177.73	6.63		n.a.	—	0.23	9.59E-06	n.a.	—	0.83	1.52E-12	n.a.	—
1244.48	6.67		n.a.	—	0.23	9.59E-06	n.a.	—	<D.L.	—	n.a.	—
1294.98	6.70		n.a.	—	0.22	9.13E-06	n.a.	—	<D.L.	—	n.a.	—
1367.98	6.70		n.a.	—	0.22	9.13E-06	n.a.	—	<D.L.	—	n.a.	—

<D.L.: Below detection limit; n.a.: Not analyzed.

Detection limits: Si=7.83×10^{-3} *M*, Mg=1.23×10^{-7} *M*, Ni=1.36×10^{-6} *M*, Mn=1.82×10^{-13} *M*, Ca=1.5×10^{-6} *M*.

Figure 1

Diagram showing the variation in concentrations of Si, Mg, Ca, Ni, and Mn as a function of time during reaction between deionized, air-CO_2-saturated water with San Carlos olivine ($Fo_{90.5}$; 250-500 μm size fraction). The experiment was conducted for 1368 hours using a flow-through reactor at 300°C and 300 bars. The fluid flow rate was maintained at 12 mL/day, except for an interval of 19 hours (mostly at night) after 440 hours of reaction, during which time the fluid reservoir had to be refilled. The missing data represent analyses for which concentrations were below the detection limit (see discussion in text).


1000
100
10
1
0.1
0.01
Concentration (milliMolar)
0
200
400
600
800
1000
1200
1400
Time in hours
Si
Mg
Ni
Mn
Ca

sample, i.e., they reached peaks near the start of the experiment. The concentration of Si decreased sharply with progress of the experiment, and dropped below the detection limit (2.2 mg/L or 7.8×10^{-3} M) in the fourth sample. The concentrations of Ni and Mn decreased very sharply in the second sample and then decreased gradually to below their respective detection limits after 316 hours of reaction. After the stoppage in fluid flow (440-459 hours), the concentration of these elements again increased to detectable levels. The Ni concentration then decreased to below the detection limit after 693 hours of reaction. Mn concentrations fluctuated at near the detection limit until approximately 1200 hours after which they were consistently below detection. The concentration-time profile of Ca is similar to those of Si, Ni and Mn, except that Ca reached its peak concentration (9.7×10^{-6} M) in the second sample, and was not detected in the first sample (detection limit, 60 µg/L or 1.5×10^{-6} M). Ca concentrations decreased below detection levels after 840 hours. The behaviour of Mg was in sharp contrast to that of the other elements. After a sharp decrease from 4.57×10^{-6} to 0.91×10^{-6} M between the first and second samples, Mg concentrations increased steadily to a value of 5.94×10^{-6} M after 363 hours of reaction, and then decreased to a value of 5.02×10^{-6} M just before the stoppage in fluid flow. After restoration of fluid flow, Mg concentrations increased to above 8.0×10^{-6} M, establishing a steady state plateau concentration. A further increase in Mg concentration occurred after approximately 1000 hours of reaction, and a second steady state plateau Mg concentration of approximately 9.5×10^{-6} M was established, which was maintained for the remainder of the experiment. The concentration of Fe was below its detection limit (70 mg/L) throughout the duration of the experiment. Calculations using the temperature jump option of the EQ3/6 software package (Wolery, 1992) indicate that pH reached a steady state value of 6.3 after 500 hours of reaction and remained approximately constant for the rest of the experiment.

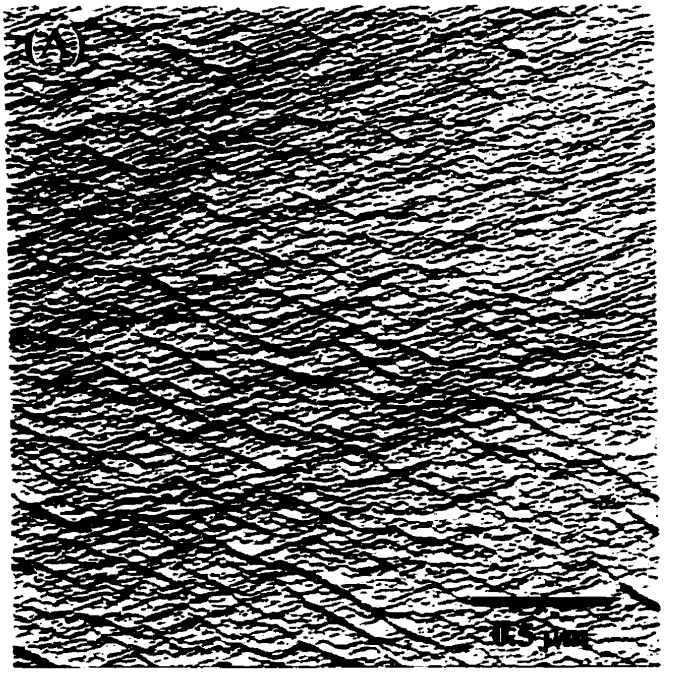
SEM and TEM investigations of the starting materials and run products

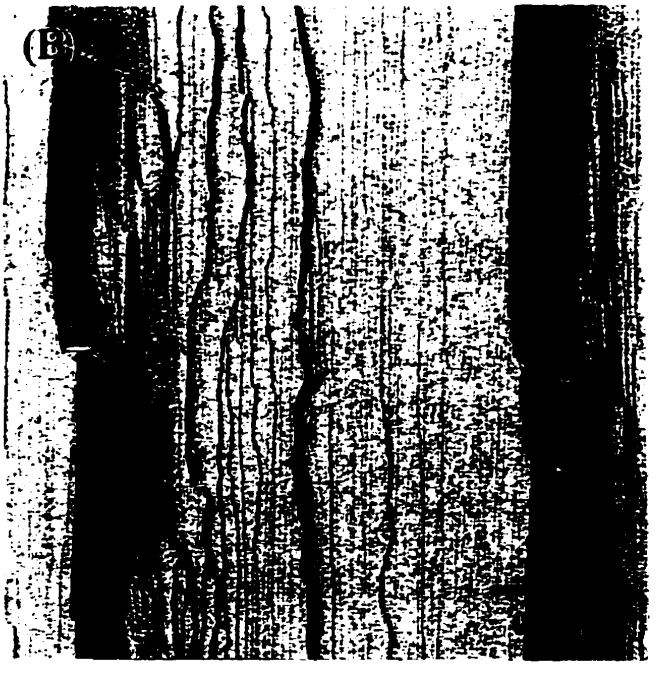
Starting material

TEM images of high resolution Pt/C replicas obtained from unreacted olivine reveal fractures, which reflect its internal structure (Figures 2a, b) or present smooth

Figure 2

TEM images of Pt/C replicas showing surface morphologies of unreacted starting San Carlos olivine. A) Fragment showing three families of fractures characterized by ordered, fine-scale steps. B) Fractured surface showing evidence of internal structure in two crystallographic orientations (diagonal in the image). These two faces may correspond to the (010) and (100) cleavage planes. [Scale bars: 1 micron].


(A)
1.5 μm


(B)

surfaces and contain opened fluid inclusions with radially distributed fractures, caused by decrepitation (see Wannamaker et al., 1990), and dislocations indicating alteration of the surface prior to crushing.

Dissolution features

A variety of etch features were evident on the Pt/C replicas of the olivine surfaces after reaction (Figures 3 and 4). These were more readily observable on olivine grains sampled from near the inlet of the reaction cell. The type of etch feature depended on the orientation of the original fractured surface relative to the internal structure. The replicas generally display two or three orthogonal directions of preferential dissolution, resulting in: 1) humocky surfaces covered with mounds that display a layered structure (Figure 3a); 2) unidirectional linear features produced by the intersection of two directions of dissolution parallel to the surface (Figure 3b); and 3) orthogonal linear features due to preferential dissolution along planes with intersections normal to the surface.

Secondary minerals

Olivine grains were progressively more shielded by secondary minerals towards the outlet of the reaction cell. The spatial distribution and grain size of the secondary minerals varied strongly with the species. Observation with the SEM revealed the presence of brucite (EDS analyses suggest an iron-poor variety) in the form of large pseudo-hexagonal, tabular crystals measuring more than 50 μm in diameter and up to 10 μm in thickness (Figure 5). These crystals are very sparse near the inlet, and at least ten times more abundant near the outlet, but are similar in size at both locations. The distribution and size of the brucite crystals indicate that the solution remained only marginally supersaturated with respect to this mineral along the length of the reaction cell. Magnetite was also observed with the SEM. This mineral formed octahedral crystals, which, in contrast to those of brucite, are homogeneously distributed, but generally larger near the outlet than at the inlet (15-20 μm versus <10 μm). Serpentine plates and fibers, although observable with the SEM, were too small (< 3 μm) for their detailed character or

Figure 3

TEM Images of Pt/C replicas of fragments from the top of the reaction cell (inlet) displaying dissolution and precipitation features. A) Large scale corrosion features characterized by mounds (etch figures) with crystallographic orientation. B) Tabular crystals of lizardite (L) showing a trigonal symmetry on etched olivine. A large magnetite crystal is also present (M). [Scale bars: 1 micron].

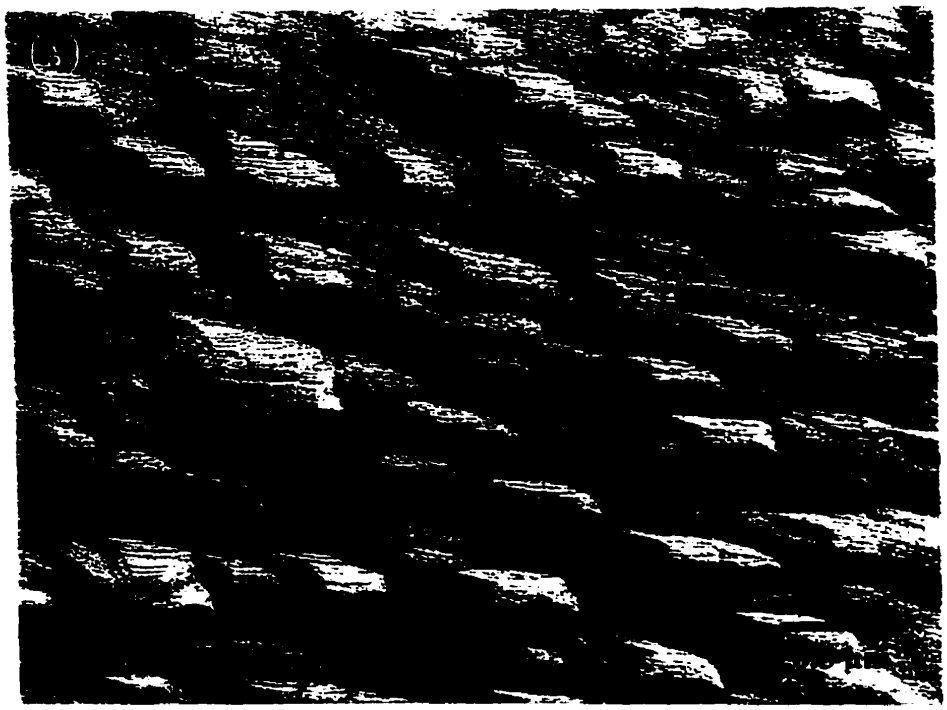




Figure 4

TEM images of Pt/C replicas of fragments from the center of the reaction cell exhibiting: A) Epitaxially oriented and randomly adsorbed lizardite (L) plates on olivine. Note the dissolution features which reveal the internal structure of the olivine; B) Large polygonal (P) and conical (C) serpentine fibers, and incipient growth of a cylindrical serpentine phase (Ctl); C) Oriented lizardite (L) on etched olivine. [Scale bars: 1 micron].

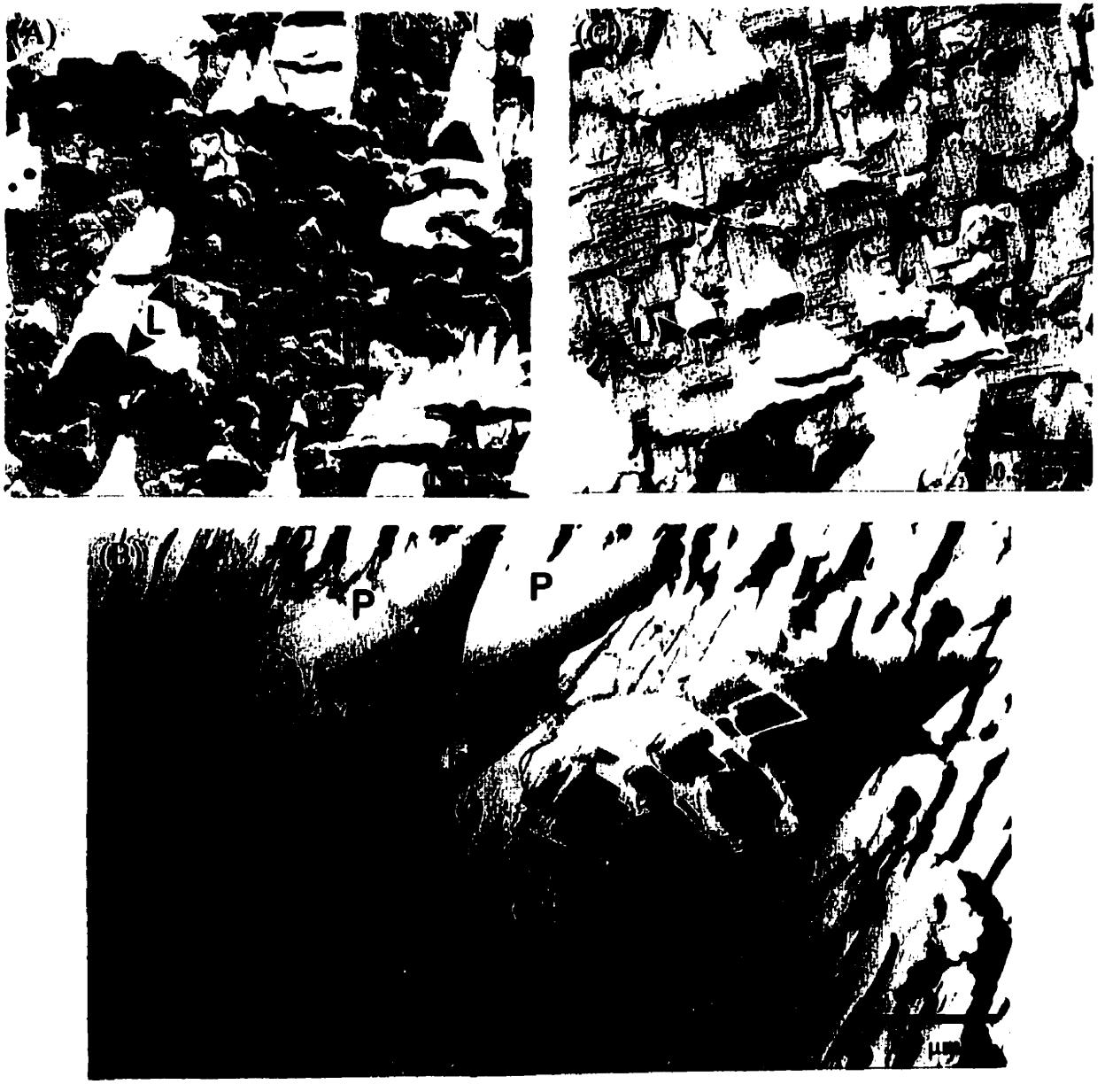
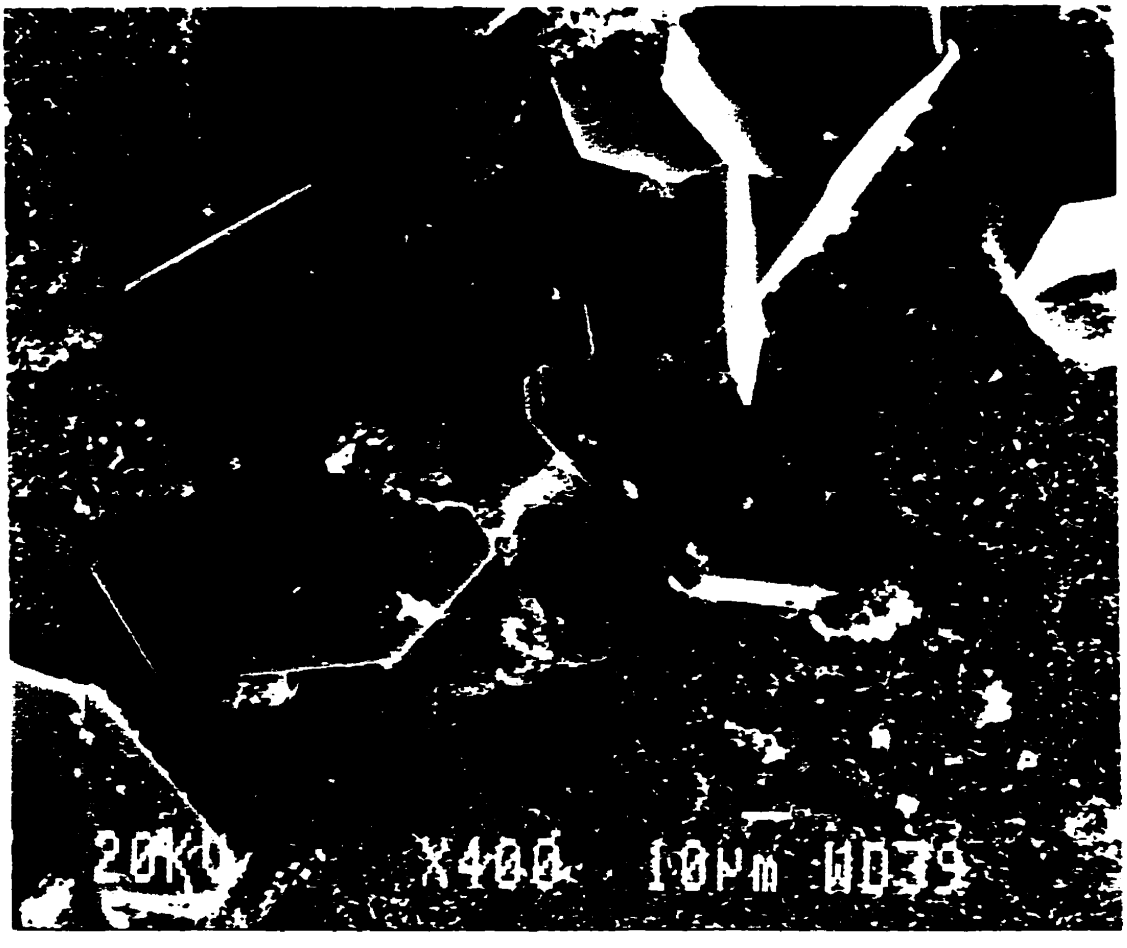

(A)
L
(C)
(B)
P
P

Figure 5

SEM image of "large" euhedral crystals of brucite. [Scale bar: 10 microns].


20KV X400 10µm WD39

distribution to be satisfactorily determined using this instrument. EDS analyses of thick fibrous bundles of serpentine indicate a Mg/(Mg+Fe) atomic ratio of approximately 0.96.

Investigation of the reacted olivine surface using TEM revealed the presence of at least four distinctly different serpentine phases characterized by plate-like, conical, polygonal and cylindrical morphologies, respectively. Serpentine on the surfaces of olivine fragments, collected from the top of the reaction cell (inlet), consists mainly of platy, trigonal lizardite crystals measuring from 700 to 1,100 nm in diameter. Rarely, a small nucleus of conical serpentine protrudes from the surface of the lizardite crystals (Figure 3b). Cylindrical chrysotile was not observed.

Olivine from the center of the reaction cell has been overgrown by several serpentine phases. The earliest serpentine to crystallize was lizardite, which forms pseudohexagonal to trigonal platelets (Figure 4a, b and c). Lizardite crystals (150 to 500 nm in diameter) oriented with their *c*-axis parallel to the olivine surface clearly nucleated and grew topotaxially with respect to the olivine substrate (Figure 4b and c). All such crystals are oriented parallel to each other, and commonly display a slight bend which curves along an axis parallel to the olivine substrate. They are linked to the olivine surface along one of its principal crystallographic directions, as revealed by dissolution features (Figure 4a and c), and are more abundant and more tightly clustered towards the outlet than towards the inlet of the reaction cell. Other lizardite crystals have their *c*-axis perpendicular to the olivine surface and occur as randomly oriented crystals measuring from 80 to 300 nm in diameter. Rare, isolated crystals measuring up to 1000 nm in diameter were also observed (Figure 4b). The crystals, which measure < 300 nm in diameter, form a population identical to the topotaxially oriented ones. They frequently mold the olivine surface irregularities, and are interpreted to have adhered in this position during extraction of the olivine from the reaction cell. The larger lizardite crystals are part of the generation which occurs near the inlet of the reaction cell.

The other serpentine phases in the central part of the reaction cell display fibrous morphologies. The most common of these phases consists of large cones (up to 600 nm in diameter at the base) which appear to be formed of connected trigonal plates of lizardite joined together to form a fiber with a serrated basal contour (Figure 4c). Smaller conical

fibers have more uniform outlines, but textures rarely suggest a continuous wrapping of the serpentine sheets along the entire length of the fiber (Yada and Iishi, 1974, 1977; Devouard, 1995). One other commonly observed serpentine habit is that of a cone of cylindrical shape near the low diameter extremity of the fiber, grading to a 15-sectored (inferred) polygonal arrangement of uniform prismatic crystal faces where the radius of the fiber is > 300 nm (Figure 4b). The latter is greater than the "critical" diameter of 100 nm inferred by Papp (1990) for the transition from cylindrical chrysotile to polygonal serpentines in natural samples. However, the identity of these polygonal cones as true polygonal fibers remains to be verified through high resolution examination of sections cut perpendicular to the fiber axis. Cylindrical chrysotile fibers are very minor and are generally observed extending from the conical or large lizardite crystals (Figure 4b). Only one example was observed of a lizardite crystal connected to a cylindrical chrysotile crystal with the curling axis perpendicular to the olivine substrate. The above observations suggest a dependence of chrysotile formation on the availability of a previously formed lizardite substrate. Moody (1976) observed a similar relationship in her experimental investigation of serpentinization of iron-bearing olivine (at temperatures of 300-375°C and pressures of 500-2000 bars) in which lizardite formed early and chrysotile gradually predominated.

Surfaces of the olivine fragments from the bottom part of the reaction cell (outlet) have considerably higher abundances of neo-formed material than those higher up in the reaction cell. In most cases, large aggregates of newly formed phases, which were not dissolved during HF treatment, still adhere to the replica (Figure 6a). High-resolution transmission electron microscopy (HRTEM) of ultrathin sections of the fibrous, conical phase confirmed the identification of serpentine (Figure 6b). At least two types of conical serpentine fibers can be recognized based on width to length ratios and conical angles: 1) long (up to 4 μm), narrow (< 200 nm) fibers with a wide range of conical aperture (16 to 57°); and 2) wider (> 200 nm) and generally shorter fibers with cone apertures > 34°. Both types of fiber form bundles that radiate from the surfaces of large (~ 1 μm) crystals of trigonal outline (Figure 6a). EDS analyses of the latter crystals indicate that they are

Figure 6

TEM images of Pt/C replicas of fragments from the bottom part of the reaction cell (outlet) showing: A) Large aggregate of newly formed serpentine phases still adhering to the replica, consisting of crystals with trigonal outlines and two types of conical fibers (long, narrow fibers, and short, thicker fibers). [Scale bar: 1 micron]. B) HRTEM images of ultrathin section cut perpendicular to a fiber. Note the curled, layered structure.


(A)
0.5 μm
(B)

composed of a Mg-Fe silicate, suggesting that fibrous serpentine growth was controlled by a lizardite template. X-ray diffraction analysis of the secondary minerals removed from the olivine surfaces by gentle grinding in alcohol revealed only serpentines, brucite and magnetite, thereby confirming the TEM observations.

DISCUSSION

Reaction Progress

The fluid

Experimental data and thermodynamic calculations (see Chernosky et al., 1988, and references therein) indicate that forsteritic olivine is unstable in the presence of H_2O below a temperature of 350°C, at a pressure of 300 bars. During reaction with water at 300°C and 300 bars, forsteritic olivine is expected to dissolve irreversibly until complete transformation into an assemblage composed of serpentine (stable antigorite, or metastable chrysotile or lizardite), brucite and magnetite. If the rate of dissolution of this olivine is much greater than that of the precipitation of the secondary minerals (serpentine and brucite), the solution may become saturated with respect to olivine and dissolution will stop. Chemical analyses of the fluid and thermodynamic calculations indicate that the solution was undersaturated with respect to olivine during the first 100 hours of the experiment (samples 1-3). Although Si concentrations dropped below the detection limit of the instrument used for its analysis after that time, the decreasing affinity (-RT Log IAP/K) of the fluid with respect to olivine between the first and the third sample suggest that the fluid was undersaturated with respect to olivine for the duration of the experiment. The Ca concentration provides a measure of the dissolution rate of olivine. This is because Ca does not enter the structure of serpentines, brucite and magnetite, and therefore was concentrated entirely in the fluid. Elevated Ca concentrations, and thus dissolution rates, near the start of the experiment were probably due to rapid dissolution of high-energy sites, such as at the location of structural defects and topographic irregularities with low radius of curvature. Thermodynamic calculations predict that the

precipitous decrease in Si concentration in the early stages of the experiment was caused by the formation of serpentines (data for chrysotile were used in the calculations) that buffered Si to a very low, undetermined steady state value. The onset of steady state Mg concentrations and pH values coincided with saturation of the solution with respect to brucite.

Saturation with serpentine in the early stages of the experiment followed by brucite, and attainment of steady state Mg concentrations and pH is explained as follows. When serpentine started to precipitate, the activity of silica decreased, whereas the activity ratio $(a\mathrm{Mg}^{2+})/(a\mathrm{H}^{+})^2$ increased (pH and Mg concentrations increased: see Table 1 and Figure 1) in an attempt to maintain the affinity (-RT Log IAP/K) of serpentine close to zero as olivine dissolved. When brucite saturated, the activity ratio $(a\mathrm{Mg}^{2+})/(a\mathrm{H}^{+})^2$ was fixed. Although the activity of aqueous SiO_2 was not quantified for the period of brucite saturation, it is reasonable to assume that it also reached a steady state value corresponding closely to that consistent with coexistence of brucite + serpentine. A more detailed account of the hydrothermal chemistry of this and other experiments are presented in Chapter III .

It is interesting to note that the steady state fluid composition attained after 600 hours, which was controlled by the precipitation of serpentine + brucite (+ magnetite), closely approximates that predicted, by thermodynamic calculations, to be in equilibrium with serpentine + brucite (+ magnetite). In other words, dilute fluids reacting, for example, along fractures within a dunite are likely to quickly approach equilibrium with the products of serpentinization. This conclusion is based on a flow rate of 6.5×10^{-5} $m^3/m^2 \cdot s$ (this experiment), whereas fluxes during natural serpentinization are estimated to range between 10^{-10} and 10^{-12} $m^3/m^2 \cdot s$ (Macdonald, 1984). However, other parameters which may significantly affect the above conclusion when applied to natural systems include P_{H2O} (i.e., $P_{H2O} < P_{Fluid}$ and $P_{Fluid} < P_{Total}$), and the electrostatic effects produced by phyllosilicates on the fluid as it circulates along extremely small channels (Casey et al., 1993).

The solids

Morphological investigations of the run products confirmed the predictions of thermodynamic calculations, based on the composition of the effluent, that brucite and serpentine were the principal phases saturated (precipitated) during the experiment. However, although the calculations predicted that serpentine would become undersaturated, and therefore dissolve after <100 hours, SEM- and TEM-assisted observations indicate that it was stable for the duration of the experiment.

Lizardite (plate-like crystals) appears to have been the first serpentine phase to precipitate, followed by conical-polygonal prisms and cone in cone needles, and finally by minor cylindrical chrysotile. The mineralogical changes with distance from the inlet reflect the progress of the reaction with time, i.e., the early stages of alteration, which are represented by fragments at the inlet, mainly involved dissolution of the olivine (fresh, unmodified fluid meets fresh unmodified rock), whereas the later stages of alteration, recognized in fragments near the outlet, were characterised largely by precipitation of secondary phases (reacted fluid becomes saturated with minerals).

The serpentine paragenesis is lizardite followed by polygonal and conical serpentine, and finally by chrysotile. This paragenesis is reflected by the relative abundance of these phases from the inlet through the center to the outlet, i.e., by: 1) lizardite >> conical serpentine, 2) lizardite > conical serpentine >> polygonal serpentine > cylindrical chrysotile, and 3) conical serpentine>lizardite. Note that, because observations on samples from the outlet were made on undissolved minerals from the backs of replicas, a detailed textural characterization of all the serpentine phases could not be achieved, and it is therefore possible that cylindrical chrysotile was overlooked.

As mentioned earlier, the topotactic lizardite crystals display a slight curvature with an axis parallel to the olivine substrate. It appears plausible, from examination of Figure 4b, that the conical serpentine formed from the agglomeration of such lizardite crystals. The passage from large, widely spaced lizardite crystals near the inlet of the reaction cell to abundant smaller crystals in the middle suggests that there was a corresponding gradient of increased concentration of components in the fluid (increasing degree of supersaturation). Topotactically oriented lizardite on the olivine surfaces

provides evidence that pseudomorphic replacement of olivine proceeds along specific crystallographic planes, and that the process is by dissolution-precipitation at the interface. With further progress of topotactically oriented pseudomorphism, diffusion (through the serpentine-covered olivine grains) becomes the main mode of transport of water and dissolved species (Wegner and Ernst, 1983). The pseudomorphic process leads ultimately to the development of the hourglass textures observed in thin sections cut from serpentinized olivine-rich rocks (see Wicks et al., 1977, and Prichard, 1979).

Relationships between saturation index and serpentine morphology

Thermodynamic analysis and phase equilibrium studies (Evans et al., 1976; Day et al., 1985; Chernosky et al., 1988) suggest that chrysotile is metastable at temperatures greater than 250°C in the system MgO-SiO_2-H_2O. Above that temperature and at low pressure, antigorite is the stable serpentine phase up to approximately 500°C. Thermodynamic data for end-member and near end-member lizardite are not available. The pressure-temperature conditions under which it might be stable are therefore a matter of debate (Chernosky et al., 1988). Field and experimental investigations, and theoretical considerations (Chernosky, 1975; Moody, 1976; O'Hanley, 1987; O'Hanley and Wicks, 1995) suggest that chrysotile might be the stable high temperature serpentine relative to lizardite. O'Hanley and Wicks (1995) estimated that the transition from lizardite to chrysotile occurs at a temperature of approximately 200°C based on field, paragenetic, stable isotope and phase equilibrium relationships, whereas Grauby et al. (1998) suggested, based on hydrothermal synthesis experiments, that lizardite (Mg end-member) is more stable than chrysotile at 300°C and 700 bars.

Under the pressure-temperature conditions of our experiment, antigorite was the phase expected to form stably. However, antigorite is very difficult to produce experimentally from hydrothermal treatment of olivine (addition of excess Si is generally required), implying that there are appreciable kinetic barriers to its nucleation and growth from serpentinizing fluids (Dungan, 1977). Chrysotile and lizardite are the serpentines that generally form during synthesis experiments. We therefore conclude that the

assemblage chrysotile + lizardite + brucite formed metastably during our experiment. The question that then follows, is which of chrysotile and lizardite was the "most" stable.

Crystallization and growth of a mineral from solution require supersaturation, a state that, by definition, is out of equilibrium. Accordingly, a number of metastable phases may crystallize and persist if supersaturation is sufficient and maintained (e.g., open system). Furthermore, heterogeneous nucleation on a foreign surface may favour the crystallization of one or more of the phases at a lower level of supersaturation than would be required for homogeneous nucleation in the body of the solution.

The critical energy required for nucleation of a phase from solution comprises contributions from the work required to form both the bulk and the surface of the solid as follows:

$$\Delta G^*_{hom} = \Delta G_{vol} + \Delta G_{surf} \quad (1)$$

in which:

$$\Delta G_{surf} = \Delta S\sigma \quad (2)$$

where S represents the surface area and σ the surface energy. Recent theories for heterogeneous nucleation consider short range and long range interfacial and molecular interaction energies (Upreti and Walton, 1966; Walton, 1969; Wu and Nancollas, 1996). According to Walton (1969), the interfacial energy between two solid phases, e.g., serpentine and olivine, may be expressed as:

$$\sigma_{Srp\text{-}Fo} = \sigma_{Srp} + \sigma_{Fo} - \Sigma\, U_{Srp\text{-}Fo} \quad (3)$$

where U represents the energetic contribution of the interaction of atoms between the two surfaces. If the interface is incoherent, dislocations will develop and the interfacial energy expression is modified to:

$$\sigma_{Srp\text{-}Fo} = \sigma_{Srp} + (\sigma_{Fo}\text{-}\sigma_X) - (\Sigma\, U_{Srp\text{-}Fo} - U_{disloc.} - U_X) \quad (4)$$

where $U_{disloc.}$ and U_X represent a decrease in net interaction due to dislocations, and distortion and strain, respectively. It can be seen from equations (3) and (4) that the greater is the structural compatibility between the phases in contact, the lower is the interfacial energy. As a result, the phase which is the most compatible with the surface of the host for heterogeneous nucleation possesses the lowest critical free energy ($G^*_{het.}$). It should be stressed here that the larger the interfacial surface area between nucleus and substrate relative to the total surface area of the nucleus, the larger are the energetic effects on the total free energy of that nucleus. Taking, as an example, the case where a serpentine phase, lizardite or chrysotile, nucleates on an olivine surface, it can be readily deduced that lizardite, with its flat-layered structure, as opposed to the rolled structure of chrysotile, would be the better candidate for a structural match with olivine and offer a larger interfacial surface area of contact.

In principle, the orientation of a serpentine nucleus with respect to that of the olivine substrate may influence the growth history of that serpentine crystal. For example, a lizardite crystal nucleating with its *c*-axis parallel to an olivine surface might progress towards chrysotile as its size increases sufficiently to enable curvature towards an equilibrium value (Devouard, 1995; Baronnet and Devouard, 1996). A lizardite nucleus with its *c*-axis perpendicular to an olivine surface, i.e., with the sheet structure parallel to the olivine surface, would offer the greatest interfacial surface area, and, as such, have the least potential for curling. The curled structure of chrysotile perpendicular to the fiber axis would offer the poorest structural match with olivine, and bonding with the hydrogens of the outer layers of the chrysotile cylinders would only occur along one direction, the direction of the fiber axis. In that respect, it is interesting to note that direct replacement of olivine by chrysotile has never been observed in natural samples (O'Hanley, 1991).

Finally, it can be seen from equation (5), below, that, although the surface energy contribution to the total nucleation energy of chrysotile may be lowered by heterogeneous nucleation, the elastic energy stored in chrysotile fibers (Devouard, 1995; Baronnet and

Devouard, 1996), due to the curved nature of the structure, represents a further contribution to the total energy, which is not found in lizardite.

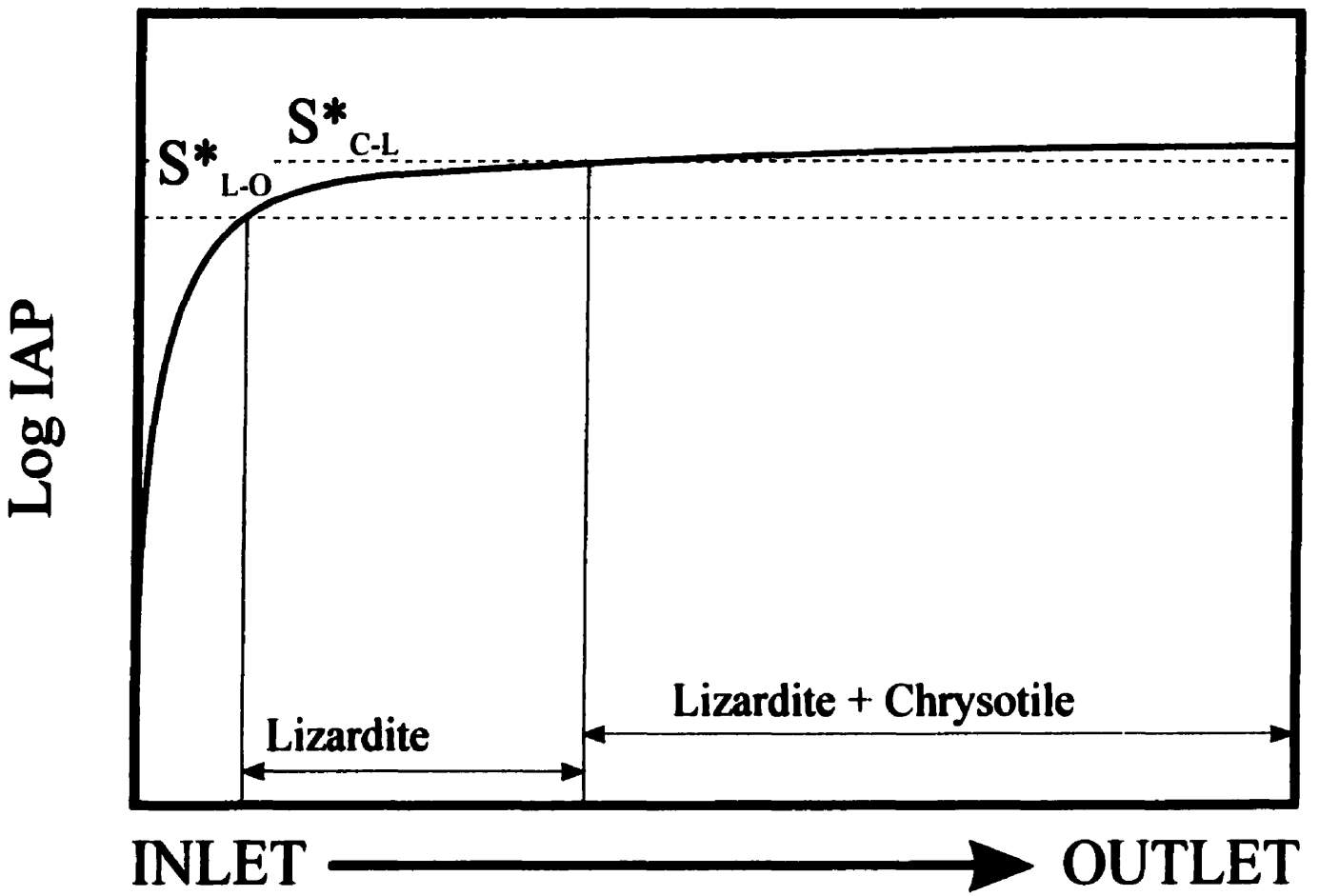
$$\Delta G^*_{chr} = \Delta G_{vol} + \Delta G_{surf} + \Delta G_{elast} + \Delta G_{interf} \quad (5)$$

In view of the above discussion, we propose that the heterogeneous nucleation of lizardite by olivine was favoured relative to that of chrysotile and that, consequently, lizardite crystallized at lower levels of supersaturation than chrysotile. The appearance of chrysotile only near the outlet of the reaction cell, where the solution is expected to have contained greater concentrations of dissolved species, is evidence that chrysotile grew at greater levels of supersaturation than lizardite. We also propose that formation of lizardite catalyzed the crystallization of chrysotile by providing a surface with maximum structural and energetic compatibility (Figure 7).

Our experimental results do not permit us to establish the relative stability of lizardite and chrysotile. There are, nevertheless, some experimental data reported by Grauby et al. (1998), which suggest that lizardite may have been the stable form of serpentine in our experiment. These authors found, during long duration hydrothermal synthesis experiments, using gels at 300°C and 700 bars, that the sequence of formation of the serpentine minerals with increased time of reaction was chrysotile → polygonal serpentine → lizardite. They interpreted this sequence as being the result of decreasing degrees of supersaturation, and ripening controlled by the reduction in elastic energy stored in the conical and cylindrical serpentines. The sequence of crystallization observed in our study and in that of Grauby et al. (1998) is the same when viewed as a function of the degree of supersaturation of the solution. In our open-system experiment, reaction progressed from low to elevated degrees of supersaturation as fluid flowed through the reaction cell, whereas in Grauby et al.'s (1998) closed-system experiment, dissolution of the gel resulted in early, highly supersaturated solutions which then gradually equilibrated with time.

Figure 7

Schematic representation of the proposed steady state ion activity product profile with respect to lizardite and chrysotile (both phases are assumed to have identical compositions), based on the observed serpentine zonation through the reaction cell. The stratification of the phases from the inlet to the outlet of the reaction cell suggests that reactions proceeded until a fixed-time steady state ion activity product profile, influenced by the relative rates of dissolution of olivine and precipitation of secondary minerals, was achieved. The composition of the fluid allowed heterogeneous nucleation of lizardite on olivine near the inlet, and heterogeneous nucleation of chrysotile on lizardite nearer to the outlet. This establishes that nucleation of chrysotile requires higher degrees of supersaturation than is necessary for nucleation of lizardite from reaction of forsteritic olivine with water at the temperature and pressure of the experiment, but provides no information regarding which phase was the more "stable". (Abbreviations: $S^*_{L\text{-}O}$: Critical level of supersaturation for heterogeneous nucleation of lizardite on olivine, $S^*_{C\text{-}L}$: Critical level of supersaturation for heterogeneous nucleation of chrysotile on lizardite).


S*C-L
S*L-O
Log IAP
Lizardite
Lizardite + Chrysotile
INLET
OUTLET

CONCLUSIONS

This study demonstrates that simulation experiments under conditions approaching those of natural systems have an important role to play in understanding hydrothermal alteration. In particular, the detailed characterization of starting and reacted materials, and of neo-formed minerals is essential to understand the processes of fluid-rock interaction. The high resolution imaging technique used in this study provided a means to characterize in detail the nature of reactant and product minerals, and the relationships between them. These relationships are intimately linked to the evolution of the chemistry of the fluid in which the minerals dissolve and grow. In our open-system experiment, we conclude that the concentration of dissolved species increased along the reaction cell towards the outlet as a result of the irreversible dissolution of olivine. Throughout the reaction cell and at lower levels of supersaturation, the serpentinization reaction was dominated by heterogeneous nucleation of lizardite on olivine. At higher levels of supersaturation, i.e., near the outlet, chrysotile formed through heterogeneous nucleation on lizardite. This agrees with observations of natural samples in which lizardite almost invariably forms before chrysotile. The experimental results also explain the observation that chrysotile is almost never observed in contact with olivine.

Chrysotile and polygonal serpentine are common in veins cutting serpentinites, whereas lizardite is rare. Because of this cross-cutting relationship, the formation of chrysotile veins is commonly explained as being the result of later, higher temperature tectonic events. Based on the results of this study, we offer an alternative interpretation. In and along veins, the water/rock ratio is extremely high and thus the fluid is likely to remain supersaturated in respect to a particular phase for much longer periods of time than would be the case in the main body of the rock. Chrysotile could therefore be metastable with respect to lizardite over a wider range of pressure and temperature conditions than previously suspected.

ACKNOWLEDGEMENTS

This research was made possible through grants from NSERC and JM Asbestos Inc. to AEW-J, HV and RFM and NSERC and FCAR scholarships to CN, and benefitted from stimulating discussions with Alain Baronnet, Fred Wicks, David Veblen, and Jeanne Paquette. The senior author is grateful to Bruce Mountain for instruction in the use of the flow-though apparatus, Michel Leroux for performing the BET measurement, Glenn Poirier for training on the electron microprobe facility, Sandra Lalli and Glenna Keating for training on the atomic absorption facilities.

REFERENCES

Baronnet, A., 1972, Growth mechanisms and polytypism in synthetic hydroxyl-bearing phlogopite. American Mineralogist, v. 57, p. 1272-1293.

Baronnet, A., 1973, Sur les origines des dislocations vis et des spirales de croissance dans les micas. Journal of Crystal Growth, v. 19, p. 193-198.

Baronnet, A. and B. Devouard, 1996, Topology and crystal growth of natural chrysotile and polygonal serpentine, Journal of Crystal Growth, v. 166, p. 952-960.

Casey, W. H., Banfield, J. F., Westrich, H. R. and L. McLaughlin, 1993, What do dissolution experiments tell us about natural weathering? Chemical Geology, v. 105, p. 1-15.

Chernosky, J. V., Jr., 1975, Aggregate refractive indices and unit cell parameters of synthetic serpentine in the system MgO-Al_2O_3-SiO_2-H_2O. American Mineralogist, v. 60, p. 200-208.

Chernosky, J. V., Jr., Berman, R. G. and L. T. Bryndzia, 1988, Stability, phase relations, and thermodynamic properties of chlorite and serpentine group minerals. *in* Hydrous Phyllosilicates (exclusive of micas), Bailey, S. W., editor. Reviews in Mineralogy. Mineralogical Society of America, v. 19, p. 295-346.

Day, H. W., Chernosky, J. V. and H. J. Kumin, 1985, Equilibria in the system MgO-SiO_2-H_2O: a thermodynamic analysis. American Mineralogist, v. 70, p. 237-248.

Devouard, B., 1995, Structure et croissance cristalline du chrysotile et des serpentines polygonales. Ph. D. Thesis, Université d'Aix-Marseille III, France, 181 p.

Dungan, M. A., 1977, Metastability in serpentine-olivine equilibria, American Mineralogist, v. 62, p. 1018-1029.

Eggleston, C. M., Hochella, M. F., Jr. and G. A. Parks, 1989, Sample preparation and ageing effects on the dissolution rate and surface composition of diopside, Geochimica et Cosmochimica Acta, v. 53, p. 797-804.

Evans, B. W., Johannes, W., Oterdoom, H. and V. Trommsdorff, 1976, Stability of chrysotile and antigorite in the serpentinite multisystem, Schweizerische Mineralogische und Petrographische Mitteilungen, v. 56, p. 79-93.

Grauby, O., Baronnet, A. and B. Devouard, 1998, Chrysotile - to - polygonal serpentines - to - lizardite reaction produced from a $MgO-SiO_2-H_2O$ (MSH) gel: 17th General Meeting of the International Mineralogical Association, August 9-14, Toronto, Canada, Abstracts and Program, p. A81.

Macdonald, A. H., 1984, Water diffusion rates through serpentinized peridotites: implications for reaction induced dynamic and chemical effects in ultramafic rocks, Ph. D. Thesis, University of Western Ontario, Canada, 265 p.

Moody, J. B., 1976, An experimental study of the serpentinization of iron-bearing olivines, Canadian Mineralogist, v. 14, p. 462-478.

Mountain, B. W., 1992, Fluid-rock interaction paths: natural and experimental examples, Ph. D. Thesis, McGill University, Canada, 354 p.

O'Hanley, D. S., 1987, A chemographic analysis of magnesian serpentines using dual networks, Canadian Mineralogist, v. 25, p. 121-133.

O'Hanley, D. S., 1991, Fault-related phenomena associated with hydration and serpentine recrystallization during serpentinization, Canadian Mineralogist, v. 29, p. 21-35.

O'Hanley, D. S. and F. J. Wicks, 1995, Conditions of formation of lizardite, chrysotile and antigorite, Cassiar, British Columbia, Canadian Mineralogist, v. 33, p. 753-773.

Papp, G., 1990, A review of the multi-layer lizardite polytypes, Annals Hist. - Nat. Mus. Natn. Hung., v. 82, p. 9-17.

Paquette, J., Vali, H. and A. Mucci, 1996, TEM study of Pt-C replicas of calcite overgrowths precipitated from electrolyte solutions, Geochimica et Cosmochimica Acta, v. 60, p. 4689-4699.

Prichard, H. M., 1979, A petrographic study of the process of serpentinization in ophiolites and the oceanic crust, Contributions to Mineralogy and Petrology, v. 68, p. 231-241.

Schwab, R. G. and D. Kastner, 1977, Präzisionsgitterkonstantenbestimmung zur festlegung röntgenographischer bestimmungskurven für synthetische olivine der

mischkristallreihe forsterit-fayalit. Neues Jahrbuch für Mineralogie Monatshefte. v. 5, p. 205-215.

Upreti, M. C. and A. G. Walton, 1966. Heterogeneous nucleation of alkali halide crystals from solution. Journal of Chemical Physics, v. 44, p. 1936-1939.

Walton, A. G., 1969. Nucleation in liquids and solutions. *in* Nucleation. Zettlemoyer, A. C., editor. Marcel Dekker Inc., New York, p. 225-307.

Wannamaker, B. J., Wong, T.-F. and B. Evans, 1990. Decrepitation and crack healing of fluid inclusions in San Carlos olivine. Journal of Geophysical Research, v. 95, p. 15,623-15,641.

Wegner, W. W. and W. G. Ernst, 1983. Experimentally determined hydration and dehydration reaction rates in the system MgO-SiO_2-H_2O. American Journal of Science, v. 283-A, p. 151-180.

Wicks, F. J., Whittaker, E. J. W. and J. Zussman, 1977. An idealized model for serpentine textures after olivine. Canadian Mineralogist, v. 15, p. 446-458.

Williams-Jones, A. E., Wood, S. A., Mountain, B. W. and C. H. Gammons, 1994. Experimental water-rock interaction: Applications to ore-forming hydrothermal systems. *in* Alteration and alteration processes associated with ore-forming systems. D. R. Lentz, editor. Geological Association of Canada Short Course Notes, v. 11, p. 131-160.

Wolery, T. J., 1992. EQ3/6, a software package for geochemical modeling of aqueous systems: package overview and installation guide (version 7.0). Lawrence Livermore National Laboratory UCRL-MA-110662, Part I, 66 p.

Wu, W. and G. H. Nancollas, 1996. Interfacial free energies and crystallization in aqueous media. Journal of Colloid and Interface Science, v. 182, p. 365-373.

Yada, K. and K. Iishi, 1974. Serpentine minerals hydrothermally synthesized and their microstructures. Journal of Crystal Growth, v. 24/25, p. 627-630.

Yada, K. and K. Iishi, 1977. Growth and microstructure of synthetic chrysotile. American Mineralogist, v. 62, p. 958-965.

INTRODUCTION TO CHAPTER III

In Chapter II, the study of the effects of fluid/rock interaction between olivine and water focused primarily on the solid products. We established that the distribution sequence of the serpentine phases corresponding to platy → polygonal → conical along the reaction cell during reaction of olivine with water reflected the level of supersaturation of the water with respect to the serpentines, and, to a lesser extent, the heterogeneous nucleation on early-formed serpentine.

In the chapter that follows, we focus our attention on the chemistry of the water reacted with the olivine, and on the chemistry of the fluids involved in two other flow-through experiments. These experiments involved the flow of water through lherzolite, and the flow of a 0.1 *M* $CaCl_2$ aqueous solution through olivine. The latter two experiments were undertaken to gain further understanding of the behaviour of Ca during serpentinization, and, by extension, of the origin of the Ca responsible for rodingitization.

CHAPTER III

CONSTRAINTS ON CALC-SILICATE ALTERATION ASSOCIATED WITH SERPENTINITES: EXPERIMENTAL AND FIELD EVIDENCE.

by

Charles Normand and Anthony E. Williams-Jones

Department of Earth and Planetary Sciences, McGill University, 3450 University Street, Montreal (Qué), Canada, H3A 2A7.

ABSTRACT

Single-pass flow-through hydrothermal experiments were conducted at 300°C and 300 bars in order to understand the behaviour of calcium during serpentinization. The starting solids were crushed San Carlos olivine ($Fo_{90.5}$) and natural lherzolite. The fluid was deionized water or 0.1 *M* H_2O-$CaCl_2$ solution, and was circulated through a solid-filled reaction cell at a flow rate of 0.5 mL/hr.

Reaction of deionized water with the olivine produced "serpentines" (lizardite and polygonal, conical and cylindrical chrysotile) and magnetite in the first few hours. Brucite formed after 550 hours of reaction when the fluid reached steady state concentrations for Mg ($7.8x10^{-6}$ *M*) and H^+ (pH of 6.33). The calculated dissolution rate for the forsteritic olivine was $5.9x10^{-14}$ mol cm^{-2} s^{-1} near the start and $9.8x10^{-14}$ mol cm^{-2} s^{-1} at the end of the experiment, respectively, which is 4 to 26 times lower than that estimated by Ponader (1989) in a similar experiment. Platy (lizardite) and fibrous (chrysotile) serpentine minerals were the only secondary minerals to form during reaction of deionized water with lherzolite. However, changes in the fluid composition with time suggest evolution toward equilibrium between "serpentine" and diopside. The Ca concentration in the fluid was $2.2x10^{-5}$ *M* at the end of the experiment (720 hours). Closed-system reaction of water with lherzolite having a bulk-rock composition the same as that used in the latter experiment would produce an equilibrium mineral assemblage composed of serpentine, brucite and diopside in the simplified CaO-MgO-SiO_2-H_2O sub-system. For comparison, the calculated Ca concentration in water required for equilibrium with end-member chrysotile-brucite-diopside at 300°C and 300 bars is 3.6×10^{-4} molal (17 ppm).

Reaction of San Carlos olivine with 0.1 *M* $CaCl_2$ solution produced two steady state plateau concentrations for Mg ($3.3x10^{-4}$ *M* from 79 to 502 hours, and $4.3x10^{-4}$ *M* from 538 to 743 hours) and Si ($2.0x10^{-4}$ *M* from 31 to 123 hours, and $1.2x10^{-4}$ *M* from 170 to 502 hours after which concentrations dropped below detection). XRD and SEM investigations revealed that the neoformed solids were chrysotile, lizardite, brucite and magnetite. No Ca-bearing phase was detected. The experimental data indicate that $CaCl_2$-

bearing fluids have the potential to serpentinize rocks composed essentially of olivine without causing widespread Ca metasomatism.

At constant pressure and temperature, transformation of peridotite to Ca-rich mineral assemblages (tremolite and diopside) during serpentinization requires the addition of silica and calcium. This can be achieved in two ways: 1) infiltration-diffusion of these components from a Ca- and Si-rich fluid derived from a Si-rich lithology at the contact with ultramafic rocks, and 2) movement of Si from a Si-rich lithology into ultramafic rocks and a corresponding movement of Ca, from the ultramafic rocks into the Si-rich lithology. The relative magnitude of these two end-member processes will depend on whether mass transfer occurs via diffusion or advection (the direction of fluid flow becomes a factor in the latter case), and on the initial differences in composition of the fluids in the serpentinite from that of the fluids in the Si-rich rocks adjacent to these serpentinites.

With progressive fluid/rock reaction, it is predicted that the complementary assemblages in the serpentinites and in the Si-rich lithologies in contact with the serpentinite would evolve from tremolite-rich in the serpentinite and feldspar- and tremolite-rich in the Si-rich lithologies, respectively, to diopside-rich in the serpentinites and chlorite-, diopside-, vesuvianite-, and grossular-rich in the Si-rich lithologies, i.e., pervasive rodingitization is predicted to occur when the Si-rich lithologies become depleted in silica as a result of the transfer of the latter to the serpentinites.

INTRODUCTION

Serpentinization is the predominant type of hydrothermal alteration affecting ultramafic rocks. It is documented in the seafloor environment in extensional (Shand, 1949; Bonatti, 1968; Cannat, 1993; Agrinier et al., 1995) and supra-subduction settings (Haggerty, 1991), in obducted ophiolite complexes (Evans and Trommsdorff, 1970; Coleman and Keith, 1971; Labotka and Albee, 1979; Laurent and Hébert, 1979; Komor et al., 1985; Coulton et al., 1995; O'Hanley and Wicks, 1995), in layered ultramafic complexes (Anhaeusser, 1976) and in ultramafic lava flows. A number of reactions have been proposed for the serpentinization of ultramafic rocks, which depend on the composition of the fluid responsible for alteration, the composition of the rock, and the reaction paths followed (Toft et al., 1990; O'Hanley and Offler, 1992). A particularly important reference reaction is that defining the limit of stability of olivine at $P_{H_2O} = P_{Total}$: Olivine + H_2O = Serpentine ± Brucite ± Magnetite. According to this reaction, the temperature at which complete serpentinization of olivine-rich peridotites may occur is below 350-365°C at pressures of 1 to 2 kilobars (Moody, 1976). However, the transformation of peridotite to serpentinite depends on the availability of water (Sanford, 1981; Macdonald, 1984; Macdonald and Fyfe, 1985; O'Hanley, 1991). Hence the occasional preservation of the original silicate minerals in peridotite outcrops.

The types of fluids which induce serpentinization depend on the lithotectonic setting in which peridotites are exposed during their alteration. The vast majority of peridotites are anhydrous rock types and the material (magma or metamorphic mantle tectonites) from which they are derived contain only very small quantities of fluid. Consequently, the serpentinization of ultramafic rocks arises from hydration by externally derived fluids. In the case of sub-seafloor, extensional and supra-subduction settings, the serpentinizing fluids are considered to be seawater-derived (Wenner and Taylor, 1973; Agrinier et al., 1995) or of metamorphic or magmatic origin (Peacock, 1987; Sakai et al., 1990; Haggerty and Chaudhuri, 1992; Ishii et al., 1992; Mottl, 1992; Scambelluri et al., 1997), respectively. It is believed that a small proportion of magmatic fluid is present in black-smoker-type fluids in extensional settings (e.g., de Ronde, 1995), but this fluid is

probably insignificant with respect to the total amount of fluid involved in the pervasive serpentinization of peridotites in these environments. Furthermore, the magmatic fluid is expected to be locally distributed above magmatic centers. When slivers of oceanic crust are detached and transported onto continental margins to form ophiolite belts, sea water, metamorphic and magmatic waters, and even meteoric waters (Barnes and O'Neil, 1969; Wenner and Taylor, 1974) may play a role in serpentinization. However, no direct analytical data are available on the composition of the fluids causing serpentinization at the temperatures, which have been estimated from oxygen isotopic studies (i.e., ~ 100-350°C). Detailed analytical data on the composition of such fluids are restricted to low temperature environments (< 30°C: Barnes and O'Neil, 1969; Haggerty, 1991). Most of the data on the composition of serpentinizing fluids comes from studies of fluid inclusions in secondary diopside, olivine and titanian clinohumite from prograde metamorphosed serpentinites in obduction and subduction settings (Peretti et al., 1992; Scambelluri et al., 1997), and from rodingites (Schandl et al. 1989, 1990; Mittwede and Schandl, 1992; O'Hanley et al., 1992; Compagnoni et al., 1998; Chapter VI). These studies indicate that the fluids involved in serpentinization are electrolyte-rich, NaCl-dominant brines with salinities that vary between ~ 0 to 25 wt. % eq. NaCl. Analyses of serpentinites commonly show quantifiable amounts of chlorine, especially at the margins of serpentine veins and at the interface between olivine and serpentine in partially serpentinized peridotites (Rucklidge, 1972; Rucklidge and Patterson, 1977; Miura et al., 1981). Boron is also enriched in serpentinites (Bonatti et al., 1984; Seyfried et al., 1984; Bergeron, 1988). It is adsorbed by serpentinite minerals at low temperature. These observations support the suggestion that a saline fluid is commonly involved in serpentinization.

There are no data on the evolution of natural serpentinizing fluids at elevated temperatures. Until direct detailed information on the composition of such fluids is obtained, experimental simulations, using synthetic fluids, provide the best means to investigate their chemical evolution. Evolution of fluid composition during closed-system seawater- or modified seawater-peridotite interaction has been documented by experiments simulating serpentinization at temperatures between 200 and 500°C,

pressures between 400 and 1000 bars (this covers a range of P-T conditions of serpentinization, which can be related to alteration in the sub-seafloor environment and during obduction of ophiolites), and fluid/rock mass ratios that varied between 5 and 50 (Seyfried and Dibble, 1980; Hajash and Chandler, 1981; Janecky and Seyfried, 1986; Menzies et al., 1993; Kholodkevich and Barinov, 1995).

Rodingites are calcium-rich metasomatic rocks believed to have formed by interaction of serpentinizing fluids with Si-Al-rich rocks. Thus, they represent a window into what fluid compositions have the potential to cause such alteration in natural systems at elevated temperatures. To evaluate the potential of serpentinizing fluids to induce rodingitization, it is essential to know the composition of such fluids and to understand the behaviour of calcium during serpentinization. For this purpose, single-pass flow-through experiments were performed on olivine and lherzolite to evaluate the potential for concentration or loss of calcium during interaction of water and $CaCl_2$-bearing fluids with peridotite, and the ability of these fluids to induce rodingitization. Thermodynamic modelling was used in conjunction with the experimental observations to evaluate the potential of more complex, NaCl-bearing fluids equilibrated with serpentinite assemblages to induce rodingitization.

HYDROTHERMAL EXPERIMENTS

EXPERIMENTAL AND ANALYTICAL METHODS

Three hydrothermal experiments were performed using a single pass, flow-through system. The apparatus ("FT2-C" built by Coretest Systems, Inc.), which is designed to study open system water-rock interaction (Williams-Jones et al., 1994; Chapter II), was operated at a temperature of 300°C and a pressure up to 500 bars. The three experiments involved reacting water with olivine and lherzolite, and a 0.1 *M* $CaCl_2$ aqueous solution with olivine.

The materials used to perform the experiments were fragments of crushed San Carlos olivine purchased from Ward's Scientific Inc. and fragments of a mantle lherzolite

xenolith from Alligator Lake, Northwest Territories, Canada, provided by Dr. Donald C. Francis. The olivine and lherzolite samples were crushed in a Bico disk grinder, sieved, and the 97-250, 250-500 and 500-850 μm size fractions retained for the olivine-$CaCl_2$-H_2O, the olivine-H_2O and the lherzolite-H_2O experiments, respectively. The purpose of using finer grains in the olivine-$CaCl_2$ solution experiment was to achieve faster reaction and maximize the potential to reach equilibrium between fluid and rock, in order to provide a benchmark for evaluating the capacity of the fluid to induce calcium metasomatism. The larger grains were used in the lherzolite-water experiments to permit better resolution of the process by which calcium is released from pyroxene-bearing peridotites undergoing serpentinization. The fragments from the three size fractions were cleaned six times in alcohol in an ultrasonic bath. SEM examination of the cleaned fragments revealed that their surfaces were essentially free of adhering particles. A portion of the fragments was retained for X-ray diffraction analysis, and the remainder stored for 12 months to allow relaxation of strain and healing of distorted sites produced during grinding (Eggleston et al., 1989). No phases other than olivine were detected by X-ray diffraction, SEM examination and electron microprobe analyses of the San Carlos sample. Olivine, orthopyroxene, clinopyroxene and Cr-spinel were identified in the lherzolite (Tables 1 and 2). Before the start of the water-olivine experiment, a N_2(30%)-He(70%) B.E.T. (Brunauer et al., 1938) measurement was conducted on a portion of the stored grains of San Carlos olivine (250-500 μm) and showed them to have a specific surface area of 0.034 m^2/g.

The mineral fragments were placed in a 10 cm long titanium reaction cell (5.2 mm i.d.) and reacted with fluid for 1368, 811 and 743 hours in the olivine-H_2O, lherzolite-H_2O and olivine-$CaCl_2$-H_2O experiments, respectively. The olivine-H_2O and lherzolite-H_2O experiments were conducted using air-CO_2-saturated deionized water. In the olivine-0.1 *M* $CaCl_2$ solution experiment, the fluid was vacuum-boiled to remove most of the CO_2. The fluid flow was set at a rate of 12 mL/day. Fluid was sampled approximately every 40 hours for pH measurement and flame AA spectrophotometric analysis. The pH of a 1 mL aliquot was measured using an ORION RESEARCH microprocessor in

Table 1. Characteristics of the materials before and after reaction.

EXPERIMENT:	Olivine-H_2O	Lherzolite-H_2O	Olivine-$CaCl_2$ solution
Starting materials			
Grain size:	250-500 μm	500-850 μm	97-250 μm
Specific surface area:	0.034 m^2/g	—	—
Weight:	4.2100 g.	4.3036 g.	4.0245 g.
Composition:	Fo_{91}	Fo_{90} (64%), Opx (21%), Cpx (13%), Sp (2%).	Fo_{91}
Ca (a.p.f.u.) in olivine:	0.002	0.002	0.002
Ca (a.p.f.u.) in opx:	—	0.03	—
Ca (a.p.f.u.) in cpx:	—	0.76	—
After reaction			
Weight:	4.2360 g.	4.3146 g.	4.5641 g.
Secondary minerals:	Serp, bru, mt	Al-liz	Serp, bru, mt

Table 2. Average of electron microprobe analyses.

	San Carlos olivine	Alligator Lake lherzolite		
		Olivine	Orthopyroxene	Clinopyroxene
Number of analyses	20	6	6	5
wt. %				
SiO_2	40.85	40.88	54.04	51.29
TiO_2	0.00	0.01	0.12	0.50
Al_2O_3	0.01	0.02	4.81	6.76
Cr_2O_3	0.02	0.01	0.40	0.78
FeO	9.02	9.45	6.09	3.03
NiO	0.31	0.32	0.09	0.04
MnO	0.14	0.14	0.14	0.09
MgO	49.58	49.53	32.85	15.37
CaO	0.07	0.06	0.81	19.49
Na_2O	n.a.	n.a.	0.13	1.84
K_2O	n.a.	n.a.	0.01	0.01
Total	100.00	100.42	99.46	99.22
Formula				
Basis of calculation	4 oxygens	4 oxygens	6 oxygens	6 oxygens
Si	0.966	0.965	1.835	1.826
Ti	0.000	0.000	0.003	0.014
Al	0.000	0.001	0.205	0.302
Cr	0.000	0.000	0.011	0.024
Fe^{2+}	0.190	0.199	0.184	0.096
Ni	0.006	0.007	0.003	0.001
Mn	0.003	0.003	0.004	0.003
Mg	1.865	1.858	1.772	0.870
Ca	0.002	0.002	0.031	0.793
Na	—	—	0.008	0.136
K	—	—	0.001	0.001
Σ Cations	3.033	3.034	4.058	4.065

n.a.: Not analyzed

combination with a pH/millivoltmeter 811® and a KCl-filled electrode calibrated against three standards. Ten mL of fluid were acidified with 1 mL of 70 %, analytical grade HNO_3 for AA spectrophotometric analyses. Si, Mg, Fe, Ni and Ca were analysed with a Perkins Elmer 3100 AA spectrophotometer. Mn was analysed with a Zeeman-corrected graphite furnace AA spectrophotometer. At the end of each experiment, the reaction cell was dried for 5 hours on a hot plate at 120°C and weighed (Table 1).

Fragments of the reacted olivine and lherzolite were selected for examination of their surface features, and for identification of the secondary minerals. Fragment-mounts from the inlet, the center and the outlet of the reaction cell were coated with carbon for examination by SEM. Pt/C replicas of the surface of reacted olivine grains from the olivine-H_2O experiment were made for TEM examination (Chapter II). SEM imaging and chemical analyses were conducted with a JSM-840A SEM equipped with a Tracor Northern energy-dispersive X-ray spectrometer, operated at 10 kV and 20 nA. The reacted grains from the olivine-H_2O and the olivine-$CaCl_2$-H_2O experiments were ground gently in alcohol to remove the secondary minerals from their surfaces, and the suspension dried on a glass slide for X-ray diffraction analysis. A Rigaku D/MAX 2400 X-ray diffractometer using Cu K_α radiation (excitation at 40 kV and 120 mA) was employed for the analyses.

EXPERIMENTAL RESULTS

Fluid chemistry

In this section, we present the results of the elemental analysis of the fluids reacted with olivine and lherzolite, and provide an interpretation for the changes in the chemical composition of the fluid with time. Before starting our description of the experiments, some introductory comments on the temporal evolution of the fluid composition, depicted later as concentration-time profiles, are in order. Olivine and orthopyroxene are unstable in the presence of an aqueous fluid under the pressure and temperature conditions of our experiments. In a closed system, the equilibrium mineral assemblage formed by reaction of olivine and lherzolite with a large amount of water at these conditions is serpentine minerals + brucite ± magnetite ± diopside, because the primary silicates dissolve

irreversibly. However, in open, flow-through systems, olivine and pyroxenes may cease to dissolve if the reacting fluid becomes saturated with respect to these minerals, a condition which occurs when the rate of precipitation of the secondary minerals is insufficient to maintain the fluid composition in equilibrium with the latter.

During the experiments presented here, the concentration of each element in each fluid sample (≈ 20 mLs on average) reflected water-rock interaction after 22-25 passes of initially fresh fluid through a cell containing the grains of the reactants. Neglecting the change in the reactive surface area of the grains of reactants during dissolution, variations in the concentrations of the elements with time in the first few hours of reaction indicate that plug flow did not occur, because steady-state concentrations would have been established from the start of the experiments. Mountain (1992) showed, by flowing water containing a Li tracer through quartz (grain-size similar to those used in our experiments), that the mode of flow was laminar. The concentration-time profiles more accurately reflect, on the one hand, a concentration effect due to laminar flow, and, on the other hand, the combined effects of the diminution of the total surface area of the reactant solids due to the precipitation of secondary minerals on their surface and the increased proportion of surface area of the latter phases. Increases and decreases in the concentrations of the different elements are a function of variations in the rates of dissolution and precipitation, and levels of supersaturation and identity of the solid phases that precipitate. Concentration plateaus with respect to time for specific elements were achieved when there was a steady state balance in the rates of dissolution and precipitation of the phases that contain this element, or when a mineral or mineral assemblage acted as a buffer, as would be expected, for example, if the fluid equilibrated with serpentine and brucite through the reactions:

$$Mg_3Si_2O_5(OH)_4 + H_2O \leftrightarrow 3Mg(OH)_2 + 2SiO_2^\circ \quad (1)$$

and

$$Mg(OH)_2 + 2H^+ \leftrightarrow Mg^{2+} + 2H_2O \quad (2).$$

Olivine-H_2O experiment

Fluid samples collected during this experiment were analysed for Ca, Fe, Ni, Mg, Mn, and Si, the results for which are reported in Table 3 and presented as concentration-time profiles in Figure 1; the concentrations of Fe were below the detection limit (1.3×10^{-6} M) for the duration of the experiment. The concentration-time profiles for Si, Ni and Mn indicate that concentrations of these elements decreased sharply after the second sample and reached their peak values (3.1×10^{-4}, 5.1×10^{-6} and 2.2×10^{-11} *M*, respectively) near the start of the experiment. The concentration of Si dropped below the detection limit (7.8×10^{-5} *M*) in the fourth sample, i.e., after 98 hours. Concentrations of Ni and Mn also decreased very sharply in the second sample, then decreased gradually, falling below their respective detection limits after 316 hours of reaction.

A stoppage in fluid flow occurred after 440 hours of reaction due to complete exhaustion of the reservoir fluid. On resumption of fluid flow (after 459 hours), the concentration of these elements returned to detectable levels. While the Ni concentration again decreased to below the detection limit, this time after 693 hours of reaction, the Mn concentration fluctuated at or near the detection limit until approximately 1200 hours into the experiment, after which concentrations of both elements were consistently below detection. The concentration-time profile of Ca is similar to those of Si, Ni and Mn, except that Ca reached its peak concentration (9.7×10^{-6} *M*) in the second sample, and was not detected in the first sample (detection limit, 60 μg/L or 1.5×10^{-6} *M*); Ca concentrations decreased below the level of detection after 840 hours. The behaviour of Mg was in sharp contrast to that of the other elements. After a sharp decrease from 4.57×10^{-6} to 0.91×10^{-6} *M* between the first and second samples, Mg concentrations increased steadily reaching a maximum value of 5.94×10^{-6} *M* after 363 hours of reaction, and then decreasing to a value of 5.02×10^{-6} *M* just before the stoppage in fluid flow at 440 hours. After restoration of fluid flow, Mg concentrations increased sharply to a steady state plateau concentration of 8.2×10^{-6} *M* between 550 and 890 hours. Thereafter Mg concentrations increased slightly to a new plateau concentration of approximately

Table 3. Composition of the air-saturated water reacted with olivine.

Time in hours	pH		Elemental concentrations									
	25°C	300°C*	Si		Mg		Ni		Mn		Ca	
			mg/L	*M*	mg/L	*M*	mg/L	*M*	µg/L	*M*	mg/L	*M*
43.12	6.68	6.05	8.77	3.12E-04	0.11	4.57E-06	0.30	5.11E-06	12.33	2.24E-11	<D.L.	—
69.87	6.38	6.31	3.66	1.30E-04	0.02	9.13E-07	0.12	2.08E-06	1.10	2.00E-12	0.39	9.69E-06
97.95	6.23	6.16	2.41	8.58E-05	0.04	1.83E-06	0.16	2.65E-06	1.18	2.14E-12	0.20	4.99E-06
126.25	6.29	6.24	<D.L.	—	0.07	2.74E-06	0.16	2.65E-06	1.23	2.24E-12	0.22	5.54E-06
167.25	6.21	6.15	<D.L.	—	0.07	2.74E-06	0.16	2.65E-06	2.35	4.28E-12	0.14	3.60E-06
208.33	6.53	6.15	<D.L.	—	0.08	3.20E-06	0.12	2.08E-06	1.47	2.67E-12	0.12	3.05E-06
241.33	6.47	6.20	<D.L.	—	0.10	4.11E-06	0.10	1.70E-06	1.74	3.17E-12	0.12	3.05E-06
269.33	6.54	6.23	<D.L.	—	0.11	4.57E-06	0.10	1.70E-06	1.31	2.38E-12	0.12	3.05E-06
315.83	6.51	6.26	<D.L.	—	0.12	5.02E-06	0.09	1.51E-06	0.58	1.05E-12	0.13	3.32E-06
362.83			<D.L.	—	0.14	5.94E-06	<D.L.	—	<D.L.	—	0.13	3.32E-06
407.33	6.56	6.30	<D.L.	—	0.13	5.48E-06	<D.L.	—	<D.L.	—	0.14	3.60E-06
438.16	6.71	6.28	<D.L.	—	0.12	5.02E-06	<D.L.	—	<D.L.	—	0.14	3.60E-06
503.33	6.50	6.46	<D.L.	—	0.19	7.76E-06	0.13	2.27E-06	5.84	1.06E-11	0.26	6.37E-06
549.58	6.18	6.36	<D.L.	—	0.20	8.22E-06	0.13	2.27E-06	1.58	2.87E-12	0.09	2.22E-06
595.58	6.25	6.33	<D.L.	—	0.19	7.76E-06	0.12	2.08E-06	0.78	1.41E-12	0.08	1.94E-06
644.83	6.31	6.33	<D.L.	—	0.19	7.76E-06	0.10	1.70E-06	1.39	2.53E-12	0.08	1.94E-06
692.83	6.01	6.34	<D.L.	—	0.20	8.22E-06	<D.L.	—	<D.L.	—	0.07	1.66E-06
740.66	6.35	6.29	<D.L.	—	0.20	8.22E-06	<D.L.	—	0.79	1.43E-12	<D.L.	—
791.66	6.09	6.34	<D.L.	—	0.20	8.22E-06	<D.L.	—	<D.L.	—	0.07	1.66E-06
838.66	6.37	6.35	<D.L.	—	0.20	8.22E-06	<D.L.	—	<D.L.	—	0.07	1.66E-06
887.66	6.31	6.33	<D.L.	—	0.20	8.22E-06	<D.L.	—	<D.L.	—	<D.L.	—
935.66	6.44	6.33	n.a.	—	0.22	9.13E-06	n.a.	—	0.85	1.56E-12	n.a.	—
983.99	6.40	6.37	n.a.	—	0.24	1.00E-05	n.a.	—	<D.L.	—	n.a.	—
1033.99	6.50	6.35	n.a.	—	0.23	9.59E-06	n.a.	—	<D.L.	—	n.a.	—
1080.07	6.56	6.35	n.a.	—	0.23	9.59E-06	n.a.	—	<D.L.	—	n.a.	—
1130.15	6.61	6.33	n.a.	—	0.22	9.13E-06	n.a.	—	<D.L.	—	n.a.	—
1177.73	6.63		n.a.	—	0.23	9.59E-06	n.a.	—	0.83	1.52E-12	n.a.	—

Table 3. (Continued)

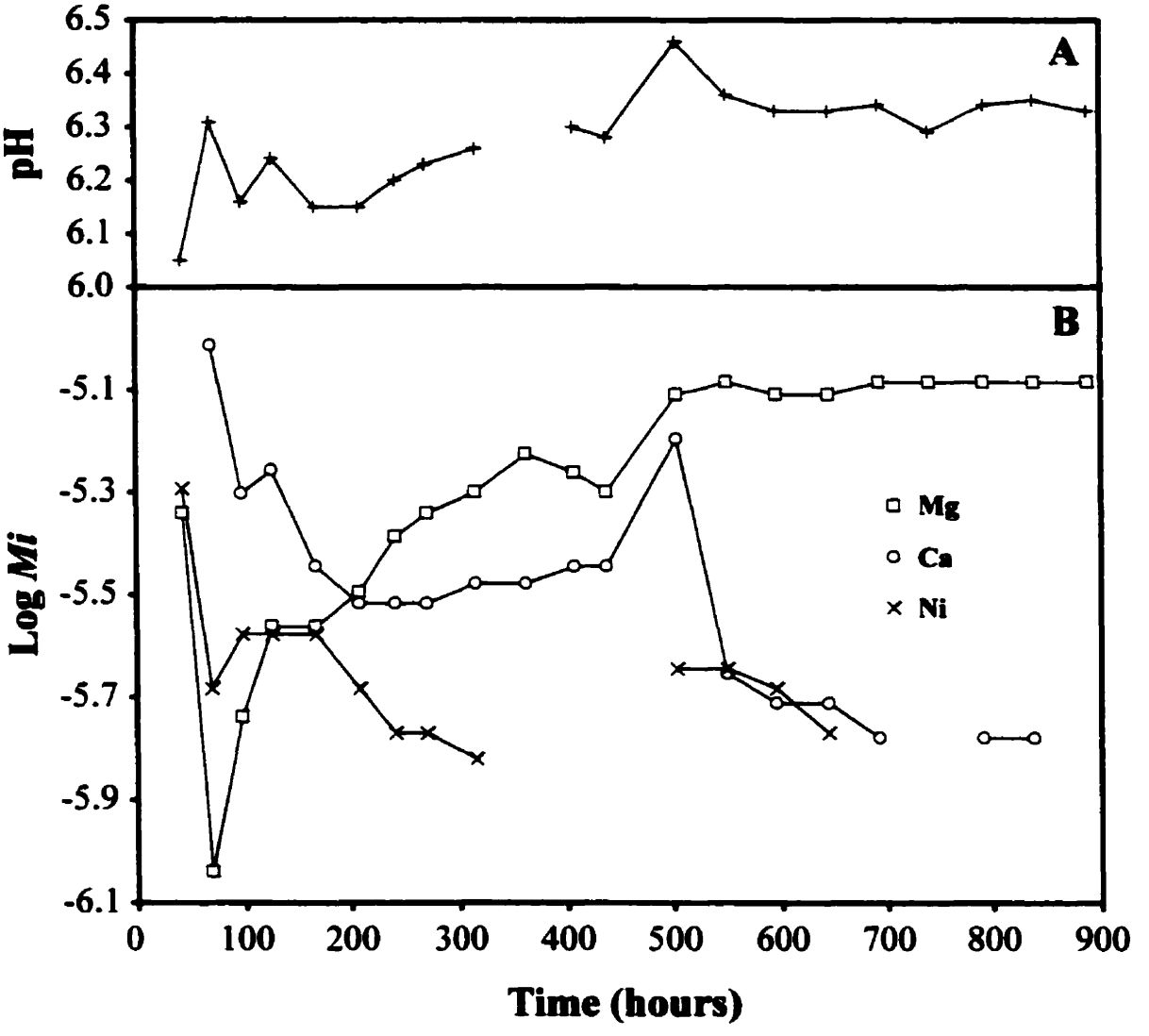
Time in hours	pH		Elemental concentrations									
	25°C	300°C*	Si		Mg		Ni		Mn		Ca	
			mg/L	*M*	mg/L	*M*	mg/L	*M*	µg/L	*M*	mg/L	*M*
1244.48	6.67		n.a.	—	0.23	9.59E-06	n.a.	—	<D.L.	—	n.a.	—
1294.98	6.70		n.a.	—	0.22	9.13E-06	n.a.	—	<D.L.	—	n.a.	—
1367.98	6.70		n.a.	—	0.22	9.13E-06	n.a.	—	<D.L.	—	n.a.	—

<D.L.: Below detection limit; n.a.: Not analyzed.

Detection limits: Si=7.83×10^{-3} *M*, Mg=1.23×10^{-7} *M*, Ni=1.36×10^{-6} *M*, Mn=1.82×10^{-13} *M*, Ca=1.5×10^{-6} *M*.

Figure 1

pH-time and concentration-time profiles for Ca, Ni and Mg in water during reaction with olivine.


A
B
pH
Log Mi
6.5
6.4
6.3
6.2
6.1
6.0
-5.1
-5.3
-5.5
-5.7
-5.9
-6.1
Mg
Ca
Ni
0
100
200
300
400
500
600
700
800
900
Time (hours)

$9.5x10^{-6}$ *M* at 980 hours, which was maintained for the remainder of the experiment. The concentration of Fe was below its detection limit (70 μg/L or $1.25x10^{-6}$ *M*) throughout the duration of the experiment.

Lherzolite-H_2O experiment

Analytical data for the concentrations of Si, Mg, Fe, and Ca in samples of fluid collected during the course of the experiment are reported in Table 4, and illustrated as a function of time in Figure 2. The concentration of Mg increased rapidly during the first 48 hours of the experiment to a first steady-state value of $1.81x10^{-6}$ *M* at 56 hours, which was maintained for the next 105 hours. Between 161 and 234 hours into the experiment, Mg concentrations decreased sharply to a new steady-state value of $4.5x10^{-7}$ *M*, which lasted until 334 hours. Thereafter, Mg concentrations decreased to below the detection limit of $1.65x10^{-7}$ *M*.

The concentration of Ca increased slowly and steadily from a level below its limit of detection (60 μg/L or $1.5x10^{-6}$ *M*) at the beginning of the experiment to a value of $5.24x10^{-6}$ *M* in the seventh sample (234 hours). After 286 hours of reaction, the Ca concentration in the fluid increased suddenly from $5x10^{-6}$ to $1.1x10^{-5}$ *M*. After this, the Ca concentration and pH continued to increase smoothly for the remainder of the experiment which lasted 811 hours (Figure 2).

The concentration of Si decreased sharply from above $1.22x10^{-3}$ *M* to $4.7x10^{-4}$ *M* during the first 56 hours of reaction, remained approximately constant at a value of $5x10^{-4}$ *M* between 56 and 129 hours, and decreased slowly to a value of $3.4x10^{-5}$ *M* after 286 hours of reaction. Thereafter, the concentration of Si decreased rapidly and dropped below the detection limit of $7.83x10^{-5}$ *M* after 405 hours of reaction.

The Fe concentration increased slowly from a value of $5.7x10^{-6}$ *M* to a maximum value of $8.2x10^{-6}$ *M* after 129 hours of reaction, and then decreased smoothly to a value of $6.5x10^{-6}$ *M* after 286 hours of reaction. At approximately 334 hours, Fe concentrations decreased sharply to below the detection limit of $1.25x10^{-6}$ *M*.

Table 4. Composition of the air-saturated water reacted with lherzolite.

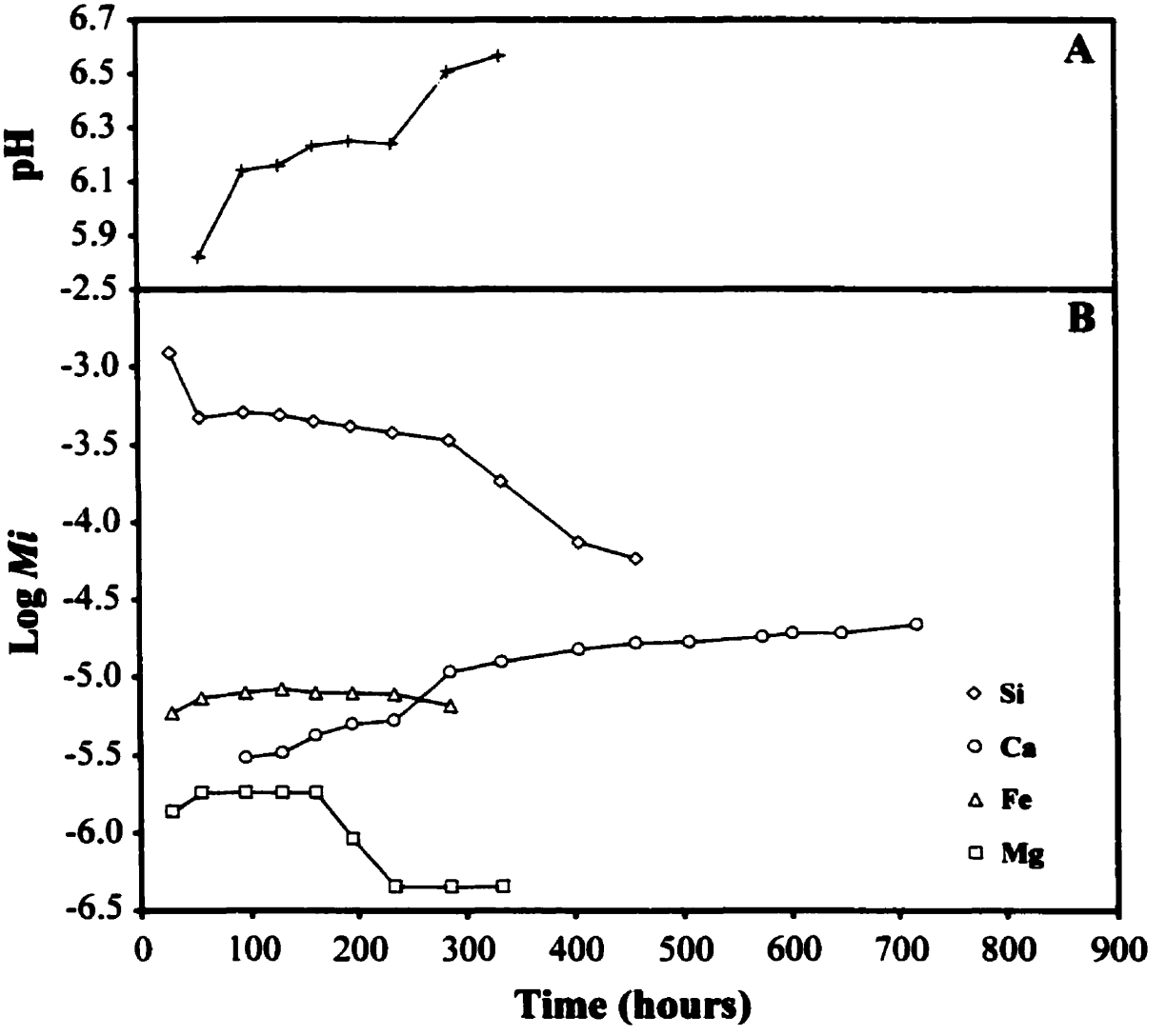
Time in hours	pH		Elemental concentrations							
	25°C	300°C*	Si		Mg		Fe		Ca	
			mg/L	*M*	mg/L	*M*	mg/L	*M*	mg/L	*M*
28.50	8.66		34.29	1.22E-03	0.004	1.65E-07	0.32	5.73E-06	<D.L.	—
55.75	6.8	5.82	13.27	4.72E-04	0.044	1.81E-06	0.40	7.16E-06	<D.L.	—
95.83	6.9	6.14	14.21	5.06E-04	0.044	1.81E-06	0.43	7.70E-06	0.12	2.99E-06
129.00	7.01	6.16	13.81	4.92E-04	0.044	1.81E-06	0.46	8.24E-06	0.13	3.24E-06
161.00	7.2	6.23	12.58	4.48E-04	0.044	1.81E-06	0.43	7.70E-06	0.17	4.24E-06
194.17	7.63	6.25	11.65	4.15E-04	0.022	9.05E-07	0.43	7.70E-06	0.2	4.99E-06
233.84	7.8	6.24	10.53	3.75E-04	0.011	4.53E-07	0.42	7.52E-06	0.21	5.24E-06
285.51	7.95	6.51	9.51	3.39E-04	0.011	4.53E-07	0.36	6.45E-06	0.43	1.07E-05
334.18	8.16	6.57	5.17	1.84E-04	0.011	4.53E-07	<D.L.	—	0.5	1.25E-05
404.85	8.28		*2.07*	*7.37E-05*	<D.L.	—	<D.L.	—	0.61	1.52E-05
457.85	8.51		*1.65*	*5.87E-05*	<D.L.	—	<D.L.	—	0.66	1.65E-05
506.02	8.51		<D.L.	—	<D.L.	—	<D.L.	—	0.67	1.67E-05
573.19	8.58		<D.L.	—	<D.L.	—	<D.L.	—	0.73	1.82E-05
600.69	—		<D.L.	—	<D.L.	—	<D.L.	—	0.77	1.92E-05
646.69	—		<D.L.	—	<D.L.	—	<D.L.	—	0.77	1.92E-05
717.69	8.7		<D.L.	—	<D.L.	—	<D.L.	—	0.87	2.17E-05
767.27	8.91		<D.L.	—	n.a.	—	n.a.	—	n.a.	—
811.27	8.78		<D.L.	—	n.a.	—	n.a.	—	n.a.	—

*: pH calculated with EQ3/6; <D.L.: Below detection limit; n.a.: Not analyzed.

Detection limits: Si=7.83×10^{-5} *M*, Mg=1.65×10^{-7} *M*, Fe=1.25×10^{-6} *M*, Ca=1.25×10^{-6} *M*.

Figure 2

pH-time and concentration-time profiles for Si, Mg, Fe, and Ca in water during reaction with lherzolite.


A
B
pH
Log Mi
Time (hours)
Si
Ca
Fe
Mg
6.7
6.5
6.3
6.1
5.9
-2.5
-3.0
-3.5
-4.0
-4.5
-5.0
-5.5
-6.0
-6.5
0
100
200
300
400
500
600
700
800
900

Olivine-0.1 M $CaCl_2$ solution experiment

Unlike the olivine-H_2O experiment, Fe was present in addition to Ca, Mg and Si in the effluent from reaction of olivine with the 0.1 *M* $CaCl_2$ solution (Table 5), although its concentration was at or near the limit of detection (0.1 mg/L or 1.79×10^{-6} *M*). A steady state concentration for Mg (3.2×10^{-4} *M*) developed from 79 to 502 hours, and a second, higher steady state concentration (4.3×10^{-4} *M*) was established from 538 to 743 hours (Figure 3). The concentration of Si also attained two steady state values (2.0×10^{-4} *M* from 31 to 123 hours, and 1.2×10^{-4} *M* from 170 to 502 hours) after which it dropped to very low concentrations. The Ca concentration in the fluid dropped to 0.093 *M* during the first 123 hours of reaction, after which it returned to its initial value.

Products of reaction

Olivine-H_2O experiment

SEM and TEM observations of the reacted olivine from this experiment were presented in detail in Chapter II and are only summarized here. Near the inlet of the reaction-cell, the olivine showed signs of extensive dissolution in the form of etch pits. Towards the outlet of the reaction cell, there were fewer signs of dissolution and the olivine grains were increasingly covered by coatings of neoformed minerals. These minerals were identified as "serpentine" (lizardite, polygonal serpentine, conical serpentine, and chrysotile), brucite (pseudohexagonal platelets) and magnetite (octahedral) based on SEM-EDS (Table 6) and XRD analyses. The total mass gain of solids after reaction was 26 mg or 0.6 % relative to the initial mass of olivine.

Lherzolite-H_2O experiment

SEM examination of the surfaces of olivine, orthopyroxene, clinopyroxene and spinel revealed that all are covered with a coating of platy (lizardite) or, rarely, fibrous (chrysotile) serpentine-group minerals (Figure 4). No other neoformed minerals were observed on the surface of the primary silicates. Titanite and a Ca-Ti oxide were identified by EDS on the inlet and outlet frits. There was an increase of 0.3 % (11 mg) of

Table 5. Composition of the 0.1 *M* $CaCl_2$ solution reacted with olivine.

Time in hours	pH		Elemental concentrations							
	25°C	300°C*	Si		Mg		Fe		Ca	
			mg/L	*M*	mg/L	*M*	mg/L	*M*	mg/L	*M*
0	5.02	4.81	<D.L.	—	0.01	4.11E-07	<D.L.	—	3993.85	0.100
31.28	7.81	4.91	6.4	2.28E-04	5.64	2.32E-04	<D.L.	—	3798.74	0.095
79.03	9.05	5.26	5.4	1.92E-04	7.62	3.14E-04	0.11	1.97E-06	3725.85	0.093
123.2	9.88	5.86	5.8	2.07E-04	7.41	3.05E-04	0.12	2.15E-06	3722.73	0.093
169.53	9.86	5.69	2.8	9.97E-05	7.51	3.09E-04	<D.L.	—	3880.69	0.097
214.2	9.88	5.72	3.1	1.10E-04	7.80	3.21E-04	<D.L.	—	3865.29	0.096
266.2	10.03	5.84	3.1	1.10E-04	8.15	3.35E-04	<D.L.	—	3906.21	0.097
332.2	10.27	5.99	3.3	1.17E-04	8.04	3.31E-04	<D.L.	—	3821.07	0.095
383.2	10.33		3.3	1.17E-04	8.10	3.33E-04	<D.L.	—	3905.11	0.097
430.2	10.16	5.95	3.6	1.28E-04	7.70	3.17E-04	<D.L.	—	3916.99	0.098
502.2	10.26	5.98	4.2	1.50E-04	8.15	3.35E-04	<D.L.	—	3881.24	0.097
538.2	10.15	5.87	2.0	7.12E-05	10.45	4.30E-04	0.13	2.33E-06	3965.50	0.099
624.7	10.34	5.94	<D.L.	—	10.34	4.25E-04	0.12	2.15E-06	3858.25	0.096
667.2	10.15	5.75	<D.L.	—	10.34	4.25E-04	0.13	2.33E-06	3990.25	0.100
742.95	10.16	5.76	<D.L.	—	10.34	4.25E-04	0.14	2.51E-06	3866.50	0.096

*: pH calculated with EQ36; <D.L.: Below detection limit.

Detection limits: Si=7.83×10^{-3} *M*, Mg=1.23×10^{-7} *M*, Fe=1.79×10^{-6} *M*, Ca=1.5×10^{-6} *M*.

Figure 3

pH-time and concentration-time profiles for Si, Mg, Fe, and Ca in the fluid during reaction of the 0.1 *M* $CaCl_2$ solution with olivine.

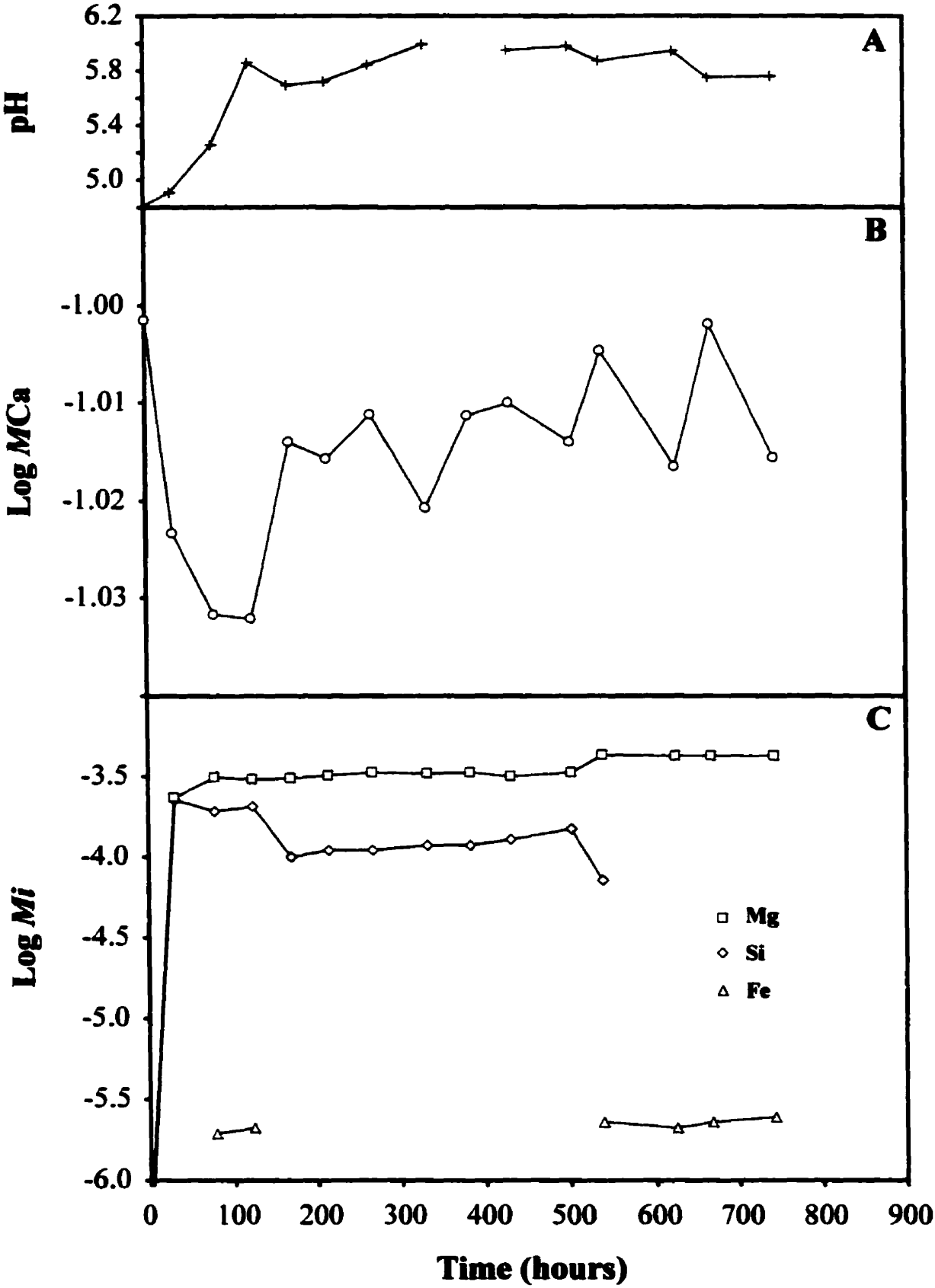

A
B
C
pH
6.2
5.8
5.4
5.0
Log MCa
-1.00
-1.01
-1.02
-1.03
Log Mi
-3.5
-4.0
-4.5
-5.0
-5.5
-6.0
Mg
Si
Fe
0
100
200
300
400
500
600
700
800
900
Time (hours)

Table 6. SEM-EDS analyses of secondary minerals formed after reaction of San Carlos olivine with water.

	Brc	Brc	Srp	Srp	Srp	Srp
wt. %						
SiO2	8.98	0.57	45.49	45.47	45.32	45.05
MgO	87.30	93.06	51.11	51.07	51.25	49.42
FeO	3.37	5.73	3.06	3.10	3.40	5.52
NiO	0.36	0.64	3.06	0.36	0.03	0.00

Brc: Brucite; Srp: Serpentine.

Figure 4

SEM photograph of (a) fibrous and (b) platy secondary serpentine on olivine from near the inlet of the reaction cell.


A
SEI
McGill 15 0kV
10μmF1 L01
X1,500


B
SEI
McGill 15 0kV
10μmF1 L01
X2,300

the total mass of solids relative to the initial mass of olivine. The surface of the original mineral was exposed in a small number of grains due to detachment of the coating during extraction of the solids from the reaction cell. These surfaces generally showed signs of dissolution in the form of etch pits. One grain of diopside displayed euhedral, oriented prism-like features but it is not certain whether they represent products of precipitation or dissolution.

By far the most abundant serpentine phase formed platelets and was interpreted to be lizardite. Fibrous serpentine (chrysotile) was observed only on one olivine grain, which had been located near the inlet of the reaction cell. The composition of the serpentine varied strongly as a function of the mineral on which it was grown. The Fe and Al contents of lizardite overgrowths decreased and increased, respectively, from olivine through orthopyroxene to clinopyroxene, consistent with the original Fe and Al contents of these minerals (Figure 5, Table 7). Lizardite grown on olivine near the outlet of the reaction cell was richer in Fe than that grown on olivine near the inlet. Chrysotile had the lowest contents of Fe and Al of any serpentine analysed.

Brucite did not form during the lherzolite-water experiment because the activity of silica in solution was too high. The absence of magnetite, however, suggests that, in contrast to the olivine-water experiment, all the available Fe was allowed to enter into the structure of the serpentines. Furthermore, inverse correlation between Si and Mg+Fe in serpentine grown on olivine suggests that Si^{4+} was substituted by Fe^{3+} in the tetrahedral layers. A reaction which might explain this absence of magnetite is:

$$Fe_3^{2+}Si_2O_5(OH)_4 + 1/3Fe_3O_4 + 2/3H_2O = Fe_2^{2+}Fe_2^{3+}SiO_5(OH)_4 + SiO_2^{\circ} + 2/3H_2 \qquad (3).$$

If this reaction took place, it would indicate that f_{H_2} was lower in the lherzolite-water experiment than in the olivine-water experiment. Because the surface area of the reactant was less in the lherzolite-water experiment (larger grain-size), the air-saturated water probably preserved its oxidizing potential more effectively.

Figure 5

Al versus Fe concentration in atoms per formula unit (a.p.f.u.) in serpentine grown on olivine (ol), orthopyroxene (opx) and clinopyroxene (cpx) from near the inlet of the reaction cell, and on olivine from near the outlet of the reaction cell during reaction of lherzolite with water. Al and Fe in the serpentine were determined from SEM-EDS analyses, and the formula of the serpentinite minerals was calculated based on 9 oxygen.

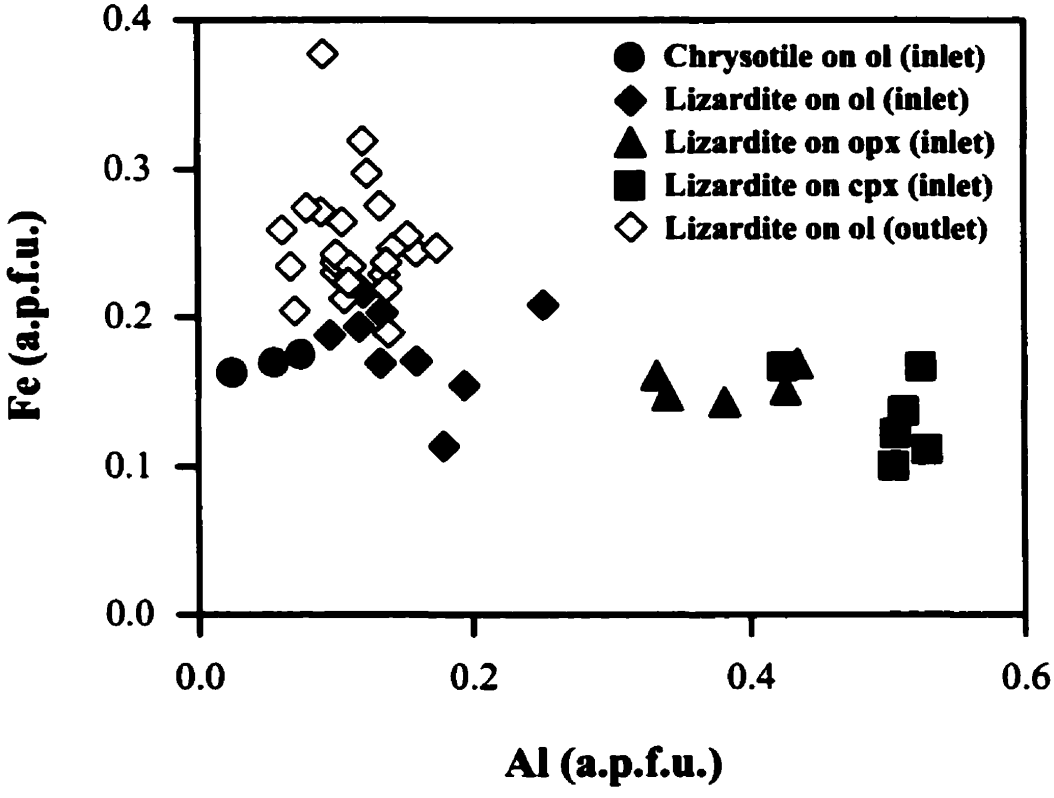

0.4
0.3
0.2
0.1
0.0
Fe (a.p.f.u.)
0.0
0.2
0.4
0.6
Al (a.p.f.u.)
Chrysotile on ol (inlet)
Lizardite on ol (inlet)
Lizardite on opx (inlet)
Lizardite on cpx (inlet)
Lizardite on ol (outlet)

Table 7a. SEM-EDS analyses of serpentine grown on olivine near the inlet of the reaction-cell during reaction of Alligator Lake lherzolite with water.

Type	Fibrous	Fibrous	Fibrous	Platy	Platy	Platy	Platy	Platy	Platy	Platy
wt. %										
SiO_2	45.46	45.39	45.68	46.11	46.12	46.12	45.25	45.04	44.75	45.76
Cr_2O_3	0.00	0.01	0.00	0.00	0.00	0.00	0.00	0.05	0.39	0.00
Al_2O_3	0.50	1.54	1.12	2.45	2.41	1.98	3.99	3.25	5.14	3.71
MgO	48.35	47.50	47.76	45.13	45.89	45.90	46.12	46.62	43.57	47.25
FeO	4.65	5.01	4.88	6.27	5.58	5.43	4.49	4.92	6.00	3.28
NiO	0.98	0.28	0.43	0.00	0.00	0.11	0.15	0.13	0.00	0.00
CaO	0.06	0.26	0.13	0.03	0.00	0.46	0.00	0.00	0.16	0.00
Na_2O	n.a.	n.a.	n.a.	n.a.	n.a.	n.a.	n.a.	n.a.	n.a.	n.a.
Formula (7 oxygens)										
Si	1.89	1.88	1.89	1.91	1.90	1.91	1.86	1.86	1.85	1.87
Cr	0.00	0.00	0.00	0.00	0.00	0.00	0.00	0.00	0.01	0.00
Al	0.02	0.08	0.05	0.12	0.12	0.10	0.19	0.16	0.25	0.18
Mg	2.99	2.93	2.95	2.78	2.82	2.83	2.83	2.87	2.69	2.88
Fe	0.16	0.17	0.17	0.22	0.19	0.19	0.15	0.17	0.21	0.11
Ni	0.03	0.01	0.01	0.00	0.00	0.00	0.01	0.00	0.00	0.00
Ca	0.00	0.01	0.01	0.00	0.00	0.02	0.00	0.00	0.01	0.00
Na	—	—	—	—	—	—	—	—	—	—
Σ Cations	5.10	5.08	5.08	5.03	5.04	5.04	5.04	5.06	5.02	5.04

n.a.: Not analyzed.

Table 7a. (Continued)

Type	Platy	Platy
wt. %		
SiO_2	44.61	44.04
Cr_2O_3	0.46	0.19
Al_2O_3	2.70	2.74
MgO	46.73	47.15
FeO	4.86	5.84
NiO	0.64	0.04
CaO	0.00	0.01
Na_2O	n.a.	n.a.
Formula (7 oxygens)		
Si	1.85	1.83
Cr	0.02	0.01
Al	0.13	0.13
Mg	2.89	2.92
Fe	0.17	0.20
Ni	0.02	0.00
Ca	0.00	0.00
Na	—	—
Σ Cations	5.08	5.10

n.a.: Not analyzed.

Table 7b. SEM-EDS analyses of serpentine grown on olivine near the outlet of the reaction-cell during reaction of Alligator Lake lherzolite with water.

Type	Platy	Platy	Platy	Platy	Platy	Platy	Platy	Platy	Platy	Platy
wt. %										
SiO_2	47.09	44.72	46.49	45.51	44.87	46.61	45.97	45.85	46.57	45.01
Cr_2O_3	0.67	0.31	0.00	0.00	0.13	0.00	0.00	0.03	0.00	0.11
Al_2O_3	3.23	3.55	2.06	2.06	1.37	2.79	2.18	1.81	2.07	2.80
MgO	41.66	44.19	44.81	45.55	46.55	43.78	45.57	44.32	44.25	45.58
FeO	7.03	7.06	6.64	6.82	6.71	6.62	6.14	7.74	6.97	6.32
NiO	0.25	0.06	0.00	0.00	0.31	0.19	0.12	0.00	0.00	0.18
CaO	0.07	0.12	0.00	0.06	0.07	0.01	0.02	0.25	0.14	0.00
Na_2O	n.a.	n.a.	n.a.	n.a.	n.a.	n.a.	n.a.	n.a.	n.a.	n.a.
Formula (7 oxygens)										
Si	1.95	1.86	1.93	1.89	1.87	1.93	1.90	1.91	1.93	1.87
Cr	0.02	0.01	0.00	0.00	0.00	0.00	0.00	0.00	0.00	0.00
Al	0.16	0.17	0.10	0.10	0.07	0.14	0.11	0.09	0.10	0.14
Mg	2.57	2.74	2.77	2.82	2.90	2.70	2.81	2.76	2.74	2.82
Fe	0.24	0.25	0.23	0.24	0.23	0.23	0.21	0.27	0.24	0.22
Ni	0.01	0.00	0.00	0.00	0.01	0.01	0.00	0.00	0.00	0.01
Ca	0.00	0.01	0.00	0.00	0.00	0.00	0.00	0.01	0.01	0.00
Na	—	—	—	—	—	—	—	—	—	—
Σ Cations	4.96	5.04	5.02	5.06	5.09	5.00	5.04	5.04	5.02	5.06

n.a.: Not analyzed.

Table 7b. (continued)

Type	Platy	Platy	Platy	Platy	Platy	Platy	Platy	Platy	Platy	Platy
wt. %										
SiO_2	45.56	47.97	46.40	45.76	46.63	47.10	46.89	46.80	46.37	46.47
Cr_2O_3	0.32	0.01	0.00	0.02	0.02	0.00	0.00	0.00	0.00	0.04
Al_2O_3	2.49	1.60	2.30	2.26	3.10	2.91	2.80	2.69	2.43	2.15
MgO	42.32	42.31	44.88	45.13	42.26	42.86	43.05	42.05	41.39	43.29
FeO	8.46	7.87	6.43	6.74	7.33	7.13	6.82	7.90	9.09	7.56
NiO	0.53	0.00	0.00	0.00	0.18	0.00	0.17	0.52	0.67	0.27
CaO	0.33	0.23	0.00	0.09	0.48	0.00	0.28	0.03	0.05	0.22
Na_2O	n.a.	n.a.	n.a.	n.a.	n.a.	n.a.	n.a.	n.a.	n.a.	n.a.
Formula (7 oxygens)										
Si	1.91	1.99	1.92	1.90	1.94	1.95	1.94	1.95	1.94	1.94
Cr	0.01	0.00	0.00	0.00	0.00	0.00	0.00	0.00	0.00	0.00
Al	0.12	0.08	0.11	0.11	0.15	0.14	0.14	0.13	0.12	0.11
Mg	2.65	2.62	2.77	2.79	2.62	2.64	2.66	2.61	2.59	2.69
Fe	0.30	0.27	0.22	0.23	0.25	0.25	0.24	0.28	0.32	0.26
Ni	0.02	0.00	0.00	0.00	0.01	0.00	0.01	0.02	0.02	0.01
Ca	0.01	0.01	0.00	0.00	0.02	0.00	0.01	0.00	0.00	0.01
Na	—	—	—	—	—	—	—	—	—	—
Σ Cations	5.02	4.97	5.02	5.04	4.99	4.98	4.99	4.99	5.00	5.01

n.a.: Not analyzed.

Table 7b. (Continued)

Type	Platy	Platy	Platy	Platy	Platy
wt. %					
SiO_2	45.87	45.88	48.33	47.18	45.36
Cr_2O_3	0.62	0.33	0.00	0.00	0.11
Al_2O_3	1.24	1.82	1.43	2.86	2.24
MgO	44.09	40.19	43.55	43.80	45.48
FeO	7.38	10.64	5.92	5.49	6.43
NiO	0.75	1.10	0.60	0.45	0.11
CaO	0.06	0.05	0.17	0.22	0.25
Na_2O	n.a.	n.a.	n.a.	n.a.	n.a.
Formula (7 oxygens)					
Si	1.92	1.95	1.99	1.94	1.89
Cr	0.02	0.01	0.00	0.00	0.00
Al	0.06	0.09	0.07	0.14	0.11
Mg	2.75	2.54	2.68	2.69	2.82
Fe	0.26	0.38	0.20	0.19	0.22
Ni	0.03	0.04	0.02	0.02	0.00
Ca	0.00	0.00	0.01	0.01	0.01
Na	—	—	—	—	—
Σ Cations	5.04	5.00	4.97	4.99	5.06

n.a.: Not analyzed.

Table 7c. SEM-EDS analyses of serpentine grown on orthopyroxene near the inlet of the reaction-cell during reaction of Alligator Lake lherzolite with water.

Type	Platy	Platy	Platy	Platy	Platy
wt. %					
SiO_2	42.65	43.14	43.17	42.63	43.35
Cr_2O_3	0.29	0.00	0.19	0.00	0.10
Al_2O_3	8.81	8.97	7.02	7.86	6.85
MgO	43.69	42.70	45.00	45.02	44.77
FeO	4.38	4.90	4.28	4.15	4.66
NiO	0.18	0.17	0.32	0.34	0.27
CaO	0.00	0.12	0.01	0.00	0.00
Na_2O	n.a.	n.a.	n.a.	n.a.	n.a.
Formula (7 oxygens)					
Si	1.75	1.77	1.78	1.76	1.79
Cr	0.01	0.00	0.01	0.00	0.00
Al	0.43	0.44	0.34	0.38	0.33
Mg	2.68	2.62	2.76	2.76	2.75
Fe	0.15	0.17	0.15	0.14	0.16
Ni	0.01	0.01	0.01	0.01	0.01
Ca	0.00	0.01	0.00	0.00	0.00
Na	—	—	—	—	—
Σ Cations	5.03	5.01	5.05	5.05	5.04

n.a.: Not analyzed.

Table 7d. SEM-EDS analyses of serpentine grown on clinopyroxene near the inlet of the reaction-cell during reaction of Alligator Lake lherzolite with water.

Type	Platy	Platy	Platy	Platy	Platy	Platy
wt. %						
SiO_2	41.62	41.74	41.89	40.81	41.34	41.22
Cr_2O_3	0.45	0.00	0.16	0.31	0.59	0.20
Al_2O_3	8.71	10.58	10.49	10.95	10.45	10.75
MgO	43.70	43.03	44.29	44.10	43.51	41.75
FeO	4.80	3.97	2.91	3.21	3.50	4.77
NiO	0.56	0.66	0.00	0.35	0.35	1.30
CaO	0.17	0.02	0.27	0.28	0.20	0.01
Na_2O	0.00	0.00	0.00	0.00	0.00	0.00
Formula (7 oxygens)						
Si	1.72	1.72	1.71	1.68	1.70	1.71
Cr	0.01	0.00	0.01	0.01	0.02	0.01
Al	0.43	0.51	0.51	0.53	0.51	0.52
Mg	2.70	2.64	2.70	2.70	2.67	2.58
Fe	0.17	0.14	0.10	0.11	0.12	0.17
Ni	0.02	0.02	0.00	0.01	0.01	0.04
Ca	0.01	0.00	0.01	0.01	0.01	0.00
Na	0.00	0.00	0.00	0.00	0.00	0.00
Σ Cations	5.06	5.03	5.03	5.05	5.04	5.03

Olivine-0.1 M $CaCl_2$ solution experiment

The olivine was altered to a much greater extent in this experiment than when reacted with deionized water. This is attributed to the smaller grain-size of the reactant (larger surface for reaction) and the slightly acidic nature of the $CaCl_2$ solution (pH ~ 4.8 at 300°C, 300 bars). The material filling the cell after reaction formed a compact mass, which was very difficult to remove. This suggests clearly that the ΔV of the overall reaction was strongly positive and sufficient to ensure that the product minerals nearly filled the initial intergranular porosity (cell volume = 2.132 cm^3; volume of olivine = 1.23 cm^3; initial porosity ~ 42%; transient water/rock ratio = 0.72). SEM examination of the run products revealed that a significant proportion of the original olivine was consumed during reaction. The total mass gain of the starting materials after reaction was 0.54 gram or 12 % relative to the original mass of olivine. Olivine grains free of coatings of neoformed minerals presented well developed euhedral outlines created by extensive dissolution. The neoformed solids were serpentine (fibrous and platy; Table 8), abundant tabular brucite, and magnetite (in cubo-octahedral crystals near the inlet, and in octahedral crystals near the outlet). No Ca-bearing phase was detected. XRD investigation of the run products confirmed the presence of serpentine, brucite and magnetite.

REACTION PROGRESS

Olivine-H_2O experiment

The concentration-time profiles in Figure 1 indicate that reaction progressed through three stages. The first stage, between the start of the experiment and 70 hours into the experiment, involved rapid dissolution of olivine. This would have been facilitated by the availability of large numbers of high energy surfaces, such as low radius-of-curvature surface features and microcracks (Eggleston et al., 1989), and is manifested by peak concentrations of Si, Mg, Ca, Ni, and Mn in the first sample. The second stage, between 70 and 500 hours, involved precipitation of serpentine minerals. During this stage, fluid composition evolved towards saturation with brucite, which occurred after 500 hours, and

Table 8. SEM-EDS analyses of secondary minerals formed after reaction of San Carlos olivine with the 0.1 *M* $CaCl_2$ solution.

	INLET					OUTLET				
	Brc	Brc	Brc	Brc	Brc	Serpentine		Serpentine		
						Fibrous	Fibrous	Fibrous	Fibrous	Platy
Atom. %										
Si	9.23	1.24	4.29	0.79	0.78	44.91	45.61	44.89	44.66	46.68
Fe	6.06	8.37	4.52	4.35	5.88	1.38	0.68	1.62	1.7	2.28
Mg	83.09	89.58	91.19	94.85	93.02	53.07	51.82	52.85	52.75	50.08
Ca	1.63	0.81	0	0	0	0.64	1.89	0.64	0.9	0.96
Cr	0	0	0	0	0.33	0	0	0	0	0

Brc: Brucite

was maintained for the remainder of the experiment (Figure 6). This third stage is represented by the coincidence of plateau Mg concentrations and plateau pH values after 500 hours.

Lherzolite-H_2O experiment

Examination of the concentration-time profiles in Figure 2 suggests that reaction progressed through four stages. The first stage, represented by the interval between the start of the experiment and 56 hours, as for the olivine-H_2O experiment, is interpreted to have involved dissolution of high-energy surfaces. This stage was followed by one during which a balance was reached between dissolution of the primary silicates, olivine and orthopyroxene, and the crystallization of serpentine as suggested by the plateau concentrations of Mg, Si and Fe between 56 and 161 hours. The higher Si and Ca concentrations relative to the olivine-H_2O experiment reflect the contribution of the pyroxene. The drop in Mg concentration and increase in Ca concentration during the third stage, i.e., between 161 and 234 hours, signal an increase in the proportion of pyroxene dissolved relative to olivine, which became increasingly overgrown by serpentine. During the fourth stage, Mg concentration was low, Si concentration decreased rapidly and there was a sudden increase in Ca concentration.

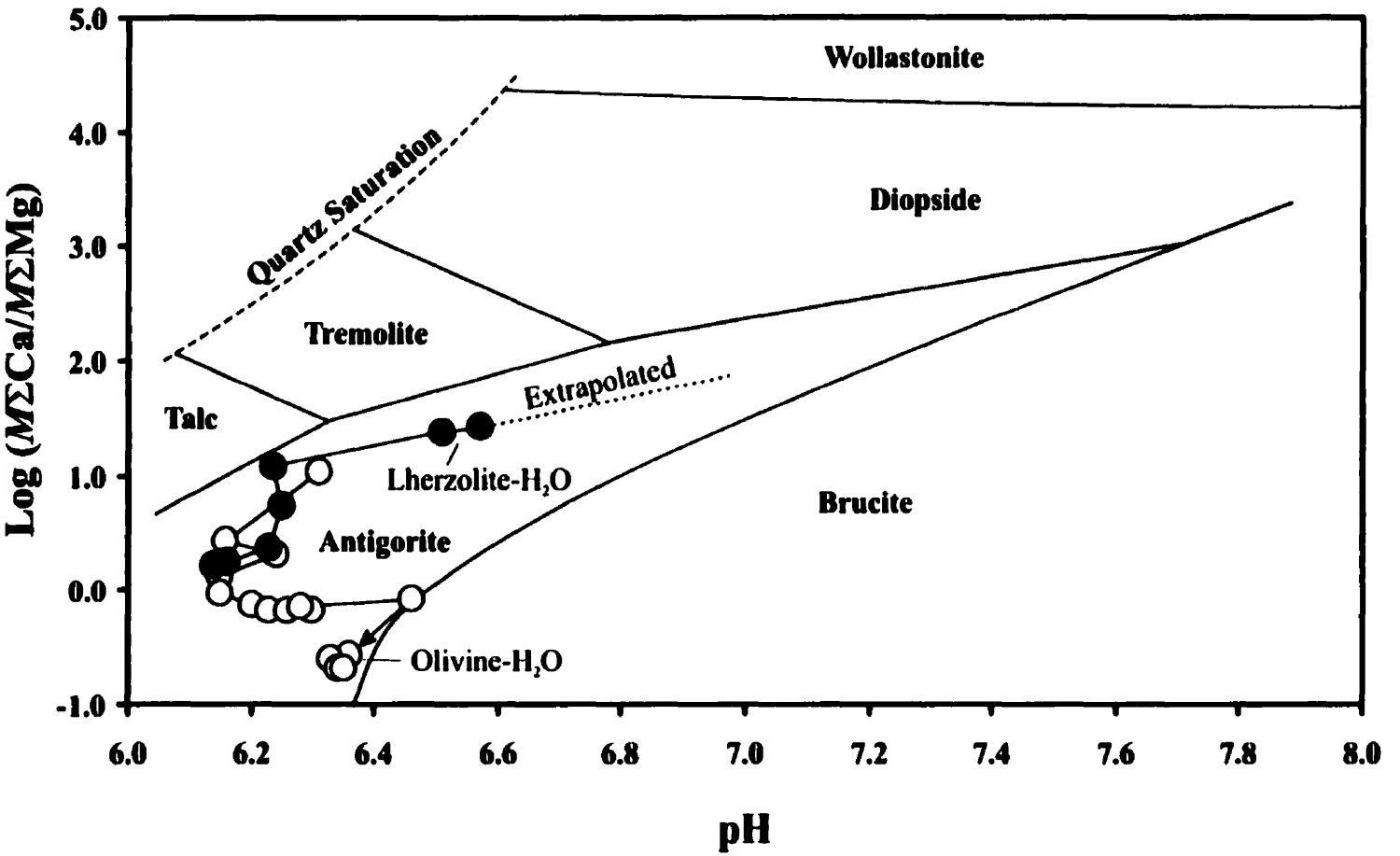
The overall fluid composition, illustrated as a function of pH and log ($M\Sigma$Ca/$M\Sigma$Mg) in Figure 6, evolved toward equilibrium with the assemblage serpentine, diopside and brucite. Fluids equilibrated with the latter assemblage contain the highest Ca and lowest SiO_2 and Mg concentrations, and have the highest pH possible for a fluid in equilibrium with a mineral assemblage containing serpentine minerals. The composition of this fluid is similar to the Ca-OH-type fluids from low temperature seeps in partially serpentinized peridotites from ophiolites described by Barnes and O'Neil (1969).

Olivine-0.1 M $CaCl_2$ solution experiment

The concentration-time profiles in Figure 3 indicate that reaction of the $CaCl_2$ solution with olivine evolved through three stages. During the first stage (the first 170

Figure 6

Fluid pH versus log ($M\Sigma Ca/M\Sigma Mg$) relationship of the fluid during reaction of water with olivine (open circles) and lherzolite (closed circles).

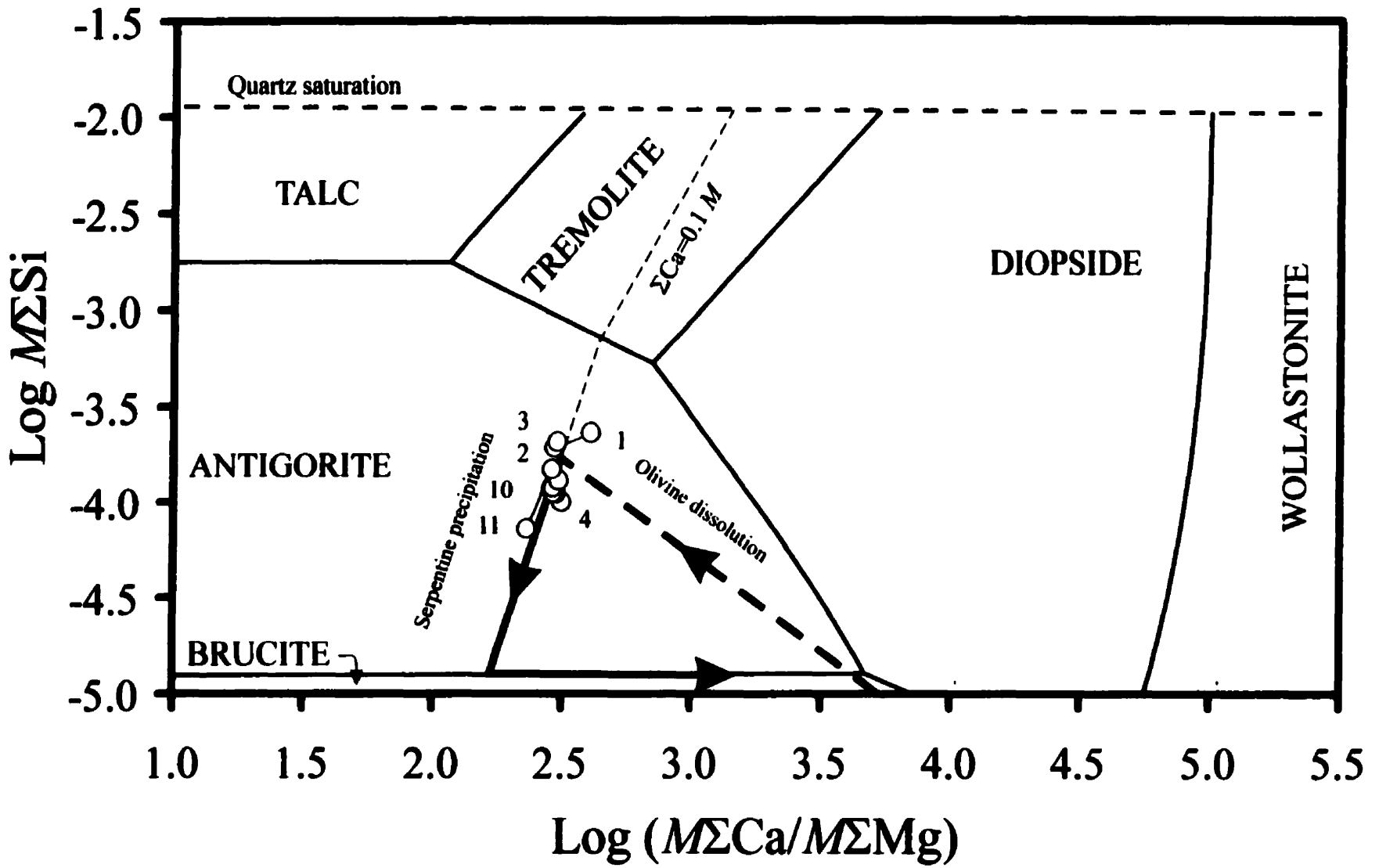

Wollastonite
Diopside
Quartz Saturation
Tremolite
Talc
Extrapolated
Lherzolite-H2O
Antigorite
Brucite
Olivine-H2O
Log (MΣCa/MΣMg)
pH
5.0
4.0
3.0
2.0
1.0
0.0
-1.0
6.0
6.2
6.4
6.6
6.8
7.0
7.2
7.4
7.6
7.8
8.0

hours of reaction), the Ca concentration in the fluid dropped slightly to 0.093 *M*, after which it returned to its initial concentration for the remainder of the experiment. This relatively small drop in Ca concentration correlates with high Si concentrations in the first three samples (as in the early stages of the experiments described above). This was presumably due, respectively, to precipitation and dissolution of a Ca-bearing phase (diopside ?) in the early stages of the experiment. The sharp drop in Si concentrations between 123 and 170 hours is interpreted to be due to the disappearance of the hypothetical Ca-bearing phase, followed by control of silica activity by precipitation of serpentine. This was accompanied by a steady state (second stage, between 170 and 502 hours) with respect to pH and Ca and Mg concentrations, representing a balance between dissolution of primary silicates and precipitation of secondary minerals. Brucite started to precipitate with a rapid drop in Si concentration to below the detection limit after 502 hours, after which a new, higher steady state of Mg concentration was established. The constant Mg concentration and pH after 502 hours suggest that the Mg and Si concentrations and pH of the fluid were buffered by the assemblage serpentine + brucite.

The reaction progress during this experiment followed a path similar to that which would take place by equilibrium reaction in a closed system, and illustrates the rapidity with which mildly saline solutions can equilibrate with the stable assemblage of secondary phases expected to form during dissolution of olivine. This is depicted on the log $M\Sigma$Si versus log ($M\Sigma$Ca/$M\Sigma$Mg) diagram in Figure 7. The reaction path between a 0.1 *M* $CaCl_2$ solution and pure forsterite shown on this diagram was calculated for 300°C and 300 bars with the EQ3/6 software package (Wolery, 1992) using the SUPCRT92 thermodynamic database (Johnson et al., 1992). The latter was modified for pressure, using equilibrium constants calculated from the more recent thermodynamic data for hydroxy-complexes of Shock et al. (1997) and chloro-complexes from Sverjensky et al. (1997). The path is valid for both closed-system and fluid-centered open-system simulations, because none of the secondary minerals back-reacts with the fluid. It can be seen from this diagram that the experimental data points plot very near to the position on the calculated reaction path where serpentine is saturated. The last data point extends along the reaction path towards brucite saturation.

Figure 7

Log $M\Sigma Si$ versus log ($M\Sigma Ca/M\Sigma Mg$) diagram illustrating the evolution of the fluid chemistry during reaction of olivine with the 0.1 *M* $CaCl_2$ solution. The thick black line represents a calculated reaction path resulting from reaction of San Carlos olivine with a 0.1 *M* $CaCl_2$ solution at a temperature of 300°C and a pressure of 300 bars (A and B Debye-Huckel parameters for activity coefficients at 300 bars calculated from Helgeson et al., 1981) using the EQ3/6 package of programs (Wolery, 1992) modified to include equilibrium constants calculated from the more recent thermodynamic data for hydroxy-complexes of Shock et al. (1997) and chloro-complexes from Sverjensky et al. (1997). Thermodynamic data for minerals were from Johnson et al. (1992). The dashed part of the line represents the change in fluid chemistry during dissolution of olivine. The solid part of the line represents the change in fluid chemistry once antigorite, then brucite become saturated. The open circles represent the composition of the experimental fluids (circles numbered 1, 2, 3, 4, 10 and 11 correspond to fluids sampled at 31.28, 79.03, 123.2, 169.53, 502.2 and 538.2 hours, respectively; see Table 5).


Quartz saturation
TALC
TREMOLITE
ΣCa=0.1 M
DIOPSIDE
WOLLASTONITE
ANTIGORITE
BRUCITE
Serpentine precipitation
Olivine dissolution
1
2
3
4
10
11
-1.5
-2.0
-2.5
-3.0
-3.5
-4.0
-4.5
-5.0
Log MΣSi
1.0
1.5
2.0
2.5
3.0
3.5
4.0
4.5
5.0
5.5
Log (MΣCa/MΣMg)

REACTION RATES

In this section, we present the results of calculations of the rate of dissolution of Fo_{91} in water and discuss the relative rates of dissolution of pyroxene with respect to olivine from reaction of lherzolite with water.

Olivine-H_2O experiment

Because Ca was not incorporated in significant quantities in the crystal structure of the secondary phases that formed during reaction (< detection limit of the SEM), dissolution rates for olivine during the experiment could be estimated from the Ca concentration of the solution and the Ca content of the olivine (0.0018 ± 0.0002 a.p.f.u. Ca, 1σ, N = 20) using the equation

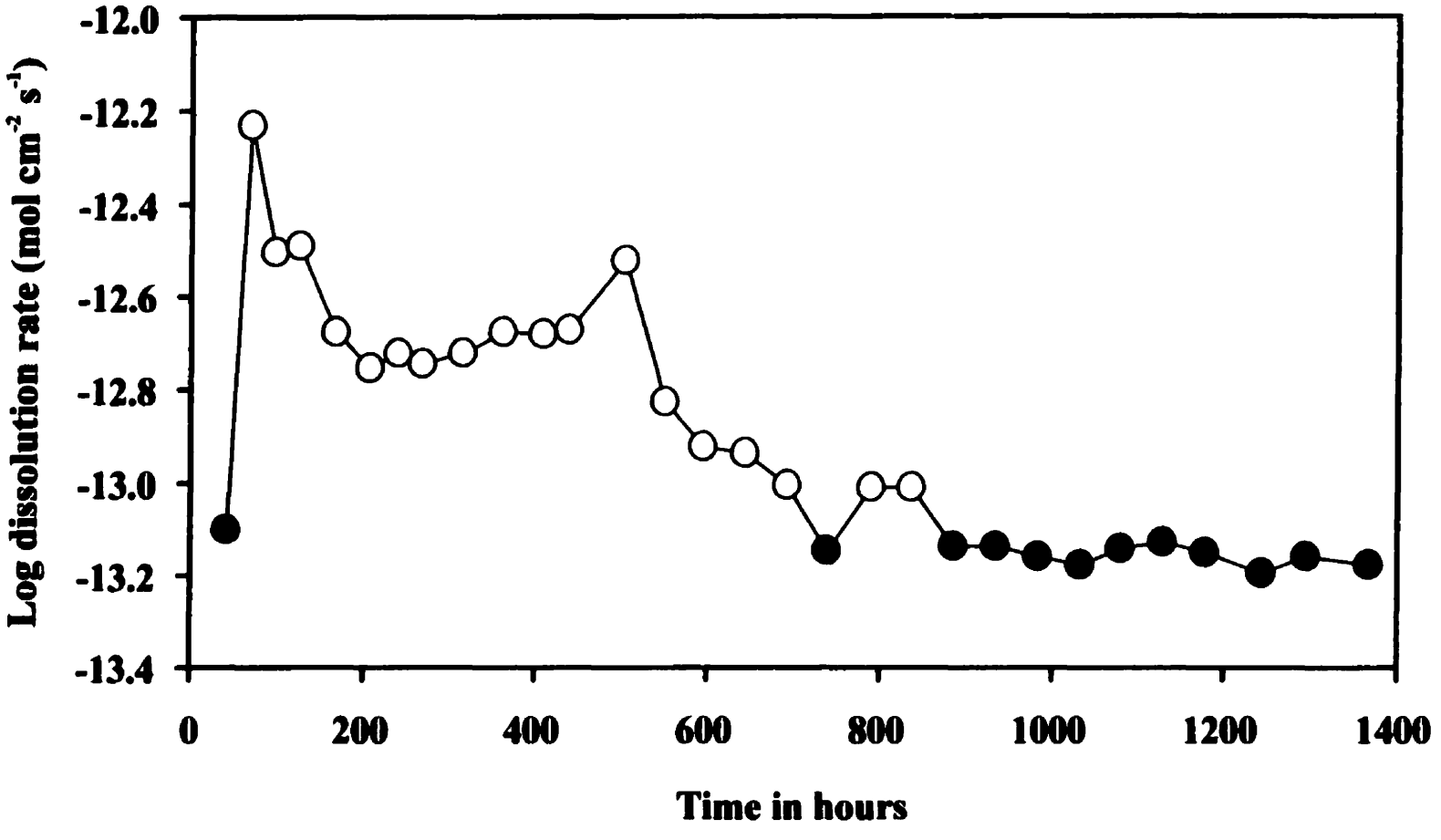
$$D.R. = (\Delta[Ca] \times V \times 10^{-6}) / (M_{Ca} \times S_T \times r_{Ca}) \quad (4)$$

of Knauss and Wolery (1986), where $\Delta[Ca]$ represents the Ca concentration of the fluid in mg/L minus that from the blank, V the flow rate in mL/sec (1.389×10^{-4}), M_{Ca} the molecular weight of Ca, S_T the total surface area of the sample (initial B.E.T. total surface area: 340 cm^2/g x 4.21 g = 1431.4 cm^2) and r_{Ca} the number of moles of Ca liberated per mole of olivine dissolved. Because the total surface area of the olivine was related to its mass, the value of the former was decreased in the rate calculation of each successive sample by an amount proportional to the mass of dissolved olivine calculated in the previous sample. However, because the amount of surface covered by secondary minerals is probably larger than the amount of lost surface calculated from the dissolved mass of olivine, the calculated dissolution rates represent maximum values as S_T would be overestimated.

The rate of dissolution of olivine, as measured by the concentration of Ca in the fluid (Figure 8), reached a maximum relatively early in the experiment (5.9×10^{-13} mol cm^{-2} s^{-1}) and then declined to a steady state value (~ 2×10^{-13} mol cm^{-2} s^{-1}), which was maintained between 167 and 438 hours. After a stoppage of 12 hours part way through

Figure 8

Log dissolution rate (mol cm^{-2} s^{-1})-time profile during reaction of water with San Carlos olivine. Open circles are rates calculated from Ca concentrations in the fluid (see text). Solid circles represent rates calculated assuming a Ca concentration at the limit of detection of the AA spectrometer of 1.5×10^{-6} *M*.


-12.0
-12.2
-12.4
-12.6
-12.8
-13.0
-13.2
-13.4
Log dissolution rate (mol cm-2 s-1)
0
200
400
600
800
1000
1200
1400
Time in hours

the experiment, the rate increased to a peak value of $3x10^{-13}$ mol cm^{-2} s^{-1} at 503 hours and then decreased abruptly to a value of $1.5x10^{-13}$ mol cm^{-2} s^{-1} at 550 hours, after which time it decreased smoothly to below $9.8x10^{-14}$ mol cm^{-2} s^{-1} after 840 hours of reaction. The maximum value (second sample after 70 hours of reaction) should provide the best estimate of the actual dissolution rate, assuming that all the high energy surfaces and finer grains were removed before the start of collection of the second fluid sample. The variations in the calculated dissolution rate should reflect the competing effects of dissolution of olivine and precipitation of secondary minerals. The steady state interval between 167 and 438 hours (Figure 8) is interpreted to correspond to a balance between the fraction of the total surface area of the olivine involved in dissolution (effective surface area ?) and that used for precipitation of neo-formed serpentine. The large decrease in the calculated dissolution rate after 503 hours can be explained by a decrease in the total surface area of olivine available for dissolution due to the precipitation of secondary minerals on its surface.

The maximum dissolution rate for olivine determined in our experiment is more than four times lower than that (2.5×10^{-12} mol cm^{-2} s^{-1}) obtained by Ponader (1989) using the same methodology. Ponader (1989) determined her rate from a flow-through study of serpentinization of olivine (Fo_{89}) also at a temperature of 300°C and a pressure of 300 bars. In her study, 1.51 g (105-149 μm size fraction versus 4.21 g of the 250-500 μm size fraction in our experiment) of olivine having a specific surface area of 0.0446 m^2/g, and offering slightly less than half of the total surface area of our experiment, was reacted with air-saturated water at a flow rate of 10.57 mLs/day (12 mLs/day for our experiment) for 576 hours (1368 hours for our experiment). The higher rate obtained by Ponader (1989) could be explained by the fact that she used smaller grains, which have a larger relative proportion of reactive surface area than larger grains (Anbeek, 1992), and by channelling of reactive fluid flow (Oelkers, 1996), which is more likely to occur with coarse grains.

Integration of the calculated dissolution rates with respect to time indicates that a maximum of 0.15 gram of forsterite should have dissolved (3.4 wt. % of the original mass) at the end of the experiment, assuming a concentration of Ca of 0.05 mg/L for

samples in which the concentration was below the detection limit of the AA spectrophotometer of 0.06 mg/L or $1.5x10^{-6}$ *M* (Table 3). The above estimate of the total amount of forsterite (containing an average of 0.00176 a.p.f.u. Ca) dissolved compares favourably with that obtained (0.14 g; 3.4 wt. % of the original mass) by summing the total amount of Ca dissolved in grams for each fluid sample, again assuming a concentration of Ca of 0.05 mg/L for samples in which the concentration was below the detection limit. The amount of dissolved forsterite calculated from the mass gain assumed to be caused by the addition of water to form the secondary minerals (the total amount of material removed in solution is negligible) in the equation:

Olivine Water

$(1.06x10^{-3})Mg_{1.81}Fe_{0.19}SiO_4 + (1.44x10^{-2})\ H_2O + (2.59x10^{-5})O_2$

=

Serpentine Brucite

$(5.31x10^{-4})Mg_{2.88}Fe_{0.22}Si_2O_5(OH)_4 + (3.81x10^{-4})Mg_{0.97}Fe_{0.03}(OH)_2 +$

Magnetite

$(2.45x10^{-5})Fe_3O_4$ (5)

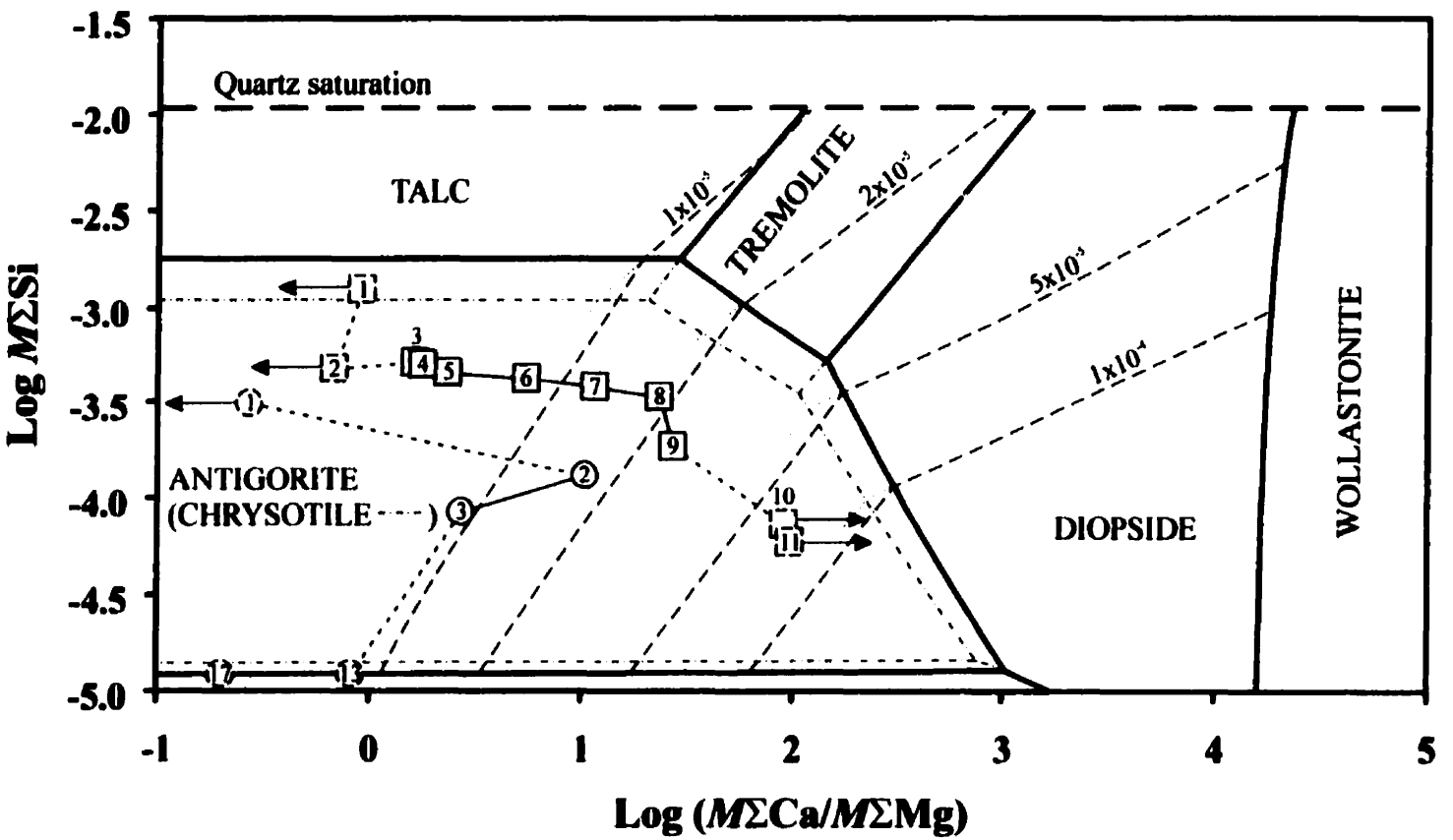
is 0.16 gram (3.7 wt. % of the original mass), i.e., a mass similar to those calculated above. Moreover, the inferred relative proportions of secondary minerals correspond closely with those that can be deduced from examination of the run products under a binocular microscope and the SEM.

Lherzolite-H_2O experiment

Because the specific surface area of the individual minerals that compose the lherzolite sample was not measured, calculation of their respective dissolution rates was not attempted. However, examination of the reaction path in Figure 9, the concentration-time profiles in Figure 2, and the experimental data in Table 4 suggest that the rates of dissolution of the primary silicates were opx>ol>cpx. The evidence for this is that;

Figure 9

Log $M\Sigma$Si versus log ($M\Sigma$Ca/$M\Sigma$Mg) diagram representing the evolution of the fluid chemistry during the olivine-water and lherzolite-water experiments. Full open circles represent chemical data for the olivine-water experiment. Dashed open circles represent the location on the diagram of a set of chemical analyses assuming a Ca concentration at the detection limit. Arrows indicate the sense of displacement of the circles for lower concentrations of Ca. Full open squares represent chemical data for the lherzolite-water experiment. Dashed open squares represent the location on the diagram of a set of chemical analyses assuming a Ca or Mg concentration at the detection limit. Arrows indicate the sense of displacement of the circles for lower concentrations of Ca (arrows pointing left) and Mg (arrows pointing right). The numbers accompanying the symbols refer to fluid analyses in Tables 3 (olivine-water experiment; numbers 1, 2 and 3 correspond to fluids sampled between 43 and 98 hours) and 4 (lherzolite-water experiment; numbers 1 to 11 correspond to fluids sampled between 28.5 and 457.9 hours).


Quartz saturation
TALC
TREMOLITE
1x10⁻³
2x10⁻³
5x10⁻³
1x10⁻⁴
WOLLASTONITE
DIOPSIDE
ANTIGORITE
(CHRYSOTILE)
-1.5
-2.0
-2.5
-3.0
-3.5
-4.0
-4.5
-5.0
Log MΣSi
-1
0
1
2
3
4
5
Log (MΣCa/MΣMg)

1) after less than 30 hours of reaction (sample 1), the fluid composition had approached that representing equilibrium between talc and serpentine; 2) the concentration of Si remained high for the next 250 hours of reaction; and 3) there was a sudden increase in the Ca concentration after 286 hours of reaction. The elevated Si concentration is interpreted to be due to the faster dissolution of orthopyroxene relative to olivine, while the increase of Ca concentrations after 286 hours is interpreted to reflect the dissolution of a much higher proportion of clinopyroxene during the later stages of the experiment. This increase in the proportion of dissolved clinopyroxene resulted from a decrease in the available proportions of free surfaces of olivine and orthopyroxene due to the precipitation of secondary minerals.

In addition to its lower dissolution rate relative to olivine and orthopyroxene, the apparent resistance of clinopyroxene to alteration also can be explained by the fact that diopside is the only one of the primary ferromagnesian silicates in lherzolite that can form a stable assemblage with serpentine and brucite in hydrothermal fluids below 350°C. In fact, most low temperature fluids seeping from partially serpentinized peridotites are supersaturated with respect to diopside (Barnes and O'Neil, 1969; Pfeifer, 1977), and this may also commonly be the case at higher temperature.

Olivine-$CaCl_2$ solution

The overall reaction between olivine and the $CaCl_2$ solution can be approximated by the reaction:

Olivine (V°: 44 cm^3/mol)

$$\mathbf{A}Mg_{1.81}Fe_{0.19}SiO_4 + (2.75\times10^{-4})H^+ + (1.38\times10^{-4})Cl^- + 0.03H_2O$$

=

Serpentine (V°: 108.5 cm^3/mol) Brucite (V°: 24.6 cm^3/mol)

$$\mathbf{B}Mg_{2.88}Fe_{0.22}Si_2O_5(OH)_4 + \mathbf{C}Mg_{0.94}Fe_{0.06}(OH)_2$$

Magnetite (V°: 44.5 cm^3/mol)

$$+ \mathbf{D}Fe_3O_4 + (4.27\times10^{-5})SiO_2^\circ + (1.37\times10^{-4})MgCl^+ + (4\times10^{-7})FeCl^+ \qquad (6).$$

This reaction was constrained using EDS and WDS analyses of the minerals and balancing the number of moles of Si, Mg and Fe released into solution by summing the amount of each in each fluid sample. In the case of Si, the lack of data for the last three fluid samples was compensated by assuming equilibration between the fluid, brucite and chrysotile. Our calculations indicate that the amount of forsterite dissolved, **A**, was 2.15×10^{-2} moles (78 % conversion versus 2.6 % with H_2O after the same reaction time), and that the amounts of serpentine, **B**, brucite, **C**, and magnetite, **D**, precipitated were 1.07×10^{-2}, 8.38×10^{-3} and 4.07×10^{-4} or 5.74×10^{-4} mole, respectively. This suggests a positive change in volume after reaction of 0.44 to 0.45 cm^3, or a volume increase of 46 to 47%, which is close to the calculated initial porosity, and corresponds to the upper limit of volume increase estimated in natural samples (Coleman and Keith, 1971; O'Hanley, 1992). Dissolution of olivine in the 0.1 *M* $CaCl_2$ solution was more than one order of magnitude faster than in the olivine-H_2O experiment due partly, as already stated above, to the smaller grain size of the reactant olivine, and partly to the more reactive nature of the solution.

DISCUSSION

The results from the flow-through experiments described above enable us to draw some general conclusions about the processes of serpentinization and the mobility of Ca through peridotites during serpentinization, both in the laboratory and in natural systems. In the following paragraphs, we analyze specific aspects of the experiments and discuss some problems relating to the source of Ca employed in the rodingitization of aluminous rocks, a process that occurs commonly in sequences of ultramafic rocks.

Olivine-H_2O experiment

The concentration of calcium in solution in each fluid sample was very low, i.e., < 0.39 mg/L. However, if it is considered that the Ca liberated during dissolution of olivine remains in solution (no adsorption or minor incorporation as a solid solution in a mineral that does not contain essential Ca) occupying a volume y within a volume x (y/x-y =

fluid/rock ratio), and that y/x-y remains constant along a column containing nx, the concentration of the latter in the fluid will increase along the column and will be limited only if a Ca-bearing phase saturates. During the olivine-H_2O experiment, x (volume of the reaction cell) was equal to 2.124 $cm^3$and y was 0.85 cm^3 (pore space). The solid phases that control the concentrations of Mg and Si, and the pH of the fluid during water-olivine interaction are serpentine and brucite. Under the temperature and pressure conditions of the experiment, the only Ca-bearing phase stable with serpentine and brucite in the system Ca-Mg-Si-O-H is diopside. The Ca concentration in water in equilibrium with serpentine + brucite + diopside (300°C, 300 bars) is 17 mg/L and would have been achieved after passage of the fluid through 44 reaction cells (calculated by multiplying the Ca concentration in an aliquot y, i.e., 0.39 mg/L, by the number of reaction cells x required to obtain 17 mg/L; the loss of water as a result of serpentinization was not considered).

Let us now consider a long, thin, newly opened fracture in olivine (containing 1.76 x 10^{-3} a.p.f.u. Ca) that has filled with water at a temperature of 300°C, and a volumetric water/rock ratio in the vicinity of this system of unity. We treat this system as a closed system. As serpentinization occurs, the amount of calcium in solution would be expected to increase rapidly, assuming that the secondary phases contain negligible amounts of this element. This would be due to the combined effects of release of Ca caused by the dissolution of the olivine and a decrease in the amount of water caused by alteration of olivine to serpentine and brucite. As a result, diopside would become saturated after only ~ 0.8 % of the olivine was consumed. At a water/rock ratio of 0.1 this value is 0.08 %, and at a water/rock ratio of 10 it is 8 %. Eventually, the calcium in the rock would be leached if the fracture was reopened a large number of times, but the amount of calcium in initially pure water is not expected to attain a value greatly exceeding 17 mg/L, if we allow supersaturation with respect to diopside, at the temperature considered.

Because the bulk solubility of the assemblage serpentine + brucite + diopside is retrograde, the above calcium content is multiplied, for example, by a factor of 5 at 200°C. Although calcium could be removed from dunitic bodies by pure water, the latter is not a very efficient medium to cause metasomatism by infiltration because enormous

amounts of water would be required to induce calcium metasomatism (rodingitization). For example, let us consider 100 grams of granite, with an original CaO content of 2.0 wt. %, and a typical product of rodingitization containing 35 wt. % CaO. If the volume of the rock was conserved after alteration, a volume of ~ 2000 L of water initially equilibrated with serpentine, brucite and diopside at a temperature of 300°C and a pressure of 300 bars would be required to produce the rodingite (this assumes that all the calcium was removed from the fluid).

Lherzolite-H_2O experiment

By contrast to dunite, water reacting with pyroxene-bearing, olivine-rich peridotite would be more prone to equilibrate with the ferromagnesian mineral assemblage serpentine + brucite + diopside ($P_{H_2O} = P_{Total}$) or olivine + serpentine + diopside ($P_{H_2O} << P_{Total}$), because diopsidic pyroxene is already present in the rock and orthopyroxenes contain much more Ca than olivine. The pyroxenes will dissolve (Mg-rich orthopyroxenes are not stable at temperatures below ~ 600-700°C in the presence of water: Day et al., 1985; Berman et al., 1986) and contribute to an increase in the Ca concentration of the fluid as long as a Ca-bearing phase is not acting to buffer its concentration within a given mineral assemblage. As stated above, our calculations indicate that diopside is the only Ca-bearing phase that forms an equilibrium assemblage with serpentine and brucite. The calculations also indicate that the latter mineral assemblage allows for maximum solubility of Ca and maximum pH, and for minimum solubility of Si and Mg in fluids equilibrated with serpentine-bearing assemblages. After the flow of water and interaction with rock for some distance through pyroxene-bearing peridotite, the dissolution of clinopyroxene is expected to be greatly reduced or effectively stopped. The pre-existing primary clinopyroxene (usually Na and Al-rich) may also be replaced by a pyroxene having a composition (closer to that of diopside-hedenbergite solid solution) reflecting the conditions of pressure and temperature during alteration, or by tremolitic amphibole. The latter would form in olivine-rich rocks under disequilibrium conditions, where high values of $\mu SiO_2°$ would occur locally at the grain-size scale of the pyroxene. As discussed above for the olivine-water experiment, the Ca

concentration of the fluid is not expected to be much greater than 17 mg/L at a temperature of 300°C and a pressure of 300 bars if diopsidic pyroxene and serpentine are in equilibrium with the fluid.

Olivine-$CaCl_2$ solution

The results of the experiment and the modelling demonstrate the large potential of hydrothermal solutions to transport Ca in dunitic rocks undergoing serpentinization, without producing Ca-metasomatism. Calculations with EQ3/6 indicate that reaction of a $CaCl_2$ solution with ultramafic rocks containing pyroxenes (harzburgites and lherzolites) under conditions of equilibrium leads to an increase in the concentration of Ca of the fluid until saturation with diopside. In order to fix the calcium through complete replacement of brucite and serpentine by an amphibole, a pyroxene or any other Ca-rich silicate (as, for example, in nephrite or diopsidite) under the temperature conditions discussed here, a source of silica external to the harzburgites and lherzolites is required. Consequently, Ca-metasomatism of serpentinized peridotites is only predicted to occur where the peridotites are in contact with or close to siliceous rocks such as felsic dykes.

IMPLICATIONS FOR RODINGITIZATION

Our treatment of the experimental results and modelling has shown that the optimum conditions for rodingitization occur when the fluid is in equilibrium with serpentine, brucite and diopside. During serpentinization of pyroxene-bearing peridotites at temperatures around 300°C, it is highly probable that equilibrium of a hydrothermal fluid with this mineral assemblage is frequently approached, as most low temperature subsurface fluids from seeps in partly serpentinized peridotites from ophiolites are supersaturated with respect to diopside (Barnes and O'Neil, 1969; Pfeifer, 1977). As stated above, this indicates that the Ca concentrations in fluids causing serpentinization probably reflect the process of replacement of primary pyroxenes by secondary pyriboles. Another explanation could be that a steady state is commonly reached where secondary

diopsidic pyroxene never nucleates because of energetic barriers, while the dissolution rate of the primary pyroxenes decreases with increasing Ca concentration in the fluid at close to the value at saturation with diopside. As long as there is pyroxene remaining in the rock and the composition of the fluid which initially enters peridotite remains undersaturated with respect to diopside, dissolution of the primary pyroxenes will occur and the composition of the fluid will tend toward that reflecting equilibrium with serpentine + brucite + diopside. This is because only a very minor increase in the concentration of Ca is required to saturate the fluid with diopside in near neutral hydrothermal fluids. In turn, this provides an explanation (in addition to the fact that diopside dissolves more slowly than olivine and orthopyroxene; see above) for why clinopyroxene is frequently the last mineral to alter completely during serpentinization. It also explains why secondary clinopyroxene is rare in retrograde serpentinites.

The composition of fluids equilibrated with secondary minerals during serpentinization was established above. In the sections that follow, we discuss the factors that can be responsible for the complete transformation of serpentinites to calc-silicate minerals, and Si-Al-rich rocks to rodingite.

Transformation of peridotite to calc-silicate rock

Serpentinites in contact with Si-rich lithologies are frequently altered to tremolite-actinolite-rich (nephrite) or diopside-hedenbergite-rich (diopsidite) rocks. Alteration of serpentinite, or peridotite to these types of calc-silicate rock is the result of Si and Ca metasomatism. Serpentinites rarely contain more than 1 wt. % CaO and generally less than 40 wt. % SiO_2, whereas nephrites and diopsidites contain between 12 and 22 wt. % CaO, and between 52 and 56 wt. % SiO_2. In nature, the sequences of mineral parageneses serpentinite → talc → nephrite (Phillips and Hess, 1936; Hockley et al., 1978; Koons, 1981), serpentinite → nephrite (Chidester et al., 1978), or serpentinite → ± talc → nephrite → ± diopsidite (Chapter V) occur commonly at the contact with felsic rocks. Assuming that minerals along the sequence serpentinite → talc → nephrite → diopsidite are replaced by each other successively and at constant volume, the replacement of a serpentine, e.g., antigorite, by talc can be expressed by the reaction:

Antigorite ($V° \sim 1742\ cm^3/mol$)

$Mg_{48}Si_{34}O_{85}(OH)_{62} + 19.2H^+ + 9.6Cl^- + 17.2SiO_2°$

=

Talc ($V° \sim 136\ cm^3/mol$)

$12.8Mg_3Si_4O_{10}(OH)_2 + 9.6MgCl^+ + 27.8H_2O$ (7),

the replacement of talc by tremolite by:

Talc ($V° \sim 136\ cm^3/mol$)

$2Mg_3Si_4O_{10}(OH)_2 + 2CaCl^+$

=

Tremolite ($V° \sim 273\ cm^3/mol$)

$Ca_2Mg_5Si_8O_{22}(OH)_2 + MgCl^+ + Cl^- + 2H^+$ (8),

and replacement of tremolite by diopside according to the reaction:

Tremolite ($V° \sim 273\ cm^3/mol$)

$Ca_2Mg_5Si_8O_{22}(OH)_2 + 2.14CaCl^+ + 0.28SiO_2° + 0.28H_2O$

=

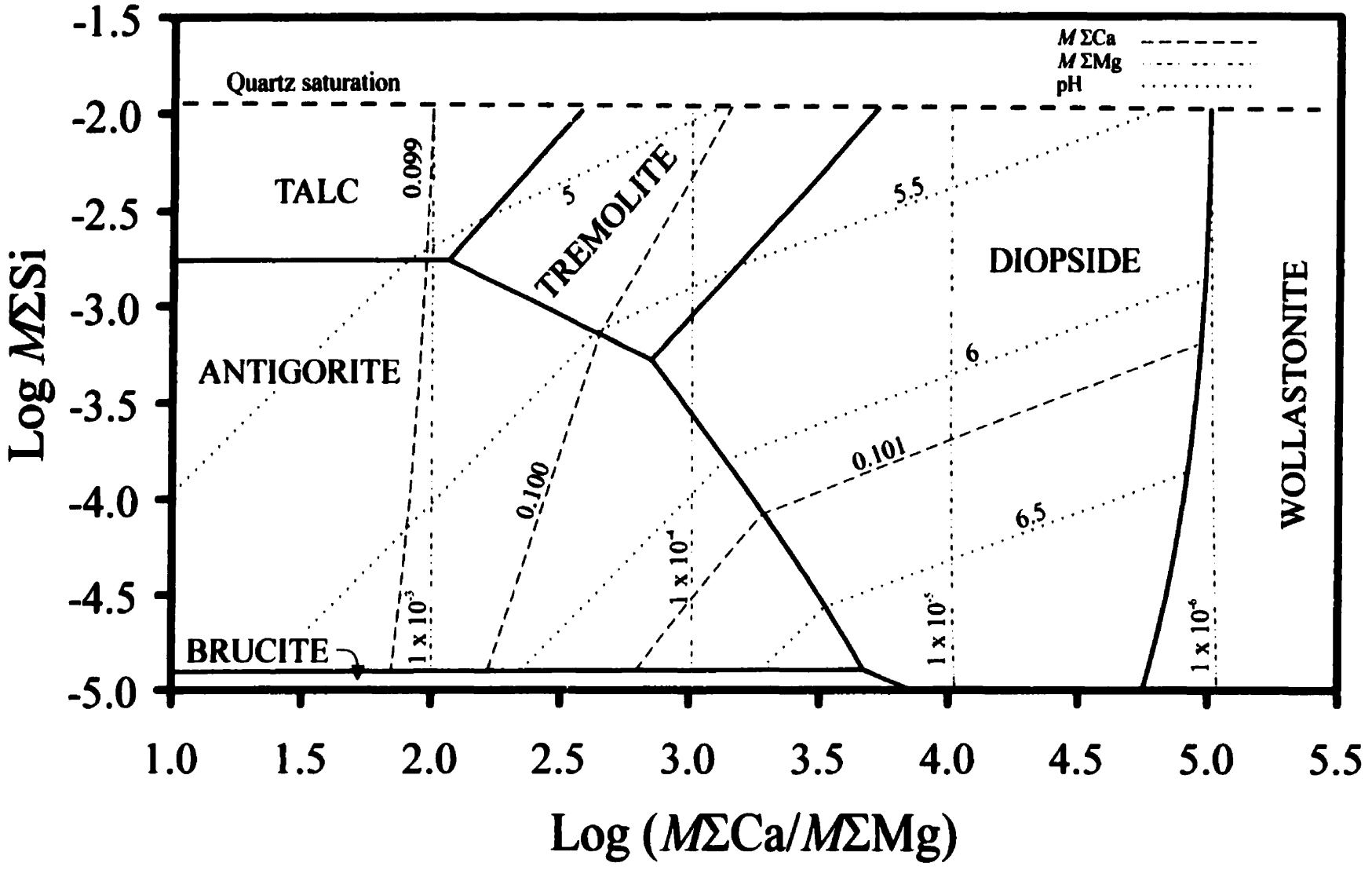
Diopside ($V° \sim 66\ cm^3/mol$)

$4.14CaMgSi_2O_6 + 0.86MgCl^+ + 1.28Cl^- + 2.56H^+$ (9).

This series of reactions suggests that the Ca required to form nephrite from serpentinite could be derived from the felsic rocks. Further indication that the Ca responsible for the formation of nephrite could be derived from felsic rocks is provided by examination of Figure 10, in which the concentrations in Si, Ca and Mg, and pH, are illustrated as a function of log $M\Sigma Si$ and log ($M\Sigma Ca/M\Sigma Mg$) at a temperature of 300°C and a pressure of 300 bars. The equilibrium Ca and Mg concentrations along a path starting in the stability

Figure 10

Log $M\Sigma$Si versus log ($M\Sigma$Ca/$M\Sigma$Mg) diagram in the system Ca-Mg-Si-O-H-Cl (0.2 *M*) involving the phases quartz, talc, antigorite, brucite, tremolite, diopside, and wollastonite. Isoconcentration contours for Ca and Mg are shown by thin dashed and dash-dotted lines, respectively, and pH contours are shown by dotted lines. A typical alteration sequence of mono-mineralic zones consisting of antigorite, then talc, then tremolite, respectively, from serpentinite to the contact with a felsic rock body suggests that the calcium responsible for the formation of the tremolite zone is derived from the felsic rocks.


MΣCa
MΣMg
pH
Quartz saturation
TALC
TREMOLITE
DIOPSIDE
WOLLASTONITE
ANTIGORITE
BRUCITE
0.099
5
5.5
6
6.5
0.101
0.100
1 x 10⁻³
1 x 10⁻⁴
1 x 10⁻⁵
1 x 10⁻⁶
-1.5
-2.0
-2.5
-3.0
-3.5
-4.0
-4.5
-5.0
Log MΣSi
1.0
1.5
2.0
2.5
3.0
3.5
4.0
4.5
5.0
5.5
Log (MΣCa/MΣMg)

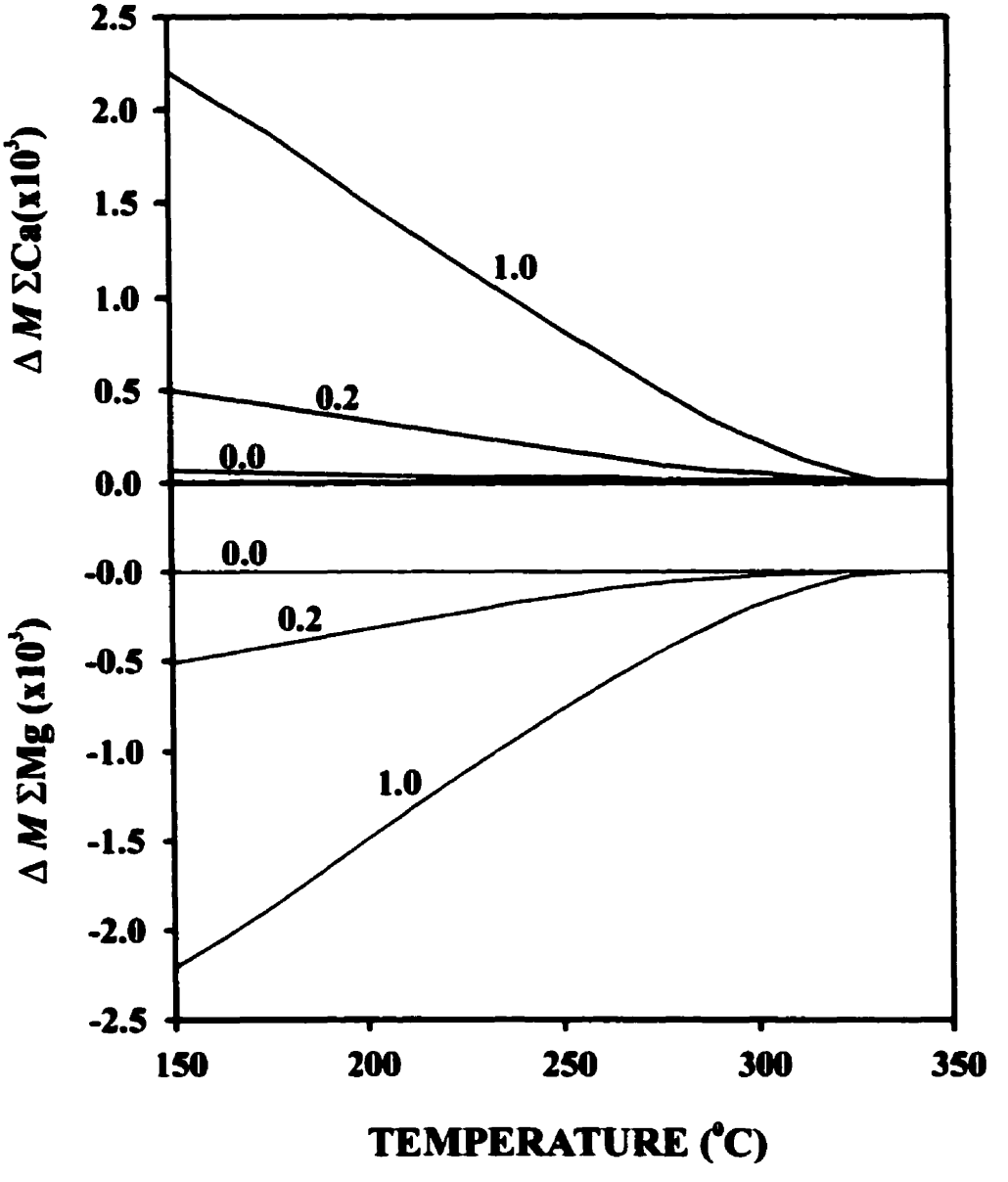
field of serpentine, and proceeding to talc, then tremolite, increase and decrease, respectively, further suggesting that Ca is derived from felsic rocks. It is also apparent from Figure 10 that fluid compositions buffered by the assemblage serpentine + brucite + diopside, while effective in inducing diopsidization of serpentinite (rodingitization of Si-Al-rich rocks) by increasing the $a\mathrm{SiO_2}°$, are not able to explain the mineral sequences described above. On the contrary, the fluids responsible for the formation of nephrite haloes in serpentinites at the contact with Si-Al-rich rocks are probably far from equilibrium with diopside. However, this explanation for the formation of nephrite ignores the possibility that there may be a temperature gradient between the serpentinite and, for example, felsic intrusive rocks, and/or that additional components like Na and Al, not considered in the simplified system (Ca-Mg-Si-O-H-Cl) used to construct Figure 10, may affect the equilibrium.

Our calculations reveal that the concentration of Ca in fluids in equilibrium with tremolite, talc and antigorite, which represents the mineral assemblage with the lowest Ca concentration in the fluid in the presence of tremolite, increases with decreasing temperature (Figure 11). This concentration difference is amplified significantly with increasing total Cl in the fluid. The calculations suggest it would be possible to derive the Ca needed to form nephrite from serpentinizing fluids in the early stages of the cooling of felsic dykes intruded in cold serpentinite.

Fluid/rock interaction paths in naturally more realistic systems, i.e., systems which include Fe, Al, Na, and K, in addition to Ca, Mg, Si, O, H, and Cl, are extremely complex because of the large variations in the relative proportions of these components that exist in rocks and fluid phases. There are, however, some useful general features reported from natural occurrences that can be used to study the problems of calc-silicate metasomatism in ultramafic bodies adjacent to felsic rocks. A number of researchers have suggested that fluid movement along positive temperature gradients could be an efficient mechanism for the precipitation of calc-silicates during alteration of plagioclase-bearing rocks (e.g., Rose et al., 1992) because of the large positive variation in the Na/Ca ratio of fluids in equilibrium with mineral assemblages containing plagioclase along such positive

Figure 11

Diagram showing the change in Ca and Mg concentrations in fluids in equilibrium with the assemblage antigorite + tremolite + talc with decreasing temperature from 350°C at a pressure of 300 bars. Relatively large decreasing and increasing concentration gradients for Ca and Mg, respectively, could be established along a reaction path passing through the stability fields of antigorite, then talc, then tremolite, towards the contact with a felsic rock body, if a steep decreasing temperature gradient exists between the felsic rock body and the host serpentinite, and is magnified by increased concentration of Cl in the fluid.


2.5
2.0
1.5
1.0
0.5
0.0
-0.0
-0.5
-1.0
-1.5
-2.0
-2.5
Δ M ΣCa(x10³)
Δ M ΣMg (x10³)
1.0
0.2
0.0
0.0
0.2
1.0
150
200
250
300
350
TEMPERATURE (°C)

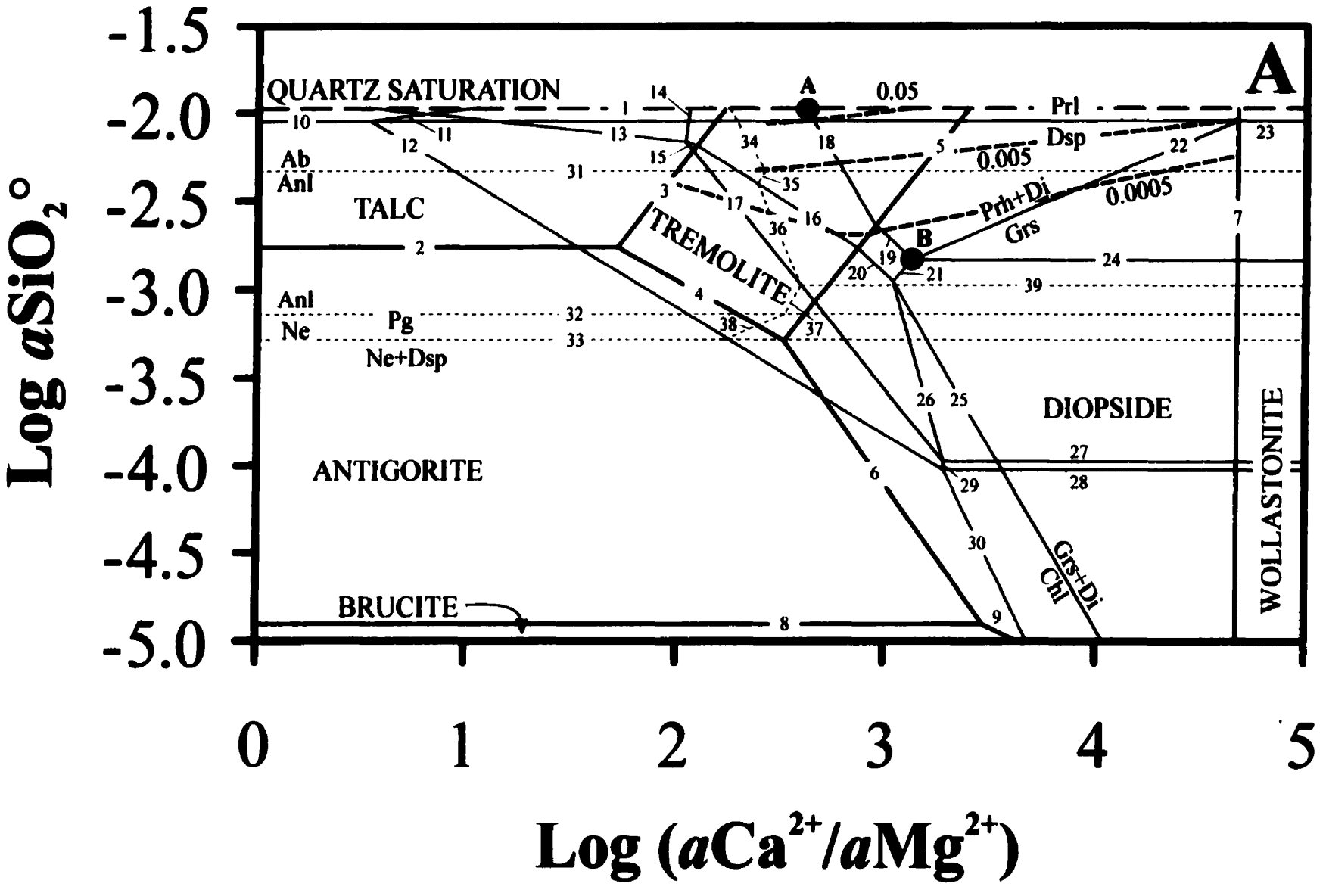
temperature gradients. Such an explanation could be applied to the alteration of serpentinites at the contact of freshly intruded felsic dykes, if the Na/Ca ratio of the fluid circulating in the serpentinites is lower than the value which would result from reaction of this fluid with the felsic rocks (Cl constant). However, experimental data provided by Berndt and Seyfried (1993) suggest that, under circumstances where equilibrium between plagioclase and coexisting fluid is not achieved, the plagioclase buffers the fluid composition.

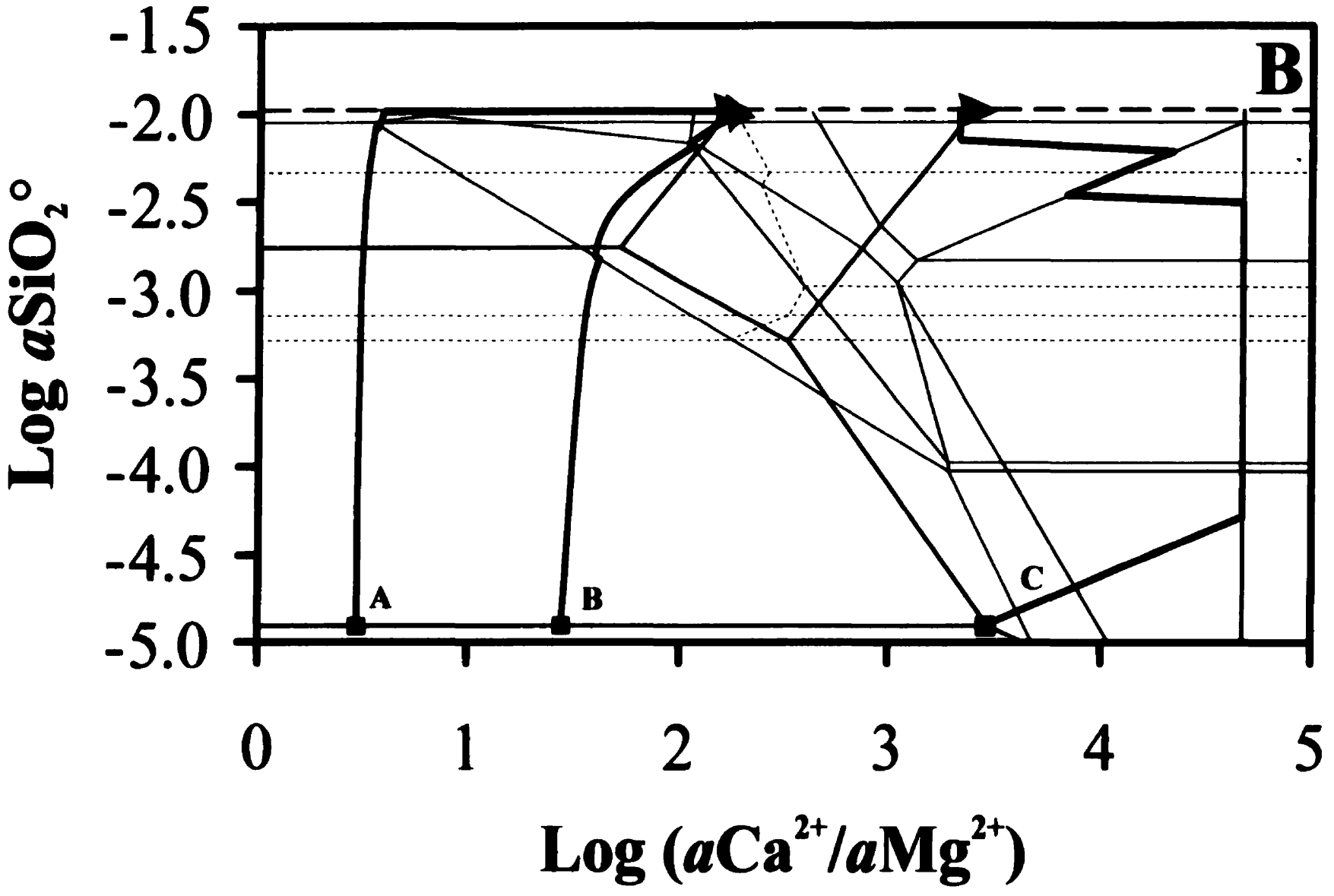
Nephrite-talc bodies occurring at the contact between serpentinites and metasedimentary rocks in thrust belts most likely formed across a constant temperature gradient. As a first approach to understanding the possible isothermal reaction paths during hydrothermal alteration at the contact between ultramafic and felsic rocks, we selected a simplified system (Na-Ca-Mg-Al-Si-O-H-Cl; Figure 12a) in which solid solutions were ignored. The scenario considered was one in which a seawater-type fluid, assumed to have reacted with upper basaltic crust in an oceanic environment (S-depleted, enriched in Ca and Cl relative to seawater: e.g., Von Damm, 1990) prior to equilibration with a model serpentinized peridotite composed of antigorite and brucite, reacts with a model plagiogranite (50 % quartz, 50 % An_{22}) at a temperature of 300°C and a pressure of 300 bars. Although black-smoker-type fluids are probably not involved in rodingitization, they provide information about the relative proportions of Na, K, Ca, and Cl in seawater-dominated fluids produced during greenschist-grade hydrothermal metamorphism of the oceanic crust. The (Na+K)/Cl molar ratios in sub-seafloor hydrothermal fluids varies between 0.70 and 0.95 (Butterfield et al., 1990; Von Damm, 1990; Butterfield and Massoth, 1994; Butterfield et al., 1994a; Butterfield et al., 1994b; de Ronde, 1995; Charlou et al., 1996). The relationship between the molar concentration of Na and Cl in these fluids is fairly constant: Na = (0.75 x Cl) + 0.03 (R^2 = 0.97, 69 pairs of values). The relationships between K and Cl, and between Ca and Cl show much wider variations: Ca = (0.09 x Cl) – 0.01 (R^2 = 0.7), K = 0.05 x Cl (R^2 = 0.5). Based on the above calculations, we selected three starting fluid compositions, each with a constant concentration of 1 *m* Cl and 0.82 *m* Na (excess Na was added to compensate for K and an arbitrary Al

Figure 12

A) Log $a SiO_2°$ versus log ($a Ca^{2+}/a Mg^{2+}$) equilibrium relationships among the phases quartz, talc, antigorite, tremolite, diopside, wollastonite, diaspore, pyrophyllite, clinochlore, margarite, zoisite, prehnite, grossular, albite, analcime, nepheline, and paragonite in the system Na-Ca-Mg-Al-Si-O-H at a temperature of 300°C and a pressure of 300 bars. The positions of the reaction boundaries were calculated using the SUPCRT92 software package (Johnson et al., 1992) and correspond to (abbreviations of minerals from Kretz, 1983): 1) Qtz = $SiO_2°$, 2) 16Tlc + $15H_2O$ = Atg + $30SiO_2°$, 3) 3Tr + $6Mg^{2+}$ + $4SiO_2°$ + $4H_2O$ = 7Tlc + 6 Ca^{2+}, 4) 48Tr + $96Mg^{2+}$ + $169H_2O$ = Atg + $96Ca^{2+}$ + $146SiO_2°$, 5) 7Di + $3Mg^{2+}$ + $2SiO_2°$ + $2H_2O$ = 2Tr + $3Ca^{2+}$, 6) 24Di +$24Mg^{2+}$ + $31H_2O$ = Atg + $24Ca^{2+}$ + $14SiO_2°$, 7) 2Wo + Mg^{2+} = Di + Ca^{2+}, 8) Atg + $17H_2O$ = 48Brc + $34SiO_2°$, 9) Di + Mg^{2+} + $2H_2O$ = 2Brc + Ca^{2+} + $2SiO_2°$, 10) Prl = 2Dsp + $4SiO_2°$, 11) 5Mrg + $5Mg^{2+}$ + $8H_2O$ + $29SiO_2°$ = 9Prl + Chl + $5Ca^{2+}$, 12) 5Mrg + $5Mg^{2+}$ + $8H_2O$ + = Chl + 18Dsp + $5Ca^{2+}$ + $7SiO_2°$, 13) Mrg + 3Tlc + Mg^{2+} + $4H_2O$ = 2Chl + Ca^{2+} + $8SiO_2°$, 14) 12Zo + $15Mg^{2+}$ + $8H_2O$ + $2SiO_2°$ = 9Mrg + 5Tlc + $15Ca^{2+}$, 15) 11Tlc + 6Zo + $12Mg^{2+}$ + $22H_2O$ = 9Chl + $12Ca^{2+}$ + $35SiO_2°$, 16) 11Tr + 14Zo + $50Mg^{2+}$ + $66H_2O$ = 21Chl + $50Ca^{2+}$ + $67SiO_2°$, 17) 18Zo + $25Mg^{2+}$ + $22H_2O$ = 5Chl + 11Mrg + $25Ca^{2+}$ + $17SiO_2°$, 18) 21Prh + $10Mg^{2+}$ = 2Tr + 14Zo + $10Ca^{2+}$ + $5SiO_2°$ + $12H_2O$, 19) 3Prh + Mg^{2+} = 2Zo + Di + Ca^{2+} + $SiO_2°$ + $2H_2O$, 20) 11Di + 4Zo + $19Mg^{2+}$ + $22H_2O$ = 6Chl + $19Ca^{2+}$ + $16SiO_2°$, 21) 6Grs + $5Mg^{2+}$ + $4SiO_2°$ + $2H_2O$ = 5Di + 4Zo + $5Ca^{2+}$, 22) 2Grs + Mg^{2+} + $2SiO_2°$ + $2H_2O$ = 2Prh + Di + Ca^{2+}, 23) Wo + Prh = Grs + $SiO_2°$ + H_2O, 24) 5Prh = 2Grs + 2Zo + $3SiO_2°$ + $4H_2O$, 25) Grs + Di + $4Mg^{2+}$ + $4H_2O$ = Chl + $4Ca^{2+}$ + $2SiO_2°$, 26) 11Grs + $25Mg^{2+}$ + $22H_2O$ = 5Chl + 4Zo + $25Ca^{2+}$ + $6SiO_2°$, 27) 2Zo = Mrg + Grs +

$SiO_2°$, 28) 3Mrg + $2H_2O$ = 10Dsp + Gr + $3SiO_2°$, 29) 9Grs + $25Mg^{2+}$ + $22H_2O$ = 5Chl + 2Mrg + $25Ca^{2+}$ + $8SiO_2°$, 30) 5Grs + $15Mg^{2+}$ + $14H_2O$ = 3Chl + 4Dsp + $15Ca^{2+}$ + $6SiO_2°$, 31) Ab + H_2O = Anl + $SiO_2°$, 32) Anl = Ne + H_2O + $SiO_2°$, 33) Pg = 2Dsp + Ne + $2SiO_2°$, 34) 21Ab + 14Zo + $20Mg^{2+}$ + $18H_2O$ = 4Tr + 21Pg + $20Ca^{2+}$ + $10SiO_2°$, 35) 21Anl + 14Zo + $20Mg^{2+}$ + $11SiO_2°$ = 4Tr + 21Pg + $20Ca^{2+}$ + $3H_2O$, 36) 11Anl + 10Zo + $20Mg^{2+}$ + $11H_2O$ = 4Chl + 11Pg + $20Ca^{2+}$ + $7SiO_2°$, 37) 9Anl + 5Mrg + $5Mg^{2+}$ + $2SiO_2°$ = 9Pg + Chl + $5Ca^{2+}$ + H_2O, 38) 9Ne + 5Mrg + $5Mg^{2+}$ + $11SiO_2°$ + $8H_2O$ = 9Pg + Chl + $5Ca^{2+}$, 39) 5Pg + 2Zo + $3H_2O$ = 5Anl + 4Mrg + $3SiO_2°$. Also shown are the isoconcentration Ca contours when a sodium mineral is saturated in the presence of diopside or tremolite. In order for feldspars, analcime or micas to persist and remain stable at low $aSiO_2°$ and in the presence of garnet during rodingitization, the Na/Ca ratio of the fluid would have to reach very high values. This can be illustrated by comparing the composition of a 1 *m* ΣCl fluid that corresponds to equilibrium with the assemblage Ab + Qtz + Zo + Prh + Tr (filled circle A) with the composition of the fluid that corresponds to equilibrium with the assemblage Anl + Grs + Zo + Prh + Di (filled circle B). The fluid composition in A is: Na = 0.813 *m*, Ca = 9.32×10^{-2} *m*, pH = 5.34 (neutral pH 5.5). In B, the composition of the fluid is: Na = 1.004 *m*, Ca = 2.38×10^{-4} *m*, pH = 7.29. Our calculations show that equilibrium reaction paths between model hydrothermal fluids previously equilibrated with serpentinites, in the system Na-Ca-Mg-Al-Si-O-H-Cl (< 1 *m*), and Si-Al-rich rocks never produce grossular-bearing assemblages containing feldspars, analcime or micas at the temperature and pressure considered. The dissolution of Si-rich minerals is necessary to produce the increase in the activity of silica required to precipitate Ca in the form of calc-silicates in rodingites. B) Reaction paths followed during reaction of fluids 1 (path A), 2 (path B) and 3 (path C) with a model plagiogranite (see text for details).


A
QUARTZ SATURATION
A
0.05
Prl
Dsp
0.005
0.0005
Prh+Di
Grs
B
Ab
Anl
TALC
TREMOLITE
Anl
Ne
Pg
Ne+Dsp
ANTIGORITE
DIOPSIDE
BRUCITE
Grs+Di
Chl
WOLLASTONITE
-1.5
-2.0
-2.5
-3.0
-3.5
-4.0
-4.5
-5.0
0
1
2
3
4
5
Log $aSiO_2$°
Log (aCa^{2+}/aMg^{2+})

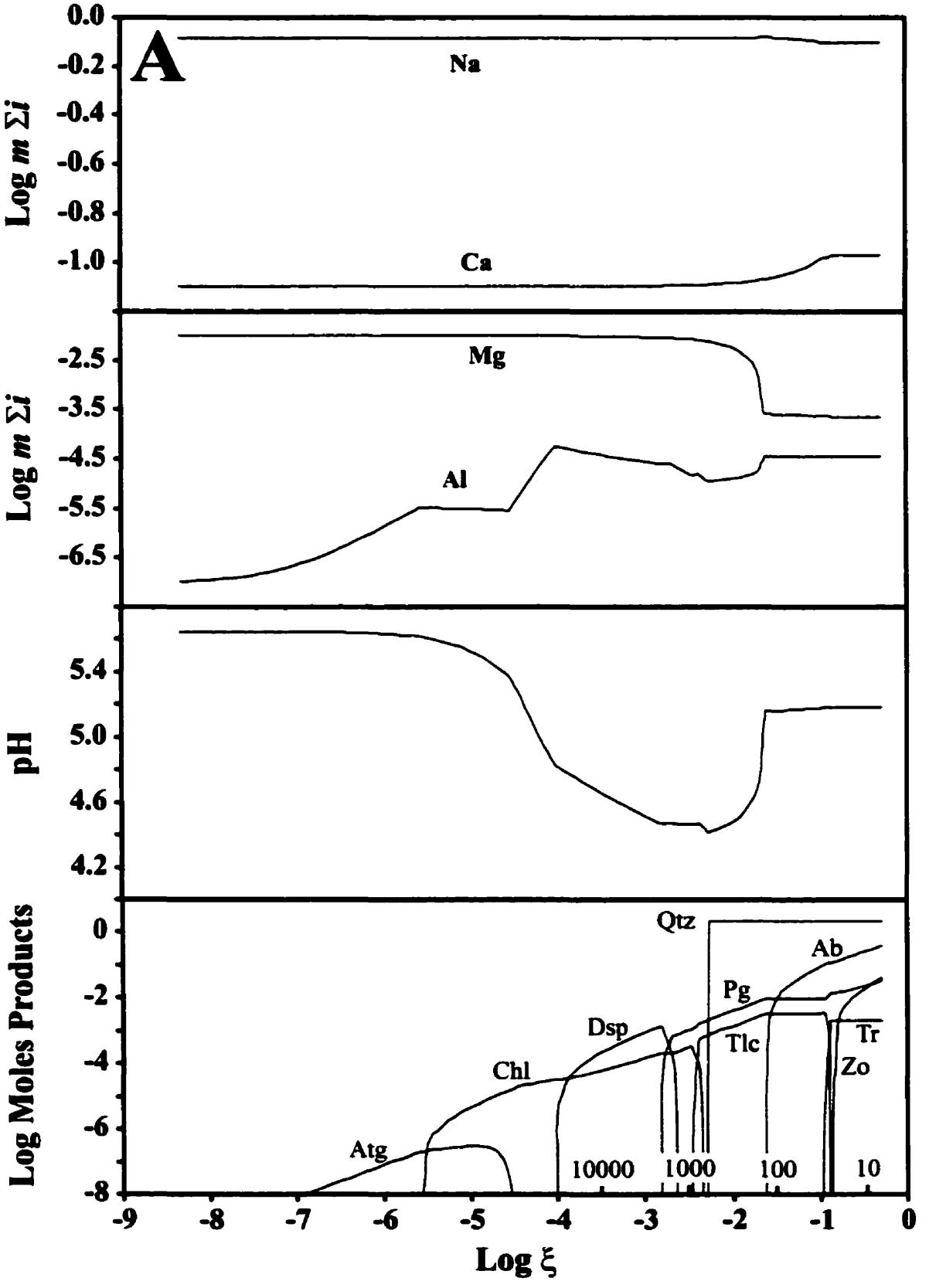

B
-1.5
-2.0
-2.5
-3.0
-3.5
-4.0
-4.5
-5.0
Log $aSiO_2^\circ$
A
B
C
0
1
2
3
4
5
Log (aCa^{2+}/aMg^{2+})

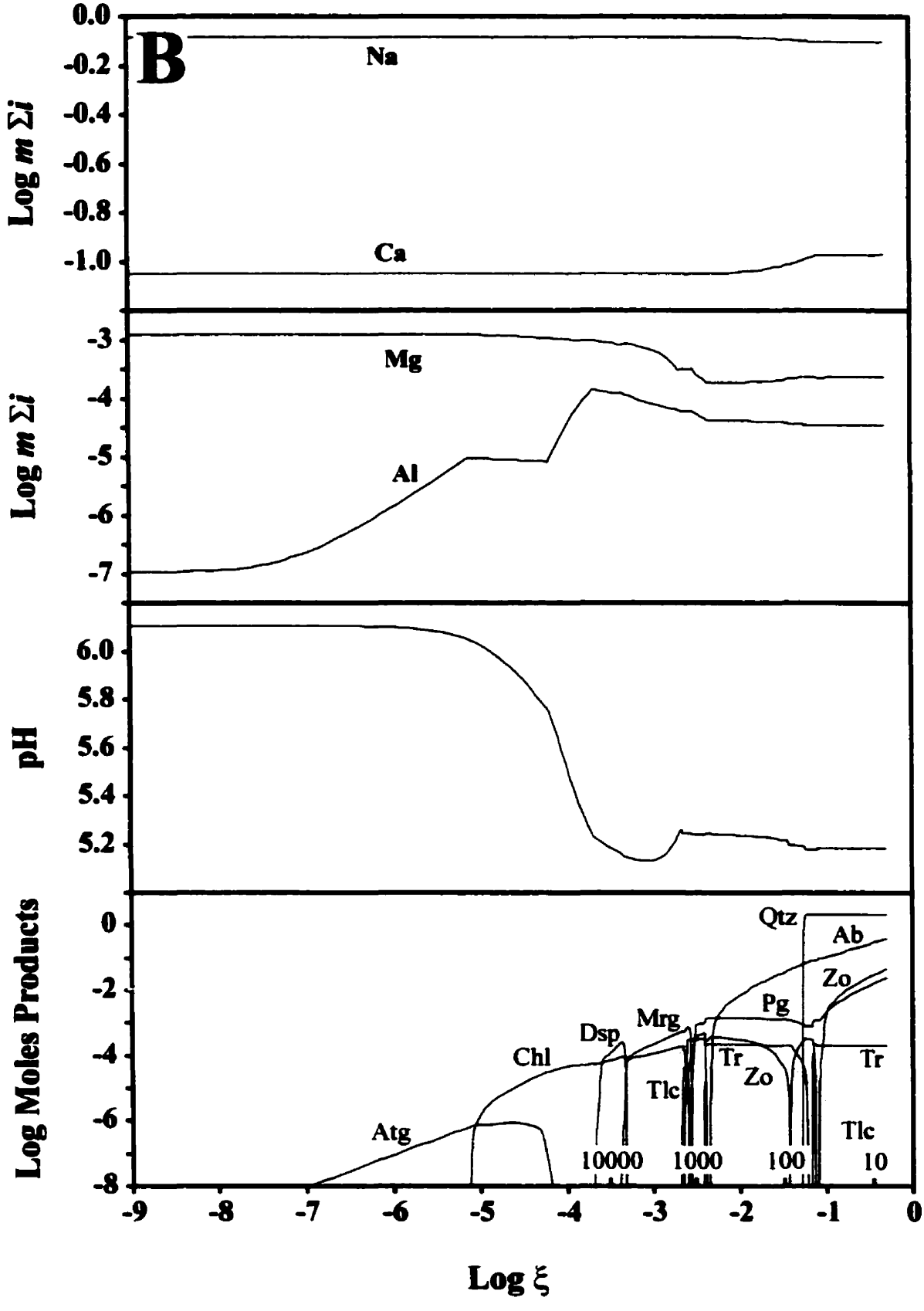
concentration of $1x10^{-7}$ *m* was used). The first fluid, A, contains 0.080 *m* Ca (pH = 5.65) and the second fluid, B, contains 0.089 *m* Ca (pH = 6.11). The compositions of fluids A and B represent equilibrium with antigorite and brucite. The third fluid, C, represents equilibrium among antigorite, brucite and diopside, and contains 0.092 *m* Ca (pH = 7.12). The dominant Ca species in all fluids is $CaCl^+$. It is important to point out here that the purpose of this exercise is not to give solutions that exactly reflect natural calc-silicate alteration processes. The modelling approach used here assumes local equilibrium and does not consider the possible complications that could arise from kinetic considerations or from the presence of counter-diffusing concentration gradients.

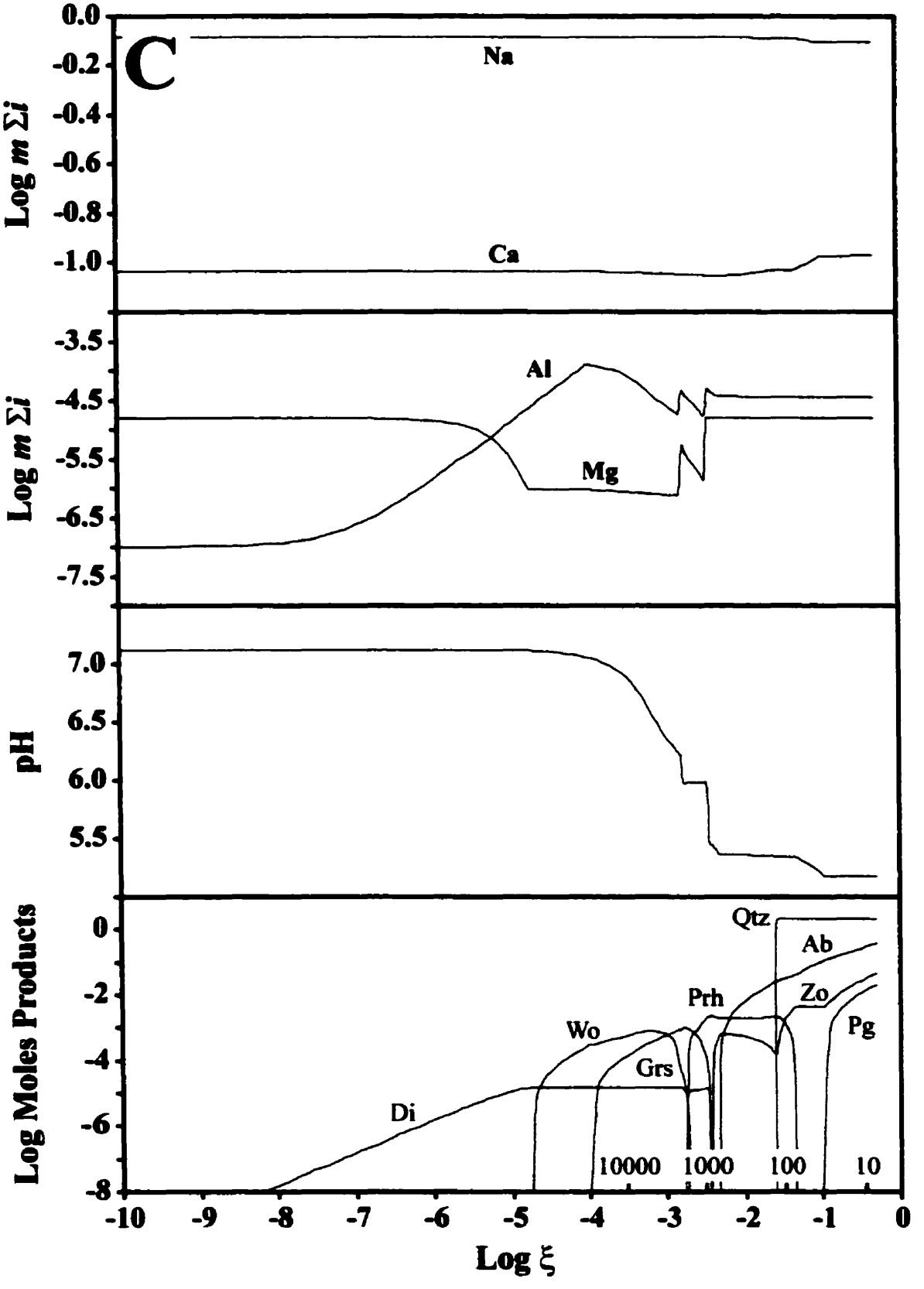
After reaction with the model plagiogranite (closed system, equilibrium reaction paths), the concentration of Ca in the first and second fluid, at any fluid/rock ratio (paths A and B, Figures 12b, 13a and 13b), increases or stays unchanged (the same is true for reaction paths calculated using only plagioclase as the reactant). According to our model, the same increasing or decreasing concentration relationships exist between Ca and Mg with respect to $a SiO_2^0$ and $a(Ca^{2+}/Mg^{2+})$ in the system Ca-Mg-Si-O-H-Cl and in the system Na-Ca-Mg-Al-Si-O-H-Cl as a result of the interaction of slightly alkaline to acidic fluids with the plagiogranite. These relationships indicate that, under isothermal conditions, the Ca responsible for the formation of nephrite in alteration sequences comprising an intervening talc zone between the nephrite and the serpentinite is derived (diffusion or advection) from adjacent dykes or metasedimentary country rocks. The calcium responsible for the formation of nephrite halos at the margin of dykes, without a talc zone, could in theory be derived from more alkaline serpentinizing fluids, whereas zones of diopsidized serpentinite would develop at the contact with Si-rich lithologies from distinctively alkaline and relatively Ca-rich serpentinizing fluids, which have compositions at or close to saturation with diopside. In the latter case, the calcium responsible for the formation of the diopsidite could be derived from the serpentinizing fluid.

Figure 13

Relationship between reaction progress and the secondary mineralogical and fluid compositions during reaction of A) fluid 1, B) fluid 2, and C) fluid 3 with a model plagiogranite (see text for details).


A
Na
Ca
Mg
Al
Log m Σi
pH
Log Moles Products
Log ξ
Qtz
Ab
Pg
Dsp
Tlc
Tr
Zo
Chl
Atg
10000
1000
100
10
0.0
-0.2
-0.4
-0.6
-0.8
-1.0
-2.5
-3.5
-4.5
-5.5
-6.5
5.4
5.0
4.6
4.2
0
-2
-4
-6
-8
-9
-8
-7
-6
-5
-4
-3
-2
-1
0


B
Na
Ca
Log m Σi
0.0
-0.2
-0.4
-0.6
-0.8
-1.0
Mg
Al
-3
-4
-5
-6
-7
pH
6.0
5.8
5.6
5.4
5.2
Log Moles Products
0
-2
-4
-6
-8
Qtz
Ab
Zo
Pg
Mrg
Dsp
Chl
Tr
Zo
Tr
Tlc
Atg
Tlc
10000
1000
100
10
-9
-8
-7
-6
-5
-4
-3
-2
-1
0
Log ξ


C
Na
Ca
Al
Mg
Log m Σi
Log m Σi
pH
Log Moles Products
Qtz
Ab
Zo
Pg
Prh
Wo
Grs
Di
10000
1000
100
10
0.0
-0.2
-0.4
-0.6
-0.8
-1.0
-3.5
-4.5
-5.5
-6.5
-7.5
7.0
6.5
6.0
5.5
0
-2
-4
-6
-8
-10
-9
-8
-7
-6
-5
-4
-3
-2
-1
0
Log ξ

Rodingitization of Si-Al-rich rocks

The very low steady state Ca concentration reached towards the end of the olivine-H_2O experiment ($1.5x10^{-6}$ *M*) does not support the idea that the calcium required to form rodingites in dunite-dominated rock sequences is derived solely from serpentinization of olivine. From the fluid compositions in the previous section, the difference in the Ca concentration between fluid 1 and fluid 3 is ~ 0.01 *m*. Reaction of fluid 1 with olivine containing 0.002 a.p.f.u. Ca could potentially saturate the fluid with diopside, if all the Ca is transferred to the fluid and Cl is maintained at 1 *m*, by reaction with 5 moles of olivine. However, as the transformation of 5 moles of olivine to serpentine + brucite requires ~ 7.5 moles of water (~ 0.9 Kg), and buffering of the fluid by rock will produce extremely saline fluids, it is very difficult to evaluate the actual potential for diopside saturation in such fluids. As already mentioned, if pyroxenes are present in the rock, however, the potential for fluids to have compositions similar to those corresponding to equilibrium between brucite, serpentine and diopside is greatly increased. Depending on the initial composition of the fluid, the Ca concentration will vary with total Cl and the ΣCations (less Ca and Mg, which adjust to equilibrium values)/Cl ratio. The effect of reacting a fluid buffered by antigorite, brucite and diopside with a felsic rock is illustrated by the reaction of the third fluid with plagiogranite from the previous section (path C; Figures 12b and 13c). The calculated reaction path indicates that there is a decrease in the Ca concentration of the fluid at elevated fluid/rock ratios, which corresponds to the formation of calc-silicate mineral assemblages, and suggests that serpentinizing fluids are a potential source of Ca for rodingitization, provided the starting composition is appropriate. Comparison of fluid compositions and mineral parageneses along paths A, B and C in Figure 12b and Figures 13a, 13b and 13c suggest that rodingites form primarily because of the very low silica activity and the relatively high pH (here 1.6 pH units higher than neutrality at saturation with diopside) of serpentinizing fluids that have initial compositions at close to or at saturation with diopside. Therefore, as long as relicts of a Ca-(Na)-rich phase (primary pyroxenes) remain in the peridotite during serpentinization, each successive batch of fluid (initially undersaturated with respect to diopside) having access to the partially serpentinized peridotite will evolve compositionally towards

saturation with diopside. Comparing the Ca concentrations in fluid A (Na, Ca and Cl typical of many sub-seafloor and other types of hydrothermal fluids), fluid B and fluid C after any stage of reaction with plagiogranite (Figures 12b and 13c) reveal that the differences among them are very small. It is evident from the data that trying to establish exactly the relative proportions of Ca contributed to rodingitization by the initial fluid (before it is allowed to interact with peridotite) and by the peridotite undergoing serpentinization is impossible. However, because the amount of Ca that can be added to the fluid as a result of reaction with ultramafic rocks is small compared to the initial value (refer again to fluids A and C), most of the Ca added to the rock during rodingitization is probably that initially in the fluid. The very small difference between the initial Ca concentration of fluid C and that of fluid C at any stage of reaction with the model plagiogranite, and the fact that fluid C has a very low pH-buffering potential, suggest that very elevated fluid/rock ratios would be required to explain the formation of rodingites from a serpentinizing fluid saturated with diopside. Preliminary multiple pass calculations based on a local equilibrium, one-dimensional 'flow-line' model (Heinrich et al., 1996) involving the reaction of diopside-saturated serpentinizing fluids with feldspar-rich rocks also suggest that very large amounts of fluids (fluid/rock ratios > 300, see Appendix I) are required to form garnet-rich rodingites.

CONCLUSIONS

Fluid inclusion and mineralogical data suggest that natural, high temperature (250-400°C) serpentinizing fluids are commonly Na- and Cl-dominant. Our experimental findings suggest that externally-derived, Ca-Cl-bearing serpentinizing fluids can circulate through peridotites without losing significant Ca. This observation has important implications for our understanding of the rodingitization of Si-Al-rich rocks and of the calc-silicate metasomatism of ultramafic rocks at the contact with the latter. Thermodynamic equilibrium calculations indicate that the amount of Ca which can be added to a Na-Ca-Cl-dominant fluid as a result of the dissolution of Ca-bearing phases

during serpentinization at low $\mu SiO_2°$ is limited by saturation with diopside, and that this amount is very small compared with the initial Ca concentration of the metasomatizing fluid. Computer simulations indicate that maximum Ca concentrations and pH values, and minimum SiO_2 concentrations are achieved when the fluid is in equilibrium with the assemblage diopside + serpentine + brucite. Fluids in equilibrium with this assemblage offer optimal conditions for rodingitization in Si-Al-rich lithologies. The data and arguments presented in this study suggest that, contrary to conventional wisdom, the proportion of Ca contributed by the host ultramafic rocks to rodingites is very small. However, the small supplementary amounts of calcium and sodium that are added to the fluid, essentially as a result of the serpentinization of the primary pyroxenes, appear to be necessary to move the pH of the fluid to values high enough to produce grossular-rich rodingites. On the other hand, the sequence of alteration serpentinite → talc → nephrite, frequently observed in nature towards contacts with Si-Al-rich rocks, probably results from the reaction of slightly alkaline to acidic fluids, derived from the latter, with the adjacent ultramafic rocks.

ACKNOWLEDGEMENTS

This research was made possible through grants from NSERC and JM Asbestos Inc. to AEW-J and NSERC and FCAR scholarships to CN. The first author is grateful to Bruce Mountain for instruction in the use of the flow-though apparatus, Michel Leroux for performing the BET measurement, Glenn Poirier for training on the electron microprobe facility, and Sandra Lalli and Glenna Keating for training on the atomic absorption facilities, all at McGill University.

REFERENCES

Agrinier, P., Hékinian, R., Bideau, D. and M. Javoy, 1995, O and H stable isotope compositions of oceanic crust and upper mantle rocks exposed in the Hess Deep near the Galapagos Triple Junction, Earth and Planetary Science Letters, v. 136, p. 183-196.

Anbeek, C., 1992, Surface roughness of minerals and implications for dissolution studies, Geochimica et Cosmochimica Acta, v. 56, p. 1461-1469.

Anhaeusser, C. R., 1976, The nature of chrysotile asbestos occurrences in southern Africa, a review, Economic Geology, v. 71, p. 96-116.

Barnes, I. and J. R. O'Neil, 1969, The relationships between fluids in some fresh Alpine-type ultramafics and possible modern serpentinization, Western United States, Geological Society of America Bulletin, v. 80, p. 1947-1960.

Bergeron, M., 1988, Distribution et comportement du bore dans la croûte océanique, Canadian Journal of Earth Sciences, v. 26, p. 782-790.

Berman, R. G., Engi, M., Greenwood, H. J. and T. H. Brown, 1986, Derivation of internally-consistent thermodynamic data by the technique of mathematical programming: a review with application to the system MgO-SiO_2-H_2O, Journal of Petrology, v. 27, p. 1331-1364.

Berndt, M. E. and W. E. Seyfried, Jr., 1993, Calcium and sodium exchange during hydrothermal alteration of calcic plagioclase at 400° C and 400 bars, Geochimica et Cosmochimica Acta, v. 57, p. 4445-4451.

Bonatti, E., 1968, Ultramafic rocks from the Mid-Atlantic Ridge, Nature, v. 219, p. 363-364.

Bonatti, E., Lawrence, J. R. and N. Morandi, 1984, Serpentinization of oceanic peridotites: temperature dependence of mineralogy and boron content, Earth and Planetary Science Letters, v. 70, p. 88-94.

Brunauer, S., Emmett, P. H. and E. Teller, 1938, Adsorption of gases in multimolecular layers, Journal of the American Chemical Society, v. 60, p. 309-319.

Butterfield, D. A. and G. J. Massoth, 1994, Geochemistry of north Cleft segment vent fluids: temporal changes in chlorinity and their possible relation to recent volcanism, Journal of Geophysical Research, v. 99, p. 4951-4968.

Butterfield, D. A., Massoth, G. J., McDuff, R. E., Lupton, J. E. and M. D. Lilley, 1990, Geochemistry of hydrothermal fluids from Axial Seamount hydrothermal emissions study vent field, Juan de Fuca Ridge: subseafloor boiling and subsequent fluid-rock interaction, Journal of Geophysical Research, v. 95, p. 12,859-12,921.

Butterfield, D. A., McDuff, R. E., Mottl, M. J., Lilley, M. D., Lupton, J. E. and G. J. Massoth, 1994a, Gradients in the composition of hydrothermal fluids from the Endeavor segment vent field: phase separation and brine loss, Journal of Geophysical Research, v. 99, p. 9561-9583.

Butterfield, D. A., McDuff, R. E., Franklin, J. and C. G. Wheat, 1994b, Geochemistry of hydrothermal vent fluids from Middle Valley, Juan de Fuca ridge, Proceedings of the Ocean Drilling Program, Scientific Results, v. 139, p. 395-410.

Cannat, M., 1993, Emplacement of mantle rocks in the seafloor at mid-ocean ridges, Journal of Geophysical Research, v. 98, p. 4163-4172.

Charlou, J. L., Fouquet, Y., Donval, J. P. and J. M. Auzende, 1996, Mineral and gas chemistry of hydrothermal fluids on an ultrafast spreading ridge: East Pacific Rise, 17° to 19°S (Naudur cruise, 1993) phase separation processes controlled by volcanic and tectonic activity, Journal of Geophysical Research, v. 101, p. 15,899-15,919.

Chidester, A. H., Albee, A. L. and W. M. Cady, 1978, Petrology, structure, and genesis of the Asbestos-bearing ultramafic rocks of the Belvidere Mountain area in Vermont, U. S. Geological Survey Professional Paper 1016, 88 p.

Coleman, R. G. and T. E. Keith, 1971, A chemical study of serpentinization – Burro Mountain, California, Journal of Petrology, v. 12, p. 311-328.

Compagnoni, R., Conte, R., Facchinelli, A., Orione, P., Rossetti, P. and C. Trossarelli, 1998, The rodingite of Bellecombe (Val d'Aosta, Italy): a petrographic and fluid inclusion study (abstract), International Mineralogical Association, 17th General Meeting, August 9-14, 1998, Toronto, Canada, Abstracts and Programme, p. A77.

Coulton, A. J., Harper, G. D. and D. S. O'Hanley, 1995, Oceanic versus emplacement age serpentinization in the Josephine ophiolite: implications for the nature of the Moho at intermediate and slow spreading ridges, Journal of Geophysical Research, v. 100, p. 22,245-22,260.

Day, H. W., Chernosky, J. V. and H. J. Kumin, 1985, Equilibria in the system $MgO-SiO_2-H_2O$: a thermodynamic analysis, American Mineralogist, v. 70, p. 237-248.

de Ronde, C. E. J., 1995, Fluid chemistry and isotopic characteristics of seafloor hydrothermal systems and associated VMS deposits: potential for magmatic contributions, *in* Magmas, Fluids and Ore Deposits, Thompson, J. F. H., editor, Mineralogical Association of Canada Short Course Series, v. 23, p. 479-509.

Eggleston, C. M., Hochella, M. F., Jr. and G. A. Parks, 1989, Sample preparation and ageing effects on the dissolution rate and surface composition of diopside, Geochimica et Cosmochimica Acta, v. 53, p. 797-804.

Evans, B. W. and V. Trommsdorff, 1970, Regional metamorphism of ultramafic rocks in the Central Alps: parageneses in the system $CaO-MgO-SiO_2-H_2O$, Schweizerische Mineralogische und Petrographische Mitteilungen, v. 50, p. 481-492.

Haggerty, J. A., 1991, Evidence from fluid seeps atop serpentinite seamounts in the Mariana Forearc: clues for emplacement of the seamounts and their relationship to forearc tectonics, Marine Geology, v.102, p. 293-309.

Haggerty, J. A. and S. Chaudhuri, 1992, Strontium isotopic composition of the interstitial waters from Leg 125: Mariana and Bonin forearcs, Proceedings of the Ocean Drilling Program, Scientific Results, v. 125, p. 397-400.

Hajash, A. and G. W. Chandler, 1981, An experimental investigation of high-temperature interactions between seawater and rhyolite, andesite, basalt and peridotite, Contributions to Mineralogy and Petrology, v. 78, p. 240-254.

Heinrich, C. A., Walshe, J. L. and B. P. Harrold, 1996, Chemical mass transfer modelling of ore-forming hydrothermal systems: current practice and problems, Ore Geology Reviews, v. 10, p. 319-338.

Helgeson, H. C., Kirkham, D. H. and G. C. Flowers, 1981, Theoretical prediction of the thermodynamic behavior of aqueous electrolytes at high pressures and temperatures:

IV. Calculation of activity coefficients, osmotic coefficients, and apparent molal and standard and relative partial molal properties to 600°C and 5 kb, American Journal of Science, v. 281, p. 1249-1516.

Hockley, J. J., Birch, W. D. and H. K. Worner, 1978, A nephrite deposit in the great serpentine belt of New South Wales, Journal of the Geological Society of Australia, v. 25, p. 249-254.

Ishii, T., Robinson, P. T., Maekawa, H. and R. Fiske, 1992, Petrological studies of peridotites from diapiric serpentinite seamounts in the Izu-Ogasawara-Mariana forearc, Leg 125, Proceedings of the Ocean Drilling Program, Scientific Results, v. 125, p. 445-485.

Janecky, D. R. and W. E. Seyfried, Jr., 1986, Hydrothermal serpentinization of peridotite within the oceanic crust: experimental investigations of mineralogy and major element chemistry, Geochimica et Cosmochimica Acta, v. 50, p. 1357-1378.

Johnson, J. W., Oelkers, E. H. and H. C. Helgeson, 1992, SUPCRT92: a software package for calculating the standard molal thermodynamic properties of minerals, gases, aqueous species, and reactions from 1 to 5000 bars and 0° to 1000°C, Computers and Geoscience, v. 17, p. 899-947.

Kholodkevich, I. V. and N. N. Barinov, 1995, Some features of harzburgite-seawater interaction at increased P-T conditions, *in* Proceedings of the 8th International Symposium on Water-Rock Interaction, Vladivostok, Russia, 15-19 August 1995, Kharaka, Y. K. and O. V. Chudaev, editors, A. A. Balkema, Rotterdam, Brookfield, p. 801-804.

Knauss, K. G. and T. J. Wolery, 1986, Dependence of albite dissolution kinetics on pH and time at 25°C and 70°C, Geochimica et Cosmochimica Acta, v. 50, p. 2481-2497.

Komor, S. C., Elthon, D. and J. F. Casey, 1985, Serpentinization of cumulate ultramafic rocks from the North Arm Mountain massif of the Bay of Islands ophiolite, Geochimica et Cosmochimica Acta, v. 49, p. 2331-2338.

Koons, P. O., 1981, A study of natural and experimental metasomatic assemblages in an ultramafic-quartzofeldspathic metasomatic system from the Haast schist, South Island, New Zealand, Contributions to Mineralogy and Petrology, v. 78, p. 189-195.

Kretz, R., 1983, Symbols for rock-forming minerals, American Mineralogist, v. 68, p. 277-279.

Labotka, T. C. and A. L. Albee, 1979, Serpentinization of the Belvidere Mountain ultramafic body, Vermont: mass balance and reaction at the metasomatic front, Canadian Mineralogist, v. 17, p. 831-845.

Laurent, R. and Y. Hébert, 1979, Paragenesis of serpentine assemblages in Harzburgite tectonite and dunite cumulate from the Québec Appalachians, Canadian Mineralogist, v.17, p. 857-869.

Macdonald, A. H., 1984, Water diffusion rates through serpentinized peridotites: implications for reaction induced dynamic and chemical effects in ultramafic rocks, Ph. D. Thesis, University of Western Ontario, Canada, 265 p.

Macdonald, A. H. and W. S. Fyfe, 1985, Rate of serpentinization in seafloor environments, Tectonophysics, v. 116, p. 123-135.

Menzies, M. A., Long, A., Ingram, G., Tatnell, M. and D. Janecky, 1993, MORB peridotite-sea water interaction: experimental constraints on the behaviour of trace elements, $^{87}Sr/^{86}Sr$ and $^{143}Nd/^{144}Nd$ ratios, *in* Magmatic Processes and Plate Tectonics, Prichard, H. M., Alabaster, T., Harris, N. B. W. and C. R. Neary, editors, Geological Society Special Publication No. 76, p. 309-322.

Mittwede, S. K. and E. S. Schandl, 1992, Rodingites from the southern Appalachian Piedmont, Southern Carolina, USA, European Journal of Mineralogy, v. 4, p. 7-16.

Miura, Y., Rucklidge, J. and G. L. Nord, Jr., 1981, The occurrence of chlorine in serpentine minerals, Contributions to Mineralogy and Petrology, v. 76, p. 17-23.

Moody, J. B., 1976, An experimental study of the serpentinization of iron-bearing olivines, Canadian Mineralogist, v. 14, p.462-478.

Mottl, M. J., 1992, Pore waters from serpentinite seamounts in the Mariana and Izu-Bonin forearcs, Leg 125, Evidence for volatiles from the subducting slab, Proceedings of the Ocean Drilling Program, Scientific Results, v. 125, p. 373-385.

Mountain, B. W., 1992, Fluid-rock interaction paths: natural and experimental examples, Ph. D. Thesis, McGill University, Canada, 354 p.

Oelkers, E. H., 1996, Physical and chemical properties of rocks and fluids for chemical mass transport calculations, *in* Reactive transport in porous media, Lichtner, P. C., Steefel, C. I. and E. H. Oelkers, editors, Mineralogical Society of America, Reviews in Mineralogy, v. 34, p. 131-191.

O'Hanley, D. S., 1991, Fault-related phenomena associated with hydration and serpentine recrystallization during serpentinization, Canadian Mineralogist, v. 29, p. 21-35.

O'Hanley, D. S., 1992, Solution to the volume problem in serpentinization, Geology, v. 20, p. 705-708.

O'Hanley, D. S. and R. Offler, 1992, Characterization of multiple serpentinization, Woodsreef, New South Wales, Canadian Mineralogist, v. 30, p. 1113-1126.

O'Hanley, D. S., Schandl, E. S. and F. J. Wicks, 1992, The origin of rodingites from Cassiar, British Columbia, and their use to estimate T and $P(H_2O)$ during serpentinization, Geochimica et Cosmochimica Acta, v. 56, p. 97-108.

O'Hanley, D. S. and F. J. Wicks, 1995, Conditions of formation of lizardite, chrysotile and antigorite, Cassiar, British Columbia, Canadian Mineralogist, v. 33, p. 753-773.

Peacock, S. M., 1987, Thermal effects of metamorphic fluids in subduction zones, Geology, v. 15, p. 1057-1060.

Peretti, A, Dubessy, J., Mullis, J., Frost, B. R. and V. Trommsdorff, 1992, Highly reducing conditions during Alpine metamorphism of the Malenco peridotite (Sondrio, northern Italy) indicated by mineral paragenesis and H_2 in fluid inclusions, Contributions to Mineralogy and Petrology, v. 112, p. 329-340.

Pfeifer, H. -R., 1977, A model for fluids in metamorphosed ultramafic rocks, Schweizerische Mineralogische und Petrographische Mitteilungen, v. 57, p. 361-396.

Phillips, A. H. and H. H. Hess, 1936, Metamorphic differentiation at contacts between serpentinite and siliceous country rocks, American Mineralogist, v. 21, p. 333-362.

Ponader, H. B., 1989, Experimental hydrothermal dissolution of forsterite, enstatite, diopside and labradorite, Ph. D. thesis, Stanford University, 184 p.

Rose, N. M., Bird, D. K. and J. G. Liou, 1992, Experimental investigation of mass transfer - albite, Ca-Al-silicates, and aqueous solutions, American Journal of Sciences, v. 292, p. 21-57.

Rucklidge, J., 1972, Chlorine in partially serpentinized dunite, Economic Geology, v. 67, p. 38-40.

Rucklidge, J. C. and G. C. Patterson, 1977, The role of chlorine in serpentinization, Contributions to Mineralogy and Petrology, v. 65, p. 39-44.

Sakai, R., Kusakabe, M., Noto, M. and T. Ishii, 1990, Origin of waters responsible for serpentinization of the Izu-Ogasawara-Mariana forearc seamounts in view of hydrogen and oxygen isotope ratios, Earth and Planetary Science Letters, v. 100, p. 291-303.

Sanford, R. F., 1981, Mineralogical and chemical effects of hydration reactions and applications to serpentinization, American Mineralogist, v. 66, p. 290-297.

Scambelluri, M., Piccardo, G. B., Philippot, P., Robbiano, A. and L. Negretti, 1997, High salinity fluid inclusions formed from recycled seawater in deeply subducted alpine serpentinite, Earth and Planetary Science Letters, v. 148, p. 485-499.

Schandl, E. S., O'Hanley, D. S. and F. J. Wicks, 1989, Rodingites in serpentinized ultramafic rocks of the Abitibi greenstone belt, Ontario, Canadian Mineralogist, v. 27, p. 579-591.

Schandl, E. S., O'Hanley, D. S., Wicks, F. J. and T. K. Kyser, 1990, Fluid inclusions in rodingites: a geothermometer for serpentinization, Economic Geology, v. 85, p. 1273-1276.

Seyfried, W. E., Jr. and W. E. Dibble, Jr., 1980, Seawater-peridotite interaction at 300°C and 500 bars: implications for the origin of oceanic serpentinites, Geochimica et Cosmochimica Acta, v. 44, p. 309-321.

Seyfried, W. E., Jr., Janecky, D. R. and M. J. Mottl, 1984, Alteration of the oceanic crust: implications for geochemical cycles of lithium and boron, Geochimica et Cosmochimica Acta, v. 48, p. 557-569.

Shand, S. J., 1949, Rocks of the mid-Atlantic ridge, Journal of Geology, v. 57, p. 89-92.

Shock, E. L., Sassani, D. C., Willis, M. and D. A. Sverjensky, 1997, Inorganic species in geologic fluids: correlations among standard molal thermodynamic properties of aqueous ions and hydroxide complexes, Geochimica et Cosmochimica Acta, v. 61, p. 907-950.

Sverjensky, D. A., Shock, E. L. and H. C. Helgeson, 1997, Prediction of the thermodynamic properties of aqueous metal complexes to 1000°C and 5 kb, Geochimica et Cosmochimica Acta, v. 61, p. 1359-1412.

Toft, P. B., Arkani-Hamed, J. and S. E. Haggerty, 1990, The effects of serpentinization on density and magnetic susceptibility: a petrophysical model, Physics of the Earth and Planetary Interiors, v. 65, p. 137-157.

Von Damm, K. L., 1990, Seafloor hydrothermal activity: black smoker chemistry and chimneys, Annual Reviews of Earth and Planetary Science, v. 18, p. 173-204.

Wenner, D. B. and H. P. Taylor, Jr., 1973, Oxygen and hydrogen isotope studies of the serpentinization of ultramafic rocks in oceanic environments and continental ophiolite complexes, American Journal of Science, v. 273, p. 207-239.

Wenner, D. B. and H. P. Taylor, Jr., 1974, D/H and O^{18}/O^{16} studies of serpentinization of ultramafic rocks, Geochimica et Cosmochimica Acta, v. 38, p. 1255-1286.

Williams-Jones, A. E., Wood, S. A., Mountain, B. W. and C. H. Gammons, 1994, Experimental water-rock interaction: applications to ore-forming hydrothermal systems, *in* Alteration and alteration processes associated with ore-forming systems, Lentz, D. R., editor, Geological Association of Canada Short Course Notes, v. 11, p. 131-160.

Wolery, T. J., 1992, EQ3/6, a software package for geochemical modeling of aqueous systems: package overview and installation guide (Version 7.0), Lawrence Livermore National Laboratory, UCRL-MA-110662 Part 1, 66 p.

PART II

FIELD AND LABORATORY STUDIES OF SERPENTINITES, FELSIC ROCKS AND THEIR ALTERATION PRODUCTS IN THE JM ASBESTOS MINE, ASBESTOS, QUÉBEC

§

PROLOGUE

In the first part of the thesis, the chemical factors that control serpentinization and rodingitization were studied experimentally and by way of thermodynamic modelling. In the second part of the thesis, studies of natural occurrences of rodingites are presented from the JM Asbestos mine, Asbestos, Québec. These rodingites formed by the metasomatic replacement of slate, diorite, granite, and serpentinite at the contact with granite and diorite. The origin of the felsic intrusive rocks is discussed in Chapter IV. In Chapter V, mineralogical and bulk-rock chemical mass balance analyses are used to establish the factors that controlled rodingitization after the emplacement of the felsic rocks. Microthermometric data on fluid inclusions and mineral parageneses are used in Chapters VI and VII to determine the nature of the fluids that were involved in rodingitization, and to determine the pressure and temperature conditions under which this alteration occurred. The origin and distribution of amphibole-group minerals in the JM Asbestos mine is discussed in Chapter VIII.

INTRODUCTION TO CHAPTER IV

This chapter represents the first of a series of five chapters aimed at determining the origin of the rodingites in the JM Asbestos mine, Asbestos, Québec. These rodingites represent the calc-silicate alteration products of dioritic and granitic dykes, serpentinites at the contact with these intrusive rocks, and slates at the base of the Asbestos ophiolite. In order to determine the timing and geological context of rodingitization, it was necessary first to determine the origin of the felsic intrusive rocks within the framework of the geological evolution of the Asbestos ophiolite. In this chapter, geological and textural evidence are presented that establish the relationship of the felsic dykes to the serpentinites. Previous ideas on the nature of the diorites are revised.

CHAPTER IV

K-RICH DIORITIC-MONZODIORITIC AND GRANITIC DYKE INTRUSION IN SERPENTINIZED PERIDOTITES OF THE JM ASBESTOS MINE, QUÉBEC

by

Charles Normand and Anthony E. Williams-Jones

Department of Earth and Planetary Sciences, McGill University, 3450 University Street, Montréal (Qué), Canada, H3A 2A7.

ABSTRACT

A conspicuous feature of the Asbestos ophiolite, Québec, is the presence of intrusive sheets comprising biotite-diorites and biotite-monzodiorites, cut by granodiorites, andalusite granites and later leucogranitic pegmatites. These felsic rocks cut serpentinized harzburgite and, rarely, dunite but do not extend into the adjacent rocks. Field and laboratory observations indicate that the peridotites had been substantially serpentinized prior to intrusion of these felsic rocks. The composition of the dioritic-monzodioritic rocks, i.e., their strong enrichment in hygromagmatophile elements (K, Rb, and Th) and Ce, and depletion in Nb, suggests that they formed in a subduction-obduction environment. However, the peraluminous nature of the associated granites implies that an appreciable proportion of continentally derived material (continental crust or sedimentary rocks derived from its erosion and deposited on the continental margin and seafloor) contributed to felsic magmatism.

Intrusion of the felsic rocks is interpreted to have taken place after detachment of the Asbestos ophiolite from its seafloor setting and before or during its emplacement onto the Caldwell Group sediments of the Laurentian continental margin, which had undergone early Taconian deformation between 470 and 460 Ma (Whitehead et al., 1996; Castonguay et al., 1997). Hébert and Bédard (1998) suggested that the ophiolite was emplaced onto the continent at approximately 460 Ma based on the age of baddeleyite, which replaced 472 Ma zircon in a trondhjemite dyke. The occurrence of the andalusite granites in the Asbestos ophiolite is significant because it supports the idea that the ophiolite was detached and emplaced without having been deeply buried in a subduction trench.

The nature and evolution of the felsic intrusives and their spatial and temporal relationships to the Asbestos ophiolite suggest that they were emplaced through partially serpentinized upper mantle units either; 1) above a subduction zone and close to a young fore-arc extensional zone, where obduction was initiated shortly before intrusion; or 2) as a result of the obduction of the ophiolite onto the Laurentian margin.

INTRODUCTION

An interesting and potentially significant feature of many ophiolites is the occurrence in them of felsic intrusives that display cross-cutting relationships with the serpentinized ultramafic units but do not extend into the amphibolite sole or overlying mafic units, such as in the Oman ophiolites (Lippard et al., 1986; Boudier et al., 1988; Cox et al., 1999). This association of felsic intrusions with serpentinites is particularly well exposed in the JM Asbestos mine, Québec, where swarms of biotite- to feldspar-rich, quartz-free dioritic-monzodioritic dykes and later peraluminous andalusite-, niobian rutile- and tourmaline-bearing granitic-granodioritic dykes intruded serpentinized harzburgite and dunite of the Asbestos ophiolite (trondhjemites also occur in the Asbestos ophiolite, but were not observed in the JM Asbestos mine). The dykes are rich in potassium, large-ion-lithophile (LILE) and high-field-strength elements (HFSE) and display subduction-related geochemical affinities. Comparable intrusive rocks occur in the Thetford Mines ophiolite complex, between Lac Nicolet and Thetford Mines (Figure 1).

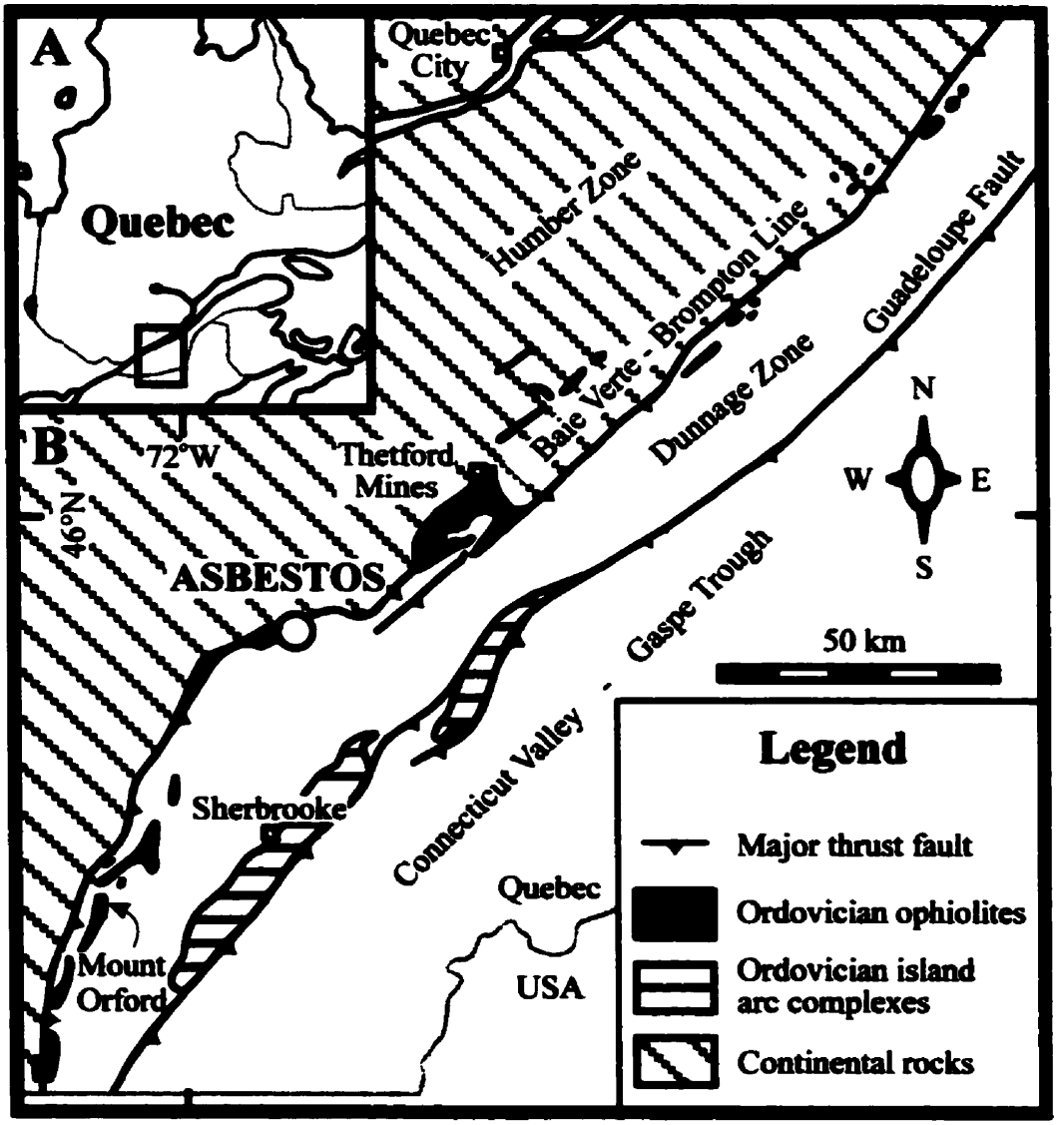
The emplacement history of the felsic intrusive rocks in the Asbestos ophiolite, especially as regards the timing of intrusion relative to the timing of serpentinization and obduction, remains largely unknown, and reconstructing this history is essential to understanding the evolution of the latter. In this paper, we present petrographic, mineralogical, structural and geochemical data, which place some constraints on the intrusive history of the felsic rocks of the Asbestos ophiolite.

TECTONIC SETTING AND METAMORPHISM

Serpentinites containing felsic intrusive bodies occur discontinuously along a narrow ophiolite belt comprising allochthonous slivers of oceanic rocks enclosed in a zone of mélange, which extends along the entire length of the Québec Appalachians, from

Figure 1

Geological map showing the distribution of ophiolitic rocks within the main lithotectonic zones of southeastern Québec (modified after Normand et al., 1996).


A
Quebec City
Quebec
Humber Zone
Baie Verte - Brompton Line
Guadeloupe Fault
Dunnage Zone
B
72°W
Thetford Mines
46°N
ASBESTOS
N
W
E
S
Gaspe Trough
50 km
Connecticut Valley
Sherbrooke
Quebec
USA
Mount Orford
Legend
Major thrust fault
Ordovician ophiolites
Ordovician island arc complexes
Continental rocks

the Québec-Vermont border to the Gaspésian peninsula (Olsen, 1961; De, 1961, 1972; St-Julien and Hubert, 1975; Williams and St-Julien, 1982; Laurent et al., 1984; Clague et al., 1985; Brodeur and Marquis, 1995). The felsic intrusive bodies occurring in the serpentinites comprise trondhjemites, diorites and subaluminous to peraluminous granitic rocks. In the discussion that follows, the Asbestos, Thetford Mines, and Orford ophiolites, which are part of this belt (Figure 1), will be considered together to provide a broader context for understanding the emplacement history of the Asbestos ophiolite.

Origin of the ophiolites

The geochemical signatures of the Thetford Mines, Asbestos and Orford ophiolites suggest that they developed in an arc environment (Hébert and Laurent, 1989; Harnois and Morency, 1989; Laurent and Hébert, 1989; Olive et al., 1997; Hébert and Bédard, 1998). Based on elevated Th/La values, positive U and Pb anomalies, negative Nb anomalies, and Nd-isotope geochemistry, Olive et al. (1997) proposed that the melts that produced the tholeiitic and boninitic mafic volcanic and intrusive rocks, which compose the Thetford Mines ophiolite, contain a significant proportion of a subduction slab-derived component comprising recycled continental crust-related material. Zircon crystals extracted from a trondhjemite dyke in the Orford ophiolite (U/Pb age of 504 ± 3 Ma: David et al., 1993; David and Marquis, 1994), from granitic rocks at the base of the Thetford Mines ophiolite (470–460 Ma; Whitehead et al., 2000) and from calc-silicate bodies in metamorphosed ultramafic rocks and volcanic rocks of the Ordovician volcanic Ascot arc complex to the East, all contain a significant component of inherited Grenvillian and older ages (1.1-2.1 Ga: David and Marquis, 1994; Trzcienski and Gromet, 1992; Trzcienski, 1994). This suggests strongly that the ophiolites formed proximal to continental blocks of Grenvillian age, or younger metasedimentary rocks derived from their erosion.

Ophiolite emplacement

The currently favoured model of emplacement of the ophiolites in the southeastern Québec Appalachians involves thrusting, or obduction, of one or more large

sheets of arc-related oceanic lithosphere onto the Laurentian continental margin (Laurent et al., 1979; Pinet and Tremblay, 1995a, 1995b; Whitehead et al., 2000). The stratigraphic position of the sediments that constitute the matrix of the mélange above the ophiolites, and the absence of high pressure schists within the mélange (Williams and St-Julien, 1982; Pinet and Tremblay, 1995a) support the latter hypothesis.

Timing of felsic intrusions

Oceanic plagiogranites from the Thetford Mines ophiolite are interpreted to have formed in an extensional setting, either axis-centered or off-axis (Pinet and Tremblay, 1995a), very shortly before obduction of the ophiolites started (Whitehead et al., 2000). A trondhjemite dyke intruded in the upper mantle peridotites of the Asbestos ophiolite (Hébert and Bédard, 1998) and the dioritic dykes from the Thetford Mines and Asbestos ophiolites (Laurent and Hébert, 1979) were also interpreted as having been emplaced during the oceanic stage of ophiolite construction. From the chemical and isotopic composition of the lavas, diabase dykes and gabbros, and the U/Pb ages of plagiogranites and trondhjemites, Hébert and Bédard (1998) concluded that the Orford (dated at 504 Ma; David et al., 1993), Thetford Mines (dated at 478-480 Ma; Dunning and Pedersen, 1988; Whitehead et al., 2000) and Asbestos (dated at 472 Ma; Hébert et al., 1998; Hébert and Bédard, 1998) ophiolites are unrelated and represent the obduction of progressively younger oceanic crust. Amphibolites from the accretionary sole of the Thetford Mines ophiolite yielded a minimum crystallization age of 477 ± 5 Ma (Ar/Ar: Whitehead et al., 1996), interpreted to represent the time at which the ophiolite was detached from the seafloor. According to Pinet and Tremblay (1995a), this age corresponds to an early intraoceanic stage of obduction, which lasted until the ophiolite was transported onto the Laurentian continental margin at ~ 470 Ma. The granitic rocks, which occur in the serpentinized peridotites of the Thetford Mines ophiolite, have chemical compositions that display continental affinity (Clague et al., 1985; Whitehead et al., 2000), and are interpreted to have been intruded at ~ 470 Ma (470 +5/-3 and 469 ± 4 Ma, U/Pb zircon ages; Whitehead et al., 2000). These granites are 3 Ma older to 17 Ma younger than amphibolites from the accretionary sole, suggesting that they were most likely intruded

after obduction was initiated (Hébert and Bédard, 1998; Whitehead et al., 2000). Similar relationships have been reported for ophiolites from other parts of the world, and it has been suggested that synchronicity of ophiolite formation and emplacement can be explained by detachment of the ophiolites at or close to a ridge axis (Dewey, 1976; Jamieson, 1986; Lippard et al., 1986; Boudier et al., 1988; LeMétour et al., 1990).

The age of emplacement of the dioritic-monzodioritic, granodioritic and granitic dykes in the JM Asbestos mine is uncertain. Limited K/Ar data on biotite from granitic rocks indicate that they crystallized or were last at a temperature > 250°C between 440 and 460 ± 23 Ma (Laurent et al., 1984). Zircon from a trondhjemite interpreted to be coeval with the formation of the Asbestos ophiolite yielded a U/Pb age of 472 Ma (Hébert and Bédard, 1998). The time at which obduction of the Asbestos ophiolite was initiated is unknown, but must have been after obduction of the Thetford Mines ophiolite, dated at 477 ± 5 Ma (Whitehead et al., 1996), and possibly shortly after 472 Ma. The data presented above suggest that the felsic dykes in the Asbestos ophiolite were intruded between 472 and 460 Ma (i.e., between the time when the ophiolite was detached from the seafloor and the time when it was metamorphosed following thrusting onto the Laurentian margin).

Metamorphic history

The ophiolites of southeastern Québec experienced a complex metamorphic history, starting with their formation in an arc environment, continuing with their deformation and emplacement onto the Laurentian continental margin during the Taconian orogeny, and culminating with their deformation during collision of continental blocks as a result of the Acadian orogeny. However, there have been few detailed studies of the metamorphic history of these ophiolites. Feininger (1981) proposed that, during detachment, the Thetford Mines ophiolite formed a slab of oceanic crust ~ 20 km thick, which was thrust westward over the seafloor and imprinted a strong, inversely zoned metamorphic aureole on the underlying basalts at pressures and temperatures reaching 5-7 kilobars and 780°C, respectively. The ophiolite was subsequently dismembered during transport onto the Laurentian margin, and only its upper 7.8 kilometers came to rest

locally upon slivers of amphibolite sole. According to Nicolas (1989), the ophiolites, which have high temperature and relatively low pressure amphibolite to granulite facies metamorphic soles with strongly inverted thermal gradients, may represent fragments of young and hot oceanic lithosphere detached near a ridge axis.

Serpentinization of the peridotites at the base of the Québec Appalachian ophiolitic sequences began in the sub-seafloor environment and continued until they were emplaced onto the Laurentian continental margin. According to Laurent (1975), early retrograde hydrothermal metamorphism of the peridotites produced a lizardite-chrysotile-magnetite-brucite-awaruite assemblage in an extensional or "static" oceanic environment. Subsequent hydrothermal metamorphism produced multiple stages of recrystallization of lizardite (Wicks and Whittaker, 1977; O'Hanley and Dyar, 1993). Chrysotile vein deposits formed during the latest stages of ophiolite transport and produced chrysotile-magnetite-brucite and antigorite-brucite assemblages (Laurent, 1975; Laurent and Hébert, 1979; O'Hanley, 1987).

Both the ancient seafloor that composes the ophiolite fragments and the rocks that formed part of the Laurentian continental margin were involved in deformation and metamorphism at several times during the Taconian and subsequent Acadian orogeny. To understand the obduction history of the ophiolites, it is necessary to compare these deformation-metamorphism episodes in space and time. $^{40}Ar/^{39}Ar$ cooling ages (muscovite) and structural data from metasedimentary rocks enclosed in the ophiolite-bearing mélange indicate that an early episode of deformation and metamorphism (greenschist facies) affected the rocks from the continental margin between 470 and 460 Ma (D_1-D_2 deformation of Castonguay et al., 1995, 1997; Whitehead et al., 1996). This likely coincided with obduction of the ophiolites onto the Laurentian continental margin (Pinet and Tremblay, 1995a). The $^{40}Ar/^{39}Ar$ data also indicate that there was localized re-heating of the metasediments at about 430-420 Ma. This episode of metamorphism was accompanied by backfolding and extension produced by tectonic wedging of slices of Grenvillian basement at depth during a later stage of the Taconian orogeny (D_3 deformation: Pinet et al., 1996; Castonguay et al., 1995, 1997). The age difference between that of the Asbestos ophiolite (472 Ma, Hébert and Bédard, 1998) and the earlier

episode of Taconian metamorphism (470-460 Ma) of continental margin sediments suggests that the Asbestos ophiolite was obducted onto the Laurentian continent very shortly after its formation. In turn, this indicates that the window of time during which the dioritic and granitic rocks could have formed was very small, if they owe their origin to the melting of sedimentary material in a subduction zone.

Large muscovite crystals from a granitic pegmatite body in the JM Asbestos deposit, mildly affected by a later episode of hydrothermal alteration, were dated by the K/Ar method at 425 ± 13 Ma (K. Sears, unpublished data), which corresponds to the age of the D_3 deformation. Similar K/Ar ages are reported for granites in the Thetford Mines ophiolite, suggesting that the latter was emplaced onto the continental margin by that time and was affected by the same D_3 deformation episode that affected the adjacent continental margin sediments.

There are few geothermobarometric data recording the metamorphic conditions in the upper parts of the Québec Appalachian ophiolites during their obduction. Laird et al. (1993) reported approximate P-T conditions for the formation of calc-silicate assemblages from gabbros and anorthositic layers in cumulate ultramafic rocks. Based on thermobarometric calculations using TWEEQU (Berman, 1991), they proposed pressures between 3 and 5 kilobars and temperatures between 300 and 400°C. Although Laird et al. (1993) did not comment on the timing and tectonic setting of metamorphism, the above pressures are probably too high to represent alteration in the sub-seafloor environment. Typically, the ultramafic portion at the base of the cumulate gabbros in ophiolite complexes lies at a depth of approximately 3 to 7 km below the seafloor (Mason, 1985), where the maximum pressure would be approximately 2.6 kilobars, assuming a 500 m column of seawater. This suggests therefore that the calc-silicate assemblages studied by Laird et al. (1993) formed or equilibrated following an episode of thickening by fault stacking after detachment of the ophiolite slivers from the oceanic lithosphere, and during transport onto the Laurentian continental margin.

The youngest metamorphic episode recognized in the Asbestos ophiolite is related to the Acadian orogeny and is recorded by K-feldspar from the amphibolite sole of the ophiolite. Whitehead et al. (1996) determined an age of 377 Ma (Ar/Ar) for this event,

during which the rocks are interpreted to have been heated to temperatures in the range 330-340°C.

MINE GEOLOGY

The JM ASBESTOS deposit is located in the basal peridotites of the Asbestos ophiolite (Figure 2) and is currently being mined by open-pit and underground methods to extract chrysotile asbestos fiber. The open pit operations exposed a section in which the base of the ophiolite is in thrust contact with argillaceous Cambrian continental slope and rise metasediments of the Caldwell Group to the NW. Serpentinized harzburgites and a dunite-pyroxenite unit are exposed in the SE portion of the pit, while amphibolites occur in the SW corner between the metasediments and the serpentinites (Hébert, 1980: Figure 2). The chrysotile ore is hosted by the serpentinized harzburgites in five tabular bodies separated from each other by shear zones containing weakly to strongly deformed sheet- and lens-like felsic intrusions.

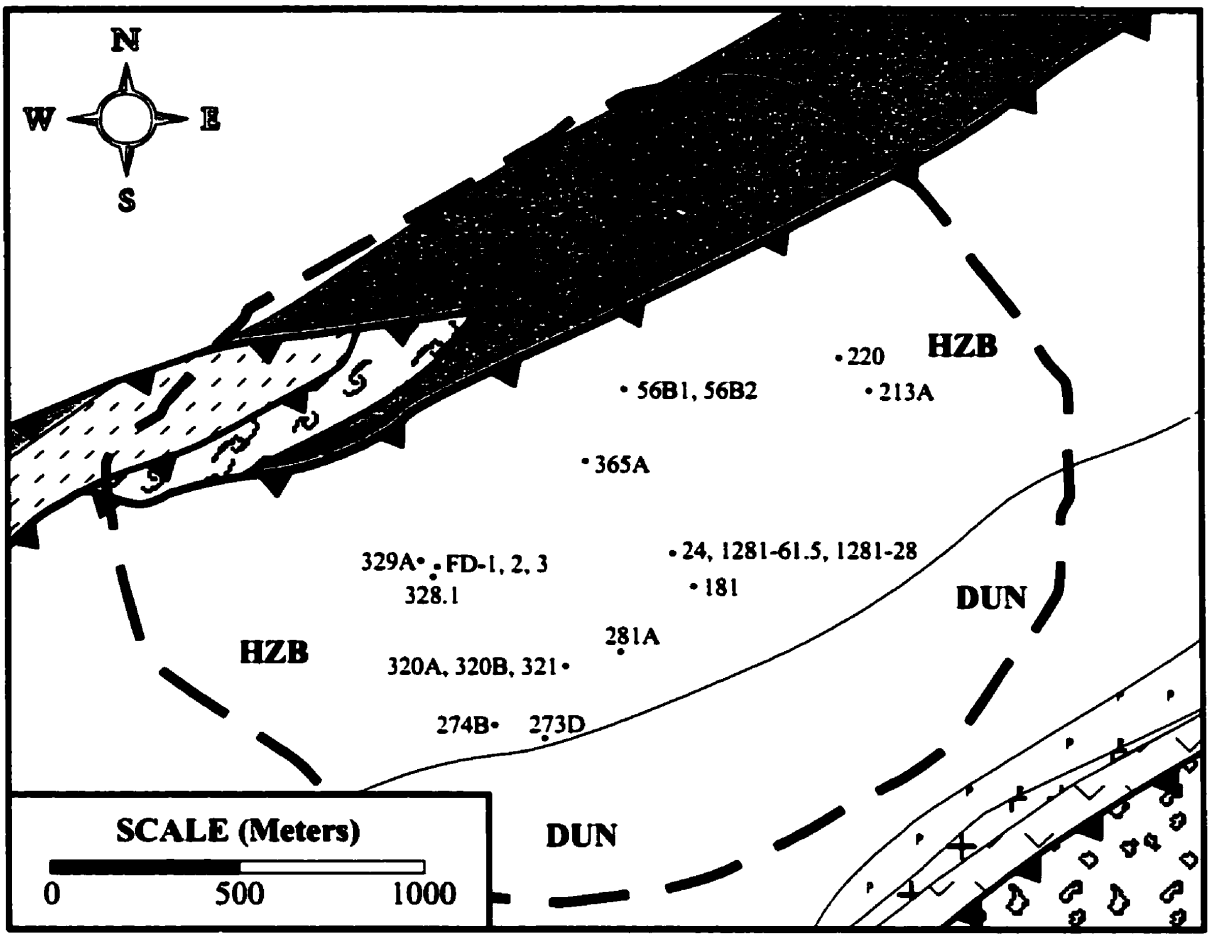
Field relationships and observations of hand samples and thin sections confirm previous conclusions (Laurent and Hébert, 1979; Hébert, 1980) that the basal part of the ophiolite sequence in the open pit is composed of harzburgite tectonites overlain by interdigitated cumulate dunites and pyroxenites. The peridotites are almost completely serpentinized. Very few samples were found which contain relict olivine.

The metasedimentary rocks, in contact with serpentinized harzburgite, consist of carbonaceous and pyritic black slates containing silty interbeds. The slates were metasomatised at their contact with the serpentinized harzburgites, and have taken on a bleached aspect over distances varying from 0.3 to 1.0 m, depending on the density of fractures.

Felsic intrusive rocks can be sub-divided into two groups. The first and oldest group comprises rocks composed of biotite, feldspars and variable proportions of an unknown pseudomorphed phenocryst phase. These intrusives were interpreted to be

Figure 2

Geological map of the Jeffrey Mine showing the location of samples discussed in this study (modified after Hébert, 1980).



LEGEND

Saint-Daniel Formation

Melange

Caldwell Group

Metagraywacke

Slate

Amphibolite

Ophiolitic Complex

Serpentinite

HZB — Harzburgite

DUN — Dunite

Pyroxenite

Gabbro

Pillowed and brecciated tholeiites

metasomatised gabbros by Olsen (1961), implying they are epidiorites, and biotite-plagioclase dioritic rocks by De (1961, 1972). They are classified as diorites and monzodiorites in this study (see below). The second group of intrusive rocks cuts the dioritic-monzodioritic rocks and comprises biotite-bearing to biotite-free granodioritic and granitic rocks.

FELSIC INTRUSIVE ROCKS

The felsic intrusives display a wide range of textures, grain-size and mineralogy, of primary and secondary nature. Most of the rocks display varying degrees of alteration and fresh rocks are rare. Extensive hydrothermal alteration produced feldspar-pyribole-, chloritic- or rodingitic-dominant mineral assemblages, which are discussed in detail in Chapter V. This study is restricted to the more commonly occurring examples of felsic intrusives, which are texturally and mineralogically homogeneous, and those that were least strongly affected by alteration.

The dioritic-monzodioritic and granodioritic-granitic rocks form sheet-like bodies (Figure 3), which can be traced for more than one kilometer along strike and at depth. The thickness of some of the largest sheets (3-5 m) is remarkably constant (John A. Millen, personal communication, 1995). Many are oriented parallel to the contact between the serpentinized harzburgites and the slates, and some are oriented perpendicular to this contact (Figure 4). Deformation textures may be strongly (foliation) or weakly (small fractures) developed.

Anthophyllite-cummingtonite (Mg/[Mg+Fe] = 0.75-0.83) rims commonly occur in serpentinite at the contacts of the dykes, or in serpentinized peridotite xenoliths enclosed in the dykes, implying that the intrusive rocks induced contact metamorphic-metasomatic alteration of the serpentinites at temperatures between ~ 550 and 725°C (below this temperature, anthophyllite-cummingtonite breaks down to form the assemblage talc + olivine, but above this temperature and at pressures of 1-2 kilobars anthophyllite-

Figure 3

Photographs showing: (A) a diorite dyke and (B) a composite dioritic-granitic dyke in serpentinized harzburgite. Darker and lighter layers in the diorite dyke in A represent biotite-rich and biotite-poor zones interpreted to have originated from flow differentiation during emplacement. The composite dyke in B shows a succession of progressively more felsic generations of granitic rocks intruded after diorite.

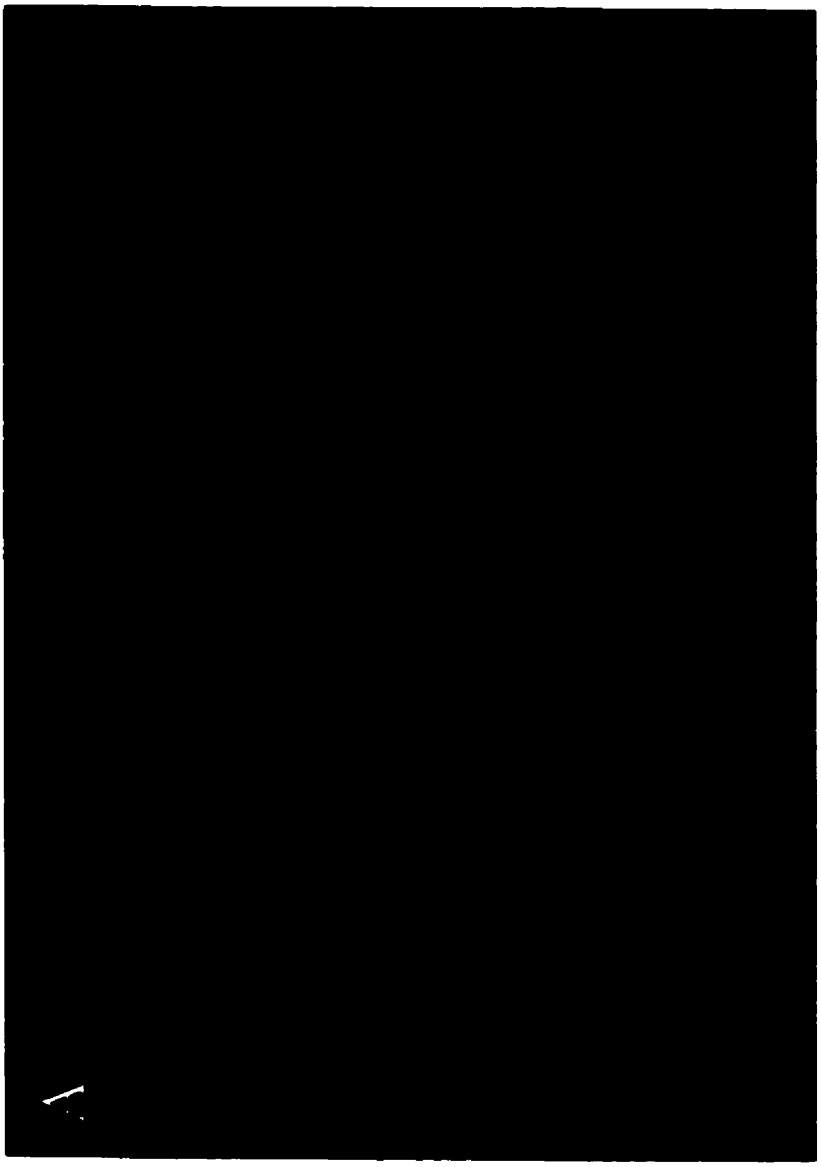
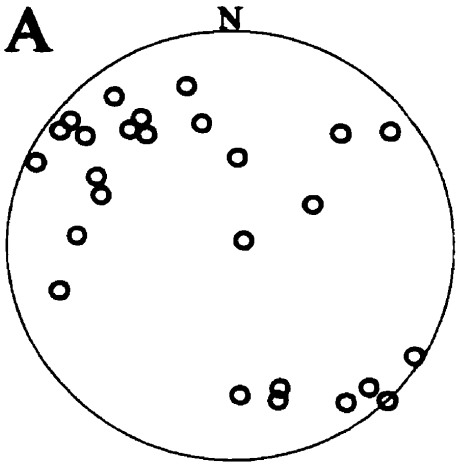
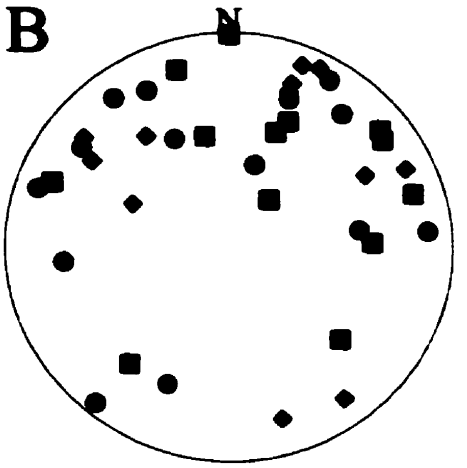


Figure 4

Equal area stereographic projections (polar, lower hemisphere) illustrating the variation in the orientation of the dioritic-monzodioritic dykes (A) and the granitoids dykes (B). The relationships among the orientation of the slate-serpentinite contact, the orientation of the most penetrative schistosity in the slate and the orientation of the joints and rodingite veins that cut the slate at the contact with serpentinite are shown in (C). The orientation of shear zones cutting serpentinized harzburgite is illustrated in (D).



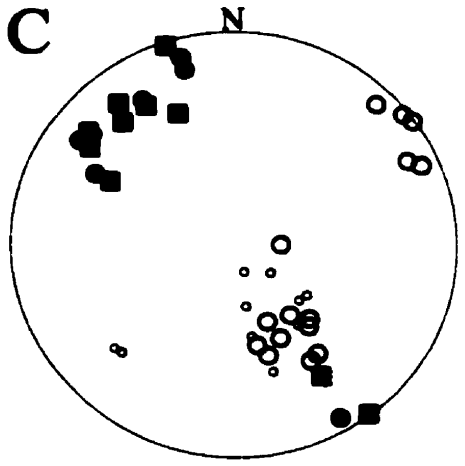
Diorite (N=27)



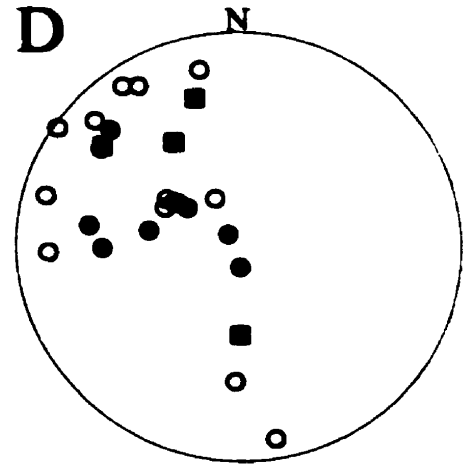
Granite (squares, N=13)

Leucogranite (circles, N=14)

Pegmatitic granite (diamonds, N=12)



- Schistosity in slates
- Orientation of slate-serpentinite contact
- Veins in slate
- Joints in slate



- S_1
- S_2
- Undifferentiated

cummingtonite breaks down to form the assemblage orthopyroxene + quartz; see Maresh and Czank, 1988, and Rasmussen et al., 1998).

General features

Dioritic-monzodioritic dykes

The dioritic intrusives commonly display alternating biotite-rich and feldspar-rich layers, in which the biotite crystals are preferentially oriented parallel to the layering. This layering is interpreted to reflect flow differentiation. It is either parallel to the sheet margins or is contorted. Individual leucocratic, feldspar-rich, and melanocratic, biotite-rich layers vary from 1 cm to several decimeters in thickness. In some intrusions, layering is absent and the rock, uniformly biotite-rich or biotite-poor, has a relatively homogeneous distribution of minerals, but the biotite nevertheless shows some preferential orientation. Inclusions of serpentinized peridotite, varying in diameter from 1 cm to 1 m, form angular blocks, or strings of ovoid lenses that are commonly aligned parallel to the layering. Contacts between the ovoid ultramafic inclusions and the intrusive rocks commonly display microscopic evidence of ductile deformation. In a few cases, the layering in the sheets was observed to run obliquely to the contact with massive, unfoliated serpentinite, and is interpreted to represent offset or rotation of large blocks along fault planes. Small amygdule-like felsic bodies (2 mm to 1 cm wide) are concentrated in some of the layers. They are composed of feldspar (albite and/or K-feldspar) ± zoisite ± grossular ± prehnite cores rimmed by diopside prisms which grew perpendicular to the walls of the bodies, suggesting open-space filling, possibly after dissolution of phenocrysts (e.g., quartz).

Granodioritic-granitic dykes

Intrusion of the granitoids appears to have occurred in pulses, with each pulse producing rocks progressively poorer in biotite, which cut the previously crystallized varieties. Granodiorites formed early, and leucocratic, andalusite- and tourmaline-bearing, and coarse-grained to pegmatitic varieties of granite were the latest to form. Relative to the diorites, a much larger proportion of the granitic intrusive sheets is oriented

perpendicular to the contact between the slates and the serpentinites (Figure 4). This orientation perpendicular to the ophiolite stratigraphy and regional structures is an indication of the intrusive nature of the felsic rocks.

The more leucocratic rocks are commonly coarse-grained to pegmatitic, and display graphic textures involving quartz and feldspars. These features were observed in the middle of dykes as well as at their contact with serpentinite. Chilled margins are never observed, suggesting that the host serpentinites were relatively hot and the magma, from which the dykes crystallized, was hydrous. Crystallization under water-saturated conditions would reduce temperature gradients in the solidifying intrusive body and, consequently, prevent the development of chilled textures. A notable feature in some pegmatites is the presence of very large clusters of andalusite crystals, measuring up to 15 cm in length, concentrated along the margins of a quartz core.

The coexistence of andalusite, K-feldspar and plagioclase in the granites indicates a minimum temperature of emplacement of ~ 640°C (minimum solidus temperature of water-saturated peraluminous melts containing an aluminosilicate; Thompson and Tracy, 1979) and a maximum pressure between 4 and 5 kilobars, assuming the P-T stability relationship between andalusite and sillimanite determined by Richardson et al. (1969). The presence of tourmaline and apatite, however, suggests that fluxing agents (boron and phosphorus: London, 1992) may have led to solidification of the granites, especially pegmatitic varieties, at lower temperature.

Mineralogy of the felsic intrusives

Diorite-Monzodiorite

The more melanocratic, biotite-rich and quartz-free felsic intrusives in the JM Asbestos deposit have mineralogical compositions that correspond to diorite, and the more leucocratic varieties to monzodiorite according to the classification of Streckheisen (1976). They classify as syenites using the R1-R2 scheme of classification of de la Roche et al. (1980; rocks composed of feldspars and biotite). The dioritic rocks can be further subdivided into those containing a pseudomorphed phase that forms phenocrysts and those which do not contain this phase. They are characterized by intergranular to ophitic

textures with the interstices between the plagioclase and the pseudomorphs, referred to above, being filled with biotite laths. All the rocks belonging to this group have been subjected to some degree of hydrothermal alteration, but the dioritic rocks are the most extensively altered (discussed below).

Thin sections from four samples of monzodiorite (JMH-329a, FD-1, FD-2, and FD-3), three samples of diorite (JMH-181, JMH-328.1, and JMH-365a) and six samples of diorite, which contain the pseudomorphed phenocrysts (JMH-24, JMH-281a, H1084-872.8, H1084-881, H1281-28, and H1281-61.5), were examined with an optical microscope and a scanning electron microscope to determine the minerals present and the textural relationships among these minerals. Wavelength dispersive and energy dispersive analyses were performed with an electron microprobe to determine the chemical composition of the minerals (Appendix II).

Biotite is the principal mafic mineral in the dioritic-monzodioritic group of rocks, and occurs in two generations. The first generation, biotite-I, forms large (up to 2 mm wide), bright red-brown pleochroic euhedra, which are generally interstitial to plagioclase crystals that have been pseudomorphed by albite + muscovite ± zoisite and to an unknown pseudomorphed phenocryst phase. According to Lalonde and Bernard (1993), the bright red colour is characteristic of Fe^{2+}-rich biotite formed under reducing conditions. Less commonly, this biotite occurs as inclusions in the plagioclase and the unknown pseudomorphs. It is markedly different from the biotite described by Laurent et al. (1984), which formed during alkaline hydrothermal alteration of granitic rocks from the Thetford-Mines area, and has lower concentrations of Ti, Fe and Al. The second generation of biotite, biotite-II, is of secondary origin and occurs only in the unknown pseudomorphs. The monzodiorite contains less than 15 vol. % biotite-I, whereas the diorite contains between 25 and 40 vol. % biotite-I. Biotite-I (Table 1) is Ti- (up to 4.1 wt. % TiO_2, average 3.4 ± 0.4 wt. %, 107 analyses) and Al-rich (average 18.8 ± 0.4 wt. % Al_2O_3), and F- and Cl-poor (F < 900 ppm, mostly below detection; Cl < 1200 ppm, average 757 ± 109 ppm 1σ), and has a Fe/(Fe+Mg) atomic ratio of 0.52 ± 0.02 (1σ). There is also a small proportion of coarse-grained, phengitic white micas. The

Table 1. Electron microprobe analyses of minerals from dioritic-monzodioritic rocks.

Mineral	Biotite-I	Plagioclase[#]	F-Apatite	C-OH-Apatite[##]
Number of analyses	115	5	35	6
Wt. % oxides				
SiO_2	35.22 (0.41)*	59.07	0.07 (0.04)	0.35
TiO_2	3.38 (0.44)	n.a.	n.a.	n.a.
Al_2O_3	18.77 (0.37)	26.44	n.a.	n.a.
Cr_2O_3	0.02 (0.03)	n.a.	n.a.	n.a.
ΣREE_2O_3	n.a.	n.a.	0.19 (0.06)	0.21
FeO	18.77 (0.54)	0.21	0.29 (0.08)	0.06
MnO	0.16 (0.02)	n.a.	0.23 (0.13)	0.00
MgO	9.88 (0.53)	0.01	0.04 (0.02)	0.00
CaO	0.02 (0.14)	7.82	54.62 (0.49)	54.43
SrO	n.a.	n.a.	0.04 (0.02)	0.02
BaO	n.a.	0.14	n.a.	n.a.
Na_2O	0.34 (0.08)	7.04	0.07 (0.03)	0.00
K_2O	10.01 (0.25)	0.45	n.a.	n.a.
P_2O_5	n.a.	0.07	41.76 (0.36)	35.27
F	0.00 (0.01)	n.a.	2.33 (0.41)	1.31
Cl	0.08 (0.01)	n.a.	0.25 (0.08)	0.02
Total	96.64 (0.60)	101.23	99.89 (0.59)	91.67
—O≡F,Cl	0.02 (0.01)	—	1.04 (0.19)	0.55
Total	96.62 (0.60)	—	98.85 (0.49)	91.11

*: average ± 1 σ. [#]: relict andesine from diorite. [##]: carbonate-fluor-apatite from leucomonzodiorite. n.a.: not analyzed.

Table 1. (continued)

Mineral	Biotite-I	Plagioclase	F-Apatite	C-OH-Apatite
Number of analyses	115	5	35	6
Cations				
Si	2.69 (0.04)	2.61	0.01 (0.01)	0.06
Ti	0.19 (0.03)	—	—	—
Al	1.69 (0.04)	1.38	—	—
Cr	0.00 (0.00)	—	—	—
ΣREE^{3+}	—	—	0.01 (0.01)	0.01
Fe^{3+}	—	0.01**	—	—
Fe^{2+}	1.20 (0.04)	—	0.04 (0.01)	0.01
Mn	0.01 (0.00)	—	0.03 (0.02)	0.00
Mg	1.12 (0.06)	0.00	0.01 (0.00)	0.00
Ca	0.00 (0.01)	0.37	9.81 (0.12)	9.42
Sr	—	—	0.00 (0.00)	0.00
Ba	—	0.00	—	—
Na	0.05 (0.01)	0.60	0.02 (0.01)	0.00
K	0.97 (0.03)	0.03	—	—
P	—	0.00	5.93 (0.06)	4.82
F	0.00 (0.00)	—	1.24 (0.22)	0.67
Cl	0.01 (0.00)	—	0.07 (0.02)	0.01
OH	—	—	0.57 (0.21)	1.38
C***	—	—	0.15 (0.11)	1.68

***: from CO_2 added to obtain 26 O-OH-F-Cl and 16 cations.

composition of this mica is typical of muscovite in peraluminous granitoid rocks.

The normative proportion of plagioclase varies between 30 and 60 vol. % in the diorites and between 60 and 70 vol. % in the monzodiorites. The composition of the plagioclase, calculated from the normative composition of the diorite, varies greatly due to late-stage hydrothermal alteration (X_{an} = 0.05 to 0.89), but is more restricted in the less altered monzodiorites, where X_{An} varies between 0.13 and 0.19. Only one grain of primary plagioclase was found in diorite (sample H1281-61.5). Electron microprobe (EMP) analyses of this grain indicate that it is an andesine with the composition $Ab_{60.4}An_{37.1}Or_{2.5}$, which contrasts with the calculated normative composition of An_{22}. This feldspar also contains between 580 and 730 ppm P_2O_5 and is associated with a Ba-rich (up to 4 wt. % BaO) K-feldspar of composition $Or_{75.4}Ab_{8.9}Cs_{7.4}An_{5.5}$. Ba-rich K-feldspar (~20 mole % celsian, EDS) also occurs in the more leucocratic sample (JMH-329A). More commonly, the original plagioclase is represented by pseudomorphs composed of a graphic-like intergrowth of albite (Ab_{89-100}), a low-Fe epidote-group mineral (< 0.3 wt. % Fe_2O_3) and muscovite. The local concentration of the epidote-group mineral in the cores of the pseudomorphs suggests that the original plagioclase crystals were normally zoned with respect to their albitic and anorthitic components. De (1961) reported a normative composition corresponding to An_{43} for plagioclase from a hornblende-biotite diorite in the Normandie mine, and Olsen (1961) reported a value of > An_{40}, based on optical properties, for plagioclase in a dioritic rock from the JM Asbestos mine.

K-feldspar occurs in small proportions (< 5 vol. %) in the dioritic rocks, but as larger crystals than plagioclase. Plagioclase crystals are frequently present as inclusions in the K-feldspar. Most K-feldspar crystals are altered to white micas. The monzodiorites contain between 16 and 23 percent by volume of K-feldspar, which locally forms large crystals (up to 5 cm) poikilitically enclosing euhedral, sericitized plagioclase, and biotite crystals (Figure 5a).

A pseudomorphically replaced mineral forms large (up to 5 mm wide) phenocrysts, which compose up to 40 percent by volume of the dioritic rocks (Figure 5b,

Figure 5

Photomicrographs of thin sections showing, in A, large crystals of poikilitic potassium feldspar (K-fs) in monzodiorite (sample FD-2) and, in B, large phenocrysts of an unidentified mineral (Ps) replaced by a fine-grained mixture of biotite-II and muscovite, albitized plagioclase (Pl) and interstitial biotite-I in diorite (sample H1281-28).


A
Pl


B
Ps
Ps
Bi

Table 2). This phase is now represented by a fine-grained mixture of Ti-poor (average 0.04 wt. % TiO_2) and Mg-rich biotite (FeO/[FeO+MgO] = 0.41; biotite II), muscovite, and varying proportions of later albite and low-Ba K-feldspar. The bulk chemical formula calculated from the mode of 107 electron microprobe analyses of the pseudomorphs is $K_{0.94}Na_{0.01}Mg_{0.72}Fe_{0.71}Mn_{0.01}Al_{2.4}Si_{2.72}O_{10}(OH)_{2.05}$. In thin section, these pseudomorphs form rectangular or 6- or 8-sided crystals, depending on the orientation of the cut, and are likely to represent hornblende, augite, or possibly cordierite (the latter has been reported from dioritic dykes in the Oman ophiolites: Peters and Kamber, 1994; Cox et al., 1999). Olsen (1961) reported the presence of rare augite inclusions in biotite-I from the dioritic rocks, and De (1961) reported the occurrence of hornblende-rich to hornblende-poor varieties of diorite from the Thetford-Mines area. De's (1961) optical parameters for this hornblende suggest that it has a Fe/(Fe+Mg) ratio in the range 0.35-0.42, i.e., a ratio similar to that of the pseudomorphs (0.41). The Al-rich composition of biotite-I (proportion of the eastonite-siderophyllite component $K(Mg,Fe)_2AlAl_2Si_2O_{10}(OH)_2$ ~ 34 %), however, is not consistent with it having formed in equilibrium with hornblende. However, it is typical of biotite coexisting with cordierite. It could also reflect reaction of the melt with the hornblende in the final stages of magma crystallization (disequilibrium conditions). The triangular diagram in Figure 6 illustrates the relative proportions of feldspars, biotite and the unknown pseudomorphed phenocryst phase in the dioritic-monzodioritic rocks. Also shown on this diagram are the relative proportions of feldspars, biotite and hornblende taken to represent the phenocryst phase in the hornblende-rich diorite sample 9/144 of De (1972) and other hornblende diorites in the Thetford Mines ophiolite (De, 1961). The diagram suggests that the Thetford Mines and Asbestos diorites are similar and that the pseudomorphed phenocrysts were originally hornblende.

The accessory minerals in the dioritic-monzodioritic rocks include apatite, zircon, monazite, allanite, titanite, and ilmenite. The diorites richest in biotite-I contain up to ~ 2 percent by volume of apatite, ~ 0.1 percent by volume of zircon and smaller proportions of the other minerals. Apatite and zircon occur commonly as euhedral, prismatic inclusions (up to 500 μm wide) in biotite-I, and, less commonly, in the unknown

Table 2. Normative and modal composition of dioritic-monzodioritic rocks.

Sample	Monzodiorite (this study)				Diorite (this study)			Diorite-Ps (this study)		
	FD-1	FD-2	FD-3	JMH-329A	JMH-328.1	JMH-365A	JMH-181	JMH-24	JMH-281A	H1084-872.8
Normative composition (wt. %)										
Qz	0.23	2.45	1.72	0	0	0	0	0	0	0
Or	21.46	17.71	15.2	17.47	2.99	20.32	6.29	3.15	0.71	4.59
Ab	49.48	43.41	49.29	54.01	18.19	3.53	29.55	34.97	34.92	31.97
An	7.56	10.98	9.92	12.16	10.75	28.95	24.53	2.15	6.82	12.76
Ne	0	0	0	1.55	0.39	5.79	4.76	1.16	2.34	1.07
Mt	0.9	0.99	0.88	0.49	2.37	1.98	1.79	2.29	2.16	2.26
Il	1.29	1.19	1.31	0.54	2.9	2.23	2.05	2.8	2.65	2.84
Ap#	1.02	1.06	1.11	0.12	1.75	1.53	1.28	2.15	1.93	1.98
Hbl	8.28	0	0	0	0	8.15	0	0	0	0
Bi	9.78	18.16	16.17	11.59	40.46	27.53	26.48	33.98	33.2	35.36
Mu	0	4.06	4.41	2.08	20.19	0	3.27	17.34	15.27	7.17
X_{Ab}^{Pl}	0.87	0.81	0.84	0.82	0.64	0.11	0.56	0.95	0.84	0.73
Modal composition										
Feldspars	n.d.	75	n.d.	88	50	n.d.	n.d.	44	46	53
Bi-I	n.d.	15	n.d.	12	50	n.d.	n.d.	22	25	36
Pseudomorphs	n.d.	5	n.d.	0	0	n.d.	n.d.	34	29	11

*: Sample 570 from Normandie mine (De, 1961), Samples 605A and 605 from Vimy mine (De, 1961), Sample 9/144 from Vimy mine (De, 1972). **: Calculated.n.d.: not determined. #: Apatite in samples 5, 6 and 7 from Olsen (1961) calculated from estimation of P_2O_5 content (regression through P_2O_5 and Zr from samples in this study).

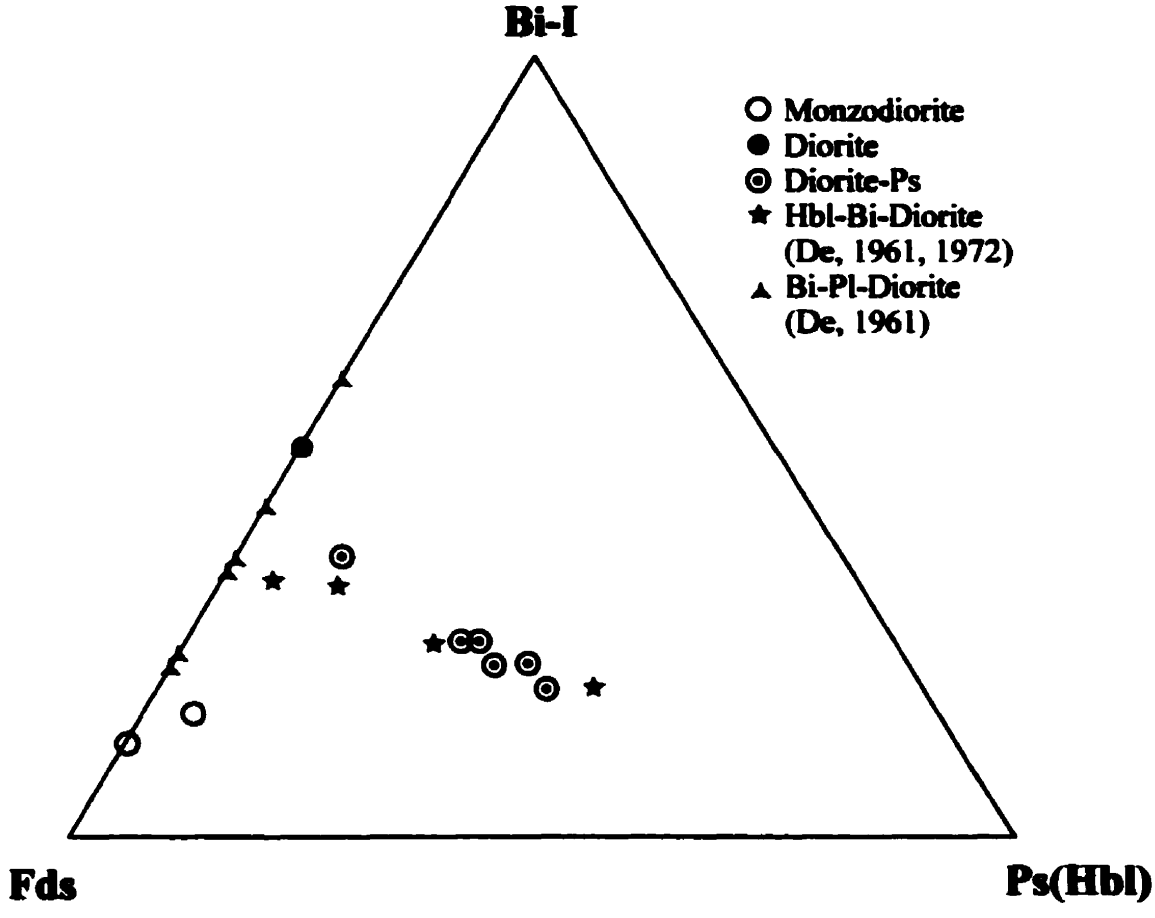
Table 2. (continued)

Sample	Diorite-Ps (this study)			Diorite (Olsen, 1961)			Hornblende Diorite (De, 1961, 1972)			
	H1084-881	H1281-28	H1281-61.5	5	6	7	570	605A	605	9/144
Normative composition (wt. %)										
Qz	0	1.96	1.7	0	6.85	12.19	5.69	n.d.	n.d.	0
Or	1.43	5.54	4.27	3.97	3.95	14.69	0	n.d.	n.d.	0
Ab	31	25.27	24.32	1	26.43	34.34	29.33	n.d.	n.d.	1.49
An	7.99	5.67	7.12	41.21	26.66	17.32	21.7	n.d.	n.d.	26.33
Ne	1.21	0	0	7.48	0	0	0	n.d.	n.d.	0
C	0	0	0	0	0	0	3.53	n.d.	n.d.	0
Hy	0	0	0	0	0	0	0	n.d.	n.d.	1.18
Ol	0	0	0	0	0	0	0	n.d.	n.d.	5.35
Mt	1.87	1.9	1.69	2.37	1.57	1.2	2.15	n.d.	n.d.	2.97
Il	2.3	1.88	1.29	2.15	2.13	1.55	1.74	n.d.	n.d.	1.59
Ap#	1.49	1.71	1.37	1.53	1.71	1.23	1.6	n.d.	n.d.	1.98
Hbl	0	0	0	0	0	0.31	0	n.d.	n.d.	42.18
Bi	35.78	31.13	30.6	36.65	25.5	17.16	31.37	n.d.	n.d.	16.92
Mu	16.92	24.93	27.64	3.64	5.22	0	0	n.d.	n.d.	0
Crd	0	0	0	0	0	0	2.9	n.d.	n.d.	0
X_{Ab}^{Pl}	0.80	0.83	0.78	0.03	0.51	0.68	0.59	—	—	0.06
Modal composition										
Feldspars	44	40	40	—	—	—	54.9*	42.7*	47.8*	31**
Bi-I	25	22	19	—	—	—	29.4*	21.5*	27.9*	17**
Pseudomorphs	31	37	41	—	—	—	4.7*	22.7*	10.7*	41**

*: Sample 570 from Normandie mine (De, 1961), Samples 605A and 605 from Vimy mine (De, 1961), Sample 9/144 from Vimy mine (De, 1972). **: Calculated. n.d.: not determined. #: Apatite in samples 5, 6 and 7 from Olsen (1961) calculated from estimation of P_2O_5 content (regression through P_2O_5 and Zr from samples in this study).

Figure 6

Triangular diagram showing the relative proportions of feldspars, biotite and the unknown pseudomorphed phenocrysts in the dioritic-monzodioritic rocks. Also shown on this diagram are the relative proportions of feldspars, biotite and hornblende (in place of the pseudomorphed phenocrysts) in the hornblende-rich diorite sample, 9/144, of De (1972) and other hornblende diorite samples from the Thetford Mines ophiolite (De, 1961). The diagram suggests that the pseudomorphs were originally hornblende.


Bi-I
Monzodiorite
Diorite
Diorite-Ps
Hbl-Bi-Diorite
(De, 1961, 1972)
Bi-Pl-Diorite
(De, 1961)
Fds
Ps(Hbl)

pseudomorphed phenocrysts. Electron microprobe analyses indicate that apatite in the dioritic rocks is a fluorine-rich variety (X_F = 0.52-0.97). Carbonate-hydroxylapatite (X_{OH} = 0.65-0.70) is present in the most leucocratic sample of monzodiorite (JMH-329A). Ilmenite was only observed in the more melanocratic diorites, usually replacing titanite in biotite-I and in the unknown pseudomorphed phenocrysts. The ilmenite contains between 5 and 9 wt. % MnO (11 to 19 mole % $MnTiO_3$, EDS analyses).

Granodiorite-granite

There are two petrographically distinct groups of granitoid rocks in the JM Asbestos mine, granites and granodiorites. Because the least altered granitic rocks are much closer to their parent rock in their major element and mineralogical composition than are the dioritic-monzodioritic rocks, less emphasis was put on detailed analyses of minerals, and much of the chemistry of the minerals was interpreted from the bulk rock compositions. The normative composition of these rocks (Table 3), calculated from bulk rock analyses, and based on the presence of phases that can be satisfactorily represented by end-member compositions, indicates that the granites contain between 27 and 36 vol. % quartz, 23 to 30 vol. % K-feldspar, 28 to 40 vol. % plagioclase, 1.4 to 9.5 vol. % biotite, and 1 to 3.5 vol. % andalusite. The granodiorites contain between 29 and 45 vol. % quartz, 10 to 16 vol. % K-feldspar, 34 to 46 vol. % plagioclase, 4.1 to 12.9 vol. % biotite, and 0.4 to 3.4 vol. % andalusite. The calculations also indicate that the plagioclase is more basic (X_{Ab}^{Plag} = 0.69-0.79), and the biotite more magnesian (X_{Ann}^{Bi} = 0.27-0.50) in the granodiorites than in the granites (X_{Ab}^{Plag} = 0.79-0.96; X_{Ann}^{Bi} = 0.52-0.70).

Examination of the accessory phases present in the granites using SEM (EDS) revealed the presence of euhedral, zoned andalusite crystals with Fe-rich cores (up to 3 wt. % FeO), tourmaline (schörl-dravite series), apatite, Nb- and Ta-rich rutile, Mn-rich ilmenite, and traces of columbite and a U-Th oxide. According to Pichavant and Manning (1984), such mineral associations are quite typical for tourmaline-bearing, S-type granitoids. Based on textural relationships, the Ti oxides, apatite and andalusite were the first minerals to form, followed by the feldspars. Quartz crystallized early in some of the

Table 3. Normative and modal composition of granodioritic-granitic rocks.

Rock type				Granite			
Sample	JMH-56B1	JMH-213A	JMH-273D	JMH-274B	Flt-F	E:53	E:75
Wt. %							
Quartz	34.14	36.1	26.93	32.49	27.53	21.28	28.21
K-feldspar	26.01	26.46	22.03	22.93	24.41	28.13	28.66
Albite	32.19	24.97	33.93	24.49	26.75	33.25	24.13
Anorthite	1.41	2.81	6.09	7.01	6.44	6.76	2.84
Phlogopite	0.42	1.73	3.4	3.01	3.71	3.61	4.28
Annite	1.21	3.38	5.47	5.21	6.01	4.71	6.62
Andalusite	4.22	3.9	1.02	4.07	4.03	1.22	3.93
Titanite	0.13	0.4	0.77	0.6	0.78	0.7	1.01
Apatite	0.26	0.26	0.37	0.18	0.33	0.35	0.33
Vol. %							
Quartz	34.07	36.24	27.12	32.88	27.90	21.36	28.56
K-feldspar	26.87	27.50	22.96	24.02	25.61	29.23	30.03
Albite	32.49	25.35	34.56	25.06	27.42	33.76	24.71
Anorthite	1.35	2.71	5.89	6.81	6.27	6.52	2.76
Phlogopite	0.40	1.67	3.29	2.92	3.61	3.48	4.16
Annite	0.97	2.72	4.42	4.23	4.89	3.80	5.38
Andalusite	3.54	3.29	0.86	3.46	3.44	1.03	3.35
Titanite	0.10	0.30	0.59	0.46	0.60	0.53	0.77
Apatite	0.21	0.22	0.31	0.15	0.28	0.29	0.28
X_{Ab}^{Pl}	0.96	0.90	0.86	0.79	0.82	0.84	0.90
X_{Ann}^{Bi}	0.70	0.61	0.57	0.59	0.57	0.52	0.56

Table 3. (continued)

Rock type	Granodiorite				
Sample	JMH-56B2	JMH-220	JMH-320A	JMH-320B	JMH-321A
Wt. %					
Quartz	29.24	38.56	43.97	33.93	38.59
K-feldspar	14.96	15.3	9.09	11.54	11.17
Albite	35.12	29.15	22.49	26.55	33.25
Anorthite	10.15	8.87	10.66	10.22	11.43
Phlogopite	4.36	2.36	5.31	6.49	2.28
Annite	2.04	2.8	6.54	7.9	2.39
Andalusite	4.03	2.63	0.75	1.67	0.49
Titanite	0.01	0.24	1.01	1.48	0.24
Apatite	0.09	0.1	0.18	0.23	0.15
Vol. %					
Quartz	29.45	38.80	44.75	34.68	38.75
K-feldspar	15.60	15.94	9.58	12.21	11.61
Albite	35.78	29.66	23.15	27.45	33.77
Anorthite	9.82	8.57	10.42	10.03	11.02
Phlogopite	4.22	2.28	5.19	6.37	2.20
Annite	1.65	2.26	5.34	6.48	1.93
Andalusite	3.41	2.23	0.64	1.44	0.41
Titanite	0.01	0.18	0.78	1.15	0.18
Apatite	0.08	0.08	0.15	0.19	0.12
X_{Ab}^{Pl}	0.79	0.78	0.69	0.73	0.76
X_{Ann}^{Bi}	0.28	0.49	0.50	0.50	0.46

leucocratic, medium-grained granites and late in the more biotite-rich granodiorites. Interestingly, pseudomorphs composed of fine-grained biotite similar to those found in the dioritic-monzodioritic rocks, were observed in some of the more biotite-rich varieties of granodiorite.

Mineralogical relationships between dioritic and granitic rocks

The modal mineralogy of the diorites and the monzodiorites is employed in this section to determine if the diorites, monzodiorites, granodiorites and granites are related. Geochemical relationships are discussed in the next section.

The presence of the unknown pseudomorphed phenocrysts in diorite and the more biotite-rich granodiorites is an indication that these rocks could be related. The proportion of the pseudomorphed phenocrysts appears to be inversely correlated with the silica content of the rocks. These phenocrysts are abundant in diorite, occur in smaller proportions in the monzodiorites, are rare in the granodiorites, and are absent from the granites. There is therefore a suggestion that the diorites, the monzodiorites and the granitoids may be linked through a process that efficiently separated early forming crystals from the magma. A likely mechanism for producing this separation is filter pressing of liquid caused by the clogging of narrow dyke conduits with early-formed crystals such as the unknown pseudomorphed phenocrysts and feldspars, and later (essentially interstitial) biotite. As a result of this process, saturation with respect to quartz would have been achieved later in the separated liquid, which is consistent with its occurrence late in the paragenesis of the granodiorites.

Geochemistry of the felsic intrusives

Bulk-rock chemical compositions were obtained from X-ray fluorescence analysis of fused pellets for major element oxides and BaO, Cr_2O_3, Ni, and Co or Ce, and pressed powder pellets for the trace elements Ga, Nb, Pb, Rb, Sr, Th, U, Y, and Zr. The analyses were performed at the Geochemical Laboratories of McGill University. The results of the chemical analyses were used to determine the primary nature of the felsic intrusive rocks and are discussed in detail in the following sections.

Diorite-Monzodiorite

The chemical compositions of pseudomorph-bearing and pseudomorph-free diorites and monzodiorites are presented in Table 4. For comparative purposes, we have included in this table analyses of a hornblende-rich hornblende-biotite diorite from the Vimy mine and a hornblende-biotite diorite from the Normandie Mine (samples 9/144 and 570 in De, 1972), both from the Black Lake area near Thetford Mines, Québec, and analyses of three biotite-rich to biotite-poor "acid rock" reported by Olsen (1961; his samples 5 to 7) from the JM Asbestos mine. Analytical data for trace elements were not provided for the hornblende-bearing diorites studied by De (1961, 1972), and comparisons between these rocks and the dioritic-monzodioritic rocks from the JM Asbestos mine are therefore restricted to the major elements and P_2O_5. Despite these limitations, the composition of the hornblende-biotite diorite (sample 570 in De, 1961, 1972) from the Normandie mine compares well with those of the dioritic rocks discussed in this study, but differs substantially from the hornblende-rich diorite (sample 9/144 in De, 1972) from the Vimy mine. The latter is substantially richer in MgO and FeO, and poorer in K_2O (Table 4).

The diorite-monzodiorite series of rocks displays relatively large variations in chemical composition, which are reflected in the modal proportions of the minerals. This is especially true for the more mobile alkali and alkali-earth elements, and, to a lesser extent, silica, and could reflect hydrothermal alteration rather than magmatic processes. However, the analytical results remain useful indicators of the relative behaviour of these elements. For example, Na_2O and SiO_2 concentrations of diorites and monzodiorites correlate positively (Figure 7a) and are highest in the most leucocratic monzodiorite. This relationship could reflect albitization as this type of alteration is ubiquitous in all aluminous rock types in contact with serpentinite. However, Na_2O correlates negatively with Zr, which is expected to have remained immobile during sodic alteration (Figure 7b). We believe that hydrothermal alteration alone could not have produced the large differences in Zr concentrations between the more mafic diorites (up to 787 ppm Zr) and

Table 4. Chemical analyses of dioritic-monzodioritic rocks.

Rock type	Monzodiorite (this study)			
Sample	FD-1	FD-2	FD-3	JMH-329A
Wt. %				
SiO_2	59.29	56.90	57.62	59.14
TiO_2	0.68	0.61	0.68	0.28
Al_2O_3	18.38	19.26	19.52	20.63
Fe_2O_3	4.11	4.47	3.98	2.20
FeO	n.a.	n.a.	n.a.	n.a.
MnO	0.06	0.07	0.06	0.04
MgO	2.91	3.35	3.07	2.39
CaO	3.18	2.75	2.57	2.4 /
Na_2O	5.83	5.03	5.72	6.60
K_2O	4.65	5.38	4.82	4.41
P_2O_5	0.43	0.44	0.46	0.05
H_2O^+	n.a.	n.a.	n.a.	n.a.
H_2O^-	n.a.	n.a.	n.a.	n.a.
CO_2	n.a.	n.a.	n.a.	n.a.
L.O.I.	1.00	1.16	1.11	1.03
ppm				
V_2O_5	n.a.	n.a.	n.a.	n.a.
BaO	1310	1639	1575	5561
Ce	n.a.	n.a.	n.a.	105
Co	20	15	<d.l.	10
Cr_2O_3	29	31	60	28
Ni	25	25	37	83
Ga	20.8	20.7	20.3	11.5
Nb	14.3	13.3	15.2	9.9
Pb	3.4	2.9	1.8	<d.l.
Rb	122.7	163.2	154.0	141.7
Sr	425.7	431.3	471.6	714.0
Th	10.1	10.0	10.8	6.5
U	<d.l.	<d.l.	<d.l.	<d.l.
Y	29.4	29.2	31.5	19.2
Zr	337.7	340.6	374.5	141.4

*: Total Fe reported as FeO, **: Calculated from regression line through Zr and P_2O_5 from this study. n.a.: not analyzed. <d.l.: below detection limit. —: not reported. Diorite-Ps: Diorite with unidentified pseudomorphs.

Table 4. (continued)

Rock type	Diorite (this study)		
Sample	JMH-328.1	JMH-181	JMH-365A
Wt. %			
SiO_2	44.48	48.86	44.79
TiO_2	1.46	1.07	1.15
Al_2O_3	21.10	21.88	20.81
Fe_2O_3	10.46	8.15	8.93
FeO	n.a.	n.a.	n.a.
MnO	0.08	0.06	0.10
MgO	7.06	4.32	5.83
CaO	3.01	5.61	7.62
Na_2O	2.14	4.49	1.65
K_2O	7.29	4.24	6.21
P_2O_5	0.71	0.54	0.64
H_2O^+	n.a.	n.a.	n.a.
H_2O^-	n.a.	n.a.	n.a.
CO_2	n.a.	n.a.	n.a.
L.O.I.	1.65	1.46	1.78
ppm			
V_2O_5	n.a.	n.a.	n.a.
BaO	2626	978	2385
Ce	n.a.	92	n.a.
Co	38	18	33
Cr_2O_3	72	30	54
Ni	69	43	70
Ga	24.9	24.8	23.2
Nb	19.6	15.2	16.7
Pb	3.6	2.3	3.4
Rb	253.4	164.6	229.1
Sr	216.6	271.3	489.5
Th	9.1	7.2	4.8
U	6.3	1.8	4.0
Y	26.6	19.2	20.2
Zr	743.2	494.4	555.9

*: Total Fe reported as FeO, **: Calculated from regression line through Zr and P_2O_5 from this study. n.a.: not analyzed. <d.l.: below detection limit. —: not reported. Diorite-Ps: Diorite with unidentified pseudomorphs.

Table 4. (continued)

Rock type	Diorite-Ps (this study)			
Sample	H1084-872.8	H1084-881	H1281-28	H1281-61.5
Wt. %				
SiO_2	48.03	47.98	48.62	48.74
TiO_2	1.47	1.16	0.94	0.64
Al_2O_3	19.05	20.71	21.77	22.98
Fe_2O_3	10.20	8.30	8.27	7.37
FeO	n.a.	n.a.	n.a.	n.a.
MnO	0.20	0.16	0.12	0.10
MgO	5.94	6.61	5.08	5.19
CaO	3.61	2.35	1.99	2.08
Na_2O	3.94	3.78	2.83	2.72
K_2O	5.38	6.18	7.31	7.42
P_2O_5	0.82	0.61	0.69	0.55
H_2O^+	n.a.	n.a.	n.a.	n.a.
H_2O^-	n.a.	n.a.	n.a.	n.a.
CO_2	n.a.	n.a.	n.a.	n.a.
L.O.I.	1.26	1.74	2.18	2.50
ppm				
V_2O_5	n.a.	n.a.	n.a.	n.a.
BaO	1541	1576	1427	1135
Ce	245	264	188	139
Co	30	36	24	20
Cr_2O_3	73	75	57	46
Ni	86	73	50	31
Ga	23.6	22.6	25.8	25.6
Nb	19.1	15.3	12.8	9.0
Pb	3.7	2.7	2.5	2.0
Rb	222.8	255.1	257.1	220.1
Sr	281.8	286.3	171.8	132.7
Th	27.5	30.9	19.6	13.8
U	6.3	5.4	5.8	4.3
Y	42.9	36.0	42.2	34.4
Zr	786.5	763.2	574.3	471.3

*: Total Fe reported as FeO, **: Calculated from regression line through Zr and P_2O_5 from this study. n.a.: not analyzed. <d.l.: below detection limit. —: not reported. Diorite-Ps: Diorite with unidentified pseudomorphs.

Table 4. (continued)

Rock type	Diorite-Ps (this study)		Diorite (Olsen, 1961)		
Sample	JMH-24	JMH-281A	5	6	7
Wt. %					
SiO_2	48.96	48.43	39.60	51.10	59.50
TiO_2	1.43	1.35	1.10	1.10	0.81
Al_2O_3	19.78	20.39	23.80	20.50	17.60
Fe_2O_3	10.23	9.64	1.06	—	—
FeO	n.a.	n.a.	8.57	6.36*	4.95*
MnO	0.10	0.10	0.10	0.04	0.04
MgO	5.48	5.48	5.85	4.50	2.85
CaO	1.59	2.38	8.90	6.20	4.20
Na_2O	4.26	4.50	1.70	3.06	4.04
K_2O	6.33	5.57	4.85	4.00	4.25
P_2O_5	0.89	0.80	0.63**	0.71**	0.52**
H_2O^+	n.a.	n.a.	2.30	—	—
H_2O^-	n.a.	n.a.	0.14	—	—
CO_2	n.a.	n.a.	—	—	—
L.O.I.	1.54	1.40	—	—	—
ppm					
V_2O_5	n.a.	n.a.	550	330	190
BaO	1962	1212	3200	1850	1950
Ce	244	227	—	—	—
Co	35	27	—	—	—
Cr_2O_3	77	67	—	—	—
Ni	146	77	—	—	—
Ga	22.8	24.9	—	—	—
Nb	18.0	18.3	—	—	—
Pb	3.4	4.5	—	—	—
Rb	239.9	226.1	—	—	—
Sr	128.6	210.9	972	355	262
Th	27.6	25.7	—	—	—
U	5.6	5.4	—	—	—
Y	46.9	43.9	—	—	—
Zr	741.7	731.0	548	622	437

*: Total Fe reported as FeO, **: Calculated from regression line through Zr and P_2O_5 from this study. n.a.: not analyzed. <d.l.: below detection limit. —: not reported. Diorite-Ps: Diorite with unidentified pseudomorphs.

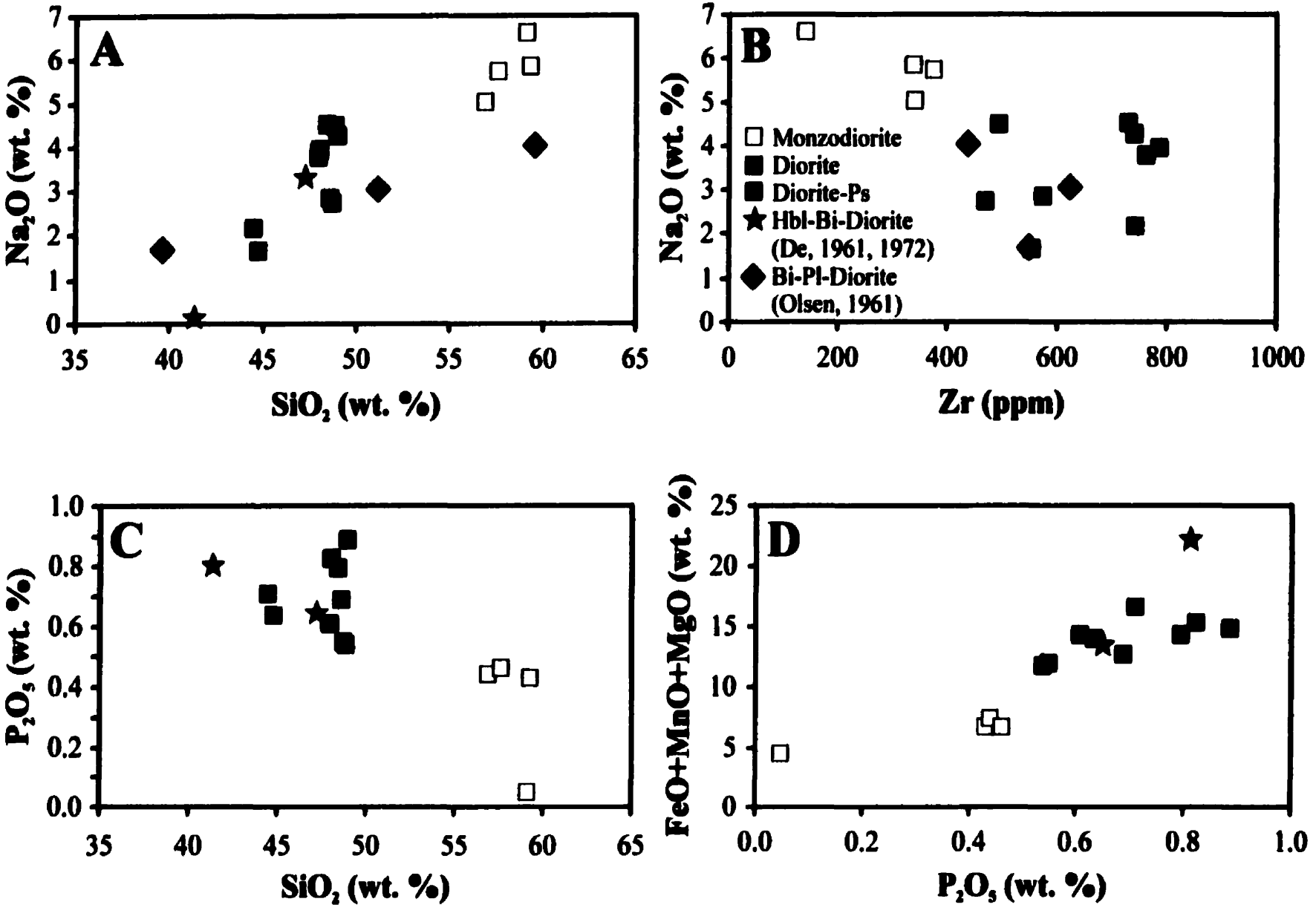
Table 4. (continued)

Rock type	Diorite (De, 1972)	
Sample	570	9/144
Wt. %		
SiO_2	47.16	41.31
TiO_2	0.88	0.81
Al_2O_3	20.82	16.36
Fe_2O_3	0.93	1.74
FeO	7.72	10.30
MnO	0.11	0.22
MgO	5.04	10.29
CaO	5.06	11.58
Na_2O	3.33	0.17
K_2O	3.12	1.72
P_2O_5	0.65	0.81
H_2O^+	4.94	4.32
H_2O^-	0.09	0.10
CO_2	0.00	0.04
L.O.I.	—	—
ppm		
V_2O_5	—	—
BaO	—	—
Ce	—	—
Co	—	—
Cr_2O_3	—	—
Ni	—	—
Ga	—	—
Nb	—	—
Pb	—	—
Rb	—	—
Sr	—	—
Th	—	—
U	—	—
Y	—	—
Zr	—	—

*: Total Fe reported as FeO, **: Calculated from regression line through Zr and P_2O_5 from this study. n.a.: not analyzed. <d.l.: below detection limit. —: not reported. Diorite-Ps: Diorite with unidentified pseudomorphs.

Figure 7

Binary diagrams showing the relationship between the concentration of Na_2O and SiO_2 (A), Na_2O and Zr (B), P_2O_5 and SiO_2 (C), and $MgO+FeO_T+MnO$ and P_2O_5 (D) in the dioritic-monzodioritic series of rocks. Diorite-Ps refers to dioritic rocks that contain the unidentified pseudomorphed phenocrysts.


A
B
C
D
Na2O (wt. %)
SiO2 (wt. %)
Zr (ppm)
P2O5 (wt. %)
FeO+MnO+MgO (wt. %)
Monzodiorite
Diorite
Diorite-Ps
Hbl-Bi-Diorite
(De, 1961, 1972)
Bi-Pl-Diorite
(Olsen, 1961)

the monzodiorites (down to 140 ppm Zr), and instead attribute these differences to the accumulation of crystals during dyke emplacement (zircon). The trends on the other diagrams in Figure 7, e.g., SiO_2 versus P_2O_5 and MgO+FeO+MnO versus P_2O_5, are also consistent with processes of crystal accumulation (mafic minerals), forming progressively more feldspar-rich rocks. The positive correlation between Na_2O and SiO_2 therefore reflects, in part, hydrothermal processes, as manifested by albitization, but also magmatic processes, because the rocks most susceptible to albitization were those that were the most differentiated, i.e., those most enriched in feldspar.

The diorites are strongly enriched in K_2O, Rb, P_2O_5, Zr, Ce, Th, and less so in Y and Nb, in proportions which increase with the proportion of biotite in the rock. The more biotite-rich varieties contain up to 0.89 wt. % P_2O_5, 787 ppm Zr, 6.3 ppm U, 264 ppm Ce, 31 ppm Th, 47 ppm Y and 20 ppm Nb (Table 4). The concentrations of P_2O_5, Zr, Ce, Th, Y, and Nb correlate with the proportions of apatite (up to ~ 2 vol. %), zircon (up to ~ 0.1 vol. %), and monazite, allanite, titanite, and ilmenite (< 1 vol. %), respectively, which are the principal carriers of these elements.

Positive correlations among Zr, P_2O_5, TiO_2, Y, Ce, and Th, and positive correlations between each of these elements or oxides and MgO and FeO (represented by biotite and the unknown pseudomorphed phase) suggest that crystal accumulation occurred during emplacement of the diorites-monzodiorites, and played an important role in their formation. Relatively low Ni (25 to 146 ppm) and Cr_2O_3 (28 to 77 ppm) values suggest that the mantle was not the source of the magmas forming these rocks. Amphibole, plagioclase and biotite fractionation may have taken place during emplacement, close to or at the actual site of intrusion of the dioritic sheets. The hornblende-rich diorite (sample 9/144 in De, 1972) from the Vimy mine, which according to our calculations contains ~ 40 % normative hornblende, represents the most fractionated member as determined by the relationship P_2O_5 versus MgO+FeO+MnO (Figure 7d). Extensive fractionation of hornblende would have served to increase the K/Na ratio of the residual liquid and increase its alumina content, enlarging the field of stability of biotite at the expense of hornblende (Cawthorn and Brown, 1976). This may explain the occurrence of the late, interstitial, Al-rich biotite-I.

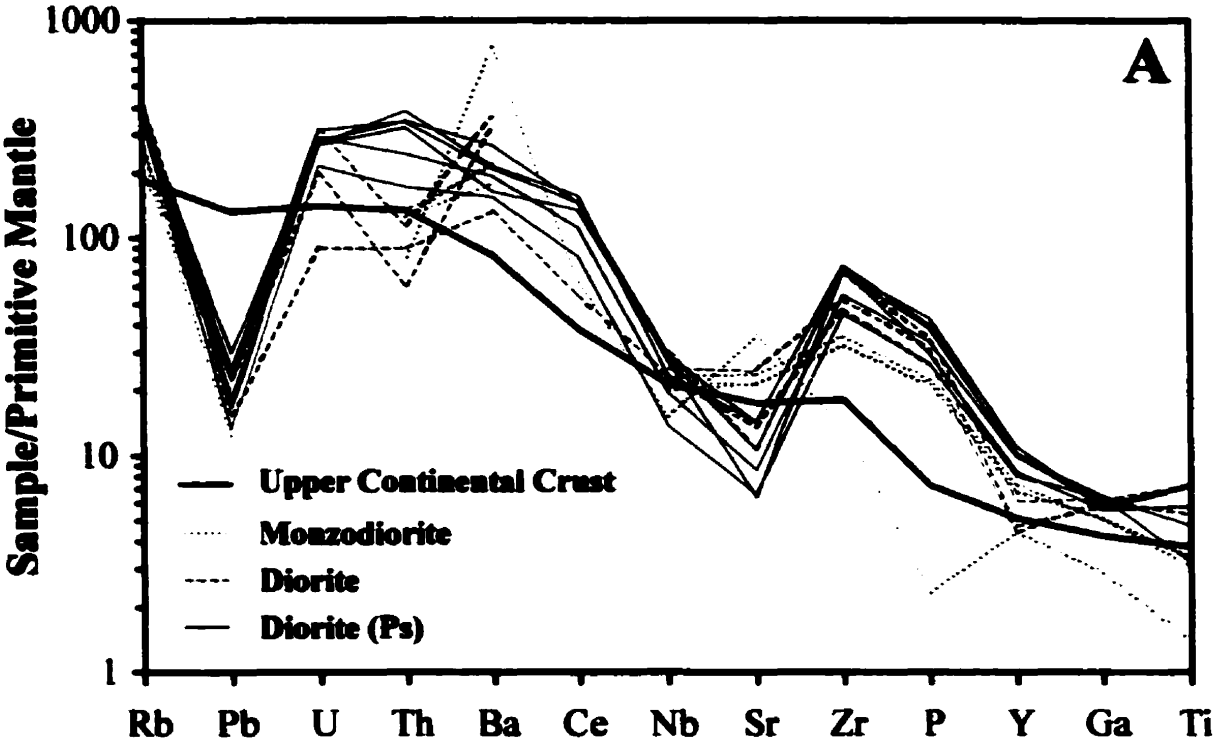
The spider diagram in Figure 8a shows the concentrations of Rb, Pb, U, Th, Ba, Ce, Nb, Sr, Zr, P, Y, Ga, and Ti in diorite-monzodiorite normalized to primitive mantle values (from Sun and McDonough, 1989). For reference, values for the upper continental crust (from Taylor and McLennan, 1985) are also shown. The most conspicuous features of this diagram are the marked enrichment in the large-ion-lithophile elements (LILE) Rb, K, and Ba, the hygromagmatophile high-field-strength elements (HFSE) Th, and Ce, and the negative anomaly in Nb. The negative anomalies in Pb and Sr are attributed to alteration of plagioclase. Although part of the enrichment can be ascribed to the cumulate nature of the diorites, particularly the more melanocratic varieties, this enrichment remains very high even in the leucocratic monzodiorites. Thus in summary, we believe that the original magma chemistry during emplacement is satisfactorily described by the variations displayed by the rocks.

Granitic rocks

Geochemically, the granitic rocks are distinguished from the dioritic-monzodioritic rocks by their higher SiO_2, lower Al_2O_3 and trace element contents, and by a more uniform composition (Table 5). Almost all the samples analysed are peraluminous and have $Al_2O_3/(Na_2O+K_2O)$ molecular ratios that range, for the granites, between 1.24 and 1.51, and, for the granodiorites, between 1.49 and 1.60. The $Al_2O_3/(CaO+Na_2O+K_2O)$ molecular ratios range between 0.98 and 1.19, for the granites, and between 0.97 and 1.16 for the granodiorites (Figure 9). This is not surprising given the presence of andalusite. The granites also have elevated P_2O_5/Zr values, and are enriched in Ba and Rb relative to granodiorites (Figure 8b). On a log Y versus log Nb diagram, the compositions of rocks of both suites plot within the fields of volcanic arc and syn-collisional granites defined by Pearce et al. (1984). Use of the log Y+Nb versus log Rb projection (Pearce et al., 1984) suggests a volcanic arc origin. However, this distinction becomes irrelevant, if it is considered that the southeastern Appalachian ophiolites represent obducted oceanic crust formed in an arc environment contaminated by continental crust. Both types would then be blended.

Figure 8

Spider diagram showing the mantle-normalized (using the concentrations of Sun and McDonough, 1989) distribution of minor and trace elements in (A) the dioritic-monzodioritic and (B) the granodioritic-granitic series of rocks. The thick line represents the values for the average upper continental crust (from Taylor and McLennan, 1981). The thin lines in (A) represent the distribution of these elements in the pseudomorph-bearing (Ps) diorites, the dashed lines the distribution in the pseudomorph-free diorites and the dotted lines the distribution in the monzodiorites. The thin lines in (B) represent the distribution of the elements in granodiorite and the dotted lines the distribution in granites.


A
1000
100
10
1
Sample/Primitive Mantle
Upper Continental Crust
Monzodiorite
Diorite
Diorite (Ps)
Rb
Pb
U
Th
Ba
Ce
Nb
Sr
Zr
P
Y
Ga
Ti

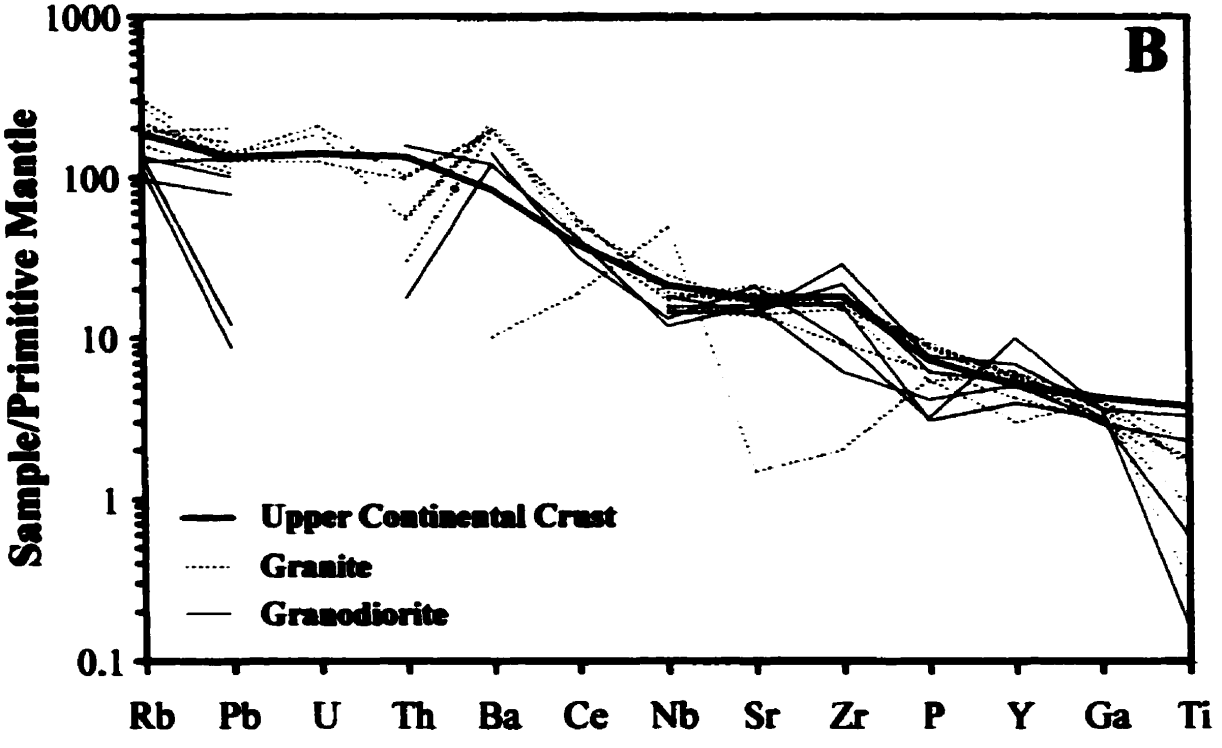

B
1000
100
10
1
0.1
Sample/Primitive Mantle
Upper Continental Crust
Granite
Granodiorite
Rb
Pb
U
Th
Ba
Ce
Nb
Sr
Zr
P
Y
Ga
Ti

Table 5. Chemical analyses of granodioritic-granitic rocks.

Rock type	Granite						
Sample	JMH-56B1	JMH-213A	JMH-273D	JMH-274B	Flt-F	E:53	E:75
Wt. %							
SiO_2	75.50	74.32	70.71	71.11	69.29	68.75	69.90
TiO_2	0.06	0.18	0.35	0.28	0.36	0.32	0.45
Al_2O_3	14.29	13.60	14.40	14.81	15.50	15.70	14.54
Fe_2O_3	0.57	1.54	2.54	2.39	2.79	2.20	3.08
MnO	0.02	0.04	0.04	0.05	0.05	0.03	0.04
MgO	0.13	0.52	1.02	0.90	1.11	1.08	1.28
CaO	0.47	0.84	1.68	1.70	1.73	1.78	1.08
Na_2O	3.79	2.94	4.02	2.89	3.17	3.94	2.87
K_2O	4.54	4.95	4.62	4.67	5.09	5.60	5.93
P_2O_5	0.12	0.13	0.20	0.11	0.18	0.18	0.19
L.O.I.	0.55	0.7	0.52	0.91	0.82	0.50	0.62
ppm							
BaO	75	1147	1562	1339	1409	1469	1440
Ce	32	n.a.	92	n.a.	96	70	85
Co	36	<d.l.	11	<d.l.	n.a.	n.a.	n.a.
Cr_2O_3	<d.l.	15	19	20	33	29	23
Ni	<d.l.	5	11	12	22	14	21
Ga	16.3	12.5	13.2	12.9	14.9	16.5	16.5
Nb	32.1	10.6	12.8	10	11.8	11.5	16.5
Pb	17	25	16.1	30.6	19.1	20.6	21.5
Rb	166.7	120.1	96.4	117.8	133.6	132.6	186.3
Sr	29.9	289.3	334.7	278.7	379.4	431.2	333.0
Th	<d.l.	<d.l.	4.6	2.4	7.8	4.4	8.1
U	<d.l.	<d.l.	<d.l.	<d.l.	2.5	3.7	4.2
Y	13	18.3	24.4	26.9	25.3	22.4	26.3
Zr	21.6	97.6	172.6	160	189.1	162.2	191.9

n.a.: not analyzed. <d.l.: below detection limit.

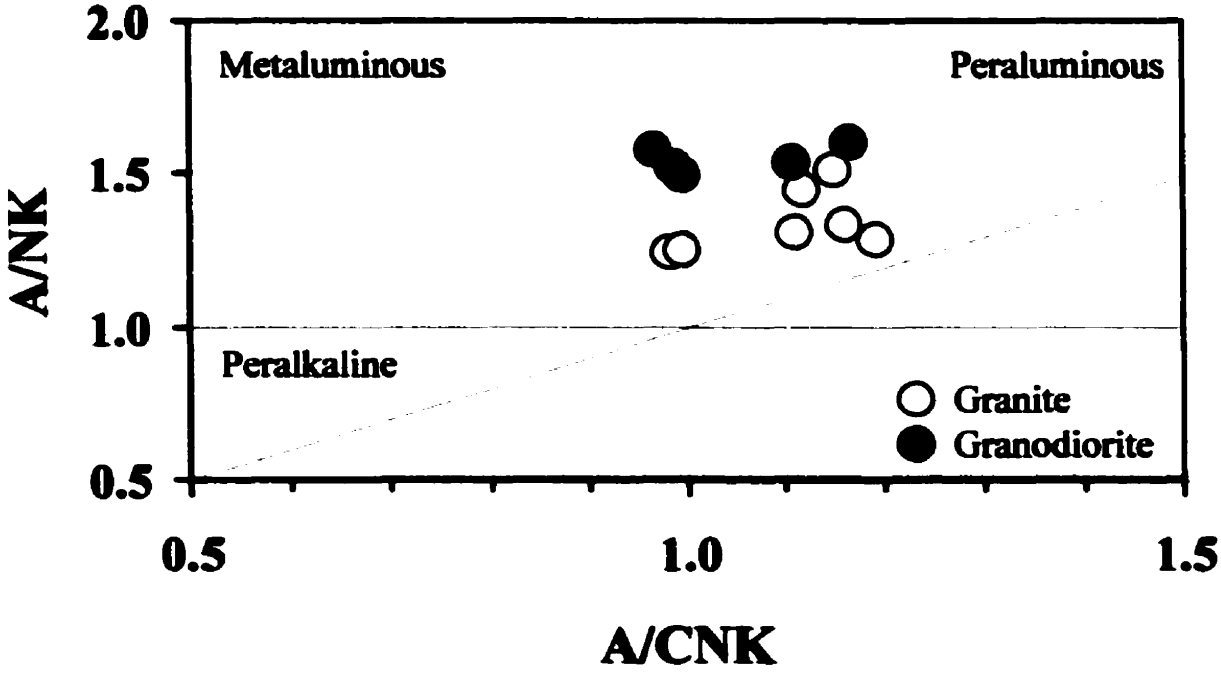
Table 5. (continued)

Rock type	Granodiorite				
Sample	JMH-56B2	JMH-220	JMH-320A	JMH-320B	JMH-321A
Wt. %					
SiO_2	70.73	74.59	74.37	69.71	75.15
TiO_2	0.03	0.12	0.46	0.65	0.12
Al_2O_3	16.39	13.81	11.64	13.50	13.44
Fe_2O_3	0.94	1.30	3.04	3.66	1.11
MnO	0.03	0.02	0.04	0.05	0.03
MgO	1.28	0.70	1.58	1.92	0.68
CaO	2.10	1.91	2.56	2.63	2.46
Na_2O	4.13	3.43	2.68	3.15	3.92
K_2O	3.20	3.10	2.76	3.42	2.37
P_2O_5	0.07	0.06	0.13	0.16	0.09
L.O.I.	1.01	0.84	0.61	0.72	0.57
ppm					
BaO	1044	877	876	1185	476
Ce	54	70	n.a.	n.a.	n.a.
Co	36	<d.l.	16	14	<d.l.
Cr_2O_3	<d.l.	15	28	48	15
Ni	<d.l.	<d.l.	20	26	7
Ga	14.6	12.6	11.7	14.3	12.3
Nb	8.8	7.8	9.4	11.9	10.2
Pb	15.2	19.4	1.3	1.8	11.7
Rb	80.5	75.3	68.9	80.9	57.8
Sr	415.5	322.4	289.6	284.3	316.1
Th	<d.l.	1.4	12.5	20.9	<d.l.
U	<d.l.	<d.l.	<d.l.	<d.l.	<d.l.
Y	43.2	17	23.4	29.6	21.8
Zr	100.2	167.4	226.3	302.7	64.9

n.a.: not analyzed. <d.l.: below detection limit.

Figure 9

A/NK versus A/CNK diagrams showing the metaluminous to peraluminous character of granodioritic and granitic rocks from the JM Asbestos deposit.


2.0
1.5
1.0
0.5
A/NK
Metaluminous
Peraluminous
Peralkaline
Granite
Granodiorite
0.5
1.0
1.5
A/CNK

Geochemical relationships between dioritic and granitoid rocks

The composition of the dioritic-monzodioritic and granitoid rocks are compared on the binary plots presented in Figure 10. The excellent correlations among TiO_2, Zr, Y, Ce, Th, Ni, and Cr_2O_3 for the two rock suites support strongly the hypothesis that they are related by fractional crystallization via a cumulate process similar to that described above.

DISCUSSION

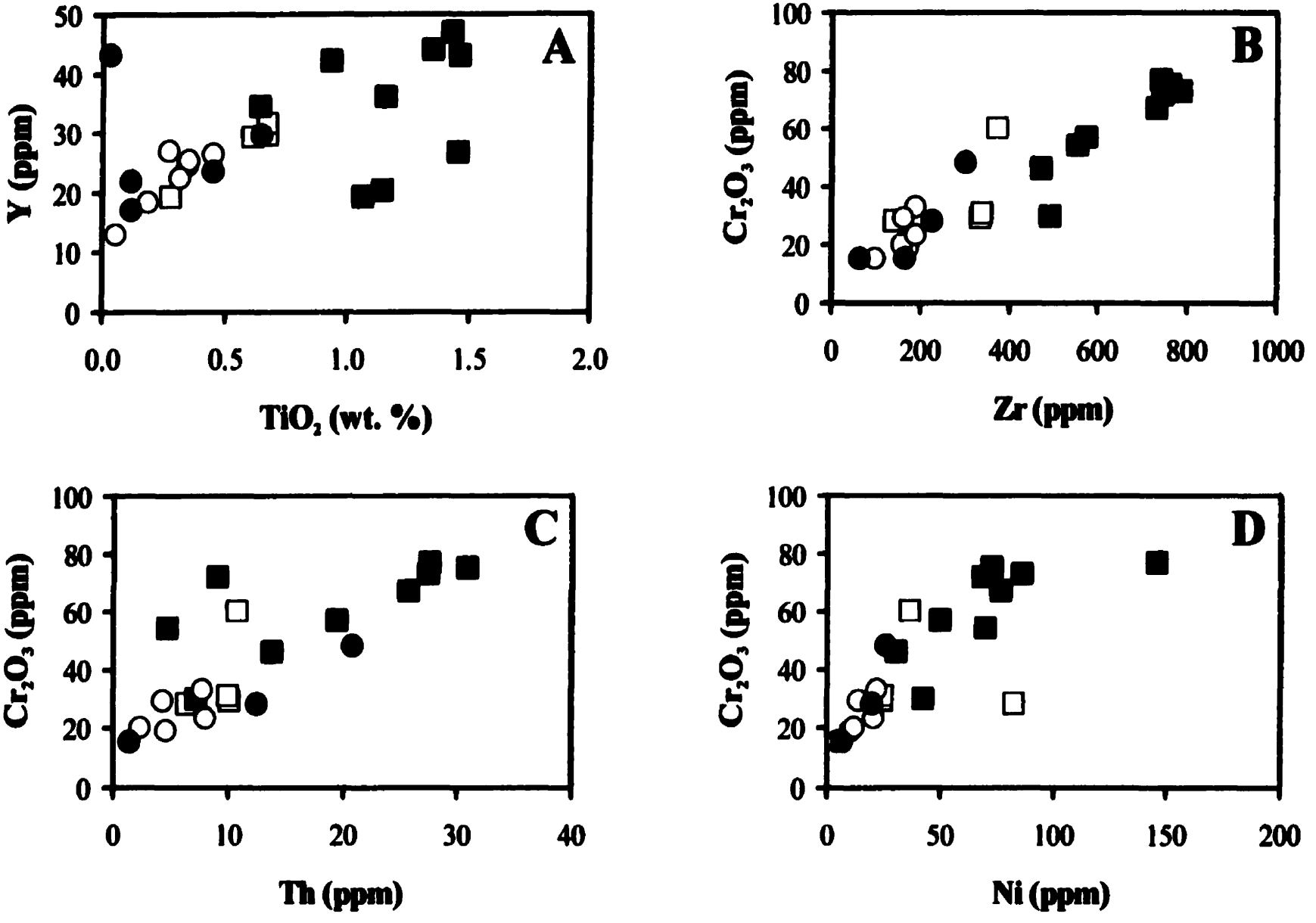
Origin of the felsic intrusive dykes

High-K diorites in subduction settings are generally associated with mature arcs or continental crust (Mason and McDonald, 1978; Le Bel et al., 1985; Meen, 1987). However, the dioritic-monzodioritic rocks in the JM Asbestos mine differ from such diorites in that they clearly appear to be the products of accumulation of early-formed crystals during crystallization of a more felsic magma. Furthermore, the inferred age of these felsic sheets (between 470 and 460 Ma), which potentially post-dates the initiation of obduction, and the fore-arc nature of the ophiolite, argue against an origin of the melts at depths associated with volcanic arc magmatism or subduction below continental crust.

The lack of age and source-identifying isotopic data limits our ability to determine the origin of the dioritic-monzodioritic and granitoid rocks. At the present time, we can only suggest, based on the geochemical data, that these felsic rocks formed in a subduction-obduction setting, from a LILE-, Th- and U-enriched source, possibly altered basaltic crust, associated pelagic sediments and continentally-derived sediments (consistent with the fore-arc setting inferred by Olive et al, 1997, and Hébert and Bédard, 1998). The lack of evidence for arc or back-arc magmatism before obduction of the Thetford Mines and Asbestos ophiolites makes it unlikely that a hydrated-metasomatised mantle wedge was the source of the magmas. Boninite-type magmatism, which characterized the later, fore-arc-related, igneous events forming the southeastern Québec Appalachian ophiolites, is believed to take place by melting of subducted oceanic crust at

Figure 10

Binary plots showing the correlation between Y and TiO_2 (A), Cr_2O_3 and Zr (B), Cr_2O_3 and Th (C), and Cr_2O_3 and Ni (D) among dioritic-monzodioritic and granodioritic-granitic intrusive rocks. This correlation is interpreted to reflect a relationship between the dioritic and granitoid rocks. Such a relationship could be attributed to fractionation (see text). Square symbols refer to the same samples as in Figure 7. Open circles represent granitic rocks and closed circles represent granodioritic rocks.


A
Y (ppm)
TiO2 (wt. %)
B
Cr2O3 (ppm)
Zr (ppm)
C
Cr2O3 (ppm)
Th (ppm)
D
Cr2O3 (ppm)
Ni (ppm)

shallow levels (< ~ 60 kilometers) in very young subduction zones where geothermal gradients along the Benioff plane are high. The shallow levels of the mantle wedge above the site of magma generation in such environments only allow for limited or for no slab-derived magma-mantle interaction (Martin, 1999). However, whether the diorites-monzodiorites and the granitoids from the Asbestos ophiolite were generated from the same source or are genetically related can only be confirmed by further dating and source-assignment isotopic geochemistry.

Emplacement of the felsic dykes

Information regarding the tectonic setting of intrusion of the dioritic and granitic rocks in the Asbestos ophiolite can be obtained from their structural position. Both types of intrusion occur exclusively in peridotites, mainly in harzburgite, and are not encountered higher in the stratigraphy of the ophiolites or in the enclosing metasedimentary rocks. The absence of the felsic intrusive rocks from the enclosing sedimentary rocks indicates that they were emplaced before the ophiolites achieved their present tectonic position. Their confinement to the peridotitic section of the ophiolites suggests that: 1) a thrust boundary exists between the lower ultramafic and upper gabbroic and volcanic parts of the ophiolite slivers, or 2) the serpentinized ultramafic cumulates acted as cold but more ductile caps above the brittle, partly serpentinized harzburgites. In the latter case, the dioritic and granitic rocks would have had to be emplaced after construction of the ophiolite to enable cooling and serpentinization.

Numerous pieces of evidence for intrusion through, at least partially, serpentinized peridotites can be observed in the field and in samples from the JM Asbestos deposit. These can be grouped into three categories: 1) structural, 2) petrographic, and 3) metamorphic. Locally, dykes occur parallel to specific sets of fracture and shear zones that affect the serpentinites, suggesting that these fractures and shear zones acted as channels for the magmatic intrusions. Where the contacts between the felsic intrusive rocks and the serpentinites are not sheared, the megascopic textures seen on cut surfaces of serpentinite samples taken far from the contact, near the contact and in serpentinite enclaves, are identical. Olivine-bearing assemblages were not

observed in serpentinite near or at the contact with felsic intrusive rocks. Bi-mineralic anthophyllite-cummingtonite rims in serpentinite at the contact with dioritic intrusives, changing sharply to antigorite forming interlocking textures or, more importantly, to lizardite pseudomorphs, suggest that the host peridotite had been serpentinized prior to intrusion of the sheets. The thickness of these amphibole rims measures less than 5 cm, irrespective of the thickness of the intrusive sheets, suggesting a metamorphic-metasomatic origin. The rims are composed of parallel fibers that grew perpendicular to the contact, indicating the flow direction of fluid and dissolved species into the serpentinite. Assuming replacement of serpentine by amphibole at constant-volume, the reaction:

$$2.48Mg_3Si_2O_5(OH)_4 + 3.04SiO_2^\circ + 0.86HCl^\circ =$$
$$Mg_7Si_8O_{22}(OH)_2 + 0.43MgCl_2^\circ + 4.39H_2O \quad (1)$$

involved consumption of SiO_2 to form anthophyllite, and liberation of Mg to form the biotite-rich zones that occur in the dykes at their contact with serpentinite. The occurrence of thin biotite veins with amphibole rims emanating from the dioritic sheets through serpentinites is further evidence that intrusion of the felsic dykes took place after a significant proportion of the peridotite had been serpentinized. If this had not been the case, i.e., the anthophyllite-cummingtonite replaced unaltered peridotite, it is unlikely that the anthophyllite-cummingtonite would have survived the subsequent serpentinization.

Application of one-dimensional conductive cooling models (Jaeger, 1957) indicate that the anthophyllite-cummingtonite rims, which, based on composition ($X_{Fe} < 0.2$) and phase equilibrium relationships, are stable above ~ 550°C (Maresh and Czank, 1988; Rasmussen et al., 1998), would only form if the felsic magma intruded at a temperature ≥ 800°C, assuming instantaneous emplacement of the dykes in serpentinites, which were at an initial temperature of 300°C. If the magma was intruded at a temperature of 700°C, the host serpentinites would have needed to have been at a temperature ≥ 400°C for anthophyllite-cummingtonite to have formed. However, because the dioritic magmas were hydrous, as indicated by the presence of biotite, it is

conceivable that small amounts of magmatic fluids could have transported heat and material through the serpentinites by advection or diffusion. Evidence for the presence of fluids during the crystallization of the granitic rocks is the occurrence of liquid-vapour-solid (NaCl) fluid inclusions coexisting with vapour-rich fluid inclusions in quartz (Chapter VI). Because fluids are much better agents of heat transport than solids (conduction), the temperature at the contact could have been raised by advection and diffusion to a value that enabled anthophyllite-cummingtonite to form, while the host serpentinites were initially at low temperature. A very sharp drop in temperature in advance of an advection-diffusion front would explain the abrupt contact between anthophyllite-cummingtonite and serpentinite.

Some of the granites and diorites are relatively fresh up to their contact with serpentinite, i.e., they did not undergo rodingitization. The presence or absence of rodingite at the contacts of dykes intruding ultramafic rocks was used as an indicator of the timing of intrusion relative to that of serpentinization by Coulton et al. (1995). They suggested that, because rodingitization is a process that takes place concomitantly with serpentinization, intrusive dykes which do not show rodingitized contacts must have been emplaced after serpentinization.

Asbestos versus Oman ophiolites

Pinet and Tremblay (1995b) drew parallels in respect to both timing and process between the obduction history of the southeastern Québec Appalachian ophiolites and that of the Oman ophiolites. In both cases, relatively rapid obduction of large sheets of young oceanic crust and upper mantle occurred without deep burial in a subduction trench. Interestingly, dioritic, granodioritic and peraluminous granitic intrusions also occur together in close association in the upper part of the harzburgite tectonites at the base of the layered series of the Oman ophiolite. A variety of interpretations have been proposed for the formation of these felsic rocks. Based on structural relationships and their chemical and Sr and Nd isotopic compositions, Lippard et al. (1986), Boudier et al. (1988) and Cox et al. (1999) suggested that the felsic intrusives were syn-obduction, derived from the partial melting of K-rich rocks at the base of the obducting ophiolite.

Lippard et al. (1986) suggested that this K-rich source of these felsic rocks was subducted continental crust. However, recent dating has shown that the ophiolite was thrust onto the Arabian continent long after the dykes were emplaced, indicating that the latter could not represent melting of subducted continental crust. A hypothesis that is consistent with the spatial and temporal obduction history of the ophiolite involves melting of trench material entrained below rapidly obducting (or at the top of subducting) young and hot oceanic crust and mantle (Boudier et al., 1988; Cox et al., 1999). Cox et al. (1999) have shown from Sr-Nd systematics that the source of the felsic rocks, ranging in composition from diorite to leucogranite, was mixed, and contained quartzofeldspathic and basaltic components. An alternative hypothesis proposed by Peters and Kamber (1994) is that the more evolved granites originated from the partial melting of older, less evolved rocks (e.g., tonalites and diorites) as a result of interaction with fluids derived from the dehydration of the basal metamorphic sole during obduction.

A hypothesis similar to that of Boudier et al. (1988) for Oman was proposed by Whitehead et al. (2000) for the genesis of the granites in the Thetford Mines ophiolite. These authors speculated that the granites could have been produced by wet or dry melting of continentally-derived or pelagic sediments as a result of shear heating, under increased rates of strain, concentrated along a narrow zone at the base of a very young (e.g., 1 Ma) and hot (> 1000°C) slab of oceanic crust. According to these authors, the injection of the granitic melt would have been facilitated by filter pressing and deformation.

The various geochemical and mineralogical features shared by both suites of K-rich felsic rocks in the JM Asbestos mine suggest that they were formed during a single event of as yet unknown duration. As discussed above, the inherited Precambrian ages of zircons in all the K-rich granitoid rocks analysed from the southeastern Québec ophiolites, and the mixed, oceanic-continental crust source of boninitic magmas, strongly support the idea that the source of the felsic dykes in the JM Asbestos mine comprised a significant component of continentally-derived material. The model proposed by Cox et al. (1999) and Whitehead et al. (2000) for the origin of felsic rocks in peridotites at the base of obducted ophiolites could be applied to the Asbestos ophiolite, if the relationship

between the age of the ophiolite and the age of the felsic rocks is similar to that for the Thetford Mines area.

CONCLUSIONS

The field, mineralogical and geochemical data presented in this study indicate that the felsic igneous rocks in the JM Asbestos deposit were intruded as melts into peridotites that had been previously serpentinized. The age relationships, although poorly known, among the felsic intrusive rocks, the ophiolites and Taconian metamorphism, suggest that intrusion of the felsic igneous rocks took place at an early stage of the obduction of the ophiolite slivers. The geochemical signature of the felsic intrusive rocks also suggests that they originated from the melting of a source enriched in incompatible elements, possibly mixed altered basalts and pelagic and continentally-derived sediments.

We conclude that the emplacement of the felsic igneous rocks in the Asbestos ophiolite and their subsequent tectonic transport took place at relatively shallow depth. The melting event, which produced these felsic rocks, probably occurred during obduction of a young and hot ophiolite slab above a young, shallow subduction zone. Until detailed petrologic and isotopic studies, and more precise age determinations are performed on the dioritic-monzodioritic and granodioritic-granitic rocks of the southeastern Québec ophiolites to establish their nature and the time at which they were emplaced, metamorphosed and altered, their origin will remain unclear.

ACKNOWLEDGEMENTS

J. A. Millen and M. Arpin, geologists at the JM Asbestos mine, provided geological information and logistical support. J. Clark is thanked for providing part of the electron microprobe analyses. This manuscript benefited from discussions with A. Hynes, R. F. Martin, J. Whitehead, and R. Hébert. Funding for this research was provided by NSERC and FCAR scholarships to CN and NSERC and FCAR research grants to AEW-J.

REFERENCES

Berman, R. G., 1991, Thermobarometry using multiequilibrium calculations: a new technique, with petrological applications, Canadian Mineralogist, v. 29, p. 833-855.

Boudier, F., Ceuleneer, G. and A. Nicolas, 1988, Shear zones, thrusts and related magmatism in the Oman ophiolite: initiation of thrusting on an oceanic ridge, Tectonophysics, v. 151, p. 275-296.

Brodeur, E. and R. Marquis, 1995, Géologie de la région d'Orford, Ministère de l'Énergie, des Mines et des Ressources du Québec, ET 93-06, 97 p.

Castonguay, S., Tremblay, A., Ruffet, G., Féraud, G. and M. Sosson, 1995, 40Ar/39Ar cooling ages of Taconian deformation and metamorphism along the Laurentian margin of the Québec Appalachians, Canada: Middle Ordovician and Silurian, Geological Society of America Abstracts with Programs, v. 27, p. A-225.

Castonguay, S., Tremblay, A., Ruffet, G., Féraud, G., Pinet, N. and M. Sosson, 1997, Ordovician and Silurian metamorphic cooling ages along the Laurentian margin of the Quebec Appalachians: bridging the gap between New England and Newfoundland, Geology, v. 25, p. 583-586.

Cawthorn, R. G. and P. A. Brown, 1976, A model for the formation and crystallization of corundum-normative calc-alkaline magmas through amphibole fractionation, Journal of Geology, v. 84, p. 467-476.

Clague, D. A., Frankel, C. S. and J. S. Eaby, 1985, The age and origin of felsic intrusions of the Thetford Mines ophiolite, Quebec, Canadian Journal of Earth Sciences, v. 22, p. 1257-1261.

Coulton, A. J., Harper, G. D. and D. S. O'Hanley, 1995, Oceanic versus emplacement age serpentinization in the Josephine ophiolite: Implications for the nature of the Moho at intermediate and slow spreading ridges, Journal of Geophysical Research, v. 100, p. 22,245-22,260.

Cox, J., Searle, M. and R. Pedersen, 1999, The petrogenesis of leucogranitic dykes intruding the northern Semail ophiolite, United Arab Emirates: field relationships, geochemistry and Sr/Nd isotope systematics, Contributions to Mineralogy and

Petrology, v. 137, p. 267-287.

David, J. and R. Marquis, 1994, Géochronologie U-Pb dans les Appalaches du Québec: application aux roches de la zone de Dunnage, La Revue Géologique du Québec, v. 1, p. 16-20.

David, J., Marquis, R. and Tremblay, A., 1993, U-Pb geochronology of the Dunnage zone, in the southwestern Quebec Appalachians, Geological Society of America Abstracts with Programs, v. 25, p. A-485.

De, A., 1961, Petrology of dikes emplaced in the ultramafic rocks of southeastern Quebec, Ph. D. dissertation, Princeton University, Princeton, 201 p.

De, A., 1972, Petrology of dikes emplaced in the ultramafic rocks of southeastern Quebec and origin of the rodingite, Geological Society of America, Memoir 132, p. 489-501.

de la Roche, H., Leterrier, J., Grandclaude, P. and M. Marchal, 1980, A classification of volcanic and plutonic rocks using R_1R_2-diagram and major-element analyses – its relationships with current nomenclature, Chemical Geology, v. 29, p. 183-210.

Dewey, J. F., 1976, Ophiolite obduction, Tectonophysics, v. 31, p. 93-120.

Dunning, G. R. and R. B. Pedersen, 1988, U/Pb ages of ophiolites and arc-related plutons of the Norwegian Caledonides: implications for the development of Iapetus, Contributions to Mineralogy and Petrology, v. 98, p. 13-23.

Feininger, T., 1981, Amphibolite associated with the Thetford Mines ophiolite complex at Belmina Ridge, Quebec, Canadian Journal of Earth Sciences, v. 18, p. 1878-1892.

Harnois, L. and M. Morency, 1989, Geochemistry of Mount Orford ophiolite complex, Northern Appalachians, Canada, Chemical Geology, v. 77, p. 133-147.

Hébert, R., 1980, Etude pétrologique des roches ophiolitiques d'Asbestos et du Mont Ham (Ham Sud), M. Sc. thesis, Université Laval, Québec, Canada, 182 p.

Hébert, R. and R. Laurent, 1989, Mineral chemistry of ultramafic and mafic plutonic rocks of the Appalachian ophiolites, Québec, Canada, Chemical Geology, v. 77, p. 265-285.

Hébert, R. and J. H. Bédard, 1998, Architecture and petrogenesis of arc ophiolites:

example from the ophiolitic complexes of southern Quebec, Geological Association of Canada, Mineralogical Association of Canada, Association des Géologues et Géophysiciens du Québec, International Association of Hydrogeologists, Canadian Geophysical Union Joint Annual Meeting, 13-15 May 1998, Québec, Québec, Canada, Fieldtrip A4 Guidebook, 51 p.

Hébert, R., Bédard, J. H., Olive, V., Huot, F. and V. Varfalvy, 1998, Ophiolites of southern Quebec Appalachians: a synthesis, Geological Association of Canada, Mineralogical Association of Canada, Association des Géologues et Géophysiciens du Québec, International Association of Hydrogeologists, Canadian Geophysical Union Joint Annual Meeting, 13-15 May 1998, Québec, Québec, Canada, Abstracts, v. 23, p. A-76.

Jaeger, J. C., 1957, The temperature in the neighborhood of a cooling intrusive sheet, American Journal of Science, v. 255, p. 306-318.

Jamieson, R. A., 1986, P-T paths from high temperature shear zones beneath ophiolites, Journal of Metamorphic Geology, v. 4, p. 3-22.

Laird, J., Trzcienski, W. E., Jr. and W. A. Bothner, 1993, High-pressure, Taconian, and subsequent polymetamorphism of southern Quebec and northern Vermont, Geological Society of America Field Trip Guidebook for the Northeastern United States, v. 2, Department of Geology and Geography, University of Massachusetts, Contribution 67, p. O 1- O 32.

Lalonde, A. E. and P. Bernard, 1993, Composition and colour of biotite from granites: two useful properties in the characterization of plutonic suites from the Hepburn internal zone of Wopmay orogen, Northwest Territories, Canadian Mineralogist, v. 31, p. 203-217.

Laurent, R., 1975, Petrology of the alpine-type serpentinites of Asbestos and Thetford Mines, Quebec, Schweizerische Mineralogische und Petrographische Mitteilungen, v. 55, p. 431-455.

Laurent, R. and Y. Hébert, 1979, Paragenesis of serpentine assemblages in harzburgite tectonite and dunite cumulate from the Quebec Appalachians, Canadian Mineralogist, v. 17, p. 857-869.

Laurent, R. and R. Hébert, 1989, The volcanic and intrusive rocks of the Québec Appalachian ophiolites (Canada) and their island-arc setting, Chemical Geology, v. 77, p. 287-302.

Laurent, R., Hébert, R. and Y. Hébert, 1979, Tectonic setting and petrological features of the Quebec Appalachian ophiolites, *in* Ophiolites of the Canadian Appalachians and Soviet Urals, Memorial University of Newfoundland Report No. 8, p. 53-77.

Laurent, R., Taner, M. F. and J. Bertrand, 1984, Mise en place et pétrologie du granite associé au complexe ophiolitique de Thetford Mines, Québec, Canadian Journal of Earth Sciences, v. 21, p. 1114-1125.

Le Bel, L., Cocherie, A., Baubron, J. -C., Fouillac, A. M. and C. J. Hawksworth, 1985, A high-K, mantle derived plutonic suite from Linga, near Arequipa (Peru), Journal of Petrology, v. 26, p. 124-148.

LeMétour, J., Rabu, D., Tegyey, M., Béchenec, F., Beurrier, M. and M. Villey, 1990, Subduction and obduction: two stages in the Eo-Alpine tectonometamorphic evolution of the Oman Mountains, *in* The geology and tectonics of the Oman region, Robertson, A. H. F., Searle, M. P. and A. C. Ries, editors, Geological Society Special Publication No. 49, p. 327-339.

Lippard, S. J., Shelton, A. W. and I. G. Gass, 1986, The ophiolite of northern Oman, Geological Society of London, Memoir 11, 178 p.

London, D., 1992, The application of experimental petrology to the genesis and crystallization of granitic rocks, Canadian Mineralogist, v. 30, p. 499-540.

Maresh, W. V. and M. Czank, 1988, Crystal chemistry, growth kinetics and phase relationships of structurally disordered (Mn^{2+}, Mg)-amphiboles, Fortschrifte der Mineralogie, v. 66, p. 69-121.

Martin, H., 1999, Adakitic magmas: modern analogues of Archean granitoids, Lithos, v. 46, p. 411-429.

Mason, R., 1985, Ophiolites, Geology Today, Sept.-Oct., p. 136-140.

Mason, D. R. and J. A. McDonald, 1978, Intrusive rocks and porphyry copper occurrences of the Papua New Guinea-Solomon Islands region: a reconnaissance study, Economic Geology, v. 73, p. 857-877.

Meen, J. K., 1987, Formation of shoshonites from calcalkaline basalt magmas: geochemical and experimental constraints from the type locality, Contributions to Mineralogy and Petrology, v. 97, p. 333-351.

Nicolas, A., 1989, Structures of ophiolites and dynamics of oceanic lithosphere, Kluwer Academic Press.

Normand, C., Gauthier, M. and M. Jébrak, 1996, The Québec Antimony deposit: an example of gudmundite-native antimony mineralization in the ophiolitic mélange of the southeastern Québec Appalachians, Economic Geology, v. 91, p. 149-163.

O'Hanley, D. S., 1987, The origin of the chrysotile asbestos veins in southeastern Quebec, Canadian Journal of Earth Sciences, v. 24, p. 1-9.

O'Hanley, D. S. and M. D. Dyar, 1993, The composition of lizardite 1T and the formation of magnetite in serpentinites, American Mineralogist, v. 78, p. 391-404.

Olive, V., Hébert, R. and M. Loubet, 1997, Isotopic and trace element constraints on the genesis of a boninitic sequence in the Thetford Mines ophiolitic complex, Quebec, Canada, Canadian Journal of Earth Sciences, v. 34, p. 1258-1271.

Olsen, E. J., 1961, High temperature acid rocks associated with serpentinite in eastern Quebec, American Journal of Science, v. 259, p. 329-347.

Pearce, J. A., Harris, N. B. W. and A. G. Tindle, 1984, Trace element discrimination diagrams for the tectonic interpretation of granitic rocks, Journal of Petrology, v. 25, p. 956-983.

Peters, T. and B. S. Kamber, 1994, Peraluminous, potassium-rich granitoids in the Semail ophiolite, Contributions to Mineralogy and Petrology, v. 118, p. 229-238.

Pichavant, M.D. and M.D. Manning, 1984, Petrogenesis of tourmaline granites and topaz granites; the contribution of experimental data. Physics of the Earth and Planetary Interiors, v. 35, p. 31-50.

Pinet, N. and A. Tremblay, 1995a, Tectonic evolution of the Quebec-Maine Appalachians: From oceanic spreading to obduction and collision in the Northern Appalachians, American Journal of Science, v. 295, p. 173-200.

Pinet, N. and A. Tremblay, 1995b, Is the Taconian orogeny of southern Quebec the result of an Oman-type obduction? Geology, v. 23, p. 121-124.

Pinet, N., Castonguay, S. and A. Tremblay, 1996, Thrusting and back thrusting in the Taconian internal zone, southern Quebec Appalachians, Canadian Journal of Earth Sciences, v. 33, p. 1283-1293.

Rasmussen, M. G., Evans, B. W. and S. M. Kuehner, 1998, Low-temperature fayalite, greenalite, and minnesotaite from the overlook gold deposit, Washington: phase relations in the system $FeO-SiO_2-H_2O$, Canadian Mineralogist, v. 36, p. 147-162.

Richardson, S. W., Gilbert, M. C. and P. M. Bell, 1969, Experimental determination of kyanite-andalusite and andalusite-sillimanite equilibria; the aluminium silicate triple point, America Journal of Science, v. 267, p. 259-272.

St-Julien, P. and C. Hubert, 1975, Evolution of the Taconian orogen in the Quebec Appalachians, American Journal of Science, v. 275-A, p. 337-362.

Streckheisen, A. L., 1976, To each plutonic rock its proper name, Earth Science Reviews, v. 12, p. 1-33.

Sun, S. -S. and W. F. McDonough, 1989, Chemical and isotopic systematics of oceanic basalts: implications for mantle composition and processes, *in* Magmatism in the ocean basins, Saunders, A. D. and M. J. Norry, editors, Geological Society Special Publication No. 42, p. 313-345.

Taylor, S. R. and S. M. McLennan, 1985, The continental crust: its composition and evolution, Blackwell Scientific, Oxford, 312 p.

Thompson, A. B. and R. J. Tracy, 1979, Model systems for anatexis of pelitic rocks II. Facies series melting and reactions in the system $CaO-KAlO_2-NaAlO_2-Al_2O_3-SiO_2-H_2O$, Contributions to Mineralogy and Petrology, v. 70, p. 429-438.

Trzcienski, W. E., Jr., 1994, Évidence des roches de Grenville recyclées dans la diamictite de Chain Lakes, les roches ultramafiques des Appalaches du Québec et dans des dykes montérégiens, La Revue Géologique du Québec, v. 1, p. 36-38.

Trzcienski, W. E., Jr. and L. P. Gromet, 1992, Inherited Precambrian zircons in ultramafic/mafic rocks of the Québec ophiolite belt, EOS, Transactions, American Geophysical Union, v. 73, p. 359-360.

Whitehead, J., Reynolds, P. H. and J. G. Spray, 1996, $^{40}Ar/^{39}Ar$ age constraints on Taconian and Acadian events in the Quebec Appalachians, Geology, v. 24, p. 359-

362.

Whitehead, J., Dunning, G. R. and J. G. Spray, 2000, U-Pb geochronology and origin of granitoid rocks in the Thetford Mines ophiolite, Canadian Appalachians, Geological Society of America Bulletin, v. 112, p. 915-928.

Wicks, F. J. and E. J. W. Whittaker, 1977, Serpentine textures and serpentinization, Canadian Mineralogist, v. 15, p. 459-488.

Williams, H. and P. St-Julien, 1982, The Baie Verte-Brompton line - Early Paleozoic continent-ocean interface in the Canadian Appalachians, Geological Association of Canada, Special Paper 24, p. 177-208.

INTRODUCTION TO CHAPTER V

In Chapter IV, the origin of the felsic intrusive rocks in the serpentinized peridotites of the JM Asbestos mine was discussed within the framework of the tectonic evolution of the Asbestos ophiolite. We established that the felsic rocks were emplaced in peridotite that had been substantially serpentinized before intrusion, and that this intrusion occurred after the start of ophiolite obduction. After emplacement of the felsic rocks and during obduction of the Asbestos ophiolite, calc-silicate alteration affected these felsic rocks, the serpentinites at their contacts, and the slates that are in thrust contact with the base of the ophiolite. The chemical factors that controlled this alteration are discussed in the following chapter.

CHAPTER V

ALTERATION OF SERPENTINITE, SLATE AND FELSIC INTRUSIVE ROCKS FROM THE JM ASBESTOS MINE, ASBESTOS, QUÉBEC: CONSTRAINTS ON RODINGITIZATION

by

Charles Normand and Anthony E. Williams-Jones

Department of Earth and Planetary Sciences, McGill University, 3450 University Street, Montreal (Qué), Canada, H3A 2A7.

ABSTRACT

A detailed mineralogical and mass transfer analysis was performed on hydrothermally altered slate, serpentinite, diorite and granite, and vesuvianite-rich calc-silicate veins from the JM Asbestos mine, Asbestos, Québec. Hydrothermal alteration resulted in the formation (veins or pervasive replacement) of feldspar-rich assemblages, rodingites and blackwall in the slate and felsic intrusive rocks, and tremolite-actinolite (nephrite)- and diopside-rich assemblages in the serpentinites. The original textures of the rocks are commonly preserved in pervasively replaced rocks, indicating that volume remained constant during alteration. Two types of alteration relationships were recognized at the contact between serpentinite and Si-Al-rich lithologies. In the first type, blackwall, rodingite and feldspar-rich assemblages form successive zones, which developed in that order, from the contact with serpentinites, in slates and some felsic intrusive rocks. In the second type, nephrite forms alteration halos adjacent to the dykes and blackwall is generally absent. Diopside replaced tremolite in nephrite adjacent to the most extensively rodingitized dykes. Geochemical analyses indicate that a substantial proportion of P_2O_5 and Zr contained in apatite and zircon in the slate and in the intrusive rocks, and Cr_2O_3, Ni and Mg contained in chromite and Mg-rich silicates in serpentinites were removed during rodingitization. These components were not redistributed across adjacent calc-silicate-altered serpentinites and Si-rich lithologies. A process that can explain extensive transport of Mg, P_2O_5, Zr, Cr_2O_3, and Ni outside, and Ca inside, the alteration zones is advection of very large amounts of fluid along or across the dyke-serpentinite and metasedimentary county rock-serpentinite contacts. The presence of a blackwall in the slates and absence of nephrite in the adjacent serpentinites suggest that fluid flowed mainly from the serpentinites to the slates during alteration. Increasing Mg solubility and decreasing Si and Ca solubility characterize the process of replacement of serpentinite by nephrite adjacent to felsic dykes. These solubility relationships could be maintained if flow of fluid was focused in the serpentinites parallel to the dykes, and if increasing SiO_2 and Ca concentration and decreasing pH gradients were established toward the dykes and normal to the direction of fluid flow.

INTRODUCTION

Serpentinized ultramafic rocks in a variety of geological settings frequently enclose or are in contact with rodingite, an unusual calc-silicate rock-type of metasomatic origin. These rocks may contain up to 35 wt. % CaO and, most typically, are composed of garnet of the grandite-hydrograndite series together with a large variety of other Ca-rich silicates, including clinopyroxene, vesuvianite, epidote-group minerals, prehnite, and wollastonite. Such serpentinite-hosted calc-silicate rocks in the Dun Mountain ultramafic body, New Zealand, were named rodingite by Bell et al. (1911) after the nearby Roding River.

Since their discovery, rodingites have been observed in many ophiolites (see a collection of papers in Bertrand and Deferne, 1980), in large layered mafic-ultramafic igneous complexes (Anhaeusser, 1979; Dreher et al., 1989), in komatiitic sills and flows (Schandl et al., 1989) and in association with ultramafic samples dredged from the seafloor (Aumento and Loubat, 1971; Honnorez and Kirst, 1975; Bideau et al., 1991). Rodingites are developed in those environments where serpentinized ultramafic rocks are in contact with lithologies richer in Al or Si. In many cases, the alteration is manifested by a bi-metasomatic association, with rodingitization producing Al-rich assemblages in the Al- and Si-rich lithologies, and nephrite (tremolite-actinolite-rich rock) and/or diopsidite (sometimes garnet-bearing; see Wares and Martin, 1980a) in the ultramafic rocks. The rocks forming rodingites represent lithologies as diverse as gabbro (Bell et al., 1911; Bloxam, 1954), anorthosite (Anhaeusser, 1979), lamprophyre (Schandl et al., 1989), basalt (Barriga and Fyfe, 1983), granite (Wares and Martin, 1980a), impure limestone (Coleman, 1966), slate (Katoh and Niida, 1983; Coleman, 1966), and greywacke (Coleman, 1967). Despite this variability in the composition of the protolith, the chemistry of the products of rodingitization (other than those after ultramafic rocks) is remarkably uniform (Coleman, 1967, 1977), and results from similarities in the composition of the secondary mineral assemblages.

The hydrothermal metasomatic origin of rodingites was first proposed by Grange (1927), but the idea was only established firmly in the literature following Coleman's

(1966, 1967) extensive studies of rodingites from the western United States and New Zealand. However, the origin of the calcium is still a matter of considerable debate and opinion is divided over whether it is derived locally from the redistribution of chemical species within the protolith during hydrothermal alteration, or whether it has been introduced from an external source, either the adjacent ultramafic rocks during serpentinization, or a more distant source (see the excellent review in Anhaeusser, 1979). Other outstanding issues, which have been given very little attention in the literature, are the manner in which metasomatic mass transfer occurs during rodingitization, i.e., primarily by infiltration or by diffusion (Plyusnina et al., 1993), and the composition of the fluids (cf. Barnes and O'Neil, 1969; Barnes et al., 1972). The latter issues are important to assess the volumes of fluids and reaction paths involved in this type of alteration.

This paper is the second of a series of five (Chapters IV, V, VI, VII, and VIII) dedicated to the study of serpentinites, slates and dioritic-monzodioritic and granodioritic-granitic rocks, and their hydrothermally altered products, in the JM Asbestos mine, Asbestos, Québec. These rocks were examined during the course of a larger project aimed at determining the distribution of amphiboles in the deposit (Chapter VIII). Here, we provide a detailed account of the distribution and nature of the alteration that overprinted the lithologies listed above. Geochemical mass balance calculations are used to identify the reactions that characterize this alteration. We also use these data to provide an estimate of the net transfer of major elements between serpentinite and felsic intrusive rocks, and between serpentinite and argillaceous country rocks. The data presented in this study help resolve outstanding questions related to rodingitization, notably that of the origin of the calcium.

TECTONIC SETTING AND METAMORPHISM

The JM Asbestos mine is located in the Asbestos ophiolite complex (Hébert, 1980), which forms one of many ophiolite slivers distributed along a thrust zone, the Baie

Verte-Brompton line (Williams and St-Julien, 1982), that marks the transition between units deposited along the margin of the Laurentian craton, and units formed and deposited in an oceanic basin. According to Hébert and Bédard (1998), the Asbestos ophiolite formed in a fore-arc environment above a SE-dipping subduction zone during the Ordovician, about 472 Ma (U/Pb crystallization age of zircon from a trondhjemite). These authors also proposed that the Asbestos ophiolite was emplaced onto the Laurentian continental margin at 460 Ma based on a U/Pb determination for baddeleyite, which replaced zircon in the trondhjemite. Most authors agree that the ophiolites located between Thetford Mines and Asbestos were detached from their seafloor roots, when still relatively hot (Pinet and Tremblay 1995a, Whitehead et al., 2000), and transported to the NW onto the Laurentian continental margin in the form of large sheets, in a manner similar to that proposed for the Oman ophiolites (Pinet and Tremblay, 1995b), thereby escaping burial in a subduction trench. The age difference between the amphibolite (477 Ma; Whitehead et al., 1996) at the base of the Thetford Mines ophiolite (30 km NW of the Asbestos ophiolite along the same structural zone), which records the approximate time at which it was detached from the seafloor, and the oceanic plagiogranites (~480 Ma; Hébert and Bédard, 1998; Whitehead et al., 2000) related to the build-up of the ophiolite, support this hypothesis.

Deformation and metamorphism of the sedimentary units on the edge of the Laurentian craton during the Taconic orogeny lasted for at least 50 Ma, based on $^{40}Ar/^{39}Ar$ cooling ages on muscovite from metagreywackes of the Caldwell Group, which identify two episodes of deformation, the first around 470-460 Ma, and the second about 430-420 Ma (Castonguay et al., 1997). It appears, from the crystallization and metamorphic ages of 472 and 460 Ma, respectively (trondhjemite; Hébert and Bédard,1998), that the Asbestos ophiolite was unrooted from its seafloor setting early in the first episode of deformation, which affected the Caldwell Group, but was emplaced on the Laurentian craton only at the end of this deformation episode. Dioritic and granitic dykes intruded the upper mantle ultramafic rocks of the ophiolite during obduction and after the peridotites were substantially serpentinized, but before thrusting over the Caldwell Group metasediments (Chapter IV).

The only available quantitative estimates of conditions during metamorphism of the Asbestos ophiolite are given by Whitehead et al. (1996). They suggested that the amphibolite at the base of the ophiolite was metamorphosed at temperatures of 300-340°C during the Acadian orogeny at ~ 377 Ma.

THE JM ASBESTOS DEPOSIT

General features

The JM Asbestos deposit is located in the basal peridotites of the Asbestos ophiolite. Mining to extract chrysotile asbestos fiber started in 1881. The open pit operations exposed a section in which the base of the ophiolite is in fault contact with Cambrian continental margin argillaceous metasediments of the Caldwell Group to the NW, and serpentinized harzburgites overlain by a dunite-pyroxenite unit to the SE (Figure 1). Chrysotile ore is hosted by the serpentinized harzburgites.

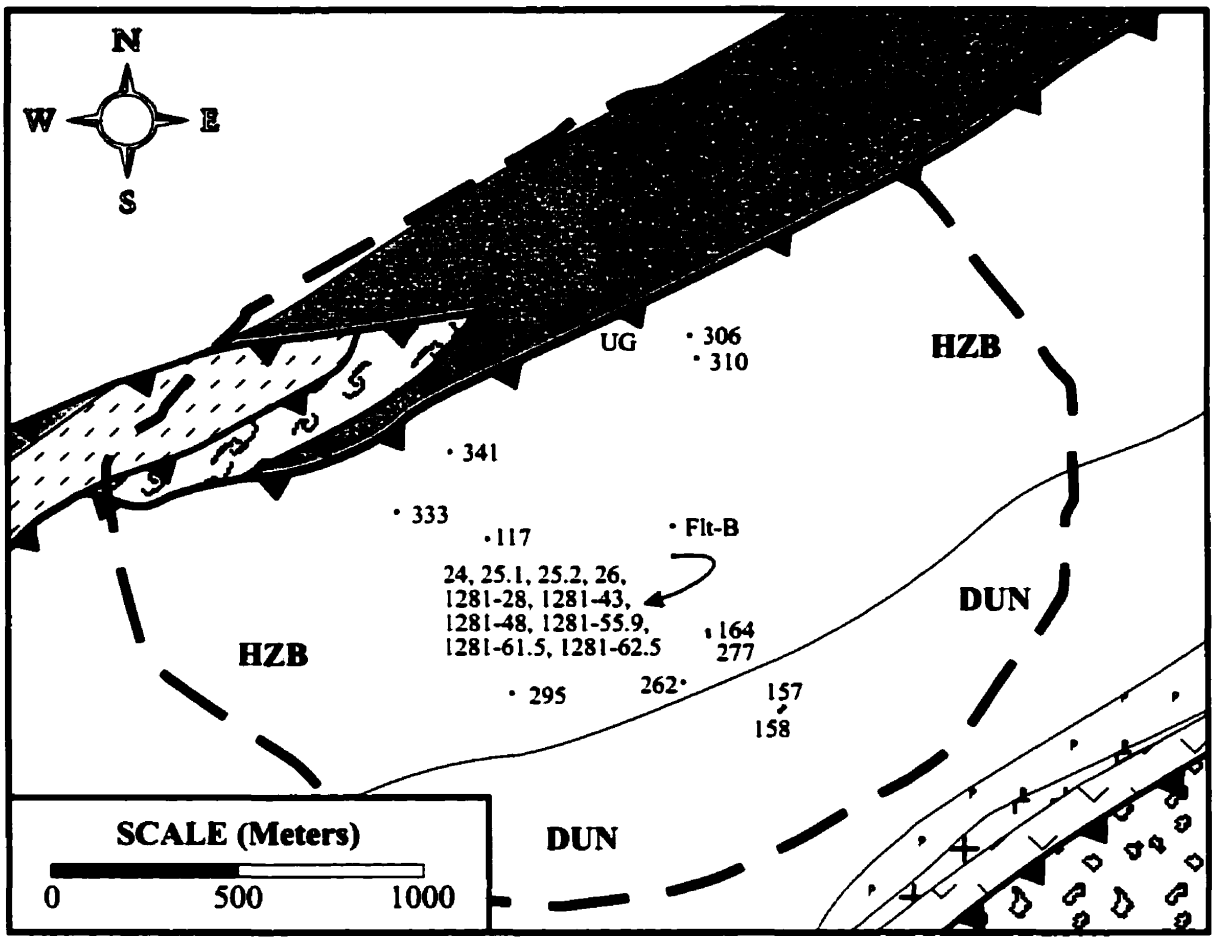
The ore zones form five tabular bodies oriented parallel to the regional structures. They are separated from each other by shear zones and sheet- and lens-like bodies of dioritic-monzodioritic and granitic intrusive rocks (Chapter IV), which display variable degrees of alteration to feldspar-pyribole assemblages and to rodingite. The contacts between the felsic intrusive rocks and the serpentinites are, for the most part, sheared, and consequently the original intrusive contact is rarely preserved. The felsic intrusive rocks are more abundant near the transition between the harzburgites and the dunite-pyroxenite unit.

Hydrothermal alteration

The harzburgites and dunites are now almost completely serpentinized. Relicts of pyroxene are uncommon and fresh olivine was observed very rarely in harzburgite. Only the pyroxenites retain substantial relicts of their primary mineralogy. Three basic types of serpentinite were identified in the harzburgite. In hand samples, the first type is

Figure 1

Geological map of the JM Asbestos chrysotile mine (modified after Hébert, 1980). The locations of the samples studied in this chapter are indicated on the map.



LEGEND

Saint-Daniel Formation

Melange

Caldwell Group

Metagraywacke

Slate

Amphibolite

Ophiolitic Complex

Serpentinite

HZB — Harzburgite

DUN — Dunite

Pyroxenite

Gabbro

Pillowed and brecciated tholeiites

characterized by dark green, massive, serpentinized harzburgite with characteristic bastite pyroxene pseudomorphs, in some cases mantled or completely replaced by magnetite. This type of rock is the host for the bulk of the chrysotile ore. In thin section, these serpentinites show pseudomorphic mesh-rim and hourglass textures and, locally, extensive recrystallization (Wicks and Whittaker, 1977; O'Hanley and Dyar, 1993). Examination of 260 samples by X-ray diffraction and 12 samples by scanning electron microscopy indicate that brucite is rare in these rocks, and that lizardite is the most abundant serpentine phase. Chromite grains are commonly replaced partially by magnetite. Awaruite (Ni_3Fe) is present in small amounts in most samples examined. The second type of serpentinite comprises chrysotile ± brucite cross and slip-fiber veins which display a marginal, dark green, massive and translucent halo grading to a more distal buff-coloured, brucite-rich zone. These veins cut the previous serpentinite type. In the third variety of serpentinite, woven and mottled-textured types occur as envelopes around shear-zones, which are also cut by chrysotile veins but less so than in massive harzburgite. The concentration of brucite in the serpentinites is proportional to the extent of shearing. This mineral is most abundant in highly fissile shear zones. Antigorite is abundant in the shear zones that enclose the dyke- and lens-like intrusive rocks, but is never seen with brucite. Adjacent to the dykes, halos of massive nephrite and/or diopsidite measuring up to two meters thick, cut by fibrous tremolite and/or diopside veins, have formed locally at the expense of the serpentinite. The absence of brucite with antigorite suggests that the latter mineral did not form simply by the thermal breakdown of lizardite via a reaction such as:

$$17\text{Lizardite} = \text{Antigorite} + 3\text{Brucite} \qquad (1),$$

but that addition of silica or removal of Mg or both accompanied alteration according to reactions like:

$$16\text{Lizardite} + 2SiO_2^{\circ} = \text{Antigorite} + H_2O \qquad (2)$$

and

$$17\text{Lizardite} + 6H^{+} = \text{Antigorite} + 3(Mg,Fe)^{+2} + 6H_2O \quad (3).$$

The proximity of silica-rich rocks and the relatively high pH of (SO_4^{2-}-CO_3^{2-}-poor) fluids equilibrated with serpentine-bearing assemblages at elevated temperatures (e.g., Pfeifer, 1977; Janecky and Seyfried, 1986), however, would favour reaction 2. Examination of a late "picrolite"-filled shear-vein by transmission electron microscopy showed that it is composed of polygonal serpentine (Vali, personal communication, 1995). Elsewhere along the orogen, unserpentinized harzburgites occur locally, whereas the dunites are invariably close to 100 % serpentinized.

As discussed above, the ultramafic rocks were subjected to two major episodes of serpentinization. The first was dominated by the formation of lizardite and the second by the formation of chrysotile veins, the local recrystallization of lizardite and the formation of antigorite and other Si-rich magnesium silicates near the contacts of serpentinite with slate (talc) and felsic igneous rocks (talc, tremolite, diopside, and anthophyllite-cummingtonite). The latter two rock-types also display various degrees of alteration near their contacts with serpentinite. Both developed albite, actinolite and fine-grained secondary biotite at an early stage, and were subsequently rodingitized.

The hornblende-bearing dioritic rocks described by De (1972) contain more CaO and less K_2O and Na_2O than the biotite-rich diorites from Asbestos. This relationship was first noted by De (1961), who suggested that replacement of hornblende by biotite or direct crystallization of biotite instead of hornblende favoured enrichment of late magmatic fluids in calcium, and that this induced rodingitization. However, the hornblende-rich diorite from Vimy Ridge (De, 1972) is significantly more enriched in FeO and MgO and depleted in Al_2O_3 than the dioritic-monzodioritic rocks from Asbestos suggesting, instead, that it crystallized from a more mafic melt than did the dioritic-monzodioritic rocks. Alternatively, these hornblende-bearing dioritic rocks may represent a more primitive product of crystallization of a magma, which initially had a composition similar to that from which the Asbestos diorites-monzodiorites crystallized. A detailed

mineralogical and chemical description of selected suites of rodingitized samples and their protoliths is given in the paragraphs that follow.

A blackwall is usually present at the contact between the serpentinites and the dykes and slates, except where the serpentinites form xenoliths totally enclosed in the igneous rocks and, in many cases, where thick halos of massive nephrite or diopsidite have formed at the contact with the felsic intrusive rocks. The blackwall is developed exclusively in the aluminous rocks and displays a sharp planar contact against the foliated biotite-rich diorites and the slates, except where veins cut across the blackwall and the diorite, in which case it swells in the direction of the vein. In some cases, the vein is filled with chlorite in the blackwall and with diopside in the adjacent diorite. In the intrusive rocks containing very coarse feldspar, the chloritization front is irregular and contains relicts of the feldspar. The blackwall was one of the latest types of alteration to form. In one example involving a dioritic precursor, a sharp chlorite front overlapped fractures that had previously displaced grossular-rich layers, as well as rodingite layers. In another example, pseudomorphous chlorite replaced grossular from the rodingitized margin of the dyke which, initially, had extended to the contact with the serpentinite.

Most, but not all, blackwall is located along sheared contacts. In many cases, blackwall is related to the vein-chrysotile stage of serpentinization. The sequence of events leading to dismemberment of the felsic intrusive sheets is as follows. During the initial stages, fractures formed perpendicular to the contact of the intrusive with the serpentinite. The fracture filling is rich in diopside near the center of the sheet and is chlorite-rich at the margins. The blackwall developed initially only at the contact and then progressed along the walls of the fractures. Later, the blackwall lined the margins of fractures across the entire width of the dyke and a cross-fiber chrysotile vein formed in the center of the fractures. Finally, the intrusive sheet split along the fractures, and sheared serpentinite was mechanically emplaced between the two separated tapered segments of intrusive, which were then completely rimmed by blackwall.

The replacement of such chemically complex rocks as diorites by essentially one mineral, chlorite, can be explained if large amounts of serpentinite-buffered fluids are permitted to flow in a dense localized network of interconnecting microfractures in the

dyke rocks near and parallel to the contact with serpentinites (Barnes et al., 1972; Halter et al., 1998), and may be viewed as an extreme example of a metasomatic side (Yardley and Lloyd, 1995) combining a strong component of hydrodynamic chemical dispersion (Steefel and Lasaga, 1992). Indeed, phase equilibrium calculations using the program PTA, version 2.0 (GEO-CALC software package: Berman et al., 1987; Brown et al., 1987, 1988), and the SUPCRT92 software package (Johnson et al., 1992), indicate that, in a fluid-buffered system where the fluid pH, activity of SiO_2 and Ca^{2+}/Mg^{2+} ratio are controlled by serpentine-bearing assemblages in the system Ca-Mg-Si-O-H, addition of Al only permits the stabilization of chlorite below 400°C.

RODINGITE MINERALOGY

In this section, we discuss the mineralogical changes which accompanied rodingitization of slate, serpentinite, and monzodioritic and granitic rocks. The rodingites form pervasive replacement bodies or veins, and are especially abundant in a strongly sheared zone that marks the transition between the harzburgites and the dunite-pyroxenite unit. The occurrence of highly porous varieties of rodingite, composed predominantly of either light-coloured grossular or green and purple vesuvianite (locally >> 90 vol. %), is limited to this zone.

Where diorite-monzodiorite has been replaced pervasively by rodingite, the protolith has been transformed partially or totally to an assemblage composed of grossular + diopside + chlorite, grossular + diopside, grossular + diopside + zoisite (clinozoisite), or grossular + diopside + zoisite (clinozoisite) + prehnite. Veins comprising similar mineral assemblages cut the rodingites and frequently extend into diorite, which has not been pervasively altered. Dark brown vesuvianite was observed only in a lens of rodingitized dioritic rock, where it forms veins with chlorite. Later pectolite- or wollastonite-rich veins are locally abundant.

Feldspar- and pyribole-rich mineral associations are the most frequent products of alteration associated with the granitic rocks. Granitic protoliths were less extensively

altered to garnet-rich mineral assemblages compared to the dioritic-monzodioritic rocks, in which garnet-rich rodingites are common. Where present in altered granitic rocks, garnet-rich mineral assemblages frequently include vesuvianite and, locally, wollastonite. Other secondary minerals locally present are margarite-rich mica, corundum and phengite, formed by replacement of large andalusite crystals in granitic pegmatites.

The textural relationships and chemical compositions of minerals were analysed by means of optical microscopy, scanning electron microscopy (SEM) and electron microprobe analyses (EPMA: Appendix II). Chemical analyses and images were obtained using a Joel Superprobe JXA-8900L WD/ED combined microanalyzer operated at 15 kV and 20 or 30 (for garnet analyses) nA using a 5 μm probe diameter and ZAF correction. The following standards were used: albite for Na, orthoclase for K, diopside for Ca, diopside for Mg (pyrope was used for garnet analyses), spessartine for Mn, andradite for Fe, chromite for Cr, orthoclase for Al (pyrope was used for garnet analyses), TiO_2 for Ti, diopside for Si (andradite was used for garnet analyses), fluorite for F and vanadinite for Cl.

The structural formula of pyroxene was calculated on the basis of 6 oxygens and 4 cations using the method of Droop (1987) for estimating of Fe^{+3}, that of zoisite-clinozoisite on the basis of 12.5 oxygens assuming all Fe is present as Fe^{+3}, and that of prehnite on the basis of 11 oxygens, assuming all Fe is present as Fe^{+3}. Two samples of the coarse-grained, orange grossular from rodingitized diorite were analysed by X-ray fluorescence spectrometry (Flt-H, Flt-I: Table 1). The values for loss on ignition (0.14, 0.11 wt. %) indicate that these garnets contain only minor quantities of water. Wet chemical analyses indicate that the garnets have $Fe^{2+}/(Fe^{2+}+Fe^{3+})$ ratios of 0.74 and 0.57, respectively. For garnet analysed with the electron microprobe, the structural formula was calculated on the basis of 12 oxygens. Part of the FeO was assigned as Fe_2O_3 in order to fill the Y site, and the totals were adjusted to 100 by adding water. The relationship between H and ΣCations (less H) resulting from these calculations indicates that H replaced Si in the structure of the garnet according to the substitution $Si^{4+} \leftrightarrow 4H^{+}$ (slope = 0.27: the slope is ~ 0.25 if all the Fe as Fe^{2+} or Fe^{3+}). The structural formula of

Table 1. X-ray fluorescence analyses of orange garnet from rodingitized diorites.

	Flt-H	Flt-I
Wt. %		
SiO_2	38.99	39.31
TiO_2	0.49	0.14
Al_2O_3	22.27	22.52
Fe_2O_3	0.50	0.93
FeO*	1.29	1.13
MnO	0.59	0.35
MgO	0.06	0.30
CaO	35.71	35.09
Na_2O	< d.l.	< d.l.
K_2O	0.040	0.190
P_2O_5	0.011	0.049
BaO	0.016	0.008
Ce	0.005	0.003
Cr_2O_3	< d.l.	0.002
Ni	< d.l.	< d.l.
L.O.I.	0.14	0.11
Total	100.11	100.13
Cations		
Si	2.94	2.96
Ti	0.03	0.01
Al	1.98	2.00
Cr	0.00	0.00
Fe^{3+}	0.03	0.05
Fe^{2+}	0.08	0.07
Mn	0.04	0.02
Mg	0.01	0.03
Ca	2.89	2.83
H	0.07	0.06

*FeO determined using ammonium metavanadate titration
< d.l.: below detection limit, L.O.I.: loss on ignition,
H calculated assuming L.O.I. = H2O

vesuvianite was calculated on the basis of 50 cations (Groat et al., 1992) and that of tremolite-actinolite was calculated based on 23 oxygens. Fe was assumed to be present as FeO in both minerals.

Rodingitized slate

A five meters zone of strongly sheared, locally talc-rich, serpentinites marks the thrust contact between the ophiolite and slates of the Caldwell Group. From their contact with serpentinite, the slates display a succession of metasomatic zones, beginning with a 2-10 cm wide blackwall, followed by a 10-60 cm thick zone of light grey rodingitized slate and an outer envelope of dark grey albite>>biotite-actinolite-rock measuring up to 2 meters thick.

Fracturing exercised a very strong control on the extent and distribution of rodingite. Where the density and width of veins are greatest, the rodingitization halo is thickest. In one location, extensive development of subhorizontal veins resulted in the formation of tongues of rodingite extending up to 1.5 meters into the slates. In most cases, however, the rodingite-vein association is restricted to the first 60 cm from the contact.

A series of four samples from an access ramp to the underground workings exemplify the rodingitization of slate and comprise; rodingite from the contact with the blackwall (UG-C: Figure 2), rodingite taken 60 cm from the contact with the blackwall at the transition between rodingite and albitized slate (UG-2), an albite-biotite-actinolite-rock taken two meters from the contact (UG-7) and an unaltered sample of slate taken three meters from the contact (UG-10). The fresh slate is composed of albite (25 vol. %), quartz (22 vol. %), muscovite (17 vol. %), calcite (12 vol. %), biotite (12 vol. %), chlorite (6 vol. %), carbon-rich matter (graphite ?; 4 vol. %), titanite (1 vol. %), pyrite (1 vol. %), and apatite (< 1 vol. %). The matrix of the slate is composed of albite, biotite, muscovite, chlorite, titanite, and quartz, whereas silty laminations comprise calcite, quartz, pyrite, and muscovite. Two meters from the contact, the slate is indurated and takes on a flinty appearance. In thin section, the matrix has been replaced extensively by fined-grained

Figure 2

Section through a sample of partially rodingitized slate. The original sedimentary layering is well preserved and continues uninterrupted from albitized slate (AS) through rodingitized slate (RS), suggesting that volume did not change as a result of calcium metasomatism.


AS
RS

albite and biotite, and radially developed fibrous aggregates of actinolite. By contrast, the silty horizons were replaced by actinolite, biotite and minor K-feldspar. No carbonates remain and only traces of quartz and pyrite are left. Traces of apatite were also noted. The relative proportion of minerals in the bulk rock is 58 vol. % albite, 18 vol. % biotite, 17 vol. % actinolite, 3 vol. % K-feldspar, and small amounts of muscovite. Undeformed veins cutting the foliation at right angle are composed of actinolite, K-feldspar and albite. A texturally and compositionally similar type of rock, formed by metasomatism of argillites, was described by Reed (1959) in the Nelson ultramafic belt of New Zealand. In the rodingite sample taken 60 cm from the contact, the matrix of the slate is replaced by prehnite, grossular and diopside (relative volumetric proportions ~ 1:0.5:0.5), while the silty laminations are replaced by diopside and turbid, brown K-feldspar. Prehnite encloses euhedral crystals of diopside and grossular. Traces of allanite, zircon and a Co-Ni arsenide are present, as well as relicts of albite from the previous zone. Rodingite from the contact provides evidence of two generations of replacement and vein development. The first generation is characterized by the association zoisite + grossular + diopside with traces of allanite, titanite and albite, whereas the second generation is represented by the association grossular + diopside + prehnite with minor amounts of K-feldspar. Compositionally, the prehnite is very close to that of its end-member (Table 2). Zoisite shows only limited solid solution with epidote (0.25 to 0.5 a.p.f.u. Fe^{3+}). Similarly, the garnet is restricted to grossular-rich compositions (Table 2). The total Fe concentration in the garnet from the pervasively rodingitized slate near the contact with serpentinite (UG-C) ranges from 0.05 to 0.10 atoms per formula unit (a.p.f.u.) and the H concentration between 0.2 and 1.2 atoms per formula unit. The garnet in veins cutting this rodingite contains between 0.06 and 0.10 a.p.f.u. Fe, and, as indicated by calculations based on the electron microprobe analyses, contains much less water (between 0 and 0.2 a.p.f.u. H) than pervasively distributed garnet (Table 2). The Fe concentrations in garnet from the pervasively rodingitized slate at 60 cm from the contact with serpentinite (UG-2) are, in general, more uniform, but vary between 0.03 and 0.08 a.p.f.u. (Table 3). This garnet is also water-rich (between 0.25 and 0.73 a.p.f.u. H). Manganese concentrations are

Table 2. Electron microprobe analyses of rodingite minerals from sample UG-C.

	Zoisite		Prehnite				Diopside				Grossular			
	Rock		Rock		Vein		Rock		Vein		Rock		Vein	
	(N=29)*	± 1 σ	(N=14)	± 1 σ	(N=20)	± 1 σ	(N=44)	± 1 σ	(N=39)	± 1 σ	(N=12)	± 1 σ	(N=11)	± 1 σ
Wt. %														
SiO_2	38.43	0.22	43.00	0.25	43.35	0.16	51.13	0.61	50.82	0.32	37.81	0.49	38.76	0.23
TiO_2	0.05	0.04	0.01	0.01	0.01	0.01	0.06	0.32	0.00	0.01	0.36	0.36	0.01	0.01
Al_2O_3	28.80	0.79	24.15	0.16	23.62	0.10	0.51	0.33	0.21	0.19	21.53	0.30	21.88	0.22
Cr_2O_3	0.04	0.05	0.00	0.01	0.01	0.01	0.01	0.04	0.01	0.01	0.01	0.01	0.00	0.01
FeO	5.31	0.93	0.13	0.05	0.25	0.09	14.65	2.03	16.85	1.20	1.13	0.20	1.17	0.23
MnO	0.17	0.16	0.02	0.01	0.02	0.02	1.51	0.65	1.82	0.67	0.21	0.05	0.33	0.14
MgO	0.04	0.03	0.00	0.00	0.00	0.01	8.34	1.51	6.92	0.82	0.00	0.00	0.00	0.00
CaO	23.96	0.31	27.40	0.11	27.11	0.21	24.23	0.23	24.23	0.18	37.74	0.16	37.72	0.24
Na_2O	0.02	0.04	0.01	0.01	0.05	0.03	0.21	0.13	0.02	0.01	0.01	0.01	0.00	0.01
K_2O	0.05	0.03	0.02	0.01	0.04	0.04	0.03	0.02	0.12	0.11	0.01	0.03	0.00	0.00
Total	96.87	0.46	94.73	0.33	94.46	0.19	100.69	0.34	101.01	0.29	98.81	0.53	99.88	0.30
Cations (refer to text for method of calculation)														
Si	2.99	0.01	2.99	0.01	3.02	0.01	1.96	0.01	1.97	0.01	2.84	0.05	2.93	0.02
Ti	0.00	0.00	0.00	0.00	0.00	0.00	0.00	0.01	0.00	0.00	0.02	0.02	0.00	0.00
Al	2.64	0.07	1.98	0.01	1.94	0.01	0.02	0.01	0.01	0.01	1.91	0.03	1.95	0.02
Cr	0.00	0.00	0.00	0.00	0.00	0.00	0.00	0.00	0.00	0.00	0.00	0.00	0.00	0.00
Fe^{3+}	0.35	0.06	0.01	0.00	0.01	0.01	0.06	0.02	0.06	0.01	0.07	0.01	0.05	0.02
Fe^{2+}	—	—	—	—	—	—	0.41	0.07	0.48	0.05	0.01	0.01	0.02	0.01
Mn^{2+}	0.01	0.01	0.00	0.00	0.00	0.00	0.05	0.02	0.06	0.02	0.01	0.00	0.02	0.01
Mg	0.00	0.00	—	—	—	—	0.48	0.08	0.40	0.04	0.00	0.00	0.00	0.00
Ca	2.00	0.02	2.04	0.01	2.02	0.02	1.00	0.01	1.01	0.01	3.04	0.02	3.06	0.02
Na	0.00	0.01	0.00	0.00	0.01	0.00	0.02	0.01	0.01	0.01	0.00	0.00	0.00	0.00
K	0.00	0.00	0.00	0.00	0.00	0.00	0.00	0.00	0.00	0.00	0.00	0.00	0.00	0.00
H	—	—	—	—	—	—	—	—	—	—	0.53	0.26	0.07	0.08

Table 3. Electron microprobe analyses of rodingite minerals from sample UG-2.

	Diopside		Prehnite		Grossular	
	(N=16)	± 1 σ	(N=11)	± 1 σ	(N=11)	± 1 σ
Wt. %						
SiO_2	52.39	0.23	42.73	0.18	37.95	0.37
TiO_2	0.01	0.01	0.16	0.17	0.80	0.16
Al_2O_3	0.49	0.14	24.13	0.14	21.70	0.09
Cr_2O_3	0.01	0.02	0.01	0.01	0.01	0.01
FeO	10.24	0.69	0.07	0.02	0.65	0.23
MnO	0.31	0.07	0.01	0.01	0.10	0.03
MgO	11.80	0.49	0.01	0.01	0.00	0.00
CaO	24.24	0.20	26.78	0.13	37.99	0.24
Na_2O	0.26	0.06	0.01	0.02	0.00	0.01
K_2O	0.03	0.01	0.03	0.02	0.02	0.04
Total	99.77	0.33	93.95	0.42	99.22	0.34
Cations (refer to text for method of calculation)						
Si	1.98	0.00	2.99	0.01	2.86	0.03
Ti	0.00	0.00	0.01	0.01	0.05	0.01
Al	0.02	0.01	1.99	0.01	1.93	0.01
Cr	0.00	0.00	0.00	0.00	0.00	0.00
Fe^{3+}	0.04	0.01	0.00	0.00	0.03	0.01
Fe^{2+}	0.28	0.02	0.00	0.00	0.01	0.01
Mn^{2+}	0.01	0.00	0.00	0.00	0.01	0.00
Mg	0.66	0.03	0.00	0.00	0.00	0.00
Ca	0.98	0.01	2.01	0.01	3.06	0.02
Na	0.02	0.00	0.00	0.00	0.00	0.00
K	0.00	0.00	0.00	0.00	0.00	0.00
H	—	—	—	—	0.37	0.17

generally low (0.004 to 0.022 a.p.f.u.) in garnet from massive rodingite and highest in garnet from veins cutting this rodingite (up to 0.04 a.p.f.u.). Titanium was retained in garnet replacing the host rock (up to 0.06 a.p.f.u.); the Ti-content of garnet is invariably below 0.002 a.p.f.u. in veins. Cr and Mg are present in very low concentrations in the garnet. Diopside from both veins and host rock displays spectacular oscillatory zoning (Figure 3), which mainly reflects variations in the relative concentrations of Fe and Mg. The number of Fe atoms per formula unit in the diopside varies from 0.27 to 0.63. The oscillatory zoning in diopside is most extensively developed in the rodingites immediately adjacent to the serpentinites, and in the veins. The data presented above contrast with those for minerals in skarns where garnet and epidote are generally richer in iron. These differences could be explained by more reducing conditions and lower iron concentrations in the fluids during the formation of rodingite.

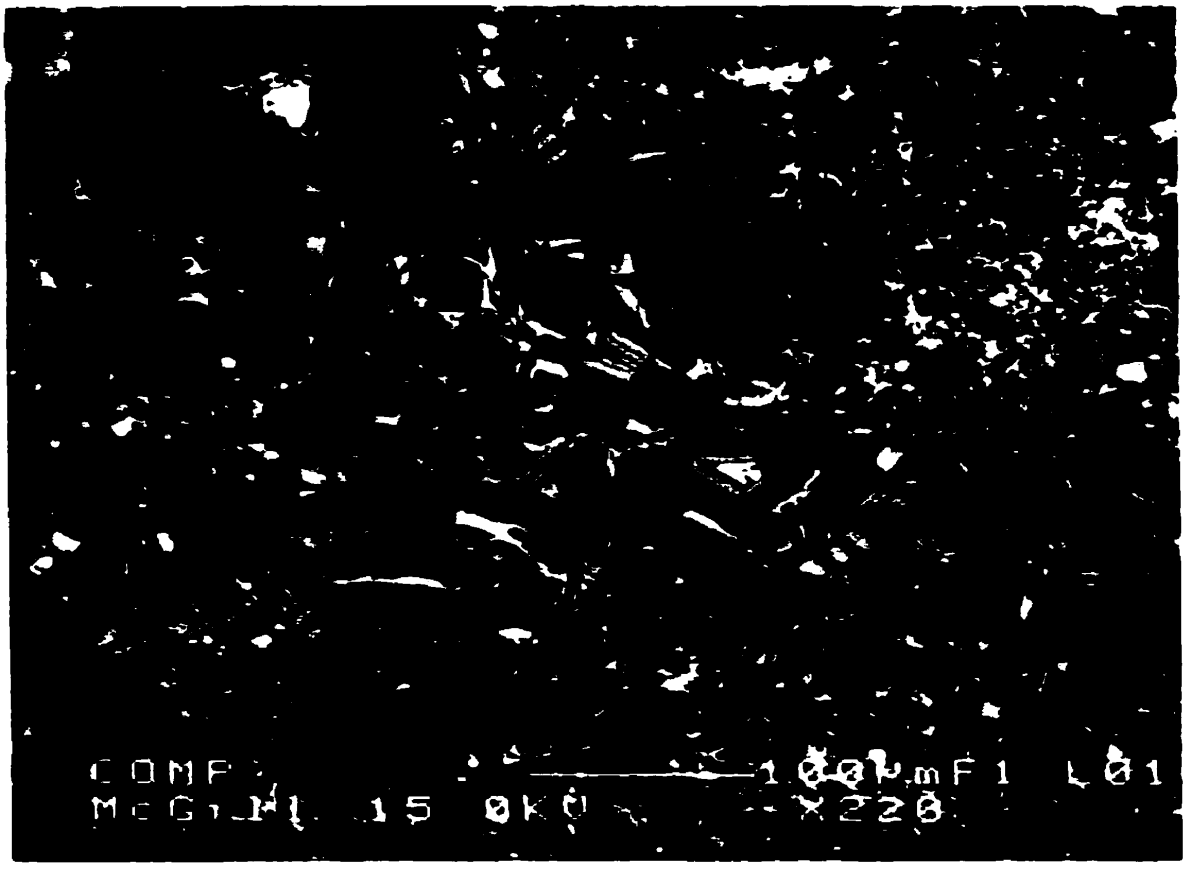
Rodingitized dioritic rocks

The diorite-monzodiorite dykes form coarse-grained rocks composed primarily of plagioclase and Ti-rich biotite. Some of the dykes, particularly the diorites, contain substantial proportions of an unknown phenocryst phase, which has been pseudomorphed by secondary micas. The monzodiorites are characterized by larger proportions of K-feldspar and lesser proportions of biotite (see Chapter IV for more details on the mineralogy and chemistry of these rocks). As in the slates, two stages of alteration have affected the dioritic-monzodioritic rocks. No completely fresh equivalent of the dioritic-monzodioritic series of rocks occurs in the JM Asbestos deposit. During the first stage of alteration, the original igneous plagioclase (andesine) was replaced by low-Ca plagioclase, muscovite and low-Fe zoisite-clinozoisite, and the unknown phenocryst-forming phase by a fine-grained mixture of low-Ti biotite and phengitic mica. Near-end-member albite, K-feldspar and minor tremolite-actinolite formed late.

The second stage of alteration was characterized by intense Ca metasomatism, forming rodingites. In the field, the rodingites, which formed from the pervasive replacement of dioritic-monzodioritic dykes, are distinguished by a uniform light, orange-

Figure 3

Backscatter SEM image of diopside showing well-developed oscillatory zoning. The sample was collected from rodingitized slate near the contact with serpentinite. Dark areas represent Mg-rich zones and light areas represent Fe-rich zones.


COMP
100µmF1 L01
15 0KV X220

pink, colour. The pervasive rodingitization can be seen to have developed from the margins of the dykes. Where dioritic-monzodioritic rocks are preserved in the cores of dykes, in all cases there is a transition from partially altered diorite to completely altered diorite at the dyke margins, which is marked by the disappearance of the primary Ti-rich biotite; this mineral was the last mineral to undergo alteration. The replacement was pseudomorphic in the early stages, and, with intensification of alteration, the minerals were recrystallized or replaced by other assemblages of minerals such that the initial texture of the rock was, in many cases, lost. Assemblages and paragenetic sequences similar to those in the host rock occur in veins, which commonly cut across the full width of a dyke. The veins usually measure from two to three cm in width, but in rare cases can reach up to eight cm wide. Most veins consist of a clinopyroxene-rich margin and an orange garnet- or prehnite-rich core. Prehnite is usually the latest mineral to have formed. In one case, however, a light pink variety of grossular had formed later and replaced prehnite in the center of a vein.

Three types of mineral assemblage were observed. The first, composed of grossular and clinopyroxene with small or negligible proportions of chlorite, is common in the narrower, completely rodingitized dykes. The second and third types are distinguished by the presence or absence of prehnite in the assemblage garnet + zoisite + clinopyroxene. Detailed electron microprobe (EDS and WDS) analysis, and textural examinations by SEM were conducted on three rodingitized samples from three different dykes containing the garnet + clinopyroxene + chlorite association (samples Flt-B, JMH-306 and JMH-295.1: Table 4), on a series of four samples from a single dyke representing weak, advanced and almost complete rodingitization (samples H1281-62.5, JMH-26, JMH-25.1 and JMH-25.2: Table 5), and on a vein sample (JMH-24: Table 5).

With the exception of a few relict Ti-rich biotite crystals, nothing remains of the primary mineralogy in the three samples representing the garnet-clinopyroxene-chlorite association. Clinopyroxene and garnet are the dominant minerals. Chlorite is present in very subordinate proportions and formed last, filling pockets and veinlets. The pocket-filling chlorite locally replaced euhedral diopside. This pseudomorphic chlorite is rich in

Table 4. Electron microprobe analyses of minerals belonging to the grossular + diopside + chlorite parageneses of rodingitized diorites.

Mineral	Grossular					
Sample	Flt-B		JMH-295.1		JMH-306	
Comments						
	(N=6)	± 1 σ	(N=6)	± 1 σ	(N=14)	± 1 σ
Wt. %						
SiO_2	38.96	0.05	39.11	0.31	39.24	0.22
TiO_2	0.73	0.04	0.44	0.29	0.34	0.32
Al_2O_3	21.74	0.14	21.78	0.21	21.94	0.27
Cr_2O_3	0.00	0.00	0.01	0.01	0.00	0.00
FeO	2.00	0.28	2.00	0.10	0.59	0.05
MnO	0.98	0.07	0.45	0.11	0.84	0.10
MgO	0.01	0.01	0.02	0.01	0.00	0.00
CaO	35.81	0.31	36.32	0.09	37.25	0.16
Na_2O	0.00	0.01	0.00	0.00	0.00	0.00
K_2O	0.00	0.00	0.00	0.00	0.00	0.01
F	—	—	—	—	—	—
Cl	—	—	—	—	—	—
Total	—	—	—	—	—	—
—O≡F,Cl	—	—	—	—	—	—
Total	100.25	0.18	100.12	0.20	100.20	0.26
Cations (refer to text for method of calculation)						
Si	2.95	0.01	2.96	0.01	2.96	0.01
Ti	0.04	0.00	0.03	0.02	0.02	0.02
Al	1.94	0.01	1.94	0.01	1.95	0.02
Cr	0.00	0.00	0.00	0.00	0.00	0.00
Fe^{3+}	0.02	0.01	0.03	0.01	0.03	0.01
Fe^{2+}	0.11	0.02	0.09	0.01	0.01	0.01
Mn^{2+}	0.06	0.00	0.03	0.01	0.05	0.01
Mg	0.00	0.00	0.00	0.00	0.00	0.00
Ca	2.91	0.02	2.94	0.01	3.01	0.01
Na	0.00	0.00	0.00	0.00	0.00	0.00
K	0.00	0.00	0.00	0.00	0.00	0.00
F	—	—	—	—	—	—
Cl	—	—	—	—	—	—
H	0.00	0.00	0.00	0.00	0.01	0.03

*Ps Di: Chlorite pseudomorphs after diopside

Table 4. (Continued)

Mineral	Diopside					
Sample	Flt-B		JMH-295.1		JMH-306	
Comments						
	(N=31)	± 1 σ	(N=10)	± 1 σ	(N=31)	± 1 σ
Wt. %						
SiO_2	51.86	0.45	50.72	0.39	50.70	0.64
TiO_2	0.14	0.50	0.00	0.00	0.55	1.11
Al_2O_3	0.47	0.31	0.12	0.11	0.38	0.33
Cr_2O_3	0.01	0.01	0.00	0.01	0.00	0.01
FeO	10.25	1.81	14.27	2.17	12.79	0.85
MnO	0.36	0.08	0.47	0.50	3.41	1.43
MgO	11.99	1.08	9.59	1.40	7.97	1.08
CaO	24.46	0.32	24.12	0.30	23.99	0.24
Na_2O	0.25	0.18	0.07	0.06	0.18	0.14
K_2O	0.03	0.02	0.02	0.01	0.02	0.01
F	—	—	—	—	—	—
Cl	—	—	—	—	—	—
Total	—	—	—	—	—	—
—O≡F,Cl	—	—	—	—	—	—
Total	99.81	0.45	99.37	0.44	99.99	0.37
Cations (refer to text for method of calculation)						
Si	1.96	0.01	1.96	0.01	1.97	0.02
Ti	0.00	0.01	0.00	0.00	0.02	0.03
Al	0.02	0.01	0.01	0.01	0.02	0.02
Cr	0.00	0.00	0.00	0.00	0.00	0.00
Fe^{3+}	0.08	0.02	0.08	0.01	0.04	0.02
Fe^{2+}	0.25	0.06	0.38	0.08	0.38	0.03
Mn^{2+}	0.01	0.00	0.02	0.02	0.11	0.05
Mg	0.67	0.06	0.55	0.08	0.46	0.06
Ca	0.99	0.01	1.00	0.01	1.00	0.01
Na	0.02	0.01	0.01	0.00	0.01	0.01
K	0.00	0.00	0.00	0.00	0.00	0.00
F	—	—	—	—	—	—
Cl	—	—	—	—	—	—
H	—	—	—	—	—	—

*Ps Di: Chlorite pseudomorphs after diopside

Table 4. (Continued)

Mineral	Chlorite							
Sample	Flt-B				JMH-295.1		JMH-306	
Comments	Pockets		Ps Di*		Veinlets		Pockets	
	(N=45)	± 1 σ	(N=13)	± 1 σ	(N=14)	± 1 σ	(N=10)	± 1 σ
Wt. %								
SiO_2	27.39	1.66	33.07	1.85	30.61	2.45	39.45	1.19
TiO_2	0.00	0.01	0.00	0.00	0.00	0.00	0.00	0.00
Al_2O_3	17.20	1.12	12.86	3.06	14.65	1.21	3.72	0.95
Cr_2O_3	0.00	0.01	0.00	0.00	0.00	0.01	0.00	0.01
FeO	24.60	5.73	7.82	1.61	14.17	8.69	5.24	3.25
MnO	3.36	0.45	2.54	0.68	3.35	1.90	0.94	0.44
MgO	15.15	4.30	29.08	1.99	23.38	7.20	36.22	3.31
CaO	0.05	0.04	0.19	0.12	0.13	0.11	0.21	0.04
Na_2O	0.03	0.02	0.05	0.02	0.03	0.02	0.04	0.02
K_2O	0.03	0.01	0.04	0.01	0.03	0.01	0.05	0.02
F	0.00	0.01	0.00	0.02	0.00	0.00	0.02	0.03
Cl	0.01	0.01	0.03	0.02	0.02	0.01	0.02	0.01
Total	87.82	0.82	85.66	0.93	86.37	1.35	85.89	1.28
—O≡F,Cl	0.00	0.00	0.01	0.01	0.00	0.00	0.01	0.01
Total	87.82	0.82	85.66	0.93	86.37	1.35	85.89	1.28
Cations (refer to text for method of calculation)								
Si	2.92	0.10	3.28	0.19	3.13	0.13	3.81	0.07
Ti	0.00	0.00	0.00	0.00	0.00	0.00	0.00	0.00
Al	2.17	0.18	1.50	0.36	1.78	0.23	0.42	0.11
Cr	0.00	0.00	0.00	0.00	0.00	0.00	0.00	0.00
Fe^{3+}	—	—	—	—	—	—	0.00	0.00
Fe^{2+}	2.21	0.53	0.65	0.14	1.24	0.83	0.43	0.27
Mn^{2+}	0.30	0.04	0.21	0.06	0.29	0.17	0.08	0.04
Mg	2.39	0.59	4.30	0.27	3.53	1.00	5.21	0.36
Ca	0.01	0.00	0.02	0.01	0.01	0.01	0.02	0.00
Na	0.01	0.00	0.01	0.00	0.01	0.00	0.01	0.00
K	0.00	0.00	0.00	0.00	0.00	0.00	0.01	0.00
F	0.00	0.00	0.00	0.01	0.00	0.00	0.01	0.01
Cl	0.00	0.00	0.00	0.00	0.00	0.00	0.00	0.00
H	—	—	—	—	—	—	—	—

*Ps Di: Chlorite pseudomorphs after diopside

Table 5. Electron microprobe analyses of minerals belonging to the grossular + zoisite + diopside ± prehnite parageneses of rodingitized diorites.

Mineral	Grossular		Zoisite			
Sample	JMH-25.2		JMH-25.2		H1281-62.5	
Comments	Rock		Rock		Rock	
	(N=7)	± 1 σ	(N=58)	± 1 σ	(N=24)	± 1 σ
Wt. %						
SiO_2	38.67	0.10	38.68	0.89	38.75	0.44
TiO_2	0.06	0.04	0.06	0.08	0.01	0.02
Al_2O_3	22.41	0.09	31.25	0.57	30.99	0.72
Cr_2O_3	0.00	0.01	0.00	0.01	0.00	0.01
FeO	2.18	0.12	2.29	0.64	3.05	0.85
MnO	1.20	0.07	0.06	0.05	0.12	0.08
MgO	0.01	0.01	0.02	0.02	0.04	0.04
CaO	35.49	0.20	24.07	0.37	24.07	0.45
Na_2O	0.00	0.00	0.02	0.09	0.03	0.09
K_2O	0.00	0.00	0.02	0.01	0.03	0.04
Total	100.02	0.29	96.49	1.03	97.11	0.58
Cations (refer to text for method of calculation)						
Si	2.93	0.01	2.99	0.04	2.99	0.02
Ti	0.00	0.00	0.00	0.00	0.00	0.00
Al	2.00	0.01	2.85	0.06	2.82	0.06
Cr	0.00	0.00	0.00	0.00	0.00	0.00
Fe^{3+}	0.00	0.00	0.15	0.04	0.20	0.06
Fe^{2+}	0.14	0.01	—	—	—	—
Mn^{2+}	0.08	0.00	0.00	0.00	0.01	0.01
Mg	0.00	0.00	0.00	0.00	0.01	0.01
Ca	2.88	0.02	2.00	0.03	1.99	0.03
Na	0.00	0.00	0.00	0.01	0.00	0.01
K	0.00	0.00	0.00	0.00	0.00	0.00
H	0.05	0.08	—	—	—	—

Table 5. (continued)

Mineral	Prehnite				Diopside		
Sample	JMH-25.2		JMH-24		JMH-25.2		H1281-62.5
Comments	Rock (Late)		Vein		Rock		Rock
	(N=21)	± 1 σ	(N=9)	± 1 σ	(N=66)	± 1 σ	(N=3)
Wt. %							
SiO_2	43.06	0.41	42.90	0.28	50.44	1.66	48.39
TiO_2	0.01	0.01	0.26	0.28	0.48	2.45	0.04
Al_2O_3	24.16	0.23	23.94	0.22	1.09	0.52	2.65
Cr_2O_3	0.01	0.01	0.01	0.01	0.01	0.01	0.00
FeO	0.12	0.04	0.03	0.02	14.80	2.31	15.84
MnO	0.03	0.03	0.04	0.01	0.81	0.32	1.13
MgO	0.01	0.03	0.00	0.00	8.25	1.32	6.54
CaO	26.97	0.36	26.21	0.29	23.80	0.54	22.45
Na_2O	0.03	0.05	0.00	0.01	0.34	0.17	0.78
K_2O	0.03	0.02	0.02	0.01	0.05	0.04	0.03
Total	94.42	0.78	93.40	0.38	100.06	1.01	97.84
Cations (refer to text for method of calculation)							
Si	3.00	0.01	3.01	0.01	1.94	0.05	1.91
Ti	0.00	0.00	0.01	0.01	0.01	0.07	0.00
Al	1.98	0.01	1.98	0.02	0.05	0.02	0.12
Cr	0.00	0.00	0.00	0.00	0.00	0.00	0.00
Fe^{3+}	0.01	0.00	0.00	0.00	0.06	0.03	0.11
Fe^{2+}	—	—	—	—	0.41	0.08	0.42
Mn^{2+}	0.00	0.00	0.00	0.00	0.03	0.01	0.04
Mg	0.00	0.00	0.00	0.00	0.47	0.07	0.39
Ca	2.01	0.02	1.97	0.02	0.98	0.02	0.95
Na	0.00	0.01	0.00	0.00	0.03	0.01	0.06
K	0.00	0.00	0.00	0.00	0.00	0.00	0.00
H	—	—	—	—	—	—	—

Mg (Mg/(Mg+Fe+Mn) from 0.80 to 0.95), whereas chlorite from the core of the pockets is Fe-rich (Mg/(Mg+Fe+Mn) down to 0.45). The original texture of the protolith has been almost completely obliterated, except for some very rough pseudomorphs of garnet and clinopyroxene after biotite. The garnet and clinopyroxene are intimately associated and neither shows signs of replacement by the other. Electron microprobe analyses show that the composition of the garnet is restricted to the grossular-rich variety, and that it contains small amounts of total Fe (< 0.15 a.p.f.u.) and virtually no water. The results of loss on ignition from the two samples of orange garnet analysed by XRF support this latter observation. The composition of the clinopyroxene shows much more inhomogeneity, with Mg varying from 0.34 to 0.75 a.p.f.u. In sample JMH-306, the proportion of Mn in the clinopyroxene reaches up to 0.23 a.p.f.u., whereas coexisting garnet contains below 0.07 a.p.f.u. Mn.

Examination of the weakly rodingitized sample (JMH-26), collected 10 cm from the footwall contact of the dyke with serpentinite, showed that the unknown pseudomorphed phenocryst phase was the most sensitive to alteration; substantial replacement by garnet and zoisite-clinozoisite was observed locally. The almost completely rodingitized diorite sample (JMH-25.2), collected 3 cm from the footwall contact of the dyke with serpentinite, contains zoned zoisite crystals (~ 31 vol. %), in which the Fe content varies between 0.10 and 0.25 a.p.f.u. Coexisting diopside (~ 52 vol. %) shows a much more homogeneous composition than in the other rodingite samples with 0.47 ± 0.07 (N = 67, 1σ) a.p.f.u. Mg. Coexisting garnet (~17 vol. %) contains 0.13-0.15 a.p.f.u. Fe and 0.07-0.08 a.p.f.u. Mn. Garnet in relict biotite contains up to 3 wt. % TiO_2. Prehnite was observed in small proportions as a late replacement of garnet. This mineral is more abundant (proportions in some samples exceeding 80 vol. %) in veins that cut the diorite dyke. Alteration was so intense that, except for biotite, the precursor minerals could rarely be identified on the basis of replacement textures. In sample H1281-62.5, however, most of the biotite remains, the plagioclase was completely replaced by zoisite, and the unknown pseudomorphed phenocryst phase was replaced predominantly by grossular.

Rodingitized granitic rocks

The early-stage alteration of the granitic rocks is characterized by the replacement of feldspars and biotite by albite, and the replacement of quartz by tremolite-actinolite. Many of the smaller dykes (< 15 cm wide) are composed entirely of feldspars (albite and K-feldspar) and pyriboles (diopside is also present). Rodingites after granitic rocks, however, are less common and, in general, less extensively developed than those formed by replacement of dioritic rocks. We will examine two examples in detail.

The first example is a rodingite that formed by replacement of a pegmatitic, leucogranitic rock (JMH-333a and JMH-333b). Two mineral assemblages were identified. A chlorite-rich assemblage with subordinate grossular and prehnite was observed in the samples that contain relict feldspar (JMH-333a). The completely rodingitized sample (JMH-333b) is macroscopically indistinguishable from the garnet-rich rodingites formed after diorite. The latter display a similar orange-coloured and granular aspect. The mineralogy of sample JMH-333b is simple: orange garnet and clinopyroxene. The orange garnet is water-poor as in the rodingitized diorites, but is less iron-rich (Table 6).

Seven samples were selected for mineralogical examination from a granitic intrusive sheet that had been strongly mylonitized at the contact with serpentinite prior to calc-silicate alteration. The alteration is divisible into three zones separated by sharp contacts. The first zone, at the contact with serpentinite, measures 4 cm in thickness, and consists of partially chloritized (blackwall-type alteration) rodingite (E:2; 38 vol. % chlorite, 32 vol. % grossular, and 30 vol. % diopside). The second zone, measuring 6 cm in thickness, is a Ca-rich (up to 41 wt. % CaO) wollastonite + vesuvianite + diopside + grossular rodingite (E:4.5; 38 vol. % diopside, 26 vol. % wollastonite, 25 vol. % vesuvianite, and 11 vol. % grossular. E:7.5; 65 vol. % wollastonite, 22 vol. % vesuvianite, 8 vol. % diopside, and 5 vol. % grossular). The third zone, which is 35 cm thick, is composed of a feldspar-pyribole assemblage (E:20, E:44). This zone is massive and takes on a bleached aspect in hand sample due to the complete replacement of the primary dark-coloured minerals by albite and K-feldspar. The garnet in the rodingitized

Table 6. Electron microprobe analyses of minerals from rodingitized granite.

Mineral	Grossular				Vesuvianite
Sample	JMH-333		E:7.5		E:7.5
	(N=10)	± 1 σ	(N=8)	± 1 σ	(N=4)
Wt. %					
SiO_2	39.27	0.23	37.53	0.45	36.10
TiO_2	0.08	0.12	0.02	0.02	0.02
Al_2O_3	22.12	0.10	21.37	1.04	17.43
Cr_2O_3	0.00	0.01	0.00	0.00	0.01
FeO	0.80	0.14	1.55	1.42	2.51
MnO	0.67	0.10	0.07	0.06	0.09
MgO	0.00	0.00	0.04	0.02	2.60
CaO	37.28	0.16	38.01	0.37	36.87
Na_2O	0.00	0.01	0.01	0.01	0.01
K_2O	0.00	0.00	0.00	0.00	0.00
Total	100.24	0.29	98.61	0.43	95.64
Cations (refer to text for method of calculation)					
Si	2.96	0.01	2.82	0.05	17.65
Ti	0.00	0.01	0.00	0.00	0.01
Al	1.96	0.01	1.89	0.08	10.05
Cr	0.00	0.00	0.00	0.00	0.00
Fe^{3+}	0.03	0.01	0.09	0.08	—
Fe^{2+}	0.02	0.01	0.01	0.01	1.03
Mn^{2+}	0.04	0.01	0.00	0.00	0.04
Mg	0.00	0.00	0.00	0.00	1.90
Ca	3.01	0.01	3.06	0.03	19.32
Na	0.00	0.00	0.00	0.00	0.01
K	0.00	0.00	0.00	0.00	0.00
H	0.01	0.02	0.62	0.24	14.22

granite is very similar to that in the massive rodingitized slate, i.e., it is water-rich and Fe-poor (Table 6). The average of four electron microprobe analyses of vesuvianite (Table 6) yield the composition $Ca_{19.32}Na_{0.01}(Mg_{1.9}, Fe_{1.03}, Mn_{0.04})Al_{10.05}Ti_{0.01}Si_{17.65}O_{78}H_{10.64}$.

Nephrite and diopsidite

Calc-silicate alteration of serpentinite is manifested most commonly by the presence of massive replacement bodies composed of tremolite ± talc ± antigorite (nephrite) or diopside ± tremolite ± antigorite after serpentinite at the contact with felsic intrusive rocks. These replacement bodies form halos measuring up to two meters thick. Mineralogical associations similar to those in the halos are present in serpentinized peridotite xenoliths enclosed in the dyke rocks. Although these xenoliths occur in both the granitic and the dioritic-monzodioritic dykes, they are more abundant in the latter. As the majority of the dyke rocks are located in shear zones, the nephrite bodies locally form isolated and boudinaged masses in sheared serpentinites. It would appear that the nephrite bodies were detached from the dykes and transported along the shear zones. Locally, minor dyke veinlets, which form apophyses off the major dykes and extend for short distances beyond the shear zones into the ore zones, are surrounded by nephrite haloes.

Careful examination of a series of samples of lizardite-chrysotile-dominant and antigorite-dominant serpentinites, nephrite and diopsidite permitted reconstruction of the paragenetic sequences of alteration minerals in the serpentinites near the margin of dykes. Spatially, from the serpentinites toward the dykes, these sequences are: 1) lizardite-chrysotile serpentinite → antigorite → talc → anthophyllite-cummingtonite → biotite (contact with dyke), and 2) lizardite-chrysotile serpentinite → nephrite → diopsidite → rodingitized felsic rock. Locally, anthophyllite-cummingtonite, which formed during intrusion of the felsic rocks, is replaced by tremolite and serpentine.

In some cases, one or more of antigorite, talc and tremolite may be missing. The tremolite appears to have nucleated and grown most commonly by pseudomorphic replacement of interlocking antigorite needles. This explains the fine-grained and very tough nature of nephrite. As the degree of alteration increased, however, the tremolite aggregates recrystallized to form coarser-grained aggregates, and, eventually, were

replaced by diopside. The replacement of tremolite by diopside in the nephrite coincided with intense rodingitization of the associated intrusive rock.

Vesuvianite-rich veins

A number of vesuvianite-dominant rodingites of dyke- or sill-like morphology and measuring up to two meters thick occur at the base of the dunite-pyroxenite unit. No traces of the original lithology remain. Because their origin is uncertain, these rodingites are tentatively referred to as "veins". Locally, a hydrothermal origin is clearly evident where stockworks of veins are filled with very coarse-grained chlorite and lesser proportions of prismatic vesuvianite. More commonly, these rodingites comprise a core which is composed almost entirely of coarse-grained, light green vesuvianite, and displays an intensively diopsidized halo extending into the serpentinite for a distance reaching up to 20 cm. These vesuvianite-rich bodies are very porous and display a variable but elevated vug porosity, visually estimated at 15-25 vol. %. Locally, breccias and fractures filled with dark green vesuvianite and rimmed by light orange-pink grossular project into the diopsidized halo. In the "veins" proper, the assemblages vesuvianite + diopside + chlorite, vesuvianite + grossular + diopside and vesuvianite + wollastonite are observed. Locally, zonal crystallization sequences are clearly evident, e.g., green vesuvianite → colourless to purple vesuvianite → wollastonite. Late-forming aragonite crystals occur in some vugs. Finally, the associations vesuvianite + wollastonite + calcite and vesuvianite + native copper + calcite were noted by Chamberlain (1980).

CHEMICAL CHANGES ACCOMPANYING RODINGITIZATION

In this section, we report the changes in chemical composition, which accompanied alteration of slates, diorites-monzodiorites, granites, and serpentinites. The chemical composition of the samples was determined by X-ray fluorescence spectrometry. SiO_2, TiO_2, Al_2O_3, Fe_2O_3, MnO, MgO, CaO, Na_2O, K_2O, P_2O_5, BaO, Co,

Cr_2O_3, Cu, Ni, and Zn were analysed in fused disks, and the trace elements Ga, Nb, Pb, Rb, Sr, Th, U, Y, and Zr in pressed powder pellets. SO_3 was determined for samples UG-C, UG-2, UG-7 (+ 1 repeat: UG-7bis)), and UG-10 (+ 1 repeat: UG-10bis) using a LECO induction furnace and ALPHA sulphur titrator. CO_2 was determined in samples UG-7bis and UG-10bis using a LECO induction furnace and absorption bulb. The detection limits, in ppm, were: SiO_2:60, TiO_2:35, Al_2O_3:120, Fe_2O_3:30, MnO:30, MgO:95, CaO:15, Na_2O:75, K_2O:25, P_2O_5:35, Co:10, BaO:17, Ce:15, Cr_2O_3:15, Cu:2, Ni:3, Zn:2, L.O.I.:100, SO_3:10, CO_2:20, and Ga-Nb-Pb-Rb-Sr-Th-U-Y-Zr:1. All analyses were performed by the Geochemical Laboratories at McGill University. The density of the samples was determined by the water displacement method.

The first step in evaluating the mass changes that occurred during alteration of a series of samples is to determine the nature of the parent rock from which the altered rocks originated, and to establish the basis for calculation (Gresens, 1967; Grant, 1986). The samples selected for analysis represented series collected from single occurrences in which the protolith could be defined as the sample which was the least altered in each series. A correlation matrix was calculated to determine which elements were related in each of these series, with particular attention being given to elements such as Zr, P, Ti, Al, Cr, Nb, Y, and Th, which have been shown to generally remain immobile during hydrothermal alteration at low temperature (< 350°C). Our calculations indicate that the assumption that Zr or P_2O_5 were immobile during rodingitization would imply an increase in volume of 33 % and 26 to 53 % for the rodingitized diorite and the rodingitized granite, respectively. Immobility of Cr_2O_3 in serpentinite during calc-silicate alteration would imply even greater increases in volume. Volume increases would have been between 43 and 166 % and 83 and 323 % if Cr_2O_3 and Ni remained immobile, respectively, during transformation of serpentinite to nephrite, and between 0 and 100 % and 66 and 194 % if Cr_2O_3 and Ni had remained immobile, respectively, after transformation of serpentinite to diopsidite. These figures are clearly excessive considering that, in some cases, the original textures of the rocks are conserved (e.g., UG-10 versus UG-2) and, in others, that the replacement is pseudomorphic (e.g., H1281-61.5 versus H1281-62.5). We therefore based our mass balance calculations on the assumption

that volume remained constant during alteration. A detailed discussion of the implications of Zr, P_2O_5, Cr_2O_3, and Ni mobility during hydrothermal alteration is presented below.

Major elements

Rodingitized slate

The four samples of slate described in the previous section were analysed (Table 7) in order to determine the origin of the Ca responsible for the rodingitization of the slate at the contact with the serpentinites. Compositions of samples were compared after correcting analyses to reflect the conservation of volume implied by the perfect preservation of sedimentary structures visible in hand samples (Figure 2) and in thin sections.

The most striking changes that occurred during the first stage of alteration, albitization, were an increase of SiO_2, Al_2O_3 and Na_2O, a decrease in CaO, and a sharp decrease in the proportions of C and S as evidenced by the disappearance of calcite and pyrite. A quantitative estimate of gains and losses of element oxides in 100 grams of albitized slate (UG-7bis) was performed by comparing the composition of the latter with that of fresh slate (UG-10bis; Table 8) at constant volume replacement. The calculated mass factor was 1.01. The total gains and losses of Ca were calculated for a linear array of cubes, each of a volume of $1cm^3$. The albitization front was 243 cm from the contact with the serpentinites (Figure 4). The corresponding mass of slate along this vector of cubes is 663 grams, and the total Ca loss, calculated assuming that albitization was uniform and preceded rodingitization, is 39 grams. The rodingitization front was located 60 cm from the contact with serpentinites, corresponding to a linear array of cubes of slate weighing 164 grams. The total amount of Ca added to form rodingite from slate was calculated to be 35 grams (based on the most completely rodingitized sample UG-2), suggesting that the Ca loss induced by albitization was almost compensated by the gain in Ca required to form the rodingite.

Field relationships and petrographic examination show that rodingites formed by the replacement of albitized slate. All samples of rodingitized slate contain variable but

Table 7. Chemical analyses of slate, albitized slate and rodingitized slate.

Sample	UG-C	UG-2	UG-7	UG-7bis	UG-10	UG-10bis
Rock type	RS	RS	AS	AS	Slate	Slate
Distance from contact with serpentinite (cm)	15	60	213	213	305	305
Density	3.08	3.12	2.77	2.77	2.73	2.73
Wt. %						
SiO_2	49.29	47.96	57.81	58.59	53.11	53.79
TiO_2	0.618	0.577	0.751	0.754	0.576	0.578
Al_2O_3	15.99	11.63	18.08	18.18	14.11	14.16
Fe_2O_3	6.88	5.62	6.47	6.44	5.89	5.88
MnO	0.457	0.281	0.098	0.093	0.084	0.083
MgO	3.57	5.53	3.7	3.62	3.76	3.64
CaO	18.49	24.91	1.59	1.31	7.55	7.28
Na_2O	1.37	0.14	7.16	7.27	2.82	2.94
K_2O	2.01	1.42	2.91	2.98	3.33	3.43
P_2O_5	0.119	0.131	0.149	0.145	0.16	0.158
L.O.I.	0.78	1.03	1.08	1.08	6.47	7.91
ppm						
BaO	1592	253	259	239	495	517
Ce	n.a.	n.a.	n.a.	80	n.a.	74
Cr_2O_3	n.a.	n.a.	n.a.	148	n.a.	129
Cu	59	47	89	n.a.	99	n.a.
Ni	34	74	47	49	61	54
Zn	53	84	33	n.a.	88	n.a.
Total	99.75	99.27	99.84	100.51	97.93	99.93
S (Wt. %)	0.003	0.002	0.040	0.030	1.080	0.970
CO_2 (Wt. %)	n.a.	n.a.	n.a.	0.450	n.a.	8.490
CO_2*	—	—	—	0.061	—	5.313
C**	—	—	—	0.389	—	3.177
ppm						
Ga	27.1	16.4	23.6	23.5	17.8	18.2
Nb	10.3	11.6	14	13.2	10.5	10.3
Pb	9.5	1.9	<d.l.	2.1	13.3	13.8
Rb	30.1	24.8	188.6	185	122.8	121.4
Sr	1059.9	57.5	157.7	150.8	350.5	343.4
Th	13.6	11	10.9	12.3	7.6	9.1
U	<d.l.	2.2	<d.l.	2	<d.l.	3.7
Y	21	22.4	21.1	20.3	23.9	24.5
Zr	115.6	132.5	162.1	155.1	140	140.2

Analyses by X-ray fluorescence except for S and CO_2 which were analysed using a LECO induction furnace. CO2*: recalculated to represent the fraction of the total carbon present in calcite. C**: excess carbon after substraction of calcite. n.a.: not analysed. <d.l.: below detection limit. RS: rodingitized slate. AS: albitized slate.

Table 8. Mass changes resulting from alteration of slate assuming volume remained constant or Zr was immobile.

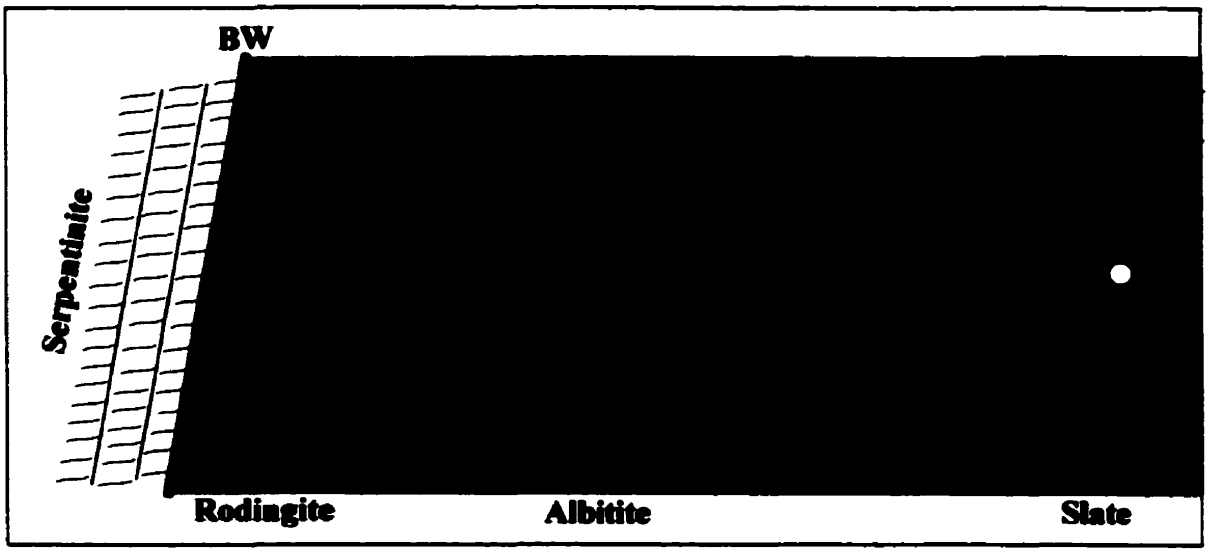
	Constant volume			
Sample	UG-C	UG-2	UG-2	UG-7bis
Precursor	UG-10bis	UG-10bis	UG-7bis	UG-10bis
Volume factor	1	1	1	1
Mass factor	1.13	1.14	1.13	1.01
Grams added-removed/100 grams precursor				
SiO_2	1.73	1.02	-3.78	5.66
TiO_2	0.12	0.08	-0.09	0.19
Al_2O_3	3.85	-0.87	-4.89	4.29
Fe_2O_3	1.87	0.54	-0.02	0.65
FeOT	1.68	0.49	-0.02	0.59
MnO	0.43	0.24	0.23	0.01
MgO	0.38	2.68	2.70	0.03
CaO	13.55	21.19	27.16	-5.95
Na_2O	-1.40	-2.78	-7.11	4.44
K_2O	-1.17	-1.81	-1.36	-0.41
P_2O_5	-0.02	-0.01	0.00	-0.01
L.O.I.	-7.03	-6.73	0.10	-6.81
S	-0.97	-0.97	-0.03	-0.94
C	—	—	—	-0.26
ppm added-removed/100 grams precursor				
BaO	1276.19	-227.86	50.14	-274.50
Ce	—	—	—	7.17
Co	—	—	—	—
Cr_2O_3	—	—	—	21.17
Cu	—	—	—	—
Ni	-15.70	30.57	35.57	-4.28
Zn	—	—	—	—
Ga	12.32	0.54	-4.76	5.64
Nb	1.30	2.96	0.06	3.09
Pb	-3.10	-11.63	0.07	-11.67
Rb	-87.50	-93.06	-156.66	66.31
Sr	850.44	-277.69	-85.09	-190.39
Th	6.22	3.47	0.27	3.38
U	—	-1.19	0.51	-1.67
Y	-0.85	1.10	5.30	-3.90
Zr	-9.99	11.23	-3.67	17.17

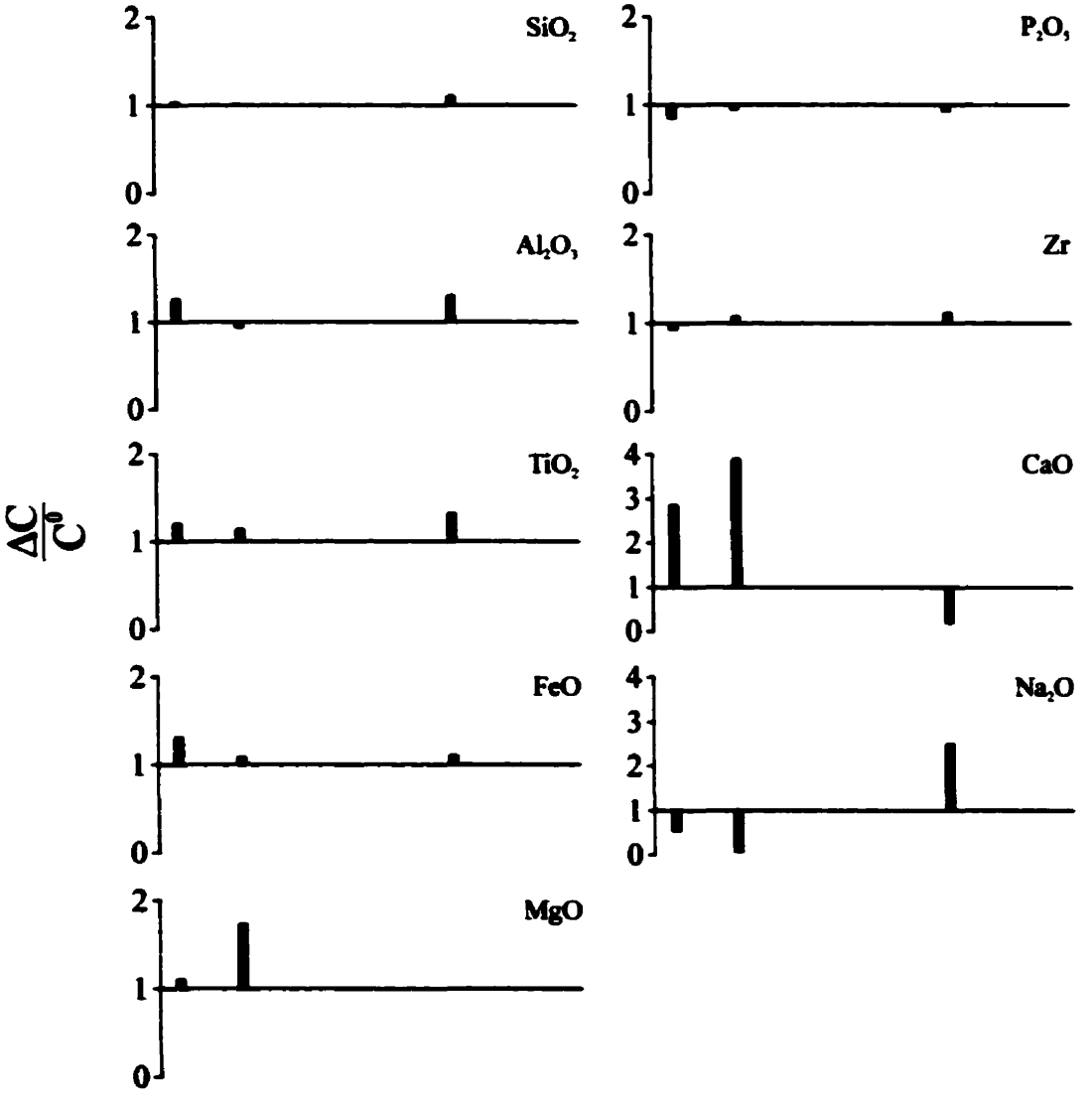
Table 8. (Continued)

	Zr immobile			
Sample	UG-C	UG-2	UG-2	UG-7bis
Precursor	UG-10bis	UG-10bis	UG-7bis	UG-10bis
Volume factor	1.08	0.93	1.04	0.89
Mass factor	1.21	1.06	1.17	0.90
Grams added-removed/100 grams precursor				
SiO_2	5.99	-3.04	-2.45	-0.83
TiO_2	0.17	0.03	-0.08	0.10
Al_2O_3	5.23	-1.85	-4.57	2.27
Fe_2O_3	2.46	0.07	0.14	-0.06
FeOT	2.22	0.06	0.12	-0.05
MnO	0.47	0.21	0.24	0.00
MgO	0.69	2.21	2.85	-0.37
CaO	15.14	19.08	27.85	-6.10
Na_2O	-1.28	-2.79	-7.11	3.63
K_2O	-0.99	-1.93	-1.32	-0.74
P_2O_5	-0.01	-0.02	0.01	-0.03
L.O.I.	-6.96	-6.82	0.13	-6.93
S	-0.97	-0.97	-0.03	-0.94
C	—	—	—	-0.26
ppm added-removed/100 grams precursor				
BaO	1413.78	-249.30	57.15	-300.96
Ce	—	—	—	-1.69
Co	—	—	—	—
Cr_2O_3	—	—	—	4.78
Cu	—	—	—	—
Ni	-12.76	24.30	37.62	-9.71
Zn	—	—	—	—
Ga	14.67	-0.85	-4.30	3.04
Nb	2.19	1.97	0.38	1.63
Pb	-2.28	-11.79	0.12	-11.90
Rb	-84.89	-95.16	-155.97	45.83
Sr	942.05	-282.56	-83.49	-207.09
Th	7.39	2.54	0.58	2.02
U	—	-1.37	0.58	-1.89
Y	0.97	-0.80	5.92	-6.15
Zr	0	0	0	0

Figure 4

Diagram showing the location of slate (UG-10), albitized slate (UG-7) and rodingitized slate (UG-2 and UG-C) samples collected near the slate-serpentinite contact. Also shown are diagrams illustrating the changes in the concentrations of SiO_2, Al_2O_3, TiO_2, FeO, MgO, P_2O_5, Zr, CaO, and Na_2O that resulted from the alteration of slate with respect to the distance from the contact with serpentinite.


BW
Serpentinite
Rodingite
Albitite
Slate


$\frac{\Delta C}{C^b}$
SiO2
P2O5
Al2O3
Zr
TiO2
CaO
FeO
Na2O
MgO
0
1
2
3
4

small proportions of relict albite. Rodingitization of slate was therefore preceded by albitization. The overall mass action equations for the transformation of 100 grams of slate (sample UG-10bis) to 101 grams of albitite (sample UG-7bis), and of 100 grams of albitite to 113 grams of rodingite (sample UG-2) are:

SLATE

$$K_{0.073}Na_{0.095}Ca_{0.13}Mg_{0.09}Mn_{0.001}Fe^{2+}_{0.074}Al_{0.278}Ti_{0.007}Si_{0.895}H_{0.741}S_{0.03}C_{0.022}O_{2.971}$$
$$+ 0.094SiO_2^\circ + 0.002Ti^{4+} + 0.097Al^{+3} + 0.008Fe^{2+} + 0.000Mn^{2+} + 0.001Mg^{+2} + 0.143Na^{+}$$
$$=$$

ALBITITE

$$K_{0.064}Na_{0.238}Ca_{0.024}Mg_{0.091}Mn_{0.001}Fe^{2+}_{0.082}Al_{0.362}Ti_{0.01}Si_{0.989}H_{0.088}S_{0.001}C_{0.001}O_{2.949}$$
$$+ 0.106Ca^{+2} + 0.009K^{+} + 0.347H^{+} + (0.029S + 0.021C + 0.306H + 0.210O) \quad (4),$$

and:

ALBITITE

$$K_{0.063}Na_{0.235}Ca_{0.023}Mg_{0.09}Mn_{0.001}Fe^{2+}_{0.081}Al_{0.357}Ti_{0.009}Si_{0.975}H_{0.116}C_{0.001}S_{0.001}O_{2.906}$$
$$+ 0.003Mn^{+2} + 0.065Mg^{+2} + 0.477Ca^{+2} + (0.536H + 0.269O)$$
$$=$$

RODINGITE

$$K_{0.034}Na_{0.005}Ca_{0.500}Mg_{0.1545}Mn_{0.005}Fe^{2+}_{0.079}Al_{0.257}Ti_{0.008}Si_{0.899}H_{0.129}S_{0.00006}O_{3.022}$$
$$+ 0.076SiO_2^\circ + 0.001Ti^{4+} + 0.100Al^{+3} + 0.001Fe^{2+} + 0.230Na^{+} + 0.030K^{+} + 0.523H^{+} +$$
$$(0.0003S + 0.0007C) \quad (5),$$

respectively.

Rodingitized dioritic rocks

Eleven samples were analysed from a major diorite sheet (Table 9), measuring 3.84 meters thick where sampled, oriented N010 and dipping ~ 75° SE. The sheet was

Table 9. Chemical analyses of altered diorite samples collected across a 3.84 m thick dyke.

Sample	JMH-25.2	H1281-62.5	JMH-25.1B
Rock type	SRD	MRD	SRD
Distance from footwall contact with serpentinite (cm)	3	4	5
Density	3.25	3.11	n.d.
Wt. %			
SiO_2	44.87	39.32	50.88
TiO_2	0.864	0.775	0.698
Al_2O_3	14.59	20.99	11.97
Fe_2O_3	8.2	13.16	9.67
MnO	0.508	0.371	0.52
MgO	4.08	5.03	3.79
CaO	25.58	12.22	18.9
Na_2O	0.4	1.04	2.64
K_2O	0.13	4.52	0.59
P_2O_5	0.382	0.598	0.304
L.O.I.	0.37	1.56	0.29
ppm			
BaO	26	283	99
Ce	92	152	95
Co	13	37	16
Cr_2O_3	29	33	<d.l.
Ni	69	37	31
Total	100.00	99.64	100.28
ppm			
Ga	20.7	26.6	15.8
Nb	14.1	8.5	14.4
Pb	4	4.1	3
Rb	9.8	287.9	33.4
Sr	1160.9	656.9	334.1
Th	17	21.8	13.1
U	<d.l.	9.8	1.2
Y	22	35	19.3
Zr	334.3	508	244.1

Analyses by X-ray fluorescence. <d.l.: below detection limit.
n.d.: not determined. SRD: strongly rodingitized diorite,
MRD: moderately rodingitized diorite. WRD: weakly rodingitized diorite.
LAD: diorite least affected by Ca-metasomatism.

Table 9. (Continued)

Sample	JMH-25.1	JMH-26	H1281-61.5	H1281-55.9
Rock type	SRD	WRD	LAD	SRD
Distance from footwall contact with serpentinite (cm)	5	10	14	84
Density	3.19	3.08	2.87	n.d.
Wt. %				
SiO_2	48.34	48.75	48.74	42.33
TiO_2	0.906	0.691	0.644	0.815
Al_2O_3	14.61	20.19	22.98	15.57
Fe_2O_3	8.8	7.79	7.37	8.11
MnO	0.405	0.195	0.095	0.511
MgO	3.83	4.57	5.19	6.69
CaO	18.77	8.59	2.08	20.78
Na_2O	2.21	3.17	2.72	0.22
K_2O	1.09	4.52	7.42	0.24
P_2O_5	0.372	0.562	0.548	0.648
L.O.I.	0.8	1.43	2.5	3.74
ppm				
BaO	179	1590	1135	33
Ce	88	155	139	161
Co	13	29	20	<d.l.
Cr_2O_3	51	38	46	50
Ni	39	50	31	48
Total	100.17	100.64	100.42	99.68
ppm				
Ga	18.8	23.6	25.6	17.8
Nb	16.8	8.5	9	11.2
Pb	2.7	4.3	2	2
Rb	62.1	168.6	220.1	14.5
Sr	379.3	727.2	132.7	62.7
Th	14.3	17.4	13.8	17.7
U	1.8	4	4.3	2.4
Y	22.7	31.4	34.4	41.7
Zr	313.4	470.3	471.3	529.9

Table 9. (Continued)

Sample	JMH-24	H1281-48	H1281-43	H1281-28
Rock type	LAD	MRD	WRD	LAD
Distance from footwall contact with serpentinite (cm)	120	156	207	363
Density	2.85	n.d.	n.d.	2.84
Wt. %				
SiO_2	48.96	42.96	47.81	48.62
TiO_2	1.432	1.111	1.008	0.94
Al_2O_3	19.78	19.55	17.8	21.77
Fe_2O_3	10.23	7.13	7.8	8.27
MnO	0.096	0.213	0.212	0.123
MgO	5.48	5.41	4.9	5.08
CaO	1.59	14.3	8.5	1.99
Na_2O	4.26	0.46	0.74	2.83
K_2O	6.33	4.29	8.54	7.31
P_2O_5	0.887	0.825	0.756	0.688
L.O.I.	1.54	3.64	1.44	2.18
ppm				
BaO	1962	635	2570	1427
Ce	244	172	194	188
Co	35	<d.l.	<d.l.	24
Cr_2O_3	77	47	36	57
Ni	146	51	61	50
Total	100.83	99.98	99.79	99.98
ppm				
Ga	22.8	21.7	15.3	25.8
Nb	18	14.3	12.2	12.8
Pb	3.4	2.2	2.1	2.5
Rb	239.9	240.5	334.5	257.1
Sr	128.6	63.4	107.5	171.8
Th	27.6	27.4	25.4	19.6
U	5.6	9.1	10.8	5.8
Y	46.9	52.2	49.9	42.2
Zr	741.7	730.5	665	574.3

located in a shear zone cutting harzburgite. Of these eleven samples, six were from a diamond drill hole (H1281) and the remainder from the open pit. The samples from the drill hole were located fifty meters above those collected from the open pit.

At the footwall contact of the sheet, the serpentinite in the open pit was sheared and replaced by antigorite over a distance of ~ 10 cm. A thin, less than 2 cm thick, biotite-bearing blackwall zone of alteration occurs in the sheet at the contact with serpentinite. The diorite was completely rodingitized to a pinkish zoisite + diopside + garnet ± prehnite assemblage over a distance of 7 cm adjacent to the blackwall (JMH-25.2), grading sharply into strongly rodingitized diorite with relict biotite to 18 cm from the contact with serpentinite (JMH-25.1). The transition between strongly rodingitized diorite and weakly-rodingitized diorite occurs within 20 cm of the contact with serpentinite where Ca concentration drops from 25.6 to 8.6 wt. % CaO (JMH-26). One meter from the contact of the sheet with serpentinite, the CaO concentration drops to 1.6 wt. % (JMH-24). At the footwall contact of the sheet, intersected in diamond-drill hole H1281, the diorite was converted to a blackwall over a distance of 3 cm, and strongly rodingitized up to 14 cm from the contact with the blackwall, where the CaO concentration drops from 12.2 (H1281-62.5) to 2.1 wt. % (H1281-61.5).

In order to avoid problems related to variations in concentrations due to fractional crystallization, only the five samples within 20 cm of the footwall contact with serpentinite were used for the mass balance calculations. The results are presented in Table 10. Partial conversion of the least altered sample H1281-61.5 to rodingite (H1281-62.5) involved an increase in the mass by a factor of 1.08, removal of SiO_2, Al_2O_3, Na_2O, and K_2O, and addition of MgO, FeO and CaO according to the reaction:

DIORITE

$$K_{0.1575}Na_{0.0878}Ca_{0.0371}Mg_{0.1287}Mn_{0.0013}Fe_{0.0923}Al_{0.4509}Ti_{0.0081}Si_{0.8111}O_{2.8355}H_{0.2775}$$
$$+ 0.1990Ca^{2+} + 0.0065Mg^{2+} + 0.0044Mn^{2+} + 0.0863Fe^{2+} + 0.0024Ti^{4+} + 0.1966H_2O$$
$$=$$

Table 10. Mass changes resulting from alteration of diorite assuming volume remained constant or Zr was immobile.

	Constant volume			Zr immobile		
Sample	H1281-62.5	JMH-25.1	JMH25.2	H1281-62.5	JMH-25.1	JMH25.2
Precursor	H1281-61.5	JMH-26	JMH-26	H1281-61.5	JMH-26	JMH-26
Volume factor	1.00	1.00	1.00	0.86	1.45	1.33
Mass factor	1.08	1.04	1.06	0.93	1.50	1.41
Grams added-removed/100 grams precursor						
SiO_2	-6.13	1.32	-1.40	-12.26	23.79	14.37
TiO_2	0.20	0.25	0.22	0.08	0.67	0.52
Al_2O_3	-0.23	-5.06	-4.79	-3.51	1.73	0.34
Fe_2O_3	6.89	1.32	0.86	4.84	5.42	3.75
FeOT	6.20	1.19	0.78	4.35	4.87	3.37
MnO	0.31	0.22	0.34	0.25	0.41	0.52
MgO	0.26	-0.60	-0.26	-0.52	1.18	1.17
CaO	11.16	10.85	18.40	9.26	19.58	27.40
Na_2O	-1.59	-0.88	-2.75	-1.76	0.15	-2.61
K_2O	-2.52	-3.39	-4.38	-3.23	-2.88	-4.34
P_2O_5	0.10	-0.18	-0.16	0.01	0.00	-0.02
L.O.I.	-0.81	-0.60	-1.04	-1.05	-0.23	-0.91
ppm added-removed/100 grams precursor						
BaO	-828.3	-1404.6	-1562.6	-872.4	-1321.4	-1553.4
Ce	25.7	-63.9	-57.9	2.0	-22.9	-25.6
Co	20.1	-15.5	-15.3	14.3	-9.5	-10.7
Cr_2O_3	-10.2	14.8	-7.4	-15.4	38.5	2.8
Ni	9.1	-9.6	22.8	3.3	8.5	47.1
Ga	3.2	-4.1	-1.8	-0.9	4.6	5.5
Nb	0.2	8.9	6.4	-1.1	16.7	11.3
Pb	2.4	-1.5	-0.1	1.8	-0.2	1.3
Rb	91.9	-104.3	-158.3	47.0	-75.4	-154.8
Sr	579.1	-334.4	497.8	476.7	-158.0	906.0
Th	9.8	-2.6	0.5	6.4	4.1	6.5
U	6.3	-2.1	-4.0	4.8	-1.3	-4.0
Y	3.5	-7.9	-8.2	-1.9	2.7	-0.4
Zr	79.2	-145.7	-117.5	0	0	0

RODINGITE

$K_{0.1040}Na_{0.0364}Ca_{0.2361}Mg_{0.1352}Mn_{0.0057}Fe_{0.1786}Al_{0.4462}Ti_{0.0105}Si_{0.7091}O_{2.8281}H_{0.1877}$

$+ 0.0535K^{+} + 0.0514Na^{+} + 0.0047Al^{3+} + 0.1020SiO_2^{\circ} + 0.4830H^{+}$ (6).

Assuming that Zr remained immobile during rodingitization would imply a volume factor of 0.86 and a mass factor of 0.93. In addition to changing the values for the stoichiometric coefficients in reaction 6, this assumption would result in Mg being subtracted instead of being added. The other components remain on the same sides of the reaction.

Conversion of the least altered sample JMH-26 to rodingite (JMH25.2) involved an increase in the mass by a factor of 1.06, removal of SiO_2, Al_2O_3, MgO, Na_2O, and K_2O, and addition of FeO and CaO according to the reaction:

DIORITE

$K_{0.0960}Na_{0.1022}Ca_{0.1532}Mg_{0.1133}Mn_{0.0027}Fe_{0.0976}Al_{0.3962}Ti_{0.0086}Si_{0.8113}O_{2.7794}H_{0.1588}$

$+ 0.3281Ca^{2+} + 0.0049Mn^{2+} + 0.0108Fe^{2+} + 0.0028Ti^{4+} + 0.0531H_2O$

=

RODINGITE

$K_{0.0030}Na_{0.0136}Ca_{0.4813}Mg_{0.1068}Mn_{0.0076}Fe_{0.1084}Al_{0.3020}Ti_{0.0114}Si_{0.7879}O_{2.7857}H_{0.0434}$

$+ 0.0930K^{+} + 0.0886Na^{+} + 0.0065Mg^{2+} + 0.0942Al^{3+} + 0.0234SiO_2^{\circ} + 0.2216H^{+}$ (7).

Assuming that Zr remained immobile during rodingitization would imply a volume factor of 1.33 and a mass factor of 1.41. In addition to changing the values for the stoichiometric coefficients in reaction 7, this assumption would result in all the major elements being added except for the alkalis Na and K.

Rodingitized granitic rocks

Results of the chemical and mass balance analyses of the seven samples from the mylonitized granitic sheet are presented in Tables 11 and 12 and illustrated in Figure 5. Alteration of granite (E:53) to wollastonite + vesuvianite + diopside + grossular-rodingite

Table 11. Chemical analyses of rodingitized, feldspar-pyribole-altered and least altered granite from a serpentinite-hosted dyke.

Sample	E:2	E:4.5	E:7.5	E:20	E:44	E:53	E:75
Rock type	SRG	SRG	SRG	FPAG	FPAG	LAG	LAG
Distance from contact with serpentinite (cm)	2	4.5	7.5	20	44	53	75
Density	3.03	3.31	3.18	2.94	2.94	2.71	2.68
Wt. %							
SiO_2	37.82	43.72	45.45	61.10	67.31	68.75	69.90
TiO_2	0.52	0.23	0.21	0.39	0.32	0.32	0.45
Al_2O_3	14.66	11.62	9.29	12.96	14.27	15.70	14.54
Fe_2O_3	4.47	1.99	1.14	2.59	2.11	2.20	3.08
MnO	0.19	0.20	0.08	0.04	0.02	0.03	0.04
MgO	18.26	7.88	1.65	1.73	1.56	1.08	1.28
CaO	17.67	32.44	41.10	12.90	4.72	1.78	1.08
Na_2O	0.16	0.10	0.05	3.08	3.09	3.94	2.87
K_2O	0.04	0.01	0.00	4.56	6.11	5.60	5.93
P_2O_5	0.25	0.13	0.12	0.20	0.18	0.18	0.19
L.O.I.	6.26	1.59	0.64	0.24	0.24	0.50	0.62
ppm							
BaO	<d.l.	<d.l.	<d.l.	1271	1642	1469	1440
Ce	73	44	61	69	65	70	85
Cr_2O_3	56	<d.l.	<d.l.	21	17	29	23
Ni	45	23	12	19	20	14	21
Total	100.33	99.91	99.74	99.92	100.11	100.24	100.14
ppm							
Ga	6.4	7.1	6.9	14.4	13.9	16.5	16.5
Nb	14.4	12	12.4	16.2	12.9	11.5	16.5
Pb	1.5	1.1	6	19.7	22.4	20.6	21.5
Rb	4.5	2.4	2.6	96.3	125.7	132.6	186.3
Sr	14.9	16.3	22.2	340.9	399.1	431.2	333
Th	15.1	5.2	7.3	8.3	5.3	4.4	8.1
U	8.4	1.3	4.4	4	2.7	3.7	4.2
Y	33.7	24	21.2	24	20.7	22.4	26.3
Zr	252.6	121.9	109.9	162.8	157.4	162.2	191.9

Analyses by X-ray fluorescence. <d.l.: below detection limit.
SRG: strongly rodingitized granite, FPAG: feldspar-pyribole-altered granite, LAG: least altered granite.

Table 12. Mass changes resulting from alteration of granite assuming volume remained constant or Zr was immobile.

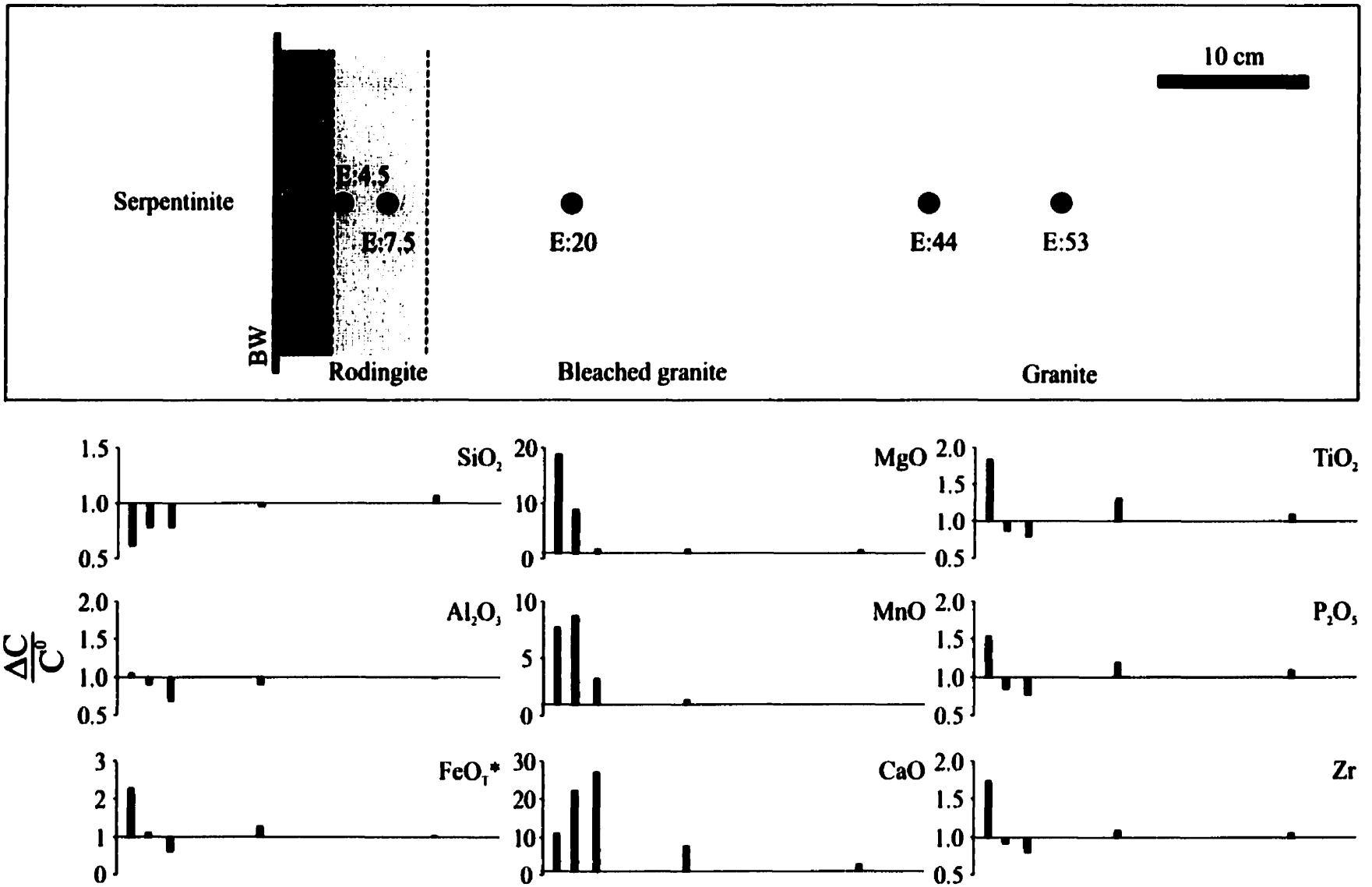
	Constant volume					
Sample	E:2	E:4.5	E:7.5	E:20	E:44	E:7.5
Precursor	E:53	E:53	E:53	E:53	E:53	E:20
Volume factor	1.00	1.00	1.00	1.00	1.00	1.00
Mass factor	1.12	1.22	1.17	1.08	1.08	1.08
Grams added-removed/100 grams precursor						
SiO_2	-26.46	-15.35	-15.42	-2.46	4.27	-11.94
TiO_2	0.27	-0.04	-0.07	0.10	0.03	-0.15
Al_2O_3	0.69	-1.51	-4.80	-1.64	-0.22	-2.91
FeOT	2.52	0.21	-0.78	0.55	0.08	-1.22
MnO	0.19	0.22	0.06	0.01	0.00	0.05
MgO	19.34	8.54	0.86	0.80	0.61	0.05
CaO	17.98	37.84	46.45	12.21	3.34	31.56
Na_2O	-3.76	-3.82	-3.88	-0.60	-0.59	-3.03
K_2O	-5.56	-5.59	-5.60	-0.65	1.03	-4.56
P_2O_5	0.10	-0.03	-0.04	0.04	0.02	-0.07
L.O.I.	6.50	1.44	0.25	-0.24	-0.24	0.45
ppm added-removed/100 grams precursor						
BaO	-1469.0	-1469.0	-1469.0	-90.1	312.4	-1271.0
Ce	11.6	-16.3	1.6	4.9	0.5	-3.0
Cr_2O_3	33.6	-29.0	-29.0	-6.2	-10.6	-21.0
Ni	36.3	14.1	0.1	6.6	7.7	-6.0
Ga	-9.3	-7.8	-8.4	-0.9	-1.4	-6.9
Nb	4.6	3.2	3.1	6.1	2.5	-2.8
Pb	-18.9	-19.3	-13.6	0.8	3.7	-13.2
Rb	-127.6	-129.7	-129.5	-28.1	3.8	-93.5
Sr	-414.5	-411.3	-405.1	-61.4	1.8	-316.9
Th	12.5	2.0	4.2	4.6	1.3	-0.4
U	5.7	-2.1	1.5	0.6	-0.8	0.8
Y	15.3	6.9	2.5	3.6	0.1	-1.1
Zr	120.2	-13.3	-33.2	14.4	8.6	-43.9

Table 12. (continued)

	Zr immobile					
Sample	E:2	E:4.5	E:7.5	E:20	E:44	E:7.5
Precursor	E:53	E:53	E:53	E:53	E:53	E:20
Volume factor	0.57	1.09	1.26	0.92	0.95	1.36
Mass factor	0.64	1.33	1.48	1.00	1.03	1.48
Grams added-removed/100 grams precursor						
SiO_2	-44.46	-10.58	-1.67	-7.88	0.61	6.23
TiO_2	0.02	-0.02	0.00	0.07	0.01	-0.07
Al_2O_3	-6.29	-0.24	-1.99	-2.79	-0.99	0.80
FeOT	0.60	0.40	-0.47	0.34	-0.02	-0.81
MnO	0.10	0.24	0.09	0.01	0.00	0.08
MgO	10.65	9.41	1.36	0.64	0.53	0.71
CaO	9.57	41.38	58.88	11.07	3.08	47.98
Na_2O	-3.84	-3.81	-3.87	-0.87	-0.76	-3.01
K_2O	-5.57	-5.59	-5.60	-1.06	0.70	-4.56
P_2O_5	-0.02	-0.01	-0.01	0.02	0.01	-0.02
L.O.I.	3.52	1.62	0.44	-0.26	-0.25	0.71
ppm added-removed/100 grams precursor						
BaO	-1469.0	-1469.0	-1469.0	-202.7	223.1	-1271.0
Ce	-23.1	-11.5	20.0	-1.3	-3.0	21.4
Cr_2O_3	7.0	-29.0	-29.0	-8.1	-11.5	-21.0
Ni	14.9	16.6	3.7	4.9	6.6	-1.2
Ga	-12.4	-7.1	-6.3	-2.2	-2.2	-4.2
Nb	-2.3	4.5	6.8	4.6	1.8	2.2
Pb	-19.6	-19.1	-11.7	-1.0	2.5	-10.8
Rb	-129.7	-129.4	-128.8	-36.7	-3.1	-92.4
Sr	-421.6	-409.5	-398.4	-91.6	-19.9	-308.0
Th	5.3	2.5	6.4	3.9	1.1	2.5
U	1.7	-2.0	2.8	0.3	-0.9	2.5
Y	-0.8	9.5	8.9	1.5	-1.1	7.4
Zr	0	0	0	0	0	0

Figure 5

Diagram showing the location of samples of granite (E:45), granite affected by feldspar-pyribole alteration (E:40, E:20) and rodingitized granite (E:7.5, E:4.5, E:2) collected near the contact of a dyke with serpentinite. Also shown are diagrams illustrating the changes in the concentrations of SiO_2, Al_2O_3, FeO, MgO, MnO, CaO, TiO_2, P_2O_5, and Zr that resulted from the alteration of granite with respect to the distance from the contact with serpentinite.


10 cm
Serpentinite
E:4.5
E:7.5
BW
Rodingite
E:20
Bleached granite
E:44
E:53
Granite
ΔC/C°
SiO2
MgO
TiO2
Al2O3
MnO
P2O5
FeOT*
CaO
Zr

(E:7.5) produced a very Ca-rich rock according to the reaction:

GRANITE

$K_{0.118}Na_{0.128}Ca_{0.032}Mg_{0.027}Fe_{0.028}Al_{0.308}Ti_{0.004}Si_{1.144}O_{2.996}H_{0.056}$

$+ 0.825Ca^{2+} + 0.001Mn^{2+} + 0.021Mg^{2+} + 0.585H_2O$

=

RODINGITE

$Na_{0.002}Ca_{0.857}Mg_{0.048}Mn_{0.001}Fe_{0.017}Al_{0.214}Ti_{0.003}Si_{0.885}O_{3.063}H_{0.084}$

$+ 0.118K^+ + 0.126Na^+ + 0.011Fe^{2+} + 0.094Al^{3+} + 0.001Ti^{4+} + 0.259SiO_2^\circ + 1.142H^+$ (8).

It is interesting to note that the identity and proportions of the elements added to form rodingite are similar for granite and slate. Next to Ca, Mn was the most enriched in the rodingites formed by replacement of the felsic intrusive rocks and slate. The enrichment is explained by the affinity of garnet and clinopyroxene for this component. The same explanation holds, to a lesser extent, for Ti, and, generally, for Fe.

Rodingitized serpentinite (nephrite and diopsidite)

The compositions of three samples of antigorite-rich serpentinite (H1281-40, H1281-47 and NEPH-2), three samples of nephrite (NEPH-1, JMH-164B and JMH-341) and two samples of diopsidite (JMH-117, JMH-164D1 and JMH-164D2) were compared with those of 23 samples of ore-bearing lizardite-chrysotile serpentinite from diamond drill hole H1281 (Table 13, Appendix III) in order to evaluate mass changes accompanying calc-silicate alteration of serpentinite (Table 14).

Serpentinites contain few immobile trace elements that can be used to evaluate mass changes during alteration. As noted earlier, Cr_2O_3 and Ni concentrations are much too low in the nephrites and diopsidites compared to those in serpentinite to be considered immobile. However, this dilution effect is not evident in the antigorite-rich serpentinites, and, because tremolite replaced antigorite pseudomorphically in the nephrite, constant volume replacement was assumed. Mass changes resulting from the

Table 13. Chemical composition of serpentinites, nephrites and diopsidites.

Sample	Average of 23 analyses		H1281-40	H1281-47
Rock type	Serpentinized harzburgite		AS	AS
Distance from contact with dyke (cm)	—		—	—
Density	2.6*		n.d	n.d
Wt. %		(± 1 σ)		
SiO_2	38.41	1.41	45.39	44.32
TiO_2	0.01	0.00	0.02	0.01
Al_2O_3	0.38	0.10	1.72	0.52
Fe_2O_3	6.96	2.62	7.26	5.34
MnO	0.09	0.01	0.12	0.10
MgO	39.70	1.23	34.05	37.68
CaO	0.01	0.02	1.49	0.08
Na_2O	0.02	0.04	0.05	<d.l.
K_2O	0.01	0.00	0.24	0.01
P_2O_5	0.01	0.00	0.01	0.01
L.O.I.	13.81	0.80	9.60	11.28
ppm				
Co	114	8	112	104
Cr_2O_3	4001	326	3171	3781
Cu	25	12	64	32
Ni	2533	138	2175	2389
Zn	68	5	89	111
Total ppm				
Nb	1.2	0.3	<d.l.	<d.l.
Pb	1.0	1.1	<d.l.	<d.l.
Rb	0.9	0.2	<d.l.	<d.l.
Sr	6.1	1.7	<d.l.	<d.l.
Th	2.3	2.8	<d.l.	<d.l.
Y	1.2	0.2	<d.l.	<d.l.
Zr	0.7	0.3	<d.l.	<d.l.

Analyses by X-ray fluorescence. <d.l.: below detection limit.
n.d.: not determined. *: average density of serpentinites (Diment, 1964).
AS: antigorite-rich altered serpentinite, N: nephrite,
D: diopsidite, R: rodingitized felsic dyke.

Table 13. (continued)

Sample	JMH-341	JMH-117	NEPH-2	NEPH-1
Rock type	N	D	AS	N
Distance from contact with dyke (cm)	5	10	10	4.5
Density	3.01	3.19	2.65	3
Wt. %				
SiO_2	55.59	54.33	49.54	56.02
TiO_2	0.01	0.01	0.01	0.02
Al_2O_3	1.11	0.33	0.10	0.78
Fe_2O_3	4.48	4.83	5.04	6.67
MnO	0.12	0.07	0.03	0.17
MgO	22.06	16.59	35.02	20.80
CaO	14.23	22.32	0.63	12.52
Na_2O	0.20	0.20	0.02	0.15
K_2O	0.08	0.07	0.04	0.26
P_2O_5	0.01	0.01	0.01	0.01
L.O.I.	2.31	0.62	9.13	2.16
ppm				
Co	n.d.	n.d.	105	56
Cr_2O_3	1670	2610	3587	2433
Cu	n.d.	n.d.	n.d.	n.d.
Ni	1175	1524	2256	1381
Zn	n.d.	n.d.	n.d.	n.d.
Total ppm				
Nb	<d.l.	<d.l.	5.3	5.5
Pb	<d.l.	<d.l.	<d.l.	<d.l.
Rb	<d.l.	<d.l.	1.4	17.1
Sr	<d.l.	<d.l.	4.4	24.2
Th	<d.l.	<d.l.	<d.l.	<d.l.
Y	<d.l.	<d.l.	4.8	6.1
Zr	<d.l.	<d.l.	<d.l.	<d.l.

Analyses by X-ray fluorescence. <d.l.: below detection limit.
n.d.: not determined. *: average density of serpentinites (Diment, 1964).
AS: antigorite-rich altered serpentinite, N: nephrite,
D: diopsidite, R: rodingitized felsic dyke.

Table 13. (continued)

Sample	JMH-164B	JMH-164D1	JMH-164D2	JMH-164D3
Rock type	N	N(D)	D	R
Distance from contact with dyke (cm)	25	10	3	—
Density	2.96	3.11	3.25	n.d.
Wt. %				
SiO_2	55.61	53.34	52.48	43.64
TiO_2	0.01	0.01	0.03	0.23
Al_2O_3	0.98	2.12	2.26	23.27
Fe_2O_3	4.69	3.70	4.91	1.16
MnO	0.18	0.22	0.22	0.06
MgO	23.16	19.21	14.25	2.48
CaO	12.06	19.30	24.56	25.81
Na_2O	0.05	0.34	0.44	0.37
K_2O	0.14	0.49	0.09	0.01
P_2O_5	0.01	0.01	0.01	0.13
L.O.I.	3.05	1.46	0.10	3.06
ppm				
Co	n.d.	n.d.	n.d.	n.d.
Cr_2O_3	1321	1675	3446	35
Cu	n.d.	n.d.	n.d.	n.d.
Ni	785	861	1426	47
Zn	n.d.	n.d.	n.d.	n.d.
Total ppm				
Nb	<d.l.	<d.l.	<d.l.	<d.l.
Pb	<d.l.	2.3	3.7	10
Rb	<d.l.	46	9.3	5.9
Sr	<d.l.	19.3	20.8	3550.2
Th	<d.l.	5	6.3	20.4
Y	<d.l.	<d.l.	<d.l.	17
Zr	<d.l.	<d.l.	<d.l.	109.3

Analyses by X-ray fluorescence. <d.l.: below detection limit.
n.d.: not determined. *: average density of serpentinites (Diment, 1964).
AS: antigorite-rich altered serpentinite, N: nephrite,
D: diopsidite, R: rodingitized felsic dyke.

Table 14. Mass changes that resulted from alteration of serpentinite assuming volume remained constant or Cr_2O_3 immobile.

	Constant volume					
Sample	NEPH-2	NEPH-1	JMH-164B	JMH-164D1	JMH-164D2	JMH-164D2
Precursor	Avg. serp.	Avg. serp.	Avg. serp.	Avg. serp.	Avg. serp.	JMH-164B
Volume factor	1.00	1.00	1.00	1.00	1.00	1.00
Mass factor	1.02	1.15	1.14	1.20	1.25	1.10
Grams added-removed/100 grams precursor						
SiO_2	12.08	26.22	24.90	25.39	27.19	2.01
TiO_2	0.00	0.01	0.01	0.01	0.03	0.02
Al_2O_3	-0.27	0.52	0.74	2.16	2.45	1.50
FeO^T	-1.64	0.66	-1.46	-2.28	-0.74	0.63
MnO	-0.05	0.11	0.11	0.18	0.18	0.06
MgO	-4.01	-15.70	-13.34	-16.73	-21.89	-7.51
CaO	0.63	14.44	13.72	23.08	30.69	14.91
Na_2O	0.00	0.15	0.04	0.38	0.53	0.43
K_2O	0.03	0.29	0.15	0.58	0.10	-0.04
P_2O_5	0.00	0.00	0.00	0.00	0.00	0.00
L.O.I.	-4.51	-11.32	-10.34	-12.06	-13.69	-2.94
ppm added-removed/100 grams precursor						
Co	-6.7	-49.1	n.d.	n.d.	n.d.	n.d.
Cr_2O_3	-345.1	-1193.8	-2497.2	-1997.6	306.4	2462.6
Ni	-234.1	-940.0	-1639.7	-1503.5	-750.9	780.7
Nb	4.2	5.2	n.d.	n.d.	n.d.	n.d.
Pb	n.d.	n.d.	n.d.	1.8	3.6	4.1
Rb	0.5	18.8	n.d.	54.1	10.7	10.2
Sr	-1.6	21.8	n.d.	17.0	19.9	22.8
Th	n.d.	n.d.	n.d.	3.7	5.6	6.9
Y	3.7	5.9	n.d.	n.d.	n.d.	n.d.

Avg. serp.: average of 23 analyses of serpentinite. n.d.: not determined.

Table 14. (continued)

	Cr_2O_3 immobile					
Sample	NEPH-2	NEPH-1	JMH-164B	JMH-164D1	JMH-164D2	JMH-164D2
Precursor	Avg. serp.	Avg. serp.	Avg. serp.	Avg. serp.	Avg. serp.	JMH-164B
Volume factor	1.09	1.43	2.66	2.00	0.93	0.35
Mass factor	1.12	1.64	3.03	2.39	1.16	0.38
Grams added-removed/100 grams precursor						
SiO_2	16.84	53.71	130.02	89.00	22.52	-35.49
TiO_2	0.00	0.02	0.03	0.02	0.03	0.00
Al_2O_3	-0.26	0.91	2.59	4.69	2.25	-0.11
FeO^T	-1.21	3.60	6.52	1.69	-1.14	-2.81
MnO	-0.05	0.19	0.45	0.45	0.16	-0.09
MgO	-0.64	-5.50	30.44	6.18	-23.16	-17.70
CaO	0.69	20.58	36.52	46.09	28.51	-2.65
Na_2O	0.00	0.22	0.13	0.79	0.49	0.12
K_2O	0.03	0.42	0.41	1.16	0.09	-0.11
P_2O_5	0.00	0.01	0.01	0.01	0.00	0.00
L.O.I.	-3.63	-10.26	-4.57	-10.32	-13.70	-3.01
ppm added-removed/100 grams precursor						
Co	3.4	-21.6	n.d.	n.d.	n.d.	n.d.
Cr_2O_3	0	0	0	0	0	0
Ni	-17.0	-262.3	-155.8	-476.7	-877.7	-238.4
Nb	4.7	7.9	n.d.	n.d.	n.d.	n.d.
Pb	n.d.	n.d.	n.d.	4.5	3.3	1.4
Rb	0.7	27.2	n.d.	109.0	9.9	3.6
Sr	-1.2	33.7	n.d.	40.0	18.0	8.0
Th	n.d.	n.d.	n.d.	9.7	5.1	2.4
Y	4.2	8.9	n.d.	n.d.	n.d.	n.d.

Avg. serp.: average of 23 analyses of serpentinite. n.d.: not determined.

formation of a calc-silicate alteration halo in serpentinite adjacent to a rodingitized felsic dyke (Table 13) were calculated for a nephrite (JMH-164B: 68 vol. % tremolite, 28 vol. % serpentine, and 4 vol. % diopside) and two diopsidites (JMH-164D1; JMH-164D2 > 98 vol. % diopside) relative to an average value for the 23 samples of serpentinite, and are illustrated in Figure 6. The overall reaction for conversion of 100 grams of serpentinite to 114 grams of nephrite (JMH-164B) is:

SERPENTINITE

$$Mg_{0.985}Mn_{0.001}Fe_{0.087}Ni_{0.004}Al_{0.008}Cr_{0.006}Si_{0.639}O_{3.143}H_{1.534}$$
$$+ 0.004K^{+} + 0.002Na^{+} + 0.241Ca^{2+} + 0.002Mn^{2+} + 0.014Al^{3+} + 0.397SiO_2^{\circ} + 0.21H^{+}$$
$$=$$

NEPHRITE

$$K_{0.004}Na_{0.002}Ca_{0.241}Mg_{0.643}Mn_{0.003}Fe_{0.066}Ni_{0.001}Al_{0.022}Cr_{0.002}Si_{1.036}O_{3.254}H_{0.378}$$
$$+ 0.342Mg^{2+} + 0.021Fe^{2+} + 0.003Ni^{2+} + 0.004Cr^{3+} + 0.683H_2O \qquad (9).$$

Because diopside replaced tremolite at the contact with the dyke during a later stage of alteration, the mass changes resulting from the formation of diopsidite may be more accurately represented by the overall reaction for conversion of 100 grams of nephrite (JMH-164B) to 110 grams of diopsidite (JMH-164D2):

NEPHRITE

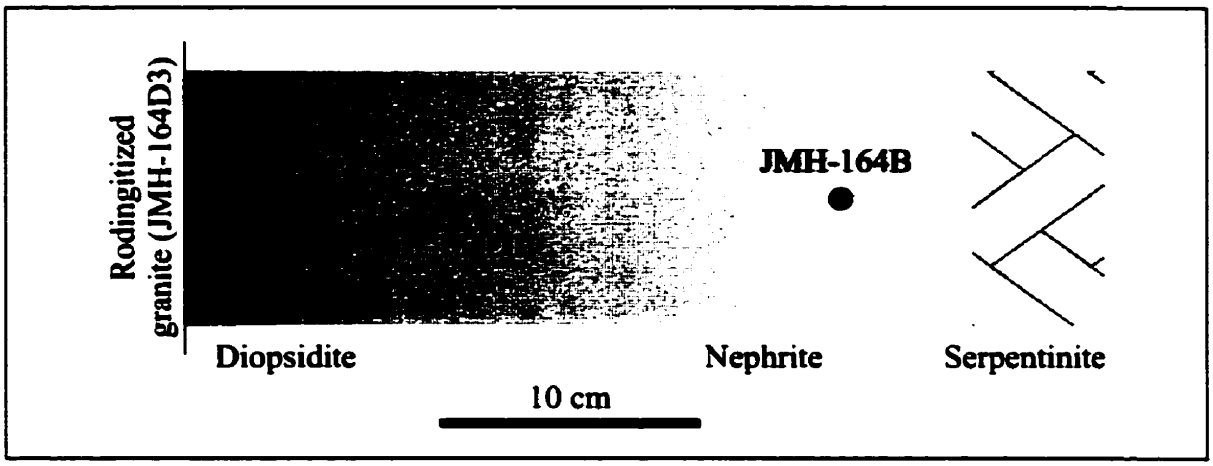
$$K_{0.002}Na_{0.002}Ca_{0.215}Mg_{0.574}Mn_{0.002}Fe_{0.059}Ni_{0.001}Al_{0.02}Cr_{0.002}Si_{0.925}O_{2.905}H_{0.338}$$
$$+ 0.014Na^{+} + 0.274Ca^{2+} + 0.001Mn^{2+} + 0.01Fe^{2+} + 0.002Ni^{2+} + 0.03Al^{3+} + 0.004Cr^{3+} +$$
$$0.05SiO_2^{\circ} + 0.003H_2O$$
$$=$$

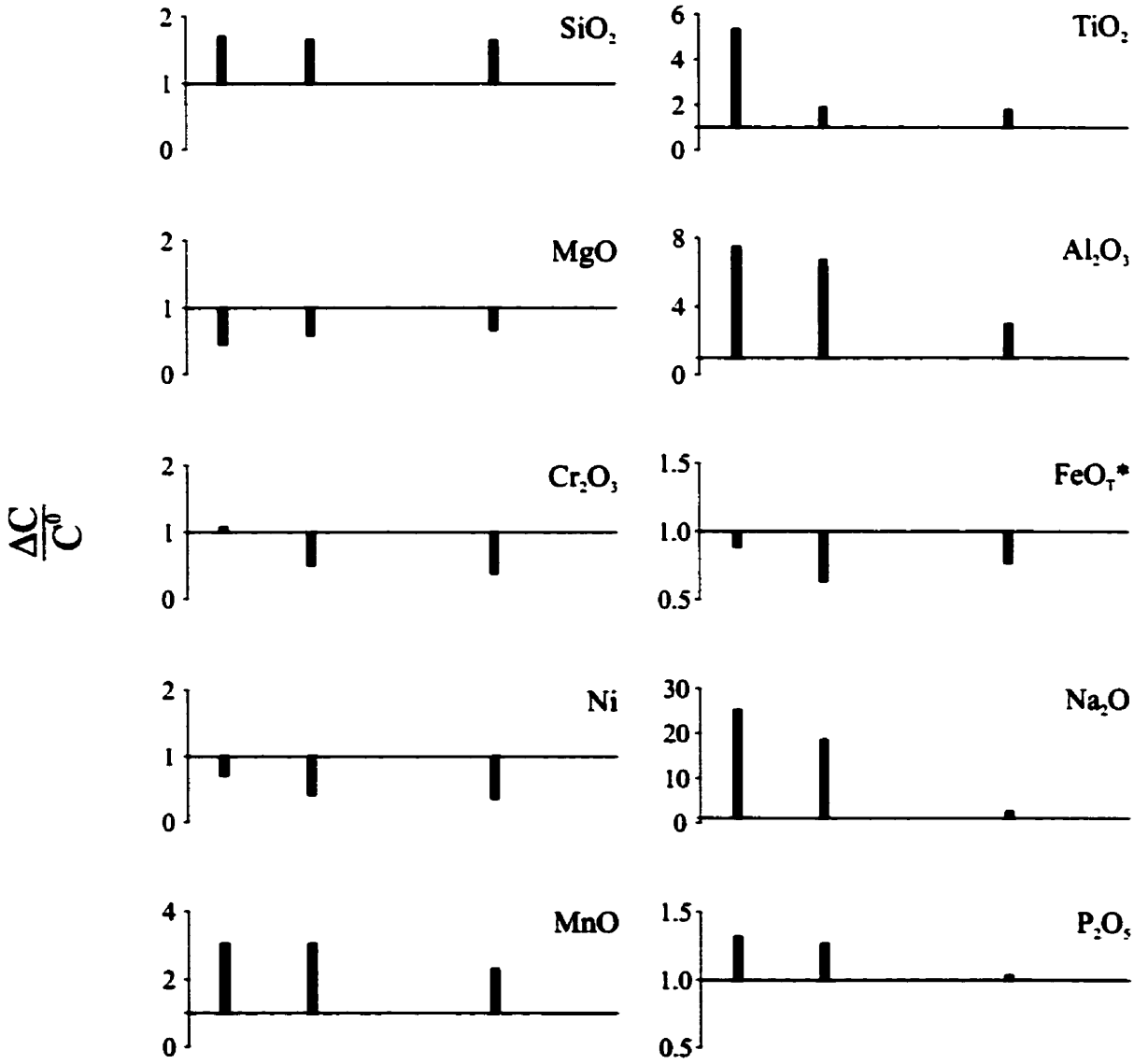
DIOPSIDITE

$$K_{0.002}Na_{0.016}Ca_{0.489}Mg_{0.395}Mn_{0.003}Fe_{0.069}Ni_{0.003}Al_{0.05}Cr_{0.006}Si_{0.975}O_{3.008}H_{0.012}$$
$$+ 0.179Mg^{2+} + 0.332H^{+} \qquad (10).$$

Figure 6

Diagram showing the location of samples of nephrite (JMH-164B and JMH-164D1) and diopsidite (JMH-164D2) collected near the contact of serpentinite with a rodingitized dyke. Also shown are diagrams illustrating the changes in the concentrations of SiO_2, MgO, Cr_2O_3, Ni, MnO, TiO_2, Al_2O_3, FeO, Na_2O, and P_2O_5 that resulted from the alteration of serpentinite with respect to the distance from the contact with the rodingitized dyke.


Rodingitized granite (JMH-164D3)
JMH-164B
Diopsidite
Nephrite
Serpentinite
10 cm


$\frac{\Delta C}{C_0}$
SiO_2
TiO_2
MgO
Al_2O_3
Cr_2O_3
FeO_T*
Ni
Na_2O
MnO
P_2O_5

Small numbers of green garnet crystals, many containing a core of chromite (see Wares and Martin, 1980a), were formed during replacement of tremolite by diopside. This explains the enrichment in Cr_2O_3, Al_2O_3, Na_2O and K_2O, which originated from the adjacent felsic intrusive, were concentrated in small proportions in the amphibole and to a greater extent in the pyroxene.

Vesuvianite-rich veins

The chemical composition of the vesuvianite-rich rocks contrasts with that of the other types of rodingite. Vesuvianite-rich rodingites at Asbestos are characterized by low or very low Ga, Zr, Nb, Y, TiO_2, and P_2O_5 contents (Table 15). These low values, the fact that the rocks are extremely vuggy, the stockwork nature and local evidence of extension normal to the "veins" all suggest that these rocks are of hydrothermal origin. Pods of grossular-rich rodingite containing high Zr and P_2O_5 (Table 15), which occur in the vesuvianite "veins", probably represent remnants of felsic dykes along which the hydrothermal solutions that deposited the vesuvianite circulated.

DISCUSSION

Rodingites in the JM Asbestos deposit were described briefly by Olsen (1961), Riordon (1975) and Hébert (1980), and studied in detail by De (1961, 1972) and Wares and Martin (1980a, b). Individual minerals or mineral occurrences were described in some detail by Grice and Williams (1979), Chamberlain (1980), Grice and Gasparrini (1981), and Grice and Robinson (1984), but no detailed information on parageneses were provided. De (1961, 1972) suggested that the rodingites formed as a result of elevated H_2O pressures in the felsic dykes during their emplacement in the serpentinites. He proposed that, during magmatic crystallization of the diorites, biotite crystallized in place of amphibole, and that this process resulted in the concentration of calcium in the residual

Table 15. Chemical composition of vesuvianite-rich "veins".

	Vesuvianite-rich "veins"			Dyke lens*
Sample	Flt-G	JMH-158	JMH-277	JMH-262
Wt. %				
SiO_2	39.74	38.42	40.87	35.93
TiO_2	0.059	0.048	0.039	0.558
Al_2O_3	22.18	17.8	15.4	19.91
Fe_2O_3	0.35	1.76	1.57	2.59
MnO	0.046	0.125	0.117	0.076
MgO	0.31	3.47	5.27	2.13
CaO	36.63	36.34	34.51	35.92
Na_2O	0.14	0.04	0.08	0.01
K_2O	0.10	<d.l.	0.05	<d.l.
P_2O_5	0.136	0.029	0.091	0.23
L.O.I.	0.33	1.72	0.88	2.39
ppm				
BaO	20	<d.l.	29	<d.l.
Ce	15	<d.l.	28	111
Co	<d.l.	<d.l.	12	<d.l.
Cr_2O_3	<d.l.	111	<d.l.	21
Ni	9	77	37	32
Total	100.03	99.77	100.1	99.76
ppm				
Ga	12	8.4	6.7	2.9
Nb	12.4	3.8	11.1	21.4
Pb	<d.l.	1.3	2	2.5
Rb	2.2	2.4	2.2	2.6
Sr	9.2	12	26.1	9.4
Th	1.7	1.7	2.1	15.5
U	4.2	<d.l.	3.7	3.7
Y	11.1	4.9	11.3	50.5
Zr	21	1	20.7	316.3

Analyses by X-ray fluorescence. <d.l.: below detection limit.
*Fine-grained, grossular-rich, lens-shaped inclusion from a vesuvianite vein.

liquid, thus permitting the formation of the calc-silicate assemblages. Similarly, he proposed that the rodingitization of the granitic rocks resulted from the interaction with a Ca-rich residual fluid left after the magmatic crystallization of Ca-poor plagioclase. However, De's (1961, 1972) proposed mechanism for the rodingitization of the felsic intrusive rocks could not explain the occurrence of calc-silicate assemblages in metasediments at the contact with serpentinites, which are similar to those in the intrusive rocks. Instead, De (1968) suggested that the rodingitization of these metasediments at the footwall contact of the Asbestos ophiolite occurred as a result of the local redistribution of chemical species during metamorphism. Wares and Martin (1980a, b) suggested that the calcium enrichment in the rodingitized dyke rocks and adjacent serpentinites at the JM Asbestos mine was the result of the interaction of these rocks with Ca-bearing fluids derived from the serpentinites. However, they did not offer an interpretation for the origin of the rodingitized slates.

Our petrographic evidence clearly indicates that the felsic intrusive rocks were completely solidified before feldspar-pyribole and, consequently, rodingitic alteration. From these premises, it is concluded that rodingitization was entirely due to post-magmatic hydrothermal processes. In the next sections, we use the mass balance calculations to evaluate the chemical controls responsible for alteration of slate, felsic intrusive rocks and serpentinite. We also discuss the implications of these calculations for the mobility of sparingly soluble high-field-strength elements (HFSE) and the origin of the calcium responsible for rodingitization.

Chemical controls of albitization and rodingitization

Alteration of Si-rich lithologies: example from the slates

It is readily apparent, without further calculation, that the mass of sodium required to form the albitized slate could not have been contributed solely by the slate. A large amount of Na was required from an external source, and was almost certainly introduced by the metasomatizing fluid. The microthermometric study of fluid inclusions in the rodingitized slate revealed that the metasomatizing fluid was a reducing (CH_4-rich, no CO_2 detected), NaCl-rich (up to 4.3 *m* NaCl eq.) brine, and that rodingitization occurred

at temperatures between 290 and 344°C and pressures between 1.7 and 2.7 kilobars (Chapter VI). Such reducing brines could induce albitization and loss of calcium through reactions like:

$$5\text{Chlorite} + 5\text{Muscovite} + 4\text{Calcite} + 61\text{Quartz} + 20Na^{+} \rightarrow$$
$$5\text{Biotite} + 2\text{Tremolite} + 20\text{Albite} + 4\text{Graphite} + 20H^{+} + 8H_2O + 4O_2\downarrow \quad (11),$$

$$\text{Calcite} + 2H^{+} + H_2O \rightarrow Ca^{2+} + CH_4 + 2O_2\downarrow \quad (12)$$

and

$$\text{Graphite} + 2H_2O \rightarrow CH_4 + O_2\downarrow \quad (13)$$

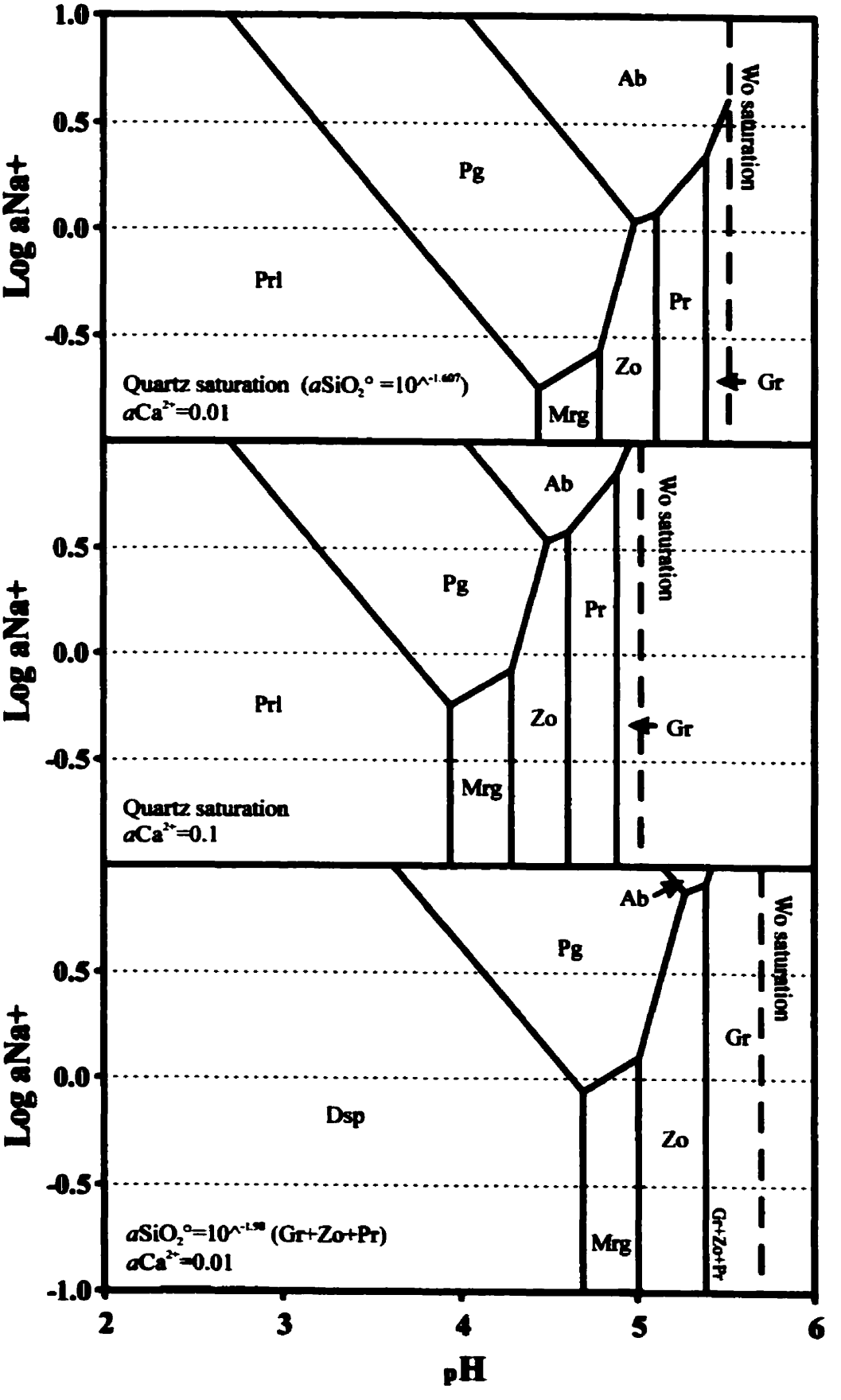
which explain satisfactorily the change in mineralogy and bulk composition of the rocks during albitization and the loss of carbon. Rodingitization of slate involved mainly the addition of Ca and the loss of Na and release of H^{+} as a result of the replacement of albite by Ca-Al-silicates. This suggests that there was a gradient of increasing pH and decreasing $a\text{SiO}_2^{\circ}$ towards the contact with serpentinite. With increasing pH, the aNa^{+} of fluids necessary to maintain saturation with Na-bearing silicates increases, and, for a fixed value of aNa^{+}, calc-silicates are stabilized at the expense of Na-bearing silicates. At high values of pH and low values of $a\text{SiO}_2^{\circ}$, extremely Na-rich solutions are necessary to stabilize Na-bearing silicates as illustrated by the Al-conservative overall reaction for the replacement of albite by grossular

$$2\text{NaAlSi}_3O_8 + 2H_2O + 3Ca^{2+} = Ca_3Al_2Si_3O_{12} + 2Na^{+} + 4H^{+} + 3\text{SiO}_2^{\circ} \quad (14),$$

and in Figure 7. At a temperature of 325°C and a pressure of 2 kilobars, the activity of SiO_2° in fluids in equilibrium with serpentine-group minerals and brucite is buffered at ~ 2.7 log units below the value at saturation with quartz if $aH_2O=1$ (calculated with the

Figure 7

pH versus log $a\mathrm{Na}^{+}$ equilibrium relationships among diaspore (Dsp), pyrophyllite (Prl), paragonite (Pg), albite (Ab), margarite (Mrg), zoisite (Zo), prehnite (Pr), grossular (Gr), and wollastonite at a temperature of 325°C and a pressure of 2 kilobars under conditions where: A) $a\mathrm{Ca}^{2+} = 0.01$ and the fluid is saturated with respect to quartz, B) $a\mathrm{Ca}^{2+} = 0.1$ and the fluid is saturated with respect to quartz, and C) $a\mathrm{Ca}^{2+} = 0.01$ and the activity of $SiO_2°$ is buffered by the assemblage zoisite + prehnite + grossular.


1.0
0.5
0.0
-0.5
-1.0
Log aNa+
Ab
Pg
Prl
Pr
Zo
Gr
Mrg
Wo saturation
Quartz saturation ($aSiO_2° = 10^{-1.607}$)
aCa^{2+}=0.01
Quartz saturation
aCa^{2+}=0.1
Dsp
$aSiO_2° = 10^{-1.98}$ (Gr+Zo+Pr)
aCa^{2+}=0.01
Gr+Zo+Pr
2
3
4
5
6
pH

thermodynamic database in the SUPCRT92 software package: Johnson et al., 1992). At close to saturation with diopside, the pH of the fluids would be > 7 in the system Ca-Mg-Si-O-H-Na-Cl (the value depends on the salinity and the Na/Cl ratio). Such serpentinite-derived fluids would offer a large potential for rodingitization while producing a fluid in which $a\mathrm{Na}^+$ increases. Although not all the Na required to form the albitized slate would have been provided by such a process, the excess Na resulting from the latter would nevertheless have been necessary to trigger albitization between rodingite and slate. With progress of reaction, the two reaction fronts, i.e., the rodingitization and albitization fronts, advanced within the slates, such that rodingite replaced albitite close to the contact with serpentinite.

Calc-silicate metasomatic alteration of serpentinite

Reaction 9 indicates that a source of silica and calcium was required, and that a significant proportion of magnesium was removed during transformation of serpentinite to nephrite. The most obvious source for the silica is the adjacent felsic intrusive rocks. The presence of blackwall-type alteration haloes in some of the felsic dykes adjacent to serpentinite suggest that the Mg removed from the serpentinite during Ca-metasomatism was, under some circumstances, transferred to the margin of the dykes. However, blackwalls are not everywhere present. Furthermore, the minor proportion of Mg calculated to have been added to form rodingites does not balance the large amount of Mg lost as a result of the formation of the thick, adjacent nephrite haloes. The series of samples JMH-164B, JMH-164D1 and JMH-164D2, which characterize the calc-silicate alteration of serpentinite over a thickness of 30 cm adjacent to a rodingitized granitic rock (JMH-164D3, identity of the protolith uncertain), exemplify the chemical changes accompanying nephrite formation. The amount of MgO released along a 30 cm long column, perpendicular to the contact of the above mentioned rodingitized dyke, and represented by cubes of serpentinite replaced by nephrite 1 cm on the side is ~ 15 grams, representing ~ 15 wt. % of the total original mass. No blackwall formed in the adjacent rodingite (JMH-164D3), which contains only 2.5 wt. % MgO, a concentration that is only marginally higher than that in most of the granitic-granodioritic rocks, and below that in

the majority of the monzodioritic-dioritic rocks. Therefore, MgO appears to have been transported beyond the actual site of sampling. Transport by diffusion appears unlikely in this case. The same behaviour is displayed by Cr_2O_3, which was removed from the serpentinites during calc-silicate alteration, but was not re-deposited in the adjacent rodingitized felsic intrusive rocks (40 ppm, in JMH-164D3) or in the blackwall-altered felsic intrusive rocks (see below). To avoid precipitation of Mg in the dykes, or formation of blackwall, the direction of fluid flow or the vector of decreasing Mg solubility during alteration must have been oriented perpendicular to serpentinite-dyke contacts and from dyke to serpentinite.

Implications of inferred fluid/rock ratios during rodingitization

Inspection of reactions 5, 6, 7, and 8 reveals that SiO_2, Al_2O_3, Na_2O, and K_2O were removed from the rocks by the fluids responsible for rodingitization. The mass balance calculations indicate that the SiO_2 and Al_2O_3 losses per 100 grams of precursor corresponding to these reactions were 3.8, 6.1, 1.4, and 15.4 grams, and 4.9, 0.2, 4.8, and 4.8 grams, respectively. In the presence of the assemblage grossular + diopside + zoisite + prehnite (e.g., sample JMH-25.2), the solubility of SiO_2 in aqueous fluids at temperatures below 350°C and pressures below 3 kilobars (Chapter VI), is < 1 g per kg H_2O. This suggests water/rock mass ratios of ≤ 14 to 154. If effects of diffusion are ignored, the large amounts of Al_2O_3 removed according to reactions 5, 6 and 8 would be an indication that even higher water/rock ratios would have been involved if the transfer of mass during alteration occurred strictly via an advecting fluid.

Numerous lines of evidence suggest that calc-silicate alteration was the result, at least in part, of transport of material by advection through hydrothermal fluids. These include the presence of veins, the swelling of blackwall alteration fronts where veins in dykes meet perpendicularly with the contact with serpentinite, the strong dilution of Zr and P in the dikes and Cr and Ni in the serpentinites, the very large amount of Ca added, and the strong oscillatory zoning (Yardley et al., 1991) in the diopside in rodingitized slate. Most likely, fractures and lithological contacts, especially the strongly sheared ones, acted as the main focus of fluid flow and element transport, while diffusion became

increasingly important away from these zones. This may be reflected by the restriction of the strong oscillatory zoning of diopside in rodingitized slate near the contact with intensely sheared serpentinites at the base of the Asbestos ophiolite, and near the margins of the veins. Numerous authors have estimated that integrated metamorphic fluid fluxes along lithological contacts, whether they are sheared or not, maybe as high as 10^6 cm^3/cm^2 (see Ferry and Gerdes, 1998). Such elevated fluid fluxes would translate into large fluid/rock ratios and would be consistent with the large fluid/rock ratios estimated in this paper for advective mass transport.

Mobility of the trace elements and P_2O_5

There are very clear dilution trends of Zr and P_2O_5 with progressive rodingitization of slate, granite and diorite. This can be interpreted in three ways. Firstly, that these components were mobile. Secondly, that these components remained effectively immobile and that the volume increased by up to 50 % during rodingitization, or, finally, that all the rodingites formed only in a "special", low-Zr and low-P_2O_5 facies of the intrusives (e.g., monzodiorites; c.f. Chapter IV). The sharp drop in Zr concentrations within one dyke between mildly rodingitized and strongly rodingitized rocks of similar textures located at the same distance from the contact with serpentinite and the absence of chilled margins argue against the latter (Figure 8). This dilution effect is even more intensively developed for Cr_2O_3 and Ni during alteration of serpentinite to nephrite and diopsidite, where mass factors up to above 3 (JMH-164B) would characterize alteration, if these components had remained immobile.

The good correlations between Zr and P_2O_5 in the fresh and altered slate, diorite and granite, and between Cr_2O_3 and Ni in the serpentinite and its calc-silicate-rich alteration products, and projection of this correlation through the origin on binary diagrams (Figure 9) have important implications. These observations indicate that the fluids responsible for alteration remained consistently, or became repeatedly, undersaturated with respect to the minerals that carried these components, and that the rates of dissolution of these minerals (zircon, monazite and apatite in the dykes; chromite and Mg-rich silicates in the serpentinites) were very similar.

Figure 8

The variation of Zr concentration in a 3.84 m wide diorite dyke versus distance from footwall contact with serpentinite. Differences in Zr concentration between samples that were least affected (solid circles) and mildly to moderately affected (grey circles) by Ca-metasomatism reflect magmatic fractionation (solid line). The strongly rodingitized samples of diorite (open circles) are strongly depleted in Zr (dashed line), indicating that a substantial proportion of the zircon in the rock, the essential carrier of the Zr, was dissolved along the zones where rodingitization had been most intense.

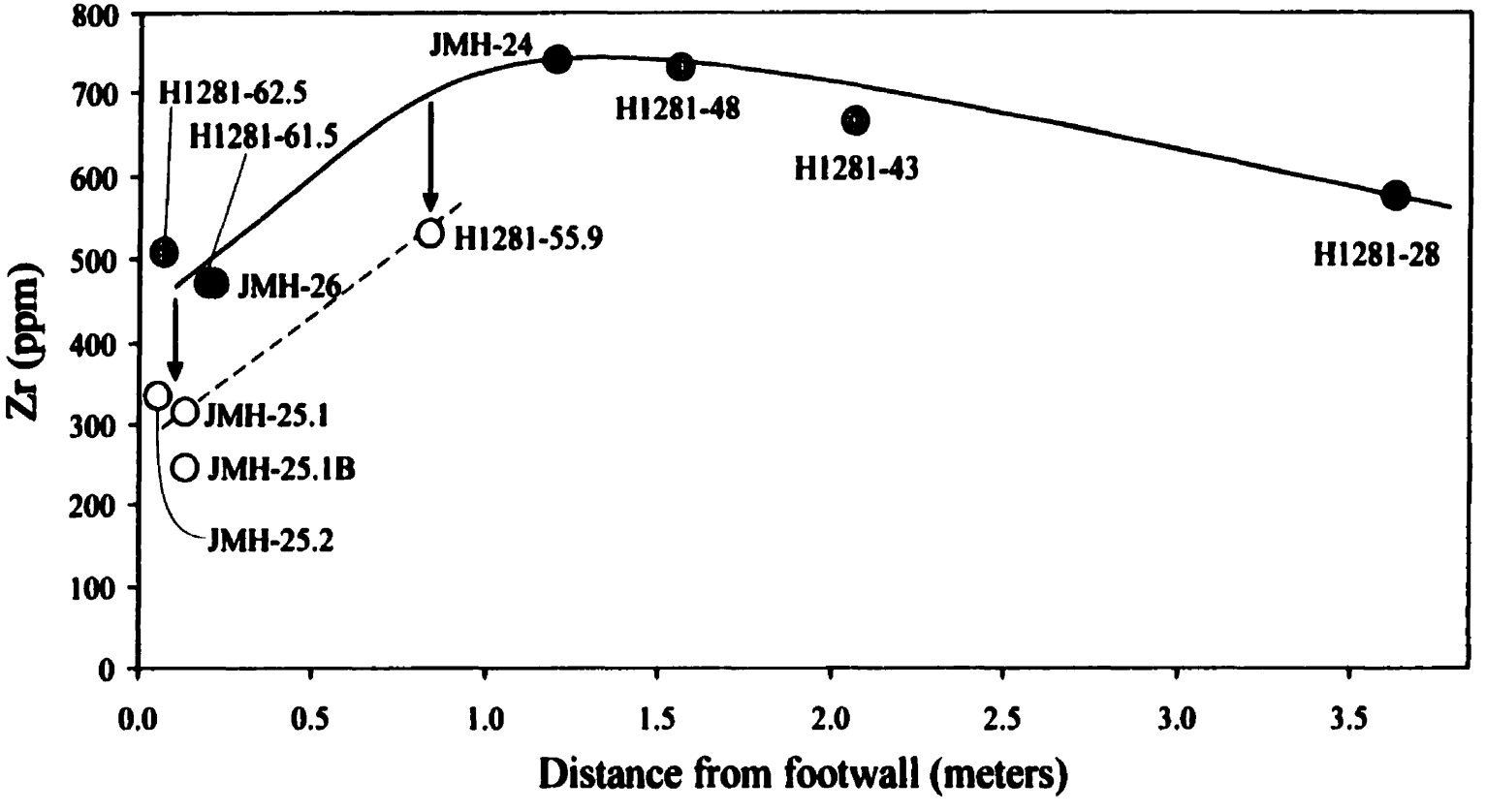
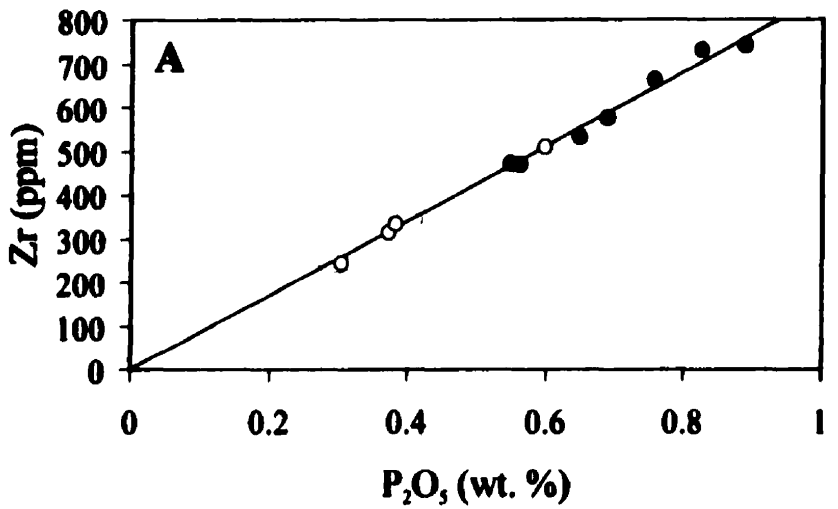
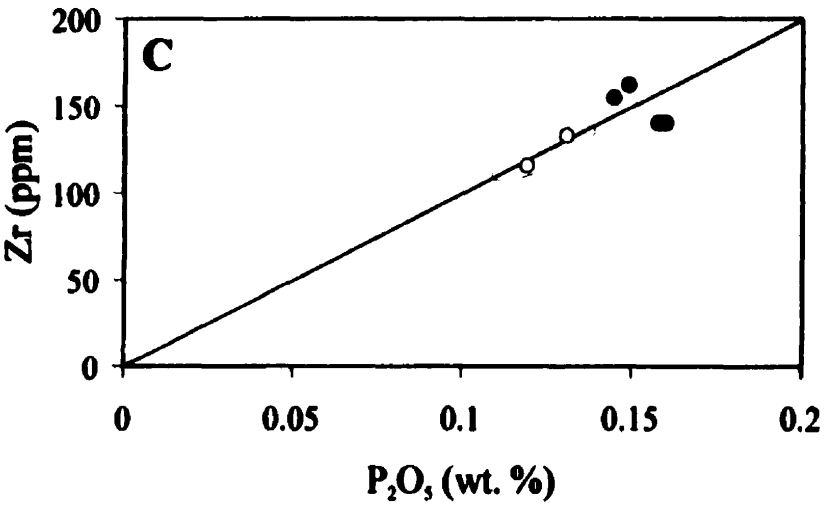
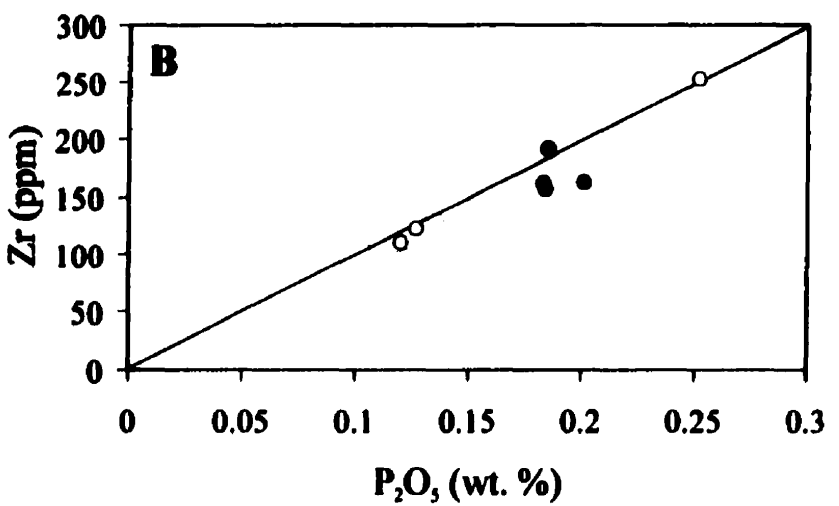

800
700
600
500
400
300
200
100
0
Zr (ppm)
0.0
0.5
1.0
1.5
2.0
2.5
3.0
3.5
Distance from footwall (meters)
JMH-24
H1281-62.5
H1281-61.5
H1281-48
H1281-43
H1281-55.9
H1281-28
JMH-26
JMH-25.1
JMH-25.1B
JMH-25.2

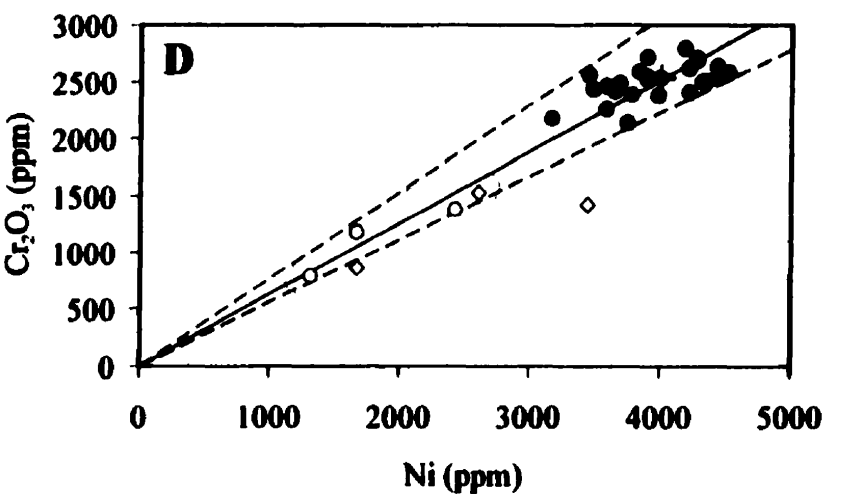
Figure 9

P_2O_5 (wt. %) versus Zr (ppm) and Ni (ppm) versus Cr_2O_3 (ppm) relationships among A) diorite least affected by Ca-metasomatism (solid circles), diorite moderately affected by Ca-metasomatism (grey circles) and strongly rodingitized diorite (open circles), B) least altered granite (solid circles), granite affected by feldspar-pyribole alteration (grey circles) and rodingitized granite (open circles), C) least altered slate (solid circles), albitized slate (grey circles) and rodingitized slate (open circles), and D) serpentinite (solid circles), serpentinite replaced by antigorite ± talc (grey circles), nephrite (open circles) and diopsidite (open diamonds).


A
Zr (ppm)
800
700
600
500
400
300
200
100
0
0
0.2
0.4
0.6
0.8
1
P_2O_5 (wt. %)


C
Zr (ppm)
200
150
100
50
0
0
0.05
0.1
0.15
0.2
P_2O_5 (wt. %)


B
Zr (ppm)
300
250
200
150
100
50
0
0
0.05
0.1
0.15
0.2
0.25
0.3
P_2O_5 (wt. %)

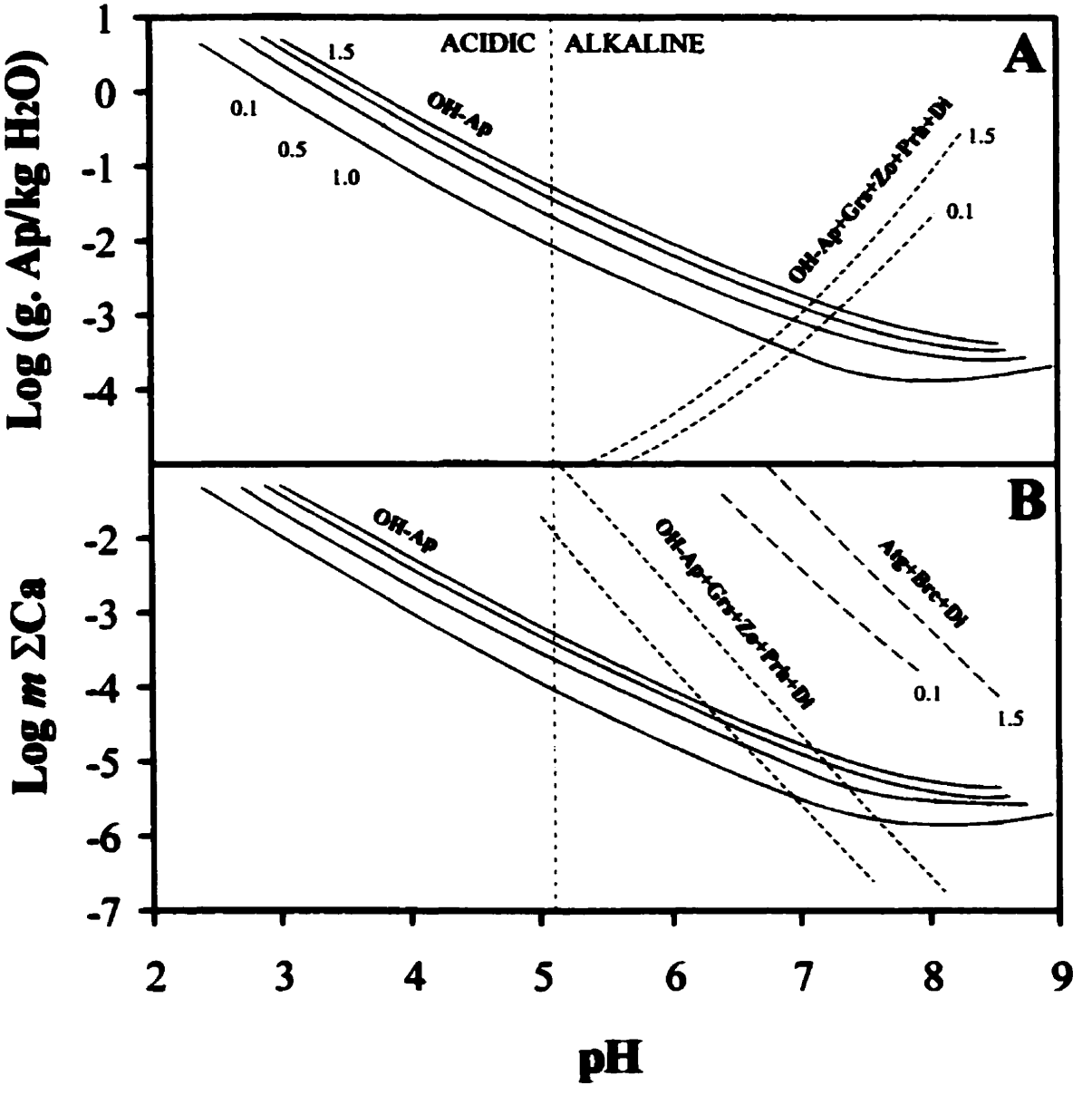

D
Cr_2O_3 (ppm)
3000
2500
2000
1500
1000
500
0
0
1000
2000
3000
4000
5000
Ni (ppm)

The concentrations of Zr and P_2O_5 in the slates and in the felsic igneous rocks were controlled by the proportions of zircon and apatite, respectively, the essential carriers of these components. These minerals, zircon in particular, are very insoluble in most hydrothermal solutions, especially when pH is near neutral. Hydrothermal solutions inducing rodingitization are expected to be alkaline, and in such solutions, the solubility of apatite in the system Ca-Na-P-Cl-O-H is very low (Figure 10). We have calculated that, at a temperature of 325°C and a pressure of 2000 bars, the solubility of OH-apatite in 0.1 to 1.5 *m* ΣCl solutions and at pH values > 6 is < 10^{-2} g/kg H_2O. In the more complex system involving equilibrium among apatite, grossular, zoisite, prehnite, and diopside at a temperature of 325°C and a pressure of 2000 bars, the solubility of OH-apatite at pH > 7 is greater than that in solutions where only OH-apatite is present. This is because the Ca concentrations in fluids in equilibrium with the calc-silicate-bearing assemblage become lower than the Ca concentrations in solutions containing only apatite (Figure 10). Assuming a situation where rodingitization is caused by the interaction of a serpentinizing fluid containing 1.5 *m* total Cl with a Si-Al-rich rock, and that the pH of the serpentinizing fluid is buffered at a value of 7, the solubility of apatite would be ~ 10^{-3} gram per kilogram of fluid. The diorites-monzodiorites contain between 1.2 and 12.8 grams of apatite per kilogram of rock. Our mass balance calculations indicate that volume-conservative replacement of UG-10bis by UG-2, E:53 by E:7.5 and JMH-26 by JMH-25.2 resulted in the removal of 0.0083, 0.042 and 0.16 gram of P_2O_5 per 100 grams of precursor, respectively. These P_2O_5 concentrations translate into 0.2, 1.0 and 3.8 grams of apatite removed per kilogram of rock. Using the value for the solubility of apatite of 10^{-3} gram per kilogram of fluid, the mass of fluid necessary to dissolve the apatite during alteration of 1 kilogram of UG-10bis to UG-2, 1 kilogram of E:53 to E:7.5 and 1 kilogram of JMH-26 to JMH-25.2, would have been 200, 1000 and 3800 kilograms, respectively. Very large water/rock ratios would thus be required to explain the proportions of apatite dissolved assuming that rodingitization occurred purely by a process of fluid infiltration.

Similar to Zr and P_2O_5, Cr_2O_3 and Ni, which are relatively insoluble in near-neutral

Figure 10

A) Solubility of OH-apatite as a function of pH in the system Na-Ca-P-O-H-Cl (total Cl concentrations of 0.1, 0.5, 1.0 and 1.5 *m*: full lines) and in equilibrium with the assemblage grossular + zoisite + prehnite + diopside in the system Na-Ca-Mg-Al-Si-O-H-P-Cl (total Cl concentrations of 0.1 and 1.5 *m*: dashed lines) at a temperature of 325°C and a pressure of 2 kilobars. B) Ca concentration versus pH in solutions in equilibrium with OH-apatite (full lines), OH-apatite + grossular + zoisite + prehnite + diopside (short dashed lines) and antigorite + brucite + diopside (long dashed lines). The temperature and pressure relationship are the same as in A. Calculations were made with the Hch package of programs (Shvarov and Bastrakov, 1999) using the original internal thermodynamic database to which were added thermodynamic data for the species $HSiO_3^-$ from SUPCRT92 (Johnson et al., 1992).


A
B
ACIDIC
ALKALINE
Log (g. Ap/kg H2O)
Log m ΣCa
pH
OH-Ap
OH-Ap+Grn+Zo+Prh+Dl
Atg+Brc+Dl
0.1
0.5
1.0
1.5
1
0
-1
-2
-3
-4
-5
-6
-7
2
3
4
5
6
7
8
9

hydrothermal solutions, are diluted in nephrite and diopsidite by up to three times their original concentrations in serpentinite (Figure 9). This implies that the water/rock ratios also had to be very large in order to explain the removal Cr_2O_3 and Ni from the serpentinites by a process of fluid infiltration.

Although Cr_2O_3 and Ni were mobile during the calc-silicate alteration of the serpentinites, they appear not to have been redeposited in significant amounts in the adjacent felsic intrusive rocks during rodingitization or during alteration to blackwall. For example, the Cr_2O_3 concentration in the rodingite sample JMH-295.1 is 66 ppm and that in the blackwall formed by its replacement (JMH-295.1b) is 63 ppm (Table 16). The Cr_2O_3 concentration in the diorite sample JMH-310.1 is 30 ppm, whereas that in the blackwall formed at the expense of this rock is also 30 ppm (Table 16). The mass balance calculations further indicate that, assuming volume was conserved, Cr_2O_3 was removed as a result of the rodingitization of diorite (-7.4 ppm per 100 g of precursor JMH-26 containing 38 ppm Cr_2O_3 for sample JMH-25.2, and -10.2 ppm per 100 g of precursor H1281-61.5 containing 46 ppm Cr_2O_3 for sample H1281-62.5) and granite (> -11.4 ppm per 100 g of precursor E:53, containing 29 ppm Cr_2O_3, for sample E:7.5). As concluded above for the MgO released during the calc-silicate alteration of serpentinites adjacent to the dykes, Cr_2O_3 appears to have been transported out of the environment where the rocks were altered, most likely by advection with fluids circulating in the serpentinites adjacent to the dykes.

Origin of the calcium responsible for rodingitization

The source of the Ca forming the calc-silicate rocks in the serpentinites, in the dykes and in the slates remains the most difficult issue to evaluate. Our mass balance calculations have revealed that the Ca needed for rodingitization of the slates is balanced by the amount of Ca removed by albitization. This hypothesis, however, can not hold in the case of the granitic rocks examined in this study, because each step in the progressive alteration of these rocks was invariably accompanied by the addition of CaO (E series of samples). Because no fresh diorite was observed, it is difficult to estimate the initial Ca

Table 16. Chemical composition of blackwall.

Sample	JMH-295.1	JMH-295.2	JMH-310.1	JMH-310.2
Rock type	Rodingite	Blackwall	Diorite	Blackwall
Wt. %				
SiO_2	39.95	32.72	46.44	32.46
TiO_2	0.775	0.734	0.821	0.401
Al_2O_3	16.81	13.59	21.16	15.06
Fe_2O_3	4.15	7.46	6.58	5.11
MnO	0.446	0.474	0.162	0.143
MgO	6.79	32.04	5.49	33.69
CaO	28.08	0.54	8.59	0.45
Na_2O	<d.l.	0.03	1.61	0.05
K_2O	0.06	0.05	6.1	0.16
P_2O_5	0.387	0.375	0.51	0.327
L.O.I.	2.24	12.15	1.6	12.26
ppm				
BaO	<d.l.	19	5551	42
Co	<d.l.	58	20	54
Cr_2O_3	66	63	30	30
Ni	36	42	85	107
Total	99.7	100.18	99.63	100.13
ppm				
Nb	14	7.7	21.3	9
Pb	13.4	11.8	9.6	8.6
Rb	2.8	1.8	186.3	11.7
Sr	15.9	5.9	1720.5	5.8
Th	8.8	2.1	5.2	<d.l.
Y	19.5	16.7	11.4	10.8
Zr	360.3	333.1	460	220.6

Analyses by X-ray fluorescence. <d.l.: below detection limit.

content of these rocks. The diorites that contain abundant pseudomorphs of the unknown phenocryst phase contain less than 3 wt. % CaO. Assuming that the bulk of the original plagioclase contained 40 mole % of the anorthite component and that the unknown pseudomorphed phenocryst phase was amphibole or clinopyroxene, the loss of CaO in the diorites that contained these phases could have been as much as 10 wt. %. Although this proportion of CaO could easily account for the formation of the rodingitized margin of the incompletely altered dykes, it can not explain the existence of other completely rodingitized dykes, some of which measure up to 1 meter thick, and are tens of meters in length. The implications of this are that transport of Ca must have taken place over distances greatly exceeding 1 meter, and that diffusion was not a major transport mechanism for Ca.

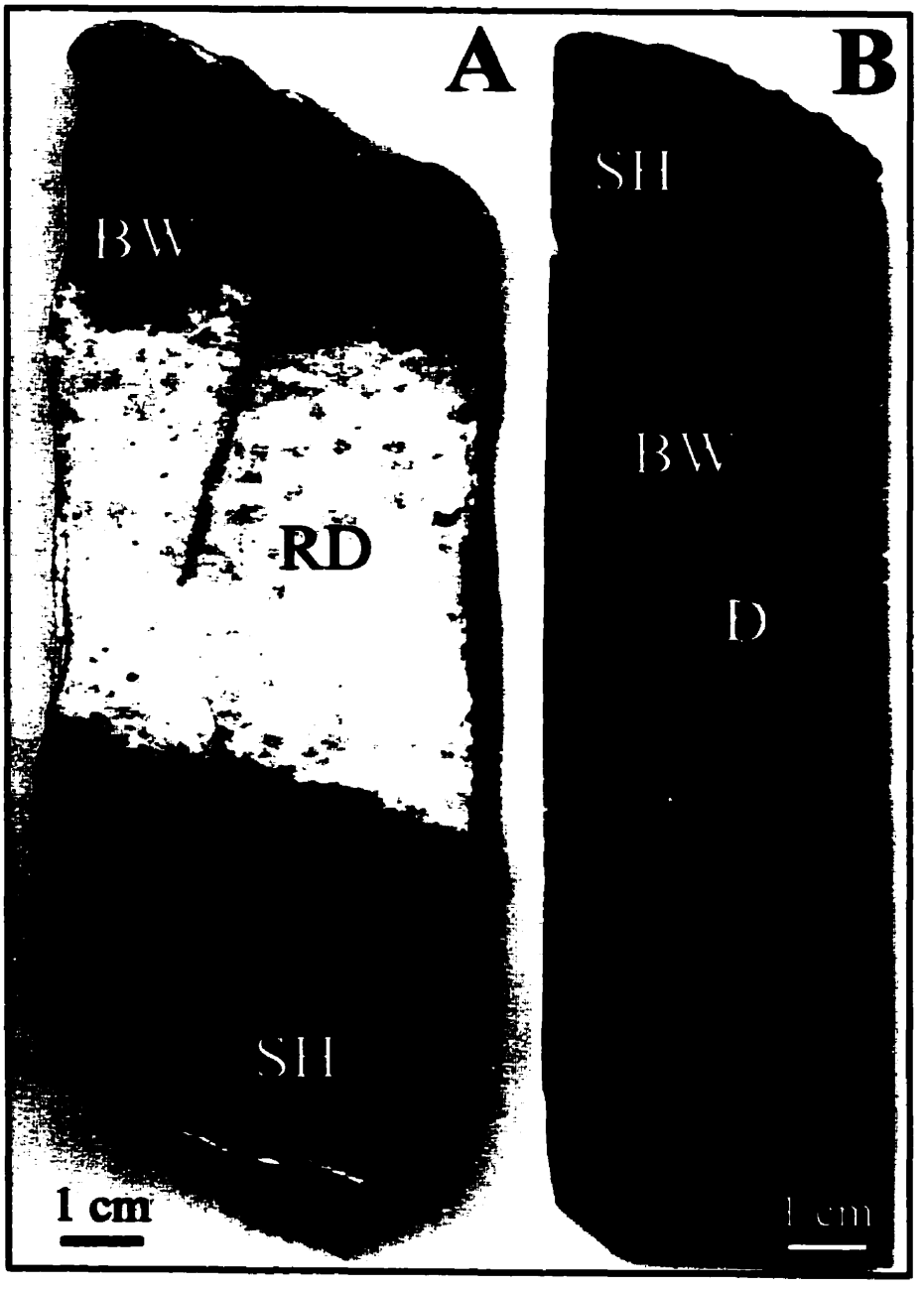
It is clear that Ca metasomatism at the contact between serpentinites and dykes is either the result of Ca transport by advection or diffusion through hydrothermal fluids, from the dykes toward the serpentinites, or from the serpentinites toward the dykes. To determine in which of these two directions transport occurred, it is necessary to determine first the sequences of mineral assemblages in a section passing through serpentinite and felsic rocks (intrusives or slate). Two general types of relationships are evident at the contacts between serpentinites and felsic rocks. In the first type, the most common succession of alteration assemblages from serpentinite to felsic rocks is, in the serpentinite, serpentinite → antigorite → talc → nephrite (diopsidite), and, in the felsic rocks, rodingite → felsic rock. In the second type, the serpentinites adjacent to the felsic rocks were not subjected to calcium-metasomatism, but a blackwall formed in the felsic rocks at the contact with the serpentinites. This blackwall replaced rodingite or directly replaced the felsic rocks. These successions represent contrasting styles of complementary alteration zonation that affected the serpentinites and the felsic rocks and may reflect the predominant direction of fluid flow during alteration. The association "nephrite in the serpentinite" and "rodingite in the felsic rocks" most probably resulted from the exchange of components between serpentinites and felsic rocks through a static fluid, a fluid circulating parallel to the contact between serpentinite and felsic rocks (Barnes et al., 1972), or a fluid emanating from the felsic rocks. The "blackwall-

rodingite" association in the felsic rocks without associated calcium-metasomatized serpentinite suggest that the fluids causing alteration circulated predominantly across the serpentinite-felsic rock contact, and into the felsic rocks. Sample Flt-B (Figure 11) provides a good example of the second type of alteration zone association. The sample shows a complete cross-section through a narrow, completely rodingitized diorite dyke with blackwall-altered margins in contact with serpentinite which present no evidence of calcium metasomatism. The contacts are not sheared and probably represent the original intrusive contact, as there is a thin rim of fibrous pyribole (see Chapter IV), now serpentinized, which grew in the serpentinite perpendicular to the contact with the dyke. Evidently, if constant volume was maintained during alteration, the calcium necessary to induce rodingitization of the diorite must have been derived from a source external to the dyke.

While the silica needed to form the nephrite halos at the margin of some of the felsic dykes most probably was derived from the dykes, the source of the calcium is less evident. These halos occur both at the margins of monzodioritic-dioritic and granitic dykes, indicating that neither the more SiO_2-rich character of the granites nor the more CaO-rich character of the diorites played a more favourable role in whether or not a nephrite halo formed. The transition serpentinite $\rightarrow$ antigorite $\rightarrow$ talc $\rightarrow$ nephrite $\rightarrow$ diopsidite towards the contact with a rodingitized dyke necessitated an increase in μSiO_2 and the ratio $\mu Ca/\mu Mg$. It was shown in Chapter III, based on fluid-solid phase equilibria in the system Ca-Mg-Si-O-H-Cl, that the Ca must have originated from the same source that provided the silica in order to explain the large removal of Mg resulting from the replacement of serpentinite by nephrite. Calculations revealed that the same relationships apply to more complex aqueous solutions in the system Na-Ca-Mg-Al-Si-O-H-Cl. However, if a case is considered where alteration occurred before the dykes reached thermal equilibrium with the host serpentinites, our calculations show that the calcium could have been derived from the serpentinizing fluids. With time, the gradient of increased silica concentration towards the dykes would have been attenuated as the extent of rodingitization of the adjacent felsic dykes increased. As a result, the activity of silica

Figure 11

A) Section through blackwall(BW)-rimmed rodingitized diorite (RD) dyke cutting serpentinized harzburgite (SH; sample Flt-B). B) Blackwall(BW)-rimmed diorite (D) dyke showing original intrusive contacts with serpentinite (SH). The serpentinites adjacent to the dykes were not subjected to Ca-metasomatism.


A
B
BW
RD
SH
SH
BW
D
1 cm
1 cm

in the solutions was lowered sufficiently to permit the replacement of tremolite by diopside (Refer to Figures 10 and 12 in Chapter III). Several lines of evidence support this idea: 1) the close association of tremolite with albite in the dyke rocks and slate; 2) the later replacement of tremolite by diopside in both dykes and nephrite; and 3) the low-level mobility of silica during rodingitization of the dioritic-monzodioritic rocks.

CONCLUSIONS

Field relationships between felsic intrusive rocks and host serpentinites in the JM Asbestos mine are consistent with the idea that their emplacement occurred in peridotites, which had been serpentinized, at least partially, prior to intrusion. This suggests that, contrary to what is frequently assumed, fluids that have equilibrated with nearly completely serpentinized peridotites can induce rodingitization as efficiently as fluids that are produced as a result of the serpentinization of fresh peridotites. The textural relationships between the precursor slates, felsic intrusive rocks and serpentinites, and their altered equivalents, suggest that volume was conserved during calc-silicate metasomatism. Rodingitization of Si-rich lithologies adjacent to serpentinites was accompanied by a very strong enrichment in Ca and Mn (both fixed in calcium silicates), a very strong depletion in volatiles (C, S, and H_2O) and alkalis, and less extensive depletion in Al and Si. Fe and Mg were either added or removed, but invariably in small proportions. Transformation of serpentinite to nephrite or diopsidite resulted from major additions of Si and Ca, and removal of Mg in proportions comparable to the amount of added Si.

Mineralogical (oscillatory zoning) and textural (veins) analyses of the rodingites suggest that the process by which mass was transferred, at least near the contacts between the Si-rich lithologies and the serpentinites, was fluid infiltration. The chemical mass balance analysis indicates that the components Zr, P_2O_5, Cr_2O_3, and Ni, which are expected to be relatively insoluble in Ca-bearing and near neutral or slightly alkaline fluids, were removed in unexpectedly large amounts. Furthermore, the Zr and P_2O_5

removed during rodingitization of the Si-rich lithologies were not redistributed in the adjacent calc-silicate-altered serpentinites, and the Cr_2O_3 and Ni removed from the serpentinites during calc-silicate alteration were not redistributed in the adjacent Si-rich lithologies. These observations suggest that very large amounts of fluids circulated through the rocks undergoing alteration and progressively dissolved the sparingly soluble minerals, zircon, apatite, and chromite. The fact that Zr, P_2O_5, Cr_2O_3, and Ni were not redistributed across the alteration zones, and the very large amounts of Ca introduced also indicate that these components must have been transported by an advecting fluid phase.

ACKNOWLEDGEMENTS

This research was made possible through grants from NSERC and JM Asbestos Inc. to AEW-J, and NSERC and FCAR scholarships to CN. Helpful discussions were had with A. Migdissov and W. H. MacLean.

REFERENCES

Anhaeusser, C. R., 1979, Rodingite occurrences in some Archean ultramafic complexes in the Barberton Mountain Land, South Africa, Precambrian Research, v. 8, p. 49-76.

Aumento, F. and H. Loubat, 1971, The Mid-Atlantic Ridge near 45° N. XVI. Serpentinized ultramafic intrusions, Canadian Journal of Earth Sciences, v. 8, p. 631-663.

Barnes, I. and J. R. O'Neil, 1969, The relationship between fluids in some fresh Alpine-type ultramafics and possible modern serpentinization, western United States, Geological Society of America Bulletin, v. 80, p. 1947-1960.

Barnes, I., Rapp, J. B., O'Neil, J. R., Sheppard, R. A. and A. J. Gude, III, 1972, Metamorphic assemblages and the direction of flow of metamorphic fluids in four instances of serpentinization, Contributions to Mineralogy and Petrology, v. 35, p. 263-276.

Barriga, F. and W. S. Fyfe, 1983, Development of rodingite in basaltic rocks in serpentinites, East Liguria, Italy, Contributions to Mineralogy and Petrology, v. 84, p. 146-151.

Bell, J. M., Clarke, E. de C. and P. Marshall, 1911, The geology of the Dun Mountain subdivision, Nelson, New Zealand Geological Survey, Bulletin 12, new series, 71 p.

Berman, R. G., Brown, T. H. and E. H. Perkins, 1987, GEØ-CALC: Software for calculation and display of P-T-X phase diagrams, American Mineralogist, v. 72, p. 861-862.

Bertrand, J. and J. Deferne, editors, 1980, Proceedings of the international symposium on tectonic inclusions and associated rocks in serpentinites, Geneva, September 1979, Archives des Sciences de la Société de Physique et d'Histoire Naturelle de Genève, v. 33.

Bideau, D., Hébert, R., Hekinian, R. and M. Cannat, 1991, Metamorphism of deep-seated rocks from the Garrett ultrafast transform (East Pacific Rise near 13°25'S), Journal of Geophysical Research, v. 96, p. 10,079-10,099.

Bloxam, T. W., 1954, Rodingite from the Girvan-Ballantrae complex, Ayrshire, Mineralogical Magazine, v. 30, p. 525-528.

Brown, T. H., Berman, R. G. and E. H. Perkins, 1987, GEØ-CALC: a software package for rapid calculation of stable pressure – temperature – activity phase diagrams, Geological Society of America, Abstracts with Programs, v. 19, p. 603.

Brown, T. H., Berman, R. G. and E. H. Perkins, 1988, GEØ-CALC: a software package for calculation and display of pressure – temperature – composition phase diagrams using an IBM or compatible personal computer, Computers and Geoscience, v. 14, p. 279-289.

Castonguay, S., Tremblay, A., Ruffet, G., Féraud, G., Pinet, N. and M. Sosson, 1997, Ordovician and Silurian metamorphic cooling ages along the Laurentian margin of the Québec Appalachians: bridging the gap between New England and Newfoundland, Geology, v. 25, p. 583-586.

Chamberlain, S. C., 1980, Wollastonite, vesuvianite, native copper and diopside from the Jeffrey mine in Asbestos, Quebec, Canada, Rocks and Minerals, p. 188-191.

Coleman, R. G., 1966, New Zealand serpentinites and associated metasomatic rocks, New Zealand Geological Survey, Bulletin No. 76, 102 p.

Coleman, R. G., 1967, Low-temperature reaction zones and alpine ultramafic rocks of California, Oregon and Washington, United States Geological Survey, Bulletin No. 1247, 49 p.

Coleman, R. G., 1977, Ophiolites: ancient oceanic lithosphere? Springer-Verlag, New York.

De, A., 1961, Petrology of dikes emplaced in the ultramafic rocks of southeastern Quebec, Ph. D. dissertation, Princeton University, Princeton, 201 p.

De, A., 1968, Post-ultramafic dykes and associated rocks in the asbestos mining areas in the Eastern Townships, Quebec, Geological Survey of Canada, Report of Activities, Paper 68-1, Part A, p. 71.

De, A., 1972, Petrology of dikes emplaced in the ultramafic rocks of southeastern Quebec and origin of the rodingite, Geological Society of America, Memoir 132, p. 489-501.

Diment, W. H., 1964, Thermal conductivity of serpentinite from Mayaguez, Puerto Rico, and other localities, *in* A study of serpentinite, the AMSOC core hole near Mayaguez, Puerto Rico, Burk., C. A., editor, National Academy of Sciences - National Research Council, Washington, D. C., Publication No. 1188, p. 92-106.

Dreher, A. M., Girardi, V. A. V. and P. Comin-Chiaramonti, 1989, Petrologia dos rodingitos do complexo máfico-ultamáfico de Cana Brava, Goiás, Revisita Brasileira de Geociências, v. 19, p. 224-236.

Droop, G. T. R., 1987, A general equation for estimating Fe^{3+} concentrations in ferromagnesian silicates and oxides from microprobe analyses, using stoichiometric criteria, Mineralogical Magazine, v. 51, p. 431-435.

Ferry, J. M. and M. L. Gerdes, 1998, Chemically reactive fluid flow during metamorphism. Annual Reviews in Earth and Planetary Sciences, v. 26, p. 255-287.

Grange, L. I., 1927, On the "rodingite" of Nelson, Transactions of the New Zealand Institute, v. 58, p. 160-166.

Grant, J. A., 1986, The isocon diagram - a simple solution to Gresens' equation for metasomatic alteration, Economic Geology, v. 81, p. 1976-1982.

Gresens, R. L., 1967, Composition-volume relationships of metasomatism, Chemical Geology, v. 2, p. 47-55.

Grice, J. D. and R. Williams, 1979, The Jeffrey mine, Asbestos, Quebec, Mineralogical Record, v. 10, p. 69-80.

Grice, J. D. and E. Gasparrini, 1981, Spertiniite, $Cu(OH)_2$, a new mineral from the Jeffrey mine, Quebec, Canadian Mineralogist, v. 19, p. 337-340.

Grice, J. D. and G. W. Robinson, 1984, Jeffreyite, $(Ca,Na)_2(Be,Al)Si_2(O,OH)_7$, a new mineral species and its relation to the melilite group, Canadian Mineralogist, v. 22, p. 443-446.

Groat, L. E., Hawthorne, F. C. and T. S. Ercit, 1992, The chemistry of vesuvianite, Canadian Mineralogist, v. 30, p. 19-48.

Halter, W. E., Williams-Jones, A. E. and D. J. Kontak, 1998, Origin and evolution of the greisenizing fluid at the East Kemptville tin deposit, Nova Scotia, Canada, Economic Geology, v. 93, p. 1026-1051.

Hébert, R., 1980, Etude pétrologique des roches ophiolitiques d'Asbestos et du Mont Ham (Ham Sud), M. Sc. Thesis, Université Laval, Québec, 182 p.

Hébert, R. and J. H. Bédard, 1998, Architecture and petrogenesis of arc ophiolites: example from the ophiolitic complexes of southern Québec, Geological Association of Canada (GAC), Mineralogical Association of Canada (MAC), Association des géologues et géophysiciens du Québec (APGGQ), International Association of Hydrogeologists (IAH), Canadian Geophysical Union (CGU) Joint Annual Meeting, 1998, Québec, Québec, Canada, Fieldtrip A4 Guidebook, 51 p.

Honnorez, J. and P. Kirst, 1975, Petrology of rodingites from the equatorial Mid-Atlantic fracture zones and their geotectonic significance, Contributions to Mineralogy and Petrology, v. 49, p. 233-257.

Janecky, D. R. and W. E. Seyfried, Jr., 1986, Hydrothermal serpentinization of peridotite within the oceanic crust: experimental investigations of mineralogy and major element chemistry, Geochimica et Cosmochimica Acta, v. 50, p. 1357-1378.

Johnson, J. W., Oelkers, E. H. and H. C. Helgeson, 1992, SUPCRT92: A software package for calculating the standard molal thermodynamic properties of minerals, gases, aqueous species, and reactions from 1 to 5000 bars and 0° to 1000°C, Computers and Geosciences, v. 17, p. 899-947.

Katoh, T. and K. Niida, 1983, Rodingites from the Kamuikotan, tectonic belt, Hokkaido, Journal of the Faculty of Science, Hokkaido University, Serie IV, v. 20, p. 151-169.

O'Hanley, D. S. and M. D. Dyar, 1993, The composition of lizardite 1*T* and the formation of magnetite in serpentinites, American Mineralogist, v. 78, p. 391-404.

Olsen, E. J., 1961, High temperature acid rocks associated with serpentinite in eastern Quebec, American Journal of Science, v. 259, p. 329-347.

Pfeifer, H. -R., 1977, A model for fluids in metamorphosed ultramafic rocks. Observations at surface and subsurface conditions (high pH spring waters), Schweizerische Mineralogische und Petrographische Mitteilungen, v. 57, p. 361-396.

Pinet, N. and A. Tremblay, 1995a, Tectonic evolution of the Quebec-Maine Appalachians: from oceanic spreading to obduction and collision in the northern

Appalachians, American Journal of Science, v. 295, p. 173-200.

Pinet, N. and A. Tremblay, 1995b, Is the Taconian orogeny of southern Quebec the result of an Oman-type obduction? Geology, v. 23, p. 121-124.

Plyusnina, L. P., Likhoidov, G. G. and G. P. Zaraisky, 1993, Physicochemical conditions of rodingite formation: experimental data, Petrology, v. 1, p. 492-502.

Reed, J. J., 1959, Soda-metasomatized argillites associated with the Nelson ultramafic belt, New Zealand Journal of Geology and Geophysics, v. 2, p. 905-915.

Riordon, P. H., 1975, Géologie des gîtes d'amiante du sud-est Québécois, Ministère des Richesses Naturelles du Québec, E.S.-18, 100 p.

Schandl, E., O'Hanley, D. S. and F. J. Wicks, 1989, Rodingites in serpentinized ultramafic rocks of the Abitibi greenstone belt, Ontario, Canadian Mineralogist, v. 27, p. 579-591.

Shvarov, Yu. V., and E. N. Bastrakov, (1999), Hch: a software package for geochemical equilibrium modelling, User's Guide, Australian Geological Survey Organisation, Record 1999/25, 61 p.

Steefel, C. I. and A. C. Lasaga, 1992, Putting transport into water-rock interaction models, Geology, v. 20, p. 680-684.

Wares, R. P. and R. F. Martin, 1980a, Rodingitization of granite and serpentinite in the Jeffrey mine, Asbestos, Quebec, Canadian Mineralogist, v. 18, p. 231-240.

Wares, R. P. and R. F. Martin, 1980b, Rodingitization of dyke rocks and enclosing serpentinites in the Jeffrey mine, Quebec Appalachians, Archives des Sciences de la Société de Physique et d'Histoire Naturelle de Genève, v. 33, p. 301-310.

Whitehead, J., Reynolds, P. H. and J. G. Spray, 1996, $^{40}Ar/^{39}Ar$ age constraints on Taconian and Acadian events in the Quebec Appalachians, Geology, v. 24, p. 359-362.

Whitehead, J., Dunning, G. R. and J. G. Spray, 2000, U-Pb geochronology and origin of granitoid rocks in the Thetford Mines ophiolite, Canadian Appalachians, Geological Society of America Bulletin, v. 112, p. 915-928.

Wicks, F. J. and E. J. W. Whittaker, 1977, Serpentine textures and serpentinization, Canadian Mineralogist, v. 15, p. 459-488.

Williams, H. and P. St-Julien, 1982, The Baie Verte-Brompton line: early Paleozoic continent-ocean interface in the Canadian Appalachians, Geological Association of Canada Special Paper 24, p. 177-207.

Yardley, B. W. D. and G. E. Lloyd, 1995, Why metasomatic fronts are really metasomatic sides, Geology, v. 23, p. 53-56.

Yardley, B. W. D., Rochelle, C. A., Barnicoat, A. C. and G. E. Lloyd, 1991, Oscillatory zoning in metamorphic minerals: an indicator of infiltration metasomatism, Mineralogical Magazine, v. 55, p. 357-365.

INTRODUCTION TO CHAPTER VI

In Chapter V, we discussed the chemical factors that controlled rodingitization of slate, felsic intrusive rocks and serpentinite. It was established, based on whole-rock geochemical mass balance calculations and geological and mineralogical observations, that rodingitization occurred as a result of the infiltration of large amounts of fluid along the tectonized and untectonized contacts between serpentinite and slate, and between serpentinite and felsic dykes.

In the following chapter, the nature of the fluids responsible for rodingitization of the felsic dykes and slates are investigated by way of petrographic, microthermometric and gas chromatographic studies of the fluid inclusions present in the rodingites.

CHAPTER VI

FLUID INCLUSIONS IN RODINGITES FROM THE JM ASBESTOS MINE, ASBESTOS, QUÉBEC

by

Charles Normand and Anthony E. Williams-Jones

Department of Earth and Planetary Sciences, McGill University, 3450 University Street, Montreal (Qué), Canada, H3A 2A7.

ABSTRACT

Fluid inclusions in rodingitized slate and in rodingitized dioritic and granitic dykes from the JM Asbestos mine, Asbestos, Québec, were investigated by means of petrographic, microthermometric and gas chromatographic analyses in order to determine the composition of the fluids involved in rodingitization and the pressure and temperature conditions under which these fluids were trapped. Available radiometric emplacement-age determinations of the felsic dykes and metamorphic-age determinations of the sedimentary country rocks adjacent to the Asbestos ophiolite were used, in conjunction with geological observations, to identify the timing and environment of rodingitization. The results indicate that three types of fluids were involved in two episodes of rodingitization during thrusting of the Asbestos ophiolite onto the Laurentian margin. The first episode involved rodingitization of diorite, granite and slate at temperatures between 300 and 350°C and pressures between 2 and 3 kbar. The fluids responsible for alteration were moderately to strongly saline (~ 2 to 4.3 *m* eq. NaCl) and Ca-rich. Relatively low salinity fluids (≤ 2 *m* eq. NaCl) were responsible for the formation of late-stage vesuvianite-rich mineral assemblages at temperatures below 200°C. The presence of CH_4 and higher order alkanes, and absence of CO_2 indicate that the fluids responsible for the rodingitization of the diorites, the granites and the slates originated from the serpentinites. The similarities in the composition of the fluids in all rock types indicate that the ophiolite was already thrust onto the slates during rodingitization.

INTRODUCTION

Rodingites are calc-silicate rocks hosted by serpentinized ultramafic rocks, and form as a result of the interaction of the serpentinizing fluids with Si-(Al)-rich lithologies in or adjacent to the ultramafic rocks (Coleman, 1966, 1967). The chemistry of the fluids responsible for rodingitization is poorly understood despite the fact that rodingite-forming minerals are known to contain primary fluid inclusions. Indeed, to our knowledge, fluid inclusion data have been reported from only four rodingite localities (Schandl et al., 1989; Schandl et al., 1990; Mittwede and Schandl, 1992; O'Hanley et al., 1992; Compagnoni et al., 1998). The data presented in these studies provide an important first step toward understanding the nature of the fluids responsible for rodingitization. They show that the fluids are brines with salinities varying from 0 to 12.8 wt. % equivalent NaCl, and that rodingitization takes place at temperatures of 270 to > 350°C and pressures of < 2.5 kbar. Initial melting temperatures of the ice at > -26.4°C indicate that the predominant salt dissolved in the fluid inclusions is NaCl. However, considerably more information is required about the chemistry of these fluids in order to be able to make a precise prediction of the reactions involved in rodingitization and identify the physicochemical parameters controlling this alteration.

In this paper, we present results from a detailed study of fluid inclusions in rodingitized slate, diorite and granite, and vesuvianite-rich veins from the JM Asbestos mine, Asbestos, Québec. The data presented here provide important additional information on the chemistry of the fluids responsible for rodingitization during obduction of oceanic crust onto a continental margin.

GEOLOGICAL SETTING

The JM Asbestos mine is located in serpentinized ultramafic rocks, which form part of an ophiolite sliver of Ordovician age, the Asbestos ophiolite, that was obducted onto the margin of the Laurentian craton during the Taconic orogeny at ~ 470-460 Ma

(Hébert and Bédard, 1998). The ultramafic rocks at the base of the Asbestos ophiolite comprise serpentinized harzburgite tectonites overlain by serpentinized cumulate dunites and pyroxenites (Hébert, 1980). The basal part of the ophiolite is in thrust contact with greenschist-grade metamorphosed slates and greywackes originally deposited on the Laurentian continental margin (Cousineau, 1990; Pinet and Tremblay, 1995). In the early stages of the obduction process, dioritic-monzodioritic and later granodioritic-granitic rocks were intruded in peridotites that were at least partially serpentinized at the base of the ophiolite (Chapter IV). With continued serpentinization and transportation of the ophiolite, these intrusive rocks were subjected to sodic-calcic and rodingitic hydrothermal alteration. These two alteration facies also developed in the continentally derived metasedimentary units (slate) below the ophiolite during thrusting of the latter onto the Laurentian continental margin (Chapter V). The fluids responsible for rodingitization were trapped in a variety of rodingite minerals and are the principal focus of this paper.

RODINGITES

A large variety of rodingitized rocks containing a complex array of mineral assemblages was observed in the field, in hand samples and in thin sections from altered serpentinite, felsic intrusive dykes that cut the serpentinite and slate in thrust contact with serpentinites. A suite of samples representative of the various types of rodingites were described in detail in Chapter V and comprise three rodingites that replaced slate (UG-C, UG-2 and JMH-301), seven samples of rodingitized diorite (JMH-24B, JMH-25.1, JMH-25.2, Flt-B, JMH-203D, JMH-306, and JMH-295), five samples of rodingitized granite (E:2, E:4.5, E:7.5, JMH-333A, and JMH-333B), and eight samples of vein-like rodingite rich in vesuvianite (GOR, MIL, Flt-100, Flt-G, JMH-157, JMH-158, JMH-262, and JMH-277). Mineral identification and textural relationships were established using an optical binocular microscope, and an electron microprobe having scanning electron microscopic capability that is equipped with wavelength and energy dispersive detectors. The essential characteristics of the different rodingite types are described below.

Rodingitized slate

Rodingitization of slate was preceded by an episode of sodic-calcic alteration, which produced a halo of albite-tremolite rock extending up to two meters from the contact with serpentinite. Relict patches of this type of alteration are commonly found in the rodingitized slate which forms a zone ~ 60 cm thick between albitized slate and a ~ 10 cm thick zone of blackwall-altered slate immediately adjacent to the serpentinites. The original sedimentary textures were preserved during albitization and rodingitization. Pervasive rodingitization of the slate produced the following calc-silicate mineral assemblages: 1) hydrogrossular + prehnite + diopside (UG-2); 2) grossular + zoisite + diopside ± prehnite (UG-C); and 3) diopside + prehnite (JMH-301). Mineral assemblages in veins are similar to those which compose the host rock, and include diopside + prehnite, grossular + diopside + prehnite and grossular + diopside.

Rodingitized diorite

The thinner dykes of rodingitized diorite (< 15 cm) are generally composed of grossular-diopside-predominant assemblages, whereas the mineral assemblages in the thicker ones (> 2 m) also include zoisite and prehnite. The mineral assemblages observed in the pervasively altered diorites include grossular + diopside + chlorite (Flt-B, JMH-306 and JMH-295), grossular + diopside, grossular + diopside + zoisite or grossular + diopside + zoisite + prehnite (JMH-25.1 and JMH-25.2) and zoisite + diopside. The veins contain highly variable proportions of the same phases present in the pervasive style of rodingitization. They are prehnite-, feldspar- (either albite or K-feldspar) or more rarely grossular-rich where they cut diorite which has not been pervasively rodingitized, and measure up to 8 cm thick. A rim of prismatic diopside crystals is commonly observed on the walls of the veins, while the core is filled with coarse-grained Ca-Al-silicate assemblages (JMH-24b). Veinlets composed of dark brown vesuvianite and chlorite were observed cutting a grossular + diopside rodingite (JMH-203D).

Rodingitized granite

Two contrasting types of mineral assemblage are present in the two dykes of rodingitized granitic rock investigated in this study. The first dyke is a pegmatitic leucogranite in which the assemblage chlorite >> grossular + late prehnite (JMH-333a) locally forms a thick zone of blackwall-type alteration near its contact with serpentinite. The pervasively rodingitized granite is composed of the assemblage grossular + diopside (JMH-333b). The second dyke is a biotite granite which was mylonitized at the margins prior to alteration. The first 4 cm of the dyke from the contact with serpentinite were altered to chlorite + hydrogrossular + diopside (E:2), and were followed in order by a 6 cm wide zone composed of wollastonite + vesuvianite + diopside + hydrogrossular (E:4.5, E:7.5), and a 35 cm wide zone of bleached albite and K-feldspar-dominant rock.

Vesuvianite-rich veins

Vesuvianite-rich veins are concentrated at the base of the cumulate dunite-pyroxenite unit near the transition into the tectonized harzburgite. They commonly display a very high vug porosity (visually estimated at up to 25 %). Many of the veins have thick haloes of diopsidized serpentinite, which are cut by vesuvianite-rich veinlets. Mineral parageneses include white grossular + green and purple vesuvianite + diopside, vesuvianite + diopside, vesuvianite + wollastonite and vesuvianite + diopside + chlorite.

FLUID INCLUSIONS

The most representative examples of fluid inclusion-bearing rodingitized dykes and slate were subjected to a detailed fluid inclusion study (Appendix IV). Twenty-four doubly polished thin sections (150-200 μm thick) were prepared from three samples of rodingitized diorite (Flt-B, JMH-25.2B and JMH-25.2D), one sample of rodingitized granite (JMH-333a), two samples of rodingitized slate (UG-C and JMH-301) and three samples of vesuvianite from vesuvianite-rich "veins" (GOR-1, GOR-2 and MIL). Selected inclusions were analysed microthermometrically using a U.S.G.S.-type heating-

freezing stage mounted on a Leitz Sm-Lux Pol polarizing microscope. Calibration was performed between –56.6 and 374°C using synthetic fluid inclusion standards of water and CO_2. Fluid inclusions were also examined in quartz from fresh, coarse-grained leucogranites but were not analysed microthermometrically.

Fluid inclusion petrography

Three types of fluid inclusions were recognized from microscopic examination of the samples at 25°C. Type 1 inclusions consisted of a single fluid phase, type 2 inclusions consisted of two immiscible liquids, and type 3 inclusions of liquid, vapour and a cubic solid interpreted to be halite.

Type 1 inclusions measure between 4 and 20 μm in diameter, and have variable shapes (irregular, tubular and rectangular). They are found in rodingitized diorite where they occur as clusters in zoisite and grossular, in the rodingitized slate where they occur as clusters in diopside, and in vesuvianite from the vesuvianite-rich veins where they are isolated.

Type 2 inclusions occur in all the rodingite-forming minerals. They are generally prismatic in diopside and vesuvianite, and oriented parallel to the *c* axis (and cleavage in diopside). In garnet and zoisite, they are prismatic, equant or irregularly shaped. Their diameter varies between < 1 μm and ~ 50 μm (one tubular inclusion in garnet in sample JMH-333 measured 150 μm in length). Type 2 inclusions were considered primary when they were large and isolated, or occurred in tight groups away from the contacts between grains. They were considered secondary when they occurred in planar arrays.

Type 3 inclusions were only observed in association with vapour-rich fluid inclusions in quartz in fresh leucogranite dykes.

Microthermometry

Cryogenic experiments

The fluid inclusions displayed an array of phase changes, which are summarized

in Table 1. All type 1 inclusions in rodingite nucleated a bubble when they were cooled to temperatures below -90°C. One inclusion in sample JMH-25.2 contained solid, liquid and gas at a temperature of -184.4°C. On being heated, these inclusions homogenized by dissolution of the bubble into the denser liquid phase. This occurred at temperatures varying between -123 and -89°C (Figure 1), suggesting that the type 1 inclusions consist of a CH_4-rich fluid. The lowest homogenization temperatures were obtained for inclusions in the rodingitized diorite (JMH-25.2; -119°C on average). Homogenization temperatures for type 1 inclusions in rodingitized slate (UG-C and JMH-301) were between -120 and -89°C. Two inclusions in purplish-coloured vesuvianite (GOR) homogenized at -90°C.

Type 2 inclusions can be divided into three sub-types based on the melting behaviour of ice and clathrate, and on whether or not a gas-liquid phase change was observed. Type 2a inclusions have low ice and clathrate melting temperatures. They occur in the rodingitized granite sample JMH-333 and in the rodingitized slate sample UG-C. Type 2b inclusions have low to moderately low ice melting temperatures and moderate to elevated clathrate melting temperatures. They occur in the samples of rodingitized diorite and slate (JMH-25.2, Flt-B, UG-C, and JMH-301). Type 2c inclusions form a sub-population of type 2b inclusions characterized by low density (see below) and occur only in vesuvianite.

After being cooled to a temperature of -196°C, type 2a inclusions contained ice, a greenish birefringent hydrate, a clathrate, and solid and vapour (and liquid?) hydrocarbons. The first phase change during heating was the melting of a solid or disappearance of liquid (difficult to distinguish) inside the inner fluid at temperatures between -196 (observed in two inclusions in sample JMH-333) and -183°C (observed in one inclusion in sample JMH-333). This suggests that the bubbles are composed of CH_4 and another component representing a system with a triple point located at lower temperature than that of CH_4. Between -102 and -85°C, a vapour bubble homogenized inside the inner fluid (liquid), suggesting further that the latter is composed predominantly of CH_4 (Figure 2). Melting of the ice started between -74 and -42°C in

Table 1. Microthermometric data.

Sample	Protolith	Mineral assemblage	Inclusion type	Inclusion origin	T_h^{V-L}		T_h^{Crit}	
					Range (Average, ± 1σ)	N*	Range (Average, ± 1σ)	N*
Flt-B	Diorite	Gr-Di-Chl	2b	P**	-88	1		
JMH-25.2	Diorite	Di-Zo-Gr-(Pr)	1	P	-100.1 to -122.9 (-119, 4)	42		
			2b	P	-86.3 to -113.6	13		
			2b	S***				
JMH-333	Granite	Gr-Di	2a	P	-83.5 to -101.9	14		
			2a	S				
			2b	P				
UG-C	Slate	Gr-Di	1	P	-88.7 to -115.6	4		
			2a	P	-84.5 to -101.5	11	-88, -88.7	2
			2b	P	-101.1	1	-85.1, -89, -103	3
			2b	S				
			2a or 2b	P				
			2a or 2b	S				
JMH-301	Slate	Di-(Pr)	1	P	-99.4 to -120.3	6		
			2b	P				
GOR	-vein-	Vs-Di	1	P	-90, -90	2		
			2c	P				
MIL	-vein-	Vs-Di	2c	P				

*: N=number of measurements, **: P=primary, ***: S=secondary, T=temperature, h=homogenization, V-L=vapour to liquid, Crit=critical, e=first ice melting, m=melting, HH="hydrohalite" (tentative), CLA=clathrate, TOT=total.

Table 1. (continued)

Sample	T_c		T_m^{HH}		T_m^{ICE}	
	Range (Average, ± 1σ)	N*	Range (Average, ± 1σ)	N*	Range (Average, ± 1σ)	N*
Flt-B	-32 to -51.7	8			-4.2 to -12.8	10
JMH-25.2						
	-28.5 to -56.8 (-43, 7)	38			-3.7 to -23.5 (-15, 5)	48
					-7	5
JMH-333	-42 to -73.6 (-54, 7)	28	-4.6 to 20.8	16	-23.4 to -27.3 (-24.4, 0.7)	25
	-45	1	3.4	1	-24	1
UG-C						
	-48 to -76 (-55, 6)	23	-6.5 to 6.7	8	-22.8 to -25.6 (-24.4, 0.6)	25
	-39 to -52.8	10	-14.3, -4.1	2	-5.5 to -24.2	13
	-45	1			-9.3	1
	-38 to -50.3	3			-23.5, -25	2
	-52	1			-24	1
JMH-301						
	-36, -63	2			-3 to -22.8	8
GOR						
	-30.6 to -42	10			-4.5 to -5.3	12
MIL	-37	1			-4.2, -4.5, -5.7	3

*: N=number of measurements, **: P=primary, ***: S=secondary, T=temperature, h=homogenization, V-L=vapour to liquid, Crit=critical, e=first ice melting, m=melting, HH="hydrohalite" (tentative), CLA=clathrate, TOT=total.

Table 1. (continued)

Sample	T_m^{CLA}		T_h^{TOT}	
	Range (Average, ± 1σ)	N*	Range (Average, ± 1σ)	N*
Flt-B	5 to 9.2	12	277 to 326 (302, 14)	18
JMH-25.2				
	-0.7 to 10.1 (6.8, 2.7)	66	286 to 333 (312, 15)	17
	8 to 9	5	222 to 275	15
JMH-333	-3.2 to -7.1 (-5.5, 1)	19	288 to 385 (344, 15)	74
			215, 251	2
	3.3	1		
UG-C				
	-1.8 to -6.4 (-4.9, 1.2)	27	300, 322.5	2
	0.2 to 11.8	13		
	9.2	1	252	1
			290 to 344 (319, 14)	26
			230, 237, 261, 269	4
JMH-301				
	-0.15 to 13.2	8		
GOR				
	4.8 to 10.8	5		
MIL			180 to 203	12

*: N=number of measurements, **: P=primary, ***: S=secondary, T=temperature, h=homogenization, V-L=vapour to liquid, Crit=critical, e=first ice melting, m=melting, HH="hydrohalite" (tentative), CLA=clathrate, TOT=total.

Figure 1

Histogram showing the distribution of total homogenization temperatures of type 1 fluid inclusions in rodingitized diorite and slate, and in vesuvianite from vesuvianite-rich veins.

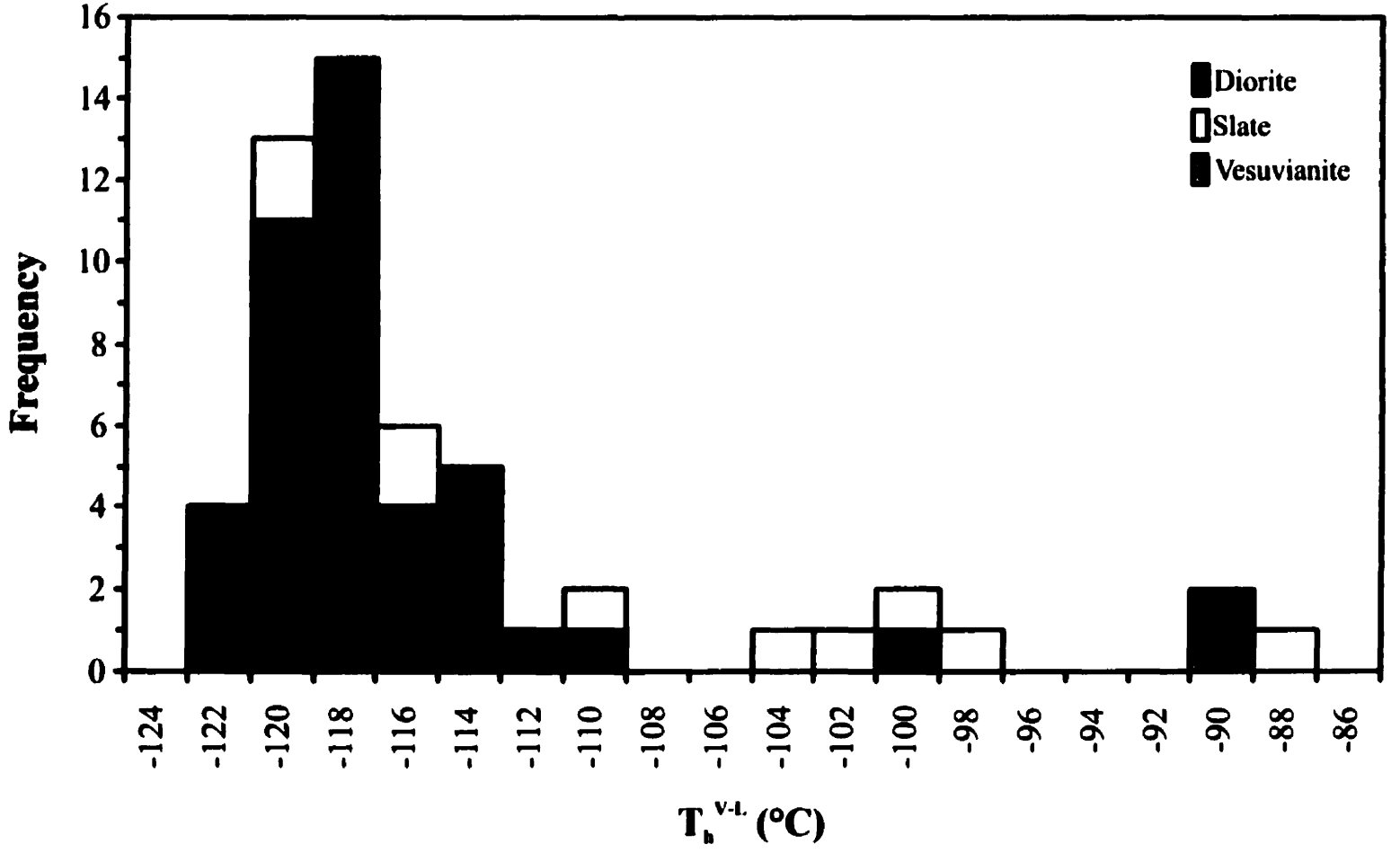
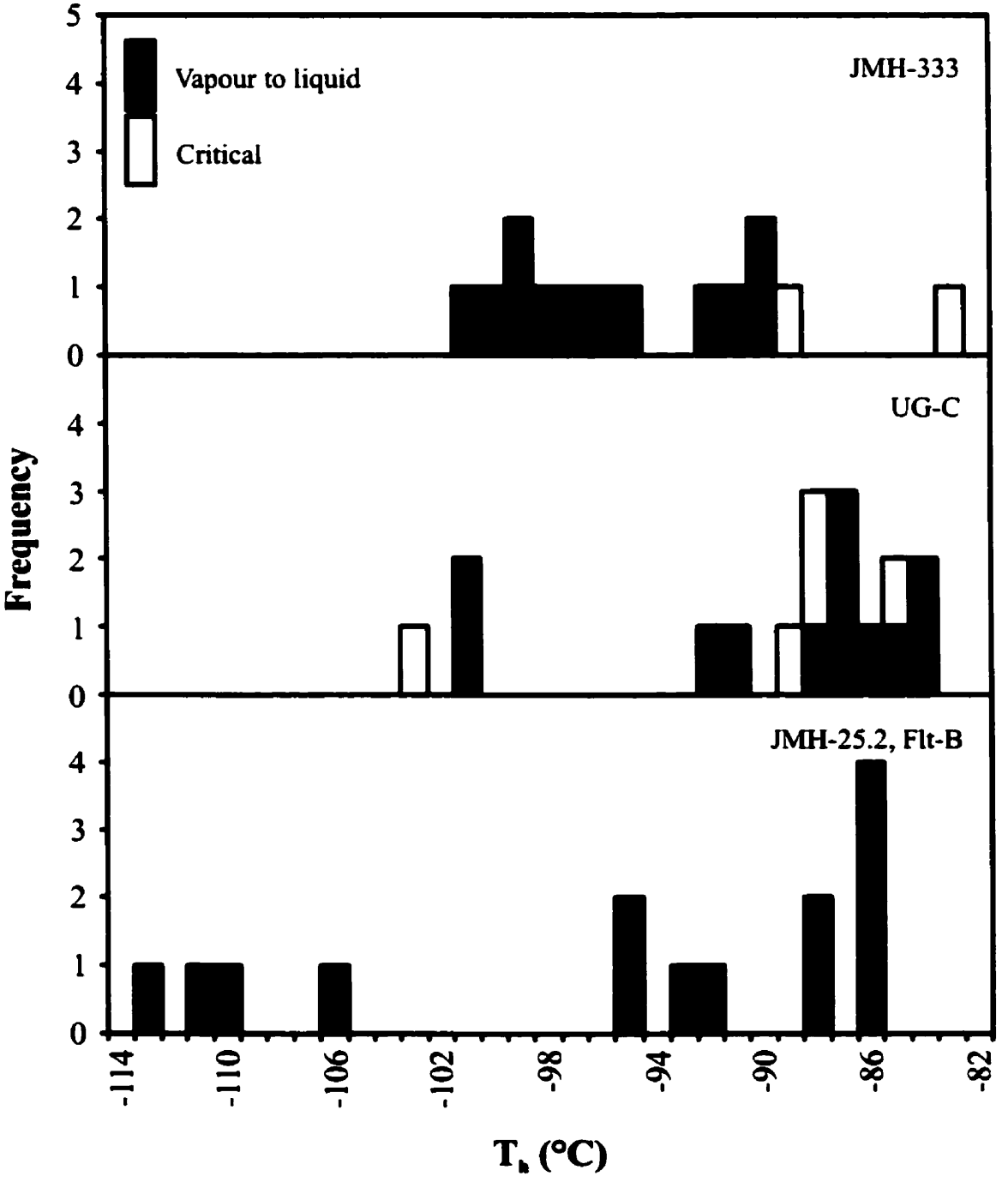

Diorite
Slate
Vesuvianite
Frequency
16
14
12
10
8
6
4
2
0
-124
-122
-120
-118
-116
-114
-112
-110
-108
-106
-104
-102
-100
-98
-96
-94
-92
-90
-88
-86
T_h^{V-L} (°C)

Figure 2

Histograms showing the distribution of vapour to liquid homogenization temperatures in the inner fluid (liquid bubble) of type 2a and 2b fluid inclusions in rodingitized granite (JMH-333), rodingitized slate (UG-C), and rodingitized diorite (JMH-25.2 and Flt-B).


Vapour to liquid
Critical
JMH-333
UG-C
JMH-25.2, Flt-B
Frequency
0
1
2
3
4
5
-114
-110
-106
-102
-98
-94
-90
-86
-82
T_h (°C)

sample JMH-333, and between -76 and -48°C in sample UG-C (Figure 3). The ice finally melted between -27.3 and -23.4°C in sample JMH-333 and between -25.6 and -22.8°C in sample UG-C (Figure 4). Upon further heating, the clathrate melted at temperatures between -7.1 and -3.2°C in sample JMH-333, and between -6.4 and -1.8°C in sample UG-C (Figure 5). The hydrate phase persisted to temperatures between -6.5 and 6.7°C in sample UG-C, and between -4.6 and 20.8°C in sample JMH-333. A pinkish solid phase was observed in two inclusions in sample UG-C and melted at a temperature of between 0.2 and 0.3°C above the melting point of the hydrate phase (-5.6 and –5.4°C). This solid is tentatively identified as halite. The calculated salinities, in terms of equivalent NaCl and uncorrected for the presence of clathrate, vary between 24 and 27 wt. % (4.1-4.6 *m* NaCl).

The concentration of initial ice melting temperatures around -52°C (Figure 3) and the occurrence of five inclusions with initial ice melting at temperatures of -67 to -76°C strongly suggests that the salts dissolved in type 2a fluid inclusions are predominantly NaCl and $CaCl_2$. The eutectic temperature of the system NaCl-$CaCl_2$-H_2O is -52°C and there is a metastable eutectic at -70°C (see Davis et al., 1990). The sequence of eutectic, final ice, hydrate and halite(?) melting temperatures of type 2a fluid inclusions in sample UG-C can be used to graphically estimate the NaCl/(NaCl+$CaCl_2$) molar ratio of these inclusions using the data presented in Williams-Jones and Samson (1990). The bulk fluid composition of two type 2a inclusions, that displayed sequences of phase change consistent with Williams-Jones and Samson (1990) data, suggest NaCl/(NaCl+$CaCl_2$) molecular ratios of 0.84 and 0.85, respectively (Na/Cl ~ 0.72).

Behaviour similar to that observed in type 2a inclusions was noted during heating of type 2b inclusions from -196 to 25°C. The main difference was in the temperature of melting of the clathrate, which varied from 0 to 13°C. Type 2b inclusions show a much wider range of clathrate and ice melting temperatures. However, these temperatures are positively correlated in type 2b inclusions, suggesting that the latter were trapped under similar conditions. The relationship between the clathrate melting temperatures and the salinity in wt. % equivalent NaCl (not corrected for the presence of clathrate and $CaCl_2$)

Figure 3

Histograms showing the distribution of the initial ice melting temperatures of type 2a and 2b fluid inclusions in rodingitized granite (JMH-333), rodingitized slate (UG-C and JMH-301), and rodingitized diorite (JMH-25.2 and Flt-B), and of type 2c fluid inclusions in vesuvianite from vesuvianite-rich veins (GOR and MIL).

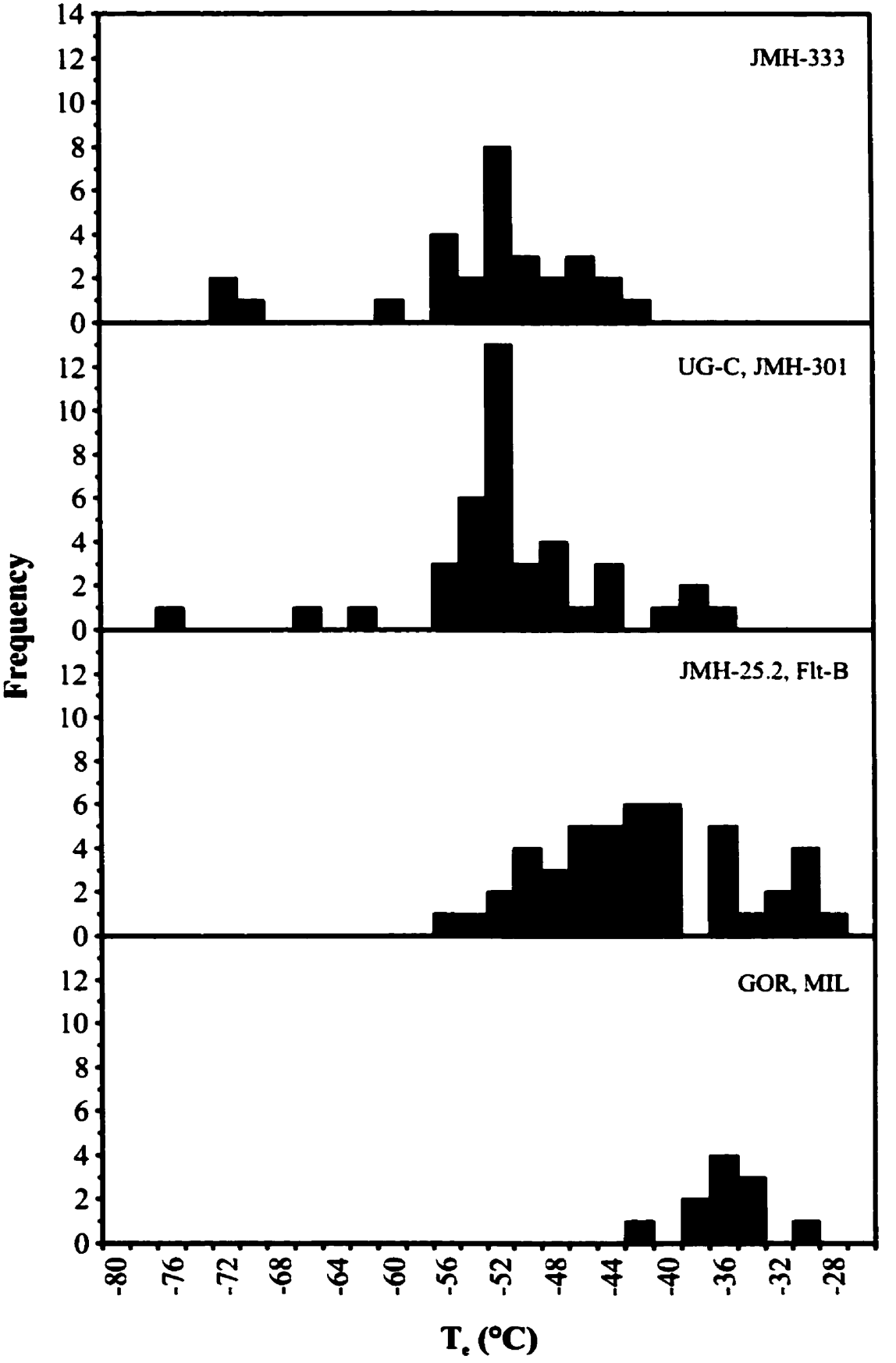

JMH-333
UG-C, JMH-301
JMH-25.2, Flt-B
GOR, MIL
Frequency
0
2
4
6
8
10
12
14
-80
-76
-72
-68
-64
-60
-56
-52
-48
-44
-40
-36
-32
-28
T$_e$ (°C)

Figure 4

Histograms showing the distribution of the final ice melting temperatures of type 2a and 2b fluid inclusions in rodingitized granite (JMH-333), rodingitized slate (UG-C and JMH-301), and rodingitized diorite (JMH-25.2 and Flt-B), and of type 2c fluid inclusions in vesuvianite from vesuvianite-rich veins (GOR and MIL).

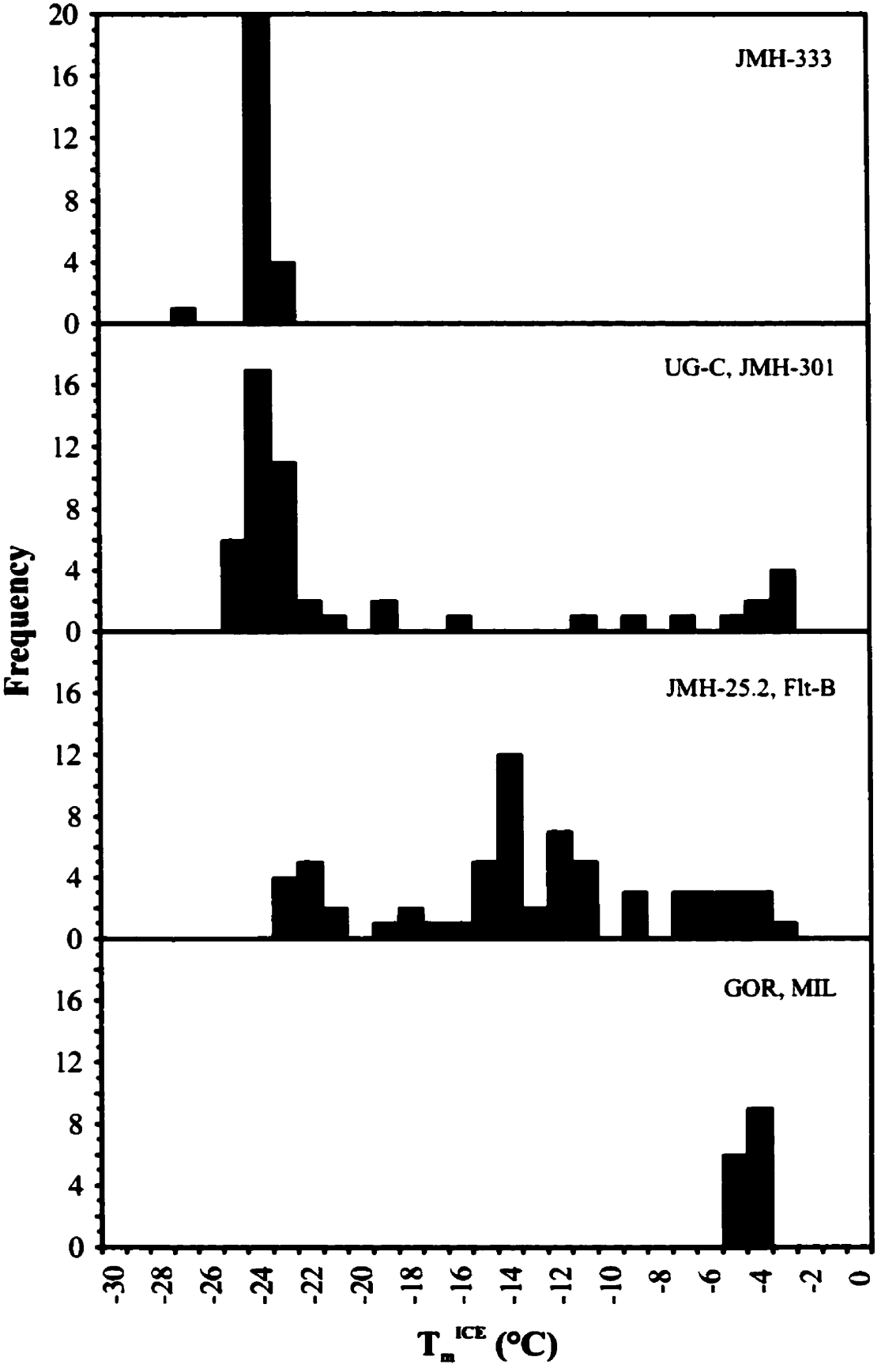
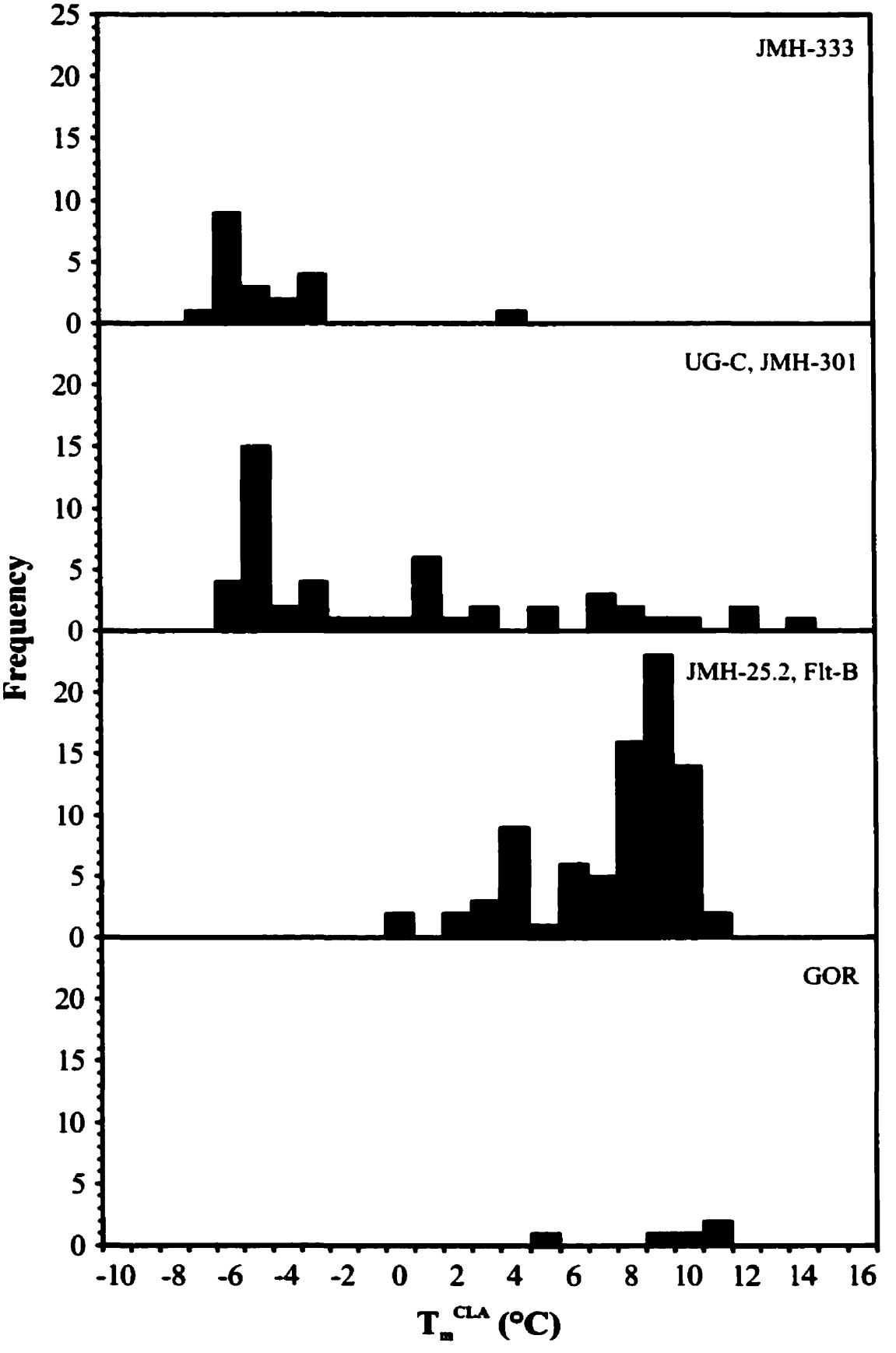

JMH-333
UG-C, JMH-301
JMH-25.2, Flt-B
GOR, MIL
Frequency
0
4
8
12
16
20
-30
-28
-26
-24
-22
-20
-18
-16
-14
-12
-10
-8
-6
-4
-2
0
T_m^{ICE} (°C)

Figure 5

Histograms showing the distribution of the final clathrate melting temperatures of type 2a and 2b fluid inclusions in rodingitized granite (JMH-333), rodingitized slate (UG-C and JMH-301), and rodingitized diorite (JMH-25.2 and Flt-B), and of type 2c fluid inclusions in vesuvianite from vesuvianite-rich veins (GOR).


JMH-333
UG-C, JMH-301
JMH-25.2, Flt-B
GOR
Frequency
25
20
15
10
5
0
-10 -8 -6 -4 -2 0 2 4 6 8 10 12 14 16
T_m^{CLA} (°C)

of type 2 inclusions is illustrated in Figure 6. Curves for internal inclusion pressures of 50, 100 and 150 bars for the system CH_4-NaCl-H_2O (from Diamond, 1994) are also shown for comparative purposes. The data indicate that type 2b inclusions are denser than type 2a inclusions, and, consistent with their coexistence with high-density type 1 inclusions, that they were thus trapped at higher pressure and/or lower temperature. The higher homogenization temperatures of type 2a fluid inclusions in sample JMH-333 relative to type 2b inclusions in sample JMH-25.2 indicate that the lower clathrate melting temperatures in sample JMH-333 result from trapping at higher temperatures.

Whereas in types 2a and 2b inclusions a vapour bubble formed in the inner fluid at low temperatures (< -82°C), this was not the case in type 2c inclusions. This suggests that the bubble in these inclusions contains a much lower proportion of CH_4, i.e., that it is composed predominantly of water vapour. The ice began to melt between -42 and -35°C, and finally melted between -5.7 and -4.5°C. Clathrate was the last solid phase to melt in type 2c inclusions, and did so between 4.8 and 10.8°C. The clathrate was very difficult to observe, further suggesting that only very small proportions of CH_4 were dissolved in the vapour bubble.

X_{CH_4} estimates

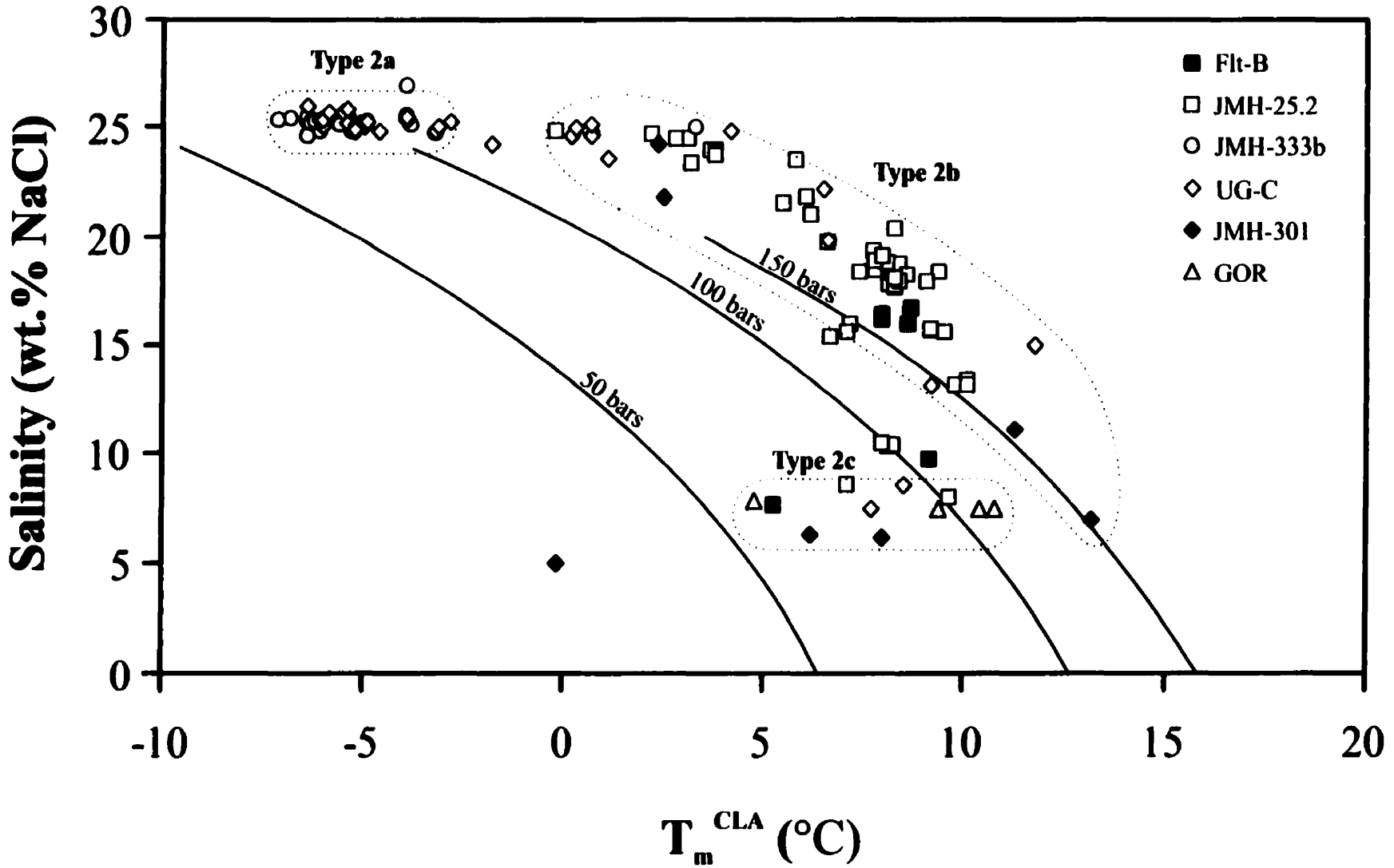
The mole fraction of CH_4 ($X_{CH_4}=nCH_4/[nCH_4+nH_2O+nNaCl]$) in type 2 fluid inclusions was estimated by calculating the number of moles n of CH_4, H_2O and NaCl in each inclusion using the following relationship:

$$n_{CH_4} = \frac{V_{CH_4} \cdot \rho_{CH_4}}{M_{CH_4}} + n'_{CH_4}$$

(where V_{CH_4} is the optically estimated volumetric fraction of bubble at 25°C; ρ_{CH_4} is the density of CH_4 obtained from homogenization data and molar volume data in Thiéry et al., 1994; M_{CH_4} is the molecular weight of CH_4; and n'_{CH_4} is the number of moles of CH_4 dissolved in the aqueous portion of the inclusion at 25°C, estimated from tables in Duan et al., 1992):

Figure 6

Diagram showing the relationship between the melting temperature of the clathrate and the salinity (uncorrected for the presence of clathrate) of type 2a, type 2b and type 2c fluid inclusions. Also shown, are isobars for comparative purposes at pressures of 50, 100 and 150 bars for the system CH_4-NaCl-H_2O (from Diamond, 1994). Type 2c fluid inclusions form a distinct population. Because the volatile compositions determined from gas chromatographic analyses of samples JHM-333 (containing only type 2a fluid inclusions), UG-C (containing type 2a and type 2b fluid inclusions) and JMH-25.2 (containing primarily type 2b fluid inclusions and no type 2a inclusions) are similar, the inferred lower internal pressure of type 2a fluid inclusions is interpreted to reflect trapping under pressure conditions similar to type 2b fluid inclusions but at higher temperature.


Salinity (wt.% NaCl)
30
25
20
15
10
5
0
-10
-5
0
5
10
15
20
T_m^{CLA} (°C)
Type 2a
Type 2b
Type 2c
150 bars
100 bars
50 bars
Flt-B
JMH-25.2
JMH-333b
UG-C
JMH-301
GOR

$$n_{H_2O} = \frac{V_{aq} \cdot \rho_{aq} \cdot (100 - wt.\%NaCl)}{M_{H_2O} \cdot 100}$$

$$n_{NaCl} = \frac{V_{aq} \cdot \rho_{aq} \cdot wt.\%NaCl}{M_{NaCl} \cdot 100}$$

The calculations suggest that X_{CH_4} varies between ≈ 0.01 and 0.03 in type 2a inclusions, and between ≈ 0.02 and 0.04 in type 2b inclusions (Figure 7). The mole fraction of CH_4 in type 2c inclusions could not be calculated because of the absence of a CH_4-dominant phase, but may be assumed to be < 0.01.

Heating experiments

Almost all inclusions > 10 μm, whether or not they had been frozen previously, decrepitated upon being heated above 100°C, confirming that the fluid inclusions have high density (elevated internal pressure).

Complete homogenization of type 2a inclusions in sample JMH-333 occurred at temperatures between 288 and 385°C, and there was a tight clustering of homogenization temperatures at 344 ± 15°C (Figure 8). In sample Flt-B, the homogenization temperatures of type 2b inclusions varied between 277 and 326°C, and in sample JMH-25.2, between 286 and 333°C. Secondary inclusions in sample JMH-25.2 (cryogenic data similar to those of low salinity type 2b and 2c inclusions) homogenized at temperatures between 222 and 275°C. Homogenization temperatures of primary inclusions in rodingitized slate (UG-C) were concentrated primarily between 290 and 344°C. Five secondary inclusions homogenized at temperatures between 230 and 269°C. Primary type 2c inclusions of prismatic habit in vesuvianite (MIL) homogenized at a mean temperature of 191°C.

Gas chromatographic analyses

Gas chromatographic analyses of the inclusion fluids in samples UG-C, JMH-333,

Figure 7

Histograms showing the distribution of the calculated molar fractions of CH_4 in type 2a and type 2b fluid inclusions (see text).

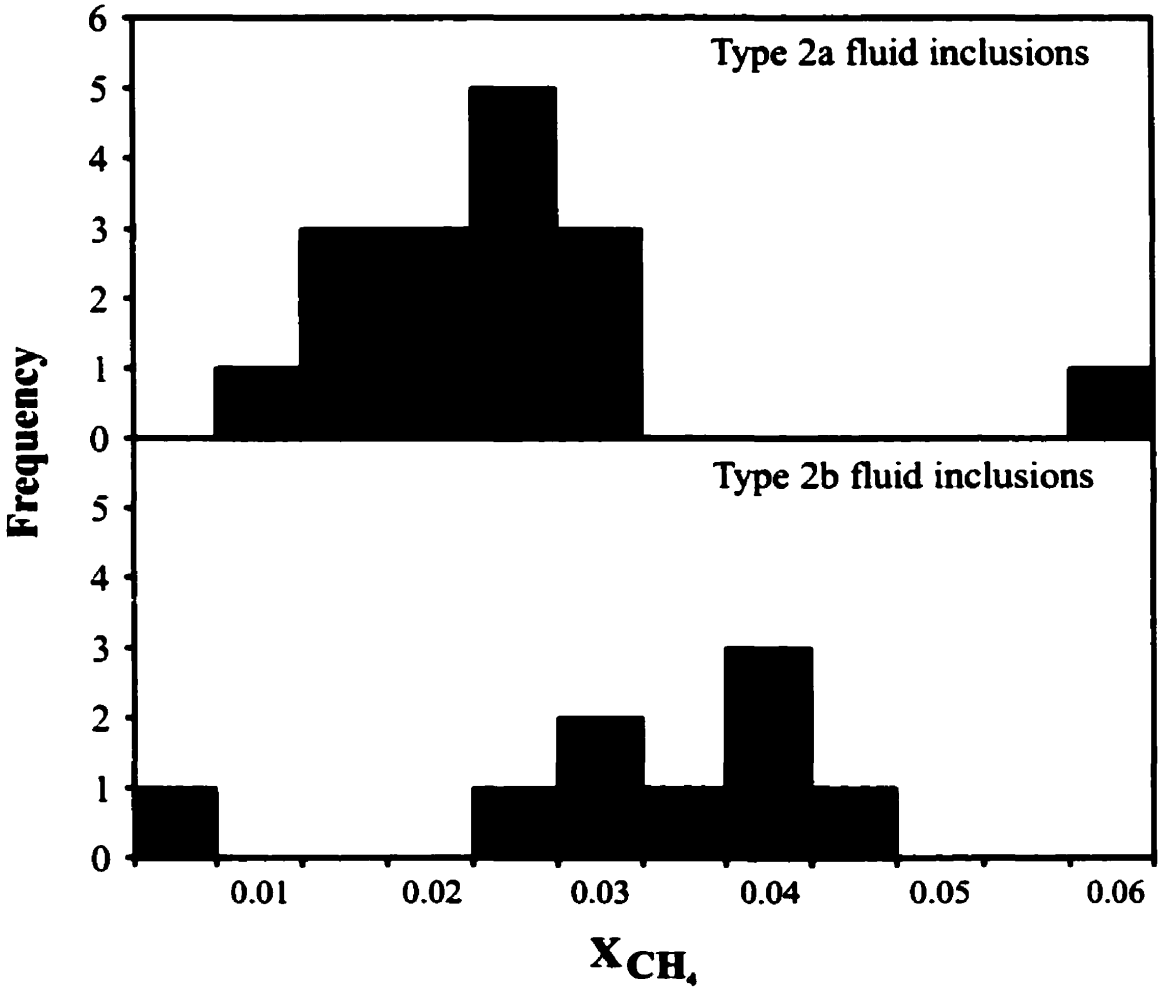
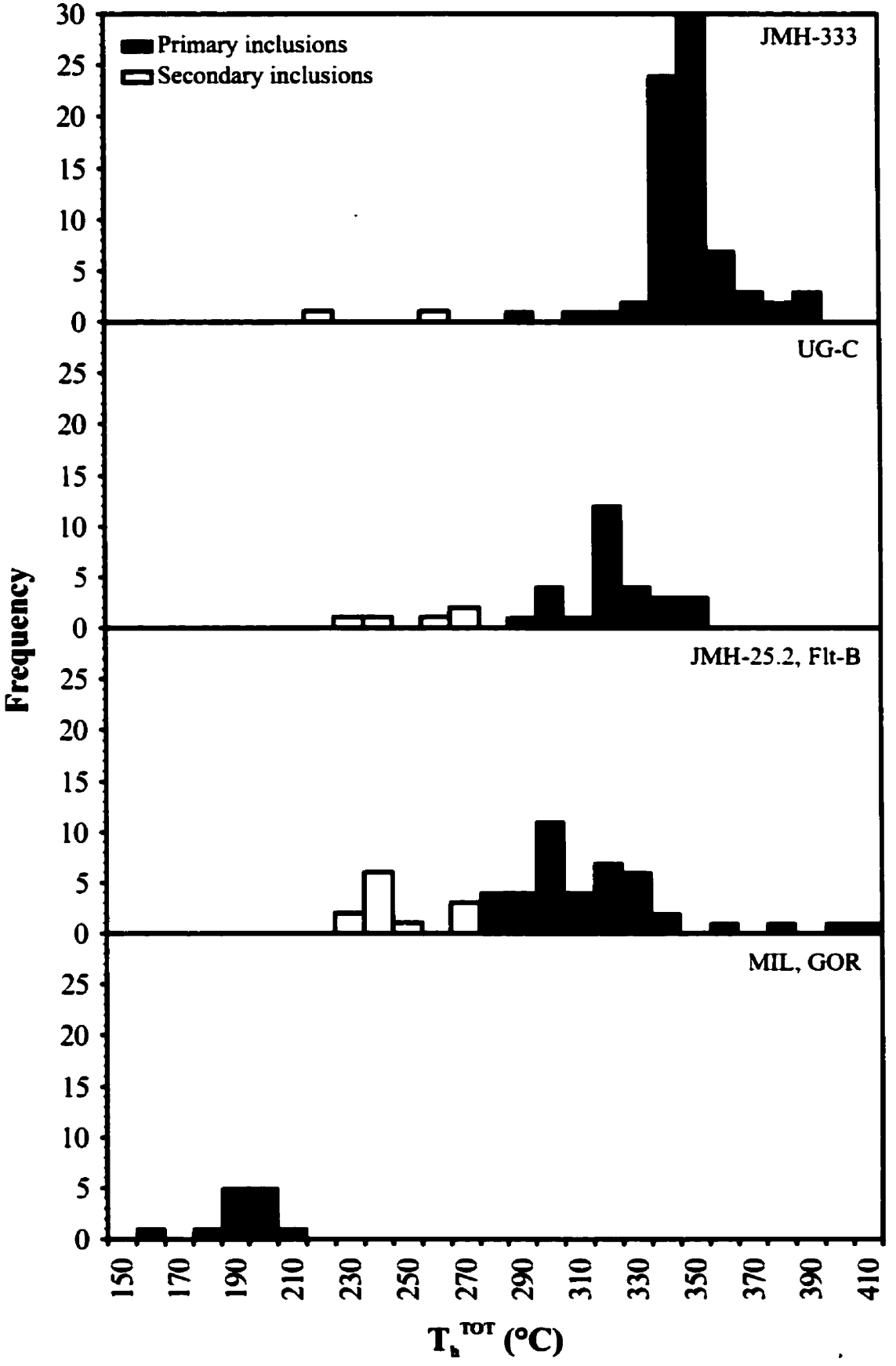

Type 2a fluid inclusions
Type 2b fluid inclusions
Frequency
0
1
2
3
4
5
6
0.01
0.02
0.03
0.04
0.05
0.06
X_{CH_4}

Figure 8

Histograms showing the distribution of the temperatures of total homogenization of type 2a and 2b fluid inclusions in rodingitized granite (JMH-333), rodingitized slate (UG-C), and rodingitized diorite (JMH-25.2 and Flt-B), and of type 2c fluid inclusions in vesuvianite from vesuvianite-rich veins (MIL and GOR).


Primary inclusions
Secondary inclusions
JMH-333
UG-C
JMH-25.2, Flt-B
MIL, GOR
Frequency
0
5
10
15
20
25
30
150
170
190
210
230
250
270
290
310
330
350
370
390
410
T_h^{TOT} (°C)

JMH-25.2, JMH-157, JMH-158, Flt-100a, Flt-100b, and GOR confirmed the presence of CH_4. The latter formed the principal carbonic species in the volatile mixtures. Hydrocarbons detected in addition to CH_4 are C_2H_6, C_3H_8, *n*-C_4H_{10}, *n*-C_5H_{12}, and smaller proportions of C_2H_2 or C_2H_4, C_3H_6, and *i*-C_4H_{10}. The bulk $C_{2+}/(C_{2+}+CH_4)$ gas ratios of the samples vary between 0.002 (JMH-157.3) and 0.08 (GOR). CO_2 was not detected in any of the samples.

Small amounts of N_2 or CO or Ar or H_2 were also detected. However, co-elution of N_2, CO, Ar, and H_2 does not permit differentiation between these species by gas chromatographic analysis using He as the carrier gas. Assuming that the species was N_2, the calculated bulk fluid $N_2/(N_2+CH_4)$ molar ratio would be ~ 0.09 for the rodingitized felsic intrusive rocks and slates, and ~ 0.21 for vesuvianite and wollastonite samples (Figure 9). The similarity of the values of this ratio among the samples of rodingitized felsic intrusive rocks and slates suggests that the difference in the inferred internal pressure of type 2a and type 2b inclusions is not due to large variations in the proportion of the volatiles, but is real. However, the proportions of this unidentified species in the samples from vesuvianite-rich veins, which contain type 1 and type 2c inclusions, are significantly higher. Raman spectroscopy and gas chromatographic analysis using N_2 carrier gas is required to determine the identity of the unknown species.

Details on the analytical procedures and results, and a discussion of the origin of the hydrocarbons are presented in Chapter VII.

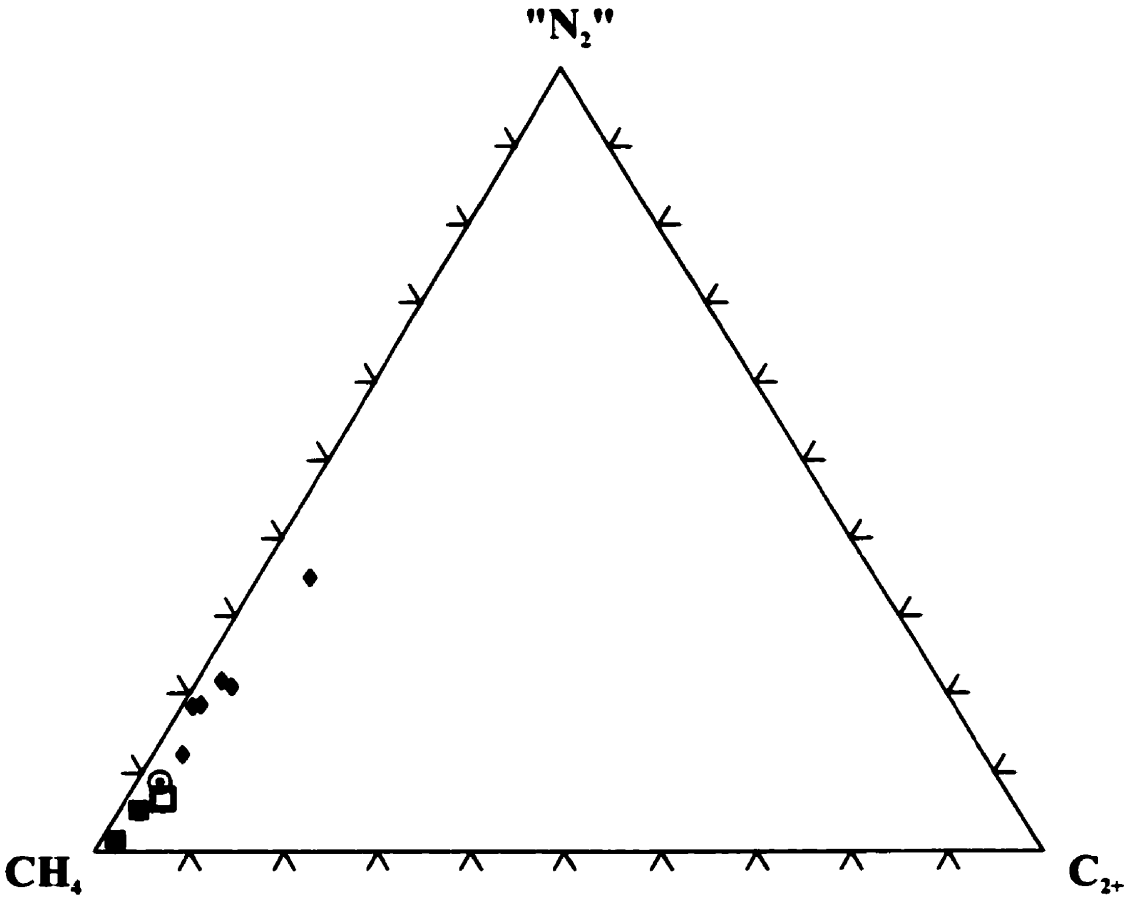
DISCUSSION

Trapping conditions

The pressure and temperature conditions under which the rodingites formed can be estimated using the fluid inclusion data and the mineral parageneses. The homogenization temperatures of type 1 and type 2 inclusions can be used to estimate their trapping conditions assuming that they were trapped at the same pressure and

Figure 9

Triangular diagram showing the relative proportions of CH_4, C_{2+} hydrocarbons and the unidentified species, assuming it is N_2, in rodingitized diorite, granite and slate, and in vesuvianite-rich veins.



■ Rodingitized diorite (JMH-25.2a, 25.2b)

□ Rodingitized granite (JMH-333, 333bis)

⊙ Rodingitized slate (UG-C)

♦ Vesuvianite and wollastonite

temperature. Microthermometric and bulk gas chromatographic data suggest that type 1 inclusions in rodingitized diorite and slate are composed of > 89 to 97 % CH_4. The isochores for type 1 inclusions were calculated assuming, as a first order approximation, that the carbonic phase in type 1 inclusions is pure CH_4. The equation of state of Holloway (1981) was employed for this purpose. Assuming that the type 2 inclusions were trapped at their homogenization temperature, the isochores for the type 1 inclusions indicate that the corresponding pressure of entrapment of type 2b inclusions in rodingitized diorite (JMH-25.2b) was ~ 2.5 kbar (Figure 10a). This pressure would be a minimum if the unidentified species was N_2, H_2 or Ar. Because the fluid inclusions in the vesuvianite samples contain significant proportions of the unknown species, no attempt was made to estimate the entrapment pressure of type 2c inclusions. However, if the two type 1 inclusions observed in vesuvianite were trapped at the same time as the type 2c inclusions, their homogenization temperature of -90°C would suggest a minimum pressure of entrapment of ~ 1 kbar. The wider range of homogenization temperatures of type 1 inclusions recorded from sample UG-C does not permit a tight constraint to be placed on the pressure conditions during rodingitization of slate. Assuming that the type 2 inclusions in rodingitized slate (UG-C and JMH-301) were trapped at their homogenization temperature, the isochores for the type 1 inclusions indicate that the corresponding pressure of entrapment of type 2b inclusions was > 1.5-2.7 kbar. Because type 1 inclusions do not occur in sample JMH-333, only minimum pressure and temperature conditions can be estimated for this sample during rodingitization. Assuming that the type 2 inclusions in sample JMH-333 were trapped at their homogenization temperature, the isochores of type 2a inclusions would intersect the saturation curve for a 4.3 *m* NaCl solution with $X_{CH_4} = 0.025$ at a minimum pressure of ~ 2 kbar. The pressure was probably similar to that during rodingitization of diorite and slate.

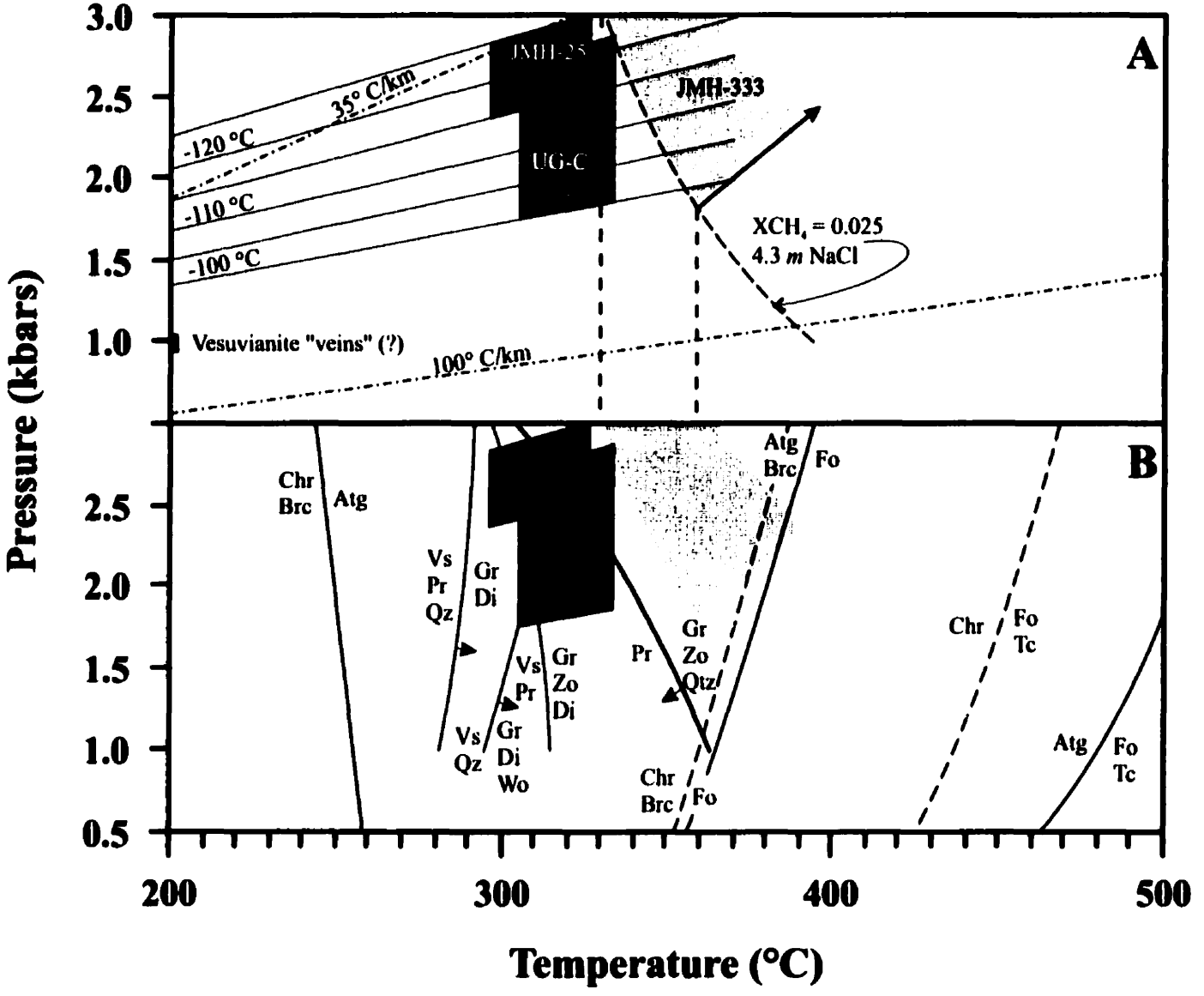
Evolution of mineral parageneses

The absence of vesuvianite in early parageneses from rodingitized diorites and the presence (rare) of late chlorite-vesuvianite veins cutting grossular-diopside-bearing

Figure 10

Diagrams illustrating the pressure and temperature conditions under which the fluid inclusions were trapped (A) and the mineral assemblages formed (B) during rodingitization of slate (UG-C), diorite (JMH-25.2) and granite (JMH-333). The dotted lines in A represent the isochores for type 1 fluid inclusions homogenizing between -100 and -125°C in rodingitized diorite and slate, assuming they are composed of pure CH_4. The dark grey box represents the conditions of trapping of type 2b fluid inclusions in the rodingitized diorite sample JMH-25.2, assuming they coexisted with type 1 fluid inclusions. The medium grey box represent the conditions of trapping of type 2a and type 2b fluid inclusions in the rodingitized slate sample UG-C, assuming they coexisted with type 1 fluid inclusions. The lighter grey area represents the inferred P-T conditions of type 2a inclusion fluids during rodingitization of the pegmatitic granite sample JMH-333, assuming trapping occurred at close to saturation with CH_4 (see text). The saturation pressure and temperature coordinates for a fluid in which $X_{CH_4} = 0.25$ and m NaCl = 4.3 in the system NaCl-H_2O-CH_4 (dashed curve) were calculated from data in Duan et al. (1992) and Lamb et al. (1996). Dash-dot lines represent geotherms.

The equilibrium boundaries for rodingite mineral assemblages (thick lines) in B were calculated with the program THERMOCALC (v2.3: Powell and Holland, 1988; Holland and Powell, 1990) using the following values for the activity of the minerals: a_{Zo}=0.72, a_{Di}=0.44, a_{Grs}=0.8, $a_{Mg\text{-}Vsv}$=0.25 (see table 2). The full thin lines in B represent equilibrium iso-reaction lines for sepentinites. The dashed lines represent metastable iso-reaction lines. Mineral abbreviations are from Kretz (1983).


A
B
JMH-25
JMH-333
UG-C
-120 °C
-110 °C
-100 °C
35° C/km
100° C/km
XCH4 = 0.025
4.3 m NaCl
Vesuvianite "veins" (?)
Chr
Brc
Atg
Vs
Pr
Gr
Di
Qz
Wo
Zo
Qtz
Fo
Tc
3.0
2.5
2.0
1.5
1.0
0.5
200
300
400
500
Pressure (kbars)
Temperature (°C)

rodingites can be used to estimate semi-quantitatively the thermal evolution of diorites during rodingitization. The fields of stability of vesuvianite-bearing and vesuvianite-free mineral assemblages relative to pressure and temperature, estimated from P-T and T-X_{CO_2} topologies in Valley et al. (1985) and Hochella et al. (1982), are consistent with those calculated with the program THERMOCALC (v2.3: Powell and Holland, 1988; Holland and Powell, 1990). According to these estimates, the assemblage diopside + zoisite + grossular (JMH-25) is stable at higher temperatures than the assemblage prehnite + vesuvianite as predicted by the reaction:

$$14\text{Prehnite} + 3\text{Vesuvianite} = 5\text{Zoisite} + 6\text{Diopside} + 23\text{Grossular} + 25H_2O \quad (1),$$

while the assemblage diopside + grossular is stable at higher temperature than the assemblage zoisite + quartz + vesuvianite as predicted by the reaction:

$$\text{Prehnite} + 5\text{Quartz} + 2\text{Vesuvianite} = 4\text{Diopside} + 12\text{Grossular} + 10H_2O \quad (2).$$

The stability fields of assemblages containing quartz, diopside, vesuvianite, prehnite, grossular, and zoisite were calculated with the program THERMOCALC v.2.3 and are represented in Figure 10b. The average activity of end-member diopside in the clinopyroxene was assumed to be equal to the mole fraction of diopside, while the average activity of zoisite, grossular and vesuvianite were calculated assuming ideal on site mixing (summarized in Table 2).

The fluid inclusion and petrographic data indicate that there were at least two episodes of rodingitization. The earlier episode corresponded to rodingitization of diorite, slate, and granite, and was followed by a second episode of rodingitization during which the vesuvianite-rich "veins" formed. The data thus define an early high temperature and a later, lower temperature (probably also lower pressure) regime of alteration. As can be seen from Figure 10, the pressure and temperature conditions estimated from type 2b fluid inclusions are consistent with the stability fields calculated for the assemblages

Table 2. Activity of end-member components in minerals from rodingites.

Mineral	Activity expression
Diopside	$a_{Di}^{Cpx} = X_{Di}^{Cpx}$ *
Zoisite	$a_{Zo}^{Ep} = X_{Zo}^{Ep} = (X_{Ca}^{A})^2 (X_{Al}^{M1,M3})^2 (X_{Al}^{M2}) (X_{Si}^{T})^3 (X_{OH}^{OH})$ **
Grossular	$a_{Gr}^{Gnt} = (X_{Ca}^{X})^3 (X_{Al}^{Y})^2 (X_{Si}^{Z})^3$ ***
Mg-Vesuvianite#	$a_{Ves}^{Mg\text{-}Ves} = X_{Ves}^{Mg\text{-}Ves} = 20.4 (X_{B}^{Mg}) (X_{AlFe}^{Mg}) (X_{AlFe}^{Al})^7 (X_{OH}^{OH})^7$ ****
Clinochlore	$a_{Clin}^{Chl} = X_{Clin}^{Chl} = 141.56 [(X_{Mg}^{O})^5 (X_{Al}^{O})] [(X_{Al}^{T}) (X_{Si}^{T})^3]$ *****

*: Ideal mixing.

**: Ideal mixing on sites.

***: Ideal mixing on sites.

****: Hoisch, 1985.

*****: Saccocia and Seyfried, 1994.

#: Mg-Vesuvianite = $Ca_{19}Mg_2Al_{11}Si_{18}O_{69}(OH)_9$ (Hoisch, 1985; Holland and Powell, 1990)

Table 2. (continued)

Mineral	Activity					
	JMH-25.2	JMH-295.1	JMH-306	Float-B	UG-C	E:7.5
Diopside	0.45 (0.05)	0.53 (0.07)	0.44 (0.05)	0.64 (0.05)	0.45 (0.07)	—
Zoisite	0.72 (0.09)	—	—	—	0.41 (0.08)	—
Grossular	0.79-0.85	0.83-0.87	0.90-0.94	0.79-0.84	0.65-0.95	0.68-0.84
Mg-Vesuvianite#	—	—	—	—	—	0.25
Clinochlore	—	0.23 (0.15)	0.11 (0.04)	0.02 to 0.44	—	—

*: Ideal mixing.

**: Ideal mixing on sites.

***: Ideal mixing on sites.

****: Hoisch, 1985.

*****: Saccocia and Seyfried, 1994.

#: Mg-Vesuvianite = $Ca_{19}Mg_2Al_{11}Si_{18}O_{69}(OH)_9$ (Hoisch, 1985; Holland and Powell, 1990)

grossular + diopside, zoisite + diopside and zoisite + grossular + diopside. The low homogenization temperatures of fluid inclusions in vesuvianite from vesuvianite-rich samples are consistent with the absence of diopside and zoisite. However, the presence of grossular and diopside, and of grossular, diopside and wollastonite with vesuvianite in some samples (e.g., E:7.5) suggests that the activity of the phases on the high temperature side of the equilibrium boundaries of Figure 10 should be much lower than calculated. Such lowered activities would be required to reconcile the fluid inclusion data, and offset the effect of the lowered activity of silica (below quartz saturation) in displacing the equilibrium of the reaction

$$2\text{Vesuvianite} + 6\text{Quartz} = 4\text{Diopside} + 11\text{Grossular} + \text{Wollastonite} + 9H_2O \qquad (3)$$

to higher temperature. More probably, vesuvianite formed over a very wide range of temperatures, i.e., between those indicated by sample JMH-333 (T_h < 360°C) and those indicated by the "vein" sample MIL (T_h 180-203°C). Because the granites must have intruded the serpentinites before rodingitization of the slates, the lower temperatures of the vesuvianite-rich "veins" must indicate a very late stage of rodingitization, recrystallization and intense veining. If the unidentified gas species was N_2, its presence in the vesuvianite-rich "veins" in proportions up to twice those in the other rodingites (see Figure 9) might indicate a progressive increase in the contribution of a fluid derived from sedimentary rocks of the Laurentian continental margin or of meteoric waters.

Spatial and temporal relationships

The occurrence of andalusite with K-feldspar and plagioclase in the later granites and granitic pegmatites implies a minimum temperature of emplacement of ~ 650°C (minimum solidus temperature of water-saturated peraluminous melts containing an aluminosilicate; Thompson and Tracy, 1979) and a maximum pressure of ~ 4 kbar (depth < 15 km). The original thickness of the crustal section of the strongly dismembered Asbestos ophiolite is unknown. However, according to Laurent et al. (1979), the thickness of the crust in the Thetford Mines ophiolite is approximately two km.

Assuming a similar thickness for the crust in the Asbestos ophiolite, the pressure at the transition between crust and mantle would have been less than 1 kbar before detachment of the ophiolite from the seafloor and before thickening as a result of thrust stacking and folding during obduction. The occurrence of some of the granitic rocks at the base of the cumulate ultramafic unit, where interdigitated harzburgites and dunite occur, would suggest intrusion at very low pressures. However, whether or not the interdigitated harzburgites and dunites represent syn-oceanic or later obduction-related features remains to be determined (Hébert and Bédard, 1998).

At the suggested time of intrusion of the felsic intrusive rocks, between 470 and 460 Ma (Chapter IV), the only rock unit that existed above the ophiolite was the Saint-Daniel Formation, which comprises, among other types of lithologies, pelagic sediments deposited on the seafloor (Pinet and Tremblay, 1995). Southeast of Asbestos, this formation is < 6 km thick. The combined thickness of this sedimentary unit (assuming it represents the original thickness) and the underlying igneous crust (2 km) indicates that the minimum depth of emplacement of the felsic intrusive rocks in the Asbestos ophiolite was 8 km, corresponding to a lithostatic pressure of > 2.2-2.4 kbar, i.e., within the range of pressures estimated from the fluid inclusion data (assuming type 1 inclusions are composed of pure CH_4).

Cross-cutting relationships indicate that the granitic rocks were intruded after the dioritic rocks, although the absolute time elapsed between the intrusion of these rocks is unknown. However, we have shown in Chapter IV that the diorites and granites could be genetically related through crystal fractionation, suggesting that their ages are similar. Consistent with this, the fluid inclusion data suggest that the granites and the diorites were rodingitized under roughly the same conditions of pressure. The similar homogenization temperatures of type 2a and type 2b fluid inclusions in samples UG-C (319 ± 14°C), JMH-25.2 (312 ± 15°C) and Flt-B (302 ± 14°C) suggest that the diorites reached thermal equilibrium with the host serpentinites before rodingitization. The higher homogenization temperatures of type 2a fluid inclusions in sample JMH-333 (344 ± 15°C) most likely reflect a local input of heat by rodingitizing fluids. It is highly unlikely that the granitic rocks retained sufficient residual heat after they were intruded to account

for this discrepancy in the homogenization temperatures. For this to have occurred, thrusting of the ophiolite over the Caldwell Group slates would have to had taken place very rapidly and immediately after granite intrusion.

CONCLUSIONS

Petrographic and fluid inclusion data indicate that there were two episodes of rodingitization involving three distinct fluids. In an early, relatively high-pressure (~ 2-3 kbar) episode, fluids of moderate to high salinity (~ 2 to < 4.3 *m* NaCl eq.) rodingitized diorite, granite and slate at temperatures of 300-350°C. A second episode of rodingitization at lower temperatures (< 270°C) and pressure, is recorded by secondary fluid inclusions in slate, diorite and granite, and by primary low-salinity (< 2 *m* NaCl eq.) fluid inclusions in vesuvianite-rich mineral assemblages (< 200°C). Gas chromatographic analyses of the inclusion fluids in the rodingites indicate that all comprise a carbonic component, in which CH_4 is the dominant species among mixtures containing short-chain alkanes. This indicates that all the fluids interacted with serpentinite. It is interesting to note that type 2a and type 2b fluid inclusions represent the most concentrated brines yet reported from rodingites and the first example of first ice melting temperatures consistent with a calcium-rich composition.

The exact nature of the inclusion fluids in the rodingites can not be resolved until more detailed analyses of their dissolved salts are performed and C-O-H stable isotopic data are obtained. Nevertheless, some general observations can be made taking into account the geological environment in which the Asbestos ophiolite evolved. The most important information concerning the fluid inclusions is that type 1, type 2a and type 2b inclusion fluids occur both in the rodingitized slates and in the rodingitized felsic dykes. Based on this, it is concluded that the rodingites formed during thrusting of the Asbestos ophiolite onto the Laurentian margin. Thus, we rule out the involvement of seawater modified in a hydrothermal system driven by mafic magmatism in or near an oceanic zone of extension. For the same reason we also rule out dehydration of deeply subducted

oceanic crust and sediments as a source for the fluid. Potential candidates for the fluids represented by the moderately to strongly saline type 2b and 2a fluid inclusions during thrusting of the Asbestos ophiolite over continental margin sediments are metamorphic waters, including evolved seawater and evolved meteoric and connate waters.

The occurrence of late aragonite in the vesuvianite-rich "veins" and along fractures in the serpentinites suggests that type 2c inclusions may comprise a more significant component of meteoric fluids.

ACKNOWLEDGEMENTS

Prokopis Kranidiotis is thanked for collecting part of the fluid inclusion data set. This research was funded by NSERC and FCAR scholarships to CN and NSERC and FCAR research grants to AEW-J.

REFERENCES

Coleman, R. G., 1966, New Zealand serpentinites and associated metasomatic rocks, New Zealand Geological Survey, Bulletin No. 76, 102 p.

Coleman, R. G., 1967, Low-temperature reaction zones and alpine ultramafic rocks of California, Oregon and Washington, United States Geological Survey, Bulletin No. 1247, 49 p.

Compagnoni, A., Conte, R., Facchinelli, A., Orione, P., Rossetti, P. and C. Trossarelli, 1998, The rodingite of Bellecombe (Val D'Aosta, Italy): a petrographic and fluid inclusion study, 17th general meeting, International Mineralogical Association, August 9-14, Toronto, Canada, Programme and Abstracts, p. A77L.

Cousineau, P. A., 1990, Le Groupe de Caldwell et le domaine océanique entre Saint-Joseph-de-Beauce et Sainte-Sabine, Ministère de l'Énergie, des Mines et des Ressources du Québec, MM 87-02, 165 p.

Davis, D. W., Lowenstein, T. K. and R. J. Spencer, 1990, Melting behavior of fluid inclusions in laboratory-grown halite crystals in the systems NaCl-H_2O, NaCl-KCl-H_2O, NaCl-$MgCl_2$-H_2O and NaCl-$CaCl_2$-H_2O, Geochimica et Cosmochimica Acta, v. 54, p. 591-601.

Diamond, L. W., 1994, Salinity of multivolatile fluid inclusions determined from clathrate hydrate stability, Geochimica et Cosmochimica Acta, v. 58, p. 19-41.

Duan, Z., Møller, N., Greenberg, J. and J. H. Weare, 1992, The prediction of methane solubility in natural waters to high ionic strength from 0 to 250°C and from 0 to 1600 bar, Geochimica et Cosmochimica Acta, v. 56, p. 1451-1460.

Hébert, R., 1980, Etude pétrologique des roches ophiolitiques d'Asbestos et du Mont Ham (Ham Sud), M. Sc. Thesis, Université Laval, Québec, 182 p.

Hébert, R. and J. H. Bédard, 1998, Architecture and petrogenesis of arc ophiolites: example from the ophiolitic complexes of southern Quebec, Geological Association of Canada, Mineralogical Association of Canada, Association des Géologues et Géophysiciens du Québec, International Association of Hydrogeologists, Canadian Geophysical Union Joint Annual Meeting, 13-15 May 1998, Québec, Québec,

Canada, Fieldtrip A4 Guidebook, 51 p.

Hochella, M. F., Jr., Liou, J. G., Keskinen, M. J. and H. S. Kim, 1982, Synthesis and stability relations of magnesium idocrase, Economic Geology, v. 77, p. 798-808.

Hoisch, T. D., 1985, The solid solution chemistry of vesuvianite, Contributions to Mineralogy and Petrology, v. 89, p. 205-214.

Holland, T. J. B. and R. Powell, 1990, An enlarged and updated internally consistent thermodynamic dataset with uncertainties and correlations: the system K_2O-Na_2O-CaO-MgO-MnO-FeO-Fe_2O_3-Al_2O_3-TiO_2-SiO_2-C-H_2-O_2, Journal of Metamorphic Geology, v. 8, p. 89-124.

Holloway, J. R., 1981, Compositions and volumes of supercritical fluids in the earth's crust, *in* Fluid Inclusions: Application to Petrology, Hollister, L. S. and M. L. Crawford, editors, Mineralogical Association of Canada Short Course Handbook, v. 6, p. 13-38.

Kretz, R., 1983, Symbols for rock-forming minerals, American Mineralogist, v. 68, p. 277-279.

Lamb, W. M., Popp, R. K. and L. A. Boockoff, 1996, The determination of phase relations in the CH_4-H_2O-NaCl system at 1 kbar, 400 to 600°C using synthetic fluid inclusions, Geochimica et Cosmochimica Acta, v. 60, p. 1885-1897.

Laurent, R., Hébert, R. and Hébert, Y., 1979, Tectonic setting and petrological features of the Quebec Appalachian ophiolites, *in* Ophiolites of the Canadian Appalachians and Soviet Urals, Memorial University of Newfoundland Report No. 8, p. 53-77.

Mittwede, S. K. and E. S. Schandl, 1992, Rodingites from the southern Appalachian Piedmont, South Carolina, USA, European Journal of Mineralogy, v. 4, p. 7-16.

O'Hanley, D. S., Schandl, E. S. and F. J. Wicks, 1992, The origin of rodingites from Cassiar, British Columbia, and their use to estimate T and $P(H_2O)$ during serpentinization, Geochimica et Cosmochimica Acta, v. 56, p. 97-108.

Pinet, N. and A. Tremblay, 1995, Tectonic evolution of the Quebec-Maine Appalachians: From oceanic spreading to obduction and collision in the Northern Appalachians, American Journal of Science, v. 295, p. 173-200.

Powell, R. and T. J. B. Holland, 1988, An internally consistent thermodynamic dataset

with uncertainties and correlations: 3. Applications to geobarometry, worked examples and a computer program, Journal of Metamorphic Geology, v. 6, p. 173-204.

Saccocia, P. J. and W. E. Seyfried, Jr., 1994, The solubility of chlorite solid solutions in 3.2 wt. % NaCl fluids from 300-400°C, 500 bars, Geochimica et Cosmochimica Acta, v. 58, p. 567-585.

Schandl, E., O'Hanley, D. S. and F. J. Wicks, 1989, Rodingites in serpentinized ultramafic rocks of the Abitibi greenstone belt, Ontario, Canadian Mineralogist, v. 27, p. 579-591.

Schandl, E., O'Hanley, D. S., Wicks, F. J. and T. K. Kyser, 1990, Fluid inclusions in rodingite: a geothermometer for serpentinization, Economic Geology, v. 85, p. 1273-1276.

Thiéry, R., van den Kerkhof, A. M. and J. Dubessy, 1994, *vX* properties of CH_4-CO_2 and CO_2-N_2 fluid inclusions: modelling for T < 31°C and P < 400 bars, European Journal of Mineralogy, v. 6, p. 753-771.

Thompson, A. B. and R. J. Tracy, 1979, Model systems for anatexis of pelitic rocks II. Facies series melting and reactions in the system CaO-$KAlO_2$-$NaAlO_2$-Al_2O_3-SiO_2-H_2O, Contributions to Mineralogy and Petrology, v. 70, p. 429-438.

Valley, J. W., Peacor, D. R., Bowman, J. R. Essene, E. J. and M. J. Allard, 1985, Crystal chemistry of a Mg-vesuvianite and implications of phase equilibria in the system CaO-MgO-Al_2O_3-SiO_2-H_2O-CO_2, Journal of Metamorphic Geology, v. 3, p. 137-153.

Williams-Jones, A. E. and I. M. Samson, 1990, Theoretical estimation of halite solubility in the system NaCl-$CaCl_2$-H_2O: applications to fluid inclusions, Canadian Mineralogist, v. 28, p. 299-304.

INTRODUCTION TO CHAPTER VII

In Chapter VI, I discussed the nature of the fluids responsible for rodingitization of the felsic intrusive rocks and slates, and determined the pressure and temperature conditions under which this calc-silicate alteration occurred. It was established that three types of fluid were present during two major episodes of alteration. The first episode took place at greater depth and at higher temperature (P ~ 2-3 kilobars, T 280-360°C) than the second episode (P < 2 kilobars, T ~ 200°C). The first episode involved the mixing of highly and moderately saline fluids (2 and 4.3 *m* eq. NaCl), and the second involved only moderately saline fluids of low density. Both episodes are recorded in the obduction history of the Asbestos ophiolite, with the later one representing the later stages of ophiolite emplacement and probably involving a greater proportion of meteoric fluids.

Gas chromatographic analyses indicated that CO_2 was not present in detectable quantities in the fluid inclusions, but that gaseous carbonic species represented by CH_4 and alkanes of higher carbon number were present in significant proportions. The significance of these hydrocarbons is discussed in the chapter that follows.

CHAPTER VII

RODINGITES: TRAPS FOR FISCHER-TROPSCH CATALYSED HYDROCARBONS IN SERPENTINITES?

by

Charles Normand and Anthony E. Williams-Jones

Department of Earth and Planetary Sciences, McGill University, 3450 University Street, Montréal (Qué), Canada, H3A 2A7.

ABSTRACT

Fluid inclusions in rodingites from the Asbestos ophiolite, Québec, sample aqueous-carbonic and carbonic fluids interpreted to have evolved during serpentinization of the host harzburgites and dunites at temperatures between 180 and 360°C and pressures of 1 to 3 kilobars. Microthermometric and gas chromatographic analyses indicate that the carbonic phase in both types of inclusions is composed mainly of methane. CO_2 was not detected. More importantly, ethane, propane, n-butane, n-pentane, and traces of acetylene or ethylene, cyclopropane and isobutane were identified in the majority of the samples analysed, in proportions which suggest that they formed under unusually high f_{CO_2} and f_{H_2}. The hydrocarbons display a Schulz-Flory distribution for C_{2+} species (CH_4 is in excess in most samples), suggesting that they could have originated from a Fischer-Tropsch-type catalytic process. However, values of the chain-growth probability factor, α, calculated for the hydrocarbon distribution vary from 0.05 to 0.23 (excluding CH_4), i.e., they are outside the range reported for Fischer-Tropsch catalysis (α>0.3 in the presence of magnetite and nickel catalysts). A viable alternative hypothesis, which has not been proposed previously for the origin of hydrocarbons in serpentinites, is equilibration of a carbonic fluid with a strongly reducing metastable (graphite supersaturated) mineral assemblage. Thermodynamic calculations, for the range of temperatures and pressures interpreted from fluid inclusion microthermometry, indicate that the full range of α values determined for the fluid inclusion hydrocarbons from the Asbestos rodingites can be explained by metastable equilibration of the fluids with cohenite (Fe_3C), magnetite (an essential mineral in serpentinites) and awaruite (Ni_3Fe). Furthermore, the calculations predict the excess CH_4 relative to the ideal Schulz-Flory distribution, which is observed in the majority of the samples.

INTRODUCTION

Although hydrocarbon gases (e.g., CH_4, C_2H_6, and C_3H_8) have been reported from numerous localities exposing partially serpentinized peridotites in ophiolites (Thayer, 1966; Barnes and O'Neil, 1969; Neal and Stanger, 1983; Abrajano et al., 1988; Lyon and Giggenbach, 1990; Fritz et al., 1992) and on the seafloor (Welhan and Craig, 1979; Mottl and Haggerty, 1989; Rona et al., 1992; Charlou et al., 1991, 1998), the mechanisms by which these hydrocarbons form and whether they are biogenic or abiogenic remain poorly understood. An example where a good case can be made for a biogenic origin of hydrocarbons associated with serpentinite, is for the seeps reported from Conical Seamount, Mariana fore-arc. Haggerty and Fisher (1992) and Mottl (1992), concluded that the complex mixtures of CH_4, C_2H_6, C_3H_8, and organic acids reported from this locality, were derived from the alkaline hydrolysis and thermal maturation of organic precursors entrained at depth in the Mariana subduction trench, and subsequently transported to near the seafloor by metamorphic fluids produced through devolatilization of the down-going slab during serpentinite diapirism. However, in most other cases of hydrocarbon seeps in serpentinites from ophiolites there is no obvious organic source, implying that the gases (mainly simple alkanes) formed via abiogenic processes. Moreover, methane gas from these serpentinites has a distinctively light carbon isotopic signature that is unlikely to result from the thermal maturation or bacterial reduction of organic matter (Abrajano et al., 1988, 1990; Fritz et al., 1992. See also Welhan, 1987, 1988).

Advocates of an abiogenic origin for hydrocarbons in serpentinites conventionally relate the formation of methane to the presence of a carbonic component, typically CO_2, in the serpentinizing fluid, and reaction of the latter with H_2 produced by the serpentinization (Moody, 1976; Apps, 1985; Frost, 1985). However, this explanation does not account for the formation of the higher hydrocarbons that occur with the methane. Fluids in equilibrium with mineral assemblages comprising serpentine-group minerals or graphite cannot achieve the low f_{O_2} and elevated f_{CO_2} conditions necessary to stabilize significant quantities of hydrocarbons of higher rank than methane.

A process, first proposed by Lancet and Anders (1970), that does lead to the formation of higher hydrocarbons during serpentinization, is Fischer-Tropsch synthesis, which is used to produce synthetic gasoline. This process involves reaction of CO or CO_2 with H_2 in the presence of a Group VIIIA metal or metal oxide catalyst, and produces mixtures rich in long-chain hydrocarbons. Evidence that Fischer-Tropsch synthesis offers a viable explanation for hydrocarbons in serpentinites was provided by Morency et al. (1986) and Berndt et al. (1996) who produced hydrogen and higher hydrocarbons through heating carbonate-bearing serpentinites and serpentinizing olivine by reaction with a CO_2-NaCl aqueous brine, respectively. Magnetite, an important byproduct of serpentinization, was interpreted by Berndt et al. (1996) to be the catalyst for hydrocarbon production in their Fischer-Tropsch synthesis. Morency et al. (1986) did not relate their results explicitly to the Fischer-Tropsch process, although they attributed the formation of hydrocarbons to thermocatalytic hydrogenation of carbon-bearing species in the presence of iron.

Another process which might produce higher hydrocarbons, and which has not been proposed previously, is equilibration of a CO_2-H_2O fluid with a metastable mineral assemblage such as cohenite (Fe_3C)-magnetite. Cohenite is a mineral which is reported to occur in retrograde, lizardite-dominant serpentinites (Eremeev and Sibilev, 1970; Shteynberg and Lagutina, 1978; Shterenberg and Stepanova, 1978; Marakushev et al., 1992), and magnetite, as noted earlier in this chapter, is common in all serpentinites. According to our calculations, C-O-H fluids that equilibrate with the metastable mineral assemblage cohenite (Fe_3C)-magnetite at elevated pressures and temperatures can form up to 7 mole % of ethane and higher hydrocarbons.

One of the stumbling blocks to resolving the issue of the origin of hydrocarbons in serpentinites is that hydrocarbon seeps are open to contamination by air or modification by biological activity. Also, they are collected potentially at very different pressure and temperature conditions to those prevailing when they formed. In principle, this problem can be overcome by analysing fluid inclusions, which have trapped these hydrocarbons. Unfortunately, serpentinites, and especially retrograde serpentinites, rarely contain minerals which are suitable hosts for fluid inclusions. Rodingites, on the other hand,

which are composed of minerals that readily trap fluid inclusions (garnet, epidote, pyroxene, and vesuvianite), are commonly present in serpentinites, having formed as a result of calcium metasomatism of felsic and adjacent ultramafic rocks by alkaline and SiO_2-poor fluids derived from the serpentinization. They therefore represent an important source for uncontaminated samples of the serpentinizing fluid, and, significantly, contain hydrocarbon-bearing fluid inclusions (Schandl et al., 1990; Compagnoni et al., 1998).

In this paper, we report the composition of the hydrocarbon gases contained in fluid inclusions from rodingitized slate, monzodiorite and granite of the JM Asbestos chrysotile deposit located in the southeastern Québec Appalachians, and use the data to evaluate mechanisms for abiogenic synthesis of hydrocarbons in serpentinites. The results of this study show that while Fischer-Tropsch synthesis can explain the distribution of hydrocarbon gases in some samples, the data are more consistent with a model in which the hydrocarbons form through reaction of a C-O-H fluid with a metastable iron oxide-iron carbide mineral assemblage during serpentinization.

GEOLOGY

The JM Asbestos chrysotile deposit, which hosts the rodingites discussed in this paper, is located in the Asbestos ophiolite, and, together with the Thetford Mines and Orford ophiolites, forms one of the larger ophiolite complexes of the southeastern Québec Appalachians. These ophiolite complexes were derived from small Ordovician arc-related oceanic basins, and occur irregularly along a narrow belt-like mélange of allochtonous rocks overlain by flysch sequences (Pinet and Tremblay, 1995a, 1995b; Hébert and Bédard, 1998). They were obducted onto the Laurentian craton during the Taconic orogeny (Ordovician-Silurian), and further deformed in the Devonian during the Acadian orogeny.

The Asbestos ophiolite forms a 2.3 km thick, dismembered sequence composed, from base to top, of slivers of amphibolite, serpentinized tectonic harzburgite, serpentinized cumulate dunite with interlayered pyroxenites, gabbros, a dyke unit, and

volcanic and sedimentary rocks (Hébert, 1980). The footwall of the ophiolite occurs in thrust contact with Cambrian age metagreywackes and slates of the Caldwell group, which were originally deposited near the edge of the Laurentian craton. During transport of the Asbestos ophiolite onto the Laurentian continental margin, dioritic-monzodioritic and peraluminous granitic rocks were intruded through the basal harzburgites and dunites. These intrusive rocks, and slates in contact with serpentinite at the base of the Asbestos ophiolite, were altered to chlorite-rich (blackwall), lime-rich (rodingite) and soda-rich (albitite) assemblages during emplacement of the ophiolite (Chapters IV and V).

Serpentinites

At least two major episodes of serpentinization affected the ultramafic rocks of the Asbestos ophiolite (Laurent, 1975; Laurent and Hébert, 1979). According to Laurent (1975) and Laurent and Hébert (1979), the first episode occurred shortly before detachment of the ophiolite from the seafloor, and continued until its emplacement onto the continental margin, while the second took place during transport of the ophiolite to its present setting. These episodes are interpreted to represent a continuum of fluid infiltration-induced alteration and recrystallization of the ultramafic rocks, and are distinguished primarily by different mineral assemblages and mineralization styles (O'Hanley, 1987; Whitehead et al., 2000; Chapter V). The first episode is believed to have led to complete alteration of the dunites and partial alteration of the harzburgites to lizardite-, magnetite- and awaruite-bearing serpentinites with minor to trace proportions of brucite. Our observations of samples from the JM asbestos mine indicate that during the second episode of serpentinization, lizardite was locally recrystallized or replaced by antigorite, and chrysotile formed veins and massive zones of replacement termed mass fiber zones. The brucite content of the rocks increased greatly during this later episode. More magnetite was formed and more, sparsely distributed, coarse-grained awaruite crystallized in the finer chrysotile veinlets. At the contact with metasediments, the serpentinites were altered to talc-rich assemblages. The alteration assemblage is more complex adjacent to felsic intrusive sheets, and in its simplest form, consists essentially of a thin metamorphic/metasomatic rim composed of parallel diopside or amphibole

(tremolite-actinolite or cummingtonite-anthophyllite) fibers that grew perpendicular to the contact. Massive bodies derived from the replacement of serpentinite by antigorite, talc, tremolite (nephrite), or diopside are commonly superimposed on the fibrous pyribole rims, and occasionally cut by cross-fiber chrysotile.

Rodingites

Blackwall, rodingites and feldspar-pyribole rocks are distributed spatially, in the order listed, from the contact of felsic intrusive sheets or slates with serpentinite towards the inside of the protolith. The blackwall zone is composed almost entirely of chlorite and varies in thickness from 1 to 5 cm. This zone is absent where a thick calc-silicate alteration halo is present in serpentinites adjacent to the felsic intrusive sheets. The rodingites are composed dominantly of calc-silicate minerals, and form zones measuring up to 1 m thick, or may replace completely the thinner intrusive sheets. The feldspar-pyribole rocks, which represent volumetrically the most extensively developed type of alteration, are composed of albite±K-feldspar±diopside-hedenbergite or albite±K-feldspar±tremolite-actinolite.

Rodingites are mineralogically complex and comprise at least three distinct paragenetic associations. Each of these parageneses occurs in the form of massive replacement bodies and veins. The earlier parageneses are characterized by the presence of orange grossular and comprise the assemblages: (1a) grossular+diopside+chlorite, (1b) grossular+diopside, (1c) grossular+diopside+zoisite, and (1d) grossular+diopside+zoisite+prehnite. The second paragenetic association is dominated by prehnite- or diopside-rich associations, and includes the assemblages: (2a) prehnite+diopside+zoisite+grossular, (2b) prehnite+diopside+grossular, (2c) prehnite+diopside, and (2d) diopside+prehnite. The latest paragenetic association is distinguished by assemblages in which light green to purple vesuvianite, white grossular or prehnite is the dominant mineral. The principal mineral assemblages in this paragenesis are: (3a) vesuvianite+diopside+chlorite, (3b) vesuvianite+diopside+wollastonite, (3c) vesuvianite+diopside+wollastonite+grossular,

(3d) grossular+vesuvianite+diopside, (3e) grossular+diopside+prehnite, (3f) grossular+diopside+prehnite+zoisite, and (3g) prehnite+grossular+diopside.

The first two paragenetic varieties of rodingite (types 1 and 2) are associated with slates and dioritic rocks, and rarely with granitic rocks. The third rodingite paragenesis is restricted mainly to the granitic rocks, although veins of type 3 rodingite were observed cutting dioritic rocks. Veins of type 2 rodingite commonly form extensions to chrysotile veins where the latter meet with felsic rocks. The timing of the formation of the early type 1 rodingites in diorites is difficult to determine. However, the presence of similar type 1 rodingites in slate and granite suggest that rodingitization occurred during obduction of the Asbestos ophiolite. A more detailed study of the calc-silicate alteration assemblages was provided in Chapter V.

FLUID INCLUSIONS

Fluid inclusions were studied in two samples of rodingitized slate (UG-C and JMH-301), two samples taken from a dyke of rodingitized diorite (JMH-25.2a and b), a sample of rodingitized, pegmatitic and feldspar-rich granitic rock (JMH-333), and five samples from vesuvianite-rich veins comprising light green prismatic (JMH-157.3), blocky olive green (JMH-157.4; in open fractures cutting light green, massive vesuvianite) and coarse-grained purple (GOR, Flt-100a) varieties of vesuvianite, and colourless, bladed wollastonite crystals (Flt-100b) interstitial to purple vesuvianite. One of the samples of rodingitized slate (UG-C) consists of a fine-grained mixture of grossular, diopside, zoisite, and prehnite (type 1d rodingite) cut by veinlets comprising larger crystals of grossular and diopside (type 1b rodingite), while the other (JMH-301) is a late stage diopsidite composed of colourless diopside with minor prehnite (type 2d rodingite). The two rodingite samples from the diorite dyke comprise orange grossular from the contact with the blackwall (JMH-25.2a: 1.5 cm from serpentinite; type 1b rodingite) and coarse-grained diopside-zoisite-grossular-prehnite rodingite (JMH-25.2b: 4.5 cm from serpentinite; type 1d rodingite), respectively. The sample of a rodingitized,

pegmatitic granitic rock (JMH-333) consists mainly of grossular and diopside, and is classified as a type 1b rodingite.

Microthermometry

Two types of primary fluid inclusion were recognized based on their appearance at room temperature. The first type (type 1) contains a single phase and nucleates a vapour bubble at temperatures < -125°C; homogenization occurs at temperatures between -123 and -84°C. In one of these inclusions, a solid nucleated at ~ -196°C (the lower temperature limit of the stage) and melted at ~ -184°C. Type 1 inclusions occur in zoisite and grossular in the rodingitized diorite samples (rodingite types 1b and 1d), in diopside in the rodingitized slate samples (type 1b rodingite), and, rarely, in vesuvianite.

The second type of inclusion comprises two phases and is divided into three subtypes (types 2a, 2b and 2c). Type 2a and 2b inclusions contain two immiscible liquids at room temperature (they are distinguished on the basis of clathrate melting temperatures: see below), while type 2c inclusions contain liquid and vapour phases. In type 2a and 2b inclusions, a vapour bubble appears in the inner, less dense phase after cooling below -125°C. No changes were observed in the vapour phase of type 2c inclusions upon cooling to -196°C. However, a solid was observed to nucleate below -184°C in the inner liquid of three type 2a inclusions in grossular from the rodingitized granitic sample. The inner liquid and vapour of type 2a and 2b inclusions generally homogenized to a liquid at temperatures between -114 and -84°C (N = 39). Two type 2a inclusions in grossular from rodigitized slate (type 1b rodingite) displayed critical behaviour at temperatures between -88 and -89°C, and three type 2b inclusions in diopside from the same sample displayed the same behaviour at temperatures between -116 and -85°C.

Type 2a inclusions contain clathrate, which melts at temperatures below -3°C (-3 to -7°C), and have high apparent (uncorrected for the presence of clathrate) salinities (24-27 wt. % eq. NaCl). They occur in grossular and diopside in the rodingitized granite and in rodingitized slate (type 1b rodingite). Type 2b inclusions have moderate to high apparent salinities (5-25 wt. % eq. NaCl) and contain a clathrate, which melts at

temperatures above 0°C (0 to 13°C). The temperature of clathrate melting in type 2b inclusions increases proportionally with decreases in the melting temperature of the ice. Type 2b fluid inclusions occur in zoisite and grossular in the rodingitized diorite samples (type 1d rodingite), and in grossular and diopside from the rodingitized slate samples (type 1b and type 2d rodingites). Type 2c inclusions have moderate salinity (apparent salinity 6-9 wt. % eq. NaCl), their clathrate melts at temperatures above 8°C, and they are restricted to vesuvianite (type 3a and 3b rodingites).

The very low homogenization temperatures of type 1 inclusions and partial homogenization temperatures of type 2a and 2b inclusions, the nucleation of a solid phase below −184°C in type 1 and type 2a inclusions, and the formation of clathrate in type 2 inclusions suggest that the type 1 inclusions and the inner liquid in type 2a and 2b inclusions consist dominantly of $CH_4 \pm N_2 \pm H_2$. Type 1 inclusions were only observed with type 2b and 2c inclusions. They occur in the same host crystal only in diopside from the rodingitized slates, in zoisite and grossular from the rodingitized dioritic rocks (type 1b and 1d rodingites), and, rarely, in vesuvianite (observed in one crystal).

Complete homogenization of type 2 inclusions occurs at temperatures between 180 and 350°C. The highest temperatures (344 ± 15°C; N = 74) were recorded by type 2a inclusions hosted in the rodingitized granite, and the lowest temperatures (191 ± 7°C; N = 12) were those of type 2c inclusions in vesuvianite. Type 2b inclusions in rodingitized diorite homogenized completely at temperatures between 277 and 333°C, whereas secondary inclusions in sample JMH-25.2a homogenized completely at temperatures between 222 and 275°C.

Gas chromatography

The gas composition of bulk samples (~ 1 g) of the various types of rodingite described above was analysed with an HP®-5890 Series-II gas chromatograph equipped with a thermal conductivity detector (TCD) and a photoionization detector (PID) connected in series. After being cleaned several times in doubly distilled water and dried on a heating plate, grains of two samples and a blank (Brazilian quartz) were introduced into three hydraulic crushing blocks online with the gas chromatograph. Before the

analyses were carried out, the crushing blocks were heated at 110°C overnight under a flow of ~ 1 mL/min. of helium carrier gas to remove air and water adsorbed to the grains. After increasing the carrier gas flow to 20 mL/min (total flow 50 mL/min), the volatile contents of the fluid inclusions were released by crushing the grains at the start of the analysis.

Volatile species were identified by comparing the retention time of the signal peaks given by the TCD and PID detectors with spectra obtained from gas mixtures of known composition. The TCD detector was used to identify and quantify N_2-CO-H_2-Ar, CH_4, CO_2, and H_2O. Co-elution of N_2, CO, H_2, and Ar does not permit differentiation between these species using He as the carrier gas. The PID detector was used to identify and quantify C_{2+} hydrocarbons. Further details on the apparatus and analytical techniques are given in Salvi and Williams-Jones (1997a, b). The results of the analyses are presented in Table 1.

Water was the principal component detected, reflecting the abundance of type 2 inclusions. Methane was by far the main carbonic species identified in all the samples analysed (> 99 mole %). By contrast, the proportion of CO_2 was below the detection limit (~ 3 nmole). In addition to methane, all the samples contained the higher hydrocarbons ethane (C_2H_6) and propane (C_3H_8). Quantifiable amounts of n-butane (n-C_4H_{10}) and n-pentane (n-C_5H_{12}) were present in five of the ten samples analysed. In some samples, there were traces of acetylene or ethylene (C_2H_2 and C_2H_4), cyclopropane (C_3H_6) and isobutane (i-C_4H_{10}). Small proportions of N_2 or H_2 or CO or Ar were detected by the thermal conduction detector, but the exact nature of these species was not determined. The gas species are similar in all types of rodingite, but the proportions of C_{2+} hydrocarbons are higher in purple vesuvianite (GOR, JMH100a) and in the rodingitized granite (JMH-333, 333bis).

Trapping pressures and temperatures of the fluid inclusions

Assuming that the type 1 inclusions were trapped synchronously and in equilibrium with the type 2 inclusions in rodingites from slate (Type 1 $T_h = -108 \pm 10$°C,

Table 1. Results of gas-chromatographic analyses of inclusion fluids in rodingites from the JM Asbestos chrysotile deposit.

	Sample UG-C	JMH-333	JMH-333bis	JMH-25.2a	JMH-25.2b	JMH-157.3
Gas content (nanomoles)						
CO_2	n.d.	n.d.	n.d.	n.d.	n.d.	n.d.
CH_4	155.846	88.087	30.870	23.585	17.796	36.053
C_2H_6	3.495	3.120	1.158	0.450	0.235	0.062
C_3H_8	0.308	0.304	0.123	0.038	0.012	0.010
n-C_4H_{10}	0.089	0.106	0.036	n.d.	n.d.	n.d.
n-C_5H_{12}	0.019	0.024	n.d.	n.d.	n.d.	n.d.
C_3H_6	present	present	n.a.	n.d.	n.d.	n.d.
i-C_4H_{10}	present	present	n.a.	n.d.	n.d.	n.d.
α (including CH_4)	0.11	0.21	0.18	0.04	0.03	0.02
α (excluding CH_4)	0.19	0.14	0.11	0.08	0.05	0.16

n.d.: not detected; n.a.: not analyzed

UG-C: Type 1b, orange grossular-diopside rodingite after slate. Mainly primary type 2a and 2b inclusions. Type 1 inclusions rare.

JMH-333: Type 1b, orange grossular-diopside rodingite after pegmatitic, feldspar-rich granitic rock. Only primary type 2a inclusions.

JMH-25.2a: Late-stage orange grossular from the contact between blackwall and rodingitized dioritic rock. Mainly secondary type 2b inclusions. Few primary type 1 and type 2b inclusions.

JMH-25.2b: Type 1c, diopside-grossular-zoisite rodingite after dioritic rock. Mainly primary type 1 and type 2b inclusions.

JMH-157.3: Light green prismatic vesuvianite from vein.

JMH-157.4: Blocky olive-green vesuvianite coating fractures in 157.3.

JMH-158: Light green prismatic vesuvianite from vein.

Flt-100a: Vug-filling purple vesuvianite from vein.

Flt-100b: Vug-filling colorless wollastonite interstitial to purple vesuvianite.

GOR: Vug-filling purple vesuvianite from vein. Mainly type 2c primary inclusions. Type 1 inclusions are very rare.

Table 1. (continued)

	JMH-157.4	JMH-158	Flt-100a	Flt-100b	GOR
Gas content (nanomoles)					
CO_2	n.d.	n.d.	n.d.	n.d.	n.d.
CH_4	12.837	9.066	137.065	225.305	27.374
C_2H_6	0.077	0.165	3.651	2.126	1.988
C_3H_8	0.012	0.025	0.707	0.226	0.279
n-C_4H_{10}	n.d.	n.a.	0.172	0.039	0.093
n-C_5H_{12}	n.d.	n.a.	0.013	n.d.	0.020
C_3H_6	n.d.	n.d.	0.042	0.057	n.d.
i-C_4H_{10}	n.d.	n.a.	0.055	n.d.	0.024
α (including CH_4)	0.03	0.05	0.12	0.06	0.17
α (excluding CH_4)	0.15	0.15	0.16	0.14	0.23

n.d.: not detected; n.a.: not analyzed

UG-C: Type 1b, orange grossular-diopside rodingite after slate. Mainly primary type 2a and 2b inclusions. Type 1 inclusions rare.

JMH-333: Type 1b, orange grossular-diopside rodingite after pegmatitic, feldspar-rich granitic rock. Only primary type 2a inclusions.

JMH-25.2a: Late-stage orange grossular from the contact between blackwall and rodingitized dioritic rock. Mainly secondary type 2b inclusions. Few primary type 1 and type 2b inclusions.

JMH-25.2b: Type 1c, diopside-grossular-zoisite rodingite after dioritic rock. Mainly primary type 1 and type 2b inclusions.

JMH-157.3: Light green prismatic vesuvianite from vein.

JMH-157.4: Blocky olive-green vesuvianite coating fractures in 157.3.

JMH-158: Light green prismatic vesuvianite from vein.

Flt-100a: Vug-filling purple vesuvianite from vein.

Flt-100b: Vug-filling colorless wollastonite interstitial to purple vesuvianite.

GOR: Vug-filling purple vesuvianite from vein. Mainly type 2c primary inclusions. Type 1 inclusions are very rare.

N = 10; Types 2a and 2b T_h = 319 ± 14°C, N = 28) and diorite (Type 1 T_h = -119 ± 4°C, N = 42; Type 2b T_h = 307 ± 15°C, N = 35), and that these inclusions consist essentially of methane, the trapping pressure would have been roughly between 1.8 and 3.0 kilobars based on the homogenization temperatures of type 1 and type 2 inclusions and the P-V-T properties of methane (using the equation of state of Holloway, 1981).

DISCUSSION

Evolution of f_{O_2}

In the absence of an aqueous or carbonic fluid, mineral assemblages in peridotites cooled to low temperatures do not undergo noticeable changes in mineralogical composition. However, in the presence of an aqueous fluid, pyroxene-bearing peridotites start to alter hydrothermally at temperatures between 650 and 800°C (below a pressure of 10 kilobars), with the formation of amphiboles and talc (Day et al., 1985). Olivine, which is generally the most abundant phase in peridotites, breaks down to serpentine (lizardite, chrysotile or antigorite), brucite and iron oxides at temperatures below 450°C via the reaction:

$$\text{Olivine} + \text{Water} \rightarrow \text{Serpentine} \pm \text{Brucite} \pm \text{Magnetite} \pm \text{Fe-Ni alloys} \pm H_2 \qquad (1)$$

(Moody, 1976). This reaction takes place spontaneously and irreversibly at low temperature, but terminates (for a given total pressure) when P_{H_2O} decreases, as a result of the consumption of water in forming the secondary hydrous phases, to a new value corresponding to a condition of equilibrium (Sanford, 1981; Macdonald and Fyfe, 1985). The number and nature of the phases involved in reaction 1 vary with the composition of the olivine, the composition of the fluid and the oxygen fugacity. However, the lack of knowledge of the thermodynamic properties of the solid solutions amongst Mg- and Fe-rich serpentine-group minerals, unfortunately, precludes characterization of the variants

of this reaction as a function of these parameters (Toft et al., 1990; O'Hanley and Dyar, 1993, 1998).

An important feature of reaction 1 is that it produces large amounts of H_2 gas through oxidation of the ferrous component of the primary mafic silicates in ultramafic rocks (Ramdohr, 1967; Frost, 1985). This oxidation of iron may proceed by hydrolysis of H_2O (Fritz et al., 1987) as in the reaction:

$$FeO_{(silicate)} + 0.5H_2O \rightarrow FeO_{1.5(silicate,\ oxide)} + 0.5H_2 \quad (2)$$

or consumption of hydrogen ions in reactions of the type:

$$Fe^{2+}_{(silicate)} + H^+ \rightarrow Fe^{3+}_{(silicate,\ oxide)} + 0.5H_2 \quad (3)$$

(Janecky and Seyfried, 1986).

Direct evidence of the production of H_2 and the strongly reducing conditions during serpentinization are provided by the common occurrence H_2-rich gas seeps (Abrajano et al., 1990; Fritz et al., 1992), and of awaruite (Ni_3Fe) with magnetite (Ramdohr, 1967) in serpentinites, more specifically in incompletely serpentinized peridotites. According to calculations of Frost (1985), the association awaruite-magnetite reflects f_{O_2} values < 4 log units below the QFM reference buffer.

Abiogenic generation of hydrocarbons

Hydrocarbons form abiogenically as a result of processes that do not involve an organic precursor for the carbon. In the case of serpentinites, the carbon source could be CO_2 or CH_4 introduced by the altering fluids or inorganic carbon-bearing phases (e.g., traces of carbonate minerals) contained in the unaltered peridotites. Much less clear is how these carbonic species are transformed into long-chain hydrocarbons during serpentinization. We can rule out simple equilibration of the serpentinizing fluid with peridotite, as the only hydrocarbon produced is methane for any reasonable set of geological conditions. It therefore follows that abiogenic hydrocarbon production in

serpentinites must proceed by a non-equilibrium or metastable process. One such process, that has been proposed previously to explain the presence of hydrocarbons in serpentinites, is Fischer-Tropsch catalysis, which is used in the commercial synthesis of petroleum products. An alternative, which has not been proposed previously, but which we suggest is equally viable, is reaction of a graphite-saturated, carbon-rich and water-poor fluid with a strongly reducing metastable mineral assemblage such as cohenite-awaruite-magnetite. In the sections that follow, we will evaluate these two mechanisms for abiogenic hydrocarbon production within the context of our analyses of the fluids present in rodingites at the J.M. Asbestos mine.

Fischer-Tropsch catalysis

Fischer-Tropsch catalysis (van der Laan and Beenackers, 1999 and references therein) is a process by which CO-H_2 or CO_2-H_2 mixtures are transformed into hydrocarbons and H_2O over a heterogeneous catalyst containing a Group VIIIA transition metal or metal oxide. During this process, CO, CO_2 and H_2 are dissociated on the surface of the metal phase and converted to CH_x species. The methyl species thus formed then combine to form hydrocarbon chains.

Most researchers describe the Fischer-Tropsch process of hydrocarbon chain growth in terms of the theory of quantum mechanics. However, Bell (1995) proposed that the hydrocarbons form a mixture in thermodynamic equilibrium with the hydrided or carbided surface of the solid catalyst. According to the quantum mechanistic interpretation, interaction between the electronic structure of the surface of the metallic catalyst and that of the carbon atoms adsorbed on the surface of the catalyst produces a change in the configuration of the electron clouds in the carbon atoms. This helps to overcome the activation energy barriers to forming C-C and C-H bonds, and therefore, permits the formation of a variety of different hydrocarbon structures. The relative proportions of hydrocarbons thus created depend on the residence time of an adsorbed carbonic species and the energy required to increase its mass. These proportions are also affected by the type of catalyst, the temperature, the pressure, the composition of the fluid, the space velocity, the time-on-stream, and modifications of the composition of the

catalyst during reaction (van der Laan and Beenackers, 1999). The probabilistic distribution of hydrocarbons in Fischer-Tropsch catalysis is described by a factor, denoted α, the chain growth probability factor (Schulz, 1935; Flory, 1936). In the case of alkanes, this factor is generally constant for the range of hydrocarbons considered in this study, and is the ratio of the molar proportion of the hydrocarbon of interest in the mixture over an analogous hydrocarbon with one less carbon atom. The distribution, termed a Schulz-Flory distribution, produces a log linear decrease in the relative proportions of hydrocarbons with increasing molecular weight.

Lancet and Anders (1970) were the first to relate Fischer-Tropsch-type processes to the production of hydrocarbons during serpentinization. Several other publications have subsequently invoked the Fischer-Tropsch process of hydrocarbon generation to explain the formation of hydrocarbons in serpentinites (Szatmari, 1989; Holm, 1996; Charlou et al., 1998). However, none of these publications or that of Lancet and Anders (1970) provided the complete analyses of hydrocarbons required to support their interpretations.

The first experiments to show that hydrocarbons can form abiogenically in reactions involving serpentinites were performed by Morency et al. (1986). By heating, i.e., de-serpentinizing, powdered samples of various kinds of serpentinized peridotites containing carbonates and magnetite, they were able to synthesize saturated, unbranched-chain hydrocarbons, from methane to hexane, as well as benzene and toluene, and substantial amounts of hydrogen gas.

Berndt et al. (1996) were the first researchers to produce higher hydrocarbons experimentally via a serpentinization reaction. They did this by reacting a CO_2-bearing (7.9 mmol/kg solution), 0.5 *m* NaCl aqueous fluid with olivine (Fo_{88}; fluid/rock ratio = 2.25) at a temperature of 300°C and a pressure of 500 bars, and produced methane, ethane and propane, along with the secondary minerals serpentine, magnetite and brucite. The distribution of the hydrocarbons showed a Schulz-Flory-type relationship with a chain growth probability factor of 0.33. Based on this, Berndt et al. (1996) concluded that the hydrocarbons formed through a Fischer-Tropsch-type process and that the secondary magnetite had provided the catalyst for the reaction. If simple equilibrium had been

reached amongst the H-C-O-containing species in the fluid phase at their experimental fO_2 conditions, virtually all the hydrocarbon fraction should have been composed of methane.

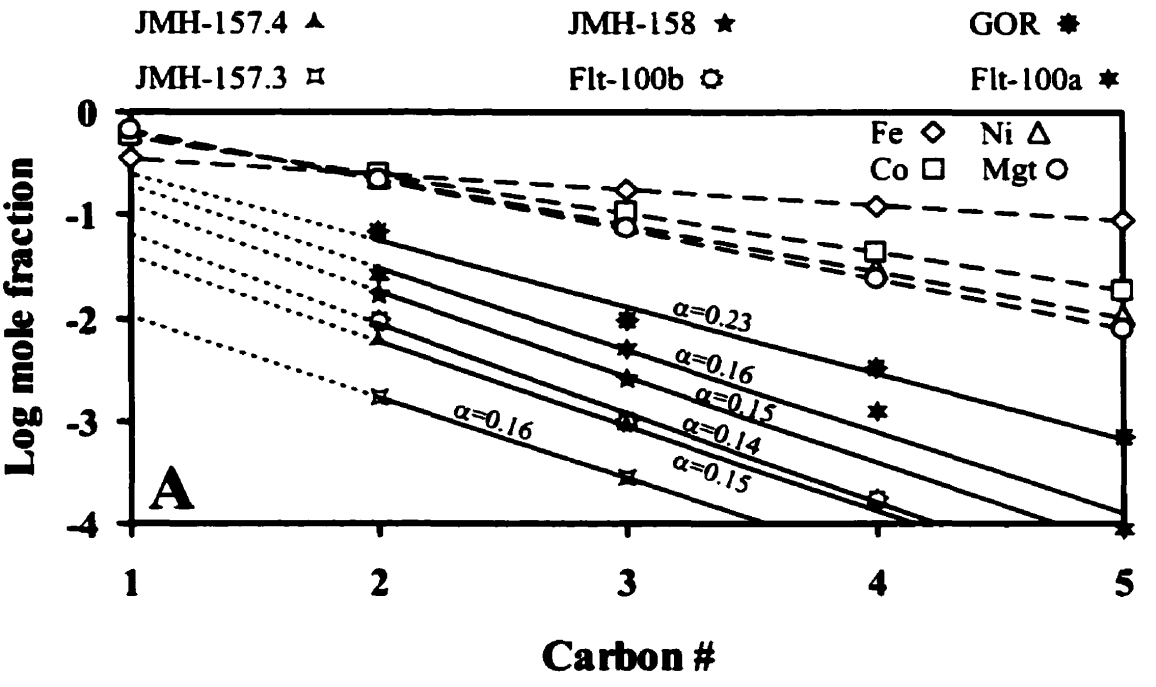
Measured alkane distribution in the Asbestos rodingites

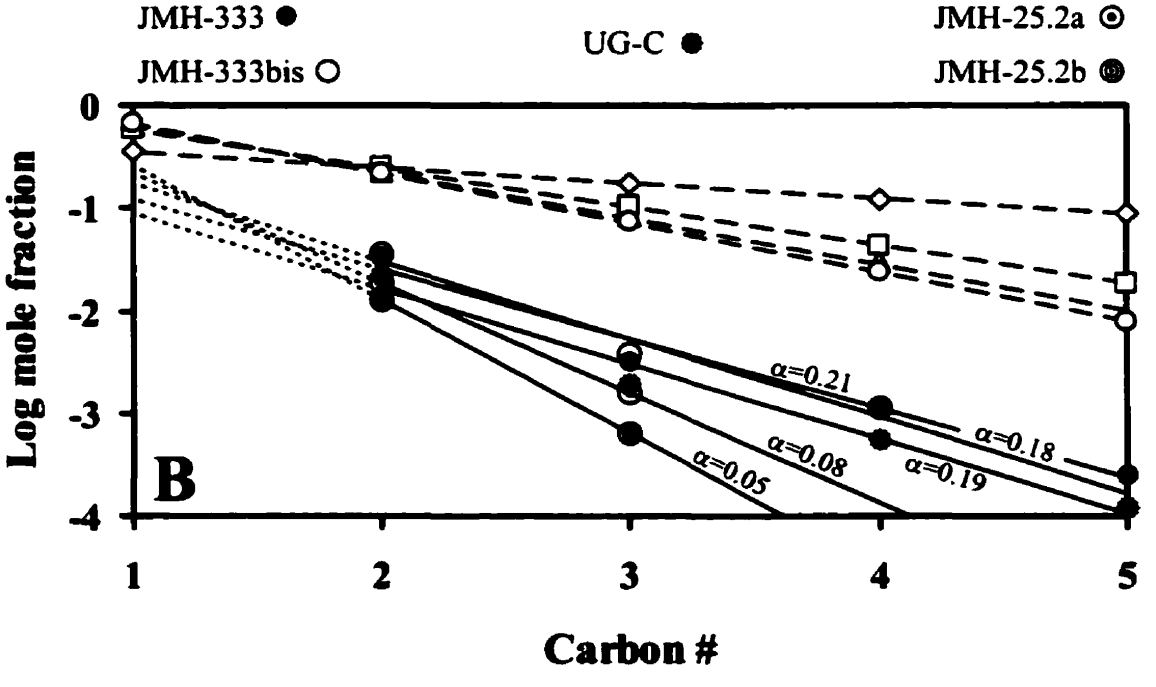
If, as has been discussed earlier, the hydrocarbons seeping from serpentinites and trapped in fluid inclusions in rodingites owe their origin to Fischer-Tropsch synthesis, they should show a Schulz-Flory distribution. In Figure 1, we show the distribution of alkanes in the rodingite samples as a function of their log mole fraction. The α value for the distribution of the hydrocarbons in each sample was calculated using the equation $\alpha=10^m$, where m is the slope obtained by linear regression through the data points (calculated without methane; solid lines). Also shown on this diagram, is the calculated distribution of these hydrocarbons for a Fischer-Tropsch synthesis catalyzed by iron, cobalt, nickel and magnetite (dashed lines).

Significantly, all samples show a more or less well-defined Schulz-Flory distribution of hydrocarbons for species with more than 2 carbon atoms. The growth probability factor, α, calculated excluding methane, varies between 0.05 and 0.08 in the samples of rodingitized diorite, is between 0.18 and 0.21 in the rodingitized granite, is 0.19 in the rodingitized slate, and is 0.23 in vesuvianite sample GOR (Table 1). The α value for the distribution of hydrocarbons in the rodingitized granite and slate, and in the vesuvianite are thus not very different from those for Fischer-Tropsch synthesis using magnetite (0.33: Berndt et al., 1996) and nickel (0.36: Kudo et al., 1993) catalysts. Moreover, as reported earlier in the paper, magnetite is an essential constituent of the Asbestos serpentinites and is commonly associated with smaller proportions of Ni-Fe alloys such as awaruite. On the other hand, the α values for hydrocarbons in rodingitized diorite are too low to reflect Fischer-Tropsch catalysis on the surface of magnetite or a metal alloy, but too elevated to be explained as having been formed in equilibrium with a stable mineral assemblage in the system Mg-Fe-Si-C-O-H. Equilibrium precipitation of graphite would limit the f_{O_2} and f_{CO_2} conditions in the fluid to values that do not permit C_{2+} hydrocarbons to form in concentrations detectable by available analytical techniques.

Figure 1

Proportions of C_1-C_5 alkanes contained in rodingite-hosted fluid inclusions from the J.M. Asbestos chrysotile Mine as a function of the carbon number (solid lines). Also shown on this diagram are the distributions of C_1-C_5 alkanes calculated using typical chain growth probability factors for Fischer-Tropsch synthesis employing iron (α=0.7), cobalt (α=0.42), nickel (α=0.36) and magnetite (α=0.33) catalysts (dashed lines). Chain growth probability factors for iron, cobalt and nickel were taken from Kudo et al. (1993), and that for magnetite from Berndt et al. (1996).


JMH-157.4
JMH-158
GOR
JMH-157.3
Flt-100b
Flt-100a
Fe
Ni
Co
Mgt
α=0.23
α=0.16
α=0.15
α=0.14
α=0.16
α=0.15
A
0
-1
-2
-3
-4
1
2
3
4
5
Log mole fraction
Carbon #


JMH-333
UG-C
JMH-25.2a
JMH-333bis
JMH-25.2b
α=0.21
α=0.18
α=0.08
α=0.19
α=0.05
B
0
-1
-2
-3
-4
1
2
3
4
5
Log mole fraction
Carbon #

Hydrocarbons in C-O-H fluids with metastable mineral assemblages

In principle, C_{2+} hydrocarbons can be produced from C-O-H fluids, if the fugacities of CO_2 and H_2 are high enough. However, in practice, this is not possible at equilibrium because saturation of the system with respect to graphite buffers the fugacities of these components to much lower values than required. On the other hand, cohenite, $(Fe,Ni,Co)_3C$, which is metastable with respect to graphite and iron below 738°C in the system Fe-C, has been reported to occur as sub-micron diameter grains in many low temperature lizardite-chrysotile-type serpentinites (Shteynberg and Lagutina, 1978). Shteynberg and Lagutina (1978) noted that these iron carbides did not occur in the unserpentinized parent peridotites, or in the serpentinites which were subsequently recrystallized to antigorite-rich assemblages. During antigorite recrystallization, cohenite was transformed into graphite and magnetite (Marakushev et al., 1992). This indicates that cohenite forms during serpentinization and suggests that exceptionally high f_{CO_2} and f_{H_2} (graphite supersaturation), i.e., conditions that would allow C_{2+} alkanes to form, accompany this alteration. During serpentinization, which is considered to proceed rapidly and at low water/rock ratio (Wegner and Ernst, 1983; Macdonald and Fyfe, 1985), consumption of water will serve to increase the bulk carbon concentration of the fluid phase, potentially to the point of effervescence of a carbon-rich fluid, an effect that would be promoted by the accompanying increase in the ionic strength of the fluid and the conversion of CO_2 to CH_4. This fluid will be out of equilibrium with the serpentinite and could have fugacities of CO_2 and H_2 high enough to stabilize cohenite and form C_{2+} hydrocarbons. It is important to point out, however, that reduction of an initially CO_2-rich fluid by H_2 is more efficient in producing C_{2+} hydrocarbons than reduction of a fluid which is initially CH_4-rich, because of the inherently higher C/H ratio of the CO_2-rich fluid.

The possibility that metastable mineral assemblages could be involved in forming hydrocarbons during serpentinization can be evaluated by comparing the fluid inclusion data obtained on the rodingite samples from Asbestos with the composition of hydrocarbons predicted from phase equilibria. Based on the pressures and temperatures recorded by the fluid inclusions, we have constructed a log f_{O_2}-log f_{CO_2} diagram

(Figure 2) calculated at 300°C and 2000 bars showing stable (solid lines) and metastable (dashed lines) equilibria among pure solid phases (forsterite, fayalite, enstatite, talc, antigorite, brucite, native iron, magnetite, FeO, hematite, siderite, magnesite, and graphite) in the system Mg-Fe-Si-C-O-H. Also shown on Figure 2 are the fields where aqueous and carbonic fluids predominate, and contours (dashed) indicating the ratios (0.001 and 0.01) of ethane over the sum of the hydrocarbons. Note that these contours parallel the graphite saturation line. The calculations were carried out with the geochemical equilibrium modelling software Hch, which uses the free energy minimization program Gibbs (Shvarov and Bastrakov, 1999). The sources for the thermodynamic data are given in the caption of Figure 2. For calculations in the gas phase, it was assumed, as a first order approximation, that $f_i = P_i$ in the mixture. The hydrocarbons included in the calculations for carbon-rich fluids comprised alkanes in the gaseous state from ethane (C_2H_6) to n-tetracosane ($C_{24}H_{50}$). The calculations show that a significant proportion of saturated, unbranched light alkanes (C_{2+}) are in metastable equilibrium (supersaturation with respect to graphite) with the metastable mineral assemblage cohenite-magnetite-ferrous oxide (point 2: Figure 2). Furthermore, the log f_{O_2} value corresponding to this assemblage lies within the range of those calculated by Frost (1985) for the assemblage awaruite-magnetite (-39.9 to -40.8) to be stable under the same pressure and temperature conditions. The calculations also show that the proportion of heavy hydrocarbons (and by inference, α) in cohenite-magnetite-ferrous oxide assemblages increases with increasing pressure and temperature (Figure 3).

The changes in composition of carbon-containing fluids resulting from reaction with a model harzburgite (Fo_{91}-En_{91}) were calculated using a simple titration model. Graphite was omitted in order to evaluate the potential of cohenite-bearing assemblages to form C_{2+} hydrocarbons. The calculations suggest that CO_2-bearing fluids with $X_{CO_2} > 0.01$ can form significant proportions of C_{2+} hydrocarbons in the presence of talc, magnesite, enstatite, and forsterite. An example showing the variations in composition of the gases and solids from reaction with a H_2O-CO_2 fluid with $X_{CO_2} = 0.1$ is presented in Figure 4. The figure shows that reaction progress is confined to fields where a hydrous

Figure 2

Log fO_2 versus logfCO_2 diagram (300°C and 2000 bars) showing stable (solid lines) and metastable (dashed lines) equilibria among pure solid phases (forsterite, fayalite, enstatite, talc, antigorite, brucite, native iron, magnetite, FeO, hematite, siderite, magnesite, and graphite) in the system Mg-Fe-Si-C-O-H. Also shown are the fields where aqueous and carbonic fluids predominate. Dotted contours indicate the ratios of ethane over the sum of the hydrocarbons for values corresponding to 0.001 and 0.01. Note that these contours parallel the graphite saturation line. All the compositions measured from fluid inclusions can be explained by equilibration of the fluid phase with the metastable assemblage cohenite-magnetite, where awaruite can coexist with magnetite (dark shaded ellipse). The thermodynamic data for the solid phases and inorganic aqueous and gaseous species were from the database provided with the geochemical equilibrium modelling software Hch, which uses the free energy minimization program Gibbs (Shvarov and Bastrakov, 1999). Thermodynamic data for the organic gaseous species were taken from Helgeson et al. (1998), while thermodynamic data for cohenite were taken from Robie et al. (1978).

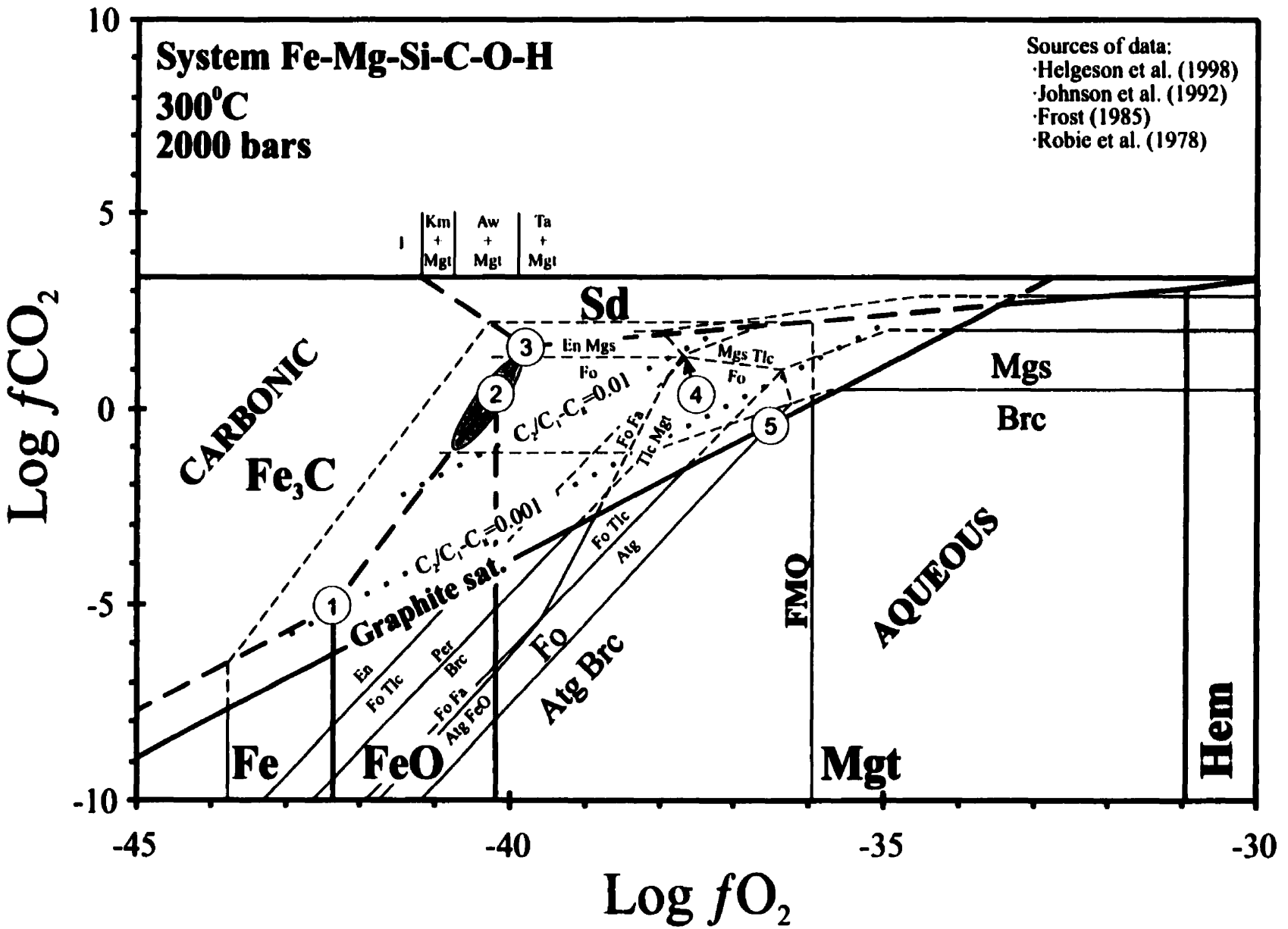

System Fe-Mg-Si-C-O-H
300°C
2000 bars
Sources of data:
·Helgeson et al. (1998)
·Johnson et al. (1992)
·Frost (1985)
·Robie et al. (1978)
Km + Mgt
Aw + Mgt
Ta + Mgt
Sd
En Mgs Fo
Mgs Tlc Fo
Mgs
Brc
CARBONIC
Fe3C
C2/C1-C4=0.01
Fo Fa
Tlc Mgt
C2/C1-C4=0.001
Graphite sat.
Fo Tlc
Atg
FMQ
AQUEOUS
Fa
Fo Tlc
Per
Brc
Fo Fa
Atg FeO
Fo
Atg Brc
Fe
FeO
Mgt
Hem
1
2
3
4
5
10
5
0
-5
-10
-45
-40
-35
-30
Log fCO2
Log fO2

Figure 3

Proportions of ethane in gaseous hydrocarbon mixtures coexisting with metastable cohenite-iron oxide(s)-bearing assemblages as a function of temperature and pressure. Formation of ethane and alkanes with higher carbon numbers is favoured by increasing pressure and increasing temperature to ~ 325-350°C. The proportions of ethane in the fluid inclusions vary between 0.002 and 0.22, i.e., well above values expected for the graphite buffer under the entrapment conditions determined from the microthermometric measurements.

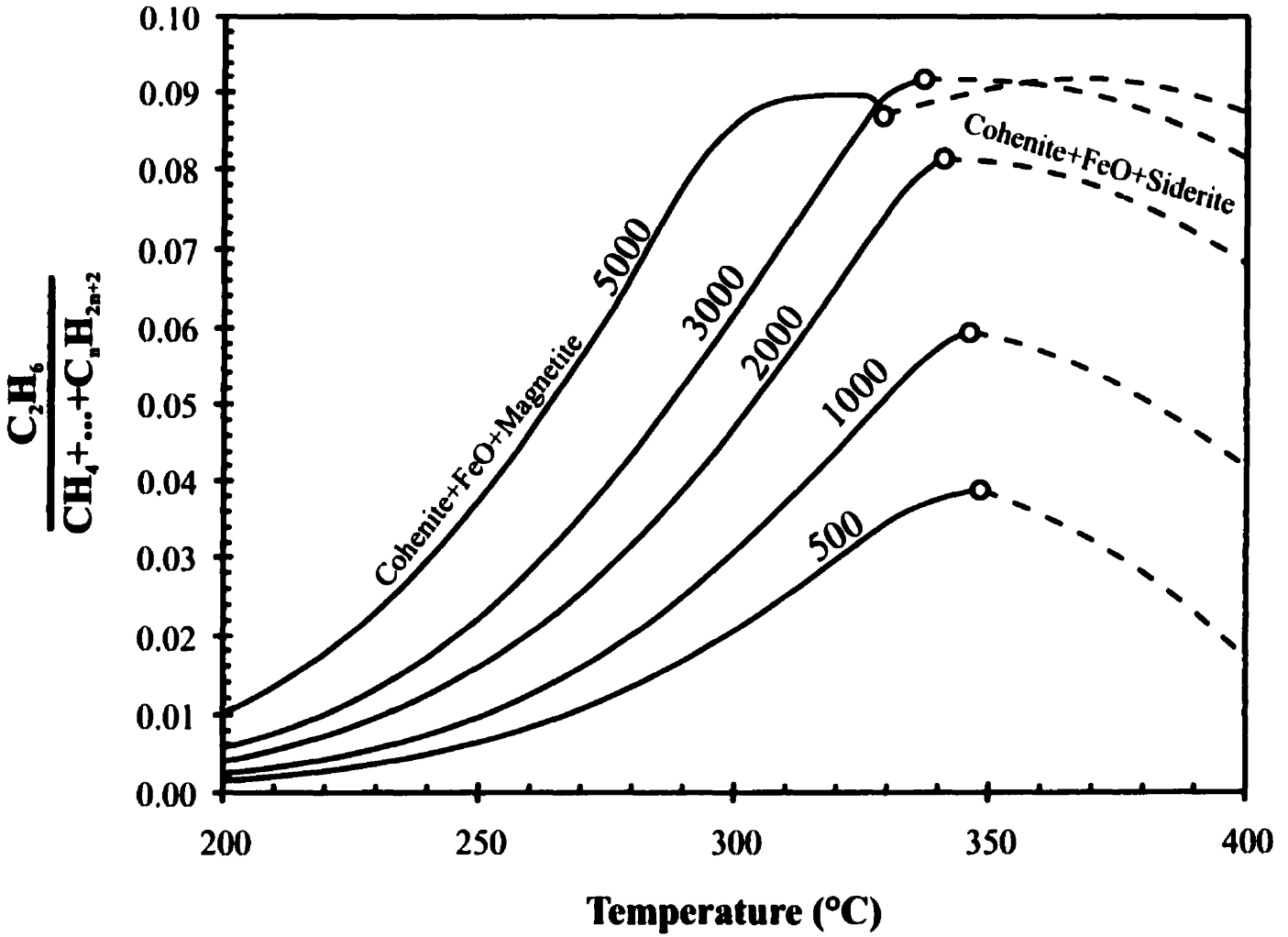
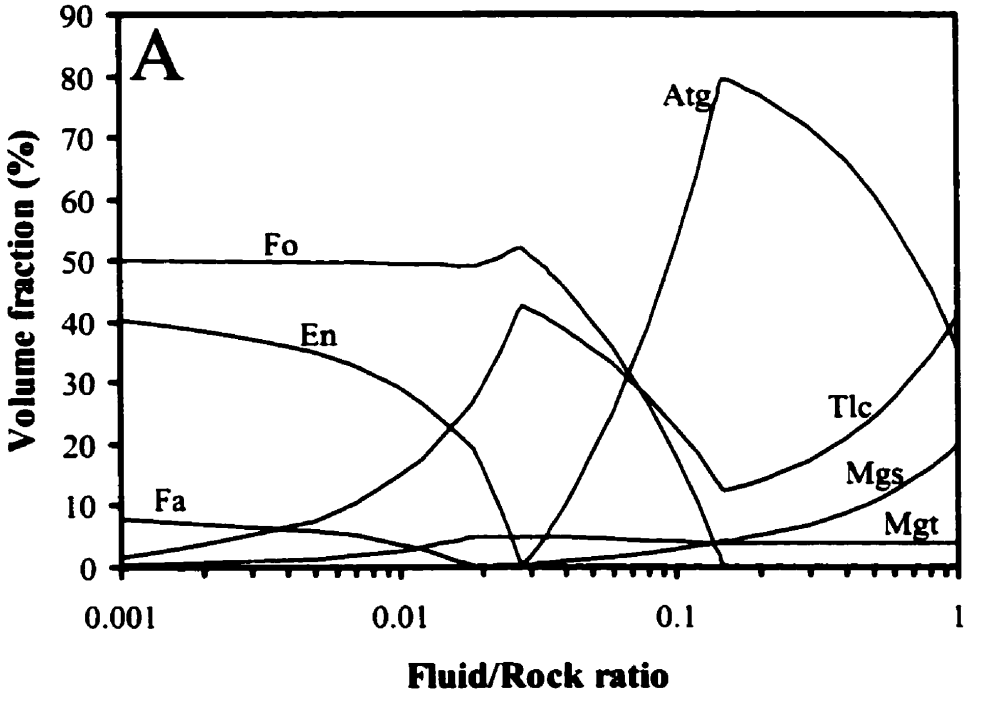
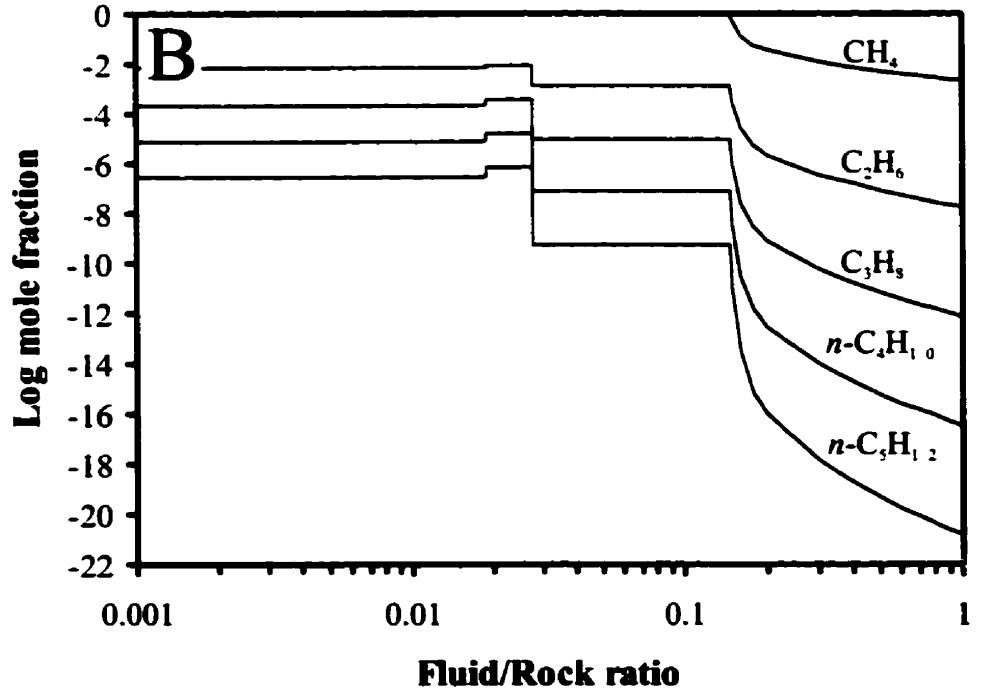
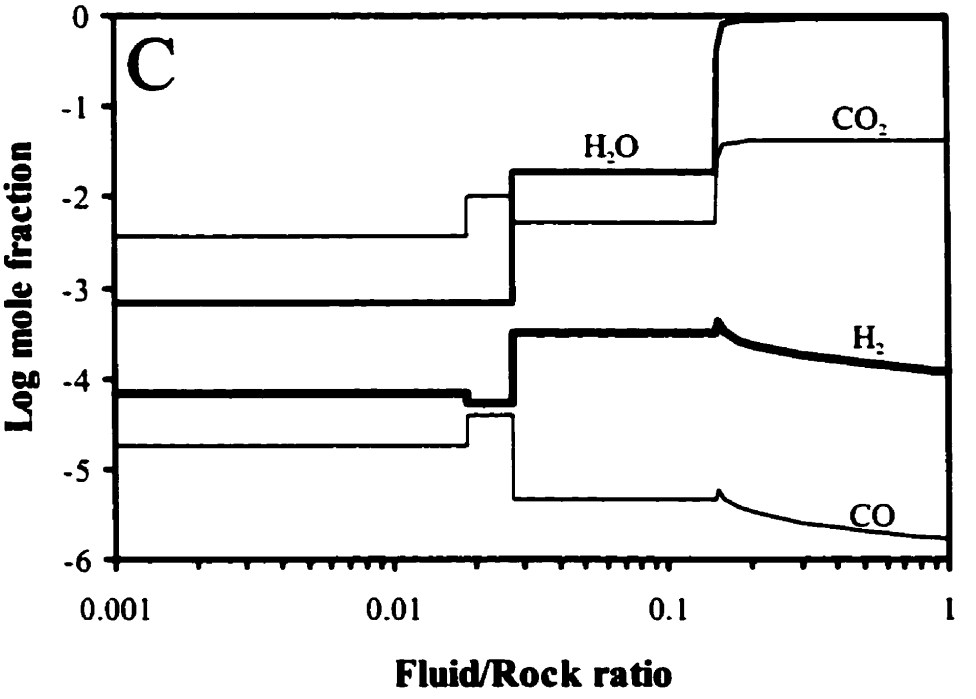

0.10
0.09
0.08
0.07
0.06
0.05
0.04
0.03
0.02
0.01
0.00
200
250
300
350
400
Temperature (°C)
$\frac{C_2H_6}{CH_4+...+C_nH_{2n+2}}$
Cohenite+FeO+Magnetite
5000
3000
2000
1000
500
Cohenite+FeO+Siderite

Figure 4

Proportions of solid (A) and fluid (B and C) phases as a function of the fluid/rock ratio during reaction of a H_2O-CO_2 (X_{CO_2} = 0.1) fluid with a model harzburgite (60%Fo_{91}-40%En_{91}). C_{2+}-rich fluids form only as a result of the reaction of CO_2-rich aqueous fluids at very low fluid/rock ratio.


A
Volume fraction (%)
90
80
70
60
50
40
30
20
10
0
Atg
Fo
En
Tlc
Mgs
Fa
Mgt
0.001
0.01
0.1
1
Fluid/Rock ratio


B
Log mole fraction
0
-2
-4
-6
-8
-10
-12
-14
-16
-18
-20
-22
CH4
C2H6
C3H8
n-C4H10
n-C5H12
0.001
0.01
0.1
1
Fluid/Rock ratio


C
0
-1
-2
-3
-4
-5
-6
Log mole fraction
H2O
CO2
H2
CO
0.001
0.01
0.1
1
Fluid/Rock ratio

silicate is present in the metastable assemblage (C_2/C_1-$C_8 < 0.01$), and that hydrocarbons appear after a precipitous drop in X_{H_2O}. Cohenite did not form in any of our reaction progress calculations because it is doubly metastable in the presence of an hydrous silicate phase. This suggests that cohenite can not form by local equilibrium processes with silicates during serpentinization. The fluid composition, however, might be driven towards the stability field of cohenite if: 1) silicates and carbonates do not form buffer assemblages, and 2) the fluid separates into two immiscible fluids, one CO_2-rich and one H_2O-rich. Migration of the CO_2-rich fluid and its mixing with H_2 liberated by serpentinization could provide the conditions of high P_{CO_2} and P_{H_2} required for cohenite formation. It is more likely, however, that cohenite forms as a result of multiple stages of reaction. During an early stage of serpentinization, magnetite, then native iron (and/or awaruite) could form via the reactions:

$$3FeO_{Silicate} + H_2O = Fe_3O_4 + H_2 \quad (4)$$

$$Fe_3O_4 + 4H_2 = 3Fe + 4H_2O \quad (5)$$

$$FeO_{Silicate} + H_2 = Fe + H_2O \quad (6)$$

Later, a CO_2-rich fluid could be reduced by the iron, resulting in the carbidization of the latter to form cohenite:

$$3Fe + CO_2 + 2H_2 = Fe_3C + 2H_2O \quad (7)$$

For this reaction to take place, reactions between silicate phases and fluid would have to be kinetically disfavoured with respect to reactions among metals, metal oxides, metal carbides, and fluid.

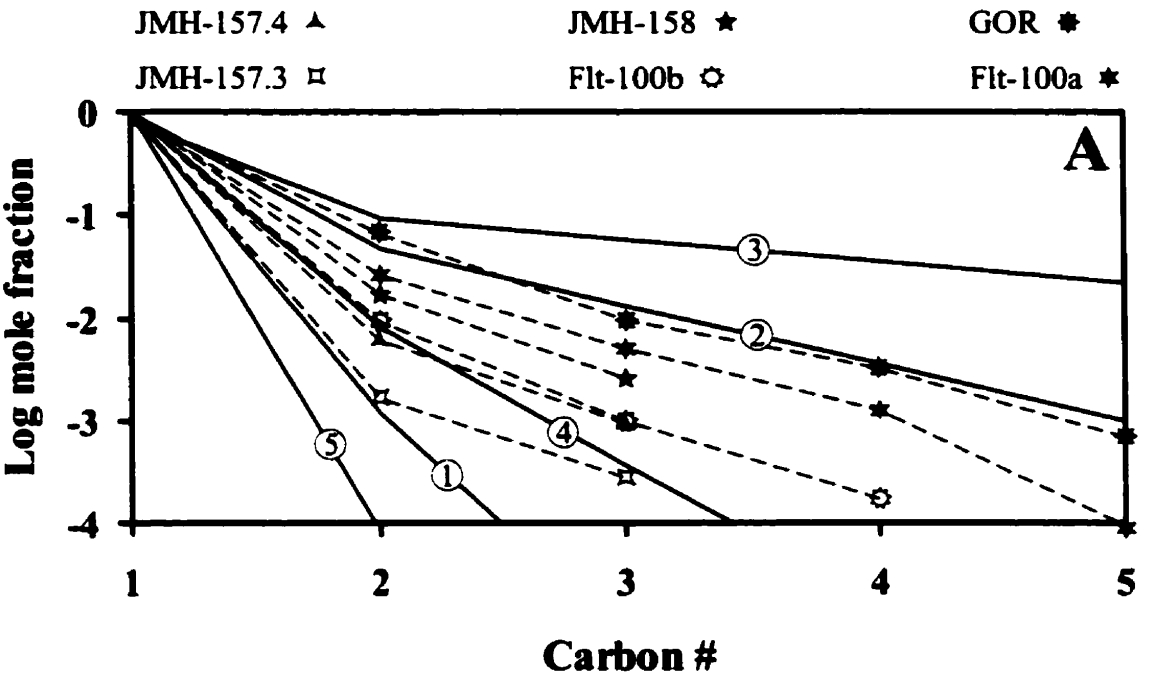
Measured versus calculated hydrocarbon distributions

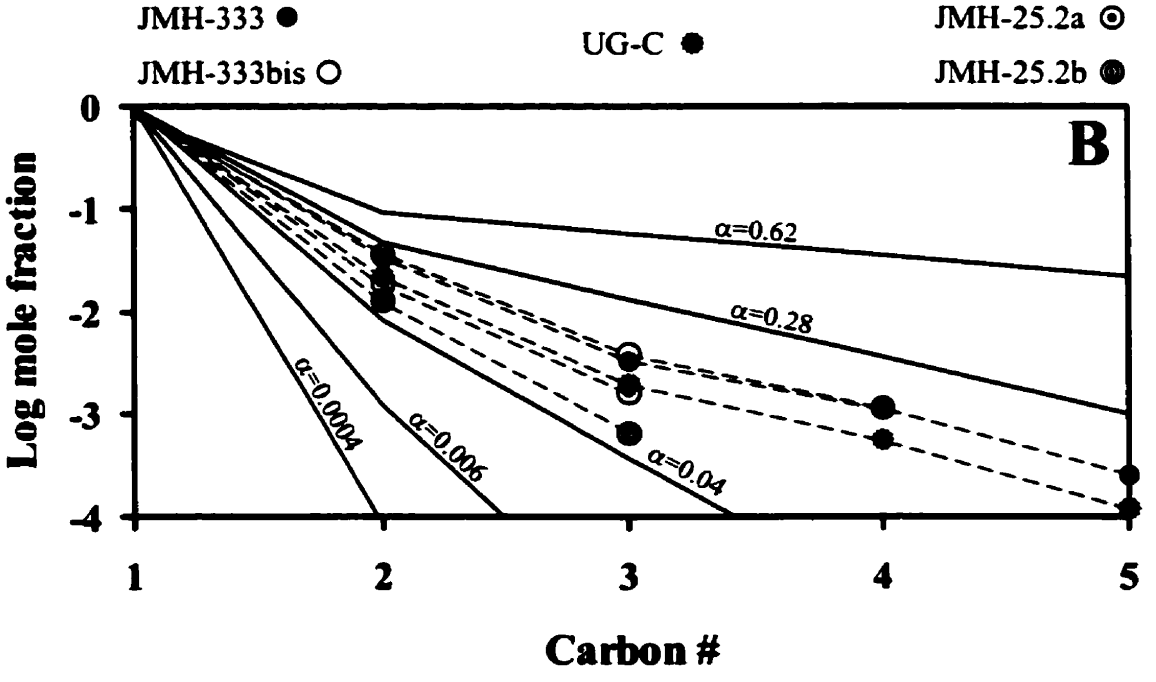
In Figure 5, we reproduce from Figure 2 the log mole fraction of hydrocarbons versus carbon number in the Asbestos rodingites (dashed lines). Also plotted on this diagram are the calculated distributions of the hydrocarbons (solid lines) in metastable equilibrium with the assemblages iron-FeO-cohenite (point 1, Figure 2), FeO-magnetite-cohenite (point 2, Figure 2), magnetite-cohenite-siderite (point 3, Figure 2), talc-magnesite-forsterite-enstatite (point 4, Figure 2), and antigorite-brucite-forsterite-graphite (point 5, Figure 2). All calculated hydrocarbon compositions, like those of the rodingite-hosted hydrocarbons, display a Schulz-Flory distribution for C_{2+} species. Moreover, in contrast to Fischer-Tropsch synthesis, the growth probability factor α has a range (0.0004 to 0.62) which encompasses all the values determined for the measured hydrocarbon distributions. As expected from the contrasting changes in thermodynamic properties of species belonging to different homologous series (see Helgeson et al., 1998), there is a break in linearity on Schulz-Flory plots between the calculated proportions of alkanes and CH_4. Homologous series for alkanes are formed by $-CH_3$ terminal species between which $-CH_2-$ species are inserted. Ethane is composed of only two terminal $-CH_3$ species, propane includes one additional $-CH_2-$ species, and so on for other higher alkanes. Each species contributes to the total free energy of the molecule in an amount proportional to the number of carbon atoms. This break between methane and other hydrocarbons is also present in the hydrocarbons extracted from the rodingites.

It is important to note that the above results are valid only for fluids containing virtually no water. All the samples studied contained aqueous-carbonic (type 2) fluid inclusions and, with the important exception of sample JMH-333, single-phase (type 1) carbonic inclusions. This indicates that C_{2+} hydrocarbons are present in type 2 aqueous-carbonic fluid inclusions and eliminates the possibility that separation of a carbonic fluid represented by type 1 inclusions occurred before formation of C_{2+} hydrocarbons. Further support for this conclusion is provided by the fairly consistent ratios between the aqueous and carbonic phases in sample JMH-333, and the tight concentration of total homogenization temperatures around 344 ± 12°C (1σ) which suggest that the aqueous and

Figure 5

Distribution of alkanes calculated (solid lines) for fluids in the presence of native iron-FeO-cohenite (point 1, Figure 2), FeO-magnetite-cohenite (point 2, Figure 2), magnetite-cohenite-siderite (point 3, Figure 2), talc-magnesite-forsterite-enstatite (point 4, Figure 2) and antigorite-brucite-forsterite-graphite (point 5, Figure 2), and measured from fluid inclusions in rodingites from the J.M. Asbestos chrysotile Mine (dashed lines). The linear variation of the logarithm of the proportions of the different alkanes with respect to the carbon number (excluding CH_4) describes a Schulz-Flory distribution and reflects the relationship $C_{n+1}/C_n = \alpha$.


JMH-157.4
JMH-158
GOR
JMH-157.3
Flt-100b
Flt-100a
A
Log mole fraction
0
-1
-2
-3
-4
1
2
3
4
5
Carbon #


JMH-333
UG-C
JMH-25.2a
JMH-333bis
JMH-25.2b
B
Log mole fraction
α=0.62
α=0.28
α=0.0004
α=0.006
α=0.04
0
-1
-2
-3
-4
1
2
3
4
5
Carbon #

carbonic components of type 2 inclusions formed an homogeneous mixture before entrapment. The CH_4-rich carbonic phase accounts for ~ 4 to 15 % of the volume of the inclusions, corresponding to molar volumes estimated, from the homogenization temperatures of the vapour in the liquid carbonic bubble (~ -90 to –100°C), to vary between 53 and 63 cm^3/mol (P-V-T data from Thiéry et al., 1994). This indicates that X_{CH_4} varies between 0.002 and 0.08 (see Chapter VI). By contrast, the saturation value of X_{CH_4} in a ~ 4.3 *m* NaCl solution, estimated from data in Duan et al. (1992) and Lamb et al. (1996), is between 0.02 and 0.03 at a temperature of 340°C and at pressures between 2 and 3 kilobars, which indicates that the aqueous phase was undersaturated with respect to a CH_4-rich fluid prior to its entrapment in JMH-333, and that the C_{2+}-bearing carbonic phase mixed with the aqueous fluid before entrapment. We propose that the conclusion that only a water-poor carbonic fluid could produce C_{2+} hydrocarbons and evidence that this fluid mixed with an aqueous fluid prior to entrapment without equilibrating with graphite-bearing serpentinite can be reconciled as follows. Fluid-dominated alteration was concentrated along shear zones, fractures and dykes where fluid flow was focussed. These same shear and fracture zones and dykes separate large blocks of less deformed peridotite towards the centers of which the fluid/rock ratio decreased, favouring the formation of CH_4-rich, C_{2+}-bearing fluids by reaction with the relict primary mafic silicates and Fe-Ni alloys. The latter fluids were able to migrate and dissolve in the aqueous fluids in the more permeable shear and fracture zones, and following a drop in temperature, separated and were trapped in rodingites together with the co-existing aqueous fluid.

CONCLUSIONS

Fischer-Tropsch synthesis is a viable mechanism for forming higher hydrocarbons (C_2-C_6 alkanes). However, the proportions of hydrocarbons must have a Schulz-Flory distribution corresponding to a α value of ~ 0.3. The hydrocarbons trapped in fluid inclusions at the J.M. Asbestos chrysotile deposit display a Schulz-Flory distribution, but

in all cases α is < 0.3. An alternative explanation for the presence of higher hydrocarbons in the JM Asbestos deposit is equilibration of a C-O-H fluid with a metastable mineral assemblage containing cohenite and magnetite. In contrast to Fischer-Tropsch synthesis, this explanation provides not only for a Schulz-Flory distribution of the hydrocarbons, but also for values of α covering the range determined for carbonic fluids trapped in the rodingites. The presence of cohenite in serpentinized peridotites provides convincing evidence that conditions favourable for the formation of higher hydrocarbons by this process can occur during serpentinization. However, significant proportions of hydrocarbons can form in the presence of a metastable mineral assemblage in serpentinized peridotite, only if the fluid is H_2O-poor and C-rich. Such fluids could form as a result of effervescence of an initially CO_2-rich fluid from a dominantly aqueous serpentinizing fluid.

ACKNOWLEDGEMENTS

Stefano Salvi, Werner Halter, Sandy Archibald, and Jane Kwak are thanked for their help in the gas chromatographic analyses and Prokopis Kranidiotis for collecting part of the fluid inclusion data set. This research was funded by NSERC and FCAR research grants to AEW-J and NSERC and FCAR scholarships to CN.

REFERENCES

Abrajano, T. A., Sturchio, N. C., Bohlke, J. K., Lyon, G. L., Poreda, R. J. and C. M. Stevens, 1988, Methane-hydrogen gas seeps, Zambales ophiolite, Philippines: Deep or shallow origin? Chemical Geology, v. 71, p. 211-222.

Abrajano, T. A., Sturchio, N. C., Kennedy, B. M., Lyon, G. L., Muehlenbachs, K. and J. K. Bohlke, 1990, Geochemistry of reduced gas related to serpentinization of the Zambales ophiolite, Philippines, Applied Geochemistry, v. 5, p. 625-630.

Apps, J. A., 1985, Methane formation during hydrolysis by mafic rocks, Lawrence Berkeley Laboratory, Annual Report 1984, p. 13-17.

Barnes, I. and J. R. O'Neil, 1969, The relationship between fluids in some fresh alpine-type ultramafics and possible modern serpentinization, Western United States, Geological Society of America Bulletin, v. 80, p. 1947-1960.

Bell, M. C., 1995, Thermodynamically controlled catalysis: equilibria in Fischer-Tropsch synthesis, Canadian Metallurgical Quarterly, v. 34, p. 331-341.

Berndt, M. E., Allen, D. E. and W. E. Seyfried Jr., 1996, Reduction of CO_2 during serpentinization of olivine at 300°C and 500 bar, Geology, v. 24, p. 351-354.

Charlou, J. L., Bougault, H., Appriou, P., Nelsen, T. and P. Rona, 1991, Different TDM/CH_4 hydrothermal plume signatures: TAG site at 26°N and serpentinized ultrabasic diapir at 15°05'N on the Mid-Atlantic Ridge, Geochimica et Cosmochimica Acta, v. 55, p. 3209-3222.

Charlou, J. L., Fouquet, Y., Bougault, H., Donval, J. P., Etoubleau, J., Jean-Baptiste, P., Dapoigny, A., Appriou, P. and P. A. Rona, 1998, Intense CH_4 plumes generated by serpentinization of ultramafic rocks at the intersection of the 15°20'N fracture zone and the Mid-Atlantic Ridge, Geochimica et Cosmochimica Acta, v. 62, p. 2323-2333.

Compagnoni, A., Conte, R., Facchinelli, A., Orione, P., Rossetti, P. and C. Trossarelli, 1998, The rodingite of Bellecombe (Val D'Aosta, Italy): a petrographic and fluid inclusion study, 17th general meeting, International Mineralogical Association, August 9-14, Toronto, Canada, Programme and Abstracts, A77L.

Day, H. W., Chernosky, J. V. and H. J. Kumin, 1985, Equilibria in the system MgO-SiO_2-H_2O: a thermodynamic analysis, American Mineralogist, v. 70, p. 237-248.

Duan, Z., Møller, N., Greenberg, J. and J. H. Weare, 1992, The prediction of methane solubility in natural waters to high ionic strength from 0 to 250°C and from 0 to 1600 bar, Geochimica et Cosmochimica Acta, v. 56, p. 1451-1460.

Eremeev, V. P. and A. K. Sibilev, 1970, Serpentinization in the Idzhim ultrabasic rock pluton and role of native iron, oregonite, and maucherite in the process, Izvestia Akadamii Nauk SSSR, Serie Geology, v. 6, p. 91-100. (in Russian).

Flory, P. J., 1936, Molecular-size distribution in linear condensation polymers, American Chemical Society Journal, v. 58, p. 1877-1884.

Fritz, P., Frape, S. K. and M. Miles, 1987, Methane in the crystalline rocks of the Canadian Shield, *in* Saline water and gases in crystalline rocks, Fritz, P. and S. K. Frappe, editors, Geological Association of Canada Special Paper 33, p. 211-223.

Fritz, P., Clark, I. D., Fontes, J. -C., Whiticar, M. J. and E. Faber, 1992, Deuterium and ^{13}C evidence for low temperature production of hydrogen and methane in a highly alkaline groundwater environment in Oman, *in* Water-Rock Interaction, Kharaka and Maest, editors, Balkema, Rotterdam, p. 793-796.

Frost, B. R., 1985, On the stability of sulfides, oxides, and native metals in serpentinite, Journal of Petrology, v. 26, p. 31-63.

Haggerty, J. A. and J. B. Fisher, 1992, Short-chain organic acids in interstitial waters from Mariana and Bonin forearc serpentinites: Leg 125, Proceedings of the oceanic drilling program, scientific results, v. 125, p. 387-395.

Hébert, R., 1980, Etude pétrologique des roches ophiolitiques d'Asbestos et du Mont Ham (Ham Sud), M. Sc. Thesis, Université Laval, Québec, 182 p.

Hébert, R. and J. H. Bédard, 1998, Architecture and petrogenesis of arc ophiolites: example from the ophiolitic complexes of southern Québec, Geological Association of Canada, Mineralogical Association of Canada, Association des géologues et géophysiciens du Québec, International Association of Hydrogeologists, Canadian Geophysical Union Joint Annual Meeting, 1998, Québec, Québec, Canada, Fieldtrip A4 Guidebook, 13-15 May 1998, 51 p.

Helgeson, H. C., Owens, C. E., Knox, A. M. and L. Richard, 1998, Calculation of the standard state molal thermodynamic properties of crystalline, liquid, and gas organic molecules at high temperatures and pressures, Geochimica et Cosmochimica Acta, v. 62, p. 985-1081.

Holloway, J. R., 1981, Composition and volumes of supercritical fluids in the earth's crust, *in* Fluid Inclusions, Hollister, L. S. and M. L. Crawford, editors, Mineralogical Association of Canada Short Course, v. 6, p. 13-38.

Holm, N. G., 1996, Serpentinization of oceanic crust and Fischer-Tropsch type synthesis of organic compounds, Origins of Life and Evolution of the Biosphere, v. 26, p. 205-206.

Janecky, D. R. and W. E. Seyfried, 1986, Hydrothermal serpentinization of peridotite within the oceanic crust: experimental investigations of mineralogy and major element chemistry, Geochimica et Cosmochimica Acta, v. 50, p. 1357-1378.

Johnson, J. W., Oelkers, E. H. and H. C. Helgeson, 1992, SUPCRT92: a software package for calculating the standard molar thermodynamic properties of minerals, gases, aqueous species, and reactions from 1 to 5000 bars and 0° to 1000°C, Computers and Geosciences, v. 18, p. 899-947.

Kudo, A., Nakagawa, S., Tsuneto, A. and T. Sakata, 1993, Electrochemical reduction of high pressure CO_2 on Ni electrodes, Journal of the Electrochemical Society, v. 140, p. 1541-1545.

Lamb, W. M., Popp, R. K. and L. A. Boockoff, 1996, The determination of phase relations in the CH_4-H_2O-NaCl system at 1 kbar, 400 to 600°C using synthetic fluid inclusions, Geochimica et Cosmochimica Acta, v. 60, p. 1885-1897.

Lancet, M. S. and E. Anders, 1970, Carbon isotope fractionation in the Fischer-Tropsch synthesis and in meteorites, Science, v. 170, p. 980-982.

Laurent, R., 1975, Petrology of the alpine-type serpentinites of Asbestos and Thetford Mines, Quebec, Schweizerische Mineralogische und Petrographische Mitteilungen, v. 55, p. 431-455.

Laurent, R. and Y. Hébert, 1979, Paragenesis of serpentine assemblages in harzburgite tectonite and dunite cumulate from the Quebec Appalachians, Canadian Mineralogist, v. 17, p. 857-869.

Lyon, G. L. and W. F. Giggenbach, 1990, Composition and origin of the hydrogen-rich gas seep, Fiordland, New Zealand, EOS, Transactions, American Geophysical Union, v. 71, p. 1717.

Macdonald, A. H. and W. S. Fyfe, 1985, Rate of serpentinization in seafloor environments, Tectonophysics, v. 116, p. 123-135.

Marakushev, A. A., Shteynberg, D. S. and M. V. Lagutina, 1992, Variations of the correlation between carbon and water contents in hydration products of meteorites and alpine-type ultramafic rocks, Doklady Akademii Nauk, v. 327, p. 575-577.

Moody, J. B., 1976, An experimental study on the serpentinization of iron-bearing olivines, Canadian Mineralogist, v. 14, p. 462-478.

Morency, M., Mineau, R., Zeller, E. and G. Dreschhoff, 1986, Are all fossil fuels really fossils? Oil & Gas Journal, June 2, p. 92-95.

Mottl, M. J., 1992, Pore waters from serpentinite seamounts in the Mariana and Izu-Bonin forearcs, Leg 125: evidence for volatiles from the subducting slab, Proceedings of the ocean drilling program, scientific results, v. 125, p. 373-385.

Mottl, M. J. and J. A. Haggerty, 1989, Upwelling of Cl-poor, S- and C-rich waters through a serpentinite seamount, Mariana forearc, ODP Leg 125, EOS, Transactions, American Geophysical Union, v. 70, p. 1382.

Neal, C. and G. Stanger, 1983, Hydrogen generation from mantle source rocks in Oman, Earth and Planetary Science Letters, v. 66, p. 315-320.

O'Hanley, D. S., 1987, The origin of the chrysotile asbestos veins in southeastern Quebec, Canadian Journal of Earth Science, v. 24, p. 1-9.

O'Hanley, D. S. and M. D. Dyar, 1993, The composition of lizardite 1T and the formation of magnetite in serpentinites, American Mineralogist, v. 78, p. 391-404.

O'Hanley, D. S. and M. D. Dyar, 1998, The composition of chrysotile and its relationship with lizardite, Canadian Mineralogist, v. 36, p. 727-739.

Pinet, N. and A. Tremblay, 1995a, Tectonic evolution of the Quebec-Maine Appalachians: from oceanic spreading to obduction and collision in the Northern Appalachians, American Journal of Science, v. 295, p. 173-200.

Pinet, N. and A. Tremblay, 1995b, Is the Taconian orogeny of southern Quebec the result of an Oman-type obduction? Geology, v. 23, p. 121-124.

Ramdohr, P., 1967, A widespread mineral association, connected with serpentinization, Neues Jahrbuch für Mineralogie Abhandlungen, v. 107, p. 241-265.

Robie, R. A., Hemingway, B. S. and J. R. Fisher, 1978, Thermodynamic properties of minerals and related substances at 298.15K (25°C) and one atmosphere (1.013 bars) and at higher temperatures, United States Geological Survey Bulletin No. 1452.

Rona, P. A., Bougault, H., Charlou, J. L., Appriou, P., Nelsen, T. A., Trefry, J. H., Eberhart, G. L., Barone, A. and H. D. Needham, 1992, Hydrothermal circulation, serpentinization, and degassing at a rift valley-fracture zone intersection: Mid-Atlantic ridge near 15°N, 45°, Geology, v. 20, p. 783-786.

Salvi, S. and A. E. Williams-Jones, 1997a, Fischer-Tropsch synthesis of hydrocarbons during sub-solidus alteration of the Strange Lake peralkaline granite, Quebec/Labrador, Canada, Geochimica et Cosmochimica Acta, v. 61, p. 83-99.

Salvi, S., and A. E. Williams-Jones, 1997b, Fluid-inclusion volatile analysis by gas chromatography: application of a wide-bore porous-polymer capillary column to the separation of organic and inorganic compounds, Canadian Mineralogist, v. 35, p. 1391-1414.

Sanford, R. F., 1981, Mineralogical and chemical effects of hydration reactions and applications to serpentinization, American Mineralogist, v. 66, p. 290-297.

Schandl, E. S., O'Hanley, D. S., Wicks, F. J. and T. K. Kyser, 1990, Fluid inclusions in rodingite: a geothermometer for serpentinization, Economic Geology, v. 85, p. 1273-1276.

Schulz, G. V., 1935, Highly polymerized compounds CXXII. The relation between reaction rate and composition of the reaction product in micropolymerization processes, Zeitschrift für Physikalische Chemie, B30, p. 379-398.

Shteynberg, D. S. and M. V. Lagutina, 1978, Carbon balance in serpentinization of ultramafic rocks, Doklady Akademii Nauk SSSR, v. 243, p. 760-763. (in Russian).

Shterenberg, L. E. and K. A. Stepanova, 1978, Graphite in sediments from the northeastern part of the Pacific Ocean (Stations No. 675 and No. 655), Doklady Akademii Nauk SSSR, v. 241, p. 460-462.

Shvarov, Y. and E. Bastrakov, 1999, HCh: a software package for geochemical equilibrium modelling, User's guide, Australian Geological Survey Organization, Record 1999/25, 61 p.

Szatmari, P., 1989, Petroleum formation by Fischer-Tropsch synthesis in plate tectonics, The American Association of Petroleum Geologists Bulletin, v. 73, p. 989-998.

Thayer, T. P., 1966, Serpentinization considered as a constant volume metasomatic process, American Mineralogist, v. 51, p. 685-710.

Thiéry, R., van den Kerkhof, A. M. and J. Dubessy, 1994, *vX* properties of CH_4-CO_2 and CO_2-N_2 fluid inclusions: modelling for T < 31°C and P < 400 bars, European Journal of Mineralogy, v. 6, p. 753-771.

Toft, P. B., Arkani-Hamed, J. and S. E. Haggerty, 1990, The effects of serpentinization on density and magnetic susceptibility: a petrophysical model, Physics of the Earth and Planetary Interiors, v. 65, p. 137-157.

van der Laan, G. P. and A. A. C. M. Beenackers, 1999, Kinetics and selectivity of the Fischer-Tropsch synthesis: a literature review, Catalysis Reviews – Science and Engineering, v. 41, p. 255-318.

Wegner, W. W. and W. G. Ernst, 1983, Experimentally determined hydration and dehydration reaction rates in the system MgO-SiO_2-H_2O, American Journal of Science, v. 283A, p. 151-180.

Welhan, J. A., 1987, Characteristics of abiotic methane in rocks, *in* Saline water and gases in crystalline rocks, Fritz, P. and S. K. Frappe, editors, Geological Association of Canada Special Paper, 33, p. 225-233.

Welhan, J. A., 1988, Origins of methane in hydrothermal systems, Chemical Geology, v. 71, p. 183-198.

Welhan, J. A. and H. Craig, 1979, Methane and hydrogen in East Pacific Rise hydrothermal fluids, Geophysical Research Letters, v. 6, p. 829-831.

Whitehead, J., Dunning, G. R. and J. G. Spray, 2000, U-Pb geochronology and origin of granitoid rocks in the Thetford Mines ophiolite, Canadian Appalachians, Geological Society of America Bulletin, v. 112, p. 915-928.

INTRODUCTION TO CHAPTER VIII

The five chapters that comprise the second part of the thesis are an extension of an industrially oriented research project supported financially by NSERC and JM Asbestos Inc., which was designed to determine the distribution of amphibole-group minerals in the JM Asbestos mine and establish the factors that controlled this distribution (Chapter VIII). The rationale for the project was that asbestiform amphiboles are known to occur in chrysotile asbestos products, and were recently recognized to be the major health hazard in this material, causing a variety of pulmonary diseases including the cancer mesothelioma. It was hoped that by establishing the distribution of the amphiboles and controls of this distribution it would be possible to reduce contamination of the chrysotile ores by amphibole, and thereby make the Asbestos products less hazardous. This chapter summarizes the results of the amphibole project.

CHAPTER VIII

CONTROLS OF AMPHIBOLE FORMATION IN CHRYSOTILE DEPOSITS: EVIDENCE FROM THE JEFFREY MINE, ASBESTOS, QUÉBEC.

by

A.E. Williams-Jones, C. Normand, J. Clark, H.Vali, R.F. Martin

Department of Earth and Planetary Sciences, McGill University, 3450 University Street, Montreal (Qué), Canada, H3A 2A7

and

A. Dufresne, A. Nayebzadeh

Department of Occupational Health, McGill University, 3450 University St., Montreal (Qué), Canada, H3A 2A7

Accepted for publication in The Canadian Mineralogist

ABSTRACT

Epidemiological studies have demonstrated strong correlations between long term exposure to asbestos fibers and a variety of pulmonary diseases, including fibrosis, lung carcinoma and a type of pleural cancer known as mesothelioma. Moreover, studies of chrysotile mine and mill workers in Québec have shown that the principal fiber in their lung tissues is not, as might be expected, chrysotile, but rather the amphibole mineral, tremolite. In view of these findings, it is essential to establish the distribution of tremolite in the mines and, in particular, to determine whether or not the chrysotile ores are tremolite-bearing.

Detailed investigations of the Jeffrey mine have revealed the presence of the following amphibole minerals: anthophyllite, cummingtonite, hornblende, and tremolite-actinolite. The bulk of the amphibole, however, is in the form of tremolite and actinolite and is found mainly in serpentinite adjacent to or as xenoliths/inclusions within felsic dykes. Appreciable quantities of amphibole are also present in pyroxenite (tremolite) and slate (actinolite) in contact with serpentinite distal to the ore zones. Significantly, the chrysotile ores are essentially amphibole-free. Most of the amphibole is fibrous but a small proportion is asbestiform according to criteria established by the U.S. Occupational Safety and Health Administration. The principal control on the formation of tremolite and actinolite in the serpentinite was an increase in $a\mathrm{SiO}^0_2$ associated with felsic dykes. Increased $a\mathrm{Ca}^{2+}$ favours tremolite-actinolite crystallization but is not a prerequisite. Anthophyllite-cummingtonite formation required both an increase in $a\mathrm{SiO}^0_2$ and high temperatures (> 600°C), which were associated with the intrusion of felsic dykes.

Amphibole is easily detected by conventional (> 2.5 wt. %) and digestion-enhanced (> 0.1 wt. %) powder X-ray diffraction analysis. Lithogeochemical analyses afford an indirect and less expensive method for screening samples for amphiboles. Amphibole-free samples contain < 15 ppm CaO, < 0.6 wt. % $\mathrm{Al_2O_3}$, and > 2,350 ppm Ni. In conjunction with conventional geological mapping, it should be possible, using these detection methods, to identify potential amphibole-rich zones and design methods to mine chrysotile ores with minimal contamination.

INTRODUCTION

During the past thirty years, there has been a growing public awareness of the health risks associated with the exploitation and use of asbestos minerals, because of epidemiological studies demonstrating strong correlations between long term exposure to asbestos fibers and a variety of pulmonary diseases, including fibrosis (asbestosis), lung carcinoma and a cancer of the pleural membrane, known as mesothelioma (Hughes and Weill, 1986). As a result, there has been considerable pressure on governments to discourage or even ban the use of asbestos products. Initially, it was assumed that health hazards posed by all asbestiform minerals are similar. However, studies by Weill et al. (1977), McDonald et al. (1983), Hughes and Weill (1986), and Hughes (1991), among others, showed that a large part of the risk was associated with amphibole-group minerals, particularly riebeckite (crocidolite) and grunerite (amosite). As a result, the exploitation and use of these asbestiform minerals has been discontinued.

At the current time only chrysotile asbestos is still being mined. Nevertheless, industrial exposure to chrysotile products can be associated with elevated incidences of lung disease, including lung carcinoma and mesothelioma, although such incidences are well below those associated with exposure to grunerite and riebeckite (Hughes and Weill, 1986; Hughes, 1991). At first, the increased health risks were attributed to the chrysotile. However, a detailed study by McDonald et al. (1989) concluded that the bulk of the increase in the incidence of lung disease, particularly mesothelioma, is due to contamination by tremolite. This conclusion is supported by a study of miners and millers from the Thetford Mines area, in which Dufresne et al. (1995 and 1996) showed that 88% of the identified lung fibers consist of tremolite, and only 4% consist of chrysotile. Preliminary results of a study by our group, of lung tissue of mine and mill workers from the Jeffrey mine, Québec, suggest that the corresponding distributions of fibers are 72% tremolite and 26% chrysotile.

In view of the above conclusion that tremolite, not chrysotile, may be the dominant factor in many of the diseases afflicting people exposed to the products of chrysotile mining, the questions that come to mind are: 1) what are the relative proportions of chrysotile and tremolite in chrysotile ore deposits, 2) what is the

distribution of tremolite in these deposits, and 3) what are the factors that control this distribution. These questions have been addressed as part of a multidisciplinary project designed to investigate the interplay of geology and human biology in the etiology of asbestos-related lung diseases. This project is centered on the Asbestos district, Québec, and the study discussed in this paper is based on results obtained from the Jeffrey mine. As a result of detailed mapping of the Jeffrey open pit, core logging, exhaustive mineralogical and geochemical studies, and a theoretical evaluation of the stability relations of amphibole-group minerals and other species in the system CaO-MgO-SiO_2-H_2O, we have been able to reconstruct the environment of amphibole crystallisation and thereby determine the origin of the amphibole contaminant in the ore.

GEOLOGICAL SETTING

The Jeffrey chrysotile deposit is found in a narrow belt of Ordovician ophiolite slivers in the Québec Appalachians, localized along the Baie Verte – Brompton Line that separates continental Cambro-Ordovician sediments to the north from oceanic crust-derived volcanic and sedimentary rocks to the south (Figure 1). In the vicinity of the mine, the ophiolite sequence consists, from north to south, of an amphibolite sole, and overlying harzburgite, dunite, pyroxenite, gabbro, basalt, and pelagic sedimentary rocks, which were thrust over continental margin sedimentary rocks of the Caldwell Group (Figure 2). The ophiolite has been extensively dismembered, with resulting transport of slices along strike, producing a thinning of the crustal parts of the sequence (Hébert et al., 1998). This dismemberment is manifested by extensive shearing and was associated with the emplacement of numerous felsic dykes (Chapter IV). During emplacement (Taconic orogeny), the ophiolites were subjected to regional mid-greenschist facies metamorphism at temperatures of 300 to 400°C, and were locally subjected to multiple reheating events at similar temperatures between the Taconic and Acadian orogenies (Laird et al., 1993; Whitehead et al., 1996).

The two major rock types of the ophiolite sequence exposed in the open pit are

Figure 1

Geological map showing the distribution of Ordovician ophiolites in southern Québec, and the location of the Jeffrey mine (Modified after Normand et al., 1996).

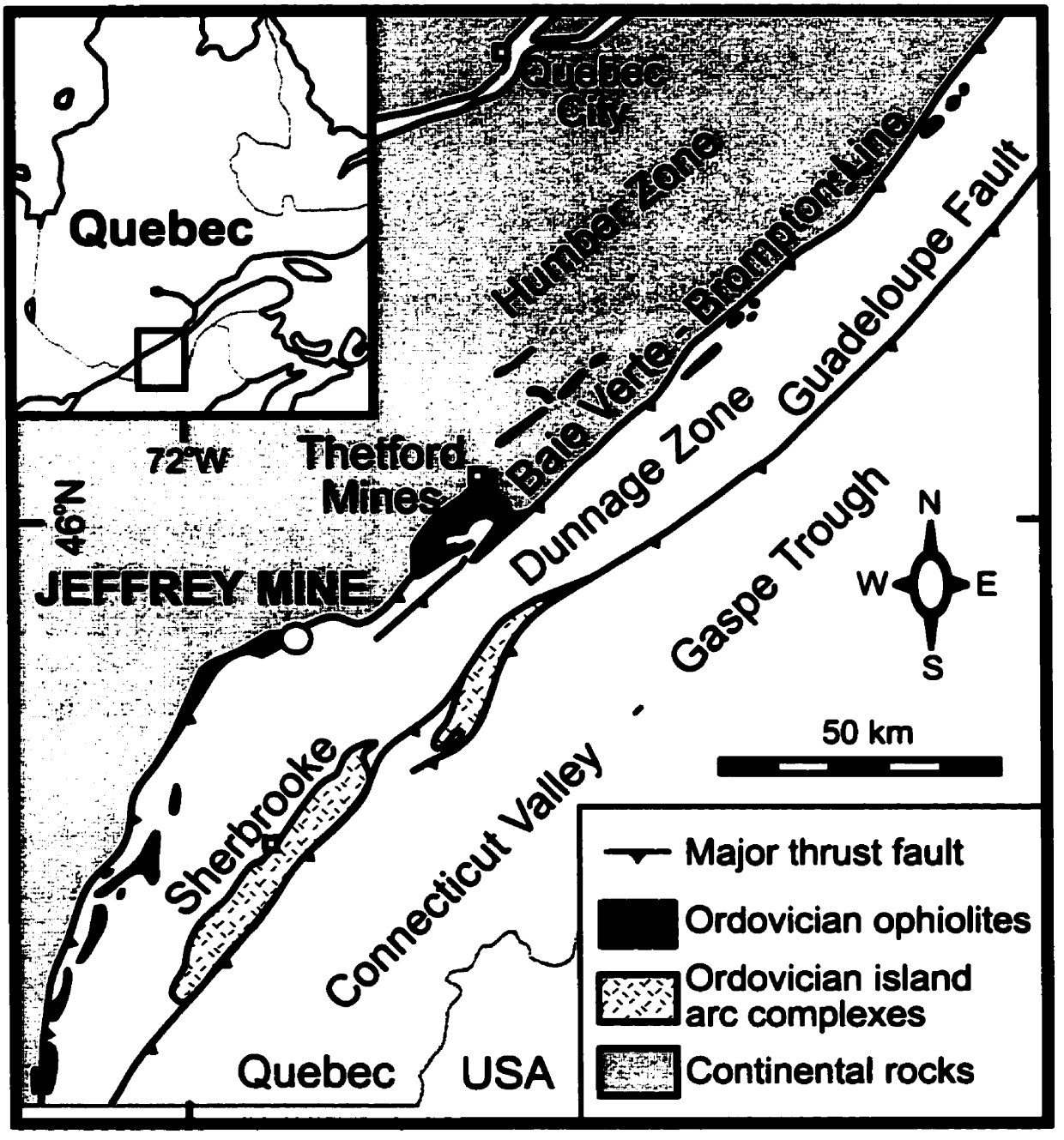
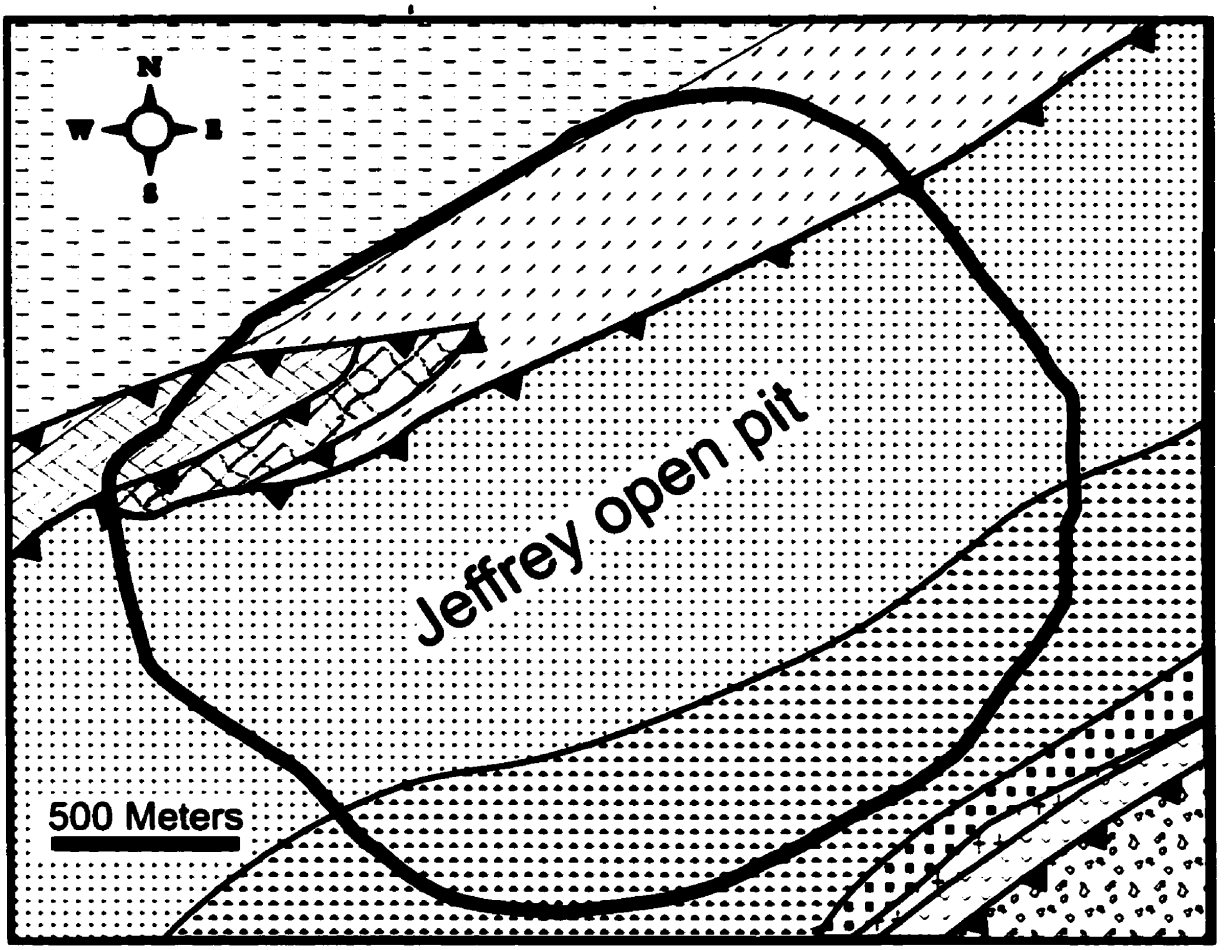

Quebec
Quebec City
Humber Zone
Baie Verte - Brompton Line
Guadeloupe Fault
72°W
Thetford Mines
46°N
JEFFREY MINE
Dunnage Zone
Gaspe Trough
N
W
E
S
50 km
Sherbrooke
Connecticut Valley
Quebec
USA
Major thrust fault
Ordovician ophiolites
Ordovician island arc complexes
Continental rocks

Figure 2

Detailed geological map of the Jeffrey mine area.



Saint-Daniel Formation

Melange

Caldwell Group

Metagraywacke

Slate

Amphibolite

Ophiolitic Complex

Serpentinite

Harzburgite

Dunite

Pyroxenite

Gabbro

Pillowed and brecciated tholeiites

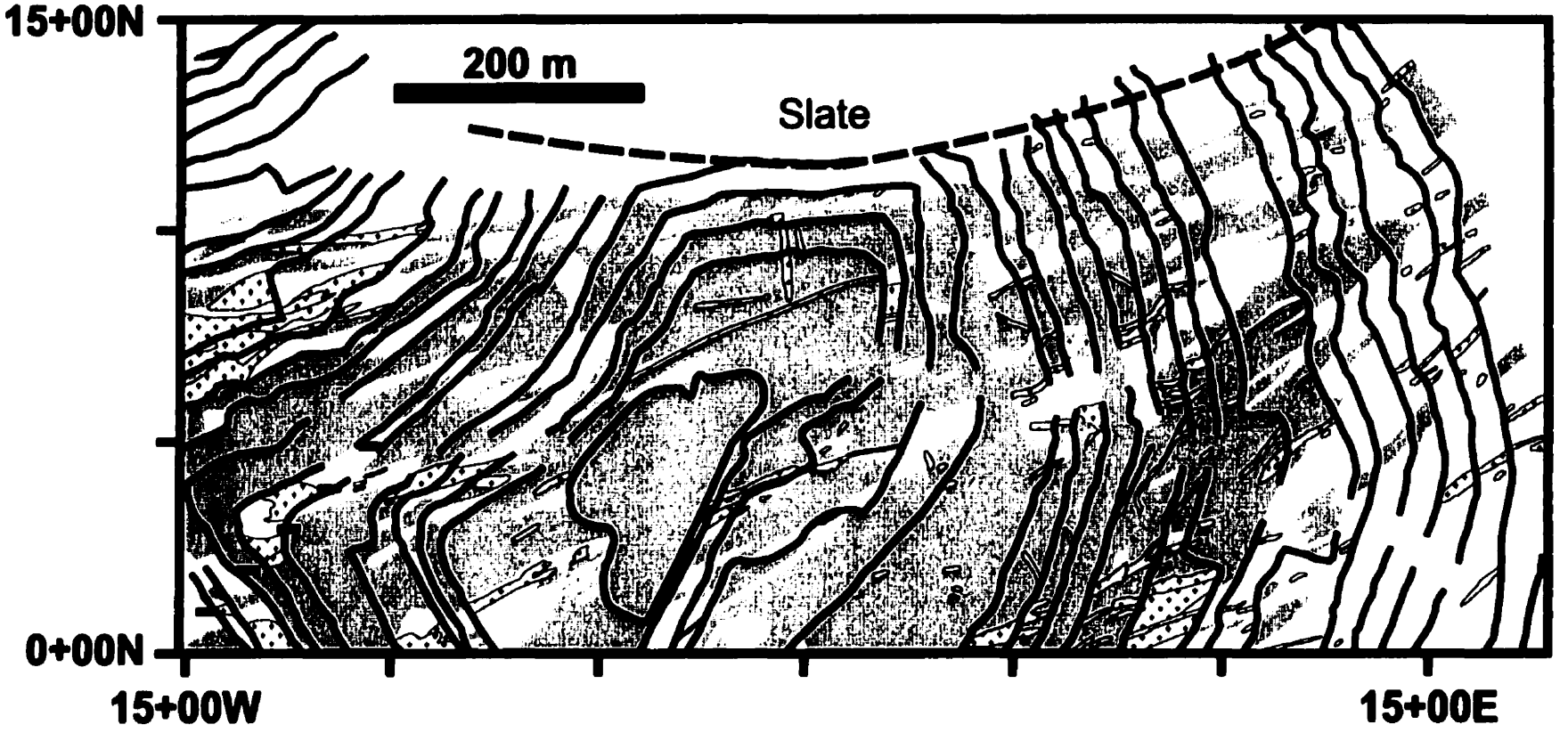
harzburgite and dunite. The latter is interlayered locally with pyroxenite, and grades into a larger body of pyroxenite on the southeastern margin of the pit. Both harzburgite and dunite were serpentinized during ridge-related hydrothermal metamorphism of the ocean-floor with further serpentinization and recrystallization of serpentine minerals taking place during tectonic emplacement of the ophiolite into its current setting (Laurent, 1975). The latter serpentinization event produced the harzburgite-hosted chrysotile ores that are currently being exploited. The serpentinites are paragenetically complex and now consist of a variety of assemblages comprising varying proportions of some or all of the following minerals; lizardite, antigorite, chrysotile, brucite, and magnetite. Ore zone serpentinite is distinguished by an abundance of veins of cross-fiber chrysotile and a concentration of brucite that is proportional to the density of chrysotile veins (up to 20 vol. % brucite). For further information on the mineralogy of the serpentinites, the reader is referred to Wicks and Whittaker (1977), Wicks and Plant (1979), and O'Hanley and Dyar (1998). The pyroxenites were also extensively altered, and now consist of tremolite, chlorite, relict clinopyroxene, talc, and lizardite.

Footwall rocks are exposed along the northwestern margins of the pit. These rocks comprise carbonaceous slates except in the western corner, where underlying greywacke and amphibolite are also exposed. The slates have been albitized over a distance of roughly two meters from their contact with serpentinite and converted to rodingite, a Ca-Al-rich metasomatic rock, in a 50 cm zone immediately adjacent to the contact.

Two types of felsic dyke rocks are present in the open pit, namely diorite-monzodiorite and granite, and are restricted mainly to the harzburgite lying largely outside the ore zones (Figure 3). Diorite-monzodiorite dykes are approximately twice as common as granitic dykes and, on the basis of cross-cutting relationships, predate the granite. Both types of dyke are mainly oriented parallel to the ophiolite stratigraphy, i.e., NE-SW, although a significant proportion of the granitic dykes and a small proportion of the diorite-monzodiorite dykes are also oriented NW-SE (Chapter IV). Dykes range in thickness from a few centimeters to several meters, and can be traced for several hundred

Figure 3

Plan of the Jeffrey open pit showing the distribution of chrysotile ores and larger felsic intrusions (based on maps provided by JM Asbestos Inc.). The solid lines demarcate benches in the pit.


15+00N
200 m
Slate
0+00N
15+00W
15+00E
Chrysotile ore zones
Felsic intrusive rocks
Undifferentiated sheared and altered serpentinite, and slate

meters along strike and vertically. Virtually all dykes are concentrated in shear zones and, in many cases, have been boudinaged and dismembered (Figure 4). In many cases, the dykes have also been extensively converted to albite and rodingite.

Potentially, the felsic dykes could have been: 1) intruded prior to serpentinization, 2) intruded post-serpentinization but prior to emplacement of the ophiolite in its current setting, 3) tectonically incorporated during emplacement, or 4) intruded post-emplacement. The fourth alternative can be eliminated because the dykes form orthogonal networks restricted to serpentinite, i.e., the dykes do not extend into the surrounding lithologies. For the same reason, i.e., the orthogonal nature of the dyke distribution, we can also rule out the third alternative; tectonic processes would have rotated any foreign bodies, particularly tabular ones, into parallelism with the regional tectonic grain. Although we cannot discount the possibility of pre-serpentinization intrusion of the dykes, we consider this unlikely on the basis of field evidence. We therefore argue that the dykes were most probably intruded after an initial stage of ridge-related serpentinization of the ocean floor, but prior to the later stages of serpentinization that occurred during ophiolite emplacement.

NATURE AND DISTRIBUTION OF AMPHIBOLE-GROUP MINERALS

The mineralogy, paragenesis and distribution of amphibole-group minerals were established by detailed mapping of the open pit, core-logging and a study of some 600 samples of various lithologies represented in the deposit using optical and electron microscopic techniques, X-ray powder-diffraction and fluorescence, and electron-microprobe analysis. With the exception of X-ray powder-diffraction analyses, the application of these methods was conventional. X-ray powder-diffraction analyses were conducted primarily to detect the presence of amphibole species. A major limitation of the conventional application of this technique is the relatively high detection-limit,

Figure 4

A lensoid fragment of a dismembered felsic dyke (light coloured) located in a zone of sheared serpentinite in the Jeffrey pit.



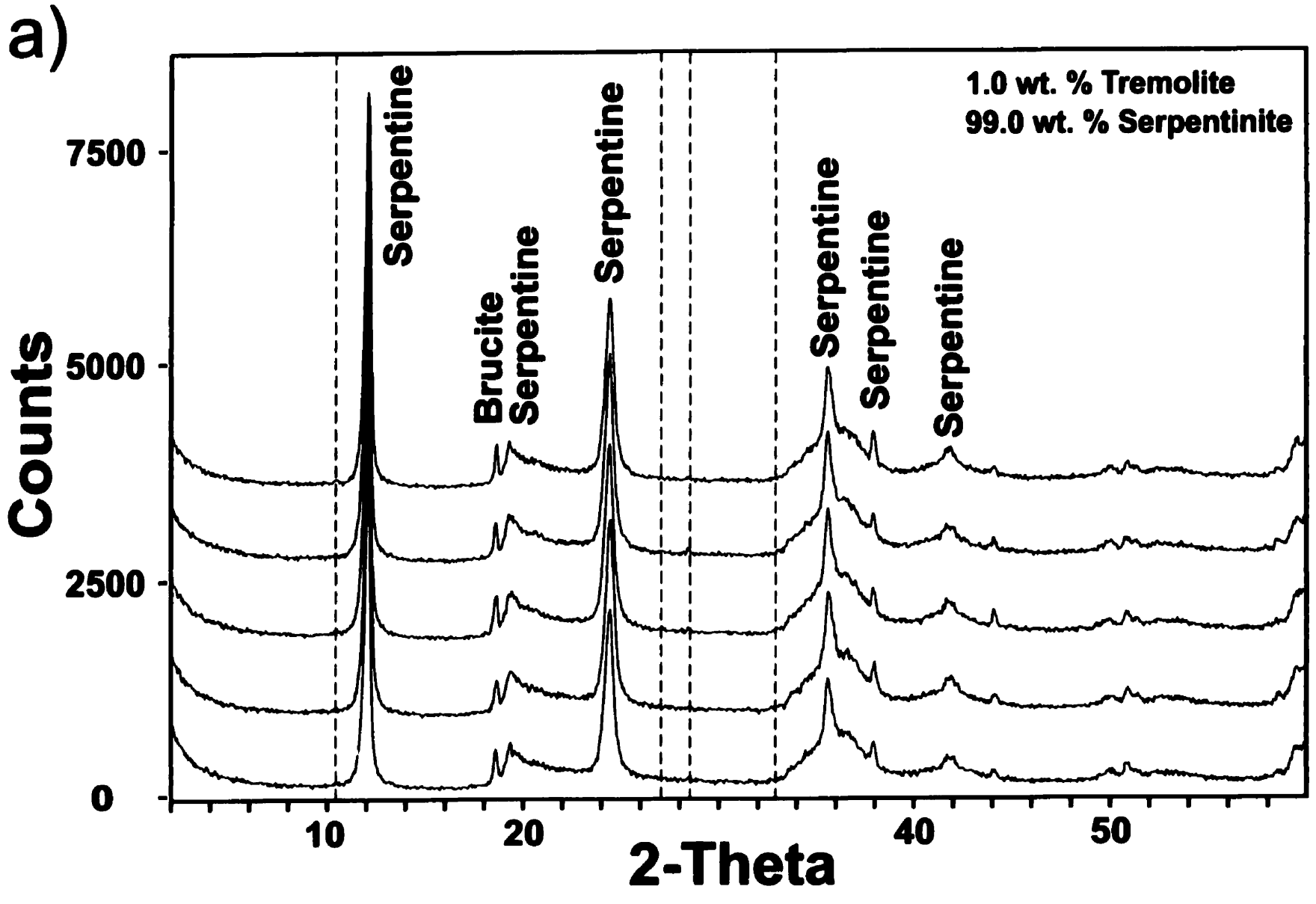
approximately 2.5 wt. % in the case of amphibole contained in serpentinite. In order to improve this level of detection, we employed a modification of the serpentine digestion method developed by Addison and Davies (1990). This procedure involved digesting samples in 2 N boiling sulphuric acid for 60 minutes, further digesting them in a boiling 4 N sodium hydroxide solution, and finally washing them repeatedly in nanopure water until pH remained neutral. This process resulted in the dissolution of the serpentine-group minerals and left the amphibole unaffected. The acid treatment served to liberate the cations, principally magnesium, and the alkali treatment broke down the silicate structure of the serpentine. Using this method, we were able to concentrate the amphibole and detect its presence to a level of ≥ 0.1 wt. % (Figure 5).

TYPES OF AMPHIBOLE

The following amphibole-group minerals were detected: anthophyllite, cummingtonite, hornblende, tremolite ($X_{Mg} > 0.75$), and actinolite ($0.55 < X_{Mg} < 0.75$), however, only tremolite and actinolite are present in significant concentrations in the open pit. Anthophyllite and cummingtonite were the earliest amphiboles to form, and are invariably intergrown. In almost all cases, both minerals are fibrous, with an aspect ratio greater than 20; their diameter typically ranges between 1 and 5 μm (Figure 6a). Tremolite and actinolite were the next amphibole-group minerals to crystallize, although in some cases they grew contemporaneously with anthophyllite and cummingtonite. Where conditions were not appropriate for the growth of anthophyllite and cummingtonite, tremolite and actinolite were the first amphiboles to form (see below). Like anthophyllite and cummingtonite, tremolite and actinolite are dominantly fibrous, with an aspect ratio greater than 20:1 (Figure 6b). However, up to 20% of tremolite crystals are non-fibrous, having an aspect ratio less than 10:1. In both cases fiber diameters are mainly between 1 and 5 μm. Actinolite commonly replaces anthophyllite and cummingtonite (Figure 6c) but the reverse is never observed, and also replaces tremolite (Figure 6d). The last amphibole to form was hornblende, which occurs as

Figure 5

A) X-ray diffractograms of five untreated samples from a 99:1 mixture of serpentine and tremolite. None of the diffractograms display peaks for tremolite (vertical dashed lines). B) A X-ray diffractogram of a 999:1 mixture of serpentine and tremolite after digestion (see text for details on digestion procedure).


a)
1.0 wt. % Tremolite
99.0 wt. % Serpentinite
Serpentine
Brucite
Serpentine
Serpentine
Serpentine
Serpentine
Serpentine
Counts
7500
5000
2500
0
10
20
40
50
2-Theta

b)

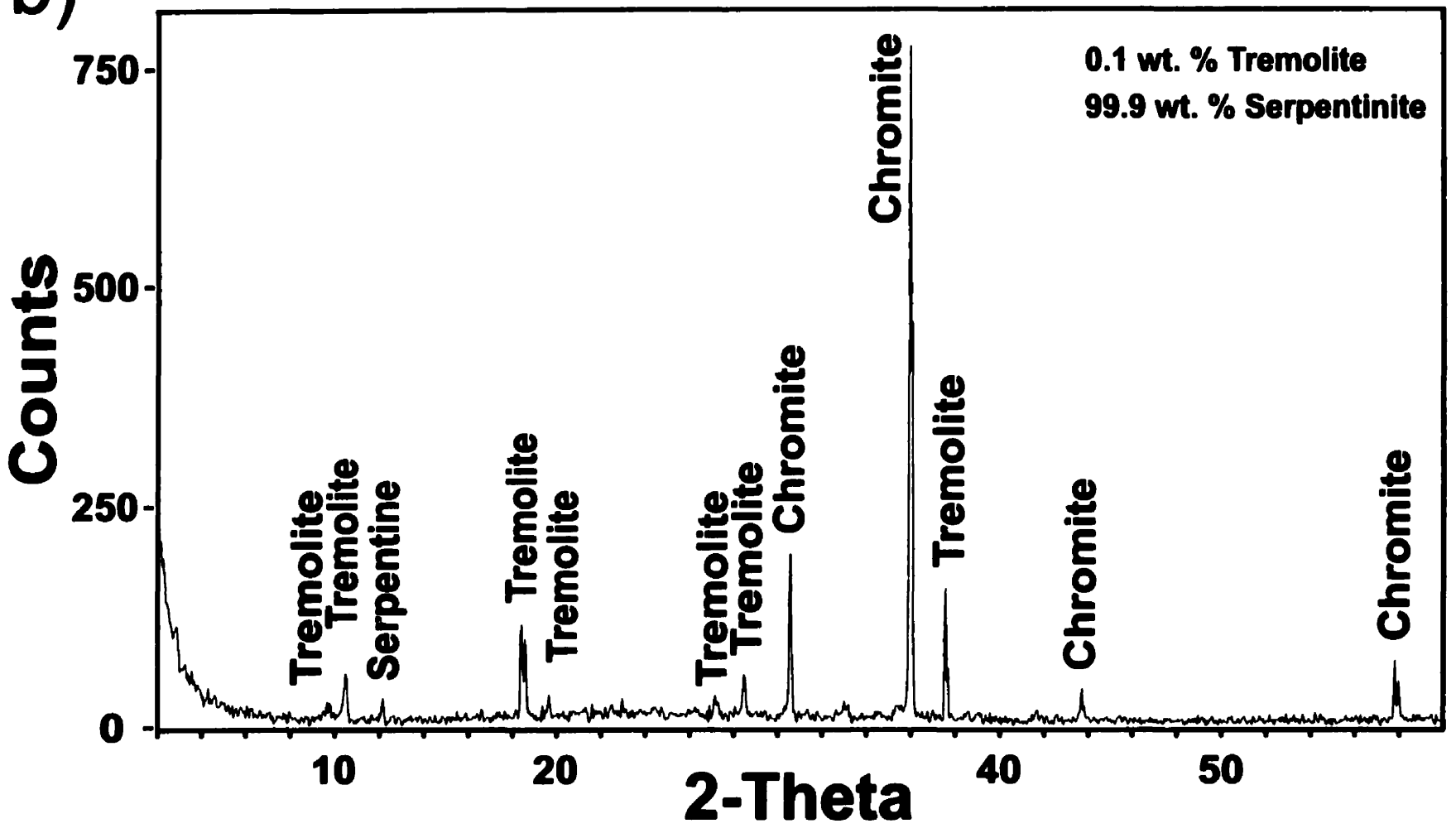
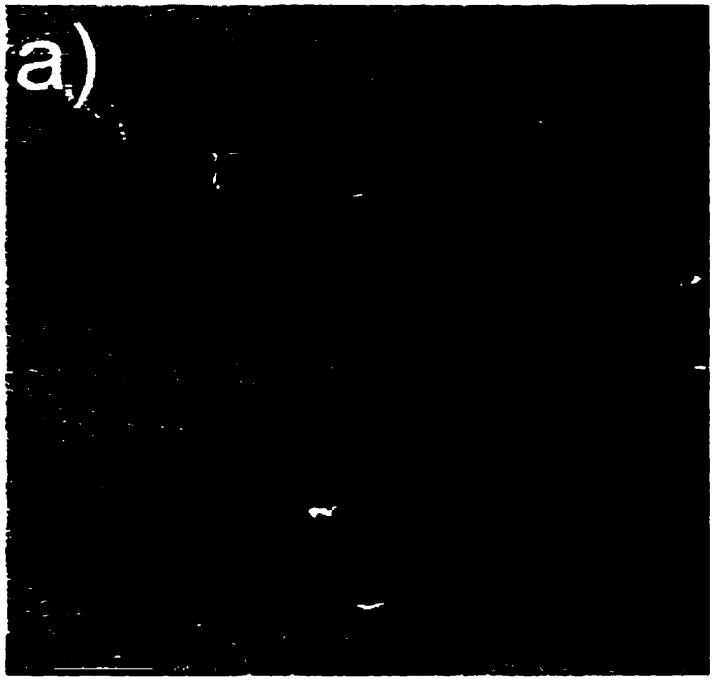
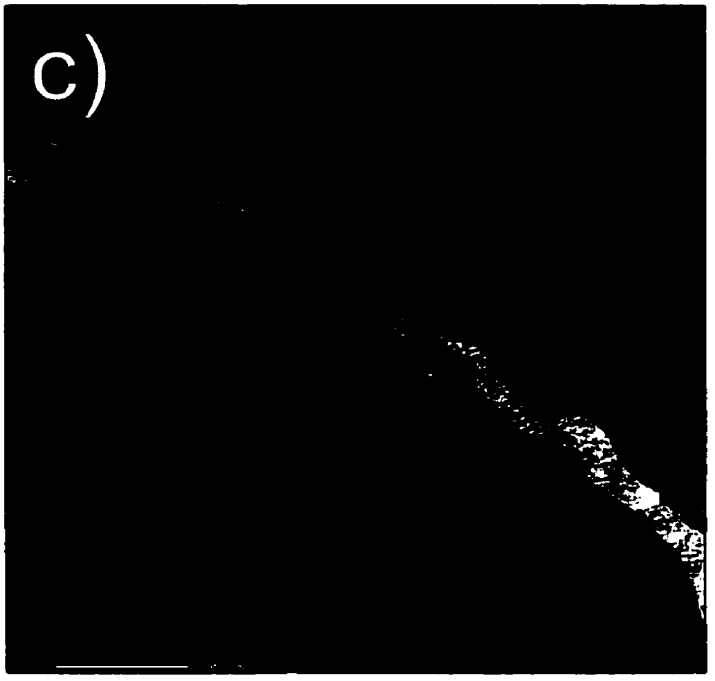

0.1 wt. % Tremolite
99.9 wt. % Serpentinite
Counts
750
500
250
0
10
20
40
50
2-Theta
Tremolite
Tremolite
Serpentine
Tremolite
Tremolite
Tremolite
Tremolite
Chromite
Chromite
Tremolite
Chromite
Chromite

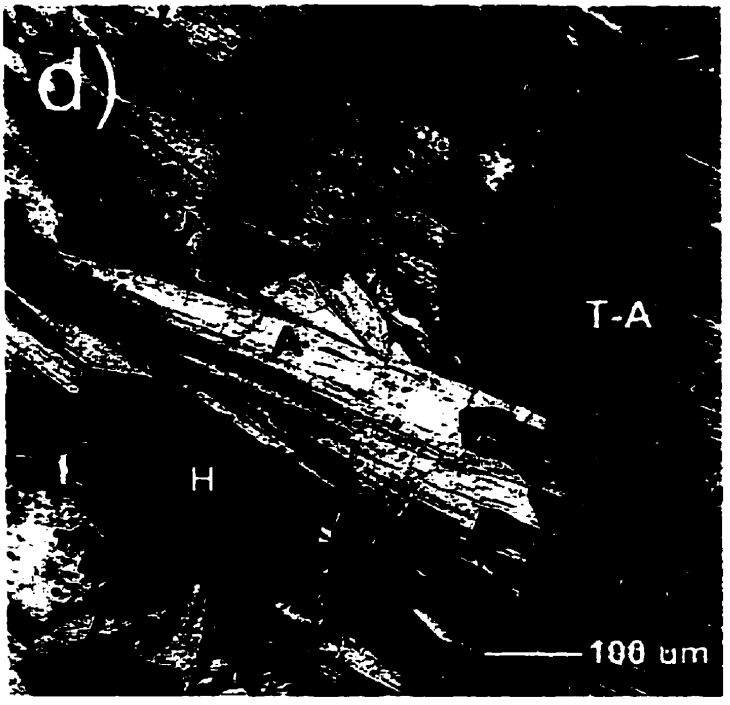
Figure 6

Electron backscatter images of: A) fibrous anthophyllite-cummingtonite (medium grey) that has replaced serpentine (darker grey) - light grey near the top left represents fracture-controlled alteration of anthophyllite-cummingtonite by actinolite; B) plagioclase (dark grey) replaced by fine-grained fibrous actinolite (light grey) in cross-fiber veins cutting a monzodiorite dyke; C) fracture-controlled actinolite (light grey) that has replaced fibrous anthophyllite-cummingtonite (dark grey); and D) early, fine-grained fibrous tremolite and actinolite (T-A) that have replaced serpentine in a serpentinite inclusion in a monzodiorite dyke and, in turn, have been overgrown by coarser fibrous actinolite (A) and late-stage, non-fibrous hornblende (H).


a)


10 um


c)


d)
T-A
H
100 um

stubby, randomly oriented subhedral crystals that replace tremolite (Figure 6d). As noted above, all amphiboles except hornblende display a dominantly fibrous habit. Nevertheless, based on the criteria of the Occupational Safety and Health Administration in the United States, only a small proportion of the fibrous amphibole is asbestiform (Langer et al., 1991). According to the above criteria, a fibrous amphibole is described as asbestiform only when its diameter is < 1 μm and the mineral occurs as bundles of flexible hair-like fibrils. As noted above, the vast majority of amphibole fibers have diameters > 1 μm. Moreover, fibrils are rarely observed.

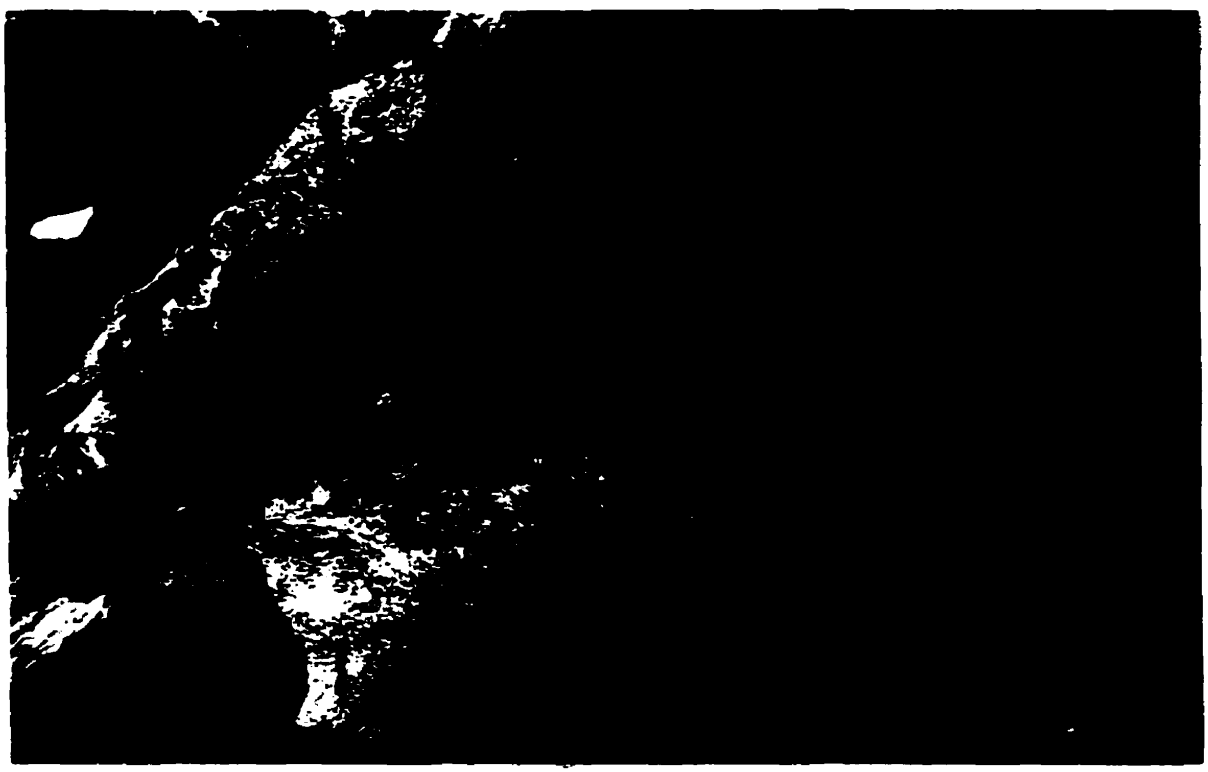
DISTRIBUTION OF AMPHIBOLE-GROUP MINERALS

Amphibole-group minerals are found mainly in or adjacent to felsic dykes, but also at the contact between slate and serpentinite or as veins in pyroxenite. Significantly, however, amphibole-group minerals are effectively absent from the chrysotile-bearing serpentinite ores; only one of 175 chrysotile-bearing samples that were analysed using X-ray diffraction contained detectable tremolite (> 0.1 wt. %, < 2.5 wt. %). Anthophyllite and cummingtonite are restricted to narrow monomineralic selvages, < 1 cm wide, around felsic dykes in serpentinite and rinds on serpentinite inclusions in felsic dykes; crystals (fibers) are commonly oriented perpendicular to the contacts.

Tremolite occurs in narrow selvages around felsic dykes, where it either replaced anthophyllite and cummingtonite or grew independently of these two minerals. However, the bulk of the tremolite is found in large masses of nephrite that are developed adjacent to felsic dykes, except where detached from the latter by shearing (Figure 7). These nephrite masses reach up to one meter in diameter, and are separated from the dykes by the narrow selvages described above. In most cases, these selvages pass inward to a narrow "blackwall" (up to 5 cm thick) of nearly monomineralic chlorite developed within the dyke and, in turn, with some exceptions, into rodingite (Chapter V). Tremolite comprises > 80 vol. % of these nephrite bodies, is randomly oriented, replaces serpentine minerals, and is locally recrystallized. Roughly 25 vol. % of the tremolite is non-fibrous

Figure 7

Nephrite block detached from a monzodiorite dyke. The light grey material extending into the center of the block is rodingite that was detached with the nephrite. Cross-fiber tremolite veins are evident near the right-hand margin of the nephrite body.



and commonly replaced antigorite. Finally, tremolite occurs as narrow (< 1 cm wide) shear and extensional fracture-fillings in pyroxenite. These veins typically comprise between 1 and 5 vol. % of the rock and host most of the asbestiform amphibole. The composition of tremolite in the three settings is similar, with X_{Mg} varying between 0.77 and 0.95.

In contrast to the amphibole-group minerals discussed above, actinolite is rarely developed in serpentinite. Rather, it occurs as disseminations and fracture fillings in albitized felsic dykes and in slate proximal to serpentinite. As noted above, the albitized rocks pass into rodingites immediately adjacent to serpentinite. Morphologically, actinolite is generally fibrous, and its composition is similar in both types of host rock ($(0.55 < X_{Mg} < 0.67)$).

The occurrence of hornblende is restricted to recrystallized parts of the nephrite bodies. There, hornblende replaces tremolite and, in turn, both minerals are locally replaced by diopside.

CONTROLS ON THE DISTRIBUTION OF AMPHIBOLE-GROUP MINERALS

Five types of amphibole are present in the Jeffrey chrysotile mine, and all occur in or adjacent to felsic dykes, which control the distribution of the bulk of the amphibole in the deposit. Tremolite and actinolite constitute over 90% of the amphibole population, and are the only amphibole-group minerals in pyroxenite and slate. These observations suggest that temperature, and/or $a\mathrm{Ca}^{2+}$, and/or $a\mathrm{SiO}^0_2$ were the principal physicochemical controls of amphibole growth in the deposit. Temperature and $a\mathrm{SiO}^0_2$ are singled out because of the association of amphibole with felsic dykes, and $a\mathrm{Ca}^{2+}$ because of the low content of Ca in the protolith and the calcic nature of the bulk of the amphibole.

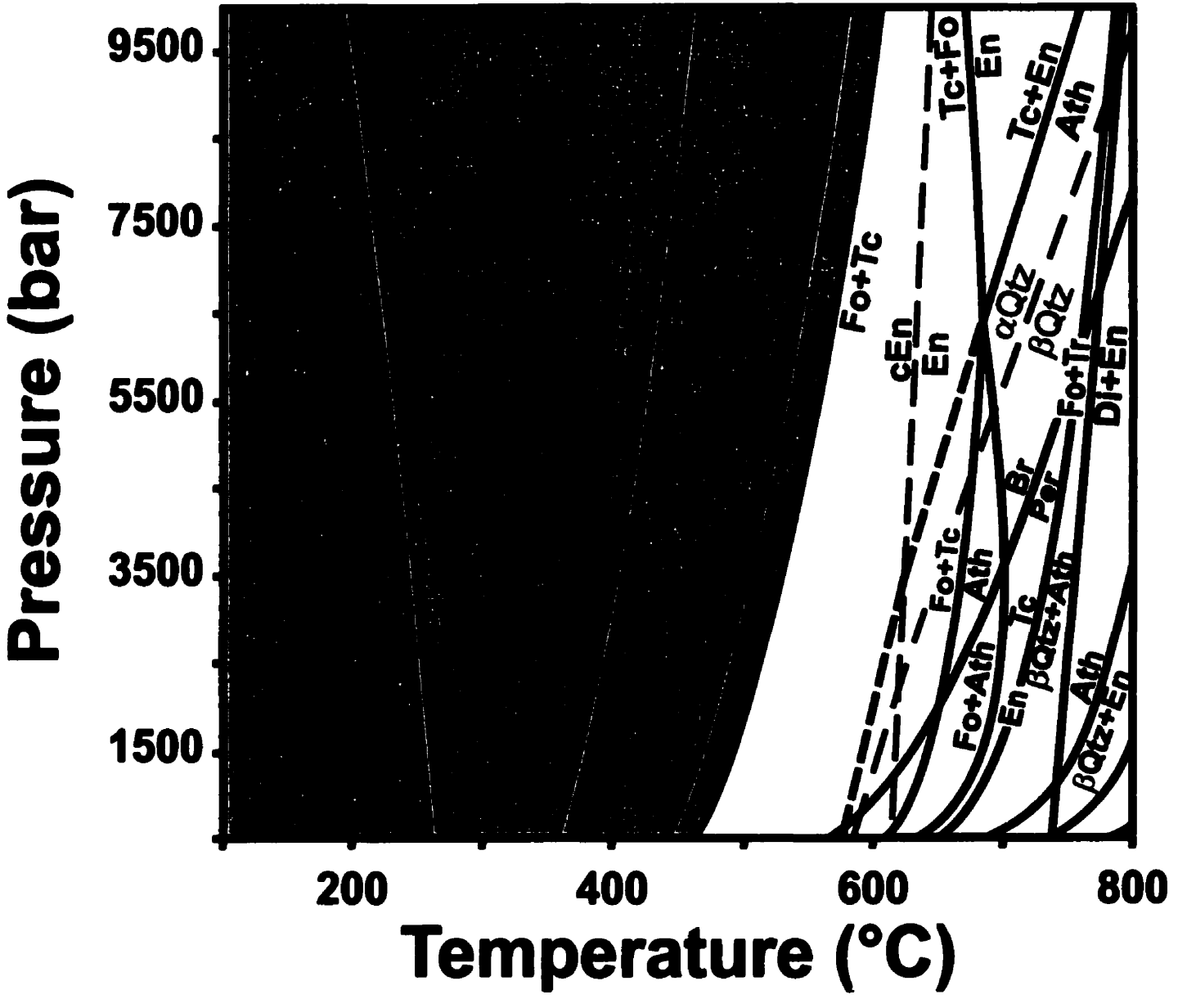
In order to evaluate the possible role of these parameters in the formation of amphibole-group minerals, it is first necessary to establish the timing of amphibole formation relative to serpentinization. From the description of the lithological

relationships provided earlier, it is evident that dyke emplacement occurred after early serpentinization but prior to final emplacement of the ophiolite. It is also clear from our description of the mode of occurrence of the amphiboles that tremolite and actinolite formed pene-contemporaneously with, or after, chrysotile; these minerals replace chrysotile (and antigorite) in bodies of nephrite, and these bodies are cut by veins in which chrysotile has been replaced by tremolite. Our description also shows that anthophyllite and cummingtonite predated or formed contemporaneously with tremolite.

In Figure 8, we show the stability relations of the various serpentine- and amphibole-group minerals in the system CaO-MgO-SiO_2-H_2O as a function of temperature and pressure. From this diagram, it is apparent that serpentinization took place at temperatures less than 500°C assuming a pressure of < 2.5 kilobars (Chapter VI), as this temperature represents the upper stability of antigorite. In reality, seafloor serpentinization probably takes place at temperatures on the order of 300 ± 75°C (Agrinier et al., 1995; Dyment et al., 1997; Alt and Shanks, 1998). Specifically, chrysotile formation probably occurred at temperatures less than 250°C (Figure 8). By contrast, anthophyllite formation is restricted to temperatures greater than 600°C (Figure 8). This prediction, coupled with the observation that anthophyllite and antigorite do not share a common field of stability, and the observed close spatial association of anthophyllite with felsic dykes, make it clear that localized heating was a major control on the formation of this amphibole. The high temperature of formation of anthophyllite, and the fact that subsequent metamorphism only heated the rocks to 300 – 400°C, further support the idea that the felsic dykes were intruded and not tectonically incorporated. The occurrence of cummingtonite only as intergrowths with anthophyllite again implies that increased temperature was the major control on the formation of cummingtonite. The bi-mineralic nature of the anthophyllite-cummingtonite zones, and the fact that these zones are chemically distinguished from the precursor serpentinite primarily by their much higher SiO_2 content, implies that $a{SiO^0}_2$ was also a major factor in the formation of anthophyllite-cummingtonite. This too is consistent with the restriction of anthophyllite to felsic dykes; the latter, having a much higher content of SiO_2 than serpentinite, are an obvious source of silica.

Figure 8

Pressure-temperature diagram showing stability relationships among serpentine minerals (antigorite, Atg; chrysotile, Ctl), tremolite (Tr), anthophyllite (Ath), brucite (Brc), diopside (Di), enstatite (En), forsterite (Fo), periclase (Per), quartz (Qtz), talc (Tlc) in the system CaO-MgO-SiO_2-H_2O. Reaction boundaries were calculated using GEØ-CALC (Berman et al., 1987). Stability fields of anthophyllite and serpentine-group minerals are indicated by light and dark shading, respectively.


Pressure (bar)
9500
7500
5500
3500
1500
200
400
600
800
Temperature (°C)
Fo+Tc
cEn
En
Tc+Fo
En
Tc+En
Ath
αQtz
βQtz
Fo+Tr
Di+En
Br
Per
Fo+Tc
Ath
Fo+Ath
En
Tc
βQtz+Ath
Ath
βQtz+En

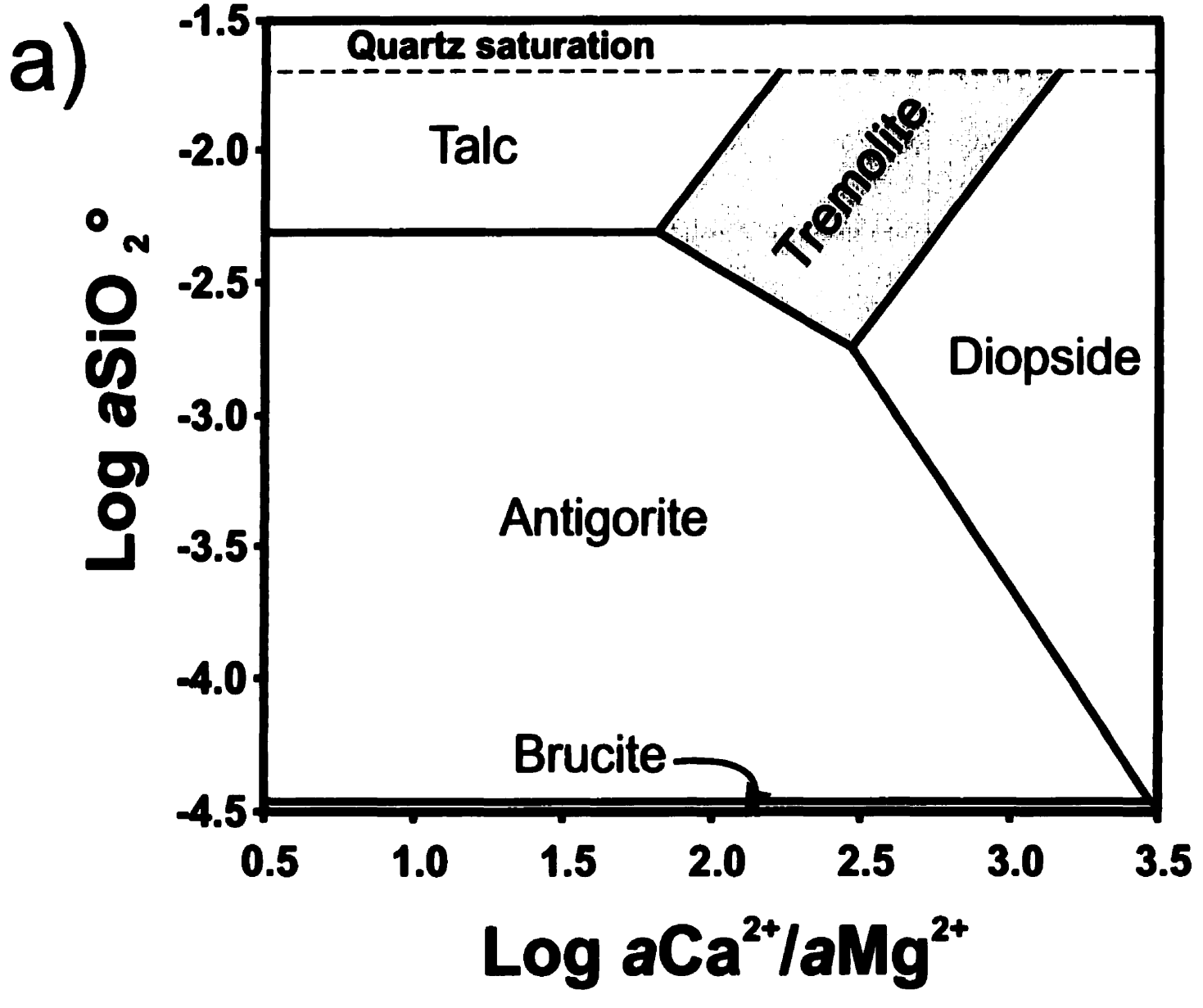
In contrast to anthophyllite-cummingtonite, tremolite and actinolite are stable to very low temperatures, i.e., below the upper stability of chrysotile (Figure 8). Studies of nephrite in serpentinites elsewhere suggest that tremolite in this environment forms at temperatures of 300 to 400°C (Yui et al., 1988; Prokhor, 1991), i.e., at temperatures similar to those of regional greenschist-facies metamorphism in the Appalachian ophiolites (Laird, et al., 1993). These findings, plus the observations that tremolite replaces anthophyllite and that some occurrences of actinolite and tremolite, e.g., in slates and altered pyroxenite, respectively, are well outside the possible influence of felsic dykes, suggest that temperature increase was not a significant factor in tremolite and actinolite formation. On the other hand, the mode of occurrence of these amphiboles, and the fact that they are substantially richer in Ca and Si than their hosts, implies that either or both $a\mathrm{SiO}^0_2$ and $a\mathrm{Ca}^{2+}$ were major factors in the formation of tremolite and actinolite.

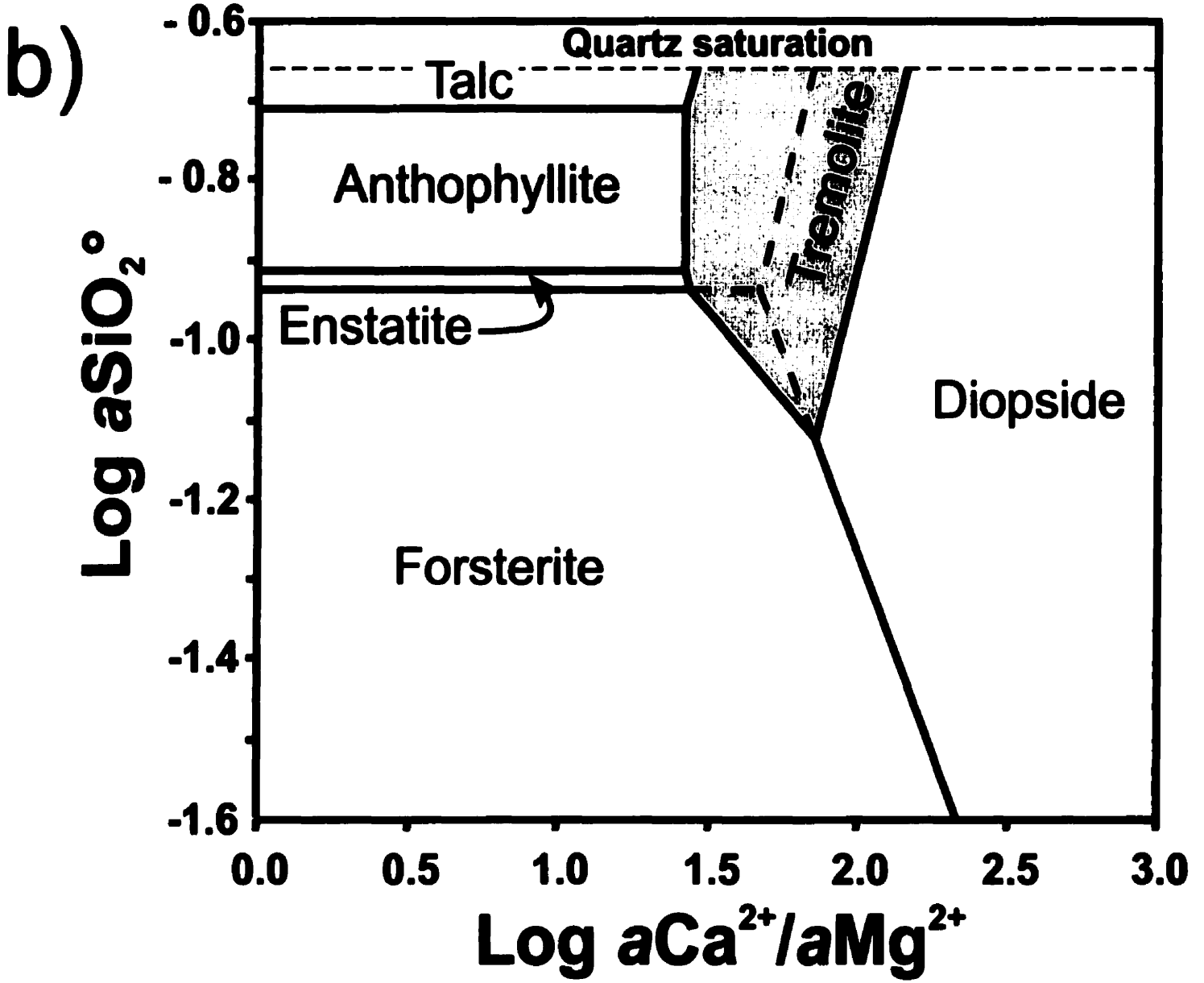
In Figure 9, we show the stability relationships of minerals in the system CaO-MgO-$\mathrm{SiO_2}$-$\mathrm{H_2O}$ as a function of log $a\mathrm{SiO_2}^0$ and log $a\mathrm{Ca}^{2+}/a\mathrm{Mg}^{2+}$ at 300 and 700°C and 2 kbar (Figures 9a and b). These diagrams demonstrate that tremolite can form directly through hydration of the primary peridotite minerals (enstatite, diopside and forsterite) at temperatures above 650°C (Figure 9b), but can only form as a result of increases in $a\mathrm{SiO}^0_2$ or $a\mathrm{Ca}^{2+}$ or both at the much lower temperatures of serpentinization (Figure 9a). However, given the presence of brucite and the absence of talc in the serpentinized harzburgites and dunites (except near dykes), the activity of silica in these rocks must have been very low, nearly three orders of magnitude below quartz saturation. In order to permit crystallization of tremolite, it would have been necessary to raise silica activity by at least 1.5 orders of magnitude. It therefore follows that $a\mathrm{SiO}^0_2$ was an essential control on tremolite formation in these rocks.

It is more difficult to evaluate the role of $a\mathrm{Ca}^{2+}$, as it is clear from Figure 9a that serpentine-group minerals, represented by antigorite, are stable over a range of $\mathrm{Ca}^{2+}/\mathrm{Mg}^{2+}$ activity ratios that completely overlap the stability field of tremolite. In other words, while an increase in $a\mathrm{SiO}^0_2$ was essential for the formation of tremolite in serpentinized harzburgite and dunite, it is not clear that a corresponding increase in $a\mathrm{Ca}^{2+}$ was required.

Figure 9

Log $aSiO^0_2$ versus log aCa^{2+}/aMg^{2+} diagrams for the system CaO-MgO-SiO_2-H_2O at 2 kbar and A) 300°C, and B) 700°C.


a)
Quartz saturation
Talc
Tremolite
Diopside
Antigorite
Brucite
-1.5
-2.0
-2.5
-3.0
-3.5
-4.0
-4.5
0.5
1.0
1.5
2.0
2.5
3.0
3.5
Log aSiO2°
Log aCa2+/aMg2+


b)
Quartz saturation
Talc
Anthophyllite
Tremolite
Enstatite
Diopside
Forsterite
- 0.6
- 0.8
-1.0
-1.2
-1.4
-1.6
Log aSiO2°
0.0
0.5
1.0
1.5
2.0
2.5
3.0
Log aCa2+/aMg2+

The relative importance of $a\mathrm{SiO}^0_2$ and $a\mathrm{Ca}^{2+}$ in forming tremolite in pyroxenite are less clear. Firstly, $a\mathrm{SiO}^0_2$ is likely to be much higher in pyroxenite than in harzburgite and dunite. Indeed, altered pyroxenite typically contains the assemblage tremolite-chlorite-serpentine-talc-clinopyroxene. Thus the activity of SiO^0_2 can be assumed to have been buffered close to the activity boundary of talc-antigorite (Figure 9b). Under such conditions, tremolite can form without increasing $a\mathrm{SiO}^0_2$. Moreover, the presence of relict clinopyroxene suggests that $a\mathrm{Ca}^{2+}$ was relatively high and perhaps sufficient to stabilize tremolite. It is thus possible that tremolite formed in pyroxenite without significant increase in either $a\mathrm{SiO}^0_2$ or $a\mathrm{Ca}^{2+}$. Assuming that local reheating and increases in $a\mathrm{SiO}^0_2$ and $a\mathrm{Ca}^{2+}$ were not controlling factors in the formation of pyroxenite-hosted tremolite, the remaining plausible hypothesis is that tremolite crystallization in these rocks was the product of essentially isochemical (except for H_2O) retrograde metamorphism. This hypothesis is supported by the stability of the assemblages diopside-tremolite-antigorite and talc-tremolite-antigorite from approximately 500°C to near-ambient temperatures (Figure 8), and the conclusion that this assemblage can be produced from pyroxenite containing the assemblage enstatite-diopside-forsterite (Figure 10).

Much of the actinolite is related to metasomatism of slate adjacent to serpentinite, which produced rodingite in contact with serpentinite, and albitite in contact with slate; the actinolite is hosted by the albitized slate. The initial bulk composition (up to 7 wt. % CaO) and mineral assemblage of the slate (biotite-muscovite-quartz-chlorite-calcite) are consistent with the development of actinolite via contact-metamorphic reactions (unbalanced) such as:

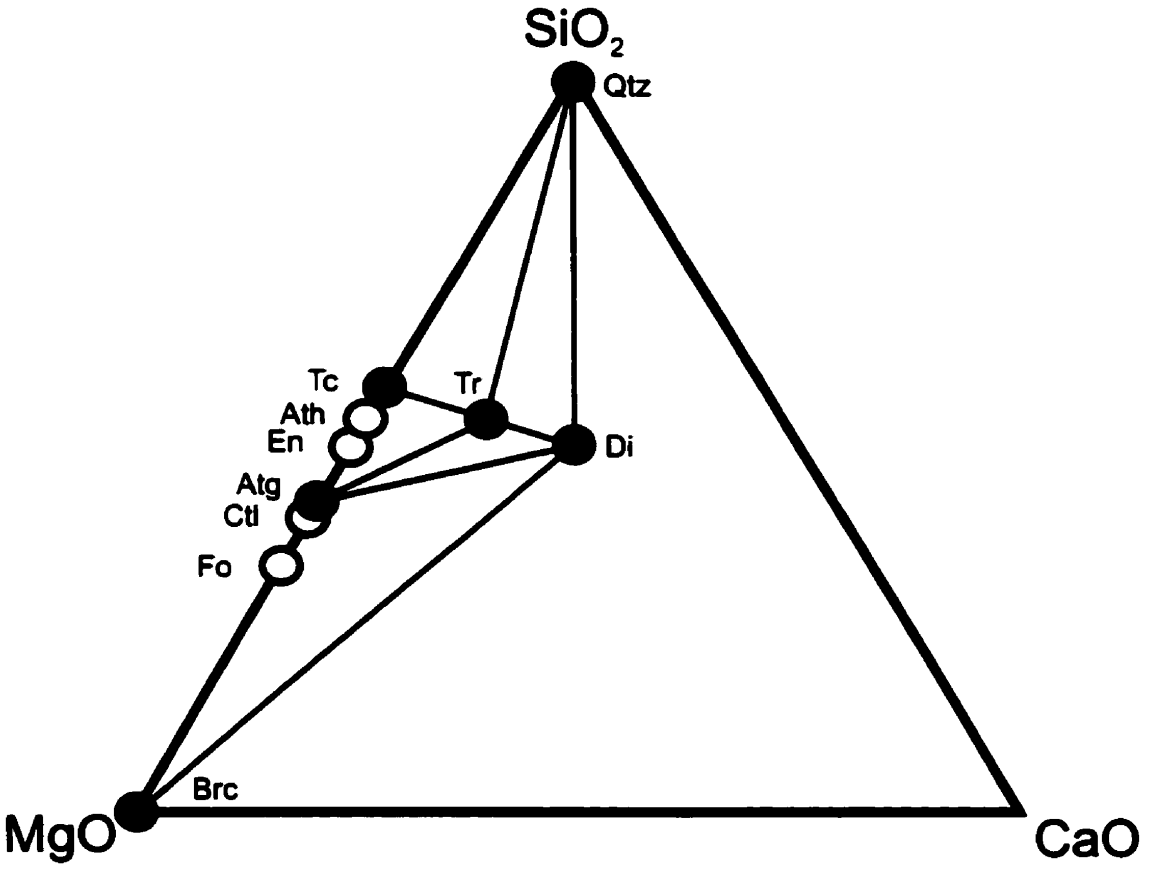
Annite + Calcite + Quartz = Actinolite + K-feldspar + CO_2 + H_2O (1)

and

Chlorite + Calcite + Quartz = Actinolite + Anorthite + CO_2 + H_2O (2).

Figure 10

Triangular projection diagram for the system CaO-MgO-SiO_2-H_2O showing stable assemblages among the minerals shown in Figure 7 at 300°C. Note that a rock containing the minerals diopside-enstatite-forsterite (shaded area) can be transformed into one containing diopside-tremolite-antigorite or tremolite-talc-antigorite. The mineral abbreviations are given in the caption to Figure 8.


SiO2
Qtz
Tc
Tr
Ath
En
Di
Atg
Ctl
Fo
Brc
MgO
CaO

However, given that the slate was albitized, and actinolite crystallization was contemporaneous with albitization, a more accurate description of actinolite formation is provided by the following (unbalanced) analogous metasomatic reactions:

$$\text{Annite} + \text{Calcite} + \text{Quartz} + Na^{+} = \text{Actinolite} + \text{Albite} + CO_2 + Ca^{2+} + K^{+} \quad (3)$$

and

$$\text{Chlorite} + \text{Calcite} + \text{Quartz} + Na^{+} = \text{Actinolite} + \text{Albite} + CO_2 + Ca^{2+} + H^{+} \quad (4)$$

On the basis of bulk-rock geochemical data, mass-balance calculations and geological relations discussed in Chapter V, we propose that actinolite in these rocks formed as a result of a metasomatic process that involved the introduction of an external, Na-rich fluid pene-contemporaneously with emplacement of the ophiolite. This metasomatism caused the albitization of the footwall slates, and concentrated calcium at or near the contact with the serpentinites, converting albitite into rodingite. The fact that the calcic amphibole is actinolite where hosted by slate, and dominantly tremolite where hosted by serpentinite and pyroxenite, is attributed to the relatively low and high Mg:Fe ratios of the slate and ultramafic rocks, respectively.

Actinolite also occurs as disseminations and veinlets in albitized felsic dykes. On the basis of textural relations, actinolite formed pene-contemporaneously with albitization, which we interpret to have been caused by a NaCl-rich fluid of possible orthomagmatic origin. We propose that the following reaction, which respects the observed mineral proportions in albitized dykes, describes the overall process of albitization and actinolite formation:

$$6\ \text{Anorthite} + 5\ \text{Annite} + 12\ Na^{+} + 48\ SiO^{0}_{2} + 4\ H_2O$$
$$=$$
$$12\ \text{Albite} + 5\ \text{K-feldspar} + 3\ \text{Actinolite} + 12\ H^{+} \quad (5).$$

The key component of this reaction in relation to actinolite is SiO^0_2, which has an extremely high stoichiometric coefficient. This again emphasises the pivotal role of high $aSiO^0_2$ in promoting amphibole formation in or adjacent to felsic dykes. Such high $aSiO^0_2$ is consistent with the fact that any hydrothermal fluids equilibrating with felsic dykes would have been saturated with quartz in the granitic varieties and close to quartz saturation in the diorites, i.e., $aSiO^0_2$ would have been very high in all cases.

APPROACHES TO IDENTIFYING AMPHIBOLE-RICH ZONES

From the perspective of the exploitation of chrysotile in the Jeffrey mine, the most important conclusion of our study is that the ores are essentially free of amphibole-group minerals. However, amphibole-group minerals are present in appreciable quantities in serpentinite associated with felsic dykes and, to a lesser extent, in pyroxenite and slate. The latter two rock types are spatially well separated from the ores and are therefore of little concern as a potential source of contamination by amphibole. The dykes, however, are concentrated in large shear zones that separate the orebody into five zones, and more importantly a significant proportion of dykes (~20%), particularly smaller ones, locally cut the ore zones. The challenge in mining the chrysotile ores is therefore to develop practices that avoid felsic dykes and their altered wallrocks, and methods of detecting such rock types.

Amphibole-bearing rocks can be identified by visual inspection, optical and electron microscopic examination, and X-ray powder-diffraction analysis. However, all of these methods have limitations. Visual inspection ignores fine-grained, disseminated amphibole; microscopic examination is time-consuming and limited to small, possibly non-representative, samples; and conventional X-ray diffraction analysis has a high detection limit (2.5 wt. %). Among the methods available for detecting amphibole directly, only X-ray diffraction analysis has the potential to provide systematic screening of appropriately sized samples. As discussed earlier, we have modified a digestion

technique developed by Addison and Davies (1990) that now permits routine detection of amphibole to better than 0.1%. Although time-consuming, this approach does permit thorough screening for amphibole-group minerals in zones scheduled for mining.

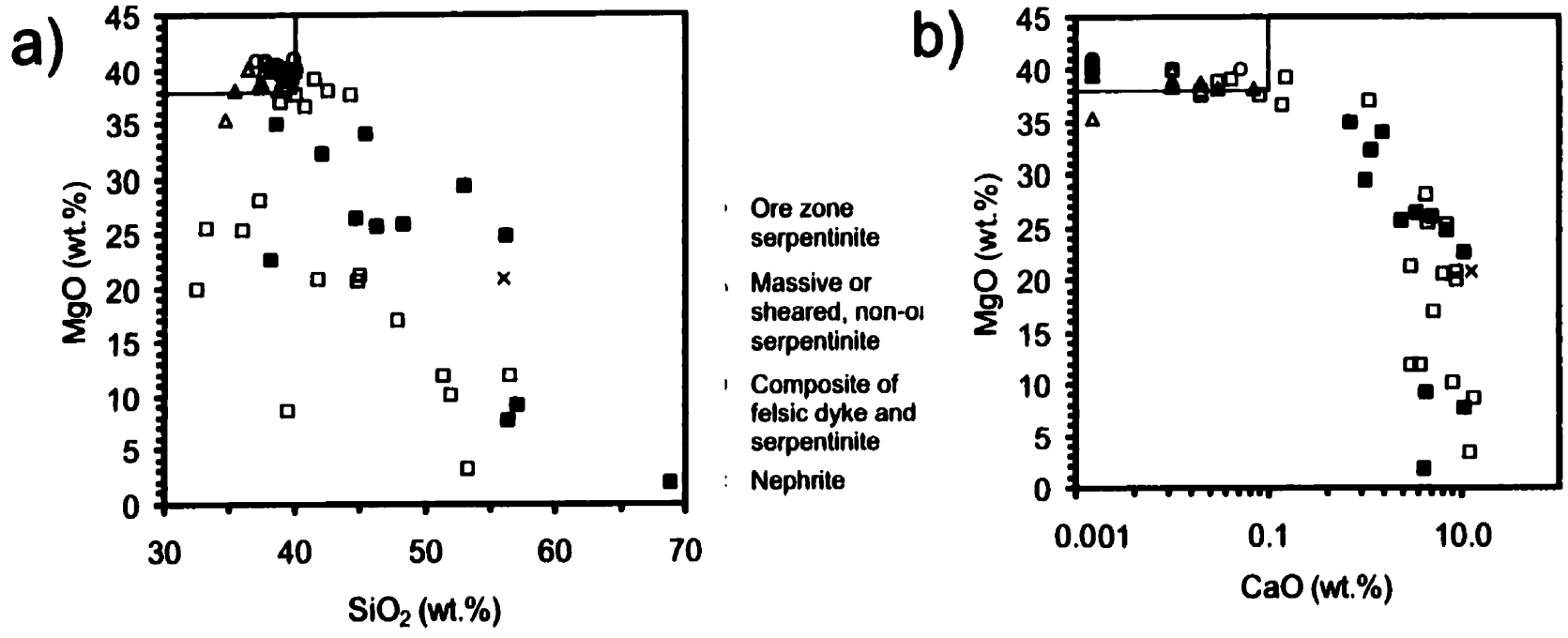
In principle, it should be possible to distinguish amphibole-rich zones from amphibole-free zones using whole-rock geochemistry. The advantage of this indirect approach to amphibole detection is that it is relatively rapid and inexpensive, and is amenable to representative sampling. In order to test the possibility of using bulk geochemistry to develop discriminants for amphibole, we analysed 56 samples of BQ drill core for major and selected elements using X-ray fluorescence spectrometry. The samples consisted of composites representing intervals ranging from 1 to 10 m in length, and varied macroscopically from homogeneous serpentinite ore through shear zone or barren serpentinite, to variable mixtures of dyke material and serpentinite. We also analysed the nephrite.

Given that amphibole in serpentinite is spatially associated with felsic dykes, and that increased $a\mathrm{SiO}^0_2$ is interpreted to have been the major factor in amphibole crystallization, it is reasonable to expect that amphibole-bearing samples would be characterized by elevated concentrations of SiO_2. By the same token, as serpentinite is dominated by Mg and Si, we would expect that an increase in SiO_2 concentration due to amphibole-producing alteration would be accompanied by a decrease in MgO concentration. In order to test the possibility of using these two elements as an amphibole discriminant, we plotted the samples described above on a diagram of wt. % MgO versus wt. % SiO_2 (Figure 11a). As can be seen from this diagram, all ore-zone serpentinite samples contain > 38 wt. % MgO and < 40 wt. % SiO_2. Some samples of non-ore serpentinite also plot in this field. By contrast, all amphibole-bearing samples contain < 35 wt. % MgO; the nephrite sample contains 20 wt. % MgO and 55 wt. % SiO_2. However, two of the twelve amphibole-bearing samples contain < 40 wt. % SiO_2. The explanation for this is that the serpentinite ores have a relatively large range in SiO_2 contents (36.5 – 40 wt. %), and thus the formation of minor tremolite (< 5 wt. %), as a result of a small addition of SiO_2, might not be evident.

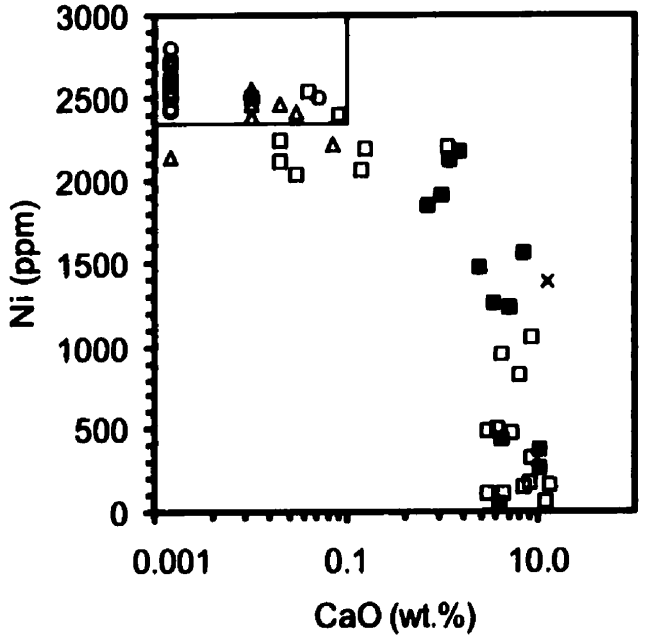
Another element that might indicate the presence of amphibole in the ore zones is

Figure 11

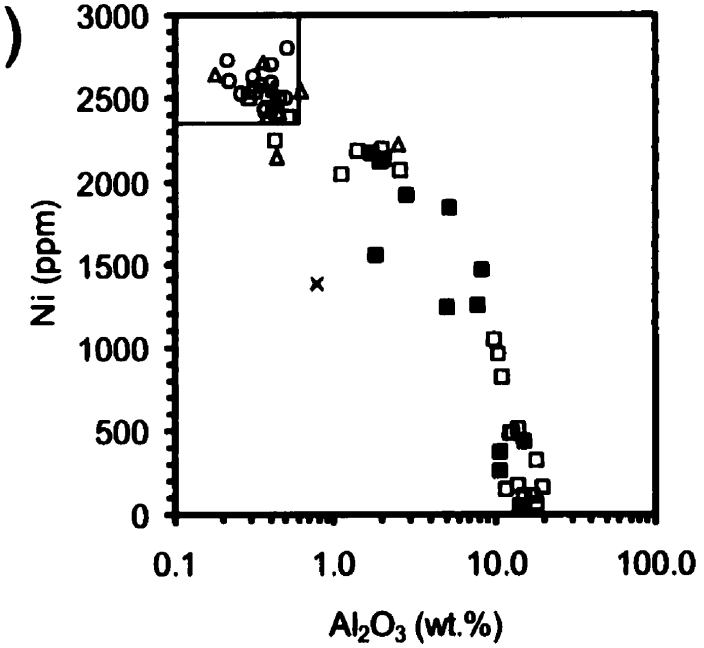
Binary plots showing the distribution of amphibole-bearing (closed symbols) and amphibole-free (open symbols) samples among ore-zone serpentinite, shear zone and massive serpentinite, composite felsic dyke and serpentinite, and nephrite: A) wt. % MgO versus wt. % SiO_2, B) wt. % CaO versus wt. % MgO, C) ppm Ni versus wt. % CaO, and D) ppm Ni versus wt. % Al_2O_3. The upper left corner of each diagram (delineated by heavy lines) represents a region predicted to be amphibole-free (forbidden region). For the purposes of illustration, all samples containing less than detectable Ca are plotted at the detection limit (15 ppm CaO).


a)
b)
MgO (wt.%)
SiO2 (wt.%)
CaO (wt.%)
0.001
0.1
10.0
Ore zone serpentinite
Massive or sheared, non-o
serpentinite
Composite of felsic dyke and serpentinite
Nephrite

c)


3000
2500
2000
1500
1000
500
0
Ni (ppm)
0.001
0.1
10.0
CaO (wt.%)

d)


3000
2500
2000
1500
1000
500
0
Ni (ppm)
0.1
1.0
10.0
100.0
Al2O3 (wt.%)

calcium; as noted earlier, tremolite is volumetrically the dominant amphibole in serpentinite. Figure 11b shows rock compositions in terms of CaO and MgO, and illustrates that most serpentinite ore samples do not contain detectable calcium (CaO < 15 ppm) and all ore samples contain < 0.1 wt. % CaO. By contrast, all tremolite-bearing samples contain > 0.7 wt. % CaO. Using ideal end-member compositions, a mixture composed of 99.9 wt. % serpentine and 0.1 wt. % tremolite would contain approximately 0.013 wt. % CaO. However, such anomalous CaO contents (one of the ore zone samples contains > 0.013 wt. % CaO) can also be explained by the presence of other Ca-bearing minerals such as diopside, which was present in the residues of some samples after modified Addison-Davies digestion. Thus in summary, the presence or absence of amphibole can be satisfactorily predicted in the Jeffrey mine by analysing bulk samples for Ca and Mg. Low SiO_2 content, contrary to expectation, does not guarantee that a sample is amphibole-free.

One of the limitations of using the high Mg content to characterize unaltered serpentinite is that the Mg proportion varies appreciably (38 to 41 wt. % MgO) because unaltered serpentinite comprises variable proportions of serpentine, brucite, chlorite, and magnetite. Given such variation, it is theoretically possible for a serpentinite sample to contain up to 15 wt. % tremolite, and yet have concentrations of Mg in the forbidden (amphibole-absent) region (>38 wt. % MgO). In view of this finding, we investigated the possibility of using a trace element not normally present in tremolite to characterise unaltered serpentinite. Three trace elements that have elevated concentrations in serpentinites are Ni, Co, and Cr. In Figure 11c, we show the distribution of the samples as a function of Ni and Ca. All ore samples contain greater than 2,350 ppm Ni and, with one exception, less than detectable concentrations of Ca (the exception contains 0.05 wt. % CaO). By contrast, tremolite-bearing samples all contain less than 2,200 ppm Ni and > 0.7 wt. % CaO. Similar results were obtained for Cr and Co versus CaO. However, the discrimination was less reliable, with one and two tremolite-bearing samples, respectively, falling in the forbidden region.

As SiO_2 did not prove to be a suitable discriminant for amphibole and as some amphibole species are not calcic, we considered other elements present in elevated concentrations in felsic dykes that could serve the role initially anticipated for Si. The

best candidate is Al, which is present in high concentrations in the felsic dykes (up to 22 wt. % Al_2O_3) and in very low concentrations in the ultramafic rocks. In Figure 11d, we show the compositions of the various samples discussed above in terms of Ni and Al_2O_3. All ore samples contain > 2,350 ppm Ni and < 0.6 wt. % Al_2O_3, whereas amphibole-bearing samples all contain < 2,200 ppm Ni and > 1.7 wt. % Al_2O_3.

RECOMMENDATIONS FOR MINING CHRYSOTILE

The bulk of the amphibole in the Jeffrey mine is associated with felsic dykes, the larger of which are concentrated in sheared and altered domains that separate individual chrysotile ore zones. Our first recommendation therefore is that extraction of ore should be limited to intervals > 2 m from obvious dyke-bearing shears. In many cases, the dykes are < 30 cm thick, and are easily overlooked. Moreover, such dykes locally cut ore zones, and the shearing associated with them may be difficult to detect, or absent. In order to ensure that such zones are detected, we recommend that drill core used to delineate ore zones be analysed for Ni, Al, and Ca, and that intervals over which concentrations of these elements fall outside the forbidden (amphibole-free) regions (see previous section) be avoided, or marked for special handling and disposal. The same recommendation applies to cuttings recovered from production blast holes. Finally, we recommend that subsets of the above samples be routinely analysed for amphibole by X-ray diffraction of residues remaining after digestion of serpentine.

CONCLUSIONS

The following are the main conclusions of our study:

1) Ore-grade serpentinite in the Jeffrey mine is essentially free of detectable amphibole. The bulk of the amphibole-group minerals occur in serpentinite adjacent to or within

felsic dykes, and is in the form of tremolite. Amphibole also occurs in pyroxenite (tremolite) distal to felsic dykes, and in slate (actinolite) in contact with serpentinite. Minor concentrations of anthophyllite, cummingtonite and hornblende are restricted to narrow (1 cm wide) contact zones between serpentinite and felsic dykes.

2) Although most of the amphibole is fibrous, only a small proportion (tremolite) qualifies as asbestiform according to criteria developed by the U.S. Occupational Safety and Health Administration.

3) The principal control on the formation of the bulk of the amphibole (tremolite) in serpentinite was an increase in $a\mathrm{SiO}^0_2$ associated with felsic dykes. Temperatures above those typical of the regional metamorphism were necessary to form anthophyllite-cummingtonite. Such high temperatures are consistent with contact metamorphism and metasomatism.

4) Amphibole-rich zones can be detected by conventional (> 2.5 wt. %) and digestion-enhanced (≥ 0.1 wt. %) X-ray diffraction techniques. An alternative and less expensive approach to amphibole detection is provided by discriminant bulk-rock geochemistry. Amphibole-free samples have concentrations of CaO, Al_2O_3 and Ni of < 15 ppm, < 0.6 wt. % and > 2,350 ppm, respectively.

5) Contamination by amphibole-group minerals can be minimized during the mining of chrysotile ores by: a) avoiding dykes and host serpentinites within two meters of the dykes; b) avoiding all shear zones along which dykes are known to be present; c) analysing diamond-drill core used to delineate ore zones and production blast-hole cuttings for Ca, Al and Ni, and using the data to identify potential amphibole-bearing zones; and d) employing digestion-enhanced X-ray diffraction analysis to confirm the absence of amphibole-group minerals in subsets of samples previously screened for amphibole using bulk-rock geochemistry.

6) Amphibole-free chrysotile can be produced from the Jeffrey mine, and other chrysotile mines elsewhere, provided that appropriate measures are taken to avoid contamination of the ores.

ACKNOWLEDGEMENTS

The research was funded by matching grants from JM Asbestos Inc. and NSERC to AEW-J, RFM, and AD. Mine geologists A.J. Millen and M. Arpin introduced the authors to the geology of the Jeffrey mine and provided logistical support. S. Smith, J. Roelofsen, K. Skaret, and J. Duggan helped in pit mapping, sampling and core logging. G. Olivo assisted in the development of the XRD digestion technique, and E. Sakoma and K. Skaret carried out the XRD analyses.

REFERENCES

Addison, J. and L. S. T. Davies, 1990, Analysis of amphibole asbestos in chrysotile and other minerals, Annals of Occupational Hygiene, v. 34, p. 159-175.

Agrinier, P., Hékinian, R., Bideau, D. and M. Javoy, M., 1995, O and H stable isotope compositions of oceanic crust and upper mantle rocks exposed in the Hess Deep near the Galapagos triple junction, Earth and Planetary Science Letters, v. 136, p. 183-196.

Alt, J. C. and W. C. Shanks, III, 1998, Sulfur in serpentinized oceanic peridotites: serpentinization process and microbial sulfate reduction, Journal of Geophysical Research, v. 103, p. 9917-9929.

Berman, R.G., Brown, P.H. and E. H. Perkins, 1987, GEØ-CALC: software for calculation and display of P-T-X phase diagrams, American Mineralogist, v. 72, p. 861-862.

Dufresne, A., Bégin, R., Churg, A. and S. Massé, 1996, Mineral fiber content of lungs in patients with mesothelioma seeking compensation in Québec, American Journal of Respiratory and Critical Care Medicine, v. 153, p. 711-718.

Dufresne, A., Harrigan, M., Massé, S. and R. Bégin, 1995, Fibers in lung tissues of mesothelioma cases among miners and millers of the Township of Asbestos, Quebec, American Journal of Industrial Medicine, v. 27, p. 581-592.

Dyment, J., Arkani-Hamed, J. and A. Ghods, 1997, Contribution of serpentinized ultramafics to marine magnetic anomalies at slow and intermediate spreading centres: insights from the shape of the anomalies, Geophysical Journal International, v. 129, p. 691-701.

Hébert, R., Bédard, J. H., Olive, V., Huot, F. and V. Varfalvy, 1998, Ophiolites of Southern Quebec Appalachians: a synthesis, Geological Association of Canada, Mineralogical Association of Canada, Association des Géologues et Géophysiciens du Québec, International Association of Hydrogeologists, Canadian Geophysical Union Joint Annual Meeting, 13-15 May 1998, Québec, Québec, Canada, Abstracts, v. 23, p. A-76.

Hughes, J. M., 1991, Epidemiology of lung cancer in relation to asbestos exposure, *in* Mineral Fibers and Health, Liddell, D. and K. Miller, editors, CRC Press, Boston, p. 135-145.

Hughes, J. M. and H. Weill, 1986, Asbestos exposure – quantitative assessment of risk. American Reviews of Respiratory Disease, v. 133, p. 5.

Laird, J., Trzcienski, W. E. Jr. and W. A. Bothner, 1993, High pressure, Taconian, and subsequent polymetamorphism of Southern Quebec and Northern Vermont, Geological Society of America Field Trip Guidebook for the Northeastern United States, v. 2, Department of Geology and Geography, University of Massachusetts, Contribution 67, p. O 1- O 32.

Langer, A. M., Nolan, R. P. and J. Addison, 1991, Distinguishing between amphibole asbestos fibers and elongate cleavage fragments of their non-asbestos analogues, *in* Mechanisms in Fiber Carcinogenesis, Brown, R. C., et al., editors, Plenum Press, New York, p. 253-267.

Laurent, R., 1975, Petrology of the Alpine-type serpentinites of Asbestos and Thetford Mines, Quebec, Schweizerische Mineralogische und Petrographische Mitteilungen, v. 55, p. 431-455.

McDonald, A. D., Fry, J. S., Woolley, A. J. and J. C. McDonald, 1983, Dust exposure and mortality in an American factory using chrysotile, amosite, and crocidolite in mainly textile manufacture, British Journal of Industrial Medicine, v. 40, p. 368.

McDonald, J. C., Armstrong, B., Case, B., Doell, D., McCaughey, W. T. E., McDonald, A. D. and P. Sébastien, 1989, Mesothelioma and asbestos fiber type, Cancer, v. 63, p. 1544-1547.

Normand, C., Gauthier, M. and M. Jébrak, 1996, The Quebec Antimony deposit: an example of gudmundite, native antimony mineralization in the ophiolitic melange of the southeastern Quebec Appalachians, Economic Geology, v. 91, p. 149-163.

O'Hanley, D. S. and M. D. Dyar, 1998, The composition of chrysotile and its relationship with lizardite, Canadian Mineralogist, v. 36, p. 727-739.

Prokhor, S. A., 1991, The genesis of nephrite and emplacement of the nephrite-bearing ultramafic complexes of East Sayan. International Geology Reviews, v. 33, p. 290-300.

Weill, H., Rossiter, C. E., Waggenspack, C., Jones, R. N. and M. M. Ziskind, 1977, Differences in lung effects resulting from chrysotile and crocidolite exposure, *in* Proceedings of Fourth International Symposium on Inhaled Particles and Vapors, Walton W. H., editor, Pergamon Press, Oxford, p. 789.

Whitehead, J., Reynolds, P. H. and J. G. Spray, 1996, $^{40}Ar/^{39}Ar$ age constraints on Taconian and Acadian events in the Quebec Appalachians, Geology, v. 24, p. 359-362.

Wicks, F. J. and A. G. Plant, 1979, Electron-microprobe and X-ray-microbeam studies of serpentine textures, Canadian Mineralogist, v. 17, p. 785-830.

Wicks, F. J. and E. J. W. Whittaker, 1977, Serpentine textures and serpentinization, Canadian Mineralogist, v. 15, p. 459-488.

Yui, T. -F., Yeh, H. -W. and C. H. Lee, 1988, Stable isotope studies of nephrite deposits from Fengtien, Taiwan, Geochimica et Cosmochimica Acta, v. 52, p. 593-602.

CHAPTER IX

CONCLUSIONS

GENERAL CONCLUSIONS

Experimental flow-through investigations of the serpentinization of olivine and lherzolite by water or 0.1 *M* $CaCl_2$ solution at a temperature of 300°C and a pressure of 300 bars revealed that:

1) Platy, polygonal, conical, and cylindrical serpentines formed during reaction of water with olivine. The spatial distribution of the serpentine-group minerals along the flow direction of the cell was lizardite-polygonal serpentine-conical serpentine>>chrysotile. This succession is interpreted to reflect the relative ease of nucleation of the various serpentine-group minerals, with those forming later, requiring the highest degree of supersaturation. An important implication of this interpretation is that the occurrence of chrysotile in veins cutting lizardite-dominant serpentinites is not a reliable indication that temperature was higher during chrysotile formation than it was during crystallization of lizardite, as is frequently suggested in the literature.
2) In all cases, the composition of the experimental serpentinizing fluids very closely approached that calculated for a fluid that would have equilibrated with the mineral assemblage predicted to form by reaction of the starting fluid with the reactant. In other words, serpentine + brucite formed during reaction of water and the $CaCl_2$ solution with olivine, and serpentine + brucite + diopside formed during reaction of water with lherzolite. This implies that the composition of natural fluids reacting with peridotites should closely approach equilibrium with the mineral assemblages predicted to form as a result of closed-system alteration, because the distances covered by fluids in nature are much greater than those covered in the experiments. The absence of brucite and diopside in some serpentinized olivine-rich and pyroxene-bearing peridotites suggest that alteration of these rocks was caused by the repeated infiltration of large amounts of diopside-undersaturated and relatively acidic and/or SiO_2-rich fluids.

3) SiO_2-poor and Ca-Cl-rich fluids can induce serpentinization of olivine without causing Ca-metasomatism. My calculations predict that Ca enrichment of a brine that initially contains Ca, by reaction with pyroxene-bearing peridotite, will be very minor due to saturation with diopside (if the precursor is rich in olivine) or tremolite (if the precursor is a pyroxenite). This explains why clinopyroxene is the primary phase most resistant in peridotites to replacement by serpentine. Although the chemistry of serpentinizing fluids may commonly approach supersaturation with respect to diopside, the fact that secondary diopside rarely occurs in retrograde serpentinites suggest that kinetic barriers generally prevent the formation of this mineral.

Field and laboratory investigations of serpentinites, slates, granites, diorites, and the altered equivalents of these rocks from the JM Asbestos mine have shown that:

1) The mantle harzburgite tectonites were extensively serpentinized, albeit locally, before detachment of the Asbestos ophiolite from its seafloor setting.
2) The diorites and granites were intruded in the mantle harzburgite tectonites after detachment of the oceanic crust and upper mantle (the Asbestos ophiolite) from their seafloor setting, and before thrusting of the ophiolite onto the Caldwell Group metasediments. The chemical composition of the diorites and granites suggests that they are genetically related, and that they originated from the melting of a source rock containing a significant proportion of continentally derived material.
3) The slates in thrust contact with the serpentinized harzburgites, and the granites and diorites that cut the serpentinized harzburgites, were affected by an early stage of sodic-calcic alteration, which was accompanied or followed by rodingitic alteration at the contact with serpentinite. Some of the felsic dykes display only sodic-calcic alteration, and others only rodingitic alteration. This indicates that sodic-calcic alteration is not necessarily a complementary facies of alteration to rodingitization.
4) The nephrite halos that formed at the expense of the serpentinites at the margin of the dykes are not everywhere associated with the most intensely rodingitized dykes. Some of these halos formed adjacent to dykes that had been affected only weakly by calc-silicate metasomatism. In fact, where halos of nephrite occur at the margins of

strongly rodingitized dykes, the amphiboles in the nephrite closest to the contact with the dykes are replaced by diopside. This suggests that the nephrites are closely associated with the early sodic-calcic stages of alteration, and that later replacement of the nephrite by diopsidite accompanied rodingitization as a result of the progressive increase in fluid/rock interaction.

5) Volume was conserved during alteration. Based on this premise, bulk-rock geochemical mass balance calculations indicate that the low-solubility components Zr and P_2O_5 present in zircon and apatite in the felsic rocks, and Cr_2O_3 in chromite in the serpentinites, were removed in unexpectedly large proportions during calc-silicate alteration. The calculations further indicate that these components were mobilized over distances that exceed the width of the alteration zones. This is interpreted to have resulted from the infiltration of very large amounts of fluid at the contact between serpentinite and slate and at the contact between serpentinite and the felsic intrusive rocks.

6) Rodingitization involved three types of fluids during two episodes of alteration. These episodes occurred following obduction of the Asbestos ophiolite onto the Laurentian continental margin during the Taconian orogeny.

7) The hydrocarbons present in the fluid inclusions from the rodingites may have originated from the reaction, at low fluid/rock ratio, of a CO_2-rich aqueous fluid with partially serpentinized peridotite or with metal alloys (awaruite) away from high permeability zones (shear zones and serpentinite-dyke contacts). My calculations revealed that the proportions of the hydrocarbons in the fluid inclusions correspond closely to those expected to compose fluids in metastable equilibrium with a mineral assemblage comprising iron carbides and iron oxides.

CONTRIBUTIONS TO KNOWLEDGE

Three aspects of this thesis contribute most significantly to our understanding of the hydrothermal alteration of peridotites, and of the more Si- and Al-rich lithologies that occur in contact with them. These are explained in the following paragraphs.

Ca sources

The origin of the Ca in rodingites has remained one of the principal concerns of those who study them. Most studies have attempted to identify a single source for the Ca, and have variously suggested that the Ca originated from the peridotites hosting the rodingites, the precursor of the rodingites, or a location distant from both the peridotites and the rodingite protolith. Based on the experimental results presented in this study and thermodynamic analysis, it is concluded that the calcium does not have a unique source. The fluids that induce serpentinization of fresh peridotites in most tectonic settings necessarily originate from outside the peridotites. Before accessing peridotites, any potential fluid, whether it is seawater or a magmatic, metamorphic, basinal, formational, or evolved meteoric fluid, will tend to equilibrate with the rock in which it is present. Most such fluids are moderately to strongly saline and contain predominantly Na, Ca and Cl. During reaction between fluid and fresh peridotites under conditions where complete serpentinization can occur, the total Na, Ca and Cl budgets of the system considered must be consistent with thermodynamic first principles, i.e., obey charge and mass balance constraints. My calculations clearly indicate that the extent of Ca exchange between Na-Ca-Cl fluids and peridotites during alteration is relatively small. Support for this conclusion is provided by the fact that Ca-rich minerals are rare in serpentinites. The highest calculated concentrations of Ca and pH correspond to equilibrium with the assemblage serpentine + brucite + diopside, but the calculated excess Ca relative to a starting fluid with any Na/Ca ratio and reasonable pH (> 3) is much less than the initial value. By virtue of this, the fluids that have the largest potential for rodingitization correspond to fluids circulating in incompletely serpentinized brucite- and pyroxene-bearing peridotites, but the Ca concentration of this fluid is not as high as one might

suspect. The calculations further indicate that the difference between the Ca concentration of a fluid equilibrated with serpentine + brucite + diopside and that of the same fluid equilibrated with, for example, grossular + zoisite + diopside + prehnite after reaction with a Si-Al-rich rock, is also much smaller than one might be inclined to assume. It is evident that there can not be a single source for the calcium involved in rodingitization.

Physicochemical controls of rodingitization

Much of the discussion in the literature concerning the origin of rodingites has concentrated on the origin of the calcium, although the required concentrations in the solutions inducing rodingitization have not been determined or even estimated. While low $\mu SiO_2°$ and high pH have been recognized as parameters playing an important role in rodingitization, this study is the first to provide a quantitative assessment of the relative importance of $\mu SiO_2°$, pH and calcium concentration in the formation of rodingites. Of these parameters, $\mu SiO_2°$ is the most sensitive, and, at the contact between serpentinite and Si-Al-rich lithologies, may vary by as much as 2.5 orders of magnitude. For a given concentration of Ca, the commonly occurring Na- and K-bearing silicates (feldspars, and micas) are not stable at low values of $\mu SiO_2°$ in the comparatively alkaline fluid responsible for alteration, relative to Ca-rich silicates. Although Ca is required for rodingitization, the concentration of this element in the fluid does not have to be high.

Origin of hydrocarbons associated with serpentinites

Methane and higher order hydrocarbons have long been known to be important components of fluids in serpentinites. Their origin has been variously attributed to the degradation of organic matter and to Fischer-Tropsch-type catalytic reactions on the surface of secondary magnetite involving a CO_2-bearing fluid and H_2 generated as a by-product of serpentinization. Hydrocarbon-bearing fluids originating from the serpentinization of ultramafic rocks occur as fluid inclusions in rodingites. These rocks are better reservoirs for the preservation of the serpentinizing fluids because the structure of the rodingite-forming minerals is less susceptible to post-entrapment leakage than serpentine-group minerals. Gas chromatographic analysis of rodingitized slate, granite

and diorite, and of vesuvianite-rich veins from the JM Asbestos mine has shown that all contain methane and short-chain *n*-alkanes up to pentane, but no CO_2. The distribution of the analysed hydrocarbons displays a Schulz-Flory relationship, which could be interpreted as evidence for their origin via a Fischer-Tropsch-type synthesis. However, the proportions of the hydrocarbons with more than one carbon atom are too small to be explained by such a process in the presence of the potential catalysts that occur in serpentinites. This study has provided an alternative hypothesis that explains satisfactorily the distribution of the hydrocarbons in serpentinizing fluids. The new interpretation involves the equilibration of a water-poor and carbon-rich fluid with a metastable iron carbide-bearing mineral assemblage. Such iron carbide-bearing mineral assemblages have been identified in incompletely serpentinized peridotites, consistent with an environment where the μH_2O is very low.

SUGGESTIONS FOR FUTURE INVESTIGATIONS

Numerous subjects that merit further study have emerged during the course of this experimental and field-related study of serpentinites and rodingites. Experiments are needed to evaluate:

1) The relative stabilities of lizardite and chrysotile.
2) Quantitatively the relative contributions of advective and diffusive mass transport during Ca-metasomatism of peridotite and adjacent Si-Al-rich lithologies. This would be an extension of Plyusnina et al.'s (1993) experiments, from which no fluid chemistry data is available. Metasomatic exchange experiments between ultramafic rocks and Si- and/or Al-rich rocks could be performed in diffusion cells and in flow-through experiments under a wider range of temperatures and using simpler systems involving olivine-quartz and olivine-feldspar pairs of minerals. Calculations are also needed to better evaluate the magnitude and relative contributions of kinetic and transport parameters involved in calcium metasomatism by simulation of open system

conditions to reproduce the various types of zoning of mineral assemblages observed in nature.

3) More precisely phase equilibrium relationships involving vesuvianite. This mineral is common in rodingites. However, its thermodynamic properties are very poorly known. There is a large potential for geothermometry using vesuvianite because it allows for a number of cation substitution schemes and mineral equilibria within the range of pressure and temperature conditions of rodingitization.
4) The thermodynamic properties of pectolite. This is one of the few rock-forming minerals for which no thermodynamic data are available. It occurs relatively commonly in rodingites and in alkaline igneous rocks. Knowledge of the phase equilibrium relationships between this and other minerals is essential to more precisely constrain the Na and Ca concentrations of the fluids responsible for the formation of assemblages containing this mineral.
5) The solubility of chromite, zircon and apatite in synthetic serpentinizing and rodingitizing fluids under temperature and pressure conditions typical for rodingitization. This information could be used to better evaluate the potential of infiltration metasomatism as an effective mechanism of rodingitization.

Further investigations of the JM Asbestos mine are required to determine:

1) The source of the felsic intrusive rocks through Nd/Sm and U/Pb analyses in order to more fully constrain the relationship between the granites and the diorites. This will shed light on the process of obduction of the ophiolite and its environment of formation. Isotopic, major and trace element analyses of the diorites that occur in the serpentinized ultramafic rocks of the Thetford Mines ophiolite should be obtained for comparison.
2) The crystallization and metamorphic ages of zircon (U-Pb), feldspar and mica (Ar-Ar), and apatite (fission track) in the felsic dykes in order to help constrain the pressure-temperature path(s) followed by the ophiolite during its emplacement on the Laurentian continental margin.

3) The identity of the first-eluted gas species observed during gas chromatographic analysis of the rodingites by using He-N_2 carrier gases, Raman spectroscopy and other mass spectrometric methods.
4) The O/H stable isotope signature of the different generations of minerals that compose the serpentinites and the rodingites, and the C/O/H stable isotope signature of the water and carbon-bearing species in the fluid inclusions from rodingites in order to constrain the origin of the fluids responsible for alteration.
5) The distribution and oxidation state of Fe in the secondary minerals formed during serpentinization of peridotites and relate this to the oxidation states of the fluids responsible for rodingitization. In this way, the temporal relationships between the various episodes of serpentinization and rodingitization could be better constrained.
6) The nature and relative proportions of the ionic species dissolved in the inclusion fluids from the rodingites by laser-ablation ICP-MS analyses or electron microprobe analyses of decrepitates. Such data will provide information on the changes that occur in the proportions of the alkali and alkali-earth elements dissolved in the fluid during rodingitization. This information could be used to constrain the reaction paths and chemical evolution of fluid and rock attending rodingitization.
7) The presence or absence of Fe (Ni) carbides in the serpentinites by TEM examination of magnetite and Fe-Ni alloys.

REFERENCES

Abrajano, T. A., Sturchio, N. C., Bohlke, J. K., Lyon, G. L., Poreda, R. J. and C. M. Stevens, 1988, Methane-hydrogen gas seeps, Zambales ophiolite, Philippines: deep or shallow origin? Chemical Geology, v. 71, p. 211-222.

Abrajano, T. A., Sturchio, N. C., Kennedy, B. M., Lyon, G. L., Muehlenbachs, K. and J. K. Bohlke, 1990, Geochemistry of reduced gas related to serpentinization of the Zambales ophiolite, Philippines, Applied Geochemistry, v. 5, p. 625-630.

Addison, J. and L. S. T. Davies, 1990, Analysis of amphibole asbestos in chrysotile and other minerals, Annals of Occupational Hygiene, v. 34, p. 159-175.

Agricola, G., 1556, De Re Metallica, Hoover, H. C. and C. H. Hoover, English translation, 1950, Dover Publications, New York, 630 p.

Agrinier, P., Hékinian, R., Bideau, D. and M. Javoy, M., 1995, O and H stable isotope compositions of oceanic crust and upper mantle rocks exposed in the Hess Deep near the Galapagos triple junction, Earth and Planetary Science Letters, v. 136, p. 183-196.

Alt, J. C. and W. C. Shanks, III, 1998, Sulfur in serpentinized oceanic peridotites: serpentinization process and microbial sulfate reduction, Journal of Geophysical Research, v. 103, p. 9917-9929.

Anbeek, C., 1992, Surface roughness of minerals and implications for dissolution studies, Geochimica et Cosmochimica Acta, v. 56, p. 1461-1469.

Anhaeusser, C. R., 1976, The nature of chrysotile asbestos occurrences in southern Africa, a review, Economic Geology, v. 71, p. 96-116.

Anhaeusser, C. R., 1979, Rodingite occurrences in some Archean ultramafic complexes in the Barberton Mountain Land, South Africa, Precambrian Research, v. 8, p. 49-76.

Apps, J. A., 1985, Methane formation during hydrolysis by mafic rocks, Lawrence Berkeley Laboratory, Annual Report 1984, p. 13-17.

Aumento, F. and H. Loubat, 1971, The Mid-Atlantic Ridge near 45° N. XVI. Serpentinized ultramafic intrusions, Canadian Journal of Earth Sciences, v. 8, p. 631-663.

Baker, G., 1958, Rodingite in nickeliferous serpentinite, near Beaconsfield, Northern Tasmania, Journal of the Geological Society of Australia, v. 6, p. 21-35.

Barnes, I. and J. R. O'Neil, 1969, The relationship between fluids in some fresh Alpine-type ultramafics and possible modern serpentinization, western United States, Geological Society of America Bulletin, v. 80, p. 1947-1960.

Barnes, I., LaMarche, V. C., Jr., and G. Himmelberg, 1967, Geochemical evidence of present-day serpentinization, Science, v. 156, p. 830-832.

Barnes, I., O'Neil, J. R. and J. J. Trescases, 1978, Present day serpentinization in New Caledonia, Oman and Yugoslavia, Geochimica et Cosmochimica Acta, v. 42, p. 144-145.

Barnes, I., Rapp, J. B., O'Neil, J. R., Sheppard, R. A. and A. J. Gude, III, 1972, Metamorphic assemblages and the direction of flow of metamorphic fluids in four instances of serpentinization, Contributions to Mineralogy and Petrology, v. 35, p. 263-276.

Barriga, F. and W. S. Fyfe, 1983, Development of rodingite in basaltic rocks in serpentinites, East Liguria, Italy, Contributions to Mineralogy and Petrology, v. 84, p. 146-151.

Baronnet, A., 1972, Growth mechanisms and polytypism in synthetic hydroxyl-bearing phlogopite, American Mineralogist, v. 57, p. 1272-1293.

Baronnet, A., 1973, Sur les origines des dislocations vis et des spirales de croissance dans les micas, Journal of Crystal Growth, v. 19, p. 193-198.

Baronnet, A. and B. Devouard, 1996, Topology and crystal growth of natural chrysotile and polygonal serpentine, Journal of Crystal Growth, v. 166, p. 952-960.

Bell, J. M., Clarke, E. de C. and P. Marshall, 1911, The geology of the Dun Mountain subdivision, Nelson, New Zealand Geological Survey, Bulletin 12, new series, 71 p.

Bell, M. C., 1995, Thermodynamically controlled catalysis: equilibria in Fischer-Tropsch synthesis, Canadian Metallurgical Quarterly, v. 34, p. 331-341.

Benson, W. N., 1926, The tectonic conditions accompanying the intrusion of basic and ultrabasic igneous rocks, Memoirs of the National Academy of Sciences, Washington, D.C., v. 19, p. 1-9.

Bergeron, M., 1988, Distribution et comportement du bore dans la croûte océanique, Canadian Journal of Earth Sciences, v. 26, p. 782-790.

Berman, R. G., 1991, Thermobarometry using multiequilibrium calculations: a new technique, with petrological applications, Canadian Mineralogist, v. 29, p. 833-855.

Berman, R. G., Brown, T. H. and E. H. Perkins, 1987, GEØ-CALC: Software for calculation and display of P-T-X phase diagrams, American Mineralogist, v. 72, p. 861-862.

Berman, R. G., Engi, M., Greenwood, H. J. and T. H. Brown, 1986, Derivation of internally-consistent thermodynamic data by the technique of mathematical programming: a review with application to the system MgO-SiO_2-H_2O, Journal of Petrology, v. 27, p. 1331-1364.

Berndt, M. E. and W. E. Seyfried, Jr., 1993, Calcium and sodium exchange during hydrothermal alteration of calcic plagioclase at 400° C and 400 bars, Geochimica et Cosmochimica Acta, v. 57, p. 4445-4451.

Berndt, M. E., Allen, D. E. and W. E. Seyfried Jr., 1996, Reduction of CO_2 during serpentinization of olivine at 300°C and 500 bar, Geology, v. 24, p. 351-354.

Bertrand, J. and J. Deferne, editors, 1980, Proceedings of the international symposium on tectonic inclusions and associated rocks in serpentinites, Geneva, September 1979, Archives des Sciences de la Société de Physique et d'Histoire Naturelle de Genève, v. 33.

Bideau, D., Hébert, R., Hekinian, R. and M. Cannat, 1991, Metamorphism of deep-seated rocks from the Garrett ultrafast transform (East Pacific Rise near 13°25'S), Journal of Geophysical Research, v. 96, p. 10,079-10,099.

Bilgrami, S. A. and R. A. Howie, 1960, The mineralogy and petrology of a rodingite dyke, Hindubagh, Pakistan, American Mineralogist, v. 45, p. 791-801.

Bloxam, T. W., 1954, Rodingite from the Girvan-Ballantrae complex, Ayrshire, Mineralogical Magazine, v. 30, p. 525-528.

Bøe, R., 1985, Rodingite from Lindås, western Norway, Norsk Geologisk Tidsskrift, v. 65, p. 301-320.

Bonatti, E., 1968, Ultramafic rocks from the Mid-Atlantic Ridge, Nature, v. 219, p. 363-364.

Bonatti, E., Lawrence, J. R. and N. Morandi, 1984, Serpentinization of oceanic peridotites: temperature dependence of mineralogy and boron content, Earth and Planetary Science Letters, v. 70, p. 88-94.

Boudier, F., Ceuleneer, G. and A. Nicolas, 1988, Shear zones, thrusts and related magmatism in the Oman ophiolite: initiation of thrusting on an oceanic ridge, Tectonophysics, v. 151, p. 275-296.

Brodeur, E. and R. Marquis, 1995, Géologie de la région d'Orford, Ministère de l'Énergie, des Mines et des Ressources du Québec, ET 93-06, 97 p.

Brown, T. H., Berman, R. G. and E. H. Perkins, 1987, GEØ-CALC: a software package for rapid calculation of stable pressure – temperature – activity phase diagrams, Geological Society of America, Abstracts with Programs, v. 19, p. 603.

Brown, T. H., Berman, R. G. and E. H. Perkins, 1988, GEØ-CALC: a software package for calculation and display of pressure – temperature – composition phase diagrams using an IBM or compatible personal computer, Computers and Geoscience, v. 14, p. 279-289.

Brunauer, S., Emmett, P. H. and E. Teller, 1938, Adsorption of gases in multimolecular layers, Journal of the American Chemical Society, v. 60, p. 309-319.

Butterfield, D. A. and G. J. Massoth, 1994, Geochemistry of north Cleft segment vent fluids: temporal changes in chlorinity and their possible relation to recent volcanism, Journal of Geophysical Research, v. 99, p. 4951-4968.

Butterfield, D. A., Massoth, G. J., McDuff, R. E., Lupton, J. E. and M. D. Lilley, 1990, Geochemistry of hydrothermal fluids from Axial Seamount hydrothermal emissions study vent field, Juan de Fuca Ridge: subseafloor boiling and subsequent fluid-rock interaction, Journal of Geophysical Research, v. 95, p. 12,859-12,921.

Butterfield, D. A., McDuff, R. E., Mottl, M. J., Lilley, M. D., Lupton, J. E. and G. J. Massoth, 1994, Gradients in the composition of hydrothermal fluids from the Endeavor segment vent field: phase separation and brine loss, Journal of Geophysical Research, v. 99, p. 9561-9583.

Butterfield, D. A., McDuff, R. E., Franklin, J. and C. G. Wheat, 1994, Geochemistry of hydrothermal vent fluids from Middle Valley, Juan de Fuca ridge, Proceedings of the Ocean Drilling Program, Scientific Results, v. 139, p. 395-410.

Cannat, M., 1993, Emplacement of mantle rocks in the seafloor at mid-ocean ridges, Journal of Geophysical Research, v. 98, p. 4163-4172.

Capedri, S., Garuti, G. and A. Rossi, 1978, Rodingites from Pindos. Constraints on the "rodingite problem", Neues Jahrbuch für Mineralogie Abhandlungen, v. 133, p. 242-263.

Caruso, L. J. and J. V. Chernosky, Jr., 1979, The stability of lizardite, Canadian Mineralogist, v. 17, p. 757-769.

Casey, W. H., Banfield, J. F., Westrich, H. R. and L. McLaughlin, 1993, What do dissolution experiments tell us about natural weathering? Chemical Geology, v. 105, p. 1-15.

Castonguay, S., Tremblay, A., Ruffet, G., Féraud, G. and M. Sosson, 1995, $^{40}Ar/^{39}Ar$ cooling ages of Taconian deformation and metamorphism along the Laurentian margin of the Québec Appalachians, Canada: Middle Ordovician and Silurian, Geological Society of America Abstracts with Programs, v. 27, p. A-225.

Castonguay, S., Tremblay, A., Ruffet, G., Féraud, G., Pinet, N. and M. Sosson, 1997, Ordovician and Silurian metamorphic cooling ages along the Laurentian margin of the Québec Appalachians: bridging the gap between New England and Newfoundland, Geology, v. 25, p. 583-586.

Cawthorn, R. G. and P. A. Brown, 1976, A model for the formation and crystallization of corundum-normative calc-alkaline magmas through amphibole fractionation, Journal of Geology, v. 84, p. 467-476.

Chamberlain, S. C., 1980, Wollastonite, vesuvianite, native copper and diopside from the Jeffrey mine in Asbestos, Quebec, Canada, Rocks and Minerals, p. 188-191.

Charlou, J. L., Fouquet, Y., Donval, J. P. and J. M. Auzende, 1996, Mineral and gas chemistry of hydrothermal fluids on an ultrafast spreading ridge: East Pacific Rise, 17° to 19°S (Naudur cruise, 1993) phase separation processes controlled by volcanic and tectonic activity, Journal of Geophysical Research, v. 101, p. 15,899-15,919.

Charlou, J. L., Bougault, H., Appriou, P., Nelsen, T. and P. Rona, 1991, Different TDM/CH_4 hydrothermal plume signatures: TAG site at 26°N and serpentinized

ultrabasic diapir at 15°05'N on the Mid-Atlantic Ridge, Geochimica et Cosmochimica Acta, v. 55, p. 3209-3222.

Charlou, J. L., Fouquet, Y., Bougault, H., Donval, J. P., Etoubleau, J., Jean-Baptiste, P., Dapoigny, A., Appriou, P. and P. A. Rona, 1998, Intense CH_4 plumes generated by serpentinization of ultramafic rocks at the intersection of the 15°20'N fracture zone and the Mid-Atlantic Ridge, Geochimica et Cosmochimica Acta, v. 62, p. 2323-2333.

Chernosky, J. V., Jr., 1975, Aggregate refractive indices and unit cell parameters of synthetic serpentine in the system MgO-Al_2O_3-SiO_2-H_2O, American Mineralogist, v. 60, p. 200-208.

Chernosky, J. V., Jr., Berman, R. G. and L. T. Bryndzia, 1988, Stability, phase relations, and thermodynamic properties of chlorite and serpentine group minerals, *in* Hydrous Phyllosilicates (exclusive of micas), Bailey, S. W., editor, Reviews in Mineralogy, Mineralogical Society of America, v. 19, p. 295-346.

Chidester, A. H., Albee, A. L. and W. M. Cady, 1978, Petrology, structure, and genesis of the Asbestos-bearing ultramafic rocks of the Belvidere Mountain area in Vermont, U. S. Geological Survey Professional Paper 1016, 88 p.

Clague, D. A., Frankel, C. S. and J. S. Eaby, 1985, The age and origin of felsic intrusions of the Thetford Mines ophiolite, Quebec, Canadian Journal of Earth Sciences, v. 22, p. 1257-1261.

Coleman, R. G., 1963, Serpentinites, rodingites and tectonic inclusions in Alpine-type mountain chains, Geological Society of America Special Paper 73.

Coleman, R. G., 1966, New Zealand serpentinites and associated metasomatic rocks, New Zealand Geological Survey, Bulletin No. 76, 102 p.

Coleman, R. G., 1967, Low-temperature reaction zones and alpine ultramafic rocks of California, Oregon and Washington, United States Geological Survey, Bulletin No. 1247, 49 p.

Coleman, R. G., 1977, Ophiolites: ancient oceanic lithosphere? Springer-Verlag, New York.

Coleman, R. G. and T. E. Keith, 1971, A chemical study of serpentinization – Burro Mountain, California, Journal of Petrology, v. 12, p. 311-328.

Compagnoni, A., Conte, R., Facchinelli, A., Orione, P., Rossetti, P. and C. Trossarelli, 1998, The rodingite of Bellecombe (Val D'Aosta, Italy): a petrographic and fluid inclusion study, 17th general meeting, International Mineralogical Association, August 9-14, Toronto, Canada, Programme and Abstracts, p. A77L.

Coulton, A. J., Harper, G. D. and D. S. O'Hanley, 1995, Oceanic versus emplacement age serpentinization in the Josephine ophiolite: Implications for the nature of the Moho at intermediate and slow spreading ridges, Journal of Geophysical Research, v. 100, p. 22,245-22,260.

Cousineau, P. A., 1990, Le Groupe de Caldwell et le domaine océanique entre Saint-Joseph-de-Beauce et Sainte-Sabine, Ministère de l'Énergie, des Mines et des Ressources du Québec, MM 87-02, 165 p.

Cox, J., Searle, M. and R. Pedersen, 1999, The petrogenesis of leucogranitic dykes intruding the northern Semail ophiolite, United Arab Emirates: field relationships, geochemistry and Sr/Nd isotope systematics, Contributions to Mineralogy and Petrology, v. 137, p. 267-287.

David, J. and R. Marquis, 1994, Géochronologie U-Pb dans les Appalaches du Québec: application aux roches de la zone de Dunnage, La Revue Géologique du Québec, v. 1, p. 16-20.

David, J., Marquis, R. and Tremblay, A., 1993, U-Pb geochronology of the Dunnage zone, in the southwestern Quebec Appalachians, Geological Society of America Abstracts with Programs, v. 25, p. A-485.

Davis, D. W., Lowenstein, T. K. and R. J. Spencer, 1990, Melting behavior of fluid inclusions in laboratory-grown halite crystals in the systems NaCl-H_2O, NaCl-KCl-H_2O, NaCl-$MgCl_2$-H_2O and NaCl-$CaCl_2$-H_2O, Geochimica et Cosmochimica Acta, v. 54, p. 591-601.

Day, H. W., Chernosky, J. V. and H. J. Kumin, 1985, Equilibria in the system MgO-SiO_2-H_2O: a thermodynamic analysis, American Mineralogist, v. 70, p. 237-248.

De, A., 1961, Petrology of dikes emplaced in the ultramafic rocks of southeastern Quebec, Ph. D. dissertation, Princeton University, Princeton, 201 p.

De, A., 1968, Post-ultramafic dykes and associated rocks in the asbestos mining areas in the Eastern Townships, Quebec, Geological Survey of Canada, Report of Activities, Paper 68-1, Part A, p. 71.

De, A., 1972, Petrology of dikes emplaced in the ultramafic rocks of southeastern Quebec and origin of the rodingite, Geological Society of America, Memoir 132, p. 489-501.

de la Roche, H., Leterrier, J., Grandclaude, P. and M. Marchal, 1980, A classification of volcanic and plutonic rocks using R_1R_2-diagram and major-element analyses – its relationships with current nomenclature, Chemical Geology, v. 29, p. 183-210.

de Ronde, C. E. J., 1995, Fluid chemistry and isotopic characteristics of seafloor hydrothermal systems and associated VMS deposits: potential for magmatic contributions, *in* Magmas, Fluids and Ore Deposits, Thompson, J. F. H., editor, Mineralogical Association of Canada Short Course Series, v. 23, p. 479-509.

de Waal, S. A., 1969, On the origin of hydrogrossularite and other calcium silicates in serpentinites, Transactions of the Geological Society of South Africa, v. 72, p. 23-27.

Devirts, A. L., Gagauz, F. G., Grinenko, V. A., Lagutina, Y. P., Pereversov, V. V. and Y. A. Shukolyukov, 1993, Origin of hydrogen in Kempirsay-intrusion ultramafites, Geochemistry International, v. 30, p. 139-144.

Devouard, B., 1995, Structure et croissance cristalline du chrysotile et des serpentines polygonales, Ph. D. Thesis, Université d'Aix-Marseille III, France, 181 p.

Dewey, J. F., 1976, Ophiolite obduction, Tectonophysics, v. 31, p. 93-120.

Diamond, L. W., 1994, Salinity of multivolatile fluid inclusions determined from clathrate hydrate stability, Geochimica et Cosmochimica Acta, v. 58, p. 19-41.

Diment, W. H., 1964, Thermal conductivity of serpentinite from Mayaguez, Puerto Rico, and other localities, *in* A study of serpentinite, the AMSOC core hole near Mayaguez, Puerto Rico, Burk., C. A., editor, National Academy of Sciences - National Research Council, Washington, D. C., Publication No. 1188, p. 92-106.

Dreher, A. M., Girardi, V. A. V. and P. Comin-Chiaramonti, 1989, Petrologia dos rodingitos do complexo máfico-ultamáfico de Cana Brava, Goiás, Revisita Brasileira de Geociências, v. 19, p. 224-236.

Droop, G. T. R., 1987, A general equation for estimating Fe^{3+} concentrations in ferromagnesian silicates and oxides from microprobe analyses, using stoichiometric criteria, Mineralogical Magazine, v. 51, p. 431-435.

Duan, Z., Møller, N., Greenberg, J. and J. H. Weare, 1992, The prediction of methane solubility in natural waters to high ionic strength from 0 to 250°C and from 0 to 1600 bar, Geochimica et Cosmochimica Acta, v. 56, p. 1451-1460.

Dubinska, E., 1997, Rodingites and amphibolites from the serpentinites surrounding Sowie Góry block (Lower Silesia, Poland): record of supra-subduction zone magmatism and serpentinization, Neues Jahrbuch für Mineralogie Abhandlungen, v. 171, p. 239-279.

Dufresne, A., Bégin, R., Churg, A. and S. Massé, 1996, Mineral fiber content of lungs in patients with mesothelioma seeking compensation in Québec, American Journal of Respiratory and Critical Care Medicine, v. 153, p. 711-718.

Dufresne, A., Harrigan, M., Massé, S. and R. Bégin, 1995, Fibers in lung tissues of mesothelioma cases among miners and millers of the Township of Asbestos, Quebec, American Journal of Industrial Medicine, v. 27, p. 581-592.

Dungan, M. A., 1977, Metastability in serpentine-olivine equilibria, American Mineralogist, v. 62, p. 1018-1029.

Dunning, G. R. and R. B. Pedersen, 1988, U/Pb ages of ophiolites and arc-related plutons of the Norwegian Caledonides: implications for the development of Iapetus, Contributions to Mineralogy and Petrology, v. 98, p. 13-23.

Dyment, J., Arkani-Hamed, J. and A. Ghods, 1997, Contribution of serpentinized ultramafics to marine magnetic anomalies at slow and intermediate spreading centres: insights from the shape of the anomalies, Geophysical Journal International, v. 129, p. 691-701.

Eggleston, C. M., Hochella, M. F., Jr. and G. A. Parks, 1989, Sample preparation and ageing effects on the dissolution rate and surface composition of diopside, Geochimica et Cosmochimica Acta, v. 53, p. 797-804.

Eremeev, V. P. and A. K. Sibilev, 1970, Serpentinization in the Idzhim ultrabasic rock pluton and role of native iron, oregonite, and maucherite in the process, Izvestia Akadamii Nauk SSSR, Serie Geology, v. 6, p. 91-100. (in Russian).

Evans, B. W. and V. Trommsdorff, 1970, Regional metamorphism of ultramafic rocks in the Central Alps: parageneses in the system CaO-MgO-SiO_2-H_2O, Schweizerische Mineralogische und Petrographische Mitteilungen, v. 50, p. 481-492.

Evans, B. W., Johannes, W., Oterdoom, H. and V. Trommsdorff, 1976, Stability of chrysotile and antigorite in the serpentinite multisystem, Schweizerische Mineralogische und Petrographische Mitteilungen, v. 56, p. 79-93.

Feininger, T., 1981, Amphibolite associated with the Thetford Mines ophiolite complex at Belmina Ridge, Quebec, Canadian Journal of Earth Sciences, v. 18, p. 1878-1892.

Ferry, J. M. and M. L. Gerdes, 1998, Chemically reactive fluid flow during metamorphism. Annual Reviews in Earth and Planetary Sciences, v. 26, p. 255-287.

Finlayson, A. M., 1909, The nephrite and magnesian rocks of the South Island of New Zealand, Quarterly Journal of the Geological Society of London, v. 65, p. 351-381.

Flory, P. J., 1936, Molecular-size distribution in linear condensation polymers, American Chemical Society Journal, v. 58, p. 1877-1884.

Fritz, P., Frape, S. K. and M. Miles, 1987, Methane in the crystalline rocks of the Canadian Shield, *in* Saline water and gases in crystalline rocks, Fritz, P. and S. K. Frappe, editors, Geological Association of Canada Special Paper 33, p. 211-223.

Fritz, P., Clark, I. D., Fontes, J. -C., Whiticar, M. J. and E. Faber, 1992, Deuterium and ^{13}C evidence for low temperature production of hydrogen and methane in a highly alkaline groundwater environment in Oman, *in* Water-Rock Interaction, Kharaka and Maest, editors, Balkema, Rotterdam, p. 793-796.

Frost, B. R., 1975, Contact metamorphism of serpentinite, chloritic blackwall and rodingite at Paddy-Go-Easy Pass, Central Cascades, Washington, Journal of Petrology, v. 16, p. 272-313.

Frost, B. R., 1985, On the stability of sulfides, oxides, and native metals in serpentinite, Journal of Petrology, v. 26, p. 31-63.

Fryer, P. and M. J. Mottl, 1992, Lithology, mineralogy, and origin of serpentine muds recovered from Conical and Torishima forearc seamounts: results of Leg 125 drilling, Proceedings of the Ocean Drilling Program, Scientific Results, v. 125, p. 343-362.

Graham, R. P. D., 1917, Origin of massive serpentine and chrysotile-asbestos, Black Lake-Thetford area, Quebec, Economic Geology, v. 12, p. 159-202.

Grange, L. I., 1927, On the "rodingite" of Nelson, Transactions of the New Zealand Institute, v. 58, p. 160-166.

Grant, J. A., 1986, The isocon diagram - a simple solution to Gresens' equation for metasomatic alteration, Economic Geology, v. 81, p. 1976-1982.

Grauby, O., Baronnet, A. and B. Devouard, 1998, Chrysotile - to - polygonal serpentines - to - lizardite reaction produced from a MgO-SiO_2-H_2O (MSH) gel, 17th General Meeting of the International Mineralogical Association, August 9-14, Toronto, Canada, Abstracts and Program, p. A81.

Gresens, R. L., 1967, Composition-volume relationships of metasomatism, Chemical Geology, v. 2, p. 47-55.

Grice, J. D. and R. Williams, 1979, The Jeffrey mine, Asbestos, Quebec, Mineralogical Record, v. 10, p. 69-80.

Grice, J. D. and E. Gasparrini, 1981, Spertiniite, $Cu(OH)_2$, a new mineral from the Jeffrey mine, Quebec, Canadian Mineralogist, v. 19, p. 337-340.

Grice, J. D. and G. W. Robinson, 1984, Jeffreyite, $(Ca,Na)_2(Be,Al)Si_2(O,OH)_7$, a new mineral species and its relation to the melilite group, Canadian Mineralogist, v. 22, p. 443-446.

Groat, L. E., Hawthorne, F. C. and T. S. Ercit, 1992, The chemistry of vesuvianite, Canadian Mineralogist, v. 30, p. 19-48.

Gustafson, W. I., 1974, The stability of andradite, hedenbergite, and related minerals in the system Ca-Fe-Si-O-H, Journal of Petrology, v. 15, p. 455-496.

Haggerty, J. A., 1991, Evidence from fluid seeps atop serpentinite seamounts in the Mariana Forearc: clues for emplacement of the seamounts and their relationship to forearc tectonics, Marine Geology, v.102, p. 293-309.

Haggerty, J. A. and S. Chaudhuri, 1992, Strontium isotopic composition of the interstitial waters from Leg 125: Mariana and Bonin forearcs, Proceedings of the Ocean Drilling Program, Scientific Results, v. 125, p. 397-400.

Haggerty, J. A. and J. B. Fisher, 1992, Short-chain organic acids in interstitial waters from Mariana and Bonin forearc serpentinites: Leg 125, Proceedings of the oceanic drilling program, scientific results, v. 125, p. 387-395.

Hajash, A. and G. W. Chandler, 1981, An experimental investigation of high-temperature interactions between seawater and rhyolite, andesite, basalt and peridotite, Contributions to Mineralogy and Petrology, v. 78, p. 240-254.

Hall, A. and Z. Ahmed, 1984, Rare earth content and origin of rodingites, Chemie der Erde, v. 43, p. 45-56.

Halter, W. E., Williams-Jones, A. E. and D. J. Kontak, 1998, Origin and evolution of the greisenizing fluid at the East Kemptville tin deposit, Nova Scotia, Canada, Economic Geology, v. 93, p. 1026-1051.

Harnois, L. and M. Morency, 1989, Geochemistry of Mount Orford ophiolite complex, Northern Appalachians, Canada, Chemical Geology, v. 77, p. 133-147.

Hébert, R., 1980, Etude pétrologique des roches ophiolitiques d'Asbestos et du Mont Ham (Ham Sud), M. Sc. Thesis, Université Laval, Québec, 182 p.

Hébert, R. and J. H. Bédard, 1998, Architecture and petrogenesis of arc ophiolites: example from the ophiolitic complexes of southern Québec, Geological Association of Canada (GAC), Mineralogical Association of Canada (MAC), Association des géologues et géophysiciens du Québec (APGGQ), International Association of Hydrogeologists (IAH), Canadian Geophysical Union (CGU) Joint Annual Meeting, 1998, Québec, Québec, Canada, Fieldtrip A4 Guidebook, 51 p.

Hébert, R. and R. Laurent, 1989, Mineral chemistry of ultramafic and mafic plutonic rocks of the Appalachian ophiolites, Québec, Canada, Chemical Geology, v. 77, p. 265-285.

Hébert, R., Bédard, J. H., Olive, V., Huot, F. and V. Varfalvy, 1998, Ophiolites of Southern Quebec Appalachians: a synthesis, Geological Association of Canada, Mineralogical Association of Canada, Association des Géologues et Géophysiciens du Québec, International Association of Hydrogeologists, Canadian Geophysical Union Joint Annual Meeting, 13-15 May 1998, Québec, Québec, Canada, Abstracts, v. 23, p. A-76.

Heinrich, C. A., Walshe, J. L. and B. P. Harrold, 1996, Chemical mass transfer modelling of ore-forming hydrothermal systems: current practice and problems, Ore Geology Reviews, v. 10, p. 319-338.

Helgeson, H. C., Kirkham, D. H. and G. C. Flowers, 1981, Theoretical prediction of the thermodynamic behavior of aqueous electrolytes at high pressures and temperatures: IV. Calculation of activity coefficients, osmotic coefficients, and apparent molal and standard and relative partial molal properties to 600°C and 5 kb, American Journal of Science, v. 281, p. 1249-1516.

Helgeson, H. C., Owens, C. E., Knox, A. M. and L. Richard, 1998, Calculation of the standard state molal thermodynamic properties of crystalline, liquid, and gas organic molecules at high temperatures and pressures, Geochimica et Cosmochimica Acta, v. 62, p. 985-1081.

Hochella, M. F., Jr., Liou, J. G., Keskinen, M. J. and H. S. Kim, 1982, Synthesis and stability relations of magnesium idocrase, Economic Geology, v. 77, p. 798-808.

Hockley, J. J., Birch, W. D. and H. K. Worner, 1978, A nephrite deposit in the great serpentine belt of New South Wales, Journal of the Geological Society of Australia, v. 25, p. 249-254.

Hoisch, T. D., 1985, The solid solution chemistry of vesuvianite, Contributions to Mineralogy and Petrology, v. 89, p. 205-214.

Holland, T. J. B. and R. Powell, 1990, An enlarged and updated internally consistent thermodynamic data-set with uncertainties and correlations: the system K_2O-Na_2O-CaO-MgO-MnO-FeO-Fe_2O_3-Al_2O_3-TiO_2-SiO_2-C-H_2-O_2, Journal of Metamorphic Geology, v. 8, p. 89-124.

Holloway, J. R., 1981, Compositions and volumes of supercritical fluids in the earth's crust, *in* Fluid Inclusions: Application to Petrology, Hollister, L. S. and M. L. Crawford, editors, Mineralogical Association of Canada Short Course Handbook, v. 6, p. 13-38.

Holm, N. G., 1996, Serpentinization of oceanic crust and Fischer-Tropsch type synthesis of organic compounds, Origins of Life and Evolution of the Biosphere, v. 26, p. 205-206.

Honnorez, J. and P. Kirst, 1975, Petrology of rodingites from the equatorial Mid-Atlantic fracture zones and their geotectonic significance, Contributions to Mineralogy and Petrology, v. 49, p. 233-257.

Hughes, J. M., 1991, Epidemiology of lung cancer in relation to asbestos exposure, *in* Mineral Fibers and Health, Liddell, D. and K. Miller, editors, CRC Press, Boston, p. 135-145.

Hughes, J. M. and H. Weill, 1986, Asbestos exposure – quantitative assessment of risk. American Reviews of Respiratory Disease, v. 133, p. 5.

Ishii, T., Robinson, P. T., Maekawa, H. and R. Fiske, 1992, Petrological studies of peridotites from diapiric serpentinite seamounts in the Izu-Ogasawara-Mariana forearc, Leg 125, Proceedings of the Ocean Drilling Program, Scientific Results, v. 125, p. 445-485.

Jaeger, J. C., 1957, The temperature in the neighborhood of a cooling intrusive sheet, American Journal of Science, v. 255, p. 306-318.

Jamieson, R. A., 1986, P-T paths from high temperature shear zones beneath ophiolites, Journal of Metamorphic Geology, v. 4, p. 3-22.

Janecky, D. R. and W. E. Seyfried, 1986, Hydrothermal serpentinization of peridotite within the oceanic crust: experimental investigations of mineralogy and major element chemistry, Geochimica et Cosmochimica Acta, v. 50, p. 1357-1378.

Johnson, J. W., Oelkers, E. H. and H. C. Helgeson, 1992, SUPCRT92: a software package for calculating the standard molal thermodynamic properties of minerals, gases, aqueous species, and reactions from 1 to 5000 bars and 0° to 1000°C, Computers and Geoscience, v. 17, p. 899-947.

Johannes, W., 1968, An experimental investigation of the system MgO-SiO_2-H_2O-CO_2, American Journal of Science, v. 267, p. 1083-1104.

Katoh, T. and K. Niida, 1983, Rodingites from the Kamuikotan, tectonic belt, Hokkaido, Journal of the Faculty of Science, Hokkaido University, Serie IV, v. 20, p. 151-169.

Kholodkevich, I. V. and N. N. Barinov, 1995, Some features of harzburgite-seawater interaction at increased P-T conditions, *in* Water-Rock Interaction, Kharaka, Y. K. and O. V. Chudaev, editors, Proceedings of the 8th international symposium on

water-rock interaction – WRI-8, Vladivostok, Russia, 15-19 August 1995, A. A. Balkema, Rotterdam, p. 801-804.

Knauss, K. G. and T. J. Wolery, 1986, Dependence of albite dissolution kinetics on pH and time at 25°C and 70°C, Geochimica et Cosmochimica Acta, v. 50, p. 2481-2497.

Kobayashi, S. and T. Shoji, 1988, Metasomatic process in the formation of rodingite in Boso Peninsula, Chiba, Japan, Journal of the Japanese Association of Mineralogy, Petrology and Economic Geology, v. 83, p. 514-526.

Komor, S. C., Elthon, D. and J. F. Casey, 1985, Serpentinization of cumulate ultramafic rocks from the North Arm Mountain massif of the Bay of Islands ophiolite, Geochimica et Cosmochimica Acta, v. 49, p. 2331-2338.

Koons, P. O., 1981, A study of natural and experimental metasomatic assemblages in an ultramafic-quartzofeldspathic metasomatic system from the Haast schist, South Island, New Zealand, Contributions to Mineralogy and Petrology, v. 78, p. 189-195.

Kretz, R., 1983, Symbols for rock-forming minerals, American Mineralogist, v. 68, p. 277-279.

Kudo, A., Nakagawa, S., Tsuneto, A. and T. Sakata, 1993, Electrochemical reduction of high pressure CO_2 on Ni electrodes, Journal of the Electrochemical Society, v. 140, p. 1541-1545.

Labotka, T. C. and A. L. Albee, 1979, Serpentinization of the Belvidere Mountain ultramafic body, Vermont: mass balance and reaction at the metasomatic front, Canadian Mineralogist, v. 17, p. 831-845.

Laird, J., Trzcienski, W. E. Jr. and W. A. Bothner, 1993, High pressure, Taconian, and subsequent polymetamorphism of Southern Quebec and Northern Vermont, Geological Society of America Field Trip Guidebook for the Northeastern United States, v. 2, Department of Geology and Geography, University of Massachusetts, Contribution 67, p. O 1- O 32.

Lalonde, A. E. and P. Bernard, 1993, Composition and colour of biotite from granites: two useful properties in the characterization of plutonic suites from the Hepburn internal zone of Wopmay orogen, Northwest Territories, Canadian Mineralogist, v. 31, p. 203-217.

Lamb, W. M., Popp, R. K. and L. A. Boockoff, 1996, The determination of phase relations in the CH_4-H_2O-NaCl system at 1 kbar, 400 to 600°C using synthetic fluid inclusions, Geochimica et Cosmochimica Acta, v. 60, p. 1885-1897.

Lancet, M. S. and E. Anders, 1970, Carbon isotope fractionation in the Fischer-Tropsch synthesis and in meteorites, Science, v. 170, p. 980-982.

Langer, A. M., Nolan, R. P. and J. Addison, 1991, Distinguishing between amphibole asbestos fibers and elongate cleavage fragments of their non-asbestos analogues, *in* Mechanisms in Fiber Carcinogenesis, Brown, R. C., et al., editors, Plenum Press, New York, p. 253-267.

Laurent, R., 1975, Petrology of the alpine-type serpentinites of Asbestos and Thetford Mines, Quebec, Schweizerische Mineralogische und Petrographische Mitteilungen, v. 55, p. 431-455.

Laurent, R., 1980, Regimes of serpentinization and rodingitization in Quebec Appalachian ophiolites, Archives des Sciences de la Société de Physique et d'Histoire Naturelle de Genève, v. 33, p. 311-320.

Laurent, R. and Y. Hébert, 1979, Paragenesis of serpentine assemblages in harzburgite tectonite and dunite cumulate from the Quebec Appalachians, Canadian Mineralogist, v. 17, p. 857-869.

Laurent, R. and R. Hébert, 1989, The volcanic and intrusive rocks of the Québec Appalachian ophiolites (Canada) and their island-arc setting, Chemical Geology, v. 77, p. 287-302.

Laurent, R., Hébert, R. and Y. Hébert, 1979, Tectonic setting and petrological features of the Quebec Appalachian ophiolites, *in* Ophiolites of the Canadian Appalachians and Soviet Urals, Memorial University of Newfoundland Report No. 8, p. 53-77.

Laurent, R., Taner, M. F. and J. Bertrand, 1984, Mise en place et pétrologie du granite associé au complexe ophiolitique de Thetford Mines, Québec, Canadian Journal of Earth Sciences, v. 21, p. 1114-1125.

Le Bel, L., Cocherie, A., Baubron, J. -C., Fouillac, A. M. and C. J. Hawksworth, 1985, A high-K, mantle derived plutonic suite from Linga, near Arequipa (Peru), Journal of Petrology, v. 26, p. 124-148.

LeMétour, J., Rabu, D., Tegyey, M., Béchenec, F., Beurrier, M. and M. Villey, 1990, Subduction and obduction: two stages in the Eo-Alpine tectonometamorphic evolution of the Oman Mountains, *in* The geology and tectonics of the Oman region, Robertson, A. H. F., Searle, M. P. and A. C. Ries, editors, Geological Society Special Publication No. 49, p. 327-339.

Lippard, S. J., Shelton, A. W. and I. G. Gass, 1986, The ophiolite of northern Oman, Geological Society of London, Memoir 11, 178 p.

London, D., 1992, The application of experimental petrology to the genesis and crystallization of granitic rocks, Canadian Mineralogist, v. 30, p. 499-540.

Lyon, G. L. and W. F. Giggenbach, 1990, Composition and origin of the hydrogen-rich gas seep, Fiordland, New Zealand, EOS, Transactions, American Geophysical Union, v. 71, p. 1717.

Macdonald, A. H., 1984, Water diffusion rates through serpentinized peridotites: implications for reaction induced dynamic and chemical effects in ultramafic rocks, Ph. D. Thesis, University of Western Ontario, Canada, 265 p.

Macdonald, A. H. and W. S. Fyfe, 1985, Rate of serpentinization in seafloor environments, Tectonophysics, v. 116, p. 123-135.

Marakushev, A. A., Shteynberg, D. S. and M. V. Lagutina, 1992, Variations of the correlation between carbon and water contents in hydration products of meteorites and alpine-type ultramafic rocks, Doklady Akademii Nauk, v. 327, p. 575-577.

Maresh, W. V. and M. Czank, 1988, Crystal chemistry, growth kinetics and phase relationships of structurally disordered (Mn^{2+}, Mg)-amphiboles, Fortschrifte der Mineralogie, v. 66, p. 69-121.

Martin, H., 1999, Adakitic magmas: modern analogues of Archean granitoids, Lithos, v. 46, p. 411-429.

Mason, R., 1985, Ophiolites, Geology Today, Sept.-Oct., p. 136-140.

Mason, D. R. and J. A. McDonald, 1978, Intrusive rocks and porphyry copper occurrences of the Papua New Guinea-Solomon Islands region: a reconnaissance study, Economic Geology, v. 73, p. 857-877.

McDonald, A. D., Fry, J. S., Woolley, A. J. and J. C. McDonald, 1983, Dust exposure and mortality in an American factory using chrysotile, amosite, and crocidolite in mainly textile manufacture, British Journal of Industrial Medicine, v. 40, p. 368.

McDonald, J. C., Armstrong, B., Case, B., Doell, D., McCaughey, W. T. E., McDonald, A. D. and P. Sébastien, 1989, Mesothelioma and asbestos fiber type, Cancer, v. 63, p. 1544-1547.

Meen, J. K., 1987, Formation of shoshonites from calcalkaline basalt magmas: geochemical and experimental constraints from the type locality, Contributions to Mineralogy and Petrology, v. 97, p. 333-351.

Menzies, M. A., Long, A., Ingram, G., Tatnell, M. and D. Janecky, 1993, MORB peridotite-sea water interaction: experimental constraints on the behaviour of trace elements, $^{87}Sr/^{86}Sr$ and $^{143}Nd/^{144}Nd$ ratios, *in* Magmatic Processes and Plate Tectonics, Prichard, H. M., Alabaster, T., Harris, N. B. W. and C. R. Neary, editors, Geological Society Special Publication No. 76, p. 309-322.

Mével, C. and C. Stamoudi, 1996, Hydrothermal alteration of the upper-mantle section at Hess Deep, Proceedings of the Ocean Drilling Program, Scientific Results, v. 147, p.p. 293-309.

Mittwede, S. K. and E. S. Schandl, 1992, Rodingites from the southern Appalachian Piedmont, South Carolina, USA, European Journal of Mineralogy, v. 4, p. 7-16.

Miura, Y., Rucklidge, J. and G. L. Nord, Jr., 1981, The occurrence of chlorine in serpentine minerals, Contributions to Mineralogy and Petrology, v. 76, p. 17-23.

Moody, J. B., 1976, An experimental study on the serpentinization of iron-bearing olivines, Canadian Mineralogist, v. 14, p. 462-478.

Morency, M., Mineau, R., Zeller, E. and G. Dreschhoff, 1986, Are all fossil fuels really fossils? Oil and Gas Journal, June 2, p. 92-95.

Mottl, M. J., 1992, Pore waters from serpentinite seamounts in the Mariana and Izu-Bonin forearcs, Leg 125: evidence for volatiles from the subducting slab, Proceedings of the ocean drilling program, scientific results, v. 125, p. 373-385.

Mottl, M. J. and J. A. Haggerty, 1989, Upwelling of Cl-poor, S- and C-rich waters through a serpentinite seamount, Mariana forearc, ODP Leg 125, EOS, Transactions, American Geophysical Union, v. 70, p. 1382.

Mountain, B. W., 1992, Fluid-rock interaction paths: natural and experimental examples, Ph. D. Thesis, McGill University, Canada, 354 p.

Muraoka, H., 1985, Serpentinization reaction responsible for rodingite formation of the Ashidashi ultramafic complex, southwest Japan, Journal of the Japanese Association of Mineralogy, Petrology and Economic Geology, v. 80, p. 413-428.

Neal, C. and G. Stanger, 1983, Hydrogen generation from mantle source rocks in Oman, Earth and Planetary Science Letters, v. 66, p. 315-320.

Nicolas, A., 1989, Structures of ophiolites and dynamics of oceanic lithosphere, Kluwer Academic Press.

Normand, C., Gauthier, M. and M. Jébrak, 1996, The Quebec Antimony deposit: an example of gudmundite, native antimony mineralization in the ophiolitic melange of the southeastern Quebec Appalachians, Economic Geology, v. 91, p. 149-163.

O'Brien, J. P. and K. A. Rodgers, 1973, Xonotlite and rodingites from Wairere, New Zealand, Mineralogical Magazine, v. 39, p. 233-240.

Oelkers, E. H., 1996, Physical and chemical properties of rocks and fluids for chemical mass transport calculations, *in* Reactive transport in porous media, Lichtner, P. C., Steefel, C. I. and E. H. Oelkers, editors, Mineralogical Society of America, Reviews in Mineralogy, v. 34, p. 131-191.

O'Hanley, D. S., 1987, The origin of the chrysotile asbestos veins in southeastern Quebec, Canadian Journal of Earth Sciences, v. 24, p. 1-9.

O'Hanley, D. S., 1987, A chemographic analysis of magnesian serpentines using dual networks, Canadian Mineralogist, v. 25, p. 121-133.

O'Hanley, D. S., 1991, Fault-related phenomena associated with hydration and serpentine recrystallization during serpentinization, Canadian Mineralogist, v. 29, p. 21-35.

O'Hanley, D. S., 1992, Solution to the volume problem in serpentinization, Geology, v. 20, p. 705-708.

O'Hanley, D. S. and M. D. Dyar, 1993, The composition of lizardite 1T and the formation of magnetite in serpentinites, American Mineralogist, v. 78, p. 391-404.

O'Hanley, D. S. and M. D. Dyar, 1998, The composition of chrysotile and its relationship with lizardite, Canadian Mineralogist, v. 36, p. 727-739.

O'Hanley, D. S. and R. Offler, 1992, Characterization of multiple serpentinization, Woodsreef, New South Wales, Canadian Mineralogist, v. 30, p. 1113-1126.

O'Hanley, D. S. and F. J. Wicks, 1995, Conditions of formation of lizardite, chrysotile and antigorite, Cassiar, British Columbia, Canadian Mineralogist, v. 33, p. 753-773.

O'Hanley, D. S., Chernosky, J. V., Jr. and F. J. Wicks, 1989, The stability of lizardite and chrysotile, Canadian Mineralogist, v. 27, p. 483-493.

O'Hanley, D. S., Schandl, E. S. and F. J. Wicks, 1992, The origin of rodingites from Cassiar, British Columbia, and their use to estimate T and $P(H_2O)$ during serpentinization, Geochimica et Cosmochimica Acta, v. 56, p. 97-108.

Olive, V., Hébert, R. and M. Loubet, 1997, Isotopic and trace element constraints on the genesis of a boninitic sequence in the Thetford Mines ophiolitic complex, Quebec, Canada, Canadian Journal of Earth Sciences, v. 34, p. 1258-1271.

Olsen, E. J., 1961, High temperature acid rocks associated with serpentinite in eastern Quebec, American Journal of Science, v. 259, p. 329-347.

Paquette, J., Vali, H. and A. Mucci, 1996, TEM study of Pt-C replicas of calcite overgrowths precipitated from electrolyte solutions, Geochimica et Cosmochimica Acta, v. 60, p. 4689-4699.

Papp, G., 1990, A review of the multi-layer lizardite polytypes, Annals Hist. - Nat. Mus. Natn. Hung., v. 82, p. 9-17.

Peacock, S. M., 1987, Serpentinization and infiltration metasomatism in the Trinity peridotite, Klamath province, northern California: implications for subduction zones, Contributions to Mineralogy and Petrology, v. 95, p. 55-70.

Peacock, S. M., 1987, Thermal effects of metamorphic fluids in subduction zones, Geology, v. 15, p. 1057-1060.

Peacock, S. M., 1993, Large-scale hydration of the lithosphere above subducting slabs, Chemical Geology, v. 108, p. 49-59.

Pearce, J. A., Harris, N. B. W. and A. G. Tindle, 1984, Trace element discrimination diagrams for the tectonic interpretation of granitic rocks, Journal of Petrology, v. 25, p. 956-983.

Peretti, A, Dubessy, J., Mullis, J., Frost, B. R. and V. Trommsdorff, 1992, Highly reducing conditions during Alpine metamorphism of the Malenco peridotite

(Sondrio, northern Italy) indicated by mineral paragenesis and H_2 in fluid inclusions, Contributions to Mineralogy and Petrology, v. 112, p. 329-340.

Peters, T. and B. S. Kamber, 1994, Peraluminous, potassium-rich granitoids in the Semail ophiolite, Contributions to Mineralogy and Petrology, v. 118, p. 229-238.

Pfeifer, H. -R., 1977, A model for fluids in metamorphosed ultramafic rocks. Observations at surface and subsurface conditions (high pH spring waters), Schweizerische Mineralogische und Petrographische Mitteilungen, v. 57, p. 361-396.

Phillips, A. H. and H. H. Hess, 1936, Metamorphic differentiation at contacts between serpentinite and siliceous country rocks, American Mineralogist, v. 21, p. 333-362.

Pichavant, M.D. and M.D. Manning, 1984, Petrogenesis of tourmaline granites and topaz granites; the contribution of experimental data. Physics of the Earth and Planetary Interiors, v. 35, p. 31-50.

Pinet, N. and A. Tremblay, 1995, Tectonic evolution of the Quebec-Maine Appalachians: From oceanic spreading to obduction and collision in the Northern Appalachians, American Journal of Science, v. 295, p. 173-200.

Pinet, N. and A. Tremblay, 1995, Is the Taconian orogeny of southern Quebec the result of an Oman-type obduction? Geology, v. 23, p. 121-124.

Pinet, N., Castonguay, S. and A. Tremblay, 1996, Thrusting and back thrusting in the Taconian internal zone, southern Quebec Appalachians, Canadian Journal of Earth Sciences, v. 33, p. 1283-1293.

Plyusnina, L. P., Likhoidov, G. G. and G. P. Zaraisky, 1993, Physicochemical conditions of rodingite formation: experimental data, Petrology, v. 1, p. 492-502.

Ponader, H. B., 1989, Experimental hydrothermal dissolution of forsterite, enstatite, diopside and labradorite, Ph. D. thesis, Stanford University, California, 184 p.

Potter, J. M., Pohl, D. C., Guillemette, R. N., Ponader, H. B. and J. G. Liou, 1985, A system for flow through experimental studies at hydrothermal conditions, Neues Jahrbuch für Mineralogie Monatshefte, v. 7, p. 329-335.

Powell, R. and T. J. B. Holland, 1988, An internally consistent thermodynamic dataset with uncertainties and correlations: 3. Applications to geobarometry, worked

examples and a computer program, Journal of Metamorphic Geology, v. 6, p. 173-204.

Prichard, H. M., 1979, A petrographic study of the process of serpentinization in ophiolites and the oceanic crust, Contributions to Mineralogy and Petrology, v. 68, p. 231-241.

Prokhor, S. A., 1991, The genesis of nephrite and emplacement of the nephrite-bearing ultramafic complexes of East Sayan, International Geology Reviews, v. 33, p. 290-300.

Ramdohr, P., 1967, A widespread mineral association, connected with serpentinization, Neues Jahrbuch für Mineralogie Abhandlungen, v. 107, p. 241-265.

Rasmussen, M. G., Evans, B. W. and S. M. Kuehner, 1998, Low-temperature fayalite, greenalite, and minnesotaite from the overlook gold deposit, Washington: phase relations in the system FeO-SiO_2-H_2O, Canadian Mineralogist, v. 36, p. 147-162.

Reed, J. J., 1959, Soda-metasomatized argillites associated with the Nelson ultramafic belt, New Zealand Journal of Geology and Geophysics, v. 2, p. 905-915.

Richardson, S. W., Gilbert, M. C. and P. M. Bell, 1969, Experimental determination of kyanite-andalusite and andalusite-sillimanite equilibria; the aluminium silicate triple point, America Journal of Science, v. 267, p. 259-272.

Riordon, P. H., 1975, Géologie des gîtes d'amiante du sud-est Québécois, Ministère des Richesses Naturelles du Québec, E.S.-18, 100 p.

Robie, R. A., Hemingway, B. S. and J. R. Fisher, 1978, Thermodynamic properties of minerals and related substances at 298.15K (25°C) and one atmosphere (1.013 bars) and at higher temperatures, United States Geological Survey Bulletin No. 1452.

Rona, P. A., Bougault, H., Charlou, J. L., Appriou, P., Nelsen, T. A., Trefry, J. H., Eberhart, G. L., Barone, A. and H. D. Needham, 1992, Hydrothermal circulation, serpentinization, and degassing at a rift valley-fracture zone intersection: Mid-Atlantic ridge near 15°N, 45°, Geology, v. 20, p. 783-786.

Rose, N. M., Bird, D. K. and J. G. Liou, 1992, Experimental investigation of mass transfer - albite, Ca-Al-silicates, and aqueous solutions, American Journal of Sciences, v. 292, p. 21-57.

Rucklidge, J., 1972, Chlorine in partially serpentinized dunite, Economic Geology, v. 67, p. 38-40.

Rucklidge, J. C. and G. C. Patterson, 1977, The role of chlorine in serpentinization, Contributions to Mineralogy and Petrology, v. 65, p. 39-44.

Saccocia, P. J. and W. E. Seyfried, Jr., 1994, The solubility of chlorite solid solutions in 3.2 wt. % NaCl fluids from 300-400°C, 500 bars, Geochimica et Cosmochimica Acta, v. 58, p. 567-585.

Sakai, R., Kusakabe, M., Noto, M. and T. Ishii, 1990, Origin of waters responsible for serpentinization of the Izu-Ogasawara-Mariana forearc seamounts in view of hydrogen and oxygen isotope ratios, Earth and Planetary Science Letters, v. 100, p. 291-303.

Salvi, S. and A. E. Williams-Jones, 1997, Fischer-Tropsch synthesis of hydrocarbons during sub-solidus alteration of the Strange Lake peralkaline granite, Quebec/Labrador, Canada, Geochimica et Cosmochimica Acta, v. 61, p. 83-99.

Salvi, S., and A. E. Williams-Jones, 1997, Fluid-inclusion volatile analysis by gas chromatography: application of a wide-bore porous-polymer capillary column to the separation of organic and inorganic compounds, Canadian Mineralogist, v. 35, p. 1391-1414.

Sanford, R. F., 1981, Mineralogical and chemical effects of hydration reactions and applications to serpentinization, American Mineralogist, v. 66, p. 290-297.

Sarp, H. and J. Deferne, 1978, Le bilan chimique de la rodingitization et l'origine de l'excès de chaux dans les rodingites, Schweizerische Mineralogische und Petrographische Mitteilungen, v. 58, p. 315-328.

Sarp, H., Bertrand, J. and E. Mc Near, 1976, Vuagnatite, $CaAl(OH)SiO_4$, a new natural calcium aluminium nesosilicate, American Mineralogist, v. 61, p. 825-830.

Sarp, H., Deferne, J. and B. W. Liebich, 1977, La chantalite $CaAl_2SiO_4(OH)_4$, un nouveau silicate naturel d'aluminium et de calcium, Bulletin Suisse de Minéralogie et Pétrographie, v. 57, p. 149-156.

Sarp, H., Deferne, J., Bizouard, H. and B. W. Liebich, 1979, La parthéite, $CaAl_2Si_2O_8.2H_2O$, un nouveau silicate naturel d'aluminium et de calcium, Schweizerische Mineralogische und Petrographische Mitteilungen, v. 59, p. 5-13.

Scambelluri, M., Piccardo, G. B., Philippot, P., Robbiano, A. and L. Negretti, 1997, High salinity fluid inclusions formed from recycled seawater in deeply subducted alpine serpentinite, Earth and Planetary Science Letters, v. 148, p. 485-499.

Schandl, E. S., O'Hanley, D. S. and F. J. Wicks, 1989, Rodingites in serpentinized ultramafic rocks of the Abitibi greenstone belt, Ontario, Canadian Mineralogist, v. 27, p. 579-591.

Schandl, E. S., O'Hanley, D. S., Wicks, F. J. and T. K. Kyser, 1990, Fluid inclusions in rodingites: a geothermometer for serpentinization, Economic Geology, v. 85, p. 1273-1276.

Schulz, G. V., 1935, Highly polymerized compounds CXXII. The relation between reaction rate and composition of the reaction product in micropolymerization processes, Zeitschrift für Physikalische Chemie, B30, p. 379-398.

Schwab, R. G. and D. Kastner, 1977, Präzisionsgitterkonstantenbestimmung zur festlegung röntgenographischer bestimmungskurven für synthetische olivine der mischkristallreihe forsterit-fayalit, Neues Jahrbuch für Mineralogie Monatshefte, v. 5, p. 205-215.

Seyfried, W. E., Jr. and W. E. Dibble, Jr., 1980, Seawater-peridotite interaction at 300°C and 500 bars: implications for the origin of oceanic serpentinites, Geochimica et Cosmochimica Acta, v. 44, p. 309-321.

Seyfried, W. E., Jr., Janecky, D. R. and M. J. Mottl, 1984, Alteration of the oceanic crust: implications for geochemical cycles of lithium and boron, Geochimica et Cosmochimica Acta, v. 48, p. 557-569.

Shand, S. J., 1949, Rocks of the mid-Atlantic ridge, Journal of Geology, v. 57, p. 89-92.

Shock, E. L., Sassani, D. C., Willis, M. and D. A. Sverjensky, 1997, Inorganic species in geologic fluids: correlations among standard molal thermodynamic properties of aqueous ions and hydroxide complexes, Geochimica et Cosmochimica Acta, v. 61, p. 907-950.

Shterenberg, L. E. and K. A. Stepanova, 1978, Graphite in sediments from the northeastern part of the Pacific Ocean (Stations No. 675 and No. 655), Doklady Akademii Nauk SSSR, v. 241, p. 460-462.

Shteynberg, D. S. and M. V. Lagutina, 1978, Carbon balance in serpentinization of ultramafic rocks, Doklady Akademii Nauk SSSR, v. 243, p. 760-763. (in Russian).

Shvarov, Y. and E. Bastrakov, 1999, HCh: a software package for geochemical equilibrium modelling, User's guide, Australian Geological Survey Organization, Record 1999/25, 61 p.

Sivell, W. J. and J. B. Waterhouse, 1986, The geochemistry, origin and tectonic significance of rodingites from the Dun Mountain ultramafics, D'Urville Island, New Zealand, New Zealand Journal of Geology and Geophysics, v. 29, p. 9-27.

St-Julien, P. and C. Hubert, 1975, Evolution of the Taconian orogen in the Quebec Appalachians, American Journal of Science, v. 275-A, p. 337-362.

Steefel, C. I. and A. C. Lasaga, 1992, Putting transport into water-rock interaction models, Geology, v. 20, p. 680-684.

Streckheisen, A. L., 1976, To each plutonic rock its proper name, Earth Science Reviews, v. 12, p. 1-33.

Sun, S. -S. and W. F. McDonough, 1989, Chemical and isotopic systematics of oceanic basalts: implications for mantle composition and processes, *in* Magmatism in the ocean basins, Saunders, A. D. and M. J. Norry, editors, Geological Society Special Publication No. 42, p. 313-345.

Sverjensky, D. A., Shock, E. L. and H. C. Helgeson, 1997, Prediction of the thermodynamic properties of aqueous metal complexes to 1000°C and 5 kb, Geochimica et Cosmochimica Acta, v. 61, p. 1359-1412.

Szatmari, P., 1986, Plate tectonic control of synthetic oil formation. Oil and Gas Journal, Sept. 1, 67-69.

Szatmari, P., 1989, Petroleum formation by Fischer-Tropsch synthesis in plate tectonics, The American Association of Petroleum Geologists Bulletin, v. 73, p. 989-998.

Taner, M. F. and R. Laurent, 1984, Iron-rich amesite from the Lake Asbestos mine, Black Lake, Quebec, Canadian Mineralogist, v. 22, p. 437-442.

Taylor, S. R. and S. M. McLennan, 1985, The continental crust: its composition and evolution, Blackwell Scientific, Oxford, 312 p.

Thayer, T. P., 1966, Serpentinization considered as a constant volume metasomatic process, American Mineralogist, v. 51, p. 685-710.

Thiéry, R., van den Kerkhof, A. M. and J. Dubessy, 1994, *vX* properties of CH_4-CO_2 and CO_2-N_2 fluid inclusions: modelling for T < 31°C and P < 400 bars, European Journal of Mineralogy, v. 6, p. 753-771.

Thompson, A. B. and R. J. Tracy, 1979, Model systems for anatexis of pelitic rocks II. Facies series melting and reactions in the system CaO-$KAlO_2$-$NaAlO_2$-Al_2O_3-SiO_2-H_2O, Contributions to Mineralogy and Petrology, v. 70, p. 429-438.

Tilley, C. E., 1957, On the replacement of anorthosite by hydrogrossular in the Transvaal, Transactions of the Geological Society of South Africa, v. 60, p. 15-17.

Toft, P. B., Arkani-Hamed, J. and S. E. Haggerty, 1990, The effects of serpentinization on density and magnetic susceptibility: a petrophysical model, Physics of the Earth and Planetary Interiors, v. 65, p. 137-157.

Trzcienski, W. E., Jr., 1994, Évidence des roches de Grenville recyclées dans la diamictite de Chain Lakes, les roches ultramafiques des Appalaches du Québec et dans des dykes montérégiens, La Revue Géologique du Québec, v. 1, p. 36-38.

Trzcienski, W. E., Jr. and L. P. Gromet, 1992, Inherited Precambrian zircons in ultramafic/mafic rocks of the Québec ophiolite belt, EOS, Transactions, American Geophysical Union, v. 73, p. 359-360.

Turner, F. J., 1933, The metamorphic and intrusive rocks of southern Westland, Transactions of the New Zealand Institute, v. 63, p. 269-276.

Ulmer, P. and V. Trommsdorff, 1995, Serpentine stability to mantle depths and subduction-related magmatism, Science, v. 268, p. 858-861.

Upreti, M. C. and A. G. Walton, 1966, Heterogeneous nucleation of alkali halide crystals from solution, Journal of Chemical Physics, v. 44, p. 1936-1939.

Valley, J. W., Peacor, D. R., Bowman, J. R. Essene, E. J. and M. J. Allard, 1985, Crystal chemistry of a Mg-vesuvianite and implications of phase equilibria in the system CaO-MgO-Al_2O_3-SiO_2-H_2O-CO_2, Journal of Metamorphic Geology, v. 3, p. 137-153.

van der Laan, G. P. and A. A. C. M. Beenackers, 1999, Kinetics and selectivity of the Fischer-Tropsch synthesis: a literature review, Catalysis Reviews – Science and Engineering, v. 41, p. 255-318.

Von Damm, K. L., 1990, Seafloor hydrothermal activity: black smoker chemistry and chimneys, Annual Reviews of Earth and Planetary Science, v. 18, p. 173-204.

Walton, A. G., 1969, Nucleation in liquids and solutions, *in* Nucleation, Zettlemoyer, A. C., editor, Marcel Dekker Inc., New York, p. 225-307.

Wannamaker, B. J., Wong, T.-F. and B. Evans, 1990, Decrepitation and crack healing of fluid inclusions in San Carlos olivine, Journal of Geophysical Research, v. 95, p. 15,623-15,641.

Wares, R. P. and R. F. Martin, 1980, Rodingitization of granite and serpentinite in the Jeffrey mine, Asbestos, Quebec, Canadian Mineralogist, v. 18, p. 231-240.

Wares, R. P. and R. F. Martin, 1980, Rodingitization of dyke rocks and enclosing serpentinites in the Jeffrey mine, Quebec Appalachians, Archives des Sciences de la Société de Physique et d'Histoire Naturelle de Genève, v. 33, p. 301-310.

Wegner, W. W. and W. G. Ernst, 1983, Experimentally determined hydration and dehydration reaction rates in the system MgO-SiO_2-H_2O, American Journal of Science, v. 283A, p. 151-180.

Weill, H., Rossiter, C. E., Waggenspack, C., Jones, R. N. and M. M. Ziskind, 1977, Differences in lung effects resulting from chrysotile and crocidolite exposure, *in* Proceedings of Fourth International Symposium on Inhaled Particles and Vapors, Walton W. H., editor, Pergamon Press, Oxford, p. 789.

Welhan, J. A., 1987, Characteristics of abiotic methane in rocks, *in* Saline water and gases in crystalline rocks, Fritz, P. and S. K. Frappe, editors, Geological Association of Canada Special Paper, 33, p. 225-233.

Welhan, J. A., 1988, Origins of methane in hydrothermal systems, Chemical Geology, v. 71, p. 183-198.

Welhan, J. A. and H. Craig, 1979, Methane and hydrogen in East Pacific Rise hydrothermal fluids, Geophysical Research Letters, v. 6, p. 829-831.

Wenner, D. B., 1979, Hydrogen, oxygen and carbon isotopic evidence for the origin of rodingites in serpentinized ultramafic rocks, Geochimica et Cosmochimica Acta, v. 43, p. 603-614.

Wenner, D. B. and H. P. Taylor, Jr., 1973, Oxygen and hydrogen isotope studies of the serpentinization of ultramafic rocks in oceanic environments and continental ophiolite complexes, American Journal of Science, v. 273, p. 207-239.

Wenner, D. B. and H. P. Taylor, Jr., 1974, D/H and O^{18}/O^{16} studies of serpentinization of ultramafic rocks, Geochimica et Cosmochimica Acta, v. 38, p. 1255-1286.

Whitehead, J., Dunning, G. R. and J. G. Spray, 2000, U-Pb geochronology and origin of granitoid rocks in the Thetford Mines ophiolite, Canadian Appalachians, Geological Society of America Bulletin, v. 112, p. 915-928.

Whitehead, J., Reynolds, P. H. and J. G. Spray, 1995, The sub-ophiolitic metamorphic rocks of the Québec Appalachians, Journal of Geodynamics, v. 19, p. 325-350.

Whitehead, J., Reynolds, P. H. and J. G. Spray, 1996, $^{40}Ar/^{39}Ar$ age constraints on Taconian and Acadian events in the Quebec Appalachians, Geology, v. 24, p. 359-362.

Wicks, F. J. and A. G. Plant, 1979, Electron-microprobe and X-ray-microbeam studies of serpentine textures, Canadian Mineralogist, v. 17, p. 785-830.

Wicks, F. J. and E. J. W. Whittaker, 1975, A reappraisal of the structures of the serpentine minerals, Canadian Mineralogist, v. 13, p. 227-243.

Wicks, F. J. and E. J. W. Whittaker, 1977, Serpentine textures and serpentinization, Canadian Mineralogist, v. 15, p. 459-488.

Wicks, F. J., Whittaker, E. J. W. and J. Zussman, 1977, An idealized model for serpentine textures after olivine, Canadian Mineralogist, v. 15, p. 446-458.

Williams, H. and P. St-Julien, 1982, The Baie Verte-Brompton line: early Paleozoic continent-ocean interface in the Canadian Appalachians, Geological Association of Canada Special Paper 24, p. 177-207.

Williams-Jones, A. E. and I. M. Samson, 1990, Theoretical estimation of halite solubility in the system $NaCl-CaCl_2-H_2O$: applications to fluid inclusions, Canadian Mineralogist, v. 28, p. 299-304.

Williams-Jones, A. E., Wood, S. A., Mountain, B. W. and C. H. Gammons, 1994, Experimental water-rock interaction: applications to ore-forming hydrothermal systems, *in* Alteration and alteration processes associated with ore-forming systems,

Lentz, D. R., editor, Geological Association of Canada Short Course Notes, v. 11, p. 131-160.

Wolery, T. J., 1992, EQ3/6, a software package for geochemical modeling of aqueous systems: package overview and installation guide (version 7.0), Lawrence Livermore National Laboratory UCRL-MA-110662, Part I, 66 p.

Wu, W. and G. H. Nancollas, 1996, Interfacial free energies and crystallization in aqueous media, Journal of Colloid and Interface Science, v. 182, p. 365-373.

Yada, K. and K. Iishi, 1974, Serpentine minerals hydrothermally synthesized and their microstructures, Journal of Crystal Growth, v. 24/25, p. 627-630.

Yada, K. and K. Iishi, 1977, Growth and microstructure of synthetic chrysotile, American Mineralogist, v. 62, p. 958-965.

Yale, L. B., 1983, An investigation of serpentinization and rodingitization, M. Sc. Thesis, Stanford University, California, 113 p.

Yardley, B. W. D. and G. E. Lloyd, 1995, Why metasomatic fronts are really metasomatic sides, Geology, v. 23, p. 53-56.

Yardley, B. W. D., Rochelle, C. A., Barnicoat, A. C. and G. E. Lloyd, 1991, Oscillatory zoning in metamorphic minerals: an indicator of infiltration metasomatism, Mineralogical Magazine, v. 55, p. 357-365.

Yui, T. -F., Yeh, H. -W. and C. H. Lee, 1988, Stable isotope studies of nephrite deposits from Fengtien, Taiwan, Geochimica et Cosmochimica Acta, v. 52, p. 593-602.

APPENDIX I

ALTERATION OF GRANITE BY DIOPSIDE-SATURATED SERPENTINIZING FLUIDS: MULTIPLE PASS CALCULATIONS BASED ON A LOCAL EQUILIBRIUM, ONE-DIMENSIONAL FLOW-LINE BOX MODEL.

The preliminary multiple pass calculations discussed in Chapter V were based on a local equilibrium, one-dimensional 'flow-line' box model (Heinrich et al., 1996) involving the reaction of a diopside-saturated serpentinizing fluid with a granite (sample E:75, refer to Chapter IV for composition). Temperatures of 345-340°C were chosen on the basis of fluid inclusion data from rodingitized granite (refer to Chapter VI). The starting composition of the fluid used in the modelling reflected equilibrium with the mineral assemblage antigorite + brucite + diopside. Concentrations of 1.0 *m*, 0.78 *m* and 0.05 *m* were selected for Cl, Na and K, respectively. The relative concentrations of Cl, Na and K in this fluid are consistent with those reflecting equilibrium with greenschist-grade, altered basaltic rocks, and are typical of those observed in sub-seafloor hydrothermal fluids. The Ca concentration of the fluid in equilibrium with the assemblage antigorite + brucite + diopside was calculated to be 0.09 *m*. The multiple pass calculations were performed using transient fluid/rock ratios of 3 (Table 1, Figures 1 and 2) and 10 (Table 2, Figures 3 and 4), and one representative elementary volume of rock (REV) taken to represent granite directly in contact with serpentinite. The Hch package of programs (Shvarov and Bastrakov, 1999) was used for this purpose, and employed thermodynamic data for minerals and aqueous species from SUPCRT92 (Johnson et al., 1992), Shock et al. (1997) and Sverjensky et al. (1997). According to the calculations, very large amounts of serpentinizing fluids (fluid/rock ratios > 300) would be necessary to produce rodingites in which grossular is the dominant mineral. Calculations also indicate that rodingitization would be accompanied by a 42 % reduction in the volume of the REV. The modelling approach used here assumed local equilibrium, and did not consider the possible complications that could arise from kinetic factors or from the presence of counter-diffusing concentration gradients. Future evaluations of the physico-chemical controls of rodingitization will have to address these effects. Use of a wider range of starting Na/Cl and Ca/Cl compositions will provide information on the importance of variable Ca concentrations in rodingitization.

REFERENCES

Heinrich, C. A., Walshe, J. L. and B. P. Harrold, 1996, Chemical mass transfer modelling of ore-forming hydrothermal systems: current practice and problems, Ore Geology Reviews, v. 10, p. 319-338.

Johnson, J. W., Oelkers, E. H. and H. C. Helgeson, 1992, SUPCRT92: A software package for calculating the standard molal thermodynamic properties of minerals, gases, aqueous species, and reactions from 1 to 5000 bars and 0° to 1000°C, Computers and Geoscience, vol. 17, p. 899-947.

Shock, E. L., Sassani, D. C., Willis, M. and D. A. Sverjensky, 1997, Inorganic species in geologic fluids: Correlations among standard molal thermodynamic properties of aqueous ions and hydroxide complexes, Geochimica et Cosmochimica Acta, v. 61, p. 907-950.

Shvarov, Y. and E. Bastrakov, 1999, HCh: a software package for geochemical equilibrium modelling. User's guide, Australian Geological Survey Organization, Record 1999/25, 61 p.

Sverjensky, D. A., Shock, E. L. and H. C. Helgeson, 1997, Prediction of the thermodynamic properties of aqueous metal complexes to 1000°C and 5 kb, Geochimica et Cosmochimica Acta, v. 61, p. 1359-1412.

Table 1. Calculated mineralogical (cm^3) and fluid (molal) compositions. Model 1.
Fluid/Flt E:53, 1000 passes at transient w/r(mass)=3, 1 REV. T = 345°C; P = 1000 bars.

Step	0	1	2	3	4	5	6	7	8	111	112	115	116	117	123
Quartz	24.52	27.84	31.16	34.47	37.79	41.11	44.43	46.76	47.21	2.16	1.68	0.16			
Diaspore															
Apatite-OH	0.41	0.41	0.41	0.41	0.41	0.41	0.41	0.41	0.41	0.41	0.41	0.41	0.41	0.41	0.41
Grossular															
Diopside													0.98	1.61	5.41
Tremolite	9.00	9.00	9.00	9.00	9.00	9.00	9.00	9.00	8.99	8.39	8.39	8.39	7.58	6.59	0.64
Muscovite	12.50	13.61	14.73	15.84	16.96	18.08	19.19	19.97	20.09	0.05					
Phlogopite														0.43	2.98
Margarite															
Prehnite											0.29	1.48			
Zoisite	3.81	6.48	9.16	11.83	14.51	17.18	19.86	21.88	22.65	42.05	41.91	41.14	42.10	41.97	41.19
Clinochlore															
Albite	33.28	28.15	23.02	17.89	12.75	7.62	2.49								
Microcline	26.73	23.29	19.85	16.41	12.97	9.53	6.09	2.14							
pH	5.35	5.35	5.35	5.35	5.35	5.35	5.35	5.31	5.21	5.13	5.33	5.33	5.46	5.60	5.60
Cl^-	6.2E-01	6.2E-01	6.2E-01	6.2E-01	6.2E-01	6.2E-01	6.2E-01	6.2E-01	6.1E-01	6.1E-01	6.1E-01	6.1E-01	6.1E-01	6.1E-01	6.1E-01
HCl°	7.7E-05	7.7E-05	7.7E-05	7.7E-05	7.7E-05	7.7E-05	7.7E-05	8.5E-05	1.1E-04	1.3E-04	8.1E-05	8.1E-05	5.9E-05	4.3E-05	4.3E-05
Na^+	5.1E-01	5.1E-01	5.1E-01	5.1E-01	5.1E-01	5.1E-01	5.1E-01	4.9E-01	4.8E-01	4.8E-01	4.8E-01	4.8E-01	4.8E-01	4.8E-01	4.8E-01
NaOH°	2.7E-06	2.7E-06	2.7E-06	2.7E-06	2.7E-06	2.7E-06	2.7E-06	2.3E-06	1.8E-06	1.5E-06	2.4E-06	2.4E-06	3.2E-06	4.5E-06	4.5E-06
NaCl°	3.2E-01	3.2E-01	3.2E-01	3.2E-01	3.2E-01	3.2E-01	3.2E-01	3.1E-01	3.0E-01	3.0E-01	3.0E-01	3.0E-01	3.0E-01	3.0E-01	3.0E-01
$NaHSiO_3$°	7.3E-06	7.3E-06	7.3E-06	7.3E-06	7.3E-06	7.3E-06	7.3E-06	6.5E-06	4.9E-06	4.1E-06	6.5E-06	6.5E-06	5.3E-06	2.7E-06	2.7E-06
K^+	6.4E-02	6.4E-02	6.4E-02	6.4E-02	6.4E-02	6.4E-02	6.4E-02	7.0E-02	5.9E-02	4.4E-02	4.4E-02	4.3E-02	4.3E-02	4.1E-02	4.1E-02
KOH°	5.9E-07	5.9E-07	5.9E-07	5.9E-07	5.9E-07	5.9E-07	5.9E-07	5.9E-07	4.0E-07	2.5E-07	3.8E-07	3.8E-07	5.2E-07	6.8E-07	6.8E-07
KCl°	1.0E-02	1.0E-02	1.0E-02	1.0E-02	1.0E-02	1.0E-02	1.0E-02	1.1E-02	9.5E-03	7.0E-03	6.9E-03	6.8E-03	6.8E-03	6.4E-03	6.4E-03
Ca^{2+}	4.9E-03	4.9E-03	4.9E-03	4.9E-03	4.9E-03	4.9E-03	4.9E-03	5.9E-03	7.8E-03	8.7E-03	8.8E-03	8.8E-03	8.8E-03	8.9E-03	8.9E-03
$CaOH^+$	6.4E-05	6.4E-05	6.4E-05	6.4E-05	6.4E-05	6.4E-05	6.4E-05	7.0E-05	7.3E-05	6.9E-05	1.1E-04	1.1E-04	1.5E-04	2.1E-04	2.1E-04
$CaCl^+$	3.7E-02	3.7E-02	3.7E-02	3.7E-02	3.7E-02	3.7E-02	3.7E-02	4.5E-02	5.9E-02	6.6E-02	6.7E-02	6.7E-02	6.7E-02	6.8E-02	6.8E-02
$CaCl_2$°	5.3E-03	5.3E-03	5.3E-03	5.3E-03	5.3E-03	5.3E-03	5.3E-03	6.4E-03	8.4E-03	9.3E-03	9.4E-03	9.4E-03	9.4E-03	9.6E-03	9.6E-03
$CaHSiO_3^+$	3.8E-06	3.8E-06	3.8E-06	3.8E-06	3.8E-06	3.8E-06	3.8E-06	4.1E-06	4.3E-06	4.1E-06	6.5E-06	6.5E-06	5.3E-06	2.7E-06	2.7E-06

Table 1. Calculated mineralogical (cm^3) and fluid (molal) compositions. Model 1 (Continued).

Step	0	1	2	3	4	5	6	7	8	111	112	115	116	117	123
Mg^{2+}	1.1E-05	1.1E-05	1.1E-05	1.1E-05	1.1E-05	1.1E-05	1.1E-05	1.4E-05	2.4E-05	3.7E-05	1.0E-05	1.0E-05	9.9E-06	2.0E-05	2.0E-05
$MgOH^{+}$	4.5E-07	4.5E-07	4.5E-07	4.5E-07	4.5E-07	4.5E-07	4.5E-07	4.9E-07	6.8E-07	8.9E-07	3.9E-07	3.9E-07	5.1E-07	1.4E-06	1.4E-06
$MgCl^{+}$	3.1E-05	3.1E-05	3.1E-05	3.1E-05	3.1E-05	3.1E-05	3.1E-05	3.7E-05	6.5E-05	1.0E-04	2.8E-05	2.8E-05	2.7E-05	5.3E-05	5.3E-05
$MgHSiO_3^{+}$	4.4E-09	4.4E-09	4.4E-09	4.4E-09	4.4E-09	4.4E-09	4.4E-09	4.8E-09	6.7E-09	8.7E-09	3.8E-09	3.8E-09	3.0E-09	3.0E-09	3.0E-09
Al^{3+}	1.4E-16	1.4E-16	1.4E-16	1.4E-16	1.4E-16	1.4E-16	1.4E-16	1.9E-16	4.5E-16	8.8E-16	1.2E-16	1.2E-16	5.3E-17	3.5E-17	3.5E-17
AlO_2^{-}	1.1E-05	1.1E-05	1.1E-05	1.1E-05	1.1E-05	1.1E-05	1.1E-05	9.7E-06	8.7E-06	8.5E-06	7.3E-06	7.3E-06	1.1E-05	2.7E-05	2.7E-05
$AlOH^{2+}$	5.9E-13	5.9E-13	5.9E-13	5.9E-13	5.9E-13	5.9E-13	5.9E-13	7.1E-13	1.3E-12	2.2E-12	4.8E-13	4.8E-13	2.8E-13	2.6E-13	2.6E-13
AlO^{+}	1.0E-10	1.0E-10	1.0E-10	1.0E-10	1.0E-10	1.0E-10	1.0E-10	1.1E-10	1.7E-10	2.3E-10	8.0E-11	8.0E-11	6.5E-11	8.2E-11	8.2E-11
$HAlO_2^{\circ}$	7.2E-08	7.2E-08	7.2E-08	7.2E-08	7.2E-08	7.2E-08	7.2E-08	7.2E-08	8.2E-08	9.6E-08	5.2E-08	5.2E-08	5.7E-08	1.0E-07	1.0E-07
$HSiO_3^{-}$	8.2E-06	8.2E-06	8.2E-06	8.2E-06	8.2E-06	8.2E-06	8.2E-06	7.4E-06	5.8E-06	4.9E-06	7.7E-06	7.7E-06	6.3E-06	3.2E-06	3.2E-06
SiO_2°	2.0E-02	2.0E-02	2.0E-02	2.0E-02	2.0E-02	2.0E-02	2.0E-02	2.0E-02	1.9E-02	1.9E-02	1.9E-02	1.9E-02	1.2E-02	4.3E-03	4.3E-03
PO_4^{3-}	1.8E-16	1.8E-16	1.8E-16	1.8E-16	1.8E-16	1.8E-16	1.8E-16	1.4E-16	9.1E-17	7.9E-17	6.7E-17	6.6E-17	6.0E-17	5.2E-17	5.2E-17
HPO_4^{2-}	1.8E-10	1.8E-10	1.8E-10	1.8E-10	1.8E-10	1.8E-10	1.8E-10	1.5E-10	1.3E-10	1.3E-10	7.2E-11	7.2E-11	4.8E-11	3.0E-11	3.0E-11
$H_2PO_4^{-}$	2.4E-08	2.4E-08	2.4E-08	2.4E-08	2.4E-08	2.4E-08	2.4E-08	2.2E-08	2.4E-08	2.9E-08	1.0E-08	9.9E-09	4.8E-09	2.2E-09	2.2E-09
$H_3PO_4^{\circ}$	4.6E-10	4.6E-10	4.6E-10	4.6E-10	4.6E-10	4.6E-10	4.6E-10	4.6E-10	6.5E-10	9.6E-10	2.1E-10	2.1E-10	7.4E-11	2.4E-11	2.4E-11
$P_2O_7^{4-}$	5.5E-19	5.5E-19	5.5E-19	5.5E-19	5.5E-19	5.5E-19	5.5E-19	3.8E-19	2.7E-19	2.9E-19	8.4E-20	8.3E-20	3.6E-20	1.4E-20	1.4E-20
$HP_2O_7^{3-}$	3.4E-14	3.4E-14	3.4E-14	3.4E-14	3.4E-14	3.4E-14	3.4E-14	2.6E-14	2.4E-14	3.0E-14	5.5E-15	5.5E-15	1.8E-15	5.0E-16	5.0E-16
$H_2P_2O_7^{2-}$	2.5E-13	2.5E-13	2.5E-13	2.5E-13	2.5E-13	2.5E-13	2.5E-13	2.1E-13	2.5E-13	3.8E-13	4.5E-14	4.5E-14	1.1E-14	2.2E-15	2.2E-15
$H_3P_2O_7^{-}$	2.1E-16	2.1E-16	2.1E-16	2.1E-16	2.1E-16	2.1E-16	2.1E-16	1.9E-16	2.9E-16	5.3E-16	3.9E-17	3.9E-17	6.8E-18	1.0E-18	1.0E-18
$H_4P_2O_7^{\circ}$	5.5E-19	5.5E-19	5.5E-19	5.5E-19	5.5E-19	5.5E-19	5.5E-19	5.5E-19	1.1E-18	2.3E-18	1.1E-19	1.1E-19	1.4E-20	1.5E-21	1.5E-21

Table 1. Calculated mineralogical (cm^3) and fluid (molal) compositions. Model 1 (Continued).

Step	124	125	130	131	165	166	167	265	266	317	318	452	453	454	1000
Quartz															
Diaspore									0.01	2.84	2.89	0.00			
Apatite-OH	0.41	0.41	0.41	0.41	0.41	0.41	0.41	0.41	0.41	0.41	0.41	0.41	0.41	0.41	0.41
Grossular		0.24	1.43	1.69	14.64	14.81	15.01	34.63	34.79	40.11	40.20	40.21	40.21	40.20	37.19
Diopside	5.86	5.89	6.01	6.01	0.04									0.00	2.38
Tremolite															
Muscovite															
Phlogopite	3.19	2.73	0.41												
Margarite							0.09	8.78	8.79	0.15					
Prehnite															
Zoisite	41.11	40.92	39.94	39.73	28.69	28.53	28.24	0.19							
Clinochlore	0.03	0.40	2.24	2.58	6.30	6.33	6.33	6.35	6.35	6.36	6.36	6.46	6.46	6.46	5.43
Albite															
Microcline															
pH	5.79	5.86	5.86	5.86	5.85	6.14	6.15	6.15	6.18	6.18	6.26	6.60	6.75	6.78	6.78
Cl^-	6.1E-01	6.1E-01	6.1E-01	6.1E-01	6.1E-01	6.1E-01	6.1E-01	6.1E-01	6.1E-01	6.1E-01	6.1E-01	6.1E-01	6.1E-01	6.1E-01	6.1E-01
HCl°	2.8E-05	2.4E-05	2.4E-05	2.4E-05	2.4E-05	1.2E-05	1.2E-05	1.2E-05	1.1E-05	1.1E-05	9.4E-06	4.3E-06	3.1E-06	2.9E-06	2.9E-06
Na^+	4.8E-01	4.8E-01	4.8E-01	4.8E-01	4.8E-01	4.8E-01	4.8E-01	4.8E-01	4.8E-01	4.8E-01	4.8E-01	4.8E-01	4.8E-01	4.8E-01	4.8E-01
NaOH°	6.8E-06	8.0E-06	8.0E-06	8.0E-06	7.9E-06	1.5E-05	1.6E-05	1.6E-05	1.7E-05	1.7E-05	2.0E-05	4.5E-05	6.2E-05	6.6E-05	6.6E-05
NaCl°	3.0E-01	3.0E-01	3.0E-01	3.0E-01	3.0E-01	3.0E-01	3.0E-01	3.0E-01	3.0E-01	3.0E-01	3.0E-01	3.0E-01	3.0E-01	3.0E-01	3.0E-01
$NaHSiO_3$°	2.1E-06	2.0E-06	2.0E-06	2.0E-06	2.0E-06	4.2E-07	4.2E-07	4.2E-07	3.7E-07	3.7E-07	3.1E-07	1.4E-07	3.4E-07	5.7E-07	5.7E-07
K^+	4.2E-02	4.6E-02	4.6E-02	4.6E-02	4.3E-02	4.3E-02	4.3E-02	4.3E-02	4.3E-02	4.3E-02	4.3E-02	4.3E-02	4.3E-02	4.3E-02	4.3E-02
KOH°	1.1E-06	1.4E-06	1.4E-06	1.4E-06	1.3E-06	2.5E-06	2.5E-06	2.5E-06	2.7E-06	2.7E-06	3.3E-06	7.2E-06	1.0E-05	1.1E-05	1.1E-05
KCl°	6.7E-03	7.3E-03	7.3E-03	7.2E-03	6.8E-03	6.8E-03	6.8E-03	6.8E-03	6.8E-03	6.8E-03	6.8E-03	6.8E-03	6.8E-03	6.8E-03	6.8E-03
Ca^{2+}	8.8E-03	8.6E-03	8.6E-03	8.6E-03	8.8E-03	8.8E-03	8.8E-03	8.8E-03	8.8E-03	8.8E-03	8.8E-03	8.8E-03	8.7E-03	8.7E-03	8.7E-03
$CaOH^+$	3.2E-04	3.6E-04	3.6E-04	3.6E-04	3.6E-04	7.1E-04	7.2E-04	7.2E-04	7.8E-04	7.8E-04	9.3E-04	2.1E-03	2.8E-03	3.0E-03	3.0E-03
$CaCl^+$	6.7E-02	6.6E-02	6.6E-02	6.6E-02	6.7E-02	6.7E-02	6.7E-02	6.7E-02	6.7E-02	6.7E-02	6.7E-02	6.7E-02	6.6E-02	6.6E-02	6.6E-02
$CaCl_2$°	9.5E-03	9.3E-03	9.3E-03	9.3E-03	9.4E-03	9.4E-03	9.4E-03	9.4E-03	9.4E-03	9.4E-03	9.4E-03	9.4E-03	9.3E-03	9.3E-03	9.3E-03
$CaHSiO_3^+$	2.1E-06	2.0E-06	2.0E-06	2.0E-06	2.0E-06	4.2E-07	4.1E-07	4.1E-07	3.6E-07	3.6E-07	3.1E-07	1.4E-07	3.3E-07	5.6E-07	5.6E-07

Table 1. Calculated mineralogical (cm^3) and fluid (molal) compositions. Model 1 (Continued).

Step	124	125	130	131	165	166	167	265	266	317	318	452	453	454	1000
Mg^{2+}	1.4E-05	1.1E-05	1.1E-05	1.1E-05	1.1E-05	6.7E-06	6.6E-06	6.6E-06	6.2E-06	6.2E-06	5.4E-06	2.9E-06	2.2E-06	2.1E-06	2.1E-06
$MgOH^{+}$	1.5E-06	1.4E-06	1.4E-06	1.4E-06	1.4E-06	1.6E-06	1.6E-06	1.6E-06	1.7E-06	1.7E-06	1.7E-06	2.0E-06	2.1E-06	2.2E-06	2.2E-06
$MgCl^{+}$	3.6E-05	3.0E-05	3.0E-05	3.0E-05	3.0E-05	1.8E-05	1.8E-05	1.8E-05	1.7E-05	1.7E-05	1.4E-05	7.6E-06	5.8E-06	5.5E-06	5.5E-06
$MgHSiO_3^{+}$	1.7E-09	1.3E-09	1.3E-09	1.3E-09	1.3E-09	1.6E-10	1.6E-10	1.6E-10	1.3E-10	1.3E-10	9.3E-11	2.3E-11	4.2E-11	6.7E-11	6.7E-11
Al^{3+}	1.1E-17	6.8E-18	6.8E-18	6.8E-18	7.0E-18	3.6E-18	3.6E-18	3.6E-18	2.9E-18	2.9E-18	1.7E-18	1.6E-19	9.9E-21	3.3E-21	3.3E-21
AlO_2^{-}	4.5E-05	5.3E-05	5.3E-05	5.3E-05	5.2E-05	3.9E-04	4.0E-04	4.0E-04	4.7E-04	4.7E-04	5.5E-04	1.2E-03	2.8E-04	1.2E-04	1.2E-04
$AlOH^{2+}$	1.2E-13	9.0E-14	9.0E-14	9.1E-14	9.2E-14	9.2E-14	9.2E-14	9.2E-14	8.3E-14	8.3E-14	5.8E-14	1.2E-14	1.0E-15	3.7E-16	3.7E-16
AlO^{+}	5.9E-11	5.1E-11	5.1E-11	5.1E-11	5.1E-11	1.0E-10	1.0E-10	1.0E-10	9.9E-11	9.9E-11	8.3E-11	3.8E-11	4.4E-12	1.7E-12	1.7E-12
$HAlO_2^{\circ}$	1.1E-07	1.1E-07	1.1E-07	1.1E-07	1.1E-07	4.3E-07	4.3E-07	4.3E-07	4.6E-07	4.6E-07	4.6E-07	4.6E-07	7.6E-08	3.1E-08	3.1E-08
$HSiO_3^{-}$	2.5E-06	2.4E-06	2.4E-06	2.4E-06	2.4E-06	5.0E-07	4.9E-07	4.9E-07	4.3E-07	4.3E-07	3.6E-07	1.6E-07	4.0E-07	6.7E-07	6.7E-07
SiO_2°	2.2E-03	1.8E-03	1.8E-03	1.8E-03	1.8E-03	1.9E-04	1.9E-04	1.9E-04	1.5E-04	1.5E-04	1.1E-04	2.2E-05	3.9E-05	6.1E-05	6.1E-05
PO_4^{3-}	4.6E-17	4.6E-17	4.6E-17	4.6E-17	4.4E-17	3.6E-17	3.5E-17	3.5E-17	3.4E-17	3.4E-17	3.3E-17	2.5E-17	2.3E-17	2.2E-17	2.2E-17
HPO_4^{2-}	1.7E-11	1.5E-11	1.5E-11	1.5E-11	1.4E-11	5.9E-12	5.8E-12	5.8E-12	5.2E-12	5.2E-12	4.1E-12	1.4E-12	9.4E-13	8.6E-13	8.6E-13
$H_2PO_4^{-}$	8.3E-10	6.0E-10	6.0E-10	6.0E-10	6.0E-10	1.2E-10	1.2E-10	1.2E-10	1.0E-10	1.0E-10	6.6E-11	1.1E-11	5.0E-12	4.2E-12	4.2E-12
$H_3PO_4^{\circ}$	6.0E-12	3.7E-12	3.7E-12	3.7E-12	3.7E-12	4.0E-13	3.9E-13	3.9E-13	2.9E-13	2.9E-13	1.6E-13	1.2E-14	4.0E-15	3.1E-15	3.1E-15
$P_2O_7^{4-}$	4.8E-21	3.5E-21	3.5E-21	3.5E-21	3.3E-21	5.6E-22	5.5E-22	5.5E-22	4.3E-22	4.3E-22	2.7E-22	3.4E-23	1.4E-23	1.2E-23	1.2E-23
$HP_2O_7^{3-}$	1.1E-16	6.8E-17	6.8E-17	6.8E-17	6.6E-17	5.7E-18	5.5E-18	5.5E-18	4.0E-18	4.0E-18	2.1E-18	1.2E-19	3.6E-20	2.8E-20	2.8E-20
$H_2P_2O_7^{2-}$	3.1E-16	1.6E-16	1.6E-16	1.6E-16	1.6E-16	7.0E-18	6.8E-18	6.8E-18	4.5E-18	4.5E-18	2.0E-18	5.1E-20	1.1E-20	8.1E-21	8.1E-21
$H_3P_2O_7^{-}$	9.5E-20	4.2E-20	4.2E-20	4.2E-20	4.2E-20	9.4E-22	9.0E-22	9.0E-22	5.5E-22	5.5E-22	2.0E-22	2.4E-24	3.8E-25	2.5E-25	2.5E-25
$H_4P_2O_7^{\circ}$	9.2E-23	3.5E-23	3.5E-23	3.5E-23	3.5E-23	4.0E-25	3.8E-25	3.8E-25	2.1E-25	2.1E-25	6.7E-26	3.5E-28	4.0E-29	2.5E-29	2.5E-29

Figure 1

Diagram showing the calculated changes in the volumes of minerals formed during progressive steps of alteration of granitic sample E:75 by a fluid (see text) equilibrated with the assemblage antigorite + brucite + diopside. The mineral proportions at each step were calculated for reaction at a transient fluid/rock ratio of 3.

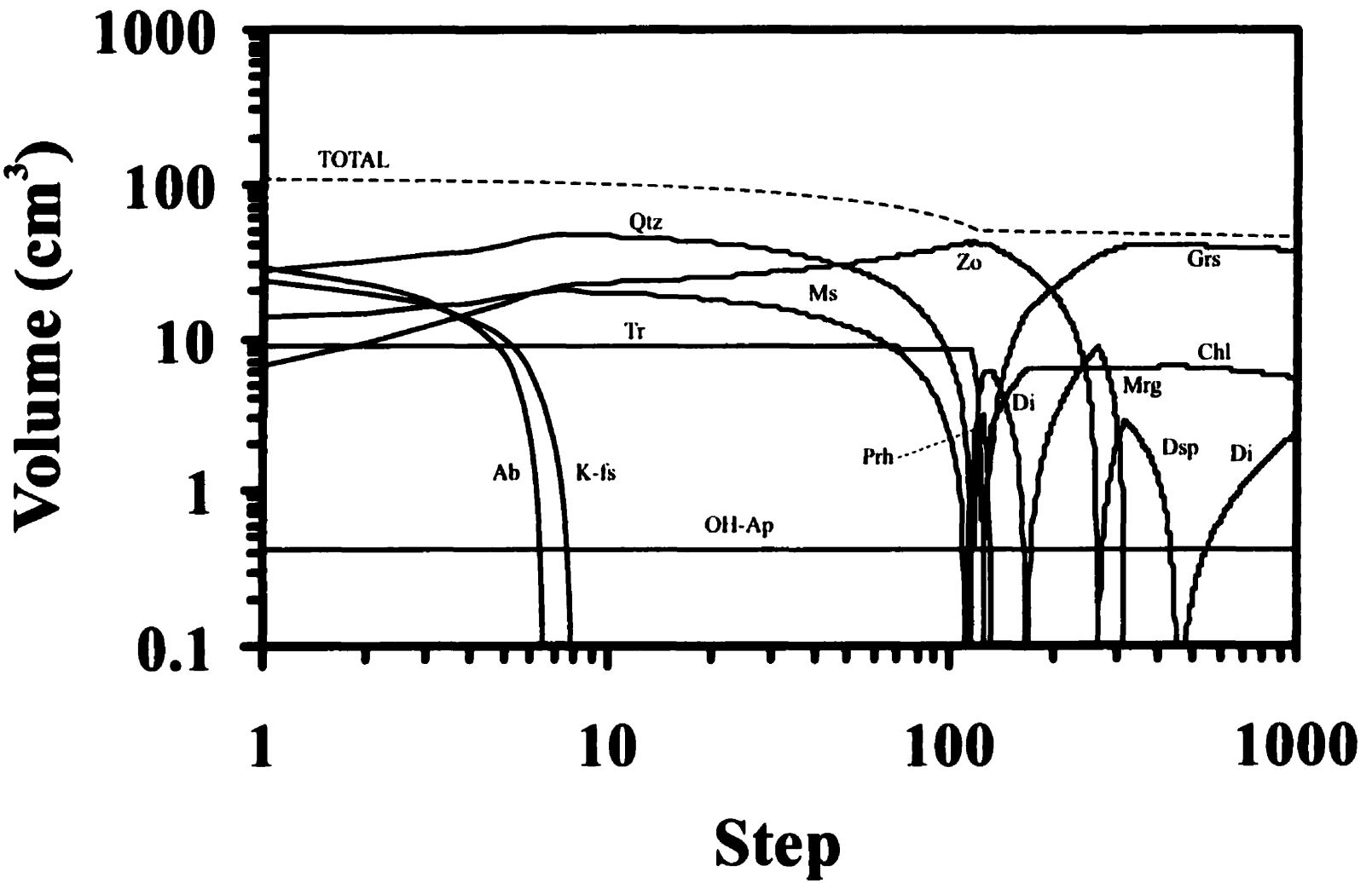
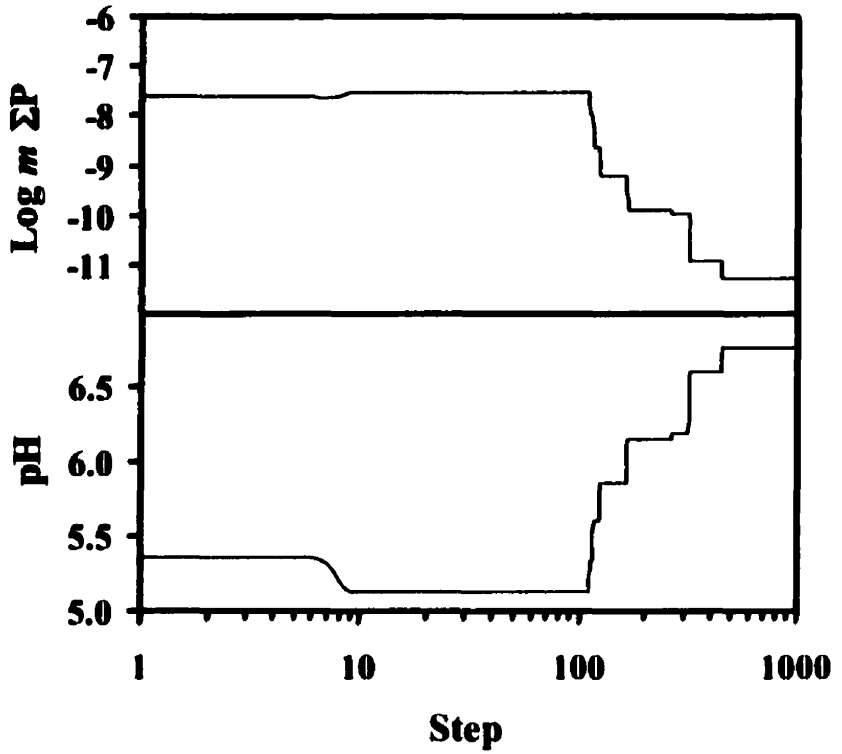

1000
100
10
1
0.1
Volume (cm3)
TOTAL
Qtz
Zo
Grs
Ms
Tr
Chl
Mrg
Di
Prh
Dsp
Di
Ab
K-fs
OH-Ap
1
10
100
1000
Step

Figure 2

A series of diagrams showing the calculated changes in fluid composition during progressive steps of alteration of the granitic sample E:75. The initial composition of the fluid corresponds to equilibrium with the assemblage antigorite + brucite + diopside. Each step represents reaction of the fluid at a transient water/rock ratio of 3 with the rock which becomes progressively more altered.


Log m ΣP
-6
-7
-8
-9
-10
-11
pH
6.5
6.0
5.5
5.0
1
10
100
1000
Step

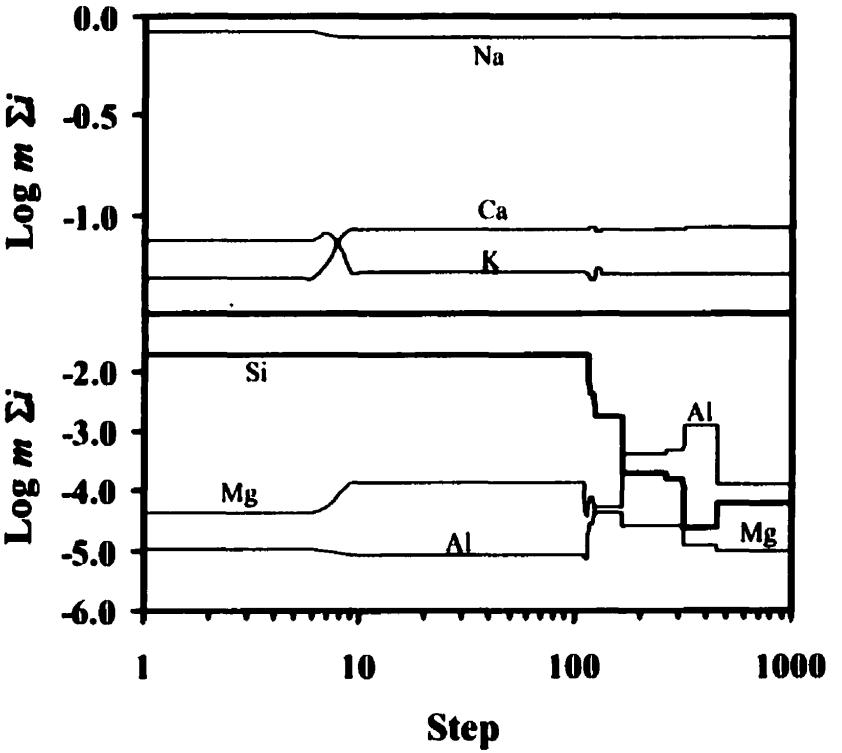

Log m Σi
0.0
-0.5
-1.0
Na
Ca
K
Log m Σi
-2.0
-3.0
-4.0
-5.0
-6.0
Si
Al
Mg
Al
Mg
1
10
100
1000
Step

Table 2. Calculated mineralogical (mol %) and fluid (molal) compositions. Model 2.
Fluid/Flt E:53, 300 passes at transient w/r(mass)=10, 1 REV. T = 340°C; P = 1000 bars.

Step	0	1	2	3	33	34	38	39	40	41	42	43
Quartz	28.16	38.45	47.25	47.16	14.02	11.76	1.65					
Diaspore												
Grossular												2.04
Diopside								1.46	8.76	12.54	15.14	14.48
Tremolite	8.39	8.73	9.06	9.18	14.35	14.60	15.70	14.74	9.15	3.36		
Muscovite	12.25	15.78	18.78	18.62	0.11							
Phlogopite										2.47	3.01	2.15
Margarite												
Prehnite						1.93	11.45	11.16				
Zoisite	9.03	16.84	23.76	25.04	71.53	71.71	71.20	72.64	82.09	81.63	81.37	79.71
Clinochlore											0.48	1.62
Albite	22.08	8.67										
Microcline	20.10	11.53	1.15									
pH	5.36	5.36	5.33	5.17	5.15	5.32	5.32	5.47	5.56	5.62	5.84	5.86
Cl^-	6.3E-01	6.3E-01	6.3E-01	6.2E-01	6.2E-01	6.2E-01	6.2E-01	6.2E-01	6.2E-01	6.2E-01	6.2E-01	6.2E-01
HCl°	7.0E-05	7.0E-05	7.5E-05	1.1E-04	1.1E-04	7.6E-05	7.6E-05	5.4E-05	4.4E-05	3.8E-05	2.3E-05	2.2E-05
Na^+	5.2E-01	5.2E-01	5.0E-01	4.9E-01	4.9E-01	4.9E-01	4.9E-01	4.9E-01	4.9E-01	4.9E-01	4.9E-01	4.9E-01
NaOH°	2.7E-06	2.7E-06	2.5E-06	1.6E-06	1.6E-06	2.3E-06	2.3E-06	3.3E-06	4.0E-06	4.6E-06	7.6E-06	8.0E-06
NaCl°	3.1E-01	3.1E-01	3.1E-01	2.9E-01	2.9E-01	2.9E-01	2.9E-01	2.9E-01	2.9E-01	2.9E-01	2.9E-01	2.9E-01
$NaHSiO_3$°	7.7E-06	7.7E-06	7.0E-06	4.7E-06	4.5E-06	6.7E-06	6.7E-06	6.0E-06	4.0E-06	2.9E-06	2.2E-06	2.2E-06
K^+	6.3E-02	6.3E-02	6.7E-02	4.8E-02	4.5E-02	4.4E-02	4.4E-02	4.4E-02	4.4E-02	4.1E-02	4.3E-02	4.4E-02
KOH°	5.8E-07	5.8E-07	5.8E-07	2.8E-07	2.6E-07	3.7E-07	3.7E-07	5.2E-07	6.3E-07	6.9E-07	1.2E-06	1.3E-06
KCl°	9.5E-03	9.5E-03	1.0E-02	7.1E-03	6.7E-03	6.5E-03	6.5E-03	6.5E-03	6.5E-03	6.1E-03	6.4E-03	6.6E-03

Table 2. Calculated mineralogical (mol %) and fluid (molal) compositions. Model 2 (Continued).

Step	0	1	2	3	33	34	38	39	40	41	42	43
Ca^{2+}	5.4E-03	5.4E-03	6.2E-03	9.2E-03	9.4E-03	9.5E-03	9.5E-03	9.5E-03	9.5E-03	9.6E-03	9.5E-03	9.4E-03
$CaOH^+$	6.7E-05	6.7E-05	7.1E-05	7.3E-05	7.2E-05	1.1E-04	1.1E-04	1.5E-04	1.8E-04	2.1E-04	3.5E-04	3.7E-04
$CaCl^+$	3.9E-02	3.9E-02	4.4E-02	6.5E-02	6.6E-02	6.6E-02	6.7E-02	6.7E-02	6.7E-02	6.8E-02	6.7E-02	6.6E-02
$CaCl_2^\circ$	5.3E-03	5.3E-03	6.0E-03	8.7E-03	8.9E-03	9.0E-03	9.0E-03	9.0E-03	9.0E-03	9.1E-03	9.0E-03	8.9E-03
$CaHSiO_3^+$	4.1E-06	4.1E-06	4.4E-06	4.4E-06	4.4E-06	6.5E-06	6.5E-06	5.9E-06	3.9E-06	2.9E-06	2.2E-06	2.1E-06
Mg^{2+}	1.2E-05	1.2E-05	1.4E-05	3.3E-05	3.6E-05	1.2E-05	1.2E-05	9.7E-06	1.4E-05	2.0E-05	1.3E-05	1.2E-05
$MgOH^+$	4.4E-07	4.4E-07	4.7E-07	7.9E-07	8.3E-07	4.1E-07	4.1E-07	4.6E-07	8.5E-07	1.4E-06	1.4E-06	1.4E-06
$MgCl^+$	3.0E-05	3.0E-05	3.4E-05	8.4E-05	9.1E-05	3.0E-05	3.0E-05	2.4E-05	3.6E-05	5.0E-05	3.2E-05	3.0E-05
$MgHSiO_3^+$	4.5E-09	4.5E-09	4.8E-09	8.2E-09	8.6E-09	4.2E-09	4.2E-09	3.0E-09	3.0E-09	3.1E-09	1.5E-09	1.4E-09
Al^{3+}	1.5E-16	1.5E-16	1.8E-16	7.1E-16	8.1E-16	1.5E-16	1.5E-16	5.4E-17	4.1E-17	3.5E-17	8.6E-18	7.3E-18
AlO_2^-	1.0E-05	1.0E-05	9.7E-06	8.5E-06	8.4E-06	7.4E-06	7.4E-06	1.0E-05	1.8E-05	2.6E-05	4.9E-05	5.2E-05
$AlOH^{2+}$	5.8E-13	5.8E-13	6.7E-13	1.8E-12	2.0E-12	5.4E-13	5.4E-13	2.8E-13	2.6E-13	2.5E-13	1.0E-13	9.2E-14
AlO^+	1.1E-10	1.1E-10	1.1E-10	2.1E-10	2.2E-10	8.9E-11	8.9E-11	6.4E-11	7.3E-11	8.2E-11	5.5E-11	5.2E-11
$HAlO_2^\circ$	7.3E-08	7.3E-08	7.3E-08	9.3E-08	9.6E-08	5.7E-08	5.7E-08	5.7E-08	7.9E-08	1.0E-07	1.1E-07	1.2E-07
$HSiO_3^-$	8.6E-06	8.6E-06	8.0E-06	5.5E-06	5.3E-06	7.8E-06	7.8E-06	7.0E-06	4.7E-06	3.4E-06	2.6E-06	2.6E-06
SiO_2°	1.9E-02	1.9E-02	1.9E-02	1.9E-02	1.9E-02	1.9E-02	1.9E-02	1.2E-02	6.5E-03	4.1E-03	1.9E-03	1.8E-03

Table 2. Calculated mineralogical (mol %) and fluid (molal) compositions. Model 2 (Continued).

Step	45	46	57	58	59	85	86	100	101	139	140	141	300
Quartz													
Diaspore							0.02	5.27	5.35	0.07			
Grossular	6.14	8.33	33.99	35.82	37.11	70.38	71.56	81.84	82.22	86.75	86.82	86.80	84.27
Diopside	13.15	12.29	0.73									0.03	4.63
Tremolite													
Muscovite													
Phlogopite	0.42												
Margarite					0.58	15.65	16.07	0.47					
Prehnite													
Zoisite	76.39	74.59	53.25	51.70	49.83	1.62							
Clinochlore	3.89	4.78	12.03	12.48	12.48	12.35	12.35	12.42	12.43	13.17	13.18	13.17	11.10
Albite													
Microcline													
pH	5.86	5.86	5.86	5.94	6.16	6.16	6.19	6.19	6.50	6.66	6.76	6.84	6.84
Cl^-	6.2E-01	6.2E-01	6.2E-01	6.2E-01	6.2E-01	6.2E-01	6.2E-01	6.2E-01	6.2E-01	6.2E-01	6.2E-01	6.2E-01	6.2E-01
HCl°	2.2E-05	2.2E-05	2.2E-05	1.8E-05	1.1E-05	1.1E-05	1.0E-05	1.0E-05	5.0E-06	3.5E-06	2.8E-06	2.3E-06	2.3E-06
Na^+	4.9E-01	4.9E-01	4.9E-01	4.9E-01	4.9E-01	4.9E-01	4.9E-01	4.9E-01	4.9E-01	4.9E-01	4.9E-01	4.9E-01	4.9E-01
NaOH°	8.0E-06	8.0E-06	8.0E-06	9.6E-06	1.6E-05	1.6E-05	1.7E-05	1.7E-05	3.5E-05	5.0E-05	6.3E-05	7.6E-05	7.6E-05
NaCl°	2.9E-01	2.9E-01	2.9E-01	2.9E-01	2.9E-01	2.9E-01	2.9E-01	2.9E-01	2.9E-01	2.9E-01	2.9E-01	2.9E-01	2.9E-01
$NaHSiO_3$°	2.2E-06	2.2E-06	2.2E-06	1.4E-06	4.4E-07	4.4E-07	4.0E-07	4.0E-07	1.9E-07	1.3E-07	2.0E-07	5.7E-07	5.7E-07
K^+	4.4E-02	4.4E-02	4.4E-02	4.4E-02	4.4E-02	4.4E-02	4.4E-02	4.4E-02	4.4E-02	4.4E-02	4.4E-02	4.4E-02	4.4E-02
KOH°	1.3E-06	1.3E-06	1.3E-06	1.5E-06	2.5E-06	2.5E-06	2.7E-06	2.7E-06	5.6E-06	8.0E-06	1.0E-05	1.2E-05	1.2E-05
KCl°	6.6E-03	6.5E-03	6.5E-03	6.5E-03	6.5E-03	6.5E-03	6.5E-03	6.5E-03	6.5E-03	6.5E-03	6.5E-03	6.5E-03	6.5E-03

Table 2. Calculated mineralogical (mol %) and fluid (molal) compositions. Model 2 (Continued).

Step	45	46	57	58	59	85	86	100	101	139	140	141	300
Ca^{2+}	9.4E-03	9.4E-03	9.5E-03	9.5E-03	9.5E-03	9.5E-03	9.5E-03	9.5E-03	9.5E-03	9.5E-03	9.4E-03	9.3E-03	9.3E-03
$CaOH^+$	3.7E-04	3.7E-04	3.7E-04	4.4E-04	7.3E-04	7.3E-04	7.8E-04	7.8E-04	1.6E-03	2.3E-03	2.9E-03	3.4E-03	3.4E-03
$CaCl^+$	6.6E-02	6.6E-02	6.6E-02	6.6E-02	6.7E-02	6.7E-02	6.7E-02	6.7E-02	6.6E-02	6.6E-02	6.6E-02	6.6E-02	6.6E-02
$CaCl_2^\circ$	8.9E-03	8.9E-03	9.0E-03	9.0E-03	9.0E-03	9.0E-03	9.0E-03	9.0E-03	9.0E-03	9.0E-03	8.9E-03	8.9E-03	8.9E-03
$CaHSiO_3^+$	2.1E-06	2.1E-06	2.1E-06	1.4E-06	4.3E-07	4.3E-07	3.9E-07	3.9E-07	1.9E-07	1.3E-07	2.0E-07	5.5E-07	5.5E-07
Mg^{2+}	1.2E-05	1.2E-05	1.2E-05	1.0E-05	6.9E-06	6.9E-06	6.5E-06	6.5E-06	3.7E-06	2.8E-06	2.3E-06	2.0E-06	2.0E-06
$MgOH^+$	1.4E-06	1.4E-06	1.4E-06	1.5E-06	1.6E-06	1.6E-06	1.6E-06	1.6E-06	1.9E-06	2.0E-06	2.1E-06	2.2E-06	2.2E-06
$MgCl^+$	3.0E-05	3.0E-05	3.0E-05	2.6E-05	1.7E-05	1.7E-05	1.6E-05	1.6E-05	9.2E-06	6.9E-06	5.7E-06	4.9E-06	4.9E-06
$MgHSiO_3^+$	1.4E-09	1.4E-09	1.4E-09	7.7E-10	1.6E-10	1.6E-10	1.4E-10	1.4E-10	3.7E-11	2.0E-11	2.4E-11	5.9E-11	5.9E-11
Al^{3+}	7.3E-18	7.3E-18	7.3E-18	6.1E-18	3.7E-18	3.7E-18	3.2E-18	3.2E-18	3.6E-19	1.2E-19	2.4E-20	2.3E-21	2.3E-21
AlO_2^-	5.2E-05	5.1E-05	5.1E-05	8.9E-05	4.0E-04	4.0E-04	4.5E-04	4.5E-04	9.4E-04	1.3E-03	6.6E-04	1.3E-04	1.3E-04
$AlOH^{2+}$	9.2E-14	9.2E-14	9.2E-14	9.2E-14	9.2E-14	9.2E-14	8.5E-14	8.5E-14	2.0E-14	9.8E-15	2.4E-15	2.7E-16	2.7E-16
AlO^+	5.2E-11	5.2E-11	5.2E-11	6.3E-11	1.0E-10	1.0E-10	1.0E-10	1.0E-10	4.9E-11	3.5E-11	1.1E-11	1.4E-12	1.4E-12
$HAlO_2^\circ$	1.2E-07	1.2E-07	1.2E-07	1.7E-07	4.5E-07	4.5E-07	4.8E-07	4.8E-07	4.8E-07	4.8E-07	1.9E-07	3.0E-08	3.0E-08
$HSiO_3^-$	2.6E-06	2.6E-06	2.6E-06	1.7E-06	5.2E-07	5.2E-07	4.7E-07	4.7E-07	2.3E-07	1.6E-07	2.4E-07	6.7E-07	6.7E-07
SiO_2°	1.8E-03	1.8E-03	1.8E-03	9.7E-04	1.8E-04	1.8E-04	1.5E-04	1.5E-04	3.6E-05	1.8E-05	2.1E-05	4.9E-05	4.9E-05

Figure 3

Diagram showing the calculated changes in the relative volumes of minerals formed during stepwise alteration of granitic sample E:75 by a fluid (see text) equilibrated with the assemblage antigorite + brucite + diopside. The mineral proportions at each step were calculated for reaction at a transient fluid/rock ratio of 10.

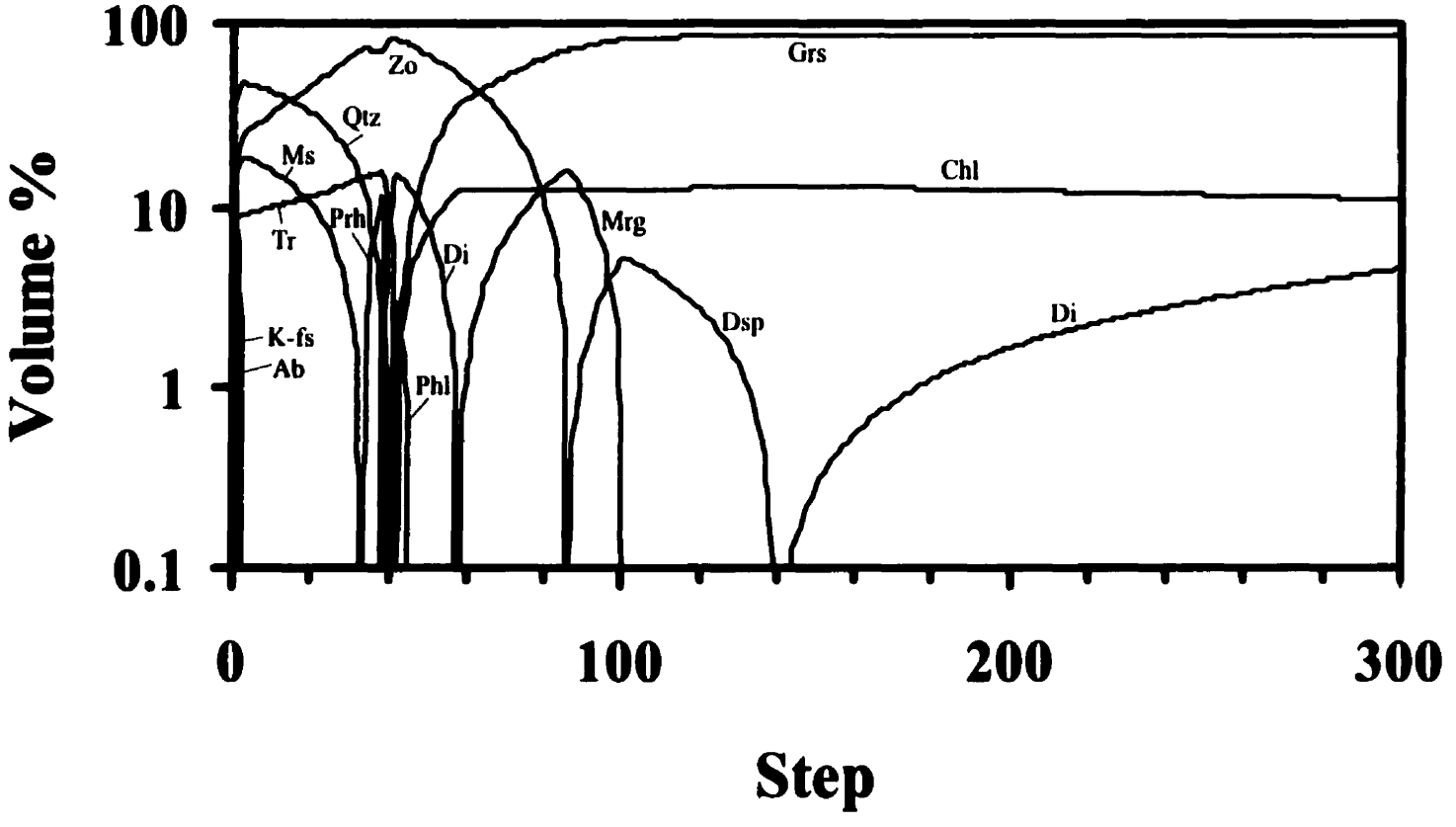
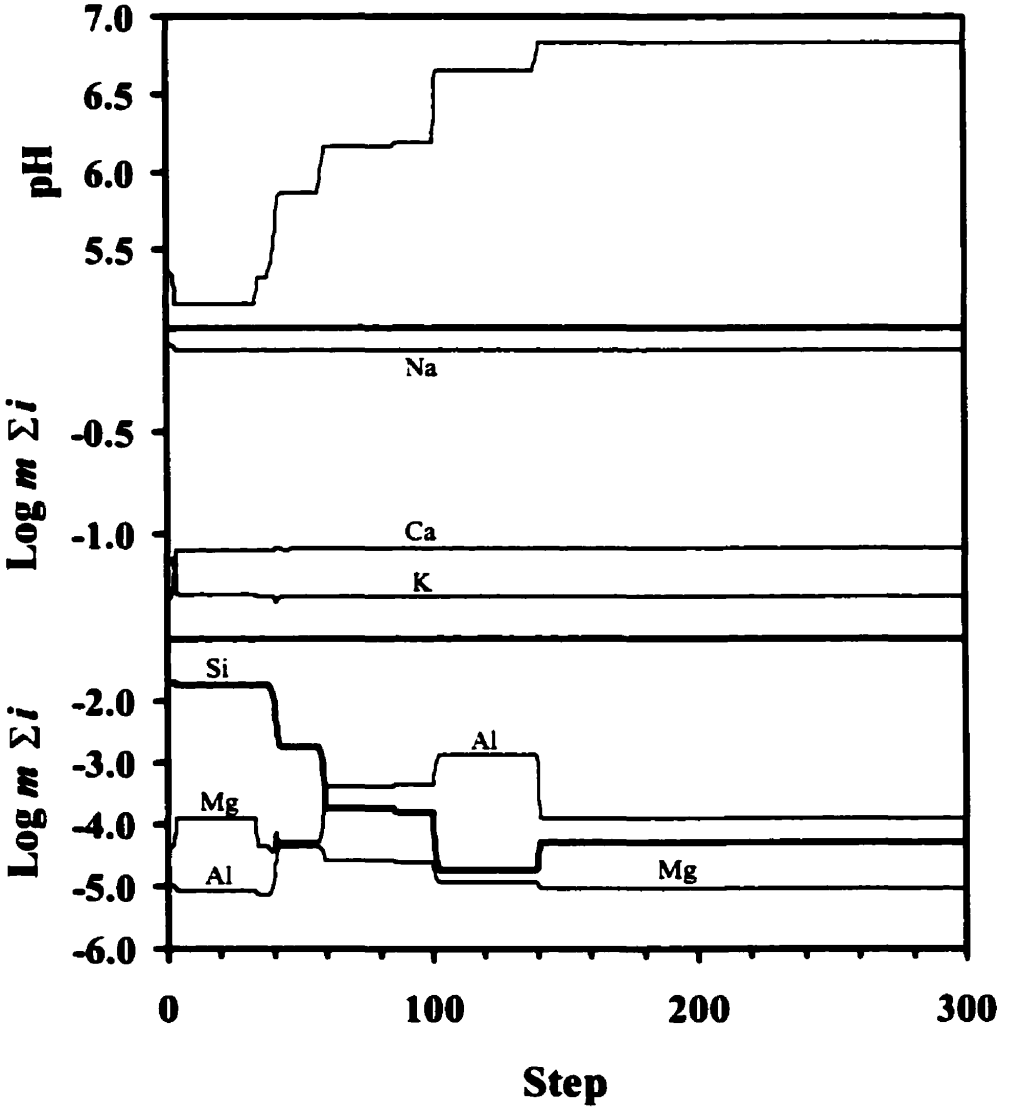

100
10
1
0.1
Volume %
0
100
200
300
Step
Zo
Qtz
Ms
Tr
Prh
Di
K-fs
Ab
Phl
Grs
Chl
Mrg
Dsp
Di

Figure 4

A series of diagrams showing the calculated changes in fluid composition during stepwise alteration of the granitic sample E:75. The initial composition of the fluid corresponds to equilibrium with the assemblage antigorite + brucite + diopside. Each step represents reaction of the fluid at a transient water/rock ratio of 10 with the rock which becomes progressively more altered.


7.0
6.5
6.0
5.5
pH
Na
-0.5
-1.0
Log m Σi
Ca
K
Si
-2.0
-3.0
-4.0
-5.0
-6.0
Log m Σi
Al
Mg
Al
Mg
0
100
200
300
Step

APPENDIX II

ELECTRON MICROPROBE ANALYSES.

Table 1. Electron microprobe analyses of actinolite.

Sample	UG7															
Circle#	5	5	5	5	5	5	5	5	3	3	3	2	2	2	2	2
Point#	1	2	3	4	5	7	15	16	1	2	5	1	3	1	2	5
Analysis#	457	458	459	460	461	463	471	472	473	474	477	482	484	487	488	491
Wt.% oxides																
SiO_2	53.59	53.34	53.50	53.51	53.25	52.66	53.73	53.79	53.39	53.46	53.84	53.97	53.80	53.69	54.09	54.75
TiO_2	0.00	0.03	0.00	0.00	0.00	0.04	0.00	0.00	0.00	0.00	0.03	0.05	0.05	0.05	0.03	0.05
Al_2O_3	0.66	0.71	0.75	0.50	0.50	1.12	0.19	0.35	0.44	0.36	0.46	0.52	0.64	0.46	0.93	2.06
Cr_2O_3	0.01	0.00	0.02	0.01	0.00	0.02	0.01	0.00	0.00	0.01	0.00	0.01	0.00	0.02	0.00	0.00
FeO	16.54	16.84	16.58	16.58	16.20	17.94	17.57	17.04	17.43	17.67	16.08	16.16	16.36	16.60	15.53	15.26
MnO	0.50	0.55	0.53	0.51	0.53	0.54	0.47	0.46	0.53	0.53	0.53	0.58	0.66	0.52	0.41	0.43
MgO	13.61	13.60	13.86	13.77	14.06	13.03	13.19	13.69	13.11	13.07	14.15	13.93	13.66	13.66	13.87	12.69
CaO	12.50	12.39	12.32	12.50	12.57	11.87	12.74	12.60	12.81	12.56	12.64	12.49	12.54	12.78	12.46	11.56
Na_2O	0.19	0.17	0.17	0.14	0.13	0.15	0.10	0.10	0.15	0.11	0.14	0.15	0.22	0.17	0.52	1.06
K_2O	0.12	0.16	0.22	0.12	0.12	0.52	0.09	0.08	0.10	0.12	0.10	0.12	0.11	0.09	0.07	0.10
F	0.00	0.00	0.00	0.01	0.02	0.00	0.00	0.00	0.00	0.00	0.00	0.01	0.00	0.00	0.00	0.00
Cl	0.00	0.01	0.02	0.01	0.01	0.01	0.00	0.01	0.02	0.01	0.03	0.02	0.02	0.01	0.02	0.01
Total	97.72	97.80	97.95	97.64	97.38	97.89	98.11	98.12	97.97	97.89	97.98	98.00	98.06	98.02	97.92	97.96
—O≡F,Cl	0.00	0.00	0.00	0.00	0.01	0.00	0.00	0.00	0.00	0.00	0.01	0.01	0.00	0.00	0.00	0.00
Total	97.72	97.80	97.94	97.64	97.36	97.89	98.10	98.12	97.97	97.89	97.97	97.98	98.05	98.02	97.92	97.96
Cations (based on 23 oxygens with all Fe as Fe^{+2})																
Si	7.83	7.82	7.84	7.82	7.75	7.78	7.93	7.91	7.87	7.87	7.88	7.89	7.89	7.88	7.88	7.94
Ti	0.00	0.00	0.00	0.00	0.00	0.00	0.00	0.00	0.00	0.00	0.00	0.01	0.01	0.00	0.00	0.01
Al	0.11	0.12	0.13	0.09	0.09	0.19	0.03	0.06	0.08	0.06	0.08	0.09	0.11	0.08	0.16	0.35
Cr	0.00	0.00	0.00	0.00	0.00	0.00	0.00	0.00	0.00	0.00	0.00	0.00	0.00	0.00	0.00	0.00
Fe^{+2}	2.02	2.07	2.03	2.03	1.97	2.22	2.17	2.10	2.15	2.18	1.97	1.98	2.01	2.04	1.89	1.85
Mn	0.06	0.07	0.07	0.06	0.06	0.07	0.06	0.06	0.07	0.07	0.07	0.07	0.08	0.06	0.05	0.05
Mg	2.97	2.97	3.03	3.00	3.05	2.87	2.90	3.00	2.88	2.87	3.08	3.04	2.99	2.99	3.01	2.74
Ca	1.96	1.95	1.93	1.96	1.96	1.88	2.01	1.99	2.02	1.98	1.98	1.96	1.97	2.01	1.94	1.80
Na	0.05	0.05	0.05	0.04	0.04	0.04	0.03	0.03	0.04	0.03	0.04	0.04	0.06	0.05	0.15	0.30
K	0.02	0.03	0.04	0.02	0.02	0.10	0.02	0.02	0.02	0.02	0.02	0.02	0.02	0.02	0.01	0.02
F	0.00	0.00	0.00	0.00	0.01	0.00	0.00	0.00	0.00	0.00	0.00	0.01	0.00	0.00	0.00	0.00
Cl	0.00	0.00	0.00	0.00	0.00	0.00	0.00	0.00	0.00	0.00	0.01	0.01	0.00	0.00	0.00	0.00
OH	2.23	2.16	2.01	2.30	2.56	2.08	1.87	1.85	2.00	2.08	1.98	1.97	1.91	1.94	2.02	1.97

Table 2. Electron microprobe analyses of andalusite and corundum.

Mineral	Andalusite									
Sample#	Chand3	Chand3	Chand3	Chand3	Chand3	Chand3	Chand3	Chand3	Chand3	Chand3
Circle#	1	1	1	1	1	1	1	1	1	1
Analysis#	6	7	8	9	10	11	12	13	14	15
Comment	Dark	Dark	Dark	Light	Light	Light	Light	Light	Dark	Dark
Wt.% oxides										
SiO_2	34.61	34.69	34.12	35.71	36.00	35.98	35.96	36.09	34.70	34.92
TiO_2	0.15	0.16	0.14	0.32	0.29	0.31	0.27	0.31	0.15	0.14
Al_2O_3	62.82	62.93	60.63	59.92	59.63	59.92	59.98	59.76	62.89	62.64
Cr_2O_3	0.00	0.00	0.01	0.00	0.00	0.00	0.00	0.09	0.03	0.00
FeO	1.15	1.10	1.06	3.07	3.12	2.93	2.82	2.88	1.07	1.05
MnO	0.00	0.01	0.02	0.01	0.01	0.00	0.01	0.00	0.01	0.00
MgO	0.02	0.01	0.00	0.09	0.08	0.07	0.07	0.09	0.01	0.02
K_2O	0.01	0.02	0.04	0.03	0.01	0.02	0.03	0.02	0.03	0.02
Total	98.75	98.92	96.01	99.14	99.13	99.24	99.15	99.24	98.89	98.79
Cations*										
Si	0.95	0.95	0.97	0.99	1.00	0.99	0.99	1.00	0.95	0.96
Ti	0.00	0.00	0.00	0.01	0.01	0.01	0.01	0.01	0.00	0.00
Al	2.04	2.04	2.02	1.96	1.95	1.95	1.95	1.95	2.04	2.03
Cr	0.00	0.00	0.00	0.00	0.00	0.00	0.00	0.00	0.00	0.00
Fe	0.03	0.03	0.03	0.07	0.07	0.07	0.07	0.07	0.02	0.02
Mn	0.00	0.00	0.00	0.00	0.00	0.00	0.00	0.00	0.00	0.00
Mg	0.00	0.00	0.00	0.00	0.00	0.00	0.00	0.00	0.00	0.00
K	0.00	0.00	0.00	0.00	0.00	0.00	0.00	0.00	0.00	0.00
Total	3.02	3.02	3.02	3.03	3.02	3.02	3.02	3.02	3.02	3.02

* Based on 5 oxygens

Table 2. Electron microprobe analyses of andalusite and corundum (continued).

Mineral	Corundum									
Sample#	Chand3	Chand3	Chand3	Chand3	Chand3	Chand3	Chand3	Chand3	Chand3	Chand3
Circle#	1	2	3	3	3	3	3	3	5	5
Analysis#	16	17	18	19	20	21	22	23	24	25
Comment	Dark								Fractures	Fractures
Wt.% oxides										
SiO_2	0.03	0.71	1.48	0.67	1.19	1.46	1.37	0.60	2.92	7.56
TiO_2	0.99	0.40	0.34	0.13	0.13	0.25	0.65	0.33	0.07	0.08
Al_2O_3	98.12	98.62	97.81	99.38	98.50	98.11	97.08	99.41	77.42	73.10
Cr_2O_3	0.00	0.00	0.03	0.01	0.00	0.03	0.00	0.00	0.00	0.00
FeO	1.09	0.61	0.12	0.15	0.07	0.12	0.33	0.13	0.30	0.43
MnO	0.00	0.01	0.00	0.01	0.01	0.01	0.00	0.01	0.01	0.00
MgO	0.00	0.00	0.00	0.00	0.01	0.02	0.01	0.00	0.01	0.01
K_2O	0.04	0.05	0.04	0.03	0.03	0.01	0.02	0.03	0.53	1.88
Total	100.27	100.39	99.81	100.37	99.92	99.99	99.46	100.51	81.26	83.06
Cations*										
Si	0.00	0.01	0.03	0.01	0.02	0.02	0.02	0.01	0.06	0.16
Ti	0.01	0.01	0.00	0.00	0.00	0.00	0.01	0.00	0.00	0.00
Al	1.97	1.97	1.96	1.98	1.97	1.96	1.95	1.98	1.91	1.77
Cr	0.00	0.00	0.00	0.00	0.00	0.00	0.00	0.00	0.00	0.00
Fe	0.02	0.01	0.00	0.00	0.00	0.00	0.00	0.00	0.01	0.01
Mn	0.00	0.00	0.00	0.00	0.00	0.00	0.00	0.00	0.00	0.00
Mg	0.00	0.00	0.00	0.00	0.00	0.00	0.00	0.00	0.00	0.00
K	0.00	0.00	0.00	0.00	0.00	0.00	0.00	0.00	0.01	0.05
Total	2.00	2.00	1.99	2.00	1.99	1.99	1.99	2.00	1.99	1.98

* Based on 3 oxygens

Table 3. Electron microprobe analyses of apatite

Sample#	JMH-329A						H1281-61.5						
Circle#	6	6	6	6	6	6	1	1	1	1	2	2	2
Analysis#	1	2	3	4	5	6	1	2	3	4	1	2	3
Wt. % oxides													
SiO_2	0.31	0.28	0.47	0.51	0.22	0.28	0.05	0.03	0.00	0.14	0.10	0.13	0.09
Ce_2O_3	0.07	0.03	0.19	0.16	0.00	0.14	0.10	0.10	0.09	0.10	0.11	0.12	0.09
La_2O_3	0.00	0.00	0.10	0.07	0.00	0.00	0.00	0.00	0.00	0.00	0.00	0.00	0.00
Nd_2O_3	0.00	0.00	0.19	0.12	0.20	0.00	0.13	0.01	0.00	0.08	0.04	0.08	0.08
FeO	0.06	0.16	0.04	0.02	0.07	0.02	0.27	0.15	0.19	0.21	0.33	0.23	0.28
MnO	0.00	0.01	0.00	0.00	0.00	0.00	0.19	0.18	0.15	0.14	0.18	0.19	0.21
MgO	0.00	0.00	0.00	0.00	0.01	0.00	0.01	0.07	0.04	0.04	0.04	0.05	0.05
CaO	54.73	53.89	54.11	54.09	54.69	55.07	56.28	55.80	54.97	55.88	54.41	54.19	55.08
SrO	0.03	0.02	0.03	0.00	0.01	0.02	0.05	0.06	0.05	0.06	0.04	0.05	0.04
Na_2O	0.00	0.01	0.00	0.00	0.00	0.00	0.07	0.07	0.06	0.10	0.06	0.07	0.08
P_2O_5	35.97	35.63	34.27	34.08	35.16	36.47	41.76	42.29	41.62	41.69	41.45	41.80	41.39
F	1.40	1.23	1.30	1.22	1.28	1.45	2.08	1.96	2.15	2.67	2.90	2.77	3.09
Cl	0.01	0.02	0.04	0.03	0.01	0.01	0.12	0.13	0.13	0.19	0.34	0.19	0.31
Total	92.60	91.26	90.73	90.30	91.65	93.46	101.13	100.84	99.44	101.31	100.00	99.86	100.78
-O=F	0.59	0.52	0.55	0.51	0.54	0.61	0.88	0.82	0.90	1.12	1.22	1.17	1.30
-O=Cl	0.00	0.00	0.01	0.01	0.00	0.00	0.03	0.03	0.03	0.04	0.08	0.04	0.07
Total	92.01	90.74	90.18	89.78	91.11	92.85	100.23	99.99	98.51	100.15	98.70	98.66	99.41
Cations (based on 26 O-OH-F-Cl and 16 cations)													
Si	0.05	0.04	0.08	0.08	0.04	0.05	0.01	0.00	0.00	0.02	0.02	0.02	0.02
Ce	0.00	0.00	0.01	0.01	0.00	0.01	0.01	0.01	0.01	0.01	0.01	0.01	0.01
La	0.00	0.00	0.01	0.00	0.00	0.00	0.00	0.00	0.00	0.00	0.00	0.00	0.00
Nd	0.00	0.00	0.01	0.01	0.01	0.00	0.01	0.00	0.00	0.00	0.00	0.00	0.00
Fe	0.01	0.02	0.01	0.00	0.01	0.00	0.04	0.02	0.03	0.03	0.05	0.03	0.04
Mn	0.00	0.00	0.00	0.00	0.00	0.00	0.03	0.03	0.02	0.02	0.03	0.03	0.03
Mg	0.00	0.00	0.00	0.00	0.00	0.00	0.00	0.02	0.01	0.01	0.01	0.01	0.01
Ca	9.51	9.28	9.34	9.30	9.47	9.62	10.30	10.15	9.85	10.18	9.75	9.69	9.93
Sr	0.00	0.00	0.00	0.00	0.00	0.00	0.01	0.01	0.00	0.01	0.00	0.00	0.00
Na	0.00	0.00	0.00	0.00	0.00	0.00	0.02	0.02	0.02	0.03	0.02	0.02	0.03
P	4.94	4.85	4.67	4.63	4.81	5.03	6.04	6.08	5.89	6.00	5.87	5.91	5.90
F	0.72	0.62	0.66	0.62	0.65	0.75	1.13	1.05	1.13	1.43	1.53	1.46	1.64
Cl	0.00	0.00	0.01	0.01	0.00	0.00	0.03	0.04	0.04	0.06	0.10	0.05	0.09
C	1.49	1.80	1.88	1.96	1.65	1.29	-0.05	0.00	0.17	-0.03	0.25	0.27	0.03
OH	1.39	1.14	1.37	1.37	1.51	1.47	0.00	0.00	0.84	0.00	0.25	0.19	0.49

Table 3. Electron microprobe analyses of apatite (continued).

Sample#	H1281-61.5	JMH-281A1									H1281-61.7
Circle#	2	1	1	1	1	3	3	3	3	3	1
Analysis#	4	1	2	3	4	1	2	3	4	5	1
Wt. % oxides											
SiO_2	0.01	0.06	0.06	0.08	0.05	0.04	0.04	0.06	0.12	0.09	0.09
Ce_2O_3	0.07	0.10	0.13	0.11	0.10	0.12	0.12	0.11	0.12	0.08	0.15
La_2O_3	0.00	0.00	0.00	0.00	0.00	0.00	0.00	0.00	0.00	0.00	0.00
Nd_2O_3	0.00	0.03	0.08	0.04	0.05	0.05	0.05	0.09	0.06	0.05	0.16
FeO	0.12	0.33	0.42	0.29	0.31	0.27	0.27	0.30	0.23	0.28	0.27
MnO	0.17	0.17	0.18	0.19	0.19	0.20	0.21	0.19	0.20	0.19	0.18
MgO	0.00	0.05	0.06	0.11	0.04	0.05	0.05	0.06	0.06	0.04	0.03
CaO	55.93	55.05	55.38	55.64	55.05	55.31	55.33	54.23	54.53	54.68	54.59
SrO	0.07	0.06	0.05	0.04	0.04	0.05	0.05	0.06	0.05	0.05	0.03
Na_2O	0.04	0.06	0.07	0.09	0.07	0.08	0.08	0.05	0.08	0.06	0.08
P_2O_5	41.48	41.19	41.76	42.12	41.49	41.41	41.30	41.69	41.80	41.83	41.10
F	1.97	3.00	1.98	2.20	2.56	2.53	2.89	2.78	2.63	3.00	3.04
Cl	0.17	0.42	0.19	0.28	0.42	0.42	0.37	0.37	0.22	0.38	0.23
Total	100.02	100.51	100.34	101.18	100.38	100.54	100.76	100.00	100.09	100.71	99.96
-O=F	0.83	1.26	0.83	0.93	1.08	1.07	1.22	1.17	1.11	1.26	1.28
-O=Cl	0.04	0.09	0.04	0.06	0.09	0.09	0.08	0.08	0.05	0.08	0.05
Total	99.15	99.16	99.47	100.19	99.20	99.38	99.45	98.74	98.93	99.36	98.62
Cations (based on 26 O-OH-F-Cl and 16 cations)											
Si	0.00	0.01	0.01	0.01	0.01	0.01	0.01	0.01	0.02	0.01	0.02
Ce	0.00	0.01	0.01	0.01	0.01	0.01	0.01	0.01	0.01	0.00	0.01
La	0.00	0.00	0.00	0.00	0.00	0.00	0.00	0.00	0.00	0.00	0.00
Nd	0.00	0.00	0.00	0.00	0.00	0.00	0.00	0.01	0.00	0.00	0.01
Fe	0.02	0.05	0.06	0.04	0.04	0.04	0.04	0.04	0.03	0.04	0.04
Mn	0.02	0.02	0.03	0.03	0.03	0.03	0.03	0.03	0.03	0.03	0.03
Mg	0.00	0.01	0.01	0.03	0.01	0.01	0.01	0.02	0.01	0.01	0.01
Ca	10.11	9.92	10.04	10.14	9.93	10.00	10.00	9.72	9.78	9.84	9.79
Sr	0.01	0.01	0.01	0.00	0.00	0.00	0.00	0.01	0.00	0.00	0.00
Na	0.01	0.02	0.02	0.03	0.02	0.03	0.03	0.02	0.02	0.02	0.02
P	5.92	5.86	5.98	6.06	5.91	5.91	5.90	5.90	5.93	5.95	5.83
F	1.05	1.60	1.06	1.19	1.36	1.35	1.54	1.47	1.39	1.59	1.61
Cl	0.05	0.12	0.05	0.08	0.12	0.12	0.10	0.11	0.06	0.11	0.07
C	0.00	0.09	0.00	-0.04	0.04	0.00	0.00	0.25	0.16	0.09	0.25
OH	0.95	0.50	0.60	0.00	0.71	0.70	0.61	0.20	0.43	0.26	0.32

Table 3. Electron microprobe analyses of apatite (continued)

Sample#	H1281-61.7						FD-3				
Circle#	1	1	1	1	1	1	1	1	1	1	2
Analysis#	2	2	4	5	6	7	1	3	4	5	1
Wt. % oxides											
SiO_2	0.04	0.11	0.08	0.06	0.11	0.07	0.06	0.00	0.02	0.09	0.06
Ce_2O_3	0.18	0.14	0.17	0.08	0.13	0.09	0.14	0.12	0.07	0.13	0.13
La_2O_3	0.00	0.00	0.00	0.00	0.00	0.00	0.00	0.00	0.00	0.00	0.00
Nd_2O_3	0.09	0.09	0.09	0.07	0.10	0.05	0.08	0.09	0.09	0.05	0.07
FeO	0.30	0.30	0.28	0.37	0.39	0.28	0.32	0.33	0.49	0.27	0.23
MnO	0.16	0.20	0.20	0.20	0.18	0.18	0.48	0.43	0.46	0.42	0.44
MgO	0.04	0.03	0.04	0.03	0.03	0.04	0.06	0.07	0.04	0.05	0.03
CaO	54.52	54.17	54.48	54.64	54.58	54.46	53.89	54.25	54.04	54.39	54.08
SrO	0.03	0.02	0.04	0.03	0.03	0.05	0.01	0.01	0.02	0.02	0.02
Na_2O	0.08	0.10	0.08	0.07	0.10	0.07	0.12	0.12	0.06	0.06	0.10
P_2O_5	42.14	41.84	42.90	42.21	42.07	41.96	41.82	42.20	42.02	41.75	41.87
F	2.91	2.10	2.05	2.20	1.99	2.05	2.47	2.20	1.97	2.11	1.97
Cl	0.25	0.18	0.18	0.20	0.18	0.19	0.22	0.21	0.28	0.28	0.21
Total	100.74	99.28	100.58	100.16	99.89	99.49	99.66	100.02	99.54	99.62	99.21
-O=F	1.22	0.89	0.86	0.93	0.84	0.86	1.04	0.93	0.83	0.89	0.83
-O=Cl	0.06	0.04	0.04	0.05	0.04	0.04	0.05	0.05	0.06	0.06	0.05
Total	99.46	98.35	99.68	99.19	99.01	98.59	98.57	99.04	98.65	98.67	98.34
Cations (based on 26 O-OH-F-Cl and 16 cations)											
Si	0.01	0.02	0.01	0.01	0.02	0.01	0.01	0.00	0.00	0.01	0.01
Ce	0.01	0.01	0.01	0.00	0.01	0.01	0.01	0.01	0.00	0.01	0.01
La	0.00	0.00	0.00	0.00	0.00	0.00	0.00	0.00	0.00	0.00	0.00
Nd	0.01	0.01	0.01	0.00	0.01	0.00	0.00	0.01	0.01	0.00	0.00
Fe	0.04	0.04	0.04	0.05	0.05	0.04	0.04	0.05	0.07	0.04	0.03
Mn	0.02	0.03	0.03	0.03	0.03	0.03	0.07	0.06	0.07	0.06	0.06
Mg	0.01	0.01	0.01	0.01	0.01	0.01	0.02	0.02	0.01	0.01	0.01
Ca	9.81	9.69	9.82	9.82	9.81	9.75	9.65	9.75	9.69	9.76	9.68
Sr	0.00	0.00	0.00	0.00	0.00	0.00	0.00	0.00	0.00	0.00	0.00
Na	0.03	0.03	0.03	0.02	0.03	0.02	0.04	0.04	0.02	0.02	0.03
P	5.99	5.91	6.11	6.00	5.98	5.94	5.92	5.99	5.96	5.92	5.92
F	1.55	1.11	1.09	1.17	1.06	1.09	1.30	1.17	1.04	1.12	1.04
Cl	0.07	0.05	0.05	0.06	0.05	0.05	0.06	0.06	0.08	0.08	0.06
C	0.07	0.26	0.00	0.05	0.06	0.19	0.24	0.09	0.17	0.16	0.25
OH	0.27	0.57	0.36	0.69	0.83	0.67	0.40	0.66	0.66	0.70	0.65

Table 3. Electron microprobe analyses of apatite (continued)

Sample#	FD-3				JMH-349A					
Circle#	2	2	3	3	1	1	1	2	2	2
Analysis#	2	3	1	4	1	2	3	1	3	4
Wt. % oxides										
SiO_2	0.02	0.09	0.07	0.03	0.12	0.13	0.15	0.08	0.10	0.04
Ce_2O_3	0.15	0.11	0.11	0.10	0.11	0.13	0.17	0.12	0.15	0.06
La_2O_3	0.00	0.00	0.00	0.00	0.00	0.00	0.00	0.00	0.00	0.00
Nd_2O_3	0.07	0.10	0.08	0.06	0.11	0.10	0.09	0.08	0.08	0.07
FeO	0.36	0.30	0.38	0.26	0.27	0.17	0.36	0.19	0.17	0.22
MnO	0.46	0.41	0.43	0.46	0.09	0.08	0.08	0.10	0.07	0.06
MgO	0.07	0.06	0.05	0.07	0.00	0.01	0.02	0.02	0.00	0.01
CaO	53.99	53.91	53.93	54.20	55.35	54.92	54.97	54.64	54.73	54.73
SrO	0.02	0.02	0.02	0.01	0.04	0.03	0.03	0.02	0.04	0.03
Na_2O	0.11	0.11	0.11	0.12	0.02	0.03	0.03	0.03	0.00	0.00
P_2O_5	41.97	41.57	41.90	41.43	42.26	41.53	41.75	42.09	41.40	41.62
F	2.19	2.00	2.20	2.40	1.98	1.78	2.06	2.19	1.76	1.75
Cl	0.20	0.18	0.24	0.23	0.26	0.22	0.29	0.37	0.16	0.17
Total	99.60	98.86	99.52	99.38	100.61	99.12	100.00	99.94	98.65	98.75
-O=F	0.92	0.84	0.92	1.01	0.83	0.75	0.87	0.92	0.74	0.73
-O=Cl	0.05	0.04	0.05	0.05	0.06	0.05	0.06	0.08	0.04	0.04
Total	98.63	97.98	98.54	98.31	99.72	98.32	99.06	98.94	97.87	97.97
Cations (based on 26 O-OH-F-Cl and 16 cations)										
Si	0.00	0.02	0.01	0.01	0.02	0.02	0.02	0.01	0.02	0.01
Ce	0.01	0.01	0.01	0.01	0.01	0.01	0.01	0.01	0.01	0.00
La	0.00	0.00	0.00	0.00	0.00	0.00	0.00	0.00	0.00	0.00
Nd	0.00	0.01	0.00	0.00	0.01	0.01	0.01	0.00	0.00	0.00
Fe	0.05	0.04	0.05	0.04	0.04	0.02	0.05	0.03	0.02	0.03
Mn	0.07	0.06	0.06	0.07	0.01	0.01	0.01	0.01	0.01	0.01
Mg	0.02	0.01	0.01	0.02	0.00	0.00	0.01	0.01	0.00	0.00
Ca	9.68	9.62	9.66	9.70	10.03	9.84	9.90	9.81	9.77	9.77
Sr	0.00	0.00	0.00	0.00	0.00	0.00	0.00	0.00	0.00	0.00
Na	0.04	0.04	0.04	0.04	0.01	0.01	0.01	0.01	0.00	0.00
P	5.94	5.86	5.93	5.86	6.05	5.88	5.94	5.97	5.84	5.87
F	1.16	1.05	1.16	1.27	1.06	0.94	1.10	1.16	0.93	0.92
Cl	0.06	0.05	0.07	0.07	0.07	0.06	0.08	0.10	0.05	0.05
C	0.19	0.33	0.22	0.27	0.00	0.20	0.04	0.14	0.32	0.30
OH	0.58	0.63	0.53	0.58	0.32	0.92	0.87	0.52	0.82	0.80

Table 4. Electron microprobe analyses of biotite.

Sample#	JMH-25							JMH-26							
Circle#	3	3	3	3	3	3	3	none							
Point#	4	8	9	10	12	13	14	1	2	3	4	5	6	7	8
Analysis#	361	365	366	367	369	370	371	286	287	288	289	290	291	292	293
Comment															
Wt. % oxides															
SiO_2	35.31	35.10	33.04	35.19	34.73	35.17	34.95	35.31	35.36	34.89	34.91	34.94	35.17	35.13	35.15
TiO_2	3.09	3.11	2.37	2.98	2.78	3.15	2.95	3.58	3.48	3.57	3.47	3.75	3.59	3.25	3.06
Al_2O_3	18.30	18.39	18.49	18.59	18.18	18.44	18.08	18.87	18.37	18.82	18.98	18.92	18.69	19.25	19.12
Cr_2O_3	0.00	0.01	0.00	0.00	0.02	0.01	0.00	0.03	0.04	0.01	0.03	0.01	0.00	0.02	0.00
FeO	19.16	18.35	21.60	18.53	19.16	18.62	18.90	19.16	18.60	19.48	19.31	18.94	18.73	18.69	19.31
MnO	0.14	0.17	0.22	0.15	0.13	0.20	0.20	0.17	0.18	0.14	0.15	0.13	0.15	0.15	0.19
MgO	9.93	10.29	10.24	10.41	10.63	10.22	10.02	9.38	9.87	9.18	9.48	9.58	9.39	9.90	9.97
CaO	0.09	0.02	0.02	0.03	0.10	0.01	0.07	0.02	0.03	0.00	0.02	0.02	0.00	0.00	0.00
Na_2O	0.26	0.32	0.16	0.28	0.24	0.31	0.25	0.36	0.21	0.36	0.33	0.37	0.36	0.40	0.36
K_2O	10.05	10.19	8.08	10.04	9.57	10.27	10.20	10.01	10.14	9.88	10.06	9.92	10.01	9.86	9.87
F	0.00	0.00	0.00	0.02	0.00	0.00	0.00	0.00	0.00	0.00	0.00	0.00	0.00	0.00	0.00
Cl	0.08	0.08	0.06	0.06	0.07	0.08	0.07	0.06	0.07	0.08	0.07	0.06	0.07	0.08	0.08
Total	96.41	96.00	94.28	96.24	95.60	96.46	95.68	96.94	96.35	96.40	96.77	96.61	96.14	96.70	97.09
—O≡F,Cl	0.02	0.02	0.01	0.02	0.02	0.02	0.02	0.01	0.02	0.02	0.02	0.01	0.02	0.02	0.02
Total	96.39	95.98	94.27	96.22	95.59	96.44	95.67	96.93	96.33	96.38	96.76	96.60	96.12	96.68	97.07
Cations (based on 12 oxygens)															
Si	2.69	2.66	2.47	2.67	2.62	2.68	2.65	2.71	2.69	2.66	2.67	2.67	2.67	2.68	2.70
Ti	0.18	0.18	0.13	0.17	0.16	0.18	0.17	0.21	0.20	0.20	0.20	0.21	0.20	0.19	0.18
Al	1.64	1.64	1.63	1.66	1.62	1.66	1.61	1.70	1.65	1.69	1.71	1.70	1.67	1.73	1.73
Cr	0.00	0.00	0.00	0.00	0.00	0.00	0.00	0.00	0.00	0.00	0.00	0.00	0.00	0.00	0.00
Fe^{+2}	1.22	1.16	1.35	1.18	1.21	1.19	1.20	1.23	1.18	1.24	1.24	1.21	1.19	1.19	1.24
Mn	0.01	0.01	0.01	0.01	0.01	0.01	0.01	0.01	0.01	0.01	0.01	0.01	0.01	0.01	0.01
Mg	1.13	1.16	1.14	1.18	1.20	1.16	1.13	1.07	1.12	1.04	1.08	1.09	1.06	1.12	1.14
Ca	0.01	0.00	0.00	0.00	0.01	0.00	0.01	0.00	0.00	0.00	0.00	0.00	0.00	0.00	0.00
Na	0.04	0.05	0.02	0.04	0.04	0.05	0.04	0.05	0.03	0.05	0.05	0.05	0.05	0.06	0.05
K	0.98	0.98	0.77	0.97	0.92	1.00	0.98	0.98	0.98	0.96	0.98	0.97	0.97	0.96	0.97
F	0.00	0.00	0.00	0.00	0.00	0.00	0.00	0.00	0.00	0.00	0.00	0.00	0.00	0.00	0.00
Cl	0.01	0.01	0.01	0.01	0.01	0.01	0.01	0.01	0.01	0.01	0.01	0.01	0.01	0.01	0.01
OH	1.84	2.03	2.86	1.91	2.22	1.81	2.19	1.57	1.86	1.84	1.66	1.73	1.96	1.69	1.50

Table 4. Electron microprobe analyses of biotite (continued).

Sample#	JMH-26														
Circle#												4	4	4	4
Point#	9	10	11	12	13	14	15	16	17	18	19	1	2	3	4
Analysis#	294	295	296	297	298	299	300	301	302	303	304	305	306	307	308
Comment												Light	Light	Light	Light
Wt. % oxides															
SiO_2	34.77	35.20	35.29	35.31	34.96	34.80	34.89	34.85	34.52	34.91	34.90	35.13	34.50	34.63	34.81
TiO_2	2.70	3.29	3.46	3.61	3.42	3.55	3.65	3.98	3.90	3.82	3.73	3.30	3.30	3.44	3.44
Al_2O_3	18.76	19.07	18.97	18.89	18.95	19.10	19.01	18.59	18.56	18.99	19.12	18.42	18.60	18.82	18.96
Cr_2O_3	0.00	0.00	0.06	0.01	0.03	0.00	0.01	0.02	0.03	0.02	0.00	0.01	0.00	0.03	0.02
FeO	19.23	18.96	18.81	19.25	18.70	18.83	18.73	18.98	18.96	18.83	18.91	18.43	18.55	18.65	18.55
MnO	0.19	0.14	0.13	0.17	0.15	0.17	0.15	0.13	0.15	0.14	0.14	0.15	0.20	0.16	0.19
MgO	9.94	9.62	9.49	9.55	9.72	9.53	9.34	9.29	9.33	9.28	9.40	9.72	9.47	9.44	9.70
CaO	0.05	0.00	0.00	0.00	0.11	0.00	0.01	0.00	0.02	0.00	0.00	0.03	0.00	0.02	0.04
Na_2O	0.15	0.40	0.38	0.40	0.37	0.29	0.40	0.37	0.35	0.37	0.41	0.33	0.35	0.41	0.31
K_2O	10.07	9.95	9.82	9.70	9.84	10.11	9.91	9.74	9.75	9.79	9.92	9.76	9.85	10.01	9.88
F	0.00	0.00	0.00	0.00	0.00	0.00	0.00	0.00	0.00	0.00	0.01	0.00	0.00	0.00	0.00
Cl	0.07	0.09	0.06	0.06	0.06	0.07	0.06	0.05	0.08	0.07	0.09	0.07	0.08	0.07	0.07
Total	95.93	96.70	96.45	96.95	96.31	96.45	96.15	95.99	95.63	96.22	96.60	95.34	94.89	95.64	95.98
—O=F,Cl	0.02	0.02	0.01	0.01	0.01	0.02	0.01	0.01	0.02	0.02	0.02	0.02	0.02	0.02	0.02
Total	95.91	96.68	96.44	96.93	96.29	96.43	96.14	95.98	95.61	96.20	96.58	95.32	94.87	95.63	95.96
Cations (based on 12 oxygens)															
Si	2.64	2.69	2.68	2.70	2.65	2.65	2.65	2.64	2.61	2.65	2.66	2.63	2.58	2.61	2.63
Ti	0.15	0.19	0.20	0.21	0.20	0.20	0.21	0.23	0.22	0.22	0.21	0.19	0.19	0.20	0.20
Al	1.68	1.72	1.70	1.70	1.70	1.72	1.70	1.66	1.65	1.70	1.72	1.63	1.64	1.67	1.69
Cr	0.00	0.00	0.00	0.00	0.00	0.00	0.00	0.00	0.00	0.00	0.00	0.00	0.00	0.00	0.00
Fe^{+2}	1.22	1.21	1.19	1.23	1.19	1.20	1.19	1.20	1.20	1.19	1.21	1.16	1.16	1.18	1.17
Mn	0.01	0.01	0.01	0.01	0.01	0.01	0.01	0.01	0.01	0.01	0.01	0.01	0.01	0.01	0.01
Mg	1.12	1.09	1.07	1.09	1.10	1.08	1.06	1.05	1.05	1.05	1.07	1.09	1.06	1.06	1.09
Ca	0.00	0.00	0.00	0.00	0.01	0.00	0.00	0.00	0.00	0.00	0.00	0.00	0.00	0.00	0.00
Na	0.02	0.06	0.06	0.06	0.05	0.04	0.06	0.05	0.05	0.05	0.06	0.05	0.05	0.06	0.05
K	0.97	0.97	0.95	0.95	0.95	0.98	0.96	0.94	0.94	0.95	0.96	0.93	0.94	0.96	0.95
F	0.00	0.00	0.00	0.00	0.00	0.00	0.00	0.00	0.00	0.00	0.00	0.00	0.00	0.00	0.00
Cl	0.01	0.01	0.01	0.01	0.01	0.01	0.01	0.01	0.01	0.01	0.01	0.01	0.01	0.01	0.01
OH	2.07	1.69	1.81	1.57	1.88	1.81	1.95	2.03	2.21	1.92	1.74	2.34	2.56	2.20	2.04

Table 4. Electron microprobe analyses of biotite (continued).

Sample#	JMH-26														
Circle#	4	4	4	4	4	4	4	4	4	4	1	1	1	1	1
Point#	5	6	7	1	2	3	4	5	6	7	1	2	3	4	5
Analysis#	309	310	311	312	313	314	315	316	317	318	504	505	506	507	508
Comment	Light	Light	Light	Dark	Dark	Dark	Dark	Dark	Dark	Dark	Csmatrix	Csmatrix	Csmatrix	Csmatrix	Csmatrix
Wt. % oxides															
SiO_2	34.69	35.10	34.89	35.39	35.52	35.36	35.06	35.18	35.73	35.21	35.07	34.84	35.13	35.10	35.15
TiO_2	3.23	3.07	3.21	3.50	3.31	3.25	3.13	3.27	2.41	3.23	3.56	3.68	3.56	3.61	3.44
Al_2O_3	19.07	19.10	18.99	19.14	19.12	18.96	19.08	18.99	18.79	18.80	18.13	18.33	18.49	18.38	18.72
Cr_2O_3	0.00	0.03	0.03	0.00	0.04	0.00	0.00	0.04	0.00	0.01	0.04	0.03	0.02	0.04	0.01
FeO	18.14	18.10	18.09	18.65	18.48	18.49	18.68	18.77	18.52	18.63	19.44	19.54	19.41	19.36	19.18
MnO	0.16	0.13	0.15	0.15	0.13	0.19	0.18	0.13	0.14	0.16	0.16	0.17	0.16	0.17	0.18
MgO	10.02	10.13	9.95	10.03	9.73	10.10	9.86	9.93	10.80	9.97	9.80	9.75	9.73	9.78	9.86
CaO	0.02	0.02	0.00	0.00	0.00	0.00	0.00	0.00	0.02	0.00	0.00	0.00	0.00	0.01	0.00
Na_2O	0.43	0.44	0.46	0.46	0.33	0.46	0.33	0.42	0.29	0.39	0.36	0.34	0.37	0.42	0.36
K_2O	9.68	9.81	9.75	9.99	9.92	9.82	10.13	10.03	10.05	10.05	9.99	10.06	10.02	9.89	10.22
F	0.00	0.00	0.00	0.00	0.00	0.00	0.00	0.00	0.00	0.00	0.00	0.00	0.00	0.00	0.00
Cl	0.08	0.07	0.08	0.07	0.07	0.07	0.06	0.07	0.08	0.07	0.07	0.08	0.07	0.08	0.08
Total	95.50	95.98	95.58	97.36	96.64	96.68	96.48	96.80	96.81	96.51	96.60	96.79	96.94	96.82	97.19
—O≡F,Cl	0.02	0.02	0.02	0.02	0.02	0.02	0.01	0.02	0.02	0.02	0.02	0.02	0.02	0.02	0.02
Total	95.48	95.97	95.57	97.35	96.62	96.66	96.47	96.79	96.79	96.49	96.58	96.77	96.92	96.80	97.17
Cations (based on 12 oxygens)															
Si	2.60	2.65	2.62	2.72	2.70	2.69	2.67	2.69	2.72	2.68	2.68	2.68	2.70	2.69	2.71
Ti	0.18	0.17	0.18	0.20	0.19	0.19	0.18	0.19	0.14	0.18	0.21	0.21	0.21	0.21	0.20
Al	1.69	1.70	1.68	1.73	1.71	1.70	1.71	1.71	1.69	1.69	1.64	1.66	1.67	1.66	1.70
Cr	0.00	0.00	0.00	0.00	0.00	0.00	0.00	0.00	0.00	0.00	0.00	0.00	0.00	0.00	0.00
Fe^{+2}	1.14	1.14	1.14	1.20	1.17	1.18	1.19	1.20	1.18	1.19	1.24	1.25	1.25	1.24	1.23
Mn	0.01	0.01	0.01	0.01	0.01	0.01	0.01	0.01	0.01	0.01	0.01	0.01	0.01	0.01	0.01
Mg	1.12	1.14	1.11	1.15	1.10	1.14	1.12	1.13	1.23	1.13	1.12	1.12	1.11	1.12	1.13
Ca	0.00	0.00	0.00	0.00	0.00	0.00	0.00	0.00	0.00	0.00	0.00	0.00	0.00	0.00	0.00
Na	0.06	0.06	0.07	0.07	0.05	0.07	0.05	0.06	0.04	0.06	0.05	0.05	0.05	0.06	0.05
K	0.93	0.94	0.93	0.98	0.96	0.95	0.98	0.98	0.98	0.98	0.98	0.99	0.98	0.97	1.00
F	0.00	0.00	0.00	0.00	0.00	0.00	0.00	0.00	0.00	0.00	0.00	0.00	0.00	0.00	0.00
Cl	0.01	0.01	0.01	0.01	0.01	0.01	0.01	0.01	0.01	0.01	0.01	0.01	0.01	0.01	0.01
OH	2.26	2.03	2.22	1.36	1.71	1.69	1.79	1.64	1.63	1.78	1.74	1.65	1.58	1.64	1.45

Table 4. Electron microprobe analyses of biotite (continued).

Sample#	JMH-26														JMH-24
Circle#	1	1	1	1	1	2	2	2	2	2	4	4	4	4	
Point#	6	7	8	9	10	1	2	3	4	5	1	2	3	4	
Analysis#	509	510	511	512	513	545	546	547	548	549	550	551	552	553	
Comment	Csmatrix	Csmatrix	Csmatrix	Csmatrix	Csmatrix	Csmatrix	Csmatrix	Csmatrix	Csmatrix	Csmatrix	Csmatrix	Csmatrix	Csmatrix	Csmatrix	
Wt. % oxides															
SiO_2	35.28	35.26	35.86	35.56	35.24	35.20	35.46	35.36	35.05	34.74	35.27	35.34	34.98	35.45	34.82
TiO_2	3.35	3.08	2.92	3.48	3.97	4.11	3.21	3.67	3.62	3.41	2.34	3.07	3.29	3.19	3.28
Al_2O_3	18.88	19.08	17.80	18.25	18.41	18.70	19.17	19.08	18.72	18.59	19.62	18.89	19.00	19.14	18.57
Cr_2O_3	0.03	0.01	0.02	0.03	0.02	0.00	0.00	0.01	0.02	0.02	0.00	0.01	0.02	0.01	0.00
FeO	18.98	19.76	19.81	19.27	19.39	18.52	18.86	18.57	18.79	18.57	18.54	18.53	18.27	18.62	18.99
MnO	0.14	0.15	0.17	0.15	0.18	0.17	0.18	0.16	0.16	0.17	0.15	0.16	0.16	0.19	0.17
MgO	9.84	9.63	9.97	9.79	9.34	9.73	9.90	9.62	9.67	9.40	10.14	10.45	9.82	10.01	9.77
CaO	0.00	0.00	0.00	0.00	0.00	0.01	0.00	0.00	0.01	0.01	0.00	0.00	0.00	0.00	0.00
Na_2O	0.39	0.31	0.11	0.15	0.33	0.35	0.41	0.41	0.36	0.30	0.48	0.36	0.37	0.40	0.39
K_2O	10.04	10.37	10.39	10.37	10.19	9.93	9.98	9.92	10.05	9.98	9.96	10.13	10.06	10.00	9.99
F	0.00	0.00	0.00	0.00	0.00	0.00	0.00	0.00	0.00	0.00	0.01	0.00	0.00	0.01	0.00
Cl	0.08	0.10	0.08	0.08	0.07	0.07	0.07	0.07	0.07	0.07	0.09	0.07	0.07	0.07	0.08
Total	97.00	97.72	97.09	97.12	97.11	96.78	97.23	96.85	96.51	95.23	96.56	96.98	96.02	97.07	96.05
—O≡F,Cl	0.02	0.02	0.02	0.02	0.02	0.02	0.02	0.01	0.02	0.02	0.02	0.01	0.02	0.02	0.02
Total	96.98	97.70	97.07	97.10	97.09	96.76	97.21	96.83	96.49	95.21	96.54	96.96	96.00	97.05	96.03
Cations (based on 12 oxygens)															
Si	2.70	2.74	2.76	2.74	2.71	2.68	2.72	2.70	2.67	2.61	2.68	2.70	2.64	2.71	2.64
Ti	0.19	0.18	0.17	0.20	0.23	0.24	0.18	0.21	0.21	0.19	0.13	0.18	0.19	0.18	0.19
Al	1.71	1.75	1.62	1.65	1.67	1.68	1.73	1.72	1.68	1.64	1.76	1.70	1.69	1.73	1.66
Cr	0.00	0.00	0.00	0.00	0.00	0.00	0.00	0.00	0.00	0.00	0.00	0.00	0.00	0.00	0.00
Fe^{+2}	1.22	1.28	1.28	1.24	1.25	1.18	1.21	1.18	1.20	1.17	1.18	1.19	1.15	1.19	1.21
Mn	0.01	0.01	0.01	0.01	0.01	0.01	0.01	0.01	0.01	0.01	0.01	0.01	0.01	0.01	0.01
Mg	1.12	1.11	1.14	1.12	1.07	1.11	1.13	1.09	1.10	1.05	1.15	1.19	1.11	1.14	1.11
Ca	0.00	0.00	0.00	0.00	0.00	0.00	0.00	0.00	0.00	0.00	0.00	0.00	0.00	0.00	0.00
Na	0.06	0.05	0.02	0.02	0.05	0.05	0.06	0.06	0.05	0.04	0.07	0.05	0.05	0.06	0.06
K	0.98	1.03	1.02	1.02	1.00	0.97	0.98	0.97	0.98	0.96	0.97	0.99	0.97	0.98	0.97
F	0.00	0.00	0.00	0.00	0.00	0.00	0.00	0.00	0.00	0.00	0.00	0.00	0.00	0.00	0.00
Cl	0.01	0.01	0.01	0.01	0.01	0.01	0.01	0.01	0.01	0.01	0.01	0.01	0.01	0.01	0.01
OH	1.54	1.19	1.50	1.49	1.49	1.65	1.43	1.61	1.78	2.40	1.75	1.55	2.02	1.50	2.01

Table 4. Electron microprobe analyses of biotite (continued).

Sample#	JMH-24														
Circle#															
Point#															
Analysis#															
Comment															
Wt. % oxides															
SiO_2	35.31	35.56	35.14	35.23	35.04	35.19	34.77	35.07	34.72	34.76	34.90	34.73	35.06	34.90	35.85
TiO_2	3.22	2.94	3.62	3.64	3.50	3.72	3.78	3.67	3.60	3.04	3.01	3.14	3.21	2.81	3.49
Al_2O_3	18.75	19.12	18.46	18.43	18.78	18.70	18.34	18.82	18.90	18.84	18.72	19.06	18.80	19.14	18.67
Cr_2O_3	0.01	0.04	0.00	0.00	0.01	0.04	0.05	0.02	0.01	0.00	0.02	0.05	0.02	0.00	0.00
FeO	18.90	18.91	18.87	18.90	19.23	19.15	19.42	19.27	19.32	18.96	17.73	18.72	19.17	19.02	17.70
MnO	0.18	0.17	0.14	0.14	0.15	0.17	0.17	0.14	0.16	0.17	0.16	0.16	0.15	0.15	0.18
MgO	9.68	9.76	9.45	9.25	9.56	9.47	9.49	9.49	9.53	9.76	10.64	9.97	9.71	10.03	10.74
CaO	0.00	0.00	0.01	0.03	0.00	0.00	0.00	0.00	0.00	0.00	0.00	0.00	0.00	0.00	0.02
Na_2O	0.42	0.40	0.44	0.35	0.40	0.33	0.34	0.37	0.38	0.42	0.25	0.35	0.39	0.43	0.32
K_2O	10.23	10.08	9.82	9.96	10.17	10.14	10.12	10.00	9.94	10.13	10.09	10.10	10.33	10.13	10.00
F	0.00	0.00	0.00	0.00	0.00	0.00	0.01	0.04	0.00	0.00	0.01	0.00	0.00	0.00	0.06
Cl	0.07	0.08	0.11	0.10	0.08	0.07	0.07	0.09	0.09	0.09	0.07	0.10	0.08	0.08	0.12
Total	96.74	97.03	96.04	96.00	96.90	96.97	96.53	96.95	96.64	96.13	95.58	96.35	96.90	96.68	97.09
—O=F,Cl	0.02	0.02	0.02	0.02	0.02	0.02	0.02	0.04	0.02	0.02	0.02	0.02	0.02	0.02	0.05
Total	96.72	97.01	96.02	95.98	96.88	96.95	96.51	96.91	96.62	96.11	95.55	96.33	96.88	96.66	97.04
Cations (based on 12 oxygens)															
Si	2.70	2.72	2.66	2.67	2.69	2.70	2.66	2.69	2.66	2.64	2.62	2.64	2.69	2.67	2.73
Ti	0.19	0.17	0.21	0.21	0.20	0.21	0.22	0.21	0.21	0.17	0.17	0.18	0.19	0.16	0.20
Al	1.69	1.73	1.65	1.65	1.70	1.69	1.66	1.70	1.70	1.69	1.66	1.71	1.70	1.72	1.67
Cr	0.00	0.00	0.00	0.00	0.00	0.00	0.00	0.00	0.00	0.00	0.00	0.00	0.00	0.00	0.00
Fe^{+2}	1.21	1.21	1.20	1.20	1.23	1.23	1.24	1.24	1.24	1.21	1.11	1.19	1.23	1.22	1.13
Mn	0.01	0.01	0.01	0.01	0.01	0.01	0.01	0.01	0.01	0.01	0.01	0.01	0.01	0.01	0.01
Mg	1.10	1.11	1.07	1.04	1.09	1.08	1.08	1.08	1.09	1.11	1.19	1.13	1.11	1.14	1.22
Ca	0.00	0.00	0.00	0.00	0.00	0.00	0.00	0.00	0.00	0.00	0.00	0.00	0.00	0.00	0.00
Na	0.06	0.06	0.07	0.05	0.06	0.05	0.05	0.06	0.06	0.06	0.04	0.05	0.06	0.06	0.05
K	1.00	0.98	0.95	0.96	1.00	0.99	0.99	0.98	0.97	0.98	0.97	0.98	1.01	0.99	0.97
F	0.00	0.00	0.00	0.00	0.00	0.00	0.00	0.01	0.00	0.00	0.00	0.00	0.00	0.00	0.01
Cl	0.01	0.01	0.01	0.01	0.01	0.01	0.01	0.01	0.01	0.01	0.01	0.01	0.01	0.01	0.02
OH	1.67	1.52	2.01	2.03	1.60	1.56	1.78	1.58	1.73	1.97	2.23	1.86	1.60	1.70	1.50

Table 4. Electron microprobe analyses of biotite (continued).

Sample#	JMH-24													H1281-61.5	
Circle#														1	1
Point#														1	2
Analysis#														594	595
Comment														matrix	
Wt. % oxides															
SiO_2	35.64	35.88	35.68	35.49	35.65	35.77	35.53	35.41	35.62	35.56	36.02	35.90	35.48	35.53	35.29
TiO_2	3.54	3.58	3.63	3.54	3.50	3.54	3.51	3.47	3.54	3.54	3.53	3.46	3.29	3.15	3.56
Al_2O_3	18.65	18.28	18.43	18.50	18.38	18.62	18.43	18.40	18.57	18.41	18.36	18.75	18.25	19.41	18.76
Cr_2O_3	0.00	0.02	0.26	0.10	0.03	0.03	0.00	0.01	0.02	0.00	0.00	0.00	0.05	0.00	0.00
FeO	18.20	18.21	18.25	18.29	18.15	18.25	18.19	17.91	17.89	18.71	18.01	17.87	18.98	19.27	19.38
MnO	0.15	0.20	0.19	0.18	0.17	0.17	0.17	0.16	0.14	0.17	0.20	0.20	0.19	0.19	0.18
MgO	10.73	10.46	10.66	10.63	10.58	10.67	10.51	10.79	10.66	10.45	10.53	10.49	10.24	9.59	9.50
CaO	0.02	0.02	0.00	0.00	0.00	0.00	0.00	0.00	0.01	0.02	0.00	0.02	0.05	0.01	0.00
Na_2O	0.35	0.27	0.32	0.23	0.29	0.24	0.29	0.30	0.19	0.29	0.33	0.27	0.18	0.40	0.35
K_2O	10.03	10.07	10.15	10.12	10.09	10.11	10.10	10.04	10.33	10.17	10.22	10.28	10.28	10.19	10.00
F	0.00	0.00	0.00	0.00	0.00	0.00	0.09	0.00	0.00	0.00	0.00	0.00	0.00	0.01	0.00
Cl	0.07	0.08	0.08	0.07	0.07	0.06	0.08	0.09	0.08	0.07	0.08	0.08	0.08	0.07	0.08
Total	97.38	97.05	97.63	97.13	96.89	97.43	96.83	96.55	97.04	97.36	97.26	97.30	97.04	97.80	97.07
—O=F,Cl	0.02	0.02	0.02	0.02	0.02	0.01	0.06	0.02	0.02	0.02	0.02	0.02	0.02	0.02	0.02
Total	97.36	97.03	97.61	97.12	96.87	97.42	96.78	96.53	97.02	97.34	97.24	97.28	97.02	97.78	97.05
Cations (based on 12 oxygens)															
Si	2.73	2.74	2.75	2.72	2.72	2.74	2.70	2.69	2.72	2.73	2.76	2.75	2.72	2.75	2.71
Ti	0.20	0.21	0.21	0.20	0.20	0.20	0.20	0.20	0.20	0.20	0.20	0.20	0.19	0.18	0.21
Al	1.69	1.65	1.67	1.67	1.65	1.68	1.65	1.65	1.67	1.67	1.66	1.69	1.65	1.77	1.70
Cr	0.00	0.00	0.02	0.01	0.00	0.00	0.00	0.00	0.00	0.00	0.00	0.00	0.00	0.00	0.00
Fe^{+2}	1.17	1.16	1.18	1.17	1.16	1.17	1.16	1.14	1.14	1.20	1.15	1.14	1.22	1.25	1.24
Mn	0.01	0.01	0.01	0.01	0.01	0.01	0.01	0.01	0.01	0.01	0.01	0.01	0.01	0.01	0.01
Mg	1.23	1.19	1.22	1.21	1.20	1.22	1.19	1.22	1.21	1.20	1.20	1.20	1.17	1.11	1.09
Ca	0.00	0.00	0.00	0.00	0.00	0.00	0.00	0.00	0.00	0.00	0.00	0.00	0.00	0.00	0.00
Na	0.05	0.04	0.05	0.03	0.04	0.04	0.04	0.04	0.03	0.04	0.05	0.04	0.03	0.06	0.05
K	0.98	0.98	1.00	0.99	0.98	0.99	0.98	0.97	1.01	1.00	1.00	1.00	1.01	1.01	0.98
F	0.00	0.00	0.00	0.00	0.00	0.00	0.02	0.00	0.00	0.00	0.00	0.00	0.00	0.00	0.00
Cl	0.01	0.01	0.01	0.01	0.01	0.01	0.01	0.01	0.01	0.01	0.01	0.01	0.01	0.01	0.01
OH	1.35	1.51	1.23	1.47	1.59	1.32	1.64	1.76	1.52	1.36	1.41	1.39	1.52	1.15	1.51

Table 4. Electron microprobe analyses of biotite (continued)

Sample#	H1281-61.5										H1281-61.7				
Circle#	3	3	3	3	3	6	6	6	6	6	2	2	2	2	
Point#	1	2	3	4	5	1	2	3	4	5	1	2	5	6	1
Analysis#	596	597	598	599	600	631	632	633	634	635	651	652	655	656	672
Comment															outer
Wt. % oxides															
SiO_2	35.18	35.33	35.54	36.03	35.08	35.10	35.52	35.36	35.40	35.61	35.44	35.63	35.13	35.51	35.62
TiO_2	3.57	3.74	3.68	2.89	3.00	3.45	3.77	3.47	3.89	3.10	2.65	2.63	2.88	2.84	3.57
Al_2O_3	19.16	19.10	19.13	18.41	19.17	18.89	19.22	18.85	18.91	18.96	19.67	19.23	18.99	18.83	19.33
Cr_2O_3	0.00	0.00	0.02	0.01	0.00	0.02	0.03	0.00	0.00	0.00	0.00	0.01	0.00	0.00	0.00
FeO	19.04	18.81	18.81	18.72	18.52	18.89	18.51	19.42	19.51	18.41	18.17	18.36	18.15	18.19	18.64
MnO	0.19	0.16	0.17	0.18	0.17	0.13	0.16	0.16	0.15	0.19	0.17	0.20	0.15	0.18	0.18
MgO	9.41	9.37	9.39	10.48	10.54	9.71	9.46	9.32	9.20	10.19	10.59	10.75	10.43	10.64	9.80
CaO	0.00	0.00	0.03	0.05	0.06	0.04	0.00	0.00	0.00	0.00	0.02	0.02	0.01	0.00	0.00
Na_2O	0.40	0.36	0.47	0.32	0.16	0.33	0.35	0.40	0.36	0.13	0.45	0.42	0.42	0.23	0.36
K_2O	10.08	10.18	9.97	9.90	9.76	10.03	10.14	9.95	10.24	10.33	9.95	9.91	9.90	10.20	9.92
F	0.00	0.00	0.00	0.00	0.00	0.01	0.00	0.00	0.00	0.00	0.00	0.00	0.00	0.00	0.00
Cl	0.08	0.07	0.11	0.11	0.08	0.07	0.07	0.07	0.08	0.09	0.08	0.09	0.08	0.08	0.08
Total	97.08	97.12	97.29	97.08	96.51	96.65	97.19	96.99	97.72	96.99	97.17	97.21	96.12	96.67	97.48
—O=F,Cl	0.02	0.02	0.03	0.02	0.02	0.02	0.02	0.02	0.02	0.02	0.02	0.02	0.02	0.02	0.02
Total	97.06	97.10	97.27	97.06	96.49	96.63	97.17	96.97	97.70	96.97	97.15	97.19	96.10	96.66	97.47
Cations (based on 12 oxygens)															
Si	2.70	2.71	2.73	2.75	2.66	2.68	2.72	2.71	2.74	2.72	2.71	2.72	2.65	2.70	2.73
Ti	0.21	0.22	0.21	0.17	0.17	0.20	0.22	0.20	0.23	0.18	0.15	0.15	0.16	0.16	0.21
Al	1.73	1.73	1.73	1.66	1.71	1.70	1.73	1.70	1.73	1.71	1.77	1.73	1.69	1.69	1.75
Cr	0.00	0.00	0.00	0.00	0.00	0.00	0.00	0.00	0.00	0.00	0.00	0.00	0.00	0.00	0.00
Fe^{+2}	1.22	1.21	1.21	1.20	1.18	1.21	1.19	1.25	1.26	1.18	1.16	1.17	1.15	1.16	1.20
Mn	0.01	0.01	0.01	0.01	0.01	0.01	0.01	0.01	0.01	0.01	0.01	0.01	0.01	0.01	0.01
Mg	1.08	1.07	1.07	1.19	1.19	1.10	1.08	1.07	1.06	1.16	1.20	1.22	1.17	1.21	1.12
Ca	0.00	0.00	0.00	0.00	0.00	0.00	0.00	0.00	0.00	0.00	0.00	0.00	0.00	0.00	0.00
Na	0.06	0.05	0.07	0.05	0.02	0.05	0.05	0.06	0.05	0.02	0.07	0.06	0.06	0.03	0.05
K	0.99	1.00	0.98	0.97	0.94	0.98	0.99	0.97	1.01	1.01	0.97	0.97	0.95	0.99	0.97
F	0.00	0.00	0.00	0.00	0.00	0.00	0.00	0.00	0.00	0.00	0.00	0.00	0.00	0.00	0.00
Cl	0.01	0.01	0.01	0.01	0.01	0.01	0.01	0.01	0.01	0.01	0.01	0.01	0.01	0.01	0.01
OH	1.50	1.48	1.40	1.50	1.78	1.71	1.44	1.55	1.19	1.55	1.45	1.43	1.97	1.70	1.30

Table 4. Electron microprobe analyses of biotite (continued).

Sample#	H1281-61.7									
Circle#										
Point#	2	3	4	5	6	7	8	9	10	11
Analysis#	673	674	675	676	677	678	679	680	681	682
Comment										
Wt. % oxides										
SiO_2	35.26	34.81	34.88	35.22	36.82	35.25	35.39	35.25	35.27	35.51
TiO_2	3.51	5.55	3.67	3.73	1.48	3.78	3.63	3.84	3.76	3.81
Al_2O_3	18.84	17.99	18.70	18.91	17.20	18.78	19.04	19.03	18.91	19.12
Cr_2O_3	0.00	0.04	0.01	0.01	0.02	0.00	0.05	0.02	0.02	0.00
FeO	18.88	17.76	18.97	18.93	17.40	19.09	18.73	19.14	18.52	18.61
MnO	0.18	0.16	0.19	0.15	0.22	0.17	0.14	0.15	0.17	0.20
MgO	9.50	9.04	9.14	9.34	12.59	9.23	9.30	9.33	9.54	9.48
CaO	0.01	1.47	0.00	0.01	0.03	0.01	0.02	0.00	0.01	0.00
Na_2O	0.35	0.35	0.32	0.27	0.05	0.35	0.35	0.33	0.37	0.33
K_2O	10.08	9.40	10.05	10.30	10.37	9.94	10.11	10.07	9.98	10.02
F	0.00	0.00	0.00	0.00	0.00	0.00	0.00	0.00	0.00	0.00
Cl	0.07	0.07	0.07	0.08	0.07	0.07	0.07	0.08	0.08	0.06
Total	96.66	96.62	95.97	96.94	96.23	96.63	96.83	97.21	96.59	97.13
—O≡F,Cl	0.01	0.02	0.01	0.02	0.01	0.01	0.02	0.02	0.02	0.01
Total	96.64	96.60	95.96	96.92	96.21	96.62	96.81	97.20	96.57	97.11
Cations (based on 12 oxygens)										
Si	2.69	2.65	2.64	2.70	2.78	2.69	2.70	2.71	2.68	2.72
Ti	0.20	0.32	0.21	0.22	0.08	0.22	0.21	0.22	0.22	0.22
Al	1.70	1.61	1.67	1.71	1.53	1.69	1.71	1.72	1.70	1.72
Cr	0.00	0.00	0.00	0.00	0.00	0.00	0.00	0.00	0.00	0.00
Fe^{+2}	1.20	1.13	1.20	1.21	1.10	1.22	1.20	1.23	1.18	1.19
Mn	0.01	0.01	0.01	0.01	0.01	0.01	0.01	0.01	0.01	0.01
Mg	1.08	1.03	1.03	1.07	1.41	1.05	1.06	1.07	1.08	1.08
Ca	0.00	0.12	0.00	0.00	0.00	0.00	0.00	0.00	0.00	0.00
Na	0.05	0.05	0.05	0.04	0.01	0.05	0.05	0.05	0.05	0.05
K	0.98	0.91	0.97	1.01	1.00	0.97	0.99	0.99	0.97	0.98
F	0.00	0.00	0.00	0.00	0.00	0.00	0.00	0.00	0.00	0.00
Cl	0.01	0.01	0.01	0.01	0.01	0.01	0.01	0.01	0.01	0.01
OH	1.71	1.73	2.04	1.58	1.91	1.72	1.62	1.44	1.74	1.47

Table 5. Electron microprobe analyses of chlorite.

Sample#	JMH-306I											
Circle#												
Analysis#	30	31	32	33	34	35	36	37	38	39	40	41
Comment	Blackwall	Blackwall	Blackwall	Blackwall	Blackwall	Blackwall	Blackwall	Blackwall	Blackwall	Blackwall	Blackwall	Blackwall
Comment	Line	Line	Line	Line	Line	Line	Line	Line	Line	Line	Line	Line
Wt. % oxides												
SiO_2	42.95	40.42	40.41	40.20	40.44	33.40	39.69	40.62	40.55	41.37	34.55	33.64
TiO_2	0.00	0.02	0.01	0.02	0.01	0.10	0.03	0.01	0.02	0.00	0.27	0.09
Al_2O_3	0.30	0.97	2.51	0.71	0.73	14.09	2.27	0.72	0.68	0.73	12.25	12.52
Cr_2O_3	0.00	0.00	0.26	0.03	0.04	0.02	0.08	0.10	0.07	0.09	0.01	0.00
FeO	4.51	2.81	3.97	2.25	2.16	5.22	2.93	2.22	2.25	2.25	5.25	8.68
MnO	0.10	0.14	0.15	0.18	0.21	0.05	0.18	0.17	0.20	0.17	0.07	0.09
MgO	38.42	38.55	37.95	39.65	39.67	32.53	38.58	39.42	39.52	40.19	33.20	31.56
CaO	0.03	0.07	0.04	0.05	0.06	0.01	0.07	0.06	0.07	0.03	0.02	0.02
Na_2O	0.00	0.00	0.01	0.01	0.02	0.00	0.01	0.01	0.02	0.00	0.02	0.02
K_2O	0.03	0.00	0.03	0.03	0.02	0.52	0.03	0.03	0.02	0.02	1.44	0.45
F	0.00	0.00	0.00	0.00	0.00	0.02	0.00	0.00	0.00	0.01	0.00	0.00
Cl	0.01	0.11	0.10	0.13	0.15	0.01	0.12	0.14	0.11	0.23	0.03	0.05
Total	86.35	83.06	85.41	83.24	83.47	85.96	83.97	83.46	83.47	85.03	87.10	87.11
—O≡F,Cl	0.00	0.03	0.02	0.03	0.03	0.01	0.03	0.03	0.03	0.06	0.01	0.01
Total	86.35	83.06	85.41	83.24	83.47	85.96	83.97	83.46	83.47	85.03	87.10	87.11
Cations (based on 14 oxygens)												
Si	4.07	3.97	3.89	3.94	3.95	3.22	3.87	3.97	3.96	3.97	3.31	3.27
Ti	0.00	0.00	0.00	0.00	0.00	0.01	0.00	0.00	0.00	0.00	0.02	0.01
Al	0.03	0.11	0.28	0.08	0.08	1.60	0.26	0.08	0.08	0.08	1.38	1.43
Cr	0.00	0.00	0.02	0.00	0.00	0.00	0.01	0.01	0.01	0.01	0.00	0.00
Fe^{+3}	0.00	0.00	0.00	0.00	0.00	0.00	0.00	0.00	0.00	0.00	0.00	0.00
Fe^{+2}	0.36	0.23	0.32	0.18	0.18	0.42	0.24	0.18	0.18	0.18	0.42	0.70
Mn	0.01	0.01	0.01	0.02	0.02	0.00	0.01	0.01	0.02	0.01	0.01	0.01
Mg	5.43	5.65	5.44	5.79	5.78	4.68	5.60	5.74	5.75	5.75	4.74	4.57
Ca	0.00	0.01	0.00	0.01	0.01	0.00	0.01	0.01	0.01	0.00	0.00	0.00
Na	0.00	0.00	0.00	0.00	0.00	0.00	0.00	0.00	0.00	0.00	0.00	0.00
K	0.00	0.00	0.00	0.00	0.00	0.06	0.00	0.00	0.00	0.00	0.18	0.06
F	0.00	0.00	0.00	0.00	0.00	0.01	0.00	0.00	0.00	0.00	0.00	0.00
Cl	0.00	0.02	0.02	0.02	0.03	0.00	0.02	0.02	0.02	0.04	0.01	0.01
OH	7.98	7.94	7.94	7.93	7.92	7.98	7.93	7.93	7.93	7.89	7.98	7.97

Table 5. Electron microprobe analyses of chlorite (continued).

Sample#	JMH-306I											
Circle#												
Analysis#	43	44	46	47	48	49	50	51	52	53	54	55
Comment	Blackwall	Blackwall	Blackwall	Blackwall	Blackwall	Blackwall	Blackwall	Blackwall	Blackwall	Blackwall	Blackwall	Blackwall
Comment	Line	Line	Line	Line	Line	Line	Line	Line	Line	Line	Line	Line
Wt. % oxides												
SiO_2	34.22	36.42	31.44	33.40	31.89	29.18	30.09	29.80	33.28	31.72	32.28	35.72
TiO_2	0.27	0.00	0.01	0.00	0.00	0.00	0.00	0.00	0.07	0.01	0.01	0.01
Al_2O_3	12.82	8.33	16.32	12.88	14.65	19.12	18.17	18.07	13.32	14.41	13.64	9.54
Cr_2O_3	0.00	0.00	0.05	0.06	0.02	0.00	0.09	0.00	0.01	0.00	0.01	0.00
FeO	5.90	5.51	8.12	7.21	8.21	11.00	9.76	10.26	11.36	12.96	11.56	3.68
MnO	0.07	0.08	0.18	0.18	0.18	0.42	0.33	0.33	0.16	0.20	0.17	0.06
MgO	32.24	34.57	30.06	31.68	30.65	26.53	28.10	27.70	28.26	26.33	28.51	35.78
CaO	0.03	0.02	0.02	0.05	0.03	0.01	0.01	0.03	0.01	0.01	0.02	0.01
Na_2O	0.01	0.06	0.02	0.04	0.02	0.01	0.01	0.01	0.07	0.03	0.03	0.00
K_2O	1.26	0.50	0.01	0.09	0.05	0.02	0.04	0.04	1.26	1.35	0.50	0.03
F	0.00	0.00	0.00	0.00	0.00	0.00	0.00	0.00	0.00	0.00	0.00	0.00
Cl	0.05	0.05	0.05	0.07	0.08	0.03	0.04	0.02	0.05	0.02	0.04	0.04
Total	86.86	85.54	86.27	85.64	85.76	86.32	86.63	86.25	87.80	87.04	86.76	84.85
—O≡F,Cl	0.01	0.01	0.01	0.02	0.02	0.01	0.01	0.01	0.01	0.01	0.01	0.01
Total	86.86	85.54	86.27	85.64	85.76	86.32	86.63	86.24	87.80	87.04	86.76	84.85
Cations (based on 14 oxygens)												
Si	3.30	3.54	3.07	3.27	3.13	2.89	2.95	2.94	3.26	3.17	3.20	3.45
Ti	0.02	0.00	0.00	0.00	0.00	0.00	0.00	0.00	0.00	0.00	0.00	0.00
Al	1.46	0.95	1.88	1.49	1.70	2.23	2.10	2.10	1.54	1.70	1.59	1.09
Cr	0.00	0.00	0.00	0.00	0.00	0.00	0.01	0.00	0.00	0.00	0.00	0.00
Fe^{+3}	0.00	0.00	0.00	0.00	0.00	0.00	0.00	0.00	0.00	0.00	0.00	0.00
Fe^{+2}	0.48	0.45	0.66	0.59	0.68	0.91	0.80	0.85	0.93	1.08	0.96	0.30
Mn	0.01	0.01	0.02	0.01	0.01	0.04	0.03	0.03	0.01	0.02	0.01	0.00
Mg	4.63	5.00	4.37	4.62	4.49	3.92	4.11	4.08	4.13	3.92	4.21	5.16
Ca	0.00	0.00	0.00	0.00	0.00	0.00	0.00	0.00	0.00	0.00	0.00	0.00
Na	0.00	0.01	0.00	0.01	0.00	0.00	0.00	0.00	0.01	0.01	0.01	0.00
K	0.15	0.06	0.00	0.01	0.01	0.00	0.00	0.00	0.16	0.17	0.06	0.00
F	0.00	0.00	0.00	0.00	0.00	0.00	0.00	0.00	0.00	0.00	0.00	0.00
Cl	0.01	0.01	0.01	0.01	0.01	0.00	0.01	0.00	0.01	0.00	0.01	0.01
OH	7.97	7.97	7.95	7.95	7.95	7.92	7.93	7.94	7.96	7.96	7.96	7.98

Table 5. Electron microprobe analyses of chlorite (continued).

Sample#	JMH-306I			JMH-306I								
Circle#				4	4	4	4	4	4	4	4	4
Analysis#	56	57	61	79	80	81	82	83	84	86	87	89
Comment	Blackwall	Blackwall	Blackwall	pocket	pocket	pocket	pocket	pocket	pocket	pocket	pocket	pocket
Comment	Line	Line	Line	margin	margin	margin	margin	margin	margin	core	core	core
Wt. % oxides												
SiO_2	32.20	32.22	35.58	40.30	39.04	37.35	38.97	38.50	41.31	39.43	38.62	40.61
TiO_2	0.02	0.05	0.00	0.00	0.00	0.00	0.00	0.00	0.00	0.00	0.00	0.00
Al_2O_3	12.73	14.97	10.62	3.55	2.18	4.72	3.73	4.83	2.90	5.06	4.07	3.12
Cr_2O_3	0.00	0.01	0.00	0.00	0.00	0.00	0.02	0.00	0.01	0.00	0.00	0.01
FeO	10.08	9.28	4.47	2.25	9.41	6.06	8.29	8.27	1.33	4.42	8.56	2.36
MnO	0.26	0.20	0.14	0.60	1.53	1.15	1.37	1.23	0.34	1.04	1.24	0.60
MgO	29.93	28.88	34.97	38.23	32.54	35.22	33.88	32.99	42.77	35.67	33.44	38.41
CaO	0.02	0.03	0.01	0.17	0.28	0.23	0.25	0.24	0.17	0.23	0.18	0.19
Na_2O	0.03	0.03	0.00	0.04	0.07	0.05	0.06	0.02	0.01	0.08	0.05	0.05
K_2O	0.29	1.25	0.01	0.05	0.04	0.05	0.06	0.06	0.01	0.07	0.06	0.06
F	0.00	0.00	0.00	0.09	0.00	0.00	0.00	0.00	0.07	0.03	0.00	0.00
Cl	0.03	0.05	0.03	0.01	0.03	0.01	0.02	0.03	0.03	0.02	0.02	0.03
Total	85.58	86.96	85.81	85.23	85.11	84.84	86.65	86.16	88.92	86.04	86.22	85.43
—O≡F,Cl	0.01	0.01	0.01	0.04	0.01	0.00	0.00	0.01	0.03	0.02	0.01	0.01
Total	85.58	86.95	85.81	85.23	85.11	84.84	86.65	86.16	88.92	86.04	86.22	85.43
Cations (based on 14 oxygens)												
Si	3.21	3.16	3.41	3.86	3.91	3.69	3.80	3.77	3.78	3.79	3.79	3.87
Ti	0.00	0.00	0.00	0.00	0.00	0.00	0.00	0.00	0.00	0.00	0.00	0.00
Al	1.50	1.73	1.20	0.40	0.26	0.55	0.43	0.56	0.31	0.57	0.47	0.35
Cr	0.00	0.00	0.00	0.00	0.00	0.00	0.00	0.00	0.00	0.00	0.00	0.00
Fe^{+3}	0.00	0.00	0.00	0.00	0.00	0.00	0.00	0.00	0.00	0.00	0.00	0.00
Fe^{+2}	0.84	0.76	0.36	0.18	0.79	0.50	0.68	0.68	0.10	0.35	0.70	0.19
Mn	0.02	0.02	0.01	0.05	0.13	0.10	0.11	0.10	0.03	0.08	0.10	0.05
Mg	4.45	4.22	5.00	5.45	4.85	5.18	4.93	4.81	5.83	5.10	4.89	5.46
Ca	0.00	0.00	0.00	0.02	0.03	0.02	0.03	0.03	0.02	0.02	0.02	0.02
Na	0.01	0.01	0.00	0.01	0.01	0.01	0.01	0.00	0.00	0.02	0.01	0.01
K	0.04	0.16	0.00	0.01	0.01	0.01	0.01	0.01	0.00	0.01	0.01	0.01
F	0.00	0.00	0.00	0.03	0.00	0.00	0.00	0.00	0.02	0.01	0.00	0.00
Cl	0.01	0.01	0.00	0.00	0.01	0.00	0.00	0.01	0.00	0.00	0.00	0.01
OH	7.95	7.95	7.97	7.85	7.73	7.81	7.77	7.79	7.90	7.81	7.79	7.89

Table 5. Electron microprobe analyses of chlorite (continued).

Sample#	JMH-306I	Flt-B										
Circle#	4	1	1	1	1	1	1	1	1	1	1	1
Analysis#	90	91	92	93	95	96	98	99	100	101	102	103
Comment	pocket	pocket	pocket	pocket	pocket	pocket	pocket	pocket	pocket	pocket	pocket	pocket
Comment	core	rim	rim	rim	rim	rim	core	core	core	core	core	core
Wt. % oxides												
SiO_2	40.32	31.01	31.79	32.07	32.87	32.00	26.79	26.95	26.85	26.67	26.89	26.53
TiO_2	0.00	0.01	0.00	0.00	0.00	0.00	0.01	0.00	0.00	0.00	0.00	0.00
Al_2O_3	3.02	15.15	14.45	13.64	13.64	14.36	17.13	16.85	16.95	17.43	17.32	17.21
Cr_2O_3	0.00	0.02	0.00	0.00	0.00	0.00	0.01	0.00	0.00	0.00	0.01	0.00
FeO	1.44	9.52	9.76	7.94	6.97	9.34	27.35	27.37	27.05	26.84	27.14	27.10
MnO	0.34	5.10	4.54	3.11	2.64	4.13	3.64	3.68	3.56	3.46	3.57	3.57
MgO	39.07	24.94	25.84	28.63	28.82	26.60	12.89	12.89	13.34	13.57	13.39	12.98
CaO	0.14	0.08	0.11	0.10	0.19	0.08	0.03	0.07	0.03	0.03	0.03	0.08
Na_2O	0.01	0.02	0.03	0.05	0.06	0.05	0.02	0.03	0.04	0.04	0.04	0.06
K_2O	0.02	0.03	0.03	0.03	0.06	0.04	0.02	0.04	0.02	0.03	0.02	0.05
F	0.00	0.00	0.00	0.00	0.00	0.00	0.00	0.00	0.00	0.00	0.00	0.00
Cl	0.01	0.00	0.02	0.02	0.03	0.02	0.01	0.01	0.02	0.00	0.02	0.02
Total	84.36	85.87	86.57	85.58	85.26	86.61	87.90	87.88	87.84	88.06	88.42	87.60
—O≡F,Cl	0.00	0.00	0.00	0.00	0.01	0.01	0.00	0.00	0.00	0.00	0.00	0.00
Total	84.36	85.87	86.57	85.58	85.26	86.61	87.90	87.88	87.84	88.06	88.42	87.60
Cations (based on 14 oxygens)												
Si	3.87	3.14	3.18	3.20	3.26	3.19	2.91	2.92	2.91	2.88	2.89	2.89
Ti	0.00	0.00	0.00	0.00	0.00	0.00	0.00	0.00	0.00	0.00	0.00	0.00
Al	0.34	1.81	1.71	1.60	1.59	1.69	2.19	2.16	2.16	2.22	2.20	2.21
Cr	0.00	0.00	0.00	0.00	0.00	0.00	0.00	0.00	0.00	0.00	0.00	0.00
Fe^{+3}	0.00	0.00	0.00	0.00	0.00	0.00	0.00	0.00	0.00	0.00	0.00	0.00
Fe^{+2}	0.12	0.81	0.82	0.66	0.58	0.78	2.48	2.48	2.45	2.42	2.44	2.47
Mn	0.03	0.44	0.39	0.26	0.22	0.35	0.33	0.34	0.33	0.32	0.32	0.33
Mg	5.59	3.76	3.86	4.26	4.26	3.95	2.08	2.08	2.15	2.18	2.15	2.10
Ca	0.01	0.01	0.01	0.01	0.02	0.01	0.00	0.01	0.00	0.00	0.00	0.01
Na	0.00	0.00	0.01	0.01	0.01	0.01	0.00	0.01	0.01	0.01	0.01	0.01
K	0.00	0.00	0.00	0.00	0.01	0.01	0.00	0.01	0.00	0.00	0.00	0.01
F	0.00	0.00	0.00	0.00	0.00	0.00	0.00	0.00	0.00	0.00	0.00	0.00
Cl	0.00	0.00	0.00	0.00	0.00	0.00	0.00	0.00	0.00	0.00	0.00	0.00
OH	7.94	7.12	7.22	7.47	7.55	7.29	7.33	7.32	7.34	7.37	7.34	7.33

Table 5. Electron microprobe analyses of chlorite (continued).

Sample#	Flt-B									Flt-B		
Circle#	1	1	1	1	1	1	1	1	1	2	2	2
Analysis#	104	105	106	107	108	109	110	111	112	126	127	128
Comment	pocket	pocket	pocket	pocket	pocket	pocket	pocket	pocket	pocket	pocket	pocket	pocket
Comment	core	core	core	core	core	core	core	core	core	filling	filling	filling
Wt. % oxides												
SiO_2	26.75	26.90	27.06	26.87	26.83	27.12	26.58	26.89	26.77	26.76	27.01	27.13
TiO_2	0.00	0.00	0.00	0.00	0.00	0.00	0.00	0.03	0.00	0.00	0.00	0.00
Al_2O_3	17.18	17.19	17.64	17.14	17.55	17.62	17.25	17.19	17.07	17.79	17.88	17.76
Cr_2O_3	0.00	0.00	0.00	0.00	0.00	0.01	0.00	0.00	0.00	0.00	0.00	0.00
FeO	26.62	27.56	27.75	27.52	27.15	27.75	28.21	26.71	26.61	26.35	25.85	25.36
MnO	3.42	3.76	3.65	3.83	3.61	3.61	3.79	3.56	3.54	3.17	3.15	3.08
MgO	13.66	12.81	13.11	12.90	13.10	12.95	12.33	13.53	13.15	13.62	13.84	14.74
CaO	0.11	0.07	0.05	0.03	0.05	0.01	0.03	0.09	0.10	0.05	0.08	0.02
Na_2O	0.05	0.02	0.07	0.02	0.07	0.02	0.00	0.02	0.07	0.00	0.01	0.02
K_2O	0.04	0.04	0.01	0.02	0.02	0.03	0.03	0.03	0.03	0.02	0.02	0.01
F	0.00	0.00	0.00	0.00	0.00	0.00	0.00	0.00	0.00	0.00	0.00	0.00
Cl	0.02	0.02	0.01	0.02	0.01	0.01	0.02	0.02	0.03	0.00	0.01	0.02
Total	87.84	88.35	89.35	88.34	88.39	89.11	88.25	88.03	87.37	87.75	87.84	88.13
—O≡F,Cl	0.00	0.00	0.00	0.00	0.00	0.00	0.00	0.00	0.01	0.00	0.00	0.01
Total	87.84	88.35	89.35	88.34	88.39	89.11	88.25	88.03	87.37	87.75	87.84	88.13
Cations (based on 14 oxygens)												
Si	2.89	2.91	2.89	2.90	2.89	2.90	2.89	2.90	2.91	2.88	2.89	2.89
Ti	0.00	0.00	0.00	0.00	0.00	0.00	0.00	0.00	0.00	0.00	0.00	0.00
Al	2.19	2.19	2.22	2.18	2.23	2.22	2.21	2.18	2.19	2.26	2.26	2.23
Cr	0.00	0.00	0.00	0.00	0.00	0.00	0.00	0.00	0.00	0.00	0.00	0.00
Fe^{+3}	0.00	0.00	0.00	0.00	0.00	0.00	0.00	0.00	0.00	0.00	0.00	0.00
Fe^{+2}	2.41	2.49	2.48	2.49	2.44	2.48	2.56	2.41	2.42	2.37	2.32	2.26
Mn	0.31	0.34	0.33	0.35	0.33	0.33	0.35	0.32	0.33	0.29	0.29	0.28
Mg	2.20	2.06	2.08	2.08	2.10	2.06	2.00	2.17	2.13	2.18	2.21	2.34
Ca	0.01	0.01	0.01	0.00	0.01	0.00	0.00	0.01	0.01	0.01	0.01	0.00
Na	0.01	0.00	0.01	0.00	0.01	0.00	0.00	0.00	0.02	0.00	0.00	0.00
K	0.01	0.01	0.00	0.00	0.00	0.00	0.00	0.00	0.00	0.00	0.00	0.00
F	0.00	0.00	0.00	0.00	0.00	0.00	0.00	0.00	0.00	0.00	0.00	0.00
Cl	0.00	0.00	0.00	0.00	0.00	0.00	0.00	0.00	0.01	0.00	0.00	0.00
OH	7.37	7.31	7.34	7.29	7.34	7.34	7.30	7.34	7.34	7.42	7.42	7.44

Table 5. Electron microprobe analyses of chlorite (continued).

Sample#	Flt-B											
Circle#	2	2	2	2	2	2	2	2	2	2	2	2
Analysis#	129	130	131	132	133	134	135	136	137	138	139	140
Comment	pocket	pocket	pocket	pocket	pocket	pocket	pocket	pocket	pocket	pocket	pocket	pocket
Comment	filling	filling	filling	filling	filling	filling	filling	filling	filling	filling	filling	filling
Wt. % oxides												
SiO_2	26.75	26.77	27.20	26.74	27.30	27.05	26.97	26.77	26.56	26.37	26.53	26.94
TiO_2	0.00	0.00	0.00	0.02	0.00	0.00	0.00	0.00	0.00	0.00	0.00	0.00
Al_2O_3	17.61	17.56	17.47	17.81	17.58	17.54	17.73	17.85	17.90	17.51	17.78	18.00
Cr_2O_3	0.00	0.00	0.00	0.00	0.00	0.00	0.03	0.00	0.00	0.02	0.00	0.00
FeO	26.22	25.95	25.53	26.15	25.36	25.33	26.32	26.35	25.34	26.48	26.48	26.36
MnO	3.14	3.21	3.08	3.20	2.99	3.08	3.21	3.12	2.88	3.12	3.12	3.07
MgO	13.68	14.16	14.76	14.05	15.01	14.97	14.08	14.09	15.15	13.89	13.71	13.87
CaO	0.04	0.06	0.02	0.06	0.07	0.06	0.10	0.06	0.04	0.04	0.03	0.09
Na_2O	0.04	0.02	0.03	0.03	0.04	0.03	0.03	0.04	0.00	0.01	0.02	0.02
K_2O	0.03	0.04	0.03	0.03	0.03	0.03	0.04	0.03	0.04	0.01	0.03	0.02
F	0.00	0.00	0.00	0.00	0.00	0.00	0.00	0.00	0.04	0.00	0.00	0.00
Cl	0.01	0.02	0.02	0.02	0.02	0.02	0.03	0.02	0.01	0.01	0.02	0.02
Total	87.52	87.79	88.13	88.10	88.40	88.09	88.52	88.32	87.92	87.46	87.72	88.38
—O≡F,Cl	0.00	0.00	0.00	0.00	0.00	0.00	0.01	0.00	0.02	0.00	0.00	0.00
Total	87.52	87.79	88.13	88.10	88.40	88.09	88.52	88.32	87.92	87.46	87.72	88.38
Cations (based on 14 oxygens)												
Si	2.89	2.88	2.90	2.87	2.90	2.88	2.88	2.86	2.84	2.86	2.86	2.88
Ti	0.00	0.00	0.00	0.00	0.00	0.00	0.00	0.00	0.00	0.00	0.00	0.00
Al	2.24	2.23	2.20	2.25	2.20	2.21	2.23	2.25	2.26	2.24	2.26	2.27
Cr	0.00	0.00	0.00	0.00	0.00	0.00	0.00	0.00	0.00	0.00	0.00	0.00
Fe^{+3}	0.00	0.00	0.00	0.00	0.00	0.00	0.00	0.00	0.00	0.00	0.00	0.00
Fe^{+2}	2.37	2.33	2.28	2.34	2.25	2.26	2.35	2.36	2.27	2.40	2.39	2.35
Mn	0.29	0.29	0.28	0.29	0.27	0.28	0.29	0.28	0.26	0.29	0.28	0.28
Mg	2.20	2.27	2.35	2.24	2.37	2.38	2.24	2.25	2.41	2.24	2.20	2.21
Ca	0.00	0.01	0.00	0.01	0.01	0.01	0.01	0.01	0.00	0.00	0.00	0.01
Na	0.01	0.01	0.01	0.01	0.01	0.01	0.01	0.01	0.00	0.00	0.00	0.00
K	0.00	0.01	0.00	0.00	0.00	0.00	0.01	0.00	0.00	0.00	0.00	0.00
F	0.00	0.00	0.00	0.00	0.00	0.00	0.00	0.00	0.01	0.00	0.00	0.00
Cl	0.00	0.00	0.00	0.00	0.00	0.00	0.00	0.00	0.00	0.00	0.00	0.00
OH	7.42	7.41	7.44	7.41	7.46	7.44	7.41	7.43	7.45	7.42	7.42	7.44

Table 5. Electron microprobe analyses of chlorite (continued).

Sample#	Flt-B										Flt-B	
Circle#	2	2	2	2	2	2	2	2	2	2	2	2
Analysis#	141	142	143	144	145	146	147	148	149	150	113	114
Comment	pocket filling	pocket filling	pocket filling	pocket filling	pocket filling	pocket filling	pocket filling	pocket filling	pocket filling	pocket filling	pseudo diopside	pseudo diopside
Comment												
Wt. % oxides												
SiO_2	26.69	26.48	26.94	26.71	26.94	26.86	27.07	26.36	26.74	26.65	32.14	32.77
TiO_2	0.00	0.01	0.00	0.00	0.01	0.00	0.00	0.00	0.00	0.00	0.01	0.00
Al_2O_3	17.94	17.44	17.87	18.27	17.89	17.95	17.94	17.63	17.74	17.57	13.61	13.68
Cr_2O_3	0.00	0.00	0.00	0.02	0.00	0.00	0.01	0.00	0.00	0.00	0.00	0.00
FeO	26.29	26.02	25.85	26.63	26.86	27.18	26.79	26.60	26.60	26.29	10.51	7.42
MnO	3.07	3.12	3.07	3.06	3.01	3.14	3.10	3.06	3.01	2.98	2.85	2.89
MgO	13.78	13.55	14.32	13.68	13.45	13.34	13.55	13.55	13.61	13.94	26.38	28.84
CaO	0.06	0.00	0.06	0.02	0.01	0.01	0.01	0.00	0.05	0.05	0.11	0.09
Na_2O	0.00	0.06	0.04	0.02	0.01	0.00	0.00	0.00	0.02	0.04	0.03	0.06
K_2O	0.04	0.03	0.03	0.03	0.01	0.02	0.01	0.03	0.03	0.04	0.04	0.03
F	0.00	0.00	0.00	0.00	0.00	0.00	0.00	0.00	0.00	0.00	0.00	0.00
Cl	0.02	0.01	0.01	0.02	0.00	0.00	0.00	0.01	0.01	0.01	0.03	0.02
Total	87.87	86.72	88.21	88.45	88.20	88.50	88.48	87.23	87.80	87.57	85.70	85.79
—O≡F,Cl	0.01	0.00	0.00	0.01	0.00	0.00	0.00	0.00	0.00	0.00	0.01	0.00
Total	87.87	86.72	88.21	88.45	88.20	88.50	88.48	87.23	87.80	87.57	85.70	85.79
Cations (based on 14 oxygens)												
Si	2.87	2.89	2.88	2.85	2.89	2.88	2.89	2.86	2.88	2.88	3.24	3.24
Ti	0.00	0.00	0.00	0.00	0.00	0.00	0.00	0.00	0.00	0.00	0.00	0.00
Al	2.27	2.24	2.25	2.30	2.26	2.27	2.26	2.26	2.25	2.23	1.62	1.60
Cr	0.00	0.00	0.00	0.00	0.00	0.00	0.00	0.00	0.00	0.00	0.00	0.00
Fe^{+3}	0.00	0.00	0.00	0.00	0.00	0.00	0.00	0.00	0.00	0.00	0.00	0.00
Fe^{+2}	2.36	2.37	2.31	2.38	2.41	2.43	2.39	2.42	2.40	2.37	0.89	0.61
Mn	0.28	0.29	0.28	0.28	0.27	0.28	0.28	0.28	0.27	0.27	0.24	0.24
Mg	2.21	2.20	2.28	2.18	2.15	2.13	2.16	2.19	2.18	2.24	3.96	4.25
Ca	0.01	0.00	0.01	0.00	0.00	0.00	0.00	0.00	0.01	0.01	0.01	0.01
Na	0.00	0.01	0.01	0.00	0.00	0.00	0.00	0.00	0.00	0.01	0.01	0.01
K	0.01	0.00	0.00	0.00	0.00	0.00	0.00	0.00	0.00	0.01	0.01	0.00
F	0.00	0.00	0.00	0.00	0.00	0.00	0.00	0.00	0.00	0.00	0.00	0.00
Cl	0.00	0.00	0.00	0.00	0.00	0.00	0.00	0.00	0.00	0.00	0.00	0.00
OH	7.43	7.42	7.44	7.44	7.45	7.43	7.44	7.43	7.45	7.45	7.51	7.51

Table 5. Electron microprobe analyses of chlorite (continued).

Sample#	Flt-B											JMH-295.1
Circle#	2	2	2	2	2	2	2	2	2	2	2	
Analysis#	115	116	117	118	119	120	121	122	123	124	125	165
Comment	pseudo	pseudo	pseudo	pseudo	pseudo	pseudo	pseudo	pseudo	pseudo	pseudo	pseudo	Blackwall
Comment	diopside	diopside	diopside	diopside	diopside	diopside	diopside	diopside	diopside	diopside	diopside	line
Wt. % oxides												
SiO_2	33.11	31.00	33.22	32.68	32.45	38.86	32.35	33.58	32.93	32.65	32.14	32.11
TiO_2	0.00	0.00	0.00	0.00	0.00	0.00	0.00	0.00	0.01	0.00	0.00	0.11
Al_2O_3	13.68	14.34	14.03	13.60	13.71	2.74	12.92	13.76	13.79	13.47	13.80	12.61
Cr_2O_3	0.00	0.00	0.00	0.00	0.00	0.00	0.00	0.00	0.01	0.00	0.00	0.00
FeO	6.49	11.53	7.25	7.19	7.32	7.49	6.36	6.60	6.93	7.25	9.29	6.35
MnO	2.35	4.38	2.52	2.60	2.57	1.50	1.86	2.01	2.33	2.44	2.69	0.20
MgO	30.58	24.48	29.21	28.77	29.22	32.31	30.32	30.41	30.38	29.19	27.94	31.73
CaO	0.23	0.15	0.13	0.21	0.14	0.57	0.20	0.24	0.14	0.16	0.13	0.09
Na_2O	0.04	0.06	0.04	0.03	0.03	0.07	0.03	0.06	0.03	0.06	0.04	0.02
K_2O	0.04	0.05	0.03	0.07	0.02	0.03	0.03	0.05	0.03	0.04	0.03	0.02
F	0.00	0.00	0.00	0.00	0.00	0.06	0.00	0.00	0.00	0.00	0.00	0.00
Cl	0.02	0.02	0.02	0.03	0.03	0.10	0.03	0.04	0.02	0.03	0.01	0.08
Total	86.52	86.01	86.43	85.17	85.49	83.69	84.09	86.75	86.57	85.29	86.07	83.30
—O=F,Cl	0.00	0.00	0.00	0.01	0.01	0.05	0.01	0.01	0.00	0.01	0.00	0.02
Total	86.52	86.01	86.43	85.17	85.49	83.69	84.09	86.75	86.57	85.29	86.07	83.30
Cations (based on 14 oxygens)												
Si	3.23	3.16	3.25	3.25	3.22	3.92	3.24	3.26	3.21	3.24	3.20	3.22
Ti	0.00	0.00	0.00	0.00	0.00	0.00	0.00	0.00	0.00	0.00	0.00	0.01
Al	1.57	1.72	1.62	1.59	1.60	0.33	1.52	1.57	1.59	1.58	1.62	1.49
Cr	0.00	0.00	0.00	0.00	0.00	0.00	0.00	0.00	0.00	0.00	0.00	0.00
Fe^{+3}	0.00	0.00	0.00	0.00	0.00	0.00	0.00	0.00	0.00	0.00	0.00	0.00
Fe^{+2}	0.53	0.98	0.59	0.60	0.61	0.63	0.53	0.54	0.57	0.60	0.77	0.53
Mn	0.19	0.38	0.21	0.22	0.22	0.13	0.16	0.16	0.19	0.21	0.23	0.02
Mg	4.44	3.72	4.26	4.26	4.32	4.86	4.52	4.40	4.42	4.32	4.15	4.75
Ca	0.02	0.02	0.01	0.02	0.02	0.06	0.02	0.02	0.01	0.02	0.01	0.01
Na	0.01	0.01	0.01	0.01	0.01	0.01	0.01	0.01	0.01	0.01	0.01	0.00
K	0.00	0.01	0.00	0.01	0.00	0.00	0.00	0.01	0.00	0.00	0.00	0.00
F	0.00	0.00	0.00	0.00	0.00	0.02	0.00	0.00	0.00	0.00	0.00	0.00
Cl	0.00	0.00	0.00	0.01	0.01	0.02	0.00	0.01	0.00	0.01	0.00	0.01
OH	7.61	7.24	7.58	7.55	7.56	7.67	7.68	7.66	7.61	7.58	7.54	7.94

Table 5. Electron microprobe analyses of chlorite (continued).

Sample#	JMH-295.1											
Circle#												
Analysis#	172	173	174	175	176	177	178	179	180	181	182	183
Comment	Blackwall	Blackwall	Blackwall	Blackwall	Blackwall	Blackwall	Blackwall	Blackwall	Blackwall	Blackwall	Blackwall	Blackwall
Comment	line	line	line	line	line	line	line	line	line	line	line	line
Wt. % oxides												
SiO_2	31.91	32.52	32.19	32.74	32.28	32.47	32.69	32.21	32.51	32.24	31.96	31.89
TiO_2	0.02	0.03	0.02	0.04	0.02	0.06	0.03	0.03	0.09	0.08	0.18	0.20
Al_2O_3	13.48	13.84	14.12	13.79	13.76	13.72	13.55	13.44	13.45	13.24	13.30	12.95
Cr_2O_3	0.02	0.00	0.00	0.00	0.00	0.00	0.00	0.01	0.00	0.00	0.01	0.00
FeO	4.91	4.83	8.79	5.26	4.71	5.13	5.52	5.28	5.82	6.55	7.77	7.28
MnO	0.14	0.13	0.40	0.14	0.13	0.15	0.16	0.16	0.19	0.26	0.28	0.30
MgO	33.10	33.29	30.92	33.04	32.73	32.77	32.60	32.85	32.67	31.97	31.28	31.44
CaO	0.10	0.08	0.06	0.10	0.11	0.10	0.08	0.07	0.06	0.12	0.08	0.11
Na_2O	0.05	0.03	0.03	0.06	0.05	0.05	0.04	0.03	0.04	0.02	0.04	0.05
K_2O	0.03	0.03	0.02	0.05	0.03	0.02	0.04	0.02	0.03	0.02	0.04	0.03
F	0.04	0.00	0.00	0.01	0.00	0.00	0.00	0.00	0.00	0.00	0.00	0.00
Cl	0.06	0.06	0.05	0.07	0.06	0.08	0.08	0.08	0.10	0.19	0.19	0.19
Total	83.83	84.82	86.57	85.28	83.85	84.53	84.77	84.15	84.94	84.64	85.09	84.38
—O≡F,Cl	0.03	0.01	0.01	0.02	0.01	0.02	0.02	0.02	0.02	0.04	0.04	0.04
Total	83.83	84.82	86.57	85.28	83.85	84.53	84.77	84.15	84.94	84.64	85.09	84.38
Cations (based on 14 oxygens)												
Si	3.16	3.17	3.15	3.19	3.19	3.19	3.20	3.18	3.19	3.19	3.17	3.18
Ti	0.00	0.00	0.00	0.00	0.00	0.00	0.00	0.00	0.01	0.01	0.01	0.01
Al	1.57	1.59	1.63	1.58	1.60	1.59	1.57	1.56	1.56	1.55	1.56	1.52
Cr	0.00	0.00	0.00	0.00	0.00	0.00	0.00	0.00	0.00	0.00	0.00	0.00
Fe^{+3}	0.00	0.00	0.00	0.00	0.00	0.00	0.00	0.00	0.00	0.00	0.00	0.00
Fe^{+2}	0.41	0.39	0.72	0.43	0.39	0.42	0.45	0.44	0.48	0.54	0.65	0.61
Mn	0.01	0.01	0.03	0.01	0.01	0.01	0.01	0.01	0.02	0.02	0.02	0.03
Mg	4.89	4.84	4.50	4.79	4.81	4.79	4.76	4.83	4.78	4.72	4.63	4.68
Ca	0.01	0.01	0.01	0.01	0.01	0.01	0.01	0.01	0.01	0.01	0.01	0.01
Na	0.01	0.00	0.01	0.01	0.01	0.01	0.01	0.00	0.01	0.00	0.01	0.01
K	0.00	0.00	0.00	0.01	0.00	0.00	0.00	0.00	0.00	0.00	0.00	0.00
F	0.01	0.00	0.00	0.00	0.00	0.00	0.00	0.00	0.00	0.00	0.00	0.00
Cl	0.01	0.01	0.01	0.01	0.01	0.01	0.01	0.01	0.02	0.03	0.03	0.03
OH	7.93	7.96	7.92	7.95	7.96	7.95	7.95	7.95	7.94	7.89	7.89	7.89

Table 5. Electron microprobe analyses of chlorite (continued).

Sample#	JMH-295.1					JMH-295.1						
Circle#						1	1	1	1	1	1	1
Analysis#	184	185	186	187	188	189	190	191	194	196	197	199
Comment	Blackwall	Blackwall	Blackwall	Blackwall	Blackwall	Veinlets	Veinlets	Veinlets	Veinlets	Veinlets	Veinlets	Veinlets
Comment	line	line	line	line	line							
Wt. % oxides												
SiO_2	32.64	33.39	34.82	33.70	37.07	32.39	32.42	30.47	33.19	32.41	26.74	30.31
TiO_2	0.23	0.32	0.13	0.63	0.07	0.01	0.00	0.00	0.00	0.00	0.00	0.00
Al_2O_3	12.10	10.06	8.05	9.49	5.98	13.12	14.21	14.36	13.17	13.98	16.78	15.00
Cr_2O_3	0.00	0.00	0.00	0.03	0.00	0.00	0.00	0.00	0.00	0.00	0.00	0.00
FeO	6.66	5.68	6.80	6.50	5.00	9.47	9.62	15.23	4.49	6.34	28.24	10.61
MnO	0.32	0.35	0.49	0.80	0.37	0.93	0.87	2.69	2.30	1.31	4.99	6.89
MgO	32.37	33.84	33.87	33.38	36.36	27.44	28.83	23.51	30.17	30.63	11.45	23.55
CaO	0.14	0.16	0.17	0.22	0.12	0.39	0.19	0.19	0.34	0.14	0.06	0.09
Na_2O	0.04	0.04	0.04	0.09	0.07	0.08	0.04	0.02	0.08	0.02	0.02	0.04
K_2O	0.05	0.03	0.03	0.02	0.05	0.06	0.03	0.04	0.05	0.04	0.03	0.03
F	0.00	0.00	0.00	0.00	0.02	0.00	0.00	0.00	0.01	0.00	0.00	0.00
Cl	0.24	0.34	0.24	0.32	0.23	0.03	0.01	0.02	0.02	0.02	0.01	0.01
Total	84.73	84.13	84.58	85.10	85.28	83.90	86.21	86.53	83.82	84.89	88.32	86.52
—O≡F,Cl	0.05	0.08	0.05	0.07	0.06	0.01	0.00	0.00	0.01	0.00	0.00	0.00
Total	84.73	84.13	84.58	85.10	85.28	83.90	86.21	86.53	83.82	84.89	88.32	86.52
Cations (based on 14 oxygens)												
Si	3.24	3.33	3.46	3.34	3.62	3.28	3.20	3.12	3.30	3.20	2.92	3.10
Ti	0.02	0.02	0.01	0.05	0.01	0.00	0.00	0.00	0.00	0.00	0.00	0.00
Al	1.42	1.18	0.94	1.11	0.69	1.57	1.65	1.73	1.54	1.63	2.16	1.81
Cr	0.00	0.00	0.00	0.00	0.00	0.00	0.00	0.00	0.00	0.00	0.00	0.00
Fe^{+3}	0.00	0.00	0.00	0.00	0.00	0.00	0.00	0.00	0.00	0.00	0.00	0.00
Fe^{+2}	0.55	0.47	0.57	0.54	0.41	0.80	0.79	1.31	0.37	0.52	2.58	0.91
Mn	0.03	0.03	0.04	0.07	0.03	0.08	0.07	0.23	0.19	0.11	0.46	0.60
Mg	4.79	5.03	5.02	4.94	5.29	4.15	4.24	3.59	4.47	4.51	1.86	3.58
Ca	0.02	0.02	0.02	0.02	0.01	0.04	0.02	0.02	0.04	0.01	0.01	0.01
Na	0.01	0.01	0.01	0.02	0.01	0.01	0.01	0.00	0.02	0.00	0.00	0.01
K	0.01	0.00	0.00	0.00	0.01	0.01	0.00	0.01	0.01	0.01	0.00	0.00
F	0.00	0.00	0.00	0.00	0.01	0.00	0.00	0.00	0.00	0.00	0.00	0.00
Cl	0.04	0.06	0.04	0.05	0.04	0.01	0.00	0.00	0.00	0.00	0.00	0.00
OH	7.87	7.83	7.84	7.76	7.85	7.83	7.85	7.53	7.60	7.77	7.07	6.80

Table 5. Electron microprobe analyses of chlorite (continued).

Sample#	JMH-295.1							UG-10
Circle#	1	1	1	1	1	1	1	
Analysis#	200	201	202	203	204	205	206	428
Comment	Veinlets	Veinlets	Veinlets	Veinlets	Veinlets	Veinlets	Veinlets	Slate
Comment								
Wt. % oxides								
SiO_2	31.91	26.15	26.19	31.45	30.89	31.49	32.54	27.55
TiO_2	0.00	0.00	0.00	0.00	0.00	0.00	0.00	0.05
Al_2O_3	14.53	16.95	16.30	14.25	14.41	14.03	14.02	20.69
Cr_2O_3	0.00	0.04	0.01	0.00	0.00	0.01	0.00	0.00
FeO	8.61	28.39	31.48	12.55	12.95	8.87	11.52	20.30
MnO	4.45	5.20	3.31	3.97	4.87	4.23	0.94	0.16
MgO	27.74	10.72	10.21	24.66	23.81	27.10	27.56	18.91
CaO	0.04	0.04	0.01	0.06	0.09	0.07	0.08	0.02
Na_2O	0.00	0.01	0.01	0.00	0.05	0.04	0.03	0.00
K_2O	0.01	0.02	0.02	0.04	0.02	0.02	0.03	0.57
F	0.00	0.00	0.00	0.00	0.00	0.00	0.00	0.00
Cl	0.00	0.00	0.01	0.01	0.02	0.03	0.02	0.02
Total	87.31	87.50	87.54	86.99	87.10	85.87	86.73	88.24
—O≡F,Cl	0.00	0.00	0.00	0.00	0.00	0.01	0.01	0.00
Total	87.31	87.50	87.54	86.99	87.10	85.87	86.73	88.24
Cations (based on 14 oxygens)								
Si	3.15	2.89	2.92	3.17	3.14	3.17	3.22	2.81
Ti	0.00	0.00	0.00	0.00	0.00	0.00	0.00	0.00
Al	1.69	2.21	2.14	1.69	1.73	1.66	1.64	2.48
Cr	0.00	0.00	0.00	0.00	0.00	0.00	0.00	0.00
Fe^{+3}	0.00	0.00	0.00	0.00	0.00	0.00	0.00	0.00
Fe^{+2}	0.71	2.63	2.94	1.06	1.10	0.75	0.95	1.73
Mn	0.37	0.49	0.31	0.34	0.42	0.36	0.08	0.01
Mg	4.08	1.77	1.70	3.71	3.60	4.06	4.06	2.87
Ca	0.00	0.00	0.00	0.01	0.01	0.01	0.01	0.00
Na	0.00	0.00	0.00	0.00	0.01	0.01	0.01	0.00
K	0.00	0.00	0.00	0.01	0.00	0.00	0.00	0.07
F	0.00	0.00	0.00	0.00	0.00	0.00	0.00	0.00
Ci	0.00	0.00	0.00	0.00	0.00	0.00	0.00	0.00
OH	7.26	7.03	7.37	7.32	7.16	7.27	7.83	7.97

Table 6. Electron microprobe analyses of feldspar.

Mineral	Albite											
Sample#	JMH-24											
Circle#	4	4	4	4	4	4	4	4	4	4	4	4
Point#												
Analysis#	5	6	7	8	9	10	11	12	13	14	15	16
Comment	large xl	large xl	large xl	large xl	large xl	large xl	large xl	large xl	large xl	large xl	large xl	large xl
SiO_2	67.72	62.94	68.57	67.00	68.88	69.47	69.50	68.80	68.57	69.33	69.07	68.04
Al_2O_3	20.26	24.03	20.00	19.36	19.83	19.69	19.67	20.08	19.86	19.76	19.55	20.43
FeO	0.16	0.43	0.02	0.03	0.01	0.04	0.06	0.03	0.04	0.00	0.01	0.09
MgO	0.07	0.09	0.00	0.00	0.00	0.00	0.00	0.00	0.01	0.01	0.00	0.03
CaO	0.08	0.08	0.37	0.89	0.22	0.19	0.05	0.56	0.65	0.13	0.25	0.20
BaO	0.00	0.00	0.00	0.00	0.00	0.00	0.00	0.00	0.00	0.00	0.00	0.00
Na_2O	11.18	8.66	11.50	11.25	11.47	11.76	11.83	11.52	11.29	11.74	11.66	11.11
K_2O	0.61	3.84	0.17	0.12	0.12	0.11	0.10	0.10	0.11	0.10	0.11	0.76
P_2O_5	0.00	0.00	0.00	1.09	0.00	0.00	0.00	0.00	0.00	0.00	0.00	0.00
Total	100.06	100.07	100.63	99.74	100.53	101.25	101.21	101.09	100.53	101.08	100.64	100.65
Cations (based on 8 oxygens)												
Si	2.96	2.80	2.98	2.94	2.99	3.00	3.00	2.98	2.98	2.99	3.00	2.96
Al	1.04	1.26	1.02	1.00	1.01	1.00	1.00	1.02	1.02	1.01	1.00	1.05
Fe^{3+}	0.01	0.02	0.00	0.00	0.00	0.00	0.00	0.00	0.00	0.00	0.00	0.00
Mg	0.00	0.01	0.00	0.00	0.00	0.00	0.00	0.00	0.00	0.00	0.00	0.00
Ca	0.00	0.00	0.02	0.04	0.01	0.01	0.00	0.03	0.03	0.01	0.01	0.01
Ba	0.00	0.00	0.00	0.00	0.00	0.00	0.00	0.00	0.00	0.00	0.00	0.00
Na	0.95	0.75	0.97	0.96	0.97	0.98	0.99	0.97	0.95	0.98	0.98	0.94
K	0.03	0.22	0.01	0.01	0.01	0.01	0.01	0.01	0.01	0.01	0.01	0.04
P	0.00	0.00	0.00	0.04	0.00	0.00	0.00	0.00	0.00	0.00	0.00	0.00

Table 6. Electron microprobe analyses of feldspar (continued).

Mineral	Albite											
Sample#	JMH-24											
Circle#	4	4	4	4	4	4	4	4	4	4	4	4
Point#												
Analysis#	17	18	19	20	21	23	24	25	26	27	28	30
Comment	large xl	large xl	large xl	large xl	large xl	large xl	large xl	large xl	large xl	large xl	large xl	large xl
SiO_2	69.27	69.25	66.20	68.77	68.70	69.95	69.04	61.52	69.45	64.82	69.29	69.39
Al_2O_3	19.61	19.65	22.38	19.53	19.69	19.60	19.56	25.78	19.83	22.38	19.51	19.68
FeO	0.04	0.02	0.38	0.06	0.00	0.01	0.00	0.74	0.04	0.62	0.07	0.00
MgO	0.01	0.00	0.04	0.03	0.01	0.00	0.00	0.12	0.00	0.09	0.00	0.00
CaO	0.07	0.20	0.11	0.05	0.32	0.05	0.14	0.03	0.16	0.11	0.08	0.26
BaO	0.00	0.00	0.00	0.00	0.00	0.00	0.00	0.00	0.00	0.00	0.00	0.00
Na_2O	11.83	11.79	9.73	11.68	11.70	11.76	11.85	7.30	11.73	9.58	11.95	11.66
K_2O	0.08	0.09	2.23	0.22	0.12	0.08	0.10	4.85	0.09	2.39	0.08	0.11
P_2O_5	0.00	0.00	0.00	0.00	0.00	0.00	0.00	0.00	0.00	0.00	0.00	0.00
Total	100.91	101.00	101.06	100.34	100.54	101.44	100.69	100.35	101.30	99.98	100.98	101.11
Cations (based on 8 oxygens)												
Si	3.00	3.00	2.89	2.99	2.99	3.01	3.00	2.74	2.99	2.86	3.00	3.00
Al	1.00	1.00	1.15	1.00	1.01	0.99	1.00	1.35	1.01	1.17	1.00	1.00
Fe^{3+}	0.00	0.00	0.01	0.00	0.00	0.00	0.00	0.03	0.00	0.02	0.00	0.00
Mg	0.00	0.00	0.00	0.00	0.00	0.00	0.00	0.01	0.00	0.01	0.00	0.00
Ca	0.00	0.01	0.00	0.00	0.01	0.00	0.01	0.00	0.01	0.01	0.00	0.01
Ba	0.00	0.00	0.00	0.00	0.00	0.00	0.00	0.00	0.00	0.00	0.00	0.00
Na	0.99	0.99	0.82	0.99	0.99	0.98	1.00	0.63	0.98	0.82	1.00	0.98
K	0.00	0.00	0.12	0.01	0.01	0.00	0.01	0.27	0.01	0.13	0.00	0.01
P	0.00	0.00	0.00	0.00	0.00	0.00	0.00	0.00	0.00	0.00	0.00	0.00

Table 6. Electron microprobe analyses of feldspar (continued).

Mineral	Perthitic Albite	Albite										
Sample#	JMH-56B1	H1281-62.5										
Circle#												
Point#		1	4	5	6	7	8	11	12	13	14	15
Analysis#	48	56	61	62	63	64	65	68	69	70	71	72
Comment	Outcircles											
SiO_2	68.37	68.91	68.60	68.66	68.85	68.48	68.49	68.25	68.88	69.08	68.98	68.63
Al_2O_3	19.36	19.61	19.46	19.31	19.52	19.46	19.56	19.53	19.60	19.49	19.54	19.27
FeO	0.01	0.31	0.23	0.30	0.30	0.32	0.27	0.07	0.21	0.07	0.10	0.15
MgO	0.00	0.01	0.00	0.00	0.00	0.00	0.00	0.00	0.00	0.00	0.00	0.00
CaO	0.10	0.06	0.07	0.15	0.20	0.18	0.13	0.06	0.02	0.04	0.10	0.07
BaO	0.00	0.00	0.00	0.00	0.00	0.00	0.00	0.00	0.00	0.00	0.00	0.00
Na_2O	11.12	11.76	11.49	11.37	11.66	11.23	11.82	10.43	11.59	11.42	11.46	11.28
K_2O	0.00	0.08	0.08	0.08	0.11	0.09	0.08	1.23	0.08	0.08	0.09	0.09
P_2O_5	0.12	0.00	0.00	0.00	0.00	0.00	0.00	0.00	0.00	0.00	0.00	0.00
Total	99.07	100.73	99.93	99.86	100.63	99.76	100.34	99.58	100.38	100.18	100.27	99.48
Cations (based on 8 oxygens)												
Si	3.00	2.99	3.00	3.00	2.99	3.00	2.99	3.00	2.99	3.01	3.00	3.01
Al	1.00	1.00	1.00	0.99	1.00	1.00	1.00	1.01	1.00	1.00	1.00	1.00
Fe^{3+}	0.00	0.01	0.01	0.01	0.01	0.01	0.01	0.00	0.01	0.00	0.00	0.01
Mg	0.00	0.00	0.00	0.00	0.00	0.00	0.00	0.00	0.00	0.00	0.00	0.00
Ca	0.00	0.00	0.00	0.01	0.01	0.01	0.01	0.00	0.00	0.00	0.00	0.00
Ba	0.00	0.00	0.00	0.00	0.00	0.00	0.00	0.00	0.00	0.00	0.00	0.00
Na	0.95	0.99	0.97	0.96	0.98	0.95	1.00	0.89	0.98	0.96	0.97	0.96
K	0.00	0.00	0.00	0.00	0.01	0.00	0.00	0.07	0.00	0.00	0.00	0.01
P	0.00	0.00	0.00	0.00	0.00	0.00	0.00	0.00	0.00	0.00	0.00	0.00

Table 6. Electron microprobe analyses of feldspar (continued).

Mineral	Albite		Albite									
Sample#	H1281-62.5		JMH-26									
Circle#			1	1	1	1	1	1	1	1	1	1
Point#	16	17	1	2	3	4	5	7	8	9	10	11
Analysis#	73	74	75	76	77	78	79	81	82	83	84	85
Comment												
SiO_2	68.84	69.17	68.01	68.96	66.49	68.62	67.45	54.96	68.73	68.67	67.69	67.80
Al_2O_3	19.28	19.38	19.39	19.46	20.80	19.55	19.93	25.35	19.48	19.70	19.99	20.09
FeO	0.12	0.14	0.02	0.04	0.10	0.06	0.08	0.63	0.12	0.15	0.30	0.06
MgO	0.00	0.00	0.00	0.00	0.00	0.00	0.00	0.00	0.00	0.00	0.00	0.00
CaO	0.05	0.04	0.25	0.08	0.82	0.38	0.70	11.47	0.11	0.29	0.95	0.74
BaO	0.00	0.00	0.00	0.00	0.00	0.00	0.00	0.00	0.00	0.00	0.00	0.00
Na_2O	10.88	11.29	11.58	11.76	10.39	11.08	11.04	6.12	11.68	11.55	11.01	10.94
K_2O	0.48	0.08	0.12	0.09	0.74	0.12	0.14	0.13	0.10	0.20	0.19	0.15
P_2O_5	0.00	0.00	0.00	0.00	0.00	0.00	0.00	0.00	0.00	0.00	0.00	0.00
Total	99.65	100.09	99.37	100.39	99.33	99.81	99.33	98.67	100.22	100.55	100.14	99.76
Cations (based on 8 oxygens)												
Si	3.01	3.01	2.99	3.00	2.93	3.00	2.97	2.53	3.00	2.99	2.96	2.97
Al	0.99	0.99	1.01	1.00	1.08	1.01	1.03	1.38	1.00	1.01	1.03	1.04
Fe^{3+}	0.00	0.01	0.00	0.00	0.00	0.00	0.00	0.02	0.00	0.01	0.01	0.00
Mg	0.00	0.00	0.00	0.00	0.00	0.00	0.00	0.00	0.00	0.00	0.00	0.00
Ca	0.00	0.00	0.01	0.00	0.04	0.02	0.03	0.57	0.01	0.01	0.04	0.03
Ba	0.00	0.00	0.00	0.00	0.00	0.00	0.00	0.00	0.00	0.00	0.00	0.00
Na	0.92	0.95	0.99	0.99	0.89	0.94	0.94	0.55	0.99	0.97	0.93	0.93
K	0.03	0.00	0.01	0.00	0.04	0.01	0.01	0.01	0.01	0.01	0.01	0.01
P	0.00	0.00	0.00	0.00	0.00	0.00	0.00	0.00	0.00	0.00	0.00	0.00

Table 6. Electron microprobe analyses of feldspar (continued).

Mineral	Albite											
Sample#	JMH-26											
Circle#	1	1	1	1	1	1	1	1	1	1	1	1
Point#	1	2	3	4	5	6	7	8	9	10	11	12
Analysis#	86	87	88	89	90	91	92	93	94	95	96	97
Comment												
SiO_2	68.56	68.52	68.41	68.39	67.59	68.59	68.65	68.36	68.77	68.32	68.15	67.77
Al_2O_3	19.85	19.67	19.59	19.63	19.51	19.56	19.72	19.71	19.61	19.77	19.63	19.88
FeO	0.03	0.05	0.15	0.10	0.40	0.02	0.01	0.05	0.09	0.08	0.06	0.03
MgO	0.00	0.00	0.00	0.00	0.00	0.00	0.00	0.00	0.00	0.00	0.00	0.00
CaO	0.43	0.36	0.43	0.17	0.86	0.26	0.31	0.31	0.42	0.47	0.38	0.62
BaO	0.00	0.00	0.00	0.00	0.00	0.00	0.00	0.00	0.00	0.00	0.00	0.00
Na_2O	11.45	11.26	11.29	11.51	10.71	11.17	11.56	11.31	11.53	11.15	11.71	11.19
K_2O	0.11	0.09	0.10	0.07	0.17	0.10	0.10	0.08	0.10	0.11	0.15	0.12
P_2O_5	0.00	0.00	0.00	0.00	0.00	0.00	0.00	0.00	0.00	0.00	0.00	0.00
Total	100.43	99.94	99.97	99.87	99.23	99.70	100.35	99.82	100.52	99.90	100.08	99.62
Cations (based on 8 oxygens)												
Si	2.98	2.99	2.99	2.99	2.98	3.00	2.99	2.99	2.99	2.99	2.98	2.97
Al	1.02	1.01	1.01	1.01	1.01	1.01	1.01	1.02	1.00	1.02	1.01	1.03
Fe^{3+}	0.00	0.00	0.01	0.00	0.01	0.00	0.00	0.00	0.00	0.00	0.00	0.00
Mg	0.00	0.00	0.00	0.00	0.00	0.00	0.00	0.00	0.00	0.00	0.00	0.00
Ca	0.02	0.02	0.02	0.01	0.04	0.01	0.01	0.01	0.02	0.02	0.02	0.03
Ba	0.00	0.00	0.00	0.00	0.00	0.00	0.00	0.00	0.00	0.00	0.00	0.00
Na	0.97	0.95	0.96	0.98	0.91	0.95	0.98	0.96	0.97	0.95	0.99	0.95
K	0.01	0.00	0.01	0.00	0.01	0.01	0.01	0.00	0.01	0.01	0.01	0.01
P	0.00	0.00	0.00	0.00	0.00	0.00	0.00	0.00	0.00	0.00	0.00	0.00

Table 6. Electron microprobe analyses of feldspar (continued).

Mineral	Albite			Albite								
Sample#	JMH-26			H1281-61.7								
Circle#	1	1	1	1	1	1	1	1	1	1	1	2
Point#	13	14	15	1	2	3	4	5	6	7	8	1
Analysis#	98	99	100	107	108	109	110	111	112	113	114	115
Comment												
SiO_2	67.89	67.99	68.26	68.54	68.41	68.70	68.82	69.16	68.61	68.94	68.22	69.25
Al_2O_3	19.74	19.96	19.89	19.60	19.77	19.79	19.76	19.77	19.74	19.68	19.06	19.55
FeO	0.04	0.02	0.06	0.18	0.09	0.10	0.09	0.12	0.08	0.12	0.40	0.08
MgO	0.00	0.00	0.00	0.10	0.02	0.00	0.02	0.01	0.00	0.00	0.48	0.00
CaO	0.39	0.54	0.42	0.27	0.23	0.34	0.21	0.22	0.27	0.14	0.54	0.07
BaO	0.00	0.00	0.00	0.00	0.00	0.00	0.00	0.03	0.01	0.00	0.09	0.00
Na_2O	11.10	11.23	11.14	11.53	11.58	11.62	11.63	11.84	11.58	11.85	11.11	11.79
K_2O	0.14	0.12	0.12	0.32	0.12	0.13	0.13	0.10	0.18	0.08	0.56	0.14
P_2O_5	0.00	0.00	0.00	0.00	0.00	0.00	0.00	0.00	0.01	0.00	0.00	0.00
Total	99.28	99.86	99.89	100.53	100.22	100.67	100.64	101.24	100.47	100.79	100.46	100.88
Cations (based on 8 oxygens)												
Si	2.98	2.97	2.98	2.98	2.98	2.98	2.99	2.99	2.99	2.99	2.98	3.00
Al	1.02	1.03	1.02	1.01	1.02	1.01	1.01	1.01	1.01	1.01	0.98	1.00
Fe^{3+}	0.00	0.00	0.00	0.01	0.00	0.00	0.00	0.00	0.00	0.00	0.01	0.00
Mg	0.00	0.00	0.00	0.01	0.00	0.00	0.00	0.00	0.00	0.00	0.03	0.00
Ca	0.02	0.03	0.02	0.01	0.01	0.02	0.01	0.01	0.01	0.01	0.03	0.00
Ba	0.00	0.00	0.00	0.00	0.00	0.00	0.00	0.00	0.00	0.00	0.00	0.00
Na	0.95	0.95	0.94	0.97	0.98	0.98	0.98	0.99	0.98	1.00	0.94	0.99
K	0.01	0.01	0.01	0.02	0.01	0.01	0.01	0.01	0.01	0.00	0.03	0.01
P	0.00	0.00	0.00	0.00	0.00	0.00	0.00	0.00	0.00	0.00	0.00	0.00

Table 6. Electron microprobe analyses of feldspar (continued).

Mineral	Albite			K-feldspar						Alkali feldspar		
Sample#	H1281-61.7			H1281-61.7						H1281-61.7		
Circle#	2	2	2	2	2	2	2	2	2	2	2	2
Point#	2	3	4	1	2	3	4	5	6			
Analysis#	116	117	118	119	120	121	122	123	124	134	135	136
Comment										dark	dark	dark
SiO_2	68.87	69.24	68.82	65.19	64.43	64.78	65.10	65.08	64.86	65.10	66.85	64.80
Al_2O_3	19.26	19.46	19.24	18.35	18.44	17.87	18.65	18.63	18.55	22.36	21.14	22.35
FeO	0.02	0.06	0.04	0.04	0.08	0.62	0.07	0.10	0.05	0.17	0.04	0.16
MgO	0.00	0.00	0.00	0.00	0.00	0.45	0.00	0.00	0.00	0.04	0.00	0.16
CaO	0.09	0.05	0.03	0.00	0.00	0.44	0.00	0.00	0.00	2.47	1.89	1.64
BaO	0.00	0.02	0.05	0.31	0.72	0.31	0.33	0.41	0.25	0.00	0.00	0.14
Na_2O	11.49	11.76	10.84	0.27	0.29	0.70	0.25	0.20	0.23	10.05	10.87	9.89
K_2O	0.12	0.10	1.55	17.05	16.92	15.50	17.23	17.21	17.20	0.65	0.15	1.28
P_2O_5	0.00	0.00	0.00	0.00	0.00	0.00	0.00	0.00	0.00	0.00	0.00	0.00
Total	99.85	100.69	100.57	101.21	100.89	100.68	101.61	101.62	101.14	100.84	100.94	100.42
Cations (based on 8 oxygens)												
Si	3.01	3.00	3.00	2.99	2.98	2.98	2.98	2.98	2.98	2.85	2.91	2.85
Al	0.99	0.99	0.99	0.99	1.01	0.97	1.01	1.01	1.01	1.15	1.08	1.16
Fe^{3+}	0.00	0.00	0.00	0.00	0.00	0.02	0.00	0.00	0.00	0.01	0.00	0.01
Mg	0.00	0.00	0.00	0.00	0.00	0.03	0.00	0.00	0.00	0.00	0.00	0.01
Ca	0.00	0.00	0.00	0.00	0.00	0.02	0.00	0.00	0.00	0.12	0.09	0.08
Ba	0.00	0.00	0.00	0.01	0.01	0.01	0.01	0.01	0.00	0.00	0.00	0.00
Na	0.97	0.99	0.92	0.02	0.03	0.06	0.02	0.02	0.02	0.85	0.92	0.84
K	0.01	0.01	0.09	1.00	1.00	0.91	1.01	1.01	1.01	0.04	0.01	0.07
P	0.00	0.00	0.00	0.00	0.00	0.00	0.00	0.00	0.00	0.00	0.00	0.00

Table 6. Electron microprobe analyses of feldspar (continued).

Mineral	Alkali feldspar								Ca-rich plagioclase			
Sample#	H1281-61.7								H1281-61.7			
Circle#	2	2	2	2	2	2	2	2	3	3	3	3
Point#									4	5	6	7
Analysis#	137	138	139	140	145	146	148	150	154	155	156	157
Comment	dark	dark	dark	dark	dark	dark	dark	dark				
SiO_2	66.23	67.18	64.98	69.71	66.05	61.51	66.80	56.82	58.86	59.17	58.75	58.12
Al_2O_3	21.50	21.28	22.54	19.19	21.27	24.49	21.28	24.34	26.86	26.41	26.55	24.86
FeO	0.05	0.02	0.22	0.10	0.04	0.80	0.14	3.41	0.27	0.18	0.17	0.67
MgO	0.00	0.00	0.22	0.01	0.01	0.35	0.05	2.20	0.00	0.00	0.00	0.38
CaO	2.35	1.69	1.68	0.20	2.07	0.65	1.22	1.06	8.35	7.91	8.09	6.09
BaO	0.01	0.01	0.04	0.03	0.06	0.00	0.09	0.04	0.09	0.01	0.27	1.85
Na_2O	10.48	10.94	10.12	11.64	10.33	7.67	10.59	6.11	6.92	7.15	6.65	5.84
K_2O	0.13	0.15	1.48	0.15	0.16	3.95	0.63	5.20	0.33	0.29	0.63	2.76
P_2O_5	0.00	0.00	0.00	0.00	0.00	0.00	0.00	0.19	0.07	0.07	0.06	0.04
Total	100.77	101.27	101.27	101.02	99.99	99.43	100.80	99.37	101.75	101.18	101.17	100.62
Cations (based on 8 oxygens)												
Si	2.89	2.91	2.84	3.01	2.90	2.76	2.91	2.60	2.59	2.62	2.61	2.64
Al	1.11	1.09	1.16	0.98	1.10	1.29	1.09	1.31	1.40	1.38	1.39	1.33
Fe^{3+}	0.00	0.00	0.01	0.00	0.00	0.03	0.00	0.13	0.01	0.01	0.01	0.03
Mg	0.00	0.00	0.01	0.00	0.00	0.02	0.00	0.15	0.00	0.00	0.00	0.03
Ca	0.11	0.08	0.08	0.01	0.10	0.03	0.06	0.05	0.39	0.37	0.38	0.30
Ba	0.00	0.00	0.00	0.00	0.00	0.00	0.00	0.00	0.00	0.00	0.00	0.03
Na	0.89	0.92	0.86	0.98	0.88	0.67	0.89	0.54	0.59	0.61	0.57	0.51
K	0.01	0.01	0.08	0.01	0.01	0.23	0.04	0.30	0.02	0.02	0.04	0.16
P	0.00	0.00	0.00	0.00	0.00	0.00	0.00	0.01	0.00	0.00	0.00	0.00

Table 6. Electron microprobe analyses of feldspar (continued).

Mineral	Ca-rich plagioclase								Alkali feldspar			
Sample#	H1281-61.7								H1281-61.7			
Circle#	3	3	3	3	3	3	3	3	3	3	3	3
Point#	8	9	10	11	12	13	14	15				
Analysis#	158	159	160	161	162	163	164	165	170	171	172	174
Comment									dark	dark	dark	dark
SiO_2	58.89	57.41	59.00	58.21	60.32	58.45	59.59	59.55	66.50	66.33	65.87	66.84
Al_2O_3	23.75	26.44	26.15	25.41	20.92	24.05	24.36	26.24	21.82	21.30	22.14	21.65
FeO	0.28	0.18	0.20	0.54	0.18	0.11	0.09	0.22	0.22	0.05	0.14	0.10
MgO	0.17	0.00	0.02	0.25	0.08	0.00	0.01	0.03	0.13	0.00	0.04	0.03
CaO	4.52	3.45	7.48	2.36	1.09	4.40	4.87	7.26	1.29	1.61	1.88	1.92
BaO	3.33	0.72	0.14	2.37	3.99	4.11	2.90	0.21	0.10	0.05	0.06	0.00
Na_2O	4.34	3.69	7.23	4.85	0.97	3.91	4.21	7.23	10.58	10.57	10.19	10.60
K_2O	5.52	7.16	0.43	6.71	12.54	5.78	5.40	0.58	0.97	0.50	0.73	0.19
P_2O_5	0.03	0.03	0.07	0.04	0.00	0.03	0.03	0.06	0.00	0.08	0.02	0.00
Total	100.82	99.08	100.71	100.72	100.09	100.84	101.45	101.37	101.61	100.49	101.08	101.33
Cations (based on 8 oxygens)												
Si	2.70	2.64	2.62	2.66	2.84	2.70	2.70	2.63	2.89	2.90	2.87	2.90
Al	1.28	1.43	1.37	1.37	1.16	1.31	1.30	1.37	1.12	1.10	1.14	1.11
Fe^{3+}	0.01	0.01	0.01	0.02	0.01	0.00	0.00	0.01	0.01	0.00	0.01	0.00
Mg	0.01	0.00	0.00	0.02	0.01	0.00	0.00	0.00	0.01	0.00	0.00	0.00
Ca	0.22	0.17	0.36	0.12	0.06	0.22	0.24	0.34	0.06	0.08	0.09	0.09
Ba	0.06	0.01	0.00	0.04	0.07	0.07	0.05	0.00	0.00	0.00	0.00	0.00
Na	0.39	0.33	0.62	0.43	0.09	0.35	0.37	0.62	0.89	0.90	0.86	0.89
K	0.32	0.42	0.02	0.39	0.75	0.34	0.31	0.03	0.05	0.03	0.04	0.01
P	0.00	0.00	0.00	0.00	0.00	0.00	0.00	0.00	0.00	0.00	0.00	0.00

Table 6. Electron microprobe analyses of feldspar (continued).

Mineral	Alkali feldspar											Albite
Sample#	H1281-61.7											H1281-6
Circle#	3	3	3	3	3	3	3	3	3	3	3	3
Point#												
Analysis#	175	176	177	178	186	187	188	189	190	191	192	193
Comment	dark	dark	dark	dark	dark	dark	dark	dark	dark	dark	dark	border
SiO_2	68.63	69.11	68.21	68.27	66.61	66.27	64.39	64.42	64.29	68.77	69.29	69.67
Al_2O_3	20.32	20.09	20.51	20.74	21.21	21.20	22.59	22.62	22.78	19.96	19.99	19.65
FeO	0.03	0.05	0.12	0.14	0.06	0.06	0.07	0.14	0.36	0.01	0.10	0.21
MgO	0.00	0.00	0.03	0.01	0.00	0.01	0.02	0.09	0.21	0.00	0.00	0.00
CaO	0.57	0.25	0.52	0.76	1.78	1.86	1.95	2.71	0.88	0.31	0.12	0.09
BaO	0.05	0.00	0.01	0.00	0.00	0.00	0.19	0.04	0.00	0.06	0.05	0.08
Na_2O	11.60	11.66	11.28	11.49	10.65	10.60	9.61	9.56	9.18	11.45	11.83	11.94
K_2O	0.21	0.12	0.27	0.28	0.20	0.24	1.52	0.71	2.16	0.24	0.12	0.12
P_2O_5	0.00	0.00	0.00	0.00	0.00	0.00	0.00	0.10	0.00	0.00	0.00	0.00
Total	101.41	101.28	100.96	101.69	100.51	100.23	100.33	100.40	99.85	100.80	101.49	101.75
Cations (based on 8 oxygens)												
Si	2.96	2.98	2.96	2.94	2.91	2.90	2.84	2.83	2.84	2.98	2.98	2.99
Al	1.03	1.02	1.05	1.05	1.09	1.10	1.18	1.17	1.19	1.02	1.02	1.00
Fe^{3+}	0.00	0.00	0.00	0.01	0.00	0.00	0.00	0.01	0.01	0.00	0.00	0.01
Mg	0.00	0.00	0.00	0.00	0.00	0.00	0.00	0.01	0.01	0.00	0.00	0.00
Ca	0.03	0.01	0.02	0.04	0.08	0.09	0.09	0.13	0.04	0.01	0.01	0.00
Ba	0.00	0.00	0.00	0.00	0.00	0.00	0.00	0.00	0.00	0.00	0.00	0.00
Na	0.97	0.98	0.95	0.96	0.90	0.90	0.82	0.81	0.79	0.96	0.99	0.99
K	0.01	0.01	0.02	0.02	0.01	0.01	0.09	0.04	0.12	0.01	0.01	0.01
P	0.00	0.00	0.00	0.00	0.00	0.00	0.00	0.00	0.00	0.00	0.00	0.00

Table 6. Electron microprobe analyses of feldspar (continued).

Mineral	Albite						
Sample#	H1281-61.7						
Circle#	3	3	3	3	3	3	3
Point#							
Analysis#	194	195	196	197	198	199	200
Comment	border	border	border	border	border	border	border
SiO_2	69.17	69.53	69.46	69.21	69.52	69.47	68.86
Al_2O_3	19.70	19.90	19.79	19.71	19.71	19.78	19.76
FeO	0.22	0.13	0.08	0.09	0.08	0.13	0.10
MgO	0.00	0.00	0.00	0.00	0.01	0.00	0.02
CaO	0.07	0.24	0.23	0.13	0.09	0.14	0.17
BaO	0.06	0.00	0.01	0.02	0.00	0.06	0.00
Na_2O	11.71	11.87	11.74	11.98	11.85	11.84	11.69
K_2O	0.43	0.12	0.12	0.12	0.09	0.10	0.12
P_2O_5	0.00	0.00	0.00	0.00	0.00	0.00	0.00
Total	101.37	101.79	101.44	101.25	101.35	101.51	100.72
Cations (based on 8 oxygens)							
Si	2.99	2.99	2.99	2.99	3.00	2.99	2.99
Al	1.00	1.01	1.01	1.00	1.00	1.00	1.01
Fe^{3+}	0.01	0.00	0.00	0.00	0.00	0.00	0.00
Mg	0.00	0.00	0.00	0.00	0.00	0.00	0.00
Ca	0.00	0.01	0.01	0.01	0.00	0.01	0.01
Ba	0.00	0.00	0.00	0.00	0.00	0.00	0.00
Na	0.98	0.99	0.98	1.00	0.99	0.99	0.98
K	0.02	0.01	0.01	0.01	0.00	0.01	0.01
P	0.00	0.00	0.00	0.00	0.00	0.00	0.00

Table 7. Electron microprobe analyses of garnet.

Sample#	JMH-25.2							Flt-1				
Circle#	1	1	1	2	2	2	2	1	1	1	1	2
Analysis#	1	2	2	1	2	3	4	1	2	3	4	1
Comment												
Wt. % oxides												
SiO_2	38.78	38.58	38.64	38.75	38.78	38.51	38.64	39.47	39.15	39.05	39.36	38.93
TiO_2	0.05	0.07	0.01	0.07	0.11	0.01	0.09	0.30	0.69	0.83	0.53	0.88
Al_2O_3	22.50	22.30	22.48	22.47	22.44	22.30	22.36	22.09	21.94	21.85	22.04	21.65
Cr_2O_3	0.00	0.00	0.00	0.00	0.03	0.00	0.00	0.03	0.00	0.00	0.02	0.00
FeO	2.20	2.22	2.40	2.03	2.08	2.18	2.16	1.95	2.02	2.11	2.00	2.09
MnO	1.20	1.24	1.33	1.15	1.19	1.15	1.11	0.29	0.29	0.35	0.28	0.44
MgO	0.01	0.01	0.02	0.01	0.01	0.02	0.00	0.00	0.01	0.02	0.01	0.03
CaO	35.61	35.57	35.13	35.60	35.74	35.42	35.37	36.46	36.49	36.29	36.39	36.35
Na_2O	0.01	0.00	0.00	0.00	0.00	0.00	0.00	0.00	0.00	0.00	0.00	0.00
K_2O	0.00	0.00	0.00	0.00	0.01	0.00	0.00	0.00	0.01	0.00	0.00	0.00
Total	100.35	100.00	100.01	100.08	100.38	99.59	99.74	100.60	100.60	100.50	100.64	100.37
Cations (refer to Chapter V for the method used in the calculation)												
Si	2.94	2.93	2.94	2.94	2.94	2.91	2.93	2.97	2.95	2.95	2.96	2.94
Ti	0.00	0.00	0.00	0.00	0.01	0.00	0.01	0.02	0.04	0.05	0.03	0.05
Al	2.01	2.00	2.01	2.01	2.00	1.99	2.00	1.96	1.95	1.94	1.95	1.93
Cr	0.00	0.00	0.00	0.00	0.00	0.00	0.00	0.00	0.00	0.00	0.00	0.00
Fe^{3+}	0.00	0.00	0.00	0.00	0.00	0.01	0.00	0.02	0.01	0.01	0.01	0.02
Fe^{2+}	0.14	0.14	0.15	0.13	0.13	0.13	0.14	0.10	0.12	0.12	0.11	0.11
Mn	0.08	0.08	0.09	0.07	0.08	0.07	0.07	0.02	0.02	0.02	0.02	0.03
Mg	0.00	0.00	0.00	0.00	0.00	0.00	0.00	0.00	0.00	0.00	0.00	0.00
Ca	2.89	2.90	2.86	2.89	2.90	2.87	2.87	2.94	2.95	2.93	2.93	2.94
H	0.00	0.00	0.00	0.00	0.00	0.20	0.13	0.00	0.00	0.00	0.00	0.00

Table 7. Electron microprobe analyses of garnet (continued).

Sample#	Flt-I	JMH-333.1									
Circle#	2	2	2	2	1	1	1	1	1	2	2	2
Analysis#	2	3	5	6	1	3	4	5	6	1	2	3
Comment												
Wt. % oxides												
SiO_2	39.24	39.52	39.36	39.50	39.55	39.22	39.33	39.21	39.33	39.24	39.50	39.41
TiO_2	0.09	0.02	0.43	0.02	0.03	0.01	0.01	0.03	0.06	0.36	0.00	0.21
Al_2O_3	22.13	22.26	22.00	22.21	22.24	22.19	22.27	22.13	22.13	21.98	22.16	22.03
Cr_2O_3	0.00	0.01	0.00	0.00	0.01	0.00	0.00	0.00	0.00	0.00	0.01	0.00
FeO	1.52	1.51	1.51	1.43	0.79	0.70	0.75	0.70	0.72	0.69	0.80	0.78
MnO	0.38	0.35	0.42	0.29	0.64	0.58	0.62	0.61	0.61	0.59	0.66	0.66
MgO	0.00	0.00	0.02	0.00	0.00	0.01	0.00	0.01	0.00	0.00	0.00	0.00
CaO	36.41	36.79	36.68	36.97	37.40	37.17	37.53	37.35	37.26	37.23	37.47	37.24
Na_2O	0.00	0.00	0.00	0.00	0.01	0.00	0.00	0.01	0.01	0.00	0.00	0.00
K_2O	0.00	0.01	0.00	0.00	0.00	0.01	0.00	0.00	0.01	0.00	0.00	0.01
Total	99.76	100.47	100.43	100.42	100.66	99.86	100.51	100.05	100.12	100.10	100.61	100.34
Cations (refer to Chapter V for the method used in the calculation)												
Si	2.96	2.97	2.96	2.97	2.97	2.96	2.96	2.96	2.97	2.96	2.97	2.97
Ti	0.00	0.00	0.02	0.00	0.00	0.00	0.00	0.00	0.00	0.02	0.00	0.01
Al	1.97	1.97	1.95	1.97	1.97	1.97	1.97	1.97	1.97	1.96	1.96	1.95
Cr	0.00	0.00	0.00	0.00	0.00	0.00	0.00	0.00	0.00	0.00	0.00	0.00
Fe^{3+}	0.03	0.03	0.02	0.03	0.03	0.03	0.03	0.03	0.03	0.02	0.04	0.03
Fe^{2+}	0.07	0.07	0.07	0.06	0.02	0.02	0.02	0.02	0.02	0.02	0.01	0.02
Mn	0.02	0.02	0.03	0.02	0.04	0.04	0.04	0.04	0.04	0.04	0.04	0.04
Mg	0.00	0.00	0.00	0.00	0.00	0.00	0.00	0.00	0.00	0.00	0.00	0.00
Ca	2.94	2.96	2.96	2.98	3.01	3.00	3.02	3.02	3.01	3.01	3.01	3.00
H	0.09	0.00	0.00	0.00	0.00	0.05	0.00	0.00	0.00	0.00	0.00	0.00

Table 7. Electron microprobe analyses of garnet (continued).

Sample#	JMH-333.1		E:0.5								Flt-B	
Circle#	2	2	1	1	1	1	3	3	3	3	1	1
Analysis#	4	5	1	2	3	4	1	2	3	4	1	2
Comment												
Wt. % oxides												
SiO_2	38.73	39.25	37.80	38.13	38.01	37.42	36.91	36.97	37.36	37.68	38.93	38.88
TiO_2	0.03	0.00	0.00	0.00	0.06	0.05	0.02	0.02	0.04	0.01	0.74	0.67
Al_2O_3	22.07	21.98	21.28	22.02	21.10	21.73	21.93	21.86	18.95	22.09	21.82	21.85
Cr_2O_3	0.00	0.00	0.00	0.01	0.00	0.00	0.00	0.00	0.00	0.00	0.00	0.00
FeO	0.99	1.12	1.52	0.68	1.68	0.93	0.84	0.88	4.95	0.91	2.26	1.90
MnO	0.83	0.87	0.10	0.02	0.20	0.03	0.02	0.07	0.10	0.05	0.94	0.89
MgO	0.01	0.01	0.04	0.04	0.03	0.05	0.04	0.04	0.07	0.02	0.01	0.01
CaO	37.19	37.00	37.81	38.23	37.53	38.27	38.34	38.12	37.42	38.36	35.77	36.02
Na_2O	0.02	0.01	0.00	0.01	0.02	0.00	0.00	0.01	0.00	0.00	0.00	0.00
K_2O	0.00	0.00	0.00	0.00	0.00	0.00	0.00	0.00	0.00	0.00	0.00	0.00
Total	99.86	100.25	98.56	99.13	98.62	98.48	98.09	97.97	98.89	99.12	100.47	100.20
Cations (refer to Chapter V for the method used in the calculation)												
Si	2.93	2.96	2.83	2.86	2.85	2.80	2.75	2.75	2.86	2.84	2.94	2.95
Ti	0.00	0.00	0.00	0.00	0.00	0.00	0.00	0.00	0.00	0.00	0.04	0.04
Al	1.97	1.96	1.88	1.95	1.87	1.92	1.93	1.92	1.71	1.96	1.95	1.95
Cr	0.00	0.00	0.00	0.00	0.00	0.00	0.00	0.00	0.00	0.00	0.00	0.00
Fe^{3+}	0.03	0.04	0.09	0.04	0.11	0.06	0.05	0.05	0.29	0.04	0.01	0.01
Fe^{2+}	0.04	0.03	0.00	0.00	0.00	0.00	0.00	0.00	0.03	0.02	0.13	0.11
Mn	0.05	0.06	0.01	0.00	0.01	0.00	0.00	0.00	0.01	0.00	0.06	0.06
Mg	0.00	0.00	0.00	0.00	0.00	0.01	0.00	0.00	0.01	0.00	0.00	0.00
Ca	3.02	2.99	3.04	3.08	3.02	3.07	3.06	3.04	3.07	3.10	2.90	2.92
H	0.05	0.00	0.64	0.40	0.60	0.71	0.90	0.96	0.31	0.41	0.00	0.00

Table 7. Electron microprobe analyses of garnet (continued).

Sample#	Flt-B	JMH-295.1i								JMH-306ii	
Circle#	1	1	1	1	1	1	1	1	1	1	1	1
Analysis#	4	5	6	7	1	2	3	4	6	7	2	3
Comment											Coarse	Coarse
Wt. % oxides												
SiO_2	39.01	38.99	39.00	38.96	38.82	38.80	38.89	39.38	39.27	39.51	39.46	39.49
TiO_2	0.72	0.77	0.77	0.69	0.72	0.69	0.70	0.13	0.13	0.27	0.15	0.09
Al_2O_3	21.78	21.88	21.53	21.60	21.66	21.55	21.57	21.93	21.97	22.00	22.32	22.05
Cr_2O_3	0.00	0.00	0.00	0.00	0.00	0.00	0.00	0.03	0.00	0.00	0.00	0.00
FeO	1.54	2.32	1.98	2.02	1.92	2.08	2.14	1.99	1.97	1.88	0.56	0.55
MnO	0.95	1.05	1.06	1.03	0.49	0.58	0.57	0.36	0.38	0.33	0.89	0.86
MgO	0.02	0.02	0.01	0.01	0.02	0.03	0.01	0.01	0.01	0.02	0.00	0.00
CaO	36.23	35.38	35.60	35.87	36.18	36.29	36.27	36.33	36.46	36.37	37.28	37.24
Na_2O	0.01	0.00	0.01	0.00	0.00	0.00	0.00	0.00	0.00	0.01	0.00	0.00
K_2O	0.00	0.00	0.00	0.00	0.00	0.00	0.00	0.00	0.00	0.01	0.00	0.00
Total	100.25	100.41	99.97	100.18	99.80	100.03	100.16	100.16	100.18	100.40	100.64	100.28
Cations (refer to Chapter V for the method used in the calculation)												
Si	2.95	2.95	2.96	2.95	2.95	2.94	2.95	2.97	2.97	2.97	2.96	2.97
Ti	0.04	0.04	0.04	0.04	0.04	0.04	0.04	0.01	0.01	0.02	0.01	0.01
Al	1.94	1.95	1.93	1.93	1.94	1.93	1.93	1.95	1.96	1.95	1.98	1.96
Cr	0.00	0.00	0.00	0.00	0.00	0.00	0.00	0.00	0.00	0.00	0.00	0.00
Fe^{3+}	0.02	0.00	0.03	0.03	0.02	0.03	0.03	0.04	0.04	0.03	0.02	0.03
Fe^{2+}	0.08	0.14	0.10	0.10	0.10	0.10	0.10	0.09	0.09	0.09	0.02	0.00
Mn	0.06	0.07	0.07	0.07	0.03	0.04	0.04	0.02	0.02	0.02	0.06	0.05
Mg	0.00	0.00	0.00	0.00	0.00	0.00	0.00	0.00	0.00	0.00	0.00	0.00
Ca	2.94	2.87	2.89	2.91	2.94	2.95	2.95	2.94	2.95	2.93	3.00	3.00
H	0.00	0.00	0.00	0.00	0.00	0.00	0.00	0.00	0.00	0.00	0.00	0.00

Table 7. Electron microprobe analyses of garnet (continued).

Sample#	JMH-306ii											
Circle#	1	1	1	2	2	2	2	2	2	2	2	2
Analysis#	4	5	14	1	2	3	4	5	8	9	1	1
Comment	Coarse	Coarse	Fine	Coarse	Coarse	Coarse	Coarse	Coarse	Fine	Fine	Fine	Fine
Wt. % oxides												
SiO_2	39.44	39.07	39.37	39.21	39.18	38.97	39.27	39.27	39.39	38.99	39.48	38.76
TiO_2	0.17	0.89	0.12	0.59	0.38	0.35	0.23	0.23	0.01	0.45	0.01	1.05
Al_2O_3	22.00	21.39	22.10	21.67	21.94	21.77	22.00	21.89	22.07	22.05	22.36	21.54
Cr_2O_3	0.01	0.00	0.00	0.00	0.00	0.00	0.00	0.00	0.01	0.00	0.00	0.00
FeO	0.56	0.54	0.73	0.60	0.56	0.55	0.58	0.55	0.59	0.64	0.56	0.63
MnO	0.78	0.75	0.92	0.77	0.79	0.77	0.82	0.85	1.03	0.82	1.08	0.71
MgO	0.00	0.00	0.01	0.00	0.00	0.00	0.00	0.01	0.00	0.00	0.00	0.00
CaO	37.34	37.47	37.07	37.31	37.16	37.33	37.51	37.31	36.89	37.30	37.13	37.18
Na_2O	0.00	0.00	0.00	0.01	0.00	0.00	0.00	0.00	0.01	0.00	0.00	0.00
K_2O	0.00	0.01	0.00	0.00	0.00	0.00	0.00	0.00	0.00	0.02	0.00	0.00
Total	100.30	100.12	100.31	100.15	100.02	99.75	100.42	100.12	99.99	100.27	100.61	99.87
Cations (refer to Chapter V for the method used in the calculation)												
Si	2.97	2.95	2.97	2.96	2.96	2.94	2.96	2.96	2.97	2.94	2.96	2.93
Ti	0.01	0.05	0.01	0.03	0.02	0.02	0.01	0.01	0.00	0.03	0.00	0.06
Al	1.95	1.91	1.96	1.93	1.95	1.94	1.95	1.95	1.96	1.96	1.98	1.92
Cr	0.00	0.00	0.00	0.00	0.00	0.00	0.00	0.00	0.00	0.00	0.00	0.00
Fe^{3+}	0.04	0.03	0.03	0.04	0.02	0.03	0.03	0.03	0.03	0.01	0.02	0.02
Fe^{2+}	0.00	0.00	0.01	0.00	0.01	0.00	0.00	0.00	0.00	0.03	0.01	0.02
Mn	0.05	0.05	0.06	0.05	0.05	0.05	0.05	0.05	0.07	0.05	0.07	0.05
Mg	0.00	0.00	0.00	0.00	0.00	0.00	0.00	0.00	0.00	0.00	0.00	0.00
Ca	3.01	3.03	2.99	3.02	3.01	3.02	3.03	3.02	2.98	3.02	2.99	3.01
H	0.00	0.00	0.00	0.00	0.00	0.10	0.00	0.00	0.00	0.00	0.00	0.05

Table 7. Electron microprobe analyses of garnet (continued).

Sample#	UG-2											UG-C
Circle#	1	1	1	1	1	1	1	1	2	2	2	1
Analysis#	1	2	3	4	5	6	7	8	2	3	6	1
Comment	matrix	matrix	matrix	matrix	matrix	matrix	matrix	matrix	matrix	matrix	matrix	matrix
Wt. % oxides												
SiO_2	37.83	37.85	37.22	37.82	37.68	38.04	38.12	37.90	38.01	38.47	38.56	37.85
TiO_2	0.88	0.83	0.77	1.00	0.82	0.77	0.93	0.92	0.83	0.59	0.43	0.46
Al_2O_3	21.74	21.74	21.71	21.72	21.72	21.77	21.81	21.73	21.74	21.48	21.59	21.62
Cr_2O_3	0.00	0.00	0.00	0.00	0.00	0.00	0.00	0.02	0.01	0.03	0.00	0.01
FeO	0.57	0.54	0.50	0.58	0.52	0.51	0.56	0.58	0.70	1.29	0.76	1.01
MnO	0.09	0.07	0.10	0.12	0.09	0.09	0.07	0.10	0.14	0.16	0.11	0.18
MgO	0.00	0.00	0.00	0.00	0.00	0.00	0.01	0.00	0.00	0.01	0.00	0.00
CaO	37.86	38.08	38.27	38.08	38.05	38.21	37.92	38.21	38.01	37.73	37.43	37.87
Na_2O	0.00	0.00	0.01	0.00	0.00	0.00	0.00	0.02	0.00	0.01	0.00	0.01
K_2O	0.02	0.00	0.00	0.00	0.00	0.01	0.00	0.00	0.03	0.01	0.15	0.00
Total	98.98	99.11	98.58	99.31	98.88	99.40	99.43	99.49	99.47	99.79	99.03	99.02
Cations (refer to Chapter V for the method used in the calculation)												
Si	2.84	2.84	2.79	2.85	2.83	2.87	2.87	2.86	2.87	2.92	2.89	2.85
Ti	0.05	0.05	0.04	0.06	0.05	0.04	0.05	0.05	0.05	0.03	0.02	0.03
Al	1.92	1.93	1.92	1.93	1.92	1.93	1.94	1.94	1.94	1.92	1.91	1.92
Cr	0.00	0.00	0.00	0.00	0.00	0.00	0.00	0.00	0.00	0.00	0.00	0.00
Fe^{3+}	0.03	0.03	0.03	0.01	0.03	0.02	0.01	0.01	0.02	0.04	0.05	0.06
Fe^{2+}	0.01	0.01	0.00	0.02	0.00	0.01	0.03	0.03	0.03	0.04	0.00	0.01
Mn	0.01	0.00	0.01	0.01	0.01	0.01	0.00	0.01	0.01	0.01	0.01	0.01
Mg	0.00	0.00	0.00	0.00	0.00	0.00	0.00	0.00	0.00	0.00	0.00	0.00
Ca	3.04	3.07	3.07	3.07	3.06	3.09	3.06	3.09	3.08	3.07	3.01	3.05
H	0.48	0.42	0.68	0.33	0.53	0.28	0.28	0.25	0.25	0.07	0.44	0.44

Table 7. Electron microprobe analyses of garnet (continued).

Sample#	UG-C											
Circle#	1	1	1	1	1	2	2	2	2	2	3	3
Analysis#	2	3	4	5	6	1	2	3	4	5	1	2
Comment	matrix	matrix	matrix	matrix	matrix	vein	vein	vein	vein	vein	vein	vein
Wt. % oxides												
SiO_2	36.76	37.44	38.30	38.41	38.17	38.90	38.67	38.63	38.98	38.99	38.64	38.84
TiO_2	0.35	0.36	0.01	0.04	0.01	0.00	0.01	0.00	0.00	0.03	0.01	0.03
Al_2O_3	21.28	21.62	21.58	21.42	21.79	21.47	21.86	21.55	21.71	21.86	22.00	22.11
Cr_2O_3	0.01	0.00	0.00	0.02	0.00	0.00	0.00	0.00	0.00	0.02	0.00	0.00
FeO	1.02	1.05	1.37	1.59	1.10	1.42	1.33	1.55	1.35	1.38	0.90	0.96
MnO	0.21	0.22	0.15	0.15	0.34	0.56	0.44	0.47	0.43	0.45	0.22	0.19
MgO	0.00	0.00	0.00	0.00	0.00	0.00	0.01	0.00	0.00	0.00	0.00	0.01
CaO	37.83	37.97	37.56	37.56	37.56	37.55	37.50	37.26	37.73	37.59	37.96	38.13
Na_2O	0.00	0.01	0.03	0.05	0.02	0.01	0.00	0.00	0.00	0.01	0.00	0.03
K_2O	0.00	0.00	0.01	0.00	0.00	0.01	0.00	0.00	0.00	0.00	0.00	0.01
Total	97.46	98.67	99.02	99.23	98.98	99.91	99.81	99.47	100.20	100.32	99.74	100.31
Cations (refer to Chapter V for the method used in the calculation)												
Si	2.73	2.81	2.88	2.90	2.87	2.95	2.93	2.92	2.95	2.95	2.92	2.93
Ti	0.02	0.02	0.00	0.00	0.00	0.00	0.00	0.00	0.00	0.00	0.00	0.00
Al	1.86	1.91	1.91	1.90	1.93	1.92	1.95	1.92	1.94	1.95	1.96	1.97
Cr	0.00	0.00	0.00	0.00	0.00	0.00	0.00	0.00	0.00	0.00	0.00	0.00
Fe^{3+}	0.06	0.07	0.09	0.09	0.07	0.08	0.05	0.08	0.07	0.05	0.04	0.03
Fe^{2+}	0.00	0.00	0.00	0.01	0.00	0.01	0.04	0.02	0.02	0.04	0.02	0.03
Mn	0.01	0.01	0.01	0.01	0.02	0.04	0.03	0.03	0.03	0.03	0.01	0.01
Mg	0.00	0.00	0.00	0.00	0.00	0.00	0.00	0.00	0.00	0.00	0.00	0.00
Ca	3.01	3.05	3.03	3.04	3.02	3.05	3.05	3.02	3.06	3.04	3.08	3.09
H	1.20	0.61	0.42	0.30	0.45	0.00	0.05	0.20	0.00	0.00	0.10	0.00

Table 7. Electron microprobe analyses of garnet (continued).

Sample#	UG-C									
Circle#	3	3	3	3	4	4	4	4	4	4
Analysis#	3	4	5	6	1	2	3	4	5	6
Comment	vein	vein	vein	vein	matrix	matrix	matrix	matrix	matrix	matrix
Wt. % oxides										
SiO_2	39.17	38.53	38.53	38.46	37.52	37.49	37.99	38.05	38.29	37.41
TiO_2	0.00	0.00	0.01	0.01	0.34	0.51	0.14	1.06	0.06	0.98
Al_2O_3	21.93	21.96	22.02	22.19	21.73	21.42	21.96	21.01	21.87	21.07
Cr_2O_3	0.00	0.00	0.00	0.00	0.00	0.00	0.02	0.03	0.01	0.00
FeO	1.05	1.01	1.00	0.93	0.98	1.05	0.89	1.28	1.22	1.02
MnO	0.22	0.23	0.22	0.20	0.21	0.20	0.25	0.19	0.25	0.16
MgO	0.01	0.00	0.01	0.00	0.00	0.00	0.01	0.01	0.00	0.00
CaO	37.68	37.86	37.83	37.89	37.76	37.65	37.91	37.60	37.71	37.95
Na_2O	0.00	0.00	0.00	0.00	0.00	0.02	0.00	0.01	0.00	0.00
K_2O	0.00	0.00	0.00	0.00	0.00	0.10	0.01	0.02	0.03	0.00
Total	100.05	99.59	99.61	99.68	98.55	98.41	99.16	99.26	99.43	98.60
Cations (refer to Chapter V for the method used in the calculation)										
Si	2.96	2.91	2.91	2.91	2.81	2.81	2.86	2.87	2.89	2.81
Ti	0.00	0.00	0.00	0.00	0.02	0.03	0.01	0.06	0.00	0.06
Al	1.95	1.95	1.96	1.98	1.92	1.89	1.95	1.87	1.95	1.86
Cr	0.00	0.00	0.00	0.00	0.00	0.00	0.00	0.00	0.00	0.00
Fe^{3+}	0.05	0.04	0.04	0.02	0.06	0.07	0.04	0.07	0.05	0.06
Fe^{2+}	0.02	0.02	0.02	0.04	0.00	0.00	0.01	0.01	0.03	0.00
Mn	0.01	0.01	0.01	0.01	0.01	0.01	0.02	0.01	0.02	0.01
Mg	0.00	0.00	0.00	0.00	0.00	0.00	0.00	0.00	0.00	0.00
Ca	3.05	3.06	3.06	3.07	3.03	3.02	3.06	3.04	3.05	3.05
H	0.00	0.17	0.16	0.14	0.67	0.73	0.38	0.31	0.24	0.65

Table 8. EDS analyses of ilmenite and chalcocite.

Mineral	Ilmenite										Chalcocite	
Sample#	1281-62.5					H1281-61.5		JMH-281A.1			JMH-25.1	
Wt. % oxides												
TiO_2	53.29	53.74	53.18	53.17	53.83	52.99	52.14	52.18	52.11	53.34		
FeO	39.65	39.32	39.79	37.96	37.45	40.53	41.40	40.86	37.02	41.38		
MnO	7.06	6.94	7.03	8.88	8.72	6.10	4.83	5.79	5.17	4.96		
Cu											79.69	79.39
S											20.31	20.61
Cations*												
Ti	1.01	1.01	1.01	1.01	1.01	1.01	1.00	1.00	1.03	1.01		
Fe	0.83	0.82	0.84	0.80	0.79	0.86	0.89	0.87	0.82	0.87		
Mn	0.15	0.15	0.15	0.19	0.19	0.13	0.10	0.13	0.12	0.11		
Cu											1.99	1.98
S											1.01	1.02

* Based on 3 oxygens for ilmenite and 3 cations for chalcocite

Table 9. Electron microprobe analyses of phengite.

Sample#	H1281-61.7		JMH-26													
Circle#	2	2	4	4	4	4	4	4	4	4	4	4	4	4	4	4
Point#	3	4	1	2	9	10	11	12	13	14	15	16	17	18	19	20
Analysis#	653	654	319	320	327	328	329	330	331	332	333	334	335	336	337	338
Wt. % oxides																
SiO_2	44.93	44.52	44.00	44.97	43.01	43.18	44.30	44.65	43.21	43.48	43.29	43.41	44.21	43.91	44.56	44.06
TiO_2	0.46	0.56	0.23	0.07	0.26	0.03	0.02	0.25	0.14	0.20	0.28	0.10	0.10	0.12	0.08	0.20
Al_2O_3	34.11	33.83	33.39	33.30	33.59	33.17	34.58	33.08	33.98	34.26	33.98	34.14	34.48	34.22	33.40	33.49
Cr_2O_3	0.00	0.00	0.00	0.00	0.00	0.00	0.00	0.00	0.00	0.00	0.00	0.00	0.00	0.00	0.00	0.00
FeO	3.66	3.48	3.21	2.97	3.92	4.11	2.38	3.11	3.18	3.18	3.31	3.01	3.03	3.07	3.16	3.46
MnO	0.02	0.02	0.01	0.00	0.01	0.03	0.00	0.00	0.02	0.01	0.02	0.00	0.01	0.00	0.00	0.02
MgO	0.83	0.78	0.97	0.74	1.10	1.28	0.69	1.01	0.73	0.69	0.77	0.76	0.69	0.95	1.13	0.87
CaO	0.00	0.00	0.00	0.00	0.00	0.00	0.01	0.02	0.00	0.01	0.00	0.02	0.02	0.01	0.00	0.00
Na_2O	0.51	0.51	0.52	1.12	0.45	0.48	0.52	0.58	0.48	0.49	0.53	0.48	0.56	0.56	0.56	0.50
K_2O	11.10	11.23	10.69	9.93	10.55	10.48	10.77	10.72	10.49	10.54	10.51	10.53	10.58	10.56	10.83	10.77
F	0.00	0.01	0.00	0.00	0.00	0.00	0.00	0.01	0.00	0.03	0.00	0.00	0.00	0.01	0.00	0.00
Cl	0.01	0.00	0.00	0.00	0.01	0.01	0.00	0.01	0.02	0.01	0.02	0.01	0.02	0.04	0.04	0.02
Total	95.62	94.93	93.02	93.11	92.89	92.75	93.26	93.43	92.23	92.86	92.70	92.45	93.68	93.43	93.77	93.38
—O≡F,Cl	0.00	0.01	0.00	0.00	0.00	0.00	0.00	0.01	0.01	0.01	0.00	0.00	0.01	0.01	0.01	0.00
Total	95.62	94.93	93.01	93.11	92.89	92.75	93.26	93.42	92.22	92.84	92.70	92.45	93.68	93.42	93.76	93.38
Cations (calculated based on 12 oxygens)																
Si	3.04	2.99	2.90	2.95	2.84	2.85	2.91	2.95	2.82	2.86	2.84	2.84	2.92	2.90	2.96	2.92
Ti	0.02	0.03	0.01	0.00	0.01	0.00	0.00	0.01	0.01	0.01	0.01	0.00	0.00	0.01	0.00	0.01
Al	2.72	2.68	2.59	2.58	2.62	2.58	2.68	2.58	2.62	2.65	2.63	2.63	2.69	2.66	2.61	2.61
Cr	0.00	0.00	0.00	0.00	0.00	0.00	0.00	0.00	0.00	0.00	0.00	0.00	0.00	0.00	0.00	0.00
Fe^{+3}	0.00	0.00	0.00	0.00	0.00	0.00	0.00	0.00	0.00	0.00	0.00	0.00	0.00	0.00	0.00	0.00
Fe^{+2}	0.21	0.20	0.18	0.16	0.22	0.23	0.13	0.17	0.17	0.17	0.18	0.16	0.17	0.17	0.18	0.19
Mn	0.00	0.00	0.00	0.00	0.00	0.00	0.00	0.00	0.00	0.00	0.00	0.00	0.00	0.00	0.00	0.00
Mg	0.08	0.08	0.10	0.07	0.11	0.13	0.07	0.10	0.07	0.07	0.08	0.07	0.07	0.09	0.11	0.09
Ca	0.00	0.00	0.00	0.00	0.00	0.00	0.00	0.00	0.00	0.00	0.00	0.00	0.00	0.00	0.00	0.00
Na	0.07	0.07	0.07	0.14	0.06	0.06	0.07	0.07	0.06	0.06	0.07	0.06	0.07	0.07	0.07	0.06
K	0.96	0.96	0.90	0.83	0.89	0.88	0.90	0.90	0.87	0.88	0.88	0.88	0.89	0.89	0.92	0.91
F	0.00	0.00	0.00	0.00	0.00	0.00	0.00	0.00	0.00	0.01	0.00	0.00	0.00	0.00	0.00	0.00
Cl	0.00	0.00	0.00	0.00	0.00	0.00	0.00	0.00	0.00	0.00	0.00	0.00	0.00	0.00	0.00	0.00
OH	1.98	2.28	3.07	3.02	3.13	3.19	2.95	2.90	3.39	3.14	3.20	3.30	2.79	2.90	2.76	2.92

Table 10. Electron microprobe analyses of prehnite.

Sample#	UG2											UGC-block1-bigvein	
Point#												1	2
Analysis#	11	12	13	14	15	16	17	18	19	20	32	426	427
Wt. % oxides													
SiO_2	42.75	42.65	42.82	42.49	42.80	42.35	42.87	42.80	42.90	42.98	42.67	43.01	42.89
TiO_2	0.34	0.06	0.27	0.00	0.06	0.00	0.29	0.12	0.09	0.52	0.06	0.00	0.02
Al_2O_3	24.13	24.09	23.94	24.29	24.27	23.93	24.19	24.16	24.14	23.95	24.31	24.16	24.07
Cr_2O_3	0.01	0.01	0.00	0.01	0.02	0.03	0.00	0.00	0.01	0.01	0.01	0.00	0.01
FeO	0.07	0.08	0.03	0.05	0.07	0.09	0.06	0.09	0.11	0.09	0.04	0.08	0.14
MnO	0.01	0.00	0.01	0.00	0.00	0.00	0.04	0.00	0.03	0.00	0.01	0.03	0.03
MgO	0.01	0.00	0.00	0.02	0.00	0.01	0.02	0.00	0.00	0.03	0.02	0.00	0.00
CaO	27.07	26.73	26.78	26.62	26.87	26.59	26.88	26.76	26.75	26.88	26.70	27.25	27.42
Na_2O	0.01	0.00	0.00	0.00	0.01	0.05	0.00	0.00	0.01	0.03	0.05	0.01	0.00
K_2O	0.03	0.02	0.10	0.02	0.02	0.03	0.03	0.01	0.03	0.02	0.03	0.02	0.02
Total	94.43	93.65	93.93	93.51	94.11	93.08	94.36	93.95	94.08	94.49	93.91	94.57	94.61
Cations (based on 12 oxygens)													
Si	2.98	2.99	3.00	2.99	2.99	2.99	2.99	2.99	3.00	2.99	2.99	2.99	2.99
Ti	0.02	0.00	0.01	0.00	0.00	0.00	0.01	0.01	0.00	0.03	0.00	0.00	0.00
Al	1.98	1.99	1.97	2.01	2.00	1.99	1.99	1.99	1.99	1.96	2.01	1.98	1.98
Cr	0.00	0.00	0.00	0.00	0.00	0.00	0.00	0.00	0.00	0.00	0.00	0.00	0.00
Fe^{+3}	0.00	0.00	0.00	0.00	0.00	0.01	0.00	0.01	0.01	0.01	0.00	0.00	0.01
Fe^{+2}	0.00	0.00	0.00	0.00	0.00	0.00	0.00	0.00	0.00	0.00	0.00	0.00	0.00
Mn^{+3}	0.00	0.00	0.00	0.00	0.00	0.00	0.00	0.00	0.00	0.00	0.00	0.00	0.00
Mg	0.00	0.00	0.00	0.00	0.00	0.00	0.00	0.00	0.00	0.00	0.00	0.00	0.00
Ca	2.02	2.01	2.01	2.00	2.01	2.01	2.01	2.00	2.00	2.00	2.00	2.03	2.05
Na	0.00	0.00	0.00	0.00	0.00	0.01	0.00	0.00	0.00	0.00	0.01	0.00	0.00
K	0.00	0.00	0.01	0.00	0.00	0.00	0.00	0.00	0.00	0.00	0.00	0.00	0.00

Table 10. Electron microprobe analyses of prehnite (continued).

Sample#	UGC-block1-bigvein							UGC-block2-bigvein							
Point#	4	5	6	7	8	9	10	1	2	3	4	5	6	7	8
Analysis#	429	430	431	432	433	434	435	520	521	522	523	524	525	526	527
Wt. % oxides															
SiO_2	43.22	42.92	43.41	43.13	43.13	43.26	43.01	42.69	43.10	42.88	43.00	42.77	42.57	42.46	42.84
TiO_2	0.00	0.01	0.00	0.00	0.03	0.03	0.00	0.00	0.02	0.00	0.00	0.01	0.00	0.01	0.00
Al_2O_3	24.08	24.50	24.12	24.28	24.36	24.30	24.27	23.94	24.04	23.82	24.04	24.11	24.08	24.12	24.18
Cr_2O_3	0.00	0.00	0.00	0.00	0.01	0.00	0.00	0.00	0.02	0.00	0.00	0.00	0.00	0.00	0.03
FeO	0.18	0.13	0.15	0.24	0.15	0.09	0.11	0.06	0.12	0.17	0.21	0.16	0.18	0.13	0.12
MnO	0.02	0.04	0.01	0.01	0.03	0.02	0.02	0.00	0.01	0.02	0.01	0.00	0.02	0.02	0.02
MgO	0.00	0.01	0.00	0.00	0.00	0.00	0.00	0.01	0.00	0.01	0.00	0.00	0.01	0.00	0.01
CaO	27.49	27.44	27.19	27.27	27.54	27.23	27.30	27.50	27.41	27.44	27.53	27.23	27.48	27.42	27.54
Na_2O	0.00	0.01	0.00	0.00	0.00	0.03	0.01	0.00	0.00	0.00	0.01	0.00	0.01	0.00	0.00
K_2O	0.02	0.02	0.02	0.02	0.00	0.01	0.02	0.02	0.03	0.01	0.03	0.03	0.03	0.02	0.03
Total	95.02	95.08	94.89	94.94	95.25	94.95	94.74	94.21	94.76	94.34	94.83	94.30	94.35	94.18	94.77
Cations (based on 12 oxygens)															
Si	2.99	2.97	3.01	2.99	2.98	3.00	2.99	2.99	2.99	2.99	2.99	2.99	2.97	2.97	2.98
Ti	0.00	0.00	0.00	0.00	0.00	0.00	0.00	0.00	0.00	0.00	0.00	0.00	0.00	0.00	0.00
Al	1.97	2.00	1.97	1.98	1.99	1.98	1.99	1.97	1.97	1.96	1.97	1.98	1.98	1.99	1.98
Cr	0.00	0.00	0.00	0.00	0.00	0.00	0.00	0.00	0.00	0.00	0.00	0.00	0.00	0.00	0.00
Fe^{+3}	0.01	0.01	0.01	0.01	0.01	0.01	0.01	0.00	0.01	0.01	0.01	0.01	0.01	0.01	0.01
Fe^{+2}	0.00	0.00	0.00	0.00	0.00	0.00	0.00	0.00	0.00	0.00	0.00	0.00	0.00	0.00	0.00
Mn^{+3}	0.00	0.00	0.00	0.00	0.00	0.00	0.00	0.00	0.00	0.00	0.00	0.00	0.00	0.00	0.00
Mg	0.00	0.00	0.00	0.00	0.00	0.00	0.00	0.00	0.00	0.00	0.00	0.00	0.00	0.00	0.00
Ca	2.04	2.04	2.02	2.02	2.04	2.02	2.03	2.06	2.04	2.05	2.05	2.04	2.06	2.06	2.05
Na	0.00	0.00	0.00	0.00	0.00	0.00	0.00	0.00	0.00	0.00	0.00	0.00	0.00	0.00	0.00
K	0.00	0.00	0.00	0.00	0.00	0.00	0.00	0.00	0.00	0.00	0.00	0.00	0.00	0.00	0.00

Table 10. Electron microprobe analyses of prehnite (continued).

Sample#	block2-bigvein		UGC-block2-zone4												
Point#	9	10	1	2	3	4	5	6	7	8	9	10	11	12	13
Analysis#	528	529	530	531	532	533	534	535	536	537	538	539	540	541	542
Wt. % oxides															
SiO_2	43.10	43.15	43.18	43.29	43.43	43.25	43.38	43.40	43.59	43.31	43.12	43.29	43.14	43.40	43.53
TiO_2	0.00	0.04	0.02	0.00	0.00	0.00	0.02	0.00	0.00	0.04	0.03	0.02	0.00	0.03	0.01
Al_2O_3	24.04	24.11	23.50	23.58	23.51	23.74	23.79	23.59	23.50	23.53	23.76	23.55	23.77	23.62	23.62
Cr_2O_3	0.01	0.00	0.00	0.00	0.00	0.00	0.00	0.00	0.00	0.00	0.00	0.02	0.00	0.04	0.02
FeO	0.09	0.05	0.16	0.13	0.31	0.20	0.20	0.19	0.43	0.38	0.31	0.32	0.26	0.17	0.20
MnO	0.03	0.00	0.01	0.05	0.05	0.06	0.01	0.03	0.04	0.03	0.00	0.03	0.00	0.02	0.03
MgO	0.00	0.00	0.00	0.00	0.00	0.00	0.00	0.00	0.03	0.00	0.00	0.00	0.00	0.01	0.00
CaO	27.34	27.46	27.15	27.14	27.01	27.31	27.19	27.29	26.73	26.82	27.09	27.23	27.39	27.32	26.79
Na_2O	0.01	0.01	0.03	0.02	0.07	0.03	0.03	0.03	0.08	0.06	0.02	0.05	0.02	0.05	0.11
K_2O	0.06	0.02	0.03	0.02	0.01	0.01	0.04	0.01	0.13	0.12	0.03	0.03	0.02	0.03	0.04
Total	94.67	94.83	94.07	94.22	94.39	94.60	94.64	94.55	94.52	94.29	94.35	94.54	94.60	94.69	94.33
Cations (based on 12 oxygens)															
Si	3.00	2.99	3.02	3.02	3.03	3.01	3.01	3.02	3.03	3.02	3.01	3.01	3.00	3.02	3.03
Ti	0.00	0.00	0.00	0.00	0.00	0.00	0.00	0.00	0.00	0.00	0.00	0.00	0.00	0.00	0.00
Al	1.97	1.97	1.94	1.94	1.93	1.95	1.95	1.94	1.93	1.94	1.95	1.93	1.95	1.94	1.94
Cr	0.00	0.00	0.00	0.00	0.00	0.00	0.00	0.00	0.00	0.00	0.00	0.00	0.00	0.00	0.00
Fe^{+3}	0.01	0.00	0.01	0.01	0.02	0.01	0.01	0.01	0.02	0.02	0.02	0.02	0.02	0.01	0.01
Fe^{+2}	0.00	0.00	0.00	0.00	0.00	0.00	0.00	0.00	0.00	0.00	0.00	0.00	0.00	0.00	0.00
Mn^{+3}	0.00	0.00	0.00	0.00	0.00	0.00	0.00	0.00	0.00	0.00	0.00	0.00	0.00	0.00	0.00
Mg	0.00	0.00	0.00	0.00	0.00	0.00	0.00	0.00	0.00	0.00	0.00	0.00	0.00	0.00	0.00
Ca	2.04	2.04	2.03	2.03	2.02	2.04	2.02	2.03	1.99	2.01	2.02	2.03	2.04	2.03	2.00
Na	0.00	0.00	0.00	0.00	0.01	0.00	0.00	0.00	0.01	0.01	0.00	0.01	0.00	0.01	0.01
K	0.01	0.00	0.00	0.00	0.00	0.00	0.00	0.00	0.01	0.01	0.00	0.00	0.00	0.00	0.00

Table 10. Electron microprobe analyses of prehnite (continued).

Sample#	zone4	JMH-24									JMH-25				
Point#	14										1	2	3	4	5
Analysis#	543	206	207	208	209	210	211	212	213	214	369	370	371	372	373
Wt. % oxides															
SiO_2	43.61	42.65	42.41	42.76	42.98	43.19	43.30	42.88	42.82	43.08	42.87	42.46	44.86	43.09	42.97
TiO_2	0.00	0.15	0.16	0.62	0.68	0.57	0.03	0.05	0.03	0.02	0.01	0.01	0.00	0.04	0.00
Al_2O_3	23.59	24.03	24.02	23.62	23.72	23.65	23.98	24.18	24.17	24.13	24.34	24.28	23.66	24.30	24.30
Cr_2O_3	0.01	0.00	0.00	0.00	0.00	0.00	0.00	0.02	0.02	0.04	0.00	0.00	0.00	0.00	0.00
FeO	0.28	0.05	0.01	0.01	0.04	0.00	0.05	0.05	0.01	0.04	0.21	0.07	0.08	0.08	0.14
MnO	0.01	0.02	0.02	0.02	0.03	0.04	0.05	0.05	0.04	0.06	0.08	0.02	0.01	0.02	0.01
MgO	0.01	0.00	0.00	0.00	0.00	0.00	0.01	0.01	0.00	0.00	0.00	0.00	0.00	0.01	0.00
CaO	27.10	26.06	26.58	26.50	26.53	26.10	26.31	25.84	25.79	26.14	27.08	27.02	24.14	27.06	27.25
Na_2O	0.08	0.00	0.00	0.01	0.02	0.01	0.00	0.01	0.00	0.00	0.00	0.00	0.99	0.01	0.02
K_2O	0.04	0.02	0.02	0.03	0.03	0.02	0.01	0.03	0.02	0.01	0.01	0.01	0.02	0.01	0.02
Total	94.73	92.97	93.23	93.57	94.04	93.57	93.73	93.10	92.89	93.53	94.60	93.87	93.76	94.63	94.71
Cations (based on 12 oxygens)															
Si	3.03	3.01	2.99	3.00	3.00	3.02	3.03	3.01	3.02	3.02	2.98	2.98	3.11	2.99	2.99
Ti	0.00	0.01	0.01	0.03	0.04	0.03	0.00	0.00	0.00	0.00	0.00	0.00	0.00	0.00	0.00
Al	1.93	2.00	2.00	1.95	1.95	1.95	1.98	2.00	2.01	1.99	2.00	2.01	1.94	1.99	1.99
Cr	0.00	0.00	0.00	0.00	0.00	0.00	0.00	0.00	0.00	0.00	0.00	0.00	0.00	0.00	0.00
Fe^{+3}	0.02	0.00	0.00	0.00	0.00	0.00	0.00	0.00	0.00	0.00	0.01	0.00	0.00	0.00	0.01
Fe^{+2}	0.00	0.00	0.00	0.00	0.00	0.00	0.00	0.00	0.00	0.00	0.00	0.00	0.00	0.00	0.00
Mn^{+3}	0.00	0.00	0.00	0.00	0.00	0.00	0.00	0.00	0.00	0.00	0.00	0.00	0.00	0.00	0.00
Mg	0.00	0.00	0.00	0.00	0.00	0.00	0.00	0.00	0.00	0.00	0.00	0.00	0.00	0.00	0.00
Ca	2.02	1.97	2.01	1.99	1.99	1.96	1.97	1.95	1.95	1.96	2.02	2.03	1.80	2.01	2.03
Na	0.01	0.00	0.00	0.00	0.00	0.00	0.00	0.00	0.00	0.00	0.00	0.00	0.13	0.00	0.00
K	0.00	0.00	0.00	0.00	0.00	0.00	0.00	0.00	0.00	0.00	0.00	0.00	0.00	0.00	0.00

Table 10. Electron microprobe analyses of prehnite (continued).

Sample#	JMH-25																
Point#	6	7	8	9	10	11	12	13	14	15	16	17	18	19	20	21	22
Analysis#	374	375	376	377	378	379	380	381	382	383	384	385	386	387	388	389	390
Wt. % oxides																	
SiO_2	42.94	42.68	42.96	43.63	42.31	43.13	42.00	43.35	43.35	43.27	43.33	43.31	43.38	43.18	43.49	43.38	43.13
TiO_2	0.00	0.00	0.00	0.00	0.00	0.00	0.00	0.00	0.01	0.00	0.00	0.00	0.00	0.00	0.01	0.03	0.00
Al_2O_3	24.22	24.11	24.28	24.35	23.79	24.29	23.34	24.28	24.24	24.19	24.13	24.27	24.29	24.21	23.93	24.16	24.12
Cr_2O_3	0.00	0.00	0.00	0.01	0.00	0.00	0.04	0.02	0.00	0.02	0.00	0.00	0.01	0.02	0.00	0.00	0.00
FeO	0.10	0.11	0.05	0.20	0.12	0.13	0.11	0.13	0.15	0.14	0.13	0.14	0.04	0.08	0.17	0.08	0.09
MnO	0.02	0.03	0.02	0.07	0.06	0.00	0.01	0.01	0.09	0.06	0.00	0.08	0.00	0.00	0.04	0.03	0.04
MgO	0.01	0.01	0.00	0.00	0.04	0.01	0.15	0.00	0.00	0.00	0.00	0.00	0.02	0.00	0.00	0.01	0.00
CaO	27.02	26.65	26.96	26.12	26.46	26.83	26.18	27.19	27.08	27.27	26.90	27.40	27.35	27.38	26.84	27.24	27.12
Na_2O	0.01	0.00	0.00	0.21	0.01	0.01	0.11	0.02	0.00	0.00	0.06	0.00	0.01	0.02	0.13	0.01	0.02
K_2O	0.02	0.03	0.01	0.02	0.04	0.08	0.05	0.02	0.03	0.03	0.04	0.03	0.03	0.02	0.01	0.01	0.01
Total	94.32	93.63	94.29	94.60	92.81	94.47	92.00	95.02	94.96	94.98	94.60	95.22	95.11	94.91	94.64	94.95	94.53
Cations (based on 12 oxygens)																	
Si	2.99	3.00	2.99	3.02	3.00	3.00	3.00	3.00	3.00	3.00	3.01	2.99	3.00	2.99	3.02	3.00	3.00
Ti	0.00	0.00	0.00	0.00	0.00	0.00	0.00	0.00	0.00	0.00	0.00	0.00	0.00	0.00	0.00	0.00	0.00
Al	1.99	1.99	1.99	1.99	1.99	1.99	1.97	1.98	1.98	1.98	1.98	1.98	1.98	1.98	1.96	1.97	1.98
Cr	0.00	0.00	0.00	0.00	0.00	0.00	0.00	0.00	0.00	0.00	0.00	0.00	0.00	0.00	0.00	0.00	0.00
Fe^{+3}	0.01	0.01	0.00	0.01	0.01	0.01	0.01	0.01	0.01	0.01	0.01	0.01	0.00	0.00	0.01	0.00	0.01
Fe^{+2}	0.00	0.00	0.00	0.00	0.00	0.00	0.00	0.00	0.00	0.00	0.00	0.00	0.00	0.00	0.00	0.00	0.00
Mn^{+3}	0.00	0.00	0.00	0.00	0.00	0.00	0.00	0.00	0.01	0.00	0.00	0.00	0.00	0.00	0.00	0.00	0.00
Mg	0.00	0.00	0.00	0.00	0.00	0.00	0.02	0.00	0.00	0.00	0.00	0.00	0.00	0.00	0.00	0.00	0.00
Ca	2.02	2.00	2.01	1.94	2.01	2.00	2.01	2.02	2.01	2.02	2.00	2.03	2.03	2.03	2.00	2.02	2.02
Na	0.00	0.00	0.00	0.03	0.00	0.00	0.02	0.00	0.00	0.00	0.01	0.00	0.00	0.00	0.02	0.00	0.00
K	0.00	0.00	0.00	0.00	0.00	0.01	0.00	0.00	0.00	0.00	0.00	0.00	0.00	0.00	0.00	0.00	0.00

Table 11. Electron microprobe analyses of the pseudomorphs.

Sample#	JMH-26						JMH-24						
Circle#	4	4	4	4	4	1	1	1	1	2	2	2	2
Point#	1	2	3	4	5		1	2	3	1	2	3	4
Analysis#	554	555	556	557	558	566	569	570	571	572	573	574	575
Comment						dark rim							
Wt. % oxides													
SiO_2	38.13	38.16	38.92	38.05	37.33	37.71	39.63	39.88	39.36	40.58	40.40	40.82	39.90
TiO_2	0.06	0.07	0.07	0.11	0.02	0.23	0.13	0.16	0.11	0.04	0.09	0.04	0.05
Al_2O_3	18.05	17.93	17.44	17.55	17.93	16.31	16.01	16.84	16.67	22.30	18.76	22.97	18.95
Cr_2O_3	0.00	0.00	0.00	0.00	0.00	0.00	0.00	0.00	0.00	0.00	0.00	0.00	0.00
FeO	17.24	18.22	18.02	18.16	18.27	19.01	15.41	14.84	15.67	12.12	14.09	11.68	14.31
MnO	0.18	0.18	0.18	0.19	0.18	0.14	0.21	0.23	0.24	0.20	0.19	0.17	0.22
MgO	11.45	11.76	12.25	11.81	11.62	12.90	13.26	12.74	13.12	10.06	11.92	9.31	11.73
CaO	0.02	0.08	0.08	0.11	0.07	0.14	0.11	0.06	0.04	0.04	0.09	0.05	0.06
Na_2O	0.06	0.07	0.07	0.06	0.06	0.02	0.04	0.06	0.06	0.05	0.06	0.10	0.04
K_2O	10.00	9.81	9.38	9.41	9.52	10.36	9.89	10.04	10.02	10.67	10.01	10.56	10.40
F	0.00	0.00	0.00	0.01	0.00	0.03	0.01	0.01	0.01	0.04	0.01	0.00	0.00
Cl	0.01	0.04	0.03	0.04	0.04	0.07	0.09	0.07	0.07	0.05	0.07	0.03	0.07
Total	95.19	96.30	96.43	95.48	95.04	96.92	94.78	94.89	95.34	96.12	95.66	95.71	95.70
— O≡F,Cl	0.00	0.01	0.01	0.01	0.01	0.03	0.03	0.02	0.02	0.03	0.02	0.01	0.02
Total	95.19	96.29	96.43	95.47	95.03	96.89	94.75	94.87	95.32	96.09	95.64	95.71	95.69
Cations (based on 12 oxygens)													
Si	2.82	2.86	2.91	2.83	2.77	2.88	2.89	2.90	2.89	2.93	2.94	2.93	2.92
Ti	0.00	0.00	0.00	0.01	0.00	0.01	0.01	0.01	0.01	0.00	0.00	0.00	0.00
Al	1.57	1.59	1.54	1.54	1.57	1.47	1.38	1.44	1.44	1.90	1.61	1.94	1.63
Cr	0.00	0.00	0.00	0.00	0.00	0.00	0.00	0.00	0.00	0.00	0.00	0.00	0.00
Fe^{+2}	1.07	1.14	1.13	1.13	1.13	1.21	0.94	0.90	0.96	0.73	0.86	0.70	0.87
Mn	0.01	0.01	0.01	0.01	0.01	0.01	0.01	0.01	0.02	0.01	0.01	0.01	0.01
Mg	1.26	1.32	1.37	1.31	1.28	1.47	1.44	1.38	1.44	1.08	1.29	1.00	1.28
Ca	0.00	0.01	0.01	0.01	0.01	0.01	0.01	0.00	0.00	0.00	0.01	0.00	0.00
Na	0.01	0.01	0.01	0.01	0.01	0.00	0.01	0.01	0.01	0.01	0.01	0.01	0.01
K	0.94	0.94	0.90	0.89	0.90	1.01	0.92	0.93	0.94	0.98	0.93	0.97	0.97
F	0.00	0.00	0.00	0.00	0.00	0.01	0.00	0.00	0.00	0.01	0.00	0.00	0.00
Cl	0.00	0.00	0.00	0.01	0.01	0.01	0.01	0.01	0.01	0.01	0.01	0.00	0.01
OH	2.37	1.86	1.78	2.25	2.46	1.59	2.55	2.49	2.29	1.89	2.12	2.05	2.10

Table 11. Electron microprobe analyses of the pseudomorphs (continued).

Sample#	JMH-24									JMH-26			
Circle#	2	6	6	7	7	7	7	7	7	1	1	1	1
Point#	5	1	2	1	2	4	5	6	7	1	2	3	4
Analysis#	576	577	578	582	583	585	586	587	588	514	515	516	517
Comment													
Wt. % oxides													
SiO_2	39.88	39.92	40.33	40.86	40.67	41.55	41.01	41.02	38.95	36.70	36.35	35.31	37.93
TiO_2	0.10	0.04	0.02	0.06	0.07	0.02	0.07	0.06	0.10	0.08	0.06	0.03	0.05
Al_2O_3	17.29	15.27	17.86	20.84	23.24	27.43	23.30	22.44	15.65	18.30	18.50	19.72	18.50
Cr_2O_3	0.00	0.00	0.03	0.00	0.00	0.00	0.00	0.00	0.00	0.02	0.00	0.00	0.00
FeO	14.92	15.59	13.71	12.81	11.85	8.81	11.43	11.89	15.73	18.36	18.42	18.21	17.72
MnO	0.19	0.26	0.17	0.22	0.17	0.15	0.15	0.18	0.23	0.12	0.11	0.16	0.15
MgO	12.17	13.71	11.39	10.40	9.69	8.05	9.14	9.53	13.01	12.11	12.00	12.16	12.20
CaO	0.08	0.24	0.29	0.10	0.10	0.08	0.06	0.06	0.10	0.14	0.06	0.03	0.08
Na_2O	0.06	0.14	0.22	0.10	0.14	0.09	0.07	0.07	0.08	0.12	0.10	0.11	0.34
K_2O	9.87	7.85	7.92	9.85	10.49	10.98	10.64	10.46	9.21	9.77	9.95	9.77	9.84
F	0.02	0.00	0.00	0.00	0.00	0.00	0.00	0.01	0.04	0.00	0.00	0.00	0.02
Cl	0.07	0.06	0.08	0.04	0.04	0.00	0.02	0.03	0.06	0.06	0.03	0.03	0.04
Total	94.63	93.07	92.00	95.27	96.44	97.17	95.89	95.74	93.12	95.75	95.56	95.53	96.85
— O=F,Cl	0.02	0.01	0.02	0.01	0.01	0.00	0.00	0.01	0.03	0.01	0.01	0.01	0.02
Total	94.61	93.05	91.98	95.26	96.43	97.17	95.88	95.73	93.09	95.74	95.56	95.52	96.83
Cations (based on 12 oxygens)													
Si	2.89	2.83	2.79	2.93	2.94	2.97	2.94	2.94	2.79	2.75	2.72	2.64	2.86
Ti	0.01	0.00	0.00	0.00	0.00	0.00	0.00	0.00	0.01	0.00	0.00	0.00	0.00
Al	1.48	1.28	1.46	1.76	1.98	2.31	1.97	1.90	1.32	1.62	1.63	1.74	1.64
Cr	0.00	0.00	0.00	0.00	0.00	0.00	0.00	0.00	0.00	0.00	0.00	0.00	0.00
Fe^{+2}	0.90	0.92	0.79	0.77	0.72	0.53	0.69	0.71	0.94	1.15	1.15	1.14	1.12
Mn	0.01	0.02	0.01	0.01	0.01	0.01	0.01	0.01	0.01	0.01	0.01	0.01	0.01
Mg	1.31	1.45	1.18	1.11	1.04	0.86	0.98	1.02	1.39	1.35	1.34	1.36	1.37
Ca	0.01	0.02	0.02	0.01	0.01	0.01	0.00	0.00	0.01	0.01	0.00	0.00	0.01
Na	0.01	0.02	0.03	0.01	0.02	0.01	0.01	0.01	0.01	0.02	0.01	0.02	0.05
K	0.91	0.71	0.70	0.90	0.97	1.00	0.97	0.96	0.84	0.93	0.95	0.93	0.95
F	0.00	0.00	0.00	0.00	0.00	0.00	0.00	0.00	0.01	0.00	0.00	0.00	0.01
Cl	0.01	0.01	0.01	0.01	0.00	0.00	0.00	0.00	0.01	0.01	0.00	0.00	0.00
OH	2.60	3.29	3.71	2.27	1.72	1.35	1.97	2.04	3.30	2.13	2.22	2.23	1.60

Table 11. Electron microprobe analyses of the pseudomorphs (continued).

Sample#	JMH-26												
Circle#	1	1	1	1	1	1	2	2	2	2	2	2	2
Point#	5	6	7	8	9	10	1	2	3	4	5	6	1
Analysis#	518	519	520	521	522	523	524	525	526	527	528	529	530
Comment							A						B
Wt. % oxides													
SiO_2	37.19	31.42	36.78	40.01	39.52	39.02	37.02	38.30	38.02	38.26	38.02	38.13	38.30
TiO_2	0.01	0.02	0.05	0.02	0.02	0.00	0.08	0.05	0.05	0.06	0.09	0.12	0.05
Al_2O_3	20.08	21.43	18.53	24.11	19.05	19.34	17.77	17.04	17.02	16.78	16.88	16.53	16.05
Cr_2O_3	0.00	0.00	0.00	0.00	0.00	0.03	0.00	0.00	0.01	0.00	0.00	0.00	0.00
FeO	17.14	19.04	16.54	13.04	16.31	15.95	18.72	18.28	18.44	18.10	17.97	17.88	18.07
MnO	0.12	0.20	0.12	0.11	0.13	0.14	0.20	0.20	0.21	0.20	0.18	0.22	0.22
MgO	11.50	15.05	13.79	8.75	11.43	11.05	12.03	12.41	12.26	12.52	12.51	12.34	12.53
CaO	0.06	0.10	0.24	0.13	0.11	0.14	0.07	0.14	0.14	0.15	0.13	0.15	0.18
Na_2O	0.12	0.14	0.14	0.53	0.08	0.10	0.07	0.09	0.10	0.10	0.08	0.13	0.09
K_2O	10.07	5.91	9.97	9.94	9.87	9.91	9.89	9.19	9.32	9.11	9.31	9.20	9.18
F	0.04	0.00	0.03	0.01	0.00	0.02	0.00	0.00	0.01	0.00	0.02	0.00	0.00
Cl	0.03	0.05	0.03	0.02	0.01	0.03	0.06	0.05	0.05	0.06	0.07	0.06	0.06
Total	96.34	93.35	96.19	96.66	96.53	95.72	95.90	95.76	95.60	95.32	95.22	94.74	94.73
¾O*F,Cl	0.02	0.01	0.02	0.01	0.00	0.02	0.01	0.01	0.02	0.01	0.02	0.01	0.01
Total	96.32	93.34	96.17	96.65	96.52	95.71	95.88	95.75	95.58	95.31	95.20	94.73	94.71
Cations (based on 12 oxygens)													
Si	2.78	2.28	2.75	2.91	2.93	2.87	2.78	2.85	2.83	2.83	2.81	2.81	2.82
Ti	0.00	0.00	0.00	0.00	0.00	0.00	0.00	0.00	0.00	0.00	0.00	0.01	0.00
Al	1.77	1.83	1.63	2.07	1.67	1.68	1.58	1.50	1.49	1.47	1.47	1.43	1.39
Cr	0.00	0.00	0.00	0.00	0.00	0.00	0.00	0.00	0.00	0.00	0.00	0.00	0.00
Fe^{+2}	1.07	1.15	1.03	0.79	1.01	0.98	1.18	1.14	1.15	1.12	1.11	1.10	1.11
Mn	0.01	0.01	0.01	0.01	0.01	0.01	0.01	0.01	0.01	0.01	0.01	0.01	0.01
Mg	1.28	1.63	1.54	0.95	1.26	1.21	1.35	1.38	1.36	1.38	1.38	1.35	1.38
Ca	0.00	0.01	0.02	0.01	0.01	0.01	0.01	0.01	0.01	0.01	0.01	0.01	0.01
Na	0.02	0.02	0.02	0.07	0.01	0.01	0.01	0.01	0.01	0.01	0.01	0.02	0.01
K	0.96	0.55	0.95	0.92	0.93	0.93	0.95	0.87	0.89	0.86	0.88	0.86	0.86
F	0.01	0.00	0.01	0.00	0.00	0.01	0.00	0.00	0.00	0.00	0.00	0.00	0.00
Cl	0.00	0.01	0.00	0.00	0.00	0.00	0.01	0.01	0.01	0.01	0.01	0.01	0.01
OH	1.84	3.22	1.91	1.62	1.72	2.11	2.06	2.11	2.20	2.32	2.37	2.59	2.60

Table 11. Electron microprobe analyses of the pseudomorphs (continued).

Sample#	JMH-26												
Circle#	2	2	2	2	2	2	2	2	2	2	2	2	2
Point#	2	3	4	5	1	2	4	5	1	2	3	4	5
Analysis#	531	532	533	534	535	536	538	539	540	541	542	543	544
Comment					C				D				
Wt. % oxides													
SiO_2	38.00	37.35	44.69	38.33	37.99	36.77	37.87	37.98	37.91	38.35	38.01	38.10	38.14
TiO_2	0.08	0.07	0.02	0.07	0.04	0.06	0.08	0.08	0.03	0.04	0.08	0.06	0.04
Al_2O_3	16.01	18.24	34.24	17.56	16.95	18.30	17.19	16.93	17.14	17.24	17.11	17.28	16.96
Cr_2O_3	0.00	0.01	0.00	0.00	0.01	0.00	0.00	0.00	0.00	0.00	0.01	0.00	0.00
FeO	17.95	18.39	3.68	18.38	18.40	18.92	18.21	18.13	18.06	18.12	18.43	18.32	18.37
MnO	0.20	0.22	0.01	0.19	0.18	0.18	0.18	0.18	0.20	0.16	0.17	0.18	0.23
MgO	12.55	11.91	1.17	11.62	12.36	11.52	12.14	12.26	12.31	12.31	12.27	12.60	12.38
CaO	0.10	0.09	0.05	0.11	0.13	0.13	0.16	0.16	0.23	0.14	0.17	0.14	0.10
Na_2O	0.08	0.09	0.81	0.55	0.08	0.21	0.10	0.08	0.08	0.08	0.09	0.06	0.07
K_2O	9.42	9.58	10.81	9.18	9.25	9.59	9.45	9.25	9.17	9.27	9.33	9.37	9.38
F	0.00	0.00	0.01	0.00	0.01	0.00	0.00	0.01	0.01	0.00	0.02	0.00	0.00
Cl	0.06	0.03	0.01	0.09	0.05	0.06	0.05	0.06	0.06	0.04	0.05	0.06	0.05
Total	94.42	95.97	95.49	96.07	95.43	95.74	95.43	95.08	95.18	95.75	95.72	96.15	95.71
½O*F,Cl	0.01	0.01	0.01	0.02	0.02	0.01	0.01	0.02	0.02	0.01	0.02	0.01	0.01
Total	94.40	95.96	95.49	96.04	95.42	95.72	95.42	95.07	95.16	95.74	95.70	96.14	95.70
Cations (based on 12 oxygens)													
Si	2.79	2.80	3.02	2.87	2.82	2.76	2.82	2.81	2.80	2.85	2.84	2.85	2.84
Ti	0.00	0.00	0.00	0.00	0.00	0.00	0.00	0.00	0.00	0.00	0.00	0.00	0.00
Al	1.39	1.61	2.73	1.55	1.49	1.62	1.51	1.48	1.50	1.51	1.50	1.53	1.49
Cr	0.00	0.00	0.00	0.00	0.00	0.00	0.00	0.00	0.00	0.00	0.00	0.00	0.00
Fe^{+2}	1.10	1.15	0.21	1.15	1.14	1.19	1.13	1.12	1.12	1.13	1.15	1.15	1.15
Mn	0.01	0.01	0.00	0.01	0.01	0.01	0.01	0.01	0.01	0.01	0.01	0.01	0.01
Mg	1.38	1.33	0.12	1.30	1.37	1.29	1.34	1.35	1.36	1.37	1.36	1.41	1.38
Ca	0.01	0.01	0.00	0.01	0.01	0.01	0.01	0.01	0.02	0.01	0.01	0.01	0.01
Na	0.01	0.01	0.11	0.08	0.01	0.03	0.01	0.01	0.01	0.01	0.01	0.01	0.01
K	0.88	0.92	0.93	0.88	0.88	0.92	0.90	0.87	0.87	0.88	0.89	0.90	0.89
F	0.00	0.00	0.00	0.00	0.00	0.00	0.00	0.00	0.00	0.00	0.00	0.00	0.00
Cl	0.01	0.00	0.00	0.01	0.01	0.01	0.01	0.01	0.01	0.01	0.01	0.01	0.01
OH	2.75	2.02	2.03	1.97	2.27	2.14	2.27	2.43	2.39	2.11	2.14	1.93	2.14

Table 11. Electron microprobe analyses of the pseudomorphs (continued).

Sample#	H1281-61.5												
Circle#	1	1	1	1	1	3	3	3	3	3	3	3	3
Point#	1	2	3	4	5	1	2	3	4	5	6	7	8
Analysis#	589	590	591	592	593	601	602	603	604	605	606	607	608
Comment													
Wt. % oxides													
SiO_2	39.69	41.48	39.53	39.78	40.57	44.12	40.75	45.99	47.07	44.72	44.47	43.11	43.97
TiO_2	0.05	0.03	0.08	0.12	0.09	0.02	0.02	0.01	0.02	0.00	0.00	0.05	0.02
Al_2O_3	16.89	21.73	17.66	15.80	16.65	27.81	22.33	29.99	33.92	29.76	28.70	25.72	28.72
Cr_2O_3	0.00	0.00	0.00	0.01	0.00	0.01	0.00	0.02	0.00	0.00	0.02	0.00	0.00
FeO	14.96	11.37	14.96	15.06	14.17	6.92	11.42	4.86	2.59	5.40	6.16	9.07	6.44
MnO	0.14	0.12	0.16	0.15	0.15	0.11	0.12	0.08	0.03	0.05	0.08	0.13	0.04
MgO	14.59	10.61	13.72	14.79	14.36	6.26	10.73	4.50	1.51	4.95	5.70	7.75	5.70
CaO	0.02	0.04	0.03	0.03	0.03	0.05	0.03	0.05	0.01	0.08	0.08	0.06	0.05
Na_2O	0.10	0.11	0.10	0.20	0.15	0.18	0.17	0.17	1.24	0.19	0.29	0.24	0.17
K_2O	10.39	10.69	10.51	10.27	10.35	11.06	10.11	11.07	10.03	11.07	10.86	10.53	11.20
F	0.02	0.04	0.04	0.06	0.04	0.03	0.00	0.00	0.00	0.00	0.01	0.00	0.00
Cl	0.07	0.05	0.05	0.15	0.06	0.03	0.04	0.04	0.02	0.04	0.05	0.05	0.03
Total	96.89	96.24	96.81	96.35	96.58	96.56	95.71	96.76	96.44	96.25	96.40	96.69	96.33
⅛O*F,Cl	0.02	0.03	0.03	0.06	0.03	0.02	0.01	0.01	0.01	0.01	0.01	0.01	0.01
Total	96.86	96.21	96.78	96.29	96.55	96.54	95.70	96.75	96.43	96.24	96.38	96.68	96.32
Cations (based on 12 oxygens)													
Si	2.96	2.99	2.94	2.95	3.00	3.09	2.92	3.17	3.17	3.09	3.09	3.06	3.06
Ti	0.00	0.00	0.00	0.01	0.01	0.00	0.00	0.00	0.00	0.00	0.00	0.00	0.00
Al	1.48	1.85	1.55	1.38	1.45	2.29	1.88	2.44	2.69	2.42	2.35	2.15	2.36
Cr	0.00	0.00	0.00	0.00	0.00	0.00	0.00	0.00	0.00	0.00	0.00	0.00	0.00
Fe^{+2}	0.93	0.69	0.93	0.93	0.88	0.40	0.68	0.28	0.15	0.31	0.36	0.54	0.37
Mn	0.01	0.01	0.01	0.01	0.01	0.01	0.01	0.00	0.00	0.00	0.00	0.01	0.00
Mg	1.62	1.14	1.52	1.63	1.58	0.65	1.14	0.46	0.15	0.51	0.59	0.82	0.59
Ca	0.00	0.00	0.00	0.00	0.00	0.00	0.00	0.00	0.00	0.01	0.01	0.00	0.00
Na	0.01	0.02	0.01	0.03	0.02	0.02	0.02	0.02	0.16	0.02	0.04	0.03	0.02
K	0.99	0.98	1.00	0.97	0.98	0.99	0.92	0.97	0.86	0.97	0.96	0.95	1.00
F	0.00	0.01	0.01	0.01	0.01	0.01	0.00	0.00	0.00	0.00	0.00	0.00	0.00
Cl	0.01	0.01	0.01	0.02	0.01	0.00	0.00	0.00	0.00	0.00	0.01	0.01	0.00
OH	1.56	1.82	1.60	1.83	1.70	1.61	2.05	1.49	1.60	1.73	1.67	1.57	1.71

Table 11. Electron microprobe analyses of the pseudomorphs (continued).

Sample#	H1281-61.5												H1281-61.7
Circle#	3	3	6	6	6	6	6	6	6	6	6	6	1
Point#	9	10	1	2	3	4	5	1	2	3	4	5	1
Analysis#	609	610	621	622	623	624	625	626	627	628	629	630	636
Comment			A					B					
Wt. % oxides													
SiO_2	44.57	43.95	42.17	42.83	43.93	44.52	45.08	44.53	44.02	43.15	44.03	44.32	42.07
TiO_2	0.03	0.00	0.06	0.07	0.02	0.04	0.00	0.00	0.00	0.06	0.01	0.02	0.02
Al_2O_3	29.29	29.07	25.83	24.52	28.48	28.88	29.78	28.65	28.61	25.84	28.58	28.46	28.14
Cr_2O_3	0.00	0.00	0.00	0.02	0.00	0.00	0.00	0.00	0.00	0.00	0.02	0.01	0.00
FeO	5.90	6.66	9.56	9.37	6.10	5.69	5.48	5.82	5.95	8.27	6.14	6.11	7.46
MnO	0.08	0.07	0.11	0.12	0.07	0.04	0.05	0.12	0.08	0.11	0.07	0.08	0.13
MgO	5.45	5.76	8.26	8.70	5.53	5.67	5.20	5.71	5.76	7.64	5.83	6.13	6.63
CaO	0.05	0.05	0.10	0.05	0.07	0.04	0.03	0.02	0.05	0.04	0.06	0.04	0.06
Na_2O	0.20	0.19	0.41	0.20	0.16	0.25	0.14	0.14	0.12	0.08	0.14	0.21	0.17
K_2O	11.25	11.25	10.37	10.83	11.06	11.12	11.35	11.52	11.55	11.18	11.62	11.16	11.02
F	0.00	0.01	0.00	0.00	0.01	0.02	0.03	0.02	0.00	0.00	0.01	0.01	0.00
Cl	0.02	0.03	0.04	0.08	0.05	0.03	0.03	0.02	0.02	0.03	0.03	0.03	0.04
Total	96.84	97.02	96.89	96.76	95.45	96.29	97.15	96.54	96.14	96.39	96.53	96.56	95.72
⅓O"F,Cl	0.01	0.01	0.01	0.02	0.02	0.02	0.02	0.01	0.01	0.01	0.01	0.01	0.01
Total	96.83	97.01	96.89	96.74	95.44	96.28	97.13	96.52	96.14	96.38	96.52	96.55	95.71
Cations (based on 12 oxygens)													
Si	3.11	3.09	3.01	3.06	3.03	3.08	3.14	3.10	3.06	3.05	3.08	3.09	2.94
Ti	0.00	0.00	0.00	0.00	0.00	0.00	0.00	0.00	0.00	0.00	0.00	0.00	0.00
Al	2.41	2.41	2.17	2.06	2.31	2.36	2.45	2.35	2.34	2.15	2.35	2.34	2.32
Cr	0.00	0.00	0.00	0.00	0.00	0.00	0.00	0.00	0.00	0.00	0.00	0.00	0.00
Fe^{+2}	0.34	0.39	0.57	0.56	0.35	0.33	0.32	0.34	0.35	0.49	0.36	0.36	0.44
Mn	0.00	0.00	0.01	0.01	0.00	0.00	0.00	0.01	0.00	0.01	0.00	0.00	0.01
Mg	0.57	0.60	0.88	0.93	0.57	0.59	0.54	0.59	0.60	0.80	0.61	0.64	0.69
Ca	0.00	0.00	0.01	0.00	0.01	0.00	0.00	0.00	0.00	0.00	0.00	0.00	0.00
Na	0.03	0.03	0.06	0.03	0.02	0.03	0.02	0.02	0.02	0.01	0.02	0.03	0.02
K	1.00	1.01	0.94	0.99	0.97	0.98	1.01	1.02	1.02	1.01	1.04	0.99	0.98
F	0.00	0.00	0.00	0.00	0.00	0.01	0.01	0.00	0.00	0.00	0.00	0.00	0.00
Cl	0.00	0.00	0.00	0.01	0.01	0.00	0.00	0.00	0.00	0.00	0.00	0.00	0.00
OH	1.47	1.40	1.48	1.55	2.10	1.72	1.33	1.61	1.79	1.71	1.62	1.60	2.00

Table 11. Electron microprobe analyses of the pseudomorphs (continued).

Sample#	H1281-61.7													
Circle#	1	1	1	1	2	2	2	2	2	2	2	2	2	2
Point#	2	3	4	5	1	2	3	4	5	6	7	8	9	10
Analysis#	637	638	639	640	641	642	643	644	645	646	647	648	649	650
Comment														
Wt. % oxides														
SiO_2	43.11	42.90	43.38	42.44	41.39	42.68	43.24	43.65	43.66	43.46	43.86	43.45	43.58	43.19
TiO_2	0.02	0.03	0.02	0.00	0.03	0.01	0.00	0.05	0.00	0.02	0.00	0.05	0.00	0.01
Al_2O_3	28.48	27.33	28.84	28.82	24.69	26.05	26.52	28.25	28.17	28.87	29.64	28.61	28.69	27.23
Cr_2O_3	0.00	0.01	0.01	0.03	0.00	0.01	0.00	0.00	0.00	0.00	0.00	0.02	0.00	0.01
FeO	7.33	8.10	6.80	6.77	9.47	8.25	8.35	6.86	6.85	6.05	5.46	6.38	6.15	7.51
MnO	0.15	0.16	0.10	0.10	0.18	0.19	0.17	0.14	0.11	0.09	0.13	0.11	0.09	0.14
MgO	6.42	7.28	6.22	6.62	8.17	7.28	7.36	6.25	6.32	5.82	5.69	5.82	5.53	6.76
CaO	0.07	0.08	0.05	0.06	0.96	0.06	0.05	0.06	0.02	0.03	0.05	0.05	0.07	0.04
Na_2O	0.19	0.16	0.24	0.23	0.20	0.10	0.15	0.18	0.18	0.18	0.20	0.16	0.17	0.14
K_2O	11.01	10.85	11.07	10.89	10.56	11.04	10.85	11.13	11.22	11.38	11.32	11.17	11.49	11.12
F	0.02	0.00	0.00	0.00	0.00	0.00	0.00	0.00	0.02	0.00	0.00	0.00	0.01	0.00
Cl	0.05	0.04	0.02	0.04	0.04	0.04	0.04	0.03	0.02	0.03	0.03	0.02	0.04	0.02
Total	96.82	96.94	96.73	95.99	95.68	95.69	96.72	96.58	96.55	95.93	96.37	95.83	95.81	96.17
½O*F,Cl	0.02	0.01	0.00	0.01	0.01	0.01	0.01	0.01	0.01	0.01	0.01	0.01	0.01	0.01
Total	96.80	96.93	96.72	95.98	95.67	95.68	96.71	96.57	96.54	95.92	96.37	95.82	95.80	96.16
Cations (based on 12 oxygens)														
Si	3.04	3.04	3.04	2.96	2.94	3.00	3.06	3.06	3.06	3.02	3.04	3.01	3.02	3.03
Ti	0.00	0.00	0.00	0.00	0.00	0.00	0.00	0.00	0.00	0.00	0.00	0.00	0.00	0.00
Al	2.36	2.28	2.38	2.37	2.06	2.16	2.21	2.33	2.33	2.36	2.43	2.34	2.35	2.25
Cr	0.00	0.00	0.00	0.00	0.00	0.00	0.00	0.00	0.00	0.00	0.00	0.00	0.00	0.00
Fe^{+2}	0.43	0.48	0.40	0.39	0.56	0.48	0.49	0.40	0.40	0.35	0.32	0.37	0.36	0.44
Mn	0.01	0.01	0.01	0.01	0.01	0.01	0.01	0.01	0.01	0.01	0.01	0.01	0.01	0.01
Mg	0.67	0.77	0.65	0.69	0.86	0.76	0.78	0.65	0.66	0.60	0.59	0.60	0.57	0.71
Ca	0.01	0.01	0.00	0.00	0.07	0.00	0.00	0.00	0.00	0.00	0.00	0.00	0.01	0.00
Na	0.03	0.02	0.03	0.03	0.03	0.01	0.02	0.02	0.02	0.02	0.03	0.02	0.02	0.02
K	0.99	0.98	0.99	0.97	0.96	0.99	0.98	1.00	1.00	1.01	1.00	0.99	1.02	1.00
F	0.00	0.00	0.00	0.00	0.00	0.00	0.00	0.00	0.00	0.00	0.00	0.00	0.00	0.00
Cl	0.01	0.01	0.00	0.00	0.01	0.00	0.00	0.00	0.00	0.00	0.00	0.00	0.00	0.00
OH	1.50	1.45	1.53	1.87	2.05	2.02	1.55	1.60	1.62	1.89	1.68	1.93	1.94	1.80

Table 11. Electron microprobe analyses of the pseudomorphs (continued).

Sample#	H1281-61.7														
Circle#	3	3	3	3	3	3	3	3	3	3	4	4	4	4	4
Point#	1	2	3	4	5	6	7	8	9	10	1	2	3	4	5
Analysis#	657	658	659	660	661	662	663	664	665	666	667	668	669	670	671
Comment															
Wt. % oxides															
SiO_2	43.35	42.05	42.33	42.57	41.98	42.75	42.13	43.04	42.59	43.42	42.48	44.15	42.16	42.63	42.39
TiO_2	0.01	0.03	0.00	0.02	0.00	0.00	0.01	0.01	0.02	0.00	0.00	0.00	0.00	0.01	0.00
Al_2O_3	28.05	29.05	28.63	28.27	28.18	27.65	26.56	28.94	27.50	28.58	28.50	28.81	27.83	28.41	28.79
Cr_2O_3	0.00	0.00	0.00	0.00	0.00	0.00	0.00	0.01	0.01	0.00	0.00	0.00	0.01	0.00	0.00
FeO	6.77	5.86	6.91	7.30	7.58	7.77	8.52	6.34	7.96	6.31	7.05	6.22	7.75	6.73	5.79
MnO	0.15	0.08	0.14	0.15	0.17	0.10	0.19	0.12	0.17	0.15	0.13	0.11	0.14	0.10	0.11
MgO	6.15	6.50	6.48	6.47	6.79	6.74	7.30	6.05	6.74	5.68	6.04	5.62	6.31	6.31	6.63
CaO	0.04	0.04	0.08	0.09	0.04	0.07	0.07	0.05	0.05	0.06	0.12	0.11	0.11	0.08	0.04
Na_2O	0.10	0.17	0.42	0.45	0.13	0.19	0.21	0.22	0.15	0.17	0.23	0.19	0.23	0.40	0.19
K_2O	11.17	11.31	10.62	10.41	11.29	10.84	10.80	11.24	11.03	11.31	10.95	10.98	10.74	10.87	11.32
F	0.00	0.02	0.01	0.00	0.00	0.00	0.00	0.00	0.02	0.00	0.00	0.00	0.01	0.00	0.01
Cl	0.02	0.02	0.03	0.02	0.02	0.02	0.05	0.02	0.02	0.03	0.03	0.04	0.02	0.03	0.00
Total	95.81	95.12	95.63	95.73	96.17	96.14	95.81	96.03	96.25	95.69	95.52	96.21	95.30	95.54	95.25
¼O"F,Cl	0.00	0.01	0.01	0.00	0.00	0.00	0.01	0.01	0.01	0.01	0.01	0.01	0.01	0.01	0.01
Total	95.80	95.10	95.62	95.73	96.17	96.13	95.80	96.03	96.24	95.68	95.52	96.20	95.29	95.53	95.24
Cations (based on 12 oxygens)															
Si	3.01	2.90	2.94	2.96	2.95	3.00	2.96	3.00	3.00	3.01	2.95	3.06	2.93	2.96	2.93
Ti	0.00	0.00	0.00	0.00	0.00	0.00	0.00	0.00	0.00	0.00	0.00	0.00	0.00	0.00	0.00
Al	2.30	2.36	2.34	2.32	2.34	2.29	2.20	2.37	2.28	2.34	2.33	2.36	2.28	2.32	2.34
Cr	0.00	0.00	0.00	0.00	0.00	0.00	0.00	0.00	0.00	0.00	0.00	0.00	0.00	0.00	0.00
Fe^{+2}	0.39	0.34	0.40	0.42	0.45	0.46	0.50	0.37	0.47	0.37	0.41	0.36	0.45	0.39	0.33
Mn	0.01	0.00	0.01	0.01	0.01	0.01	0.01	0.01	0.01	0 01	0.01	0.01	0.01	0.01	0.01
Mg	0.64	0.67	0.67	0.67	0.71	0.70	0.76	0.63	0.71	0.59	0.63	0.58	0.65	0.65	0.68
Ca	0.00	0.00	0.01	0.01	0.00	0.01	0.01	0.00	0.00	0.00	0.01	0.01	0.01	0.01	0.00
Na	0.01	0.02	0.06	0.06	0.02	0.03	0.03	0.03	0.02	0.02	0.03	0.03	0.03	0.05	0.03
K	0.99	1.00	0.94	0.92	1.01	0.97	0.97	1.00	0.99	1.00	0.97	0.97	0.95	0.96	1.00
F	0.00	0.00	0.00	0.00	0.00	0.00	0.00	0.00	0.00	0.00	0.00	0.00	0.00	0.00	0.00
Cl	0.00	0.00	0.00	0.00	0.00	0.00	0.01	0.00	0.00	0.00	0.00	0.00	0.00	0.00	0.00
OH	1.95	2.25	2.03	1.98	1.80	1.81	1.97	1.84	1.77	2.00	2.08	1.76	2.19	2.07	2.19

Table 12. Electron microprobe analyses of pyroxene.

Sample#	UG-2														
Circle#	1	1	1	1	1	1	3	3	3	3	3	3	3	3	3
Point#															
Analysis#	5	6	7	8	9	10	21	22	23	24	25	26	27	28	29
Comment	Fine	Fine	Fine	Fine	Fine	Fine	Fine	Fine	Fine	Fine	Fine	Fine	Fine	Fine	Fine
Wt. % oxides															
SiO_2	52.89	52.51	52.65	52.30	52.33	52.29	51.99	52.52	51.97	52.37	52.31	52.39	52.33	52.43	52.60
Al_2O_3	0.40	0.55	0.70	0.42	0.73	0.51	0.40	0.46	0.20	0.32	0.45	0.42	0.62	0.36	0.60
TiO_2	0.00	0.02	0.00	0.00	0.02	0.03	0.02	0.03	0.00	0.00	0.00	0.00	0.00	0.02	0.00
Cr_2O_3	0.00	0.00	0.00	0.03	0.00	0.03	0.04	0.00	0.00	0.04	0.01	0.07	0.00	0.00	0.00
FeO	8.19	9.08	8.88	9.09	9.81	8.94	8.51	8.40	9.28	9.89	9.12	9.89	9.24	9.22	7.36
Fe_2O_3	1.11	0.75	1.20	1.22	1.60	1.13	1.55	1.26	1.89	1.37	1.63	1.23	1.47	1.65	1.74
MnO	0.19	0.24	0.24	0.29	0.26	0.28	0.32	0.40	0.41	0.42	0.34	0.38	0.26	0.36	0.26
MgO	12.85	12.18	12.06	11.90	11.21	11.89	11.92	12.25	11.30	11.23	11.50	11.25	11.50	11.54	12.56
CaO	24.21	23.92	24.01	24.20	24.07	24.17	24.13	24.16	24.57	24.60	24.36	24.08	24.24	24.43	24.49
K_2O	0.02	0.02	0.02	0.03	0.01	0.01	0.03	0.01	0.03	0.02	0.04	0.03	0.04	0.03	0.04
Na_2O	0.19	0.23	0.33	0.18	0.36	0.25	0.24	0.26	0.16	0.15	0.27	0.30	0.30	0.26	0.30
Cl															
Total	100.04	99.49	100.08	99.67	100.41	99.53	99.15	99.75	99.81	100.43	100.02	100.04	100.00	100.28	99.94
Cation (based on 6 oxygens and 4 cations using the method of Droop, 1987)															
Si	1.98	1.99	1.98	1.98	1.97	1.98	1.98	1.98	1.98	1.98	1.98	1.98	1.98	1.98	1.97
Al	0.02	0.02	0.03	0.02	0.03	0.02	0.02	0.02	0.01	0.01	0.02	0.02	0.03	0.02	0.03
Ti	0.00	0.00	0.00	0.00	0.00	0.00	0.00	0.00	0.00	0.00	0.00	0.00	0.00	0.00	0.00
Cr	0.00	0.00	0.00	0.00	0.00	0.00	0.00	0.00	0.00	0.00	0.00	0.00	0.00	0.00	0.00
Fe^{2+}	0.26	0.29	0.28	0.29	0.31	0.28	0.27	0.27	0.30	0.31	0.29	0.31	0.29	0.29	0.23
Fe^{3+}	0.03	0.02	0.03	0.03	0.05	0.03	0.04	0.04	0.05	0.04	0.05	0.04	0.04	0.05	0.05
Mn	0.01	0.01	0.01	0.01	0.01	0.01	0.01	0.01	0.01	0.01	0.01	0.01	0.01	0.01	0.01
Mg	0.72	0.69	0.68	0.67	0.63	0.67	0.68	0.69	0.64	0.63	0.65	0.63	0.65	0.65	0.70
Ca	0.97	0.97	0.97	0.98	0.97	0.98	0.98	0.98	1.00	1.00	0.99	0.98	0.98	0.99	0.98
K	0.00	0.00	0.00	0.00	0.00	0.00	0.00	0.00	0.00	0.00	0.00	0.00	0.00	0.00	0.00
Na	0.01	0.02	0.02	0.01	0.03	0.02	0.02	0.02	0.01	0.01	0.02	0.02	0.02	0.02	0.02
Cl	0.00	0.00	0.00	0.00	0.00	0.00	0.00	0.00	0.00	0.00	0.00	0.00	0.00	0.00	0.00
Total	4.00	4.00	4.00	4.00	4.00	4.00	4.00	4.00	4.00	4.00	4.00	4.00	4.00	4.00	4.00

lt core = light core; dk rim = darker rim; xl = crystal; transv = transverse; transit = transition

Table 12. Electron microprobe analyses of pyroxene (continued).

Sample#	UG-2	JMH-306i													
Circle#	3	1	1	1	1	1	1	1	1	1	1	1	1	1	1
Point#															
Analysis#	30	38	39	40	41	42	43	44	45	46	47	48	49	50	51
Comment	Fine														
Wt. % oxides															
SiO_2	52.31	49.31	49.77	51.26	48.37	50.96	51.39	50.58	50.35	50.53	50.81	50.81	50.58	50.71	50.94
Al_2O_3	0.64	0.86	0.64	0.69	1.00	0.59	0.20	0.51	0.79	0.60	0.46	1.06	0.03	0.62	0.42
TiO_2	0.03	3.59	2.26	0.08	4.77	0.36	0.00	0.97	1.17	0.22	0.64	0.69	0.00	1.34	0.04
Cr_2O_3	0.00	0.00	0.00	0.04	0.03	0.00	0.00	0.00	0.02	0.01	0.00	0.00	0.00	0.00	0.00
FeO	8.83	11.62	12.37	11.48	11.21	10.23	11.35	11.50	12.08	10.66	9.62	10.80	13.12	11.74	11.86
Fe_2O_3	1.55	0.00	0.00	1.54	0.00	2.10	1.53	0.90	0.36	2.73	1.86	1.71	1.44	0.52	1.49
MnO	0.29	2.04	2.44	2.44	2.08	2.57	2.43	2.98	2.13	2.47	2.43	2.06	4.97	2.15	2.52
MgO	11.70	7.67	7.85	8.47	7.64	9.24	8.96	8.38	8.24	9.07	9.96	8.79	6.37	8.63	8.36
CaO	24.20	24.14	23.98	23.95	24.19	23.68	24.14	23.96	23.80	23.32	23.81	23.76	24.06	24.44	23.71
K_2O	0.03	0.02	0.03	0.01	0.03	0.04	0.03	0.03	0.02	0.02	0.03	0.04	0.03	0.05	0.03
Na_2O	0.33	0.35	0.27	0.35	0.30	0.33	0.14	0.25	0.38	0.30	0.19	0.49	0.01	0.23	0.25
Cl															
Total	99.89	99.59	99.59	100.29	99.63	100.09	100.16	100.04	99.33	99.90	99.83	100.20	100.62	100.43	99.63
Cation (based on 6 oxygens and 4 cations using the method of Droop, 1987)															
Si	1.98	1.91	1.94	1.97	1.88	1.96	1.98	1.96	1.96	1.95	1.95	1.95	1.98	1.95	1.98
Al	0.03	0.04	0.03	0.03	0.05	0.03	0.01	0.02	0.04	0.03	0.02	0.05	0.00	0.03	0.02
Ti	0.00	0.10	0.07	0.00	0.14	0.01	0.00	0.03	0.03	0.01	0.02	0.02	0.00	0.04	0.00
Cr	0.00	0.00	0.00	0.00	0.00	0.00	0.00	0.00	0.00	0.00	0.00	0.00	0.00	0.00	0.00
Fe^{2+}	0.28	0.38	0.40	0.37	0.36	0.33	0.37	0.37	0.39	0.34	0.31	0.35	0.43	0.38	0.39
Fe^{3+}	0.04	0.00	0.00	0.04	0.00	0.06	0.04	0.03	0.01	0.08	0.05	0.05	0.04	0.02	0.04
Mn	0.01	0.07	0.08	0.08	0.07	0.08	0.08	0.10	0.07	0.08	0.08	0.07	0.16	0.07	0.08
Mg	0.66	0.44	0.46	0.49	0.44	0.53	0.51	0.48	0.48	0.52	0.57	0.50	0.37	0.49	0.48
Ca	0.98	1.00	1.00	0.99	1.01	0.98	1.00	0.99	0.99	0.97	0.98	0.98	1.01	1.01	0.99
K	0.00	0.00	0.00	0.00	0.00	0.00	0.00	0.00	0.00	0.00	0.00	0.00	0.00	0.00	0.00
Na	0.02	0.03	0.02	0.03	0.02	0.02	0.01	0.02	0.03	0.02	0.01	0.04	0.00	0.02	0.02
Cl	0.00	0.00	0.00	0.00	0.00	0.00	0.00	0.00	0.00	0.00	0.00	0.00	0.00	0.00	0.00
Total	4.00	3.98	3.99	4.00	3.97	4.00	4.00	4.00	4.00	4.00	4.00	4.00	4.00	4.00	4.00

lt core = light core; dk rim = darker rim; xl = crystal; transv = transverse; transit = transition

Table 12. Electron microprobe analyses of pyroxene (continued).

Sample#	JMH-306i														
Circle#	1	3	3	3	3	3	3	3	3	5	5	5	5	5	5
Point#															
Analysis#	52	53	54	55	56	57	58	59	60	63	64	65	66	67	68
Comment															
Wt. % oxides															
SiO_2	50.82	51.02	51.46	51.11	50.94	50.89	51.05	50.32	51.27	50.91	51.10	51.02	51.33	51.09	50.32
Al_2O_3	0.60	0.16	0.14	0.13	0.09	0.08	0.18	0.02	0.16	0.08	0.89	0.60	0.15	0.12	0.02
TiO_2	0.15	0.00	0.00	0.02	0.00	0.00	0.00	0.00	0.00	0.00	0.38	0.22	0.00	0.00	0.00
Cr_2O_3	0.01	0.00	0.00	0.00	0.00	0.00	0.00	0.00	0.00	0.00	0.00	0.00	0.00	0.00	0.00
FeO	12.14	11.87	12.14	11.90	12.83	12.55	11.98	12.88	12.11	13.04	9.56	10.34	10.81	12.65	12.06
Fe_2O_3	1.18	1.70	0.58	1.45	1.18	1.54	1.01	1.20	1.04	1.48	2.06	2.06	1.53	1.13	1.44
MnO	2.47	3.48	3.56	3.57	4.02	4.40	3.85	5.92	3.16	4.39	1.90	2.33	3.71	3.59	6.39
MgO	8.16	8.01	8.24	7.97	7.29	7.00	7.85	5.86	8.09	6.71	9.99	9.25	8.52	7.73	6.14
CaO	23.64	24.11	24.07	24.21	23.99	24.24	23.96	23.96	24.23	24.26	23.75	23.86	24.38	23.97	23.88
K_2O	0.03	0.02	0.04	0.03	0.01	0.02	0.03	0.01	0.02	0.01	0.03	0.02	0.02	0.02	0.02
Na_2O	0.29	0.08	0.03	0.06	0.05	0.06	0.09	0.03	0.11	0.07	0.36	0.30	0.07	0.05	0.01
Cl															
Total	99.49	100.44	100.25	100.46	100.41	100.78	99.99	100.21	100.18	100.95	100.01	100.01	100.53	100.36	100.26
Cation (based on 6 oxygens and 4 cations using the method of Droop, 1987)															
Si	1.98	1.98	1.99	1.98	1.98	1.98	1.98	1.98	1.99	1.98	1.95	1.96	1.98	1.98	1.98
Al	0.03	0.01	0.01	0.01	0.00	0.00	0.01	0.00	0.01	0.00	0.04	0.03	0.01	0.01	0.00
Ti	0.00	0.00	0.00	0.00	0.00	0.00	0.00	0.00	0.00	0.00	0.01	0.01	0.00	0.00	0.00
Cr	0.00	0.00	0.00	0.00	0.00	0.00	0.00	0.00	0.00	0.00	0.00	0.00	0.00	0.00	0.00
Fe^{2+}	0.39	0.38	0.39	0.39	0.42	0.41	0.39	0.42	0.39	0.42	0.31	0.33	0.35	0.41	0.40
Fe^{3+}	0.03	0.05	0.02	0.04	0.03	0.05	0.03	0.04	0.03	0.04	0.06	0.06	0.04	0.03	0.04
Mn	0.08	0.11	0.12	0.12	0.13	0.14	0.13	0.20	0.10	0.14	0.06	0.08	0.12	0.12	0.21
Mg	0.47	0.46	0.48	0.46	0.42	0.41	0.46	0.34	0.47	0.39	0.57	0.53	0.49	0.45	0.36
Ca	0.99	1.00	1.00	1.00	1.00	1.01	1.00	1.01	1.01	1.01	0.97	0.98	1.01	1.00	1.01
K	0.00	0.00	0.00	0.00	0.00	0.00	0.00	0.00	0.00	0.00	0.00	0.00	0.00	0.00	0.00
Na	0.02	0.01	0.00	0.00	0.00	0.00	0.01	0.00	0.01	0.01	0.03	0.02	0.01	0.00	0.00
Cl	0.00	0.00	0.00	0.00	0.00	0.00	0.00	0.00	0.00	0.00	0.00	0.00	0.00	0.00	0.00
Total	4.00	4.00	4.00	4.00	4.00	4.00	4.00	4.00	4.00	4.00	4.00	4.00	4.00	4.00	4.00

lt core = light core; dk rim = darker rim; xl = crystal; transv = transverse; transit = transition

Table 12. Electron microprobe analyses of pyroxene (continued).

Sample#	JMH-306i		Flt-B												
Circle#	5	5	1	1	1	1	1	1	1	1	1	1	1	1	1
Point#															
Analysis#	69	70	72	73	74	75	76	77	78	79	80	81	82	83	84
Comment															
Wt. % oxides															
SiO_2	50.27	50.29	51.06	50.89	51.86	51.56	52.14	52.02	52.12	52.22	51.58	51.79	52.11	51.73	52.23
Al_2O_3	0.00	0.00	0.81	0.96	0.68	0.70	0.53	0.37	1.06	1.11	0.59	0.14	0.06	0.52	0.27
TiO_2	0.00	0.00	0.06	2.79	0.03	0.04	0.02	0.00	0.09	0.07	0.04	0.00	0.01	0.00	0.00
Cr_2O_3	0.00	0.00	0.02	0.03	0.00	0.02	0.00	0.00	0.00	0.00	0.00	0.00	0.00	0.00	0.02
FeO	11.54	10.58	9.91	8.26	9.03	8.13	7.99	6.20	3.91	5.55	7.39	9.64	8.16	7.19	6.61
Fe_2O_3	1.12	1.89	1.50	0.00	2.91	2.87	2.62	3.15	4.00	2.82	2.49	3.12	2.50	3.56	2.99
MnO	6.55	6.81	0.50	0.28	0.49	0.42	0.41	0.36	0.30	0.33	0.38	0.46	0.35	0.38	0.33
MgO	6.25	6.41	10.92	11.47	11.23	11.64	12.19	13.07	13.58	12.83	11.93	11.08	12.22	12.33	12.80
CaO	23.96	24.29	24.38	24.50	24.12	24.05	24.31	24.58	24.40	23.73	24.06	24.65	24.90	24.21	24.90
K_2O	0.03	0.02	0.00	0.02	0.03	0.02	0.03	0.03	0.02	0.04	0.02	0.04	0.02	0.02	0.04
Na_2O	0.00	0.01	0.00	0.49	0.32	0.33	0.22	0.17	0.58	0.70	0.38	0.08	0.01	0.27	0.15
Cl															
Total	99.72	100.31	99.14	99.69	100.71	99.76	100.45	99.94	100.06	99.40	98.86	101.01	100.35	100.20	100.35
Cation (based on 6 oxygens and 4 cations using the method of Droop, 1987)															
Si	1.98	1.97	1.96	1.92	1.96	1.95	1.96	1.95	1.94	1.96	1.96	1.96	1.96	1.95	1.96
Al	0.00	0.00	0.04	0.04	0.03	0.03	0.02	0.02	0.05	0.05	0.03	0.01	0.00	0.02	0.01
Ti	0.00	0.00	0.00	0.08	0.00	0.00	0.00	0.00	0.00	0.00	0.00	0.00	0.00	0.00	0.00
Cr	0.00	0.00	0.00	0.00	0.00	0.00	0.00	0.00	0.00	0.00	0.00	0.00	0.00	0.00	0.00
Fe^{2+}	0.38	0.35	0.32	0.26	0.28	0.26	0.25	0.19	0.12	0.17	0.24	0.30	0.26	0.23	0.21
Fe^{3+}	0.03	0.06	0.04	0.00	0.08	0.08	0.07	0.09	0.11	0.08	0.07	0.09	0.07	0.10	0.08
Mn	0.22	0.23	0.02	0.01	0.02	0.01	0.01	0.01	0.01	0.01	0.01	0.01	0.01	0.01	0.01
Mg	0.37	0.37	0.62	0.65	0.63	0.66	0.68	0.73	0.75	0.72	0.68	0.62	0.69	0.69	0.72
Ca	1.01	1.02	1.00	0.99	0.97	0.98	0.98	0.99	0.97	0.95	0.98	1.00	1.01	0.98	1.00
K	0.00	0.00	0.00	0.00	0.00	0.00	0.00	0.00	0.00	0.00	0.00	0.00	0.00	0.00	0.00
Na	0.00	0.00	0.00	0.04	0.02	0.02	0.02	0.01	0.04	0.05	0.03	0.01	0.00	0.02	0.01
Cl	0.00	0.00	0.00	0.00	0.00	0.00	0.00	0.00	0.00	0.00	0.00	0.00	0.00	0.00	0.00
Total	4.00	4.00	4.00	3.99	4.00	4.00	4.00	4.00	4.00	4.00	4.00	4.00	4.00	4.00	4.00

lt core = light core; dk rim = darker rim; xl = crystal; transv = transverse; transit = transition

Table 12. Electron microprobe analyses of pyroxene (continued).

Sample#	Flt-B														
Circle#	1	1	1	1	1	1	2	2	2	3	3	3	3	3	3
Point#															
Analysis#	85	86	87	88	89	90	92	93	94	97	98	99	100	101	102
Comment															
Wt. % oxides															
SiO_2	52.17	51.71	52.19	52.50	52.31	52.11	52.63	52.14	51.84	51.59	51.51	51.35	52.04	51.16	52.22
Al_2O_3	0.26	0.47	0.45	1.07	0.46	0.52	0.60	0.33	0.60	0.09	0.46	0.52	0.05	0.13	0.12
TiO_2	0.00	0.20	0.06	0.17	0.01	0.07	0.03	0.02	0.02	0.00	0.00	0.00	0.00	0.00	0.00
Cr_2O_3	0.00	0.01	0.00	0.03	0.00	0.02	0.00	0.02	0.00	0.00	0.00	0.00	0.00	0.00	0.01
FeO	8.15	8.80	7.69	6.66	6.56	7.48	5.58	6.64	4.46	9.18	7.09	9.08	7.36	11.41	7.32
Fe_2O_3	2.47	2.94	2.69	2.27	2.65	2.17	2.51	2.92	3.97	2.90	3.42	3.18	2.95	3.05	2.84
MnO	0.37	0.43	0.30	0.24	0.28	0.34	0.31	0.34	0.28	0.39	0.30	0.48	0.29	0.49	0.27
MgO	12.28	11.30	12.07	12.42	12.89	12.17	13.32	12.84	13.38	11.39	12.05	10.87	12.56	9.83	12.64
CaO	24.49	24.23	24.54	24.00	24.41	24.33	24.58	24.70	24.56	24.65	24.51	24.40	24.93	24.54	24.95
K_2O	0.01	0.01	0.00	0.14	0.04	0.02	0.03	0.03	0.03	0.02	0.04	0.01	0.02	0.03	0.02
Na_2O	0.13	0.33	0.32	0.59	0.29	0.35	0.38	0.17	0.41	0.04	0.26	0.25	0.04	0.05	0.06
Cl															
Total	100.31	100.43	100.31	100.08	99.89	99.60	99.97	100.13	99.54	100.24	99.65	100.14	100.25	100.69	100.45
Cation (based on 6 oxygens and 4 cations using the method of Droop, 1987)															
Si	1.96	1.95	1.96	1.96	1.96	1.97	1.96	1.96	1.95	1.96	1.95	1.95	1.96	1.96	1.96
Al	0.01	0.02	0.02	0.05	0.02	0.02	0.03	0.01	0.03	0.00	0.02	0.02	0.00	0.01	0.01
Ti	0.00	0.01	0.00	0.00	0.00	0.00	0.00	0.00	0.00	0.00	0.00	0.00	0.00	0.00	0.00
Cr	0.00	0.00	0.00	0.00	0.00	0.00	0.00	0.00	0.00	0.00	0.00	0.00	0.00	0.00	0.00
Fe^{2+}	0.26	0.28	0.24	0.21	0.21	0.24	0.17	0.21	0.14	0.29	0.22	0.29	0.23	0.36	0.23
Fe^{3+}	0.07	0.08	0.08	0.06	0.07	0.06	0.07	0.08	0.11	0.08	0.10	0.09	0.08	0.09	0.08
Mn	0.01	0.01	0.01	0.01	0.01	0.01	0.01	0.01	0.01	0.01	0.01	0.02	0.01	0.02	0.01
Mg	0.69	0.64	0.68	0.69	0.72	0.69	0.74	0.72	0.75	0.64	0.68	0.62	0.70	0.56	0.71
Ca	0.99	0.98	0.99	0.96	0.98	0.98	0.98	0.99	0.99	1.00	1.00	0.99	1.01	1.01	1.00
K	0.00	0.00	0.00	0.01	0.00	0.00	0.00	0.00	0.00	0.00	0.00	0.00	0.00	0.00	0.00
Na	0.01	0.02	0.02	0.04	0.02	0.03	0.03	0.01	0.03	0.00	0.02	0.02	0.00	0.00	0.00
Cl	0.00	0.00	0.00	0.00	0.00	0.00	0.00	0.00	0.00	0.00	0.00	0.00	0.00	0.00	0.00
Total	4.00	4.00	4.00	4.00	4.00	4.00	4.00	4.00	4.00	4.00	4.00	4.00	4.00	4.00	4.00

lt core = light core; dk rim = darker rim; xl = crystal; transv = transverse; transit = transition

Table 12. Electron microprobe analyses of pyroxene (continued).

Sample#	Flt-B			JMH-295.1										UG2	JMH-25
Circle#	3	3	3	2	2	2	2	2	2	2	2	2	2	1	1
Point#															
Analysis#	103	104	105	119	120	121	122	123	124	127	128	129	130	131	139
Comment				Coarser	Coarser	Coarser	Coarser	Coarser	Coarser	Coarser	Coarser	Coarser	Coarser		Fine
Wt. % oxides															
SiO_2	50.88	52.12	51.81	50.70	51.61	50.44	51.14	50.49	50.80	50.54	50.63	50.30	50.50	50.63	51.08
Al_2O_3	0.26	0.21	0.08	0.21	0.15	0.06	0.40	0.04	0.03	0.05	0.12	0.04	0.06	0.04	0.90
TiO_2	0.43	0.04	0.00	0.01	0.00	0.00	0.00	0.00	0.00	0.00	0.00	0.00	0.00	0.00	0.05
Cr_2O_3	0.00	0.00	0.00	0.00	0.00	0.00	0.00	0.00	0.00	0.00	0.02	0.00	0.00	0.00	0.05
FeO	14.06	8.55	7.26	9.94	8.51	14.27	8.92	11.98	13.17	14.05	14.00	14.32	8.77	9.09	11.58
Fe_2O_3	2.11	2.12	3.30	3.75	3.02	2.11	3.15	2.50	2.22	2.59	2.42	2.62	3.07	3.24	2.78
MnO	0.16	0.37	0.41	0.32	0.16	0.41	0.17	0.31	0.25	0.34	0.41	0.45	1.86	1.85	0.89
MgO	8.31	12.01	12.21	11.06	11.71	8.18	11.27	9.57	9.14	8.37	8.29	8.06	10.24	10.14	9.13
CaO	23.95	24.71	25.13	23.63	24.80	24.03	24.07	24.00	24.02	24.07	24.12	24.08	24.40	24.42	24.24
K_2O	0.03	0.01	0.03	0.04	0.01	0.03	0.02	0.02	0.02	0.02	0.01	0.02	0.02	0.02	0.05
Na_2O	0.31	0.08	0.05	0.06	0.08	0.04	0.24	0.05	0.04	0.05	0.09	0.02	0.04	0.03	0.25
Cl															
Total	100.50	100.20	100.29	99.71	100.05	99.58	99.37	98.96	99.69	100.08	100.11	99.91	98.95	99.46	101.01
Cation (based on 6 oxygens and 4 cations using the method of Droop, 1987)															
Si	1.96	1.97	1.95	1.94	1.96	1.97	1.95	1.96	1.97	1.96	1.97	1.96	1.96	1.95	1.95
Al	0.01	0.01	0.00	0.01	0.01	0.00	0.02	0.00	0.00	0.00	0.01	0.00	0.00	0.00	0.04
Ti	0.01	0.00	0.00	0.00	0.00	0.00	0.00	0.00	0.00	0.00	0.00	0.00	0.00	0.00	0.00
Cr	0.00	0.00	0.00	0.00	0.00	0.00	0.00	0.00	0.00	0.00	0.00	0.00	0.00	0.00	0.00
Fe^{2+}	0.45	0.27	0.23	0.32	0.27	0.47	0.29	0.39	0.43	0.46	0.45	0.47	0.28	0.29	0.37
Fe^{3+}	0.06	0.06	0.09	0.11	0.09	0.06	0.09	0.07	0.06	0.08	0.07	0.08	0.09	0.09	0.08
Mn	0.01	0.01	0.01	0.01	0.01	0.01	0.01	0.01	0.01	0.01	0.01	0.01	0.06	0.06	0.03
Mg	0.48	0.68	0.69	0.63	0.66	0.48	0.64	0.55	0.53	0.48	0.48	0.47	0.59	0.58	0.52
Ca	0.99	1.00	1.02	0.97	1.01	1.01	0.99	1.00	1.00	1.00	1.00	1.01	1.01	1.01	0.99
K	0.00	0.00	0.00	0.00	0.00	0.00	0.00	0.00	0.00	0.00	0.00	0.00	0.00	0.00	0.00
Na	0.02	0.01	0.00	0.00	0.01	0.00	0.02	0.00	0.00	0.00	0.01	0.00	0.00	0.00	0.02
Cl	0.00	0.00	0.00	0.00	0.00	0.00	0.00	0.00	0.00	0.00	0.00	0.00	0.00	0.00	0.00
Total	4.00	4.00	4.00	4.00	4.00	4.00	4.00	4.00	4.00	4.00	4.00	4.00	4.00	4.00	4.00

lt core = light core; dk rim = darker rim; xl = crystal; transv = transverse; transit = transition

Table 12. Electron microprobe analyses of pyroxene (continued).

Sample#	JMH-25														
Circle#	1	1	1	1	1	1	2	2	2	2	2	2	2	2	5
Point#															
Analysis#	140	141	142	143	144	147	174	175	176	177	178	179	180	181	182
Comment	Fine	Fine	Fine	Fine	Fine	Fine	Fine	Fine	Fine	Fine	Fine	Fine	Fine	Fine	Fine
Wt. % oxides															
SiO_2	50.75	51.54	51.07	51.49	50.83	50.74	51.12	51.63	50.43	51.00	50.73	51.12	50.45	50.70	52.31
Al_2O_3	1.21	1.87	0.47	1.50	0.81	1.07	0.69	0.89	1.69	0.62	0.51	0.58	0.93	1.01	1.15
TiO_2	0.37	0.77	0.03	0.02	0.03	0.05	0.03	0.06	0.04	0.03	0.03	0.00	0.04	0.05	0.00
Cr_2O_3	0.00	0.00	0.00	0.00	0.02	0.00	0.00	0.00	0.00	0.00	0.00	0.00	0.00	0.00	0.00
FeO	13.36	13.44	15.91	12.38	15.44	14.61	15.68	15.07	13.01	14.38	15.74	13.80	14.99	14.69	7.98
Fe_2O_3	1.96	0.74	1.78	2.24	1.96	2.04	1.27	1.15	2.30	2.08	1.98	2.32	2.04	2.55	1.99
MnO	0.73	0.59	1.58	0.62	1.15	1.21	1.44	0.91	0.82	0.96	1.24	1.01	1.31	1.30	0.23
MgO	8.21	8.16	6.89	8.63	6.90	7.24	7.08	7.89	8.05	7.74	6.83	8.09	7.29	7.22	11.61
CaO	23.94	23.77	23.95	23.91	23.91	23.70	23.70	23.82	23.42	24.29	23.94	24.18	23.39	23.79	24.28
K_2O	0.06	0.03	0.03	0.04	0.03	0.08	0.03	0.03	0.02	0.02	0.02	0.02	0.07	0.07	0.05
Na_2O	0.31	0.69	0.11	0.53	0.25	0.29	0.21	0.24	0.45	0.15	0.17	0.19	0.19	0.24	0.52
Cl															
Total	100.89	101.59	101.83	101.36	101.34	101.04	101.24	101.68	100.22	101.27	101.19	101.30	100.70	101.62	100.11
Cation (based on 6 oxygens and 4 cations using the method of Droop, 1987)															
Si	1.95	1.95	1.97	1.95	1.96	1.96	1.97	1.97	1.94	1.96	1.97	1.96	1.96	1.95	1.97
Al	0.05	0.08	0.02	0.07	0.04	0.05	0.03	0.04	0.08	0.03	0.02	0.03	0.04	0.05	0.05
Ti	0.01	0.02	0.00	0.00	0.00	0.00	0.00	0.00	0.00	0.00	0.00	0.00	0.00	0.00	0.00
Cr	0.00	0.00	0.00	0.00	0.00	0.00	0.00	0.00	0.00	0.00	0.00	0.00	0.00	0.00	0.00
Fe^{2+}	0.43	0.43	0.51	0.39	0.50	0.47	0.51	0.48	0.42	0.46	0.51	0.44	0.49	0.47	0.25
Fe^{3+}	0.06	0.02	0.05	0.06	0.06	0.06	0.04	0.03	0.07	0.06	0.06	0.07	0.06	0.07	0.06
Mn	0.02	0.02	0.05	0.02	0.04	0.04	0.05	0.03	0.03	0.03	0.04	0.03	0.04	0.04	0.01
Mg	0.47	0.46	0.40	0.49	0.40	0.42	0.41	0.45	0.46	0.44	0.39	0.46	0.42	0.41	0.65
Ca	0.98	0.96	0.99	0.97	0.99	0.98	0.98	0.97	0.97	1.00	0.99	0.99	0.97	0.98	0.98
K	0.00	0.00	0.00	0.00	0.00	0.00	0.00	0.00	0.00	0.00	0.00	0.00	0.00	0.00	0.00
Na	0.02	0.05	0.01	0.04	0.02	0.02	0.02	0.02	0.03	0.01	0.01	0.01	0.01	0.02	0.04
Cl	0.00	0.00	0.00	0.00	0.00	0.00	0.00	0.00	0.00	0.00	0.00	0.00	0.00	0.00	0.00
Total	4.00	4.00	4.00	4.00	4.00	4.00	4.00	4.00	4.00	4.00	4.00	4.00	4.00	4.00	4.00

lt core = light core; dk rim = darker rim; xl = crystal; transv = transverse; transit = transition

Table 12. Electron microprobe analyses of pyroxene (continued).

Sample#	JMH-25														
Circle#	5	5	5	5	5	5	5	5	5	6	6	6	6	1	1
Point#														1	2
Analysis#	183	184	185	186	189	190	191	192	194	197	198	201	202	242	243
Comment	Fine	Fine	Fine	Fine	Fine	Fine	Fine	Fine	Fine	Fine	Fine	Fine	Fine		
Wt. % oxides															
SiO_2	49.55	50.56	50.49	52.44	51.26	51.56	50.03	50.61	51.36	49.84	51.22	50.88	50.82	52.61	52.24
Al_2O_3	0.57	0.15	0.63	2.25	0.75	1.00	1.85	0.64	1.19	2.00	1.31	0.65	0.86	0.94	0.79
TiO_2	0.00	0.00	0.03	0.00	0.03	0.18	0.17	0.08	0.09	0.00	0.12	0.13	0.10	0.00	0.01
Cr_2O_3	0.00	0.00	0.00	0.00	0.00	0.00	0.00	0.01	0.00	0.00	0.00	0.00	0.00	0.00	0.01
FeO	9.09	17.53	15.30	6.97	14.08	12.95	12.13	13.59	11.94	15.70	12.51	14.80	13.63	8.34	9.12
Fe_2O_3	3.97	1.74	2.37	1.80	1.86	1.47	1.64	2.56	2.03	2.65	2.00	1.83	2.04	1.64	2.00
MnO	0.30	0.86	0.64	0.25	0.84	0.71	0.68	0.97	0.60	1.40	1.99	0.83	0.73	0.74	0.61
MgO	9.70	5.93	7.12	11.62	8.06	8.69	8.45	7.71	9.05	5.85	7.91	7.65	8.16	11.52	10.88
CaO	24.06	24.27	23.99	22.93	23.97	24.08	22.84	24.11	23.99	24.14	24.16	23.99	24.05	24.54	24.37
K_2O	0.13	0.01	0.02	0.09	0.02	0.03	0.08	0.04	0.02	0.11	0.08	0.03	0.05	0.02	0.04
Na_2O	0.29	0.08	0.21	1.11	0.27	0.37	0.56	0.27	0.44	0.17	0.33	0.19	0.22	0.39	0.44
Cl															
Total	97.66	101.11	100.80	99.45	101.13	101.04	98.43	100.60	100.72	101.87	101.63	100.97	100.64	100.73	100.49
Cation (based on 6 oxygens and 4 cations using the method of Droop, 1987)															
Si	1.94	1.97	1.96	1.97	1.97	1.97	1.95	1.96	1.96	1.92	1.95	1.96	1.96	1.97	1.97
Al	0.03	0.01	0.03	0.10	0.03	0.04	0.08	0.03	0.05	0.09	0.06	0.03	0.04	0.04	0.04
Ti	0.00	0.00	0.00	0.00	0.00	0.01	0.01	0.00	0.00	0.00	0.00	0.00	0.00	0.00	0.00
Cr	0.00	0.00	0.00	0.00	0.00	0.00	0.00	0.00	0.00	0.00	0.00	0.00	0.00	0.00	0.00
Fe^{2+}	0.30	0.57	0.50	0.22	0.45	0.41	0.40	0.44	0.38	0.51	0.40	0.48	0.44	0.26	0.29
Fe^{3+}	0.12	0.05	0.07	0.05	0.05	0.04	0.05	0.07	0.06	0.08	0.06	0.05	0.06	0.05	0.06
Mn	0.01	0.03	0.02	0.01	0.03	0.02	0.02	0.03	0.02	0.05	0.06	0.03	0.02	0.02	0.02
Mg	0.57	0.35	0.41	0.65	0.46	0.49	0.49	0.44	0.51	0.34	0.45	0.44	0.47	0.64	0.61
Ca	1.01	1.02	1.00	0.92	0.98	0.98	0.95	1.00	0.98	1.00	0.99	0.99	0.99	0.98	0.98
K	0.01	0.00	0.00	0.00	0.00	0.00	0.00	0.00	0.00	0.01	0.00	0.00	0.00	0.00	0.00
Na	0.02	0.01	0.02	0.08	0.02	0.03	0.04	0.02	0.03	0.01	0.02	0.01	0.02	0.03	0.03
Cl	0.00	0.00	0.00	0.00	0.00	0.00	0.00	0.00	0.00	0.00	0.00	0.00	0.00	0.00	0.00
Total	4.00	4.00	4.00	4.00	4.00	4.00	4.00	4.00	4.00	4.00	4.00	4.00	4.00	4.00	4.00

lt core = light core; dk rim = darker rim; xl = crystal; transv = transverse; transit = transition

Table 12. Electron microprobe analyses of pyroxene (continued).

Sample#	JMH-25														
Circle#	1	1	2	2	2	2	2	5	5	5	5	5	5	6	6
Point#	5	10	1	2	3	4	5	1	2	3	5	6	8	2	3
Analysis#	246	251	252	253	254	255	256	257	258	259	261	262	264	266	267
Comment															
Wt. % oxides															
SiO_2	51.43	50.83	50.61	50.62	50.04	50.74	50.24	50.87	51.69	50.97	50.75	50.83	50.45	49.18	49.08
Al_2O_3	0.91	1.05	1.26	0.91	1.09	0.78	0.88	0.48	1.41	0.66	1.19	0.72	0.80	0.84	0.97
TiO_2	0.08	0.29	0.03	0.04	0.04	0.01	0.04	0.00	0.00	0.00	0.09	0.18	0.00	0.38	0.06
Cr_2O_3	0.00	0.00	0.00	0.00	0.00	0.00	0.00	0.02	0.00	0.03	0.00	0.00	0.01	0.01	0.00
FeO	14.88	15.50	12.68	15.31	12.54	15.30	12.25	15.23	9.39	9.17	12.71	13.35	12.15	14.36	11.65
Fe_2O_3	0.65	0.00	2.86	2.01	3.39	2.01	3.31	1.66	2.13	3.28	2.12	1.99	3.58	2.76	4.17
MnO	0.80	1.03	0.73	1.17	0.73	1.15	0.62	0.74	0.56	0.44	0.70	0.79	0.72	0.90	0.63
MgO	7.99	7.83	8.44	7.13	8.11	7.10	8.51	7.51	10.29	10.55	8.56	8.26	8.37	6.94	8.18
CaO	23.69	22.36	23.79	23.55	23.85	23.82	23.54	23.93	23.63	24.19	23.75	24.10	24.24	23.61	23.84
K_2O	0.03	0.11	0.04	0.07	0.04	0.08	0.04	0.02	0.06	0.04	0.04	0.03	0.04	0.07	0.01
Na_2O	0.26	0.32	0.32	0.21	0.32	0.17	0.38	0.16	0.66	0.30	0.33	0.24	0.30	0.23	0.28
Cl															
Total	100.72	99.32	100.76	101.03	100.13	101.17	99.80	100.64	99.82	99.62	100.23	100.48	100.64	99.27	98.87
Cation (based on 6 oxygens and 4 cations using the method of Droop, 1987)															
Si	1.98	1.98	1.94	1.96	1.94	1.96	1.95	1.97	1.96	1.95	1.95	1.96	1.94	1.94	1.93
Al	0.04	0.05	0.06	0.04	0.05	0.04	0.04	0.02	0.06	0.03	0.05	0.03	0.04	0.04	0.04
Ti	0.00	0.01	0.00	0.00	0.00	0.00	0.00	0.00	0.00	0.00	0.00	0.01	0.00	0.01	0.00
Cr	0.00	0.00	0.00	0.00	0.00	0.00	0.00	0.00	0.00	0.00	0.00	0.00	0.00	0.00	0.00
Fe^{2+}	0.48	0.51	0.41	0.50	0.41	0.49	0.40	0.49	0.30	0.29	0.41	0.43	0.39	0.47	0.38
Fe^{3+}	0.02	0.00	0.08	0.06	0.10	0.06	0.10	0.05	0.06	0.09	0.06	0.06	0.10	0.08	0.12
Mn	0.03	0.03	0.02	0.04	0.02	0.04	0.02	0.02	0.02	0.01	0.02	0.03	0.02	0.03	0.02
Mg	0.46	0.46	0.48	0.41	0.47	0.41	0.49	0.43	0.58	0.60	0.49	0.47	0.48	0.41	0.48
Ca	0.98	0.93	0.98	0.98	0.99	0.99	0.98	0.99	0.96	0.99	0.98	1.00	1.00	1.00	1.00
K	0.00	0.01	0.00	0.00	0.00	0.00	0.00	0.00	0.00	0.00	0.00	0.00	0.00	0.00	0.00
Na	0.02	0.02	0.02	0.02	0.02	0.01	0.03	0.01	0.05	0.02	0.02	0.02	0.02	0.02	0.02
Cl	0.00	0.00	0.00	0.00	0.00	0.00	0.00	0.00	0.00	0.00	0.00	0.00	0.00	0.00	0.00
Total	4.00	4.00	4.00	4.00	4.00	4.00	4.00	4.00	4.00	4.00	4.00	4.00	4.00	4.00	4.00

lt core = light core; dk rim = darker rim; xl = crystal; transv = transverse; transit = transition

Table 12. Electron microprobe analyses of pyroxene (continued).

Sample#	JMH-25	JMH-25.2													
Circle#	6	2	2	2	2	2	2	3	3	3	4	4	4	5	5
Point#	5	1	2	3	4	5	6	2	3	4	1	2	3	1	2
Analysis#	269	270	271	272	273	274	275	277	278	279	280	281	282	283	284
Comment															
Wt. % oxides															
SiO_2	47.87	49.59	49.92	50.00	49.91	50.35	50.55	50.34	38.88	49.33	50.88	49.53	49.93	50.63	50.43
Al_2O_3	0.18	0.93	1.23	1.37	0.95	2.12	1.52	1.06	2.72	1.83	0.84	1.22	1.27	2.69	1.89
TiO_2	0.00	0.03	0.08	0.06	0.39	0.12	0.12	0.21	19.85	2.43	0.01	1.94	0.02	0.19	0.08
Cr_2O_3	0.00	0.00	0.00	0.00	0.00	0.00	0.00	0.03	0.03	0.01	0.00	0.00	0.00	0.02	0.01
FeO	12.47	12.37	11.35	13.75	12.75	13.56	13.92	14.29	6.72	13.34	12.83	12.45	12.52	10.28	10.21
Fe_2O_3	5.69	3.56	3.46	2.70	2.54	2.38	1.98	2.33	0.00	0.27	2.30	0.40	2.53	1.99	2.70
MnO	0.70	0.95	0.76	1.00	0.84	0.73	0.76	0.83	0.28	0.57	0.97	0.56	0.64	0.48	0.56
MgO	7.26	8.02	8.72	7.38	8.08	7.73	7.84	7.38	3.93	8.09	8.53	8.82	8.20	9.66	9.51
CaO	23.95	23.68	23.45	23.48	23.86	22.91	23.15	23.82	26.47	23.27	23.89	23.97	23.19	22.59	23.00
K_2O	0.01	0.05	0.03	0.04	0.05	0.09	0.08	0.02	0.04	0.06	0.04	0.06	0.05	0.11	0.09
Na_2O	0.09	0.26	0.43	0.37	0.29	0.56	0.43	0.33	0.27	0.61	0.24	0.29	0.45	0.75	0.63
Cl															
Total	98.22	99.44	99.41	100.14	99.65	100.56	100.34	100.63	99.19	99.82	100.52	99.23	98.79	99.37	99.10
Cation (based on 6 oxygens and 4 cations using the method of Droop, 1987)															
Si	1.91	1.94	1.94	1.94	1.94	1.94	1.95	1.95	1.53	1.91	1.96	1.92	1.95	1.94	1.94
Al	0.01	0.04	0.06	0.06	0.04	0.10	0.07	0.05	0.13	0.08	0.04	0.06	0.06	0.12	0.09
Ti	0.00	0.00	0.00	0.00	0.01	0.00	0.00	0.01	0.59	0.07	0.00	0.06	0.00	0.01	0.00
Cr	0.00	0.00	0.00	0.00	0.00	0.00	0.00	0.00	0.00	0.00	0.00	0.00	0.00	0.00	0.00
Fe^{2+}	0.42	0.40	0.37	0.45	0.41	0.44	0.45	0.46	0.22	0.43	0.41	0.40	0.41	0.33	0.33
Fe^{3+}	0.17	0.10	0.10	0.08	0.07	0.07	0.06	0.07	0.00	0.01	0.07	0.01	0.07	0.06	0.08
Mn	0.02	0.03	0.02	0.03	0.03	0.02	0.02	0.03	0.01	0.02	0.03	0.02	0.02	0.02	0.02
Mg	0.43	0.47	0.50	0.43	0.47	0.44	0.45	0.43	0.23	0.47	0.49	0.51	0.48	0.55	0.55
Ca	1.03	0.99	0.97	0.98	0.99	0.94	0.96	0.99	1.11	0.96	0.98	1.00	0.97	0.93	0.95
K	0.00	0.00	0.00	0.00	0.00	0.00	0.00	0.00	0.00	0.00	0.00	0.00	0.00	0.01	0.00
Na	0.01	0.02	0.03	0.03	0.02	0.04	0.03	0.02	0.02	0.05	0.02	0.02	0.03	0.06	0.05
Cl	0.00	0.00	0.00	0.00	0.00	0.00	0.00	0.00	0.00	0.00	0.00	0.00	0.00	0.00	0.00
Total	4.00	4.00	4.00	4.00	4.00	4.00	4.00	4.00	3.84	4.00	4.00	4.00	4.00	4.00	4.00

lt core = light core; dk rim = darker rim; xl = crystal; transv = transverse; transit = transition

Table 12. Electron microprobe analyses of pyroxene (continued).

Sample#	JMH-25.2					H1281-62.5			JMH-26						
Circle#	5	6	6	7	7	2	2	2	1	1	1	1	1	1	1
Point#	3	1	3	1	2	1	2	3	2	3	4	5	6	7	8
Analysis#	285	286	288	291	292	308	309	310	295	296	297	298	299	300	301
Comment															
Wt. % oxides															
SiO_2	50.32	49.66	49.59	50.09	50.50	47.48	47.96	49.72	51.61	50.65	51.38	50.95	51.00	50.97	50.55
Al_2O_3	1.17	1.10	0.91	0.90	0.84	2.08	2.29	3.57	2.26	1.70	0.67	0.40	0.53	0.71	0.72
TiO_2	0.68	0.07	0.61	0.92	0.23	0.06	0.02	0.04	0.04	0.11	0.02	0.03	0.04	0.00	0.08
Cr_2O_3	0.01	0.00	0.02	0.02	0.05	0.00	0.01	0.00	0.00	0.00	0.00	0.01	0.00	0.00	0.00
FeO	10.68	11.41	9.82	11.18	11.82	13.20	13.40	11.28	8.93	7.96	14.10	15.01	14.31	13.63	12.88
Fe_2O_3	2.26	3.30	3.16	1.98	3.12	4.20	3.55	2.96	0.56	2.59	1.33	1.69	1.82	2.30	2.02
MnO	0.51	0.94	0.50	0.49	0.59	1.29	1.41	0.69	0.25	0.35	0.53	0.76	0.54	0.57	0.65
MgO	9.57	8.53	9.66	9.33	8.92	6.22	6.01	7.38	11.02	11.30	8.27	7.75	8.06	8.11	8.57
CaO	23.70	23.51	23.68	23.91	23.60	22.89	22.75	21.71	22.55	23.28	23.60	23.65	23.64	23.67	23.42
K_2O	0.07	0.04	0.05	0.04	0.24	0.03	0.02	0.03	0.14	0.12	0.02	0.03	0.02	0.03	0.04
Na_2O	0.42	0.36	0.39	0.36	0.28	0.39	0.56	1.40	0.78	0.44	0.38	0.21	0.31	0.40	0.34
Cl															
Total	99.39	98.91	98.38	99.21	100.20	97.83	97.99	98.77	98.13	98.48	100.30	100.49	100.28	100.38	99.27
Cation (based on 6 oxygens and 4 cations using the method of Droop, 1987)															
Si	1.94	1.94	1.93	1.94	1.94	1.90	1.91	1.93	1.97	1.94	1.98	1.97	1.97	1.97	1.97
Al	0.05	0.05	0.04	0.04	0.04	0.10	0.11	0.16	0.10	0.08	0.03	0.02	0.02	0.03	0.03
Ti	0.02	0.00	0.02	0.03	0.01	0.00	0.00	0.00	0.00	0.00	0.00	0.00	0.00	0.00	0.00
Cr	0.00	0.00	0.00	0.00	0.00	0.00	0.00	0.00	0.00	0.00	0.00	0.00	0.00	0.00	0.00
Fe^{2+}	0.34	0.37	0.32	0.36	0.38	0.44	0.45	0.37	0.29	0.25	0.45	0.49	0.46	0.44	0.42
Fe^{3+}	0.07	0.10	0.09	0.06	0.09	0.13	0.11	0.09	0.02	0.07	0.04	0.05	0.05	0.07	0.06
Mn	0.02	0.03	0.02	0.02	0.02	0.04	0.05	0.02	0.01	0.01	0.02	0.03	0.02	0.02	0.02
Mg	0.55	0.50	0.56	0.54	0.51	0.37	0.36	0.43	0.63	0.64	0.48	0.45	0.46	0.47	0.50
Ca	0.98	0.98	0.99	0.99	0.97	0.98	0.97	0.90	0.92	0.96	0.97	0.98	0.98	0.98	0.98
K	0.00	0.00	0.00	0.00	0.01	0.00	0.00	0.00	0.01	0.01	0.00	0.00	0.00	0.00	0.00
Na	0.03	0.03	0.03	0.03	0.02	0.03	0.04	0.10	0.06	0.03	0.03	0.02	0.02	0.03	0.03
Cl	0.00	0.00	0.00	0.00	0.00	0.00	0.00	0.00	0.00	0.00	0.00	0.00	0.00	0.00	0.00
Total	4.00	4.00	4.00	4.00	4.00	4.00	4.00	4.00	4.00	4.00	4.00	4.00	4.00	4.00	4.00

lt core = light core; dk rim = darker rim; xl = crystal; transv = transverse; transit = transition

Table 12. Electron microprobe analyses of pyroxene (continued).

Sample#	JMH-26													
Circle#	1	1	1	1	1	1	1	1	1	1	1	1	1	1
Point#	9	10	11	12	13	14								
Analysis#	302	303	304	305	306	307	559	560	561	563	564	565	567	568
Comment							lt core	dk rim	lt core	lt core	dk rim	lt core	lt core	dk rim
Wt. % oxides														
SiO_2	49.81	50.02	50.27	49.15	49.87	49.76	50.12	52.10	52.25	50.60	50.81	49.53	49.56	52.19
Al_2O_3	0.25	0.21	0.27	0.24	0.17	0.31	0.21	2.45	0.28	0.13	3.29	0.31	0.04	1.60
TiO_2	0.05	0.00	0.02	0.02	0.00	0.03	0.00	0.06	0.06	0.01	0.01	0.04	0.01	0.03
Cr_2O_3	0.00	0.04	0.00	0.00	0.00	0.00	0.00	0.02	0.00	0.00	0.00	0.03	0.00	0.04
FeO	14.52	13.08	12.48	18.17	15.17	14.36	21.03	11.27	17.37	18.47	6.36	22.41	20.24	8.39
Fe_2O_3	2.78	3.43	3.30	3.39	2.94	2.85	0.42	0.47	0.00	0.99	4.47	0.60	0.43	2.09
MnO	0.80	0.72	0.71	1.36	0.74	1.01	2.01	0.35	1.06	2.32	0.26	3.56	4.86	0.35
MgO	7.39	8.17	8.81	4.83	6.96	7.39	2.85	11.34	6.47	4.89	12.28	1.61	2.25	11.42
CaO	23.73	24.22	23.91	23.43	24.04	23.58	22.44	21.11	22.99	23.80	20.82	23.11	23.34	23.78
K_2O	0.03	0.02	0.02	0.04	0.03	0.05	0.04	0.16	0.02	0.03	1.15	0.04	0.02	0.09
Na_2O	0.13	0.08	0.11	0.11	0.09	0.13	0.63	0.64	0.17	0.08	0.45	0.14	0.03	0.56
Cl							0.49	0.17	0.02	0.02	0.05	0.00	0.00	0.04
Total	99.49	99.97	99.91	100.74	100.02	99.47	100.12	100.09	100.68	101.33	99.93	101.38	100.78	100.55
Cation (based on 6 oxygens and 4 cations using the method of Droop, 1987)														
Si	1.96	1.95	1.95	1.95	1.96	1.96	2.01	1.96	2.02	1.99	1.91	1.99	1.99	1.96
Al	0.01	0.01	0.01	0.01	0.01	0.01	0.01	0.11	0.01	0.01	0.15	0.01	0.00	0.07
Ti	0.00	0.00	0.00	0.00	0.00	0.00	0.00	0.00	0.00	0.00	0.00	0.00	0.00	0.00
Cr	0.00	0.00	0.00	0.00	0.00	0.00	0.00	0.00	0.00	0.00	0.00	0.00	0.00	0.00
Fe^{2+}	0.48	0.43	0.40	0.60	0.50	0.47	0.71	0.36	0.56	0.61	0.20	0.75	0.68	0.26
Fe^{3+}	0.08	0.10	0.10	0.10	0.09	0.08	0.01	0.01	0.00	0.03	0.13	0.02	0.01	0.06
Mn	0.03	0.02	0.02	0.05	0.02	0.03	0.07	0.01	0.03	0.08	0.01	0.12	0.17	0.01
Mg	0.43	0.47	0.51	0.29	0.41	0.43	0.17	0.64	0.37	0.29	0.69	0.10	0.13	0.64
Ca	1.00	1.01	0.99	1.00	1.01	0.99	0.97	0.85	0.95	1.00	0.84	0.99	1.01	0.96
K	0.00	0.00	0.00	0.00	0.00	0.00	0.00	0.01	0.00	0.00	0.05	0.00	0.00	0.00
Na	0.01	0.01	0.01	0.01	0.01	0.01	0.05	0.05	0.01	0.01	0.03	0.01	0.00	0.04
Cl	0.00	0.00	0.00	0.00	0.00	0.00	0.03	0.01	0.00	0.00	0.00	0.00	0.00	0.00
Total	4.00	4.00	4.00	4.00	4.00	4.00	4.00	4.00	3.98	4.00	4.00	4.00	4.00	4.00

lt core = light core; dk rim = darker rim; xl = crystal; transv = transverse; transit = transition

Table 12. Electron microprobe analyses of pyroxene (continued).

Sample#	UGC-block1-bigvein														
Circle#	1	1	2	3	4	5	6	7	8	1	2	3	4	5	3
Point#															1
Analysis#															
Comment		xlzoned	xlzoned	xlzoned	xlzoned	xlzoned	xlzoned	xlzoned	xlzoned	xlzoned	xlzoned	xlzoned	xlzoned	xlzoned	transv
Wt. % oxides															
SiO_2	50.67	50.79	50.43	50.60	50.48	50.43	50.29	50.45	50.18	51.36	50.98	51.21	50.95	50.97	51.48
Al_2O_3	0.15	0.44	0.09	0.07	0.11	0.27	0.15	0.25	0.29	0.52	0.44	0.35	0.43	0.43	0.65
TiO_2	0.00	0.01	0.00	0.00	0.00	0.00	0.01	0.00	0.00	0.03	0.00	0.00	0.00	0.00	0.00
Cr_2O_3	0.00	0.00	0.00	0.00	0.04	0.04	0.00	0.00	0.00	0.00	0.04	0.01	0.00	0.00	0.00
FeO	14.53	15.45	16.60	16.06	16.26	15.18	17.01	14.62	14.64	12.26	13.71	13.84	13.12	12.62	12.23
Fe_2O_3	2.50	1.95	2.12	2.37	2.39	2.31	2.16	2.85	3.19	2.35	2.45	2.24	2.64	2.76	2.60
MnO	1.86	1.19	1.37	1.17	1.14	1.48	1.10	1.44	1.54	0.89	1.43	1.81	2.07	1.78	0.76
MgO	7.05	7.00	6.10	6.46	6.51	6.73	6.07	6.98	6.84	8.69	7.53	7.57	7.47	8.14	8.80
CaO	24.37	23.86	24.21	24.42	24.14	24.10	24.09	24.35	24.26	24.32	24.26	24.19	24.27	24.35	24.14
K_2O	0.00	0.02	0.03	0.02	0.03	0.04	0.02	0.02	0.00	0.01	0.01	0.03	0.03	0.01	0.03
Na_2O	0.08	0.21	0.07	0.09	0.07	0.14	0.06	0.12	0.11	0.34	0.28	0.22	0.26	0.17	0.40
Cl															
Total	101.21	100.92	101.02	101.25	101.16	100.70	100.95	101.08	101.06	100.79	101.12	101.46	101.22	101.25	101.08
Cation (based on 6 oxygens and 4 cations using the method of Droop, 1987)															
Si	1.96	1.97	1.97	1.97	1.97	1.97	1.97	1.96	1.95	1.97	1.96	1.97	1.96	1.96	1.96
Al	0.01	0.02	0.00	0.00	0.01	0.01	0.01	0.01	0.01	0.02	0.02	0.02	0.02	0.02	0.03
Ti	0.00	0.00	0.00	0.00	0.00	0.00	0.00	0.00	0.00	0.00	0.00	0.00	0.00	0.00	0.00
Cr	0.00	0.00	0.00	0.00	0.00	0.00	0.00	0.00	0.00	0.00	0.00	0.00	0.00	0.00	0.00
Fe^{2+}	0.47	0.50	0.54	0.52	0.53	0.50	0.56	0.47	0.48	0.39	0.44	0.44	0.42	0.41	0.39
Fe^{3+}	0.07	0.06	0.06	0.07	0.07	0.07	0.06	0.08	0.09	0.07	0.07	0.06	0.08	0.08	0.07
Mn	0.06	0.04	0.05	0.04	0.04	0.05	0.04	0.05	0.05	0.03	0.05	0.06	0.07	0.06	0.02
Mg	0.41	0.40	0.36	0.37	0.38	0.39	0.35	0.40	0.40	0.50	0.43	0.43	0.43	0.47	0.50
Ca	1.01	0.99	1.01	1.02	1.01	1.01	1.01	1.01	1.01	1.00	1.00	1.00	1.00	1.00	0.99
K	0.00	0.00	0.00	0.00	0.00	0.00	0.00	0.00	0.00	0.00	0.00	0.00	0.00	0.00	0.00
Na	0.01	0.02	0.00	0.01	0.01	0.01	0.00	0.01	0.01	0.03	0.02	0.02	0.02	0.01	0.03
Cl	0.00	0.00	0.00	0.00	0.00	0.00	0.00	0.00	0.00	0.00	0.00	0.00	0.00	0.00	0.00
Total	4.00	4.00	4.00	4.00	4.00	4.00	4.00	4.00	4.00	4.00	4.00	4.00	4.00	4.00	4.00

lt core = light core; dk rim = darker rim; xl = crystal; transv = transverse; transit = transition

Table 12. Electron microprobe analyses of pyroxene (continued).

Sample#	UGC-block1-bigvein														UGC-block2
Circle#	3	3	3	3	3	3	3	3	3	3	3	3	3	3	
Point#	2	3	4	5	6	7	8	9	10	11	12	13	14	15	1
Analysis#															
Comment	transv	transv	transv	transv	transv	transv	transv	transv	transv	transv	transv	transv	transv	transv	bigvein
Wt. % oxides															
SiO_2	51.37	51.28	50.97	50.76	50.99	51.10	50.99	50.81	50.31	50.85	50.75	50.70	50.90	50.89	51.01
Al_2O_3	0.74	0.34	0.23	0.12	0.04	0.08	0.09	0.05	0.07	0.06	0.13	0.04	0.07	0.04	0.68
TiO_2	0.00	0.02	0.00	0.00	0.00	0.00	0.00	0.00	0.00	0.00	0.00	0.00	0.00	0.00	0.00
Cr_2O_3	0.00	0.02	0.03	0.00	0.01	0.00	0.00	0.00	0.02	0.01	0.01	0.01	0.00	0.00	0.00
FeO	12.99	13.40	13.60	16.25	13.84	14.19	15.05	16.59	16.23	15.09	14.52	15.09	14.87	15.02	13.34
Fe_2O_3	2.30	2.08	2.37	2.17	2.13	1.79	1.91	1.78	2.07	2.24	2.09	2.28	2.40	2.16	2.14
MnO	0.84	1.30	1.65	1.22	3.04	2.97	1.42	2.22	2.85	2.62	1.78	3.09	1.44	1.79	2.13
MgO	8.25	8.17	7.88	6.64	6.95	6.99	7.15	6.00	5.57	6.55	7.36	6.03	7.26	6.98	7.41
CaO	23.83	24.41	24.17	24.19	24.52	24.33	24.53	24.27	24.05	24.35	24.22	24.55	24.47	24.39	23.95
K_2O	0.02	0.01	0.03	0.00	0.02	0.03	0.01	0.02	0.02	0.02	0.03	0.01	0.03	0.01	0.02
Na_2O	0.50	0.17	0.12	0.08	0.04	0.04	0.06	0.01	0.06	0.02	0.03	0.04	0.04	0.06	0.33
Cl															
Total	100.84	101.19	101.07	101.43	101.57	101.52	101.22	101.76	101.26	101.81	100.92	101.84	101.47	101.34	101.01
Cation (based on 6 oxygens and 4 cations using the method of Droop, 1987)															
Si	1.97	1.97	1.96	1.97	1.97	1.97	1.97	1.97	1.97	1.97	1.97	1.97	1.97	1.97	1.97
Al	0.03	0.02	0.01	0.01	0.00	0.00	0.00	0.00	0.00	0.00	0.01	0.00	0.00	0.00	0.03
Ti	0.00	0.00	0.00	0.00	0.00	0.00	0.00	0.00	0.00	0.00	0.00	0.00	0.00	0.00	0.00
Cr	0.00	0.00	0.00	0.00	0.00	0.00	0.00	0.00	0.00	0.00	0.00	0.00	0.00	0.00	0.00
Fe^{2+}	0.42	0.43	0.44	0.53	0.45	0.46	0.49	0.54	0.53	0.49	0.47	0.49	0.48	0.49	0.43
Fe^{3+}	0.07	0.06	0.07	0.06	0.06	0.05	0.06	0.05	0.06	0.07	0.06	0.07	0.07	0.06	0.06
Mn	0.03	0.04	0.05	0.04	0.10	0.10	0.05	0.07	0.09	0.09	0.06	0.10	0.05	0.06	0.07
Mg	0.47	0.47	0.45	0.38	0.40	0.40	0.41	0.35	0.32	0.38	0.43	0.35	0.42	0.40	0.43
Ca	0.98	1.00	1.00	1.01	1.02	1.01	1.02	1.01	1.01	1.01	1.01	1.02	1.01	1.01	0.99
K	0.00	0.00	0.00	0.00	0.00	0.00	0.00	0.00	0.00	0.00	0.00	0.00	0.00	0.00	0.00
Na	0.04	0.01	0.01	0.01	0.00	0.00	0.00	0.00	0.00	0.00	0.00	0.00	0.00	0.00	0.02
Cl	0.00	0.00	0.00	0.00	0.00	0.00	0.00	0.00	0.00	0.00	0.00	0.00	0.00	0.00	0.00
Total	4.00	4.00	4.00	4.00	4.00	4.00	4.00	4.00	4.00	4.00	4.00	4.00	4.00	4.00	4.00

lt core = light core; dk rim = darker rim; xl = crystal; transv = transverse; transit = transition

Table 12. Electron microprobe analyses of pyroxene (continued).

Sample#	UGC-block2									UGC-block1					
Circle#															
Point#	2	3	4	5	6	7	8	9	10	1	2	3	4	5	2
Analysis#															
Comment	bigvein	bigvein	bigvein	bigvein	bigvein	bigvein	bigvein	bigvein	bigvein	border	border	border	border	border	transit
Wt. % oxides															
SiO_2	51.24	50.49	50.62	50.76	51.00	50.93	50.93	50.44	50.46	50.08	50.69	50.98	51.74	50.87	51.06
Al_2O_3	0.14	0.11	0.16	0.04	0.10	0.05	0.06	0.17	0.12	0.02	0.03	0.53	0.42	0.07	0.36
TiO_2	0.00	0.04	0.00	0.00	0.00	0.00	0.00	0.00	0.01	0.00	0.00	0.00	0.02	0.00	0.03
Cr_2O_3	0.00	0.00	0.01	0.00	0.00	0.00	0.00	0.01	0.00	0.00	0.00	0.03	0.01	0.00	0.04
FeO	14.64	15.99	15.37	15.80	15.63	16.08	16.16	17.09	16.37	17.43	15.61	13.69	11.85	15.47	14.86
Fe_2O_3	1.89	1.81	1.91	1.20	1.66	1.78	1.88	1.92	1.49	2.03	1.83	2.10	1.95	1.60	1.78
MnO	2.03	2.84	2.19	2.81	2.39	1.46	1.51	1.55	2.92	2.63	2.99	1.17	1.13	2.73	1.35
MgO	7.32	5.77	6.53	6.08	6.41	6.70	6.72	5.89	5.47	5.02	5.99	7.92	9.47	6.34	7.30
CaO	24.28	24.08	24.03	24.20	24.30	24.20	24.24	23.82	24.11	23.99	24.24	24.10	24.31	24.26	24.17
K_2O	0.00	0.02	0.03	0.01	0.02	0.04	0.01	0.03	0.03	0.03	0.04	0.02	0.02	0.02	0.02
Na_2O	0.09	0.08	0.09	0.04	0.07	0.06	0.03	0.12	0.06	0.01	0.03	0.22	0.18	0.03	0.18
Cl															
Total	101.62	101.22	100.94	100.95	101.58	101.28	101.54	101.03	101.03	101.23	101.42	100.76	101.09	101.39	101.14
Cation (based on 6 oxygens and 4 cations using the method of Droop, 1987)															
Si	1.97	1.97	1.97	1.98	1.98	1.98	1.97	1.97	1.98	1.97	1.97	1.97	1.97	1.98	1.97
Al	0.01	0.00	0.01	0.00	0.00	0.00	0.00	0.01	0.01	0.00	0.00	0.02	0.02	0.00	0.02
Ti	0.00	0.00	0.00	0.00	0.00	0.00	0.00	0.00	0.00	0.00	0.00	0.00	0.00	0.00	0.00
Cr	0.00	0.00	0.00	0.00	0.00	0.00	0.00	0.00	0.00	0.00	0.00	0.00	0.00	0.00	0.00
Fe^{2+}	0.47	0.52	0.50	0.52	0.51	0.52	0.52	0.56	0.54	0.57	0.51	0.44	0.38	0.50	0.48
Fe^{3+}	0.05	0.05	0.06	0.04	0.05	0.05	0.05	0.06	0.04	0.06	0.05	0.06	0.06	0.05	0.05
Mn	0.07	0.09	0.07	0.09	0.08	0.05	0.05	0.05	0.10	0.09	0.10	0.04	0.04	0.09	0.04
Mg	0.42	0.34	0.38	0.35	0.37	0.39	0.39	0.34	0.32	0.29	0.35	0.46	0.54	0.37	0.42
Ca	1.00	1.01	1.00	1.01	1.01	1.01	1.01	1.00	1.01	1.01	1.01	1.00	0.99	1.01	1.00
K	0.00	0.00	0.00	0.00	0.00	0.00	0.00	0.00	0.00	0.00	0.00	0.00	0.00	0.00	0.00
Na	0.01	0.01	0.01	0.00	0.01	0.00	0.00	0.01	0.00	0.00	0.00	0.02	0.01	0.00	0.01
Cl	0.00	0.00	0.00	0.00	0.00	0.00	0.00	0.00	0.00	0.00	0.00	0.00	0.00	0.00	0.00
Total	4.00	4.00	4.00	4.00	4.00	4.00	4.00	4.00	4.00	4.00	4.00	4.00	4.00	4.00	4.00

lt core = light core; dk rim = darker rim; xl = crystal; transv = transverse; transit = transition

Table 12. Electron microprobe analyses of pyroxene (continued).

Sample#	UGC-block1												
Circle#													
Point#	3	4	5	6	7	8	9	10	11	12	1	2	4
Analysis#													
Comment	transit	transit	transit	transit	transit	transit	transit	transit	transit	transit	matrix	matrix	matrix
Wt. % oxides													
SiO_2	51.15	51.25	51.89	50.76	51.70	51.96	50.49	51.25	50.51	50.62	49.49	51.38	50.75
Al_2O_3	0.55	0.40	0.93	0.46	0.68	1.02	0.66	0.59	0.30	0.37	1.51	0.89	0.43
TiO_2	0.00	0.00	0.00	0.01	0.00	0.05	0.00	0.00	0.00	0.02	2.10	0.05	0.04
Cr_2O_3	0.00	0.00	0.00	0.00	0.01	0.00	0.01	0.00	0.01	0.00	0.06	0.01	0.02
FeO	12.46	13.63	8.81	13.71	10.95	9.19	11.06	10.43	14.61	12.84	13.47	12.23	14.43
Fe_2O_3	2.57	2.18	2.38	2.40	2.35	2.23	4.13	2.40	2.57	2.38	0.13	1.63	2.29
MnO	1.22	1.59	0.74	1.43	0.92	0.72	1.31	1.23	1.74	1.19	0.87	1.17	1.26
MgO	8.62	7.89	11.07	7.71	9.89	10.94	8.51	9.67	7.02	8.37	7.89	8.82	7.38
CaO	24.19	24.18	24.22	24.21	24.25	24.46	24.56	24.41	24.10	24.02	24.80	24.34	24.16
K_2O	0.03	0.02	0.01	0.03	0.03	0.04	0.04	0.03	0.05	0.02	0.02	0.02	0.01
Na_2O	0.22	0.20	0.37	0.15	0.25	0.28	0.27	0.22	0.11	0.16	0.18	0.24	0.19
Cl													
Total	101.01	101.35	100.41	100.87	101.02	100.90	101.04	100.23	101.02	99.99	100.51	100.79	100.96
Cation (based on 6 oxygens and 4 cations using the method of Droop, 1987)													
Si	1.96	1.97	1.96	1.96	1.96	1.96	1.94	1.96	1.96	1.96	1.91	1.96	1.96
Al	0.02	0.02	0.04	0.02	0.03	0.05	0.03	0.03	0.01	0.02	0.07	0.04	0.02
Ti	0.00	0.00	0.00	0.00	0.00	0.00	0.00	0.00	0.00	0.00	0.06	0.00	0.00
Cr	0.00	0.00	0.00	0.00	0.00	0.00	0.00	0.00	0.00	0.00	0.00	0.00	0.00
Fe^{2+}	0.40	0.44	0.28	0.44	0.35	0.29	0.35	0.33	0.47	0.42	0.43	0.39	0.47
Fe^{3+}	0.07	0.06	0.07	0.07	0.07	0.06	0.12	0.07	0.08	0.07	0.00	0.05	0.07
Mn	0.04	0.05	0.02	0.05	0.03	0.02	0.04	0.04	0.06	0.04	0.03	0.04	0.04
Mg	0.49	0.45	0.62	0.44	0.56	0.61	0.49	0.55	0.41	0.48	0.45	0.50	0.43
Ca	0.99	0.99	0.98	1.00	0.99	0.99	1.01	1.00	1.00	1.00	1.02	1.00	1.00
K	0.00	0.00	0.00	0.00	0.00	0.00	0.00	0.00	0.00	0.00	0.00	0.00	0.00
Na	0.02	0.01	0.03	0.01	0.02	0.02	0.02	0.02	0.01	0.01	0.01	0.02	0.01
Cl	0.00	0.00	0.00	0.00	0.00	0.00	0.00	0.00	0.00	0.00	0.00	0.00	0.00
Total	4.00	4.00	4.00	4.00	4.00	4.00	4.00	4.00	4.00	4.00	4.00	4.00	4.00

lt core = light core; dk rim = darker rim; xl = crystal; transv = transverse; transit = transition

Table 12. Electron microprobe analyses of pyroxene (continued).

Sample#	UGC-block2						UGC-block2				UGC-block2				
Circle#															
Point#	1	2	3	4	5	6	1	2	3	4	1	2	3	4	1
Analysis#															
Comment	Zone 1	Zone 1	Zone 1	Zone 1	Zone 1	Zone 1	Zone 2	Zone 2	Zone 2	Zone 2	Zone 3	Zone 3	Zone 3	Zone 3	Zone 5
Wt. % oxides															
SiO_2	51.30	50.80	51.31	50.27	51.94	51.16	51.62	50.79	51.68	51.59	52.06	50.71	51.42	51.79	51.35
Al_2O_3	0.33	0.17	0.41	0.14	0.72	0.39	0.43	0.31	0.60	0.59	1.04	0.23	0.75	0.75	0.81
TiO_2	0.00	0.00	0.02	0.00	0.00	0.01	0.00	0.00	0.00	0.00	0.12	0.02	0.02	0.04	0.01
Cr_2O_3	0.00	0.00	0.02	0.02	0.00	0.00	0.00	0.02	0.01	0.01	0.00	0.00	0.00	0.00	0.02
FeO	13.35	14.71	13.28	15.28	11.53	13.81	13.32	15.85	11.05	11.02	10.01	11.68	9.70	10.51	10.94
Fe_2O_3	2.21	2.28	1.99	2.60	1.57	1.92	1.74	1.66	2.24	2.57	1.82	2.45	3.18	2.15	2.50
MnO	1.66	2.40	1.44	2.44	0.86	1.80	1.25	1.53	1.24	1.18	0.89	2.55	1.26	1.31	1.28
MgO	7.93	6.78	8.22	6.00	9.49	7.56	8.47	6.74	9.56	9.60	10.40	8.04	9.91	9.84	9.28
CaO	24.34	24.21	24.29	24.30	24.28	24.23	24.31	23.93	24.42	24.30	24.01	24.66	24.47	24.17	24.02
K_2O	0.03	0.02	0.02	0.04	0.15	0.03	0.03	0.03	0.02	0.03	0.02	0.03	0.02	0.01	0.02
Na_2O	0.20	0.10	0.17	0.08	0.27	0.20	0.17	0.13	0.24	0.25	0.45	0.08	0.31	0.35	0.39
Cl															
Total	101.34	101.45	101.17	101.17	100.81	101.11	101.34	100.99	101.06	101.14	100.83	100.43	101.05	100.91	100.62
Cation (based on 6 oxygens and 4 cations using the method of Droop, 1987)															
Si	1.97	1.97	1.97	1.96	1.97	1.97	1.97	1.97	1.96	1.96	1.96	1.96	1.95	1.96	1.96
Al	0.01	0.01	0.02	0.01	0.03	0.02	0.02	0.01	0.03	0.03	0.05	0.01	0.03	0.03	0.04
Ti	0.00	0.00	0.00	0.00	0.00	0.00	0.00	0.00	0.00	0.00	0.00	0.00	0.00	0.00	0.00
Cr	0.00	0.00	0.00	0.00	0.00	0.00	0.00	0.00	0.00	0.00	0.00	0.00	0.00	0.00	0.00
Fe^{2+}	0.43	0.48	0.43	0.50	0.37	0.45	0.43	0.51	0.35	0.35	0.32	0.38	0.31	0.33	0.35
Fe^{3+}	0.06	0.07	0.06	0.08	0.04	0.06	0.05	0.05	0.06	0.07	0.05	0.07	0.09	0.06	0.07
Mn	0.05	0.08	0.05	0.08	0.03	0.06	0.04	0.05	0.04	0.04	0.03	0.08	0.04	0.04	0.04
Mg	0.45	0.39	0.47	0.35	0.54	0.43	0.48	0.39	0.54	0.54	0.58	0.46	0.56	0.56	0.53
Ca	1.00	1.00	1.00	1.02	0.99	1.00	1.00	1.00	0.99	0.99	0.97	1.02	0.99	0.98	0.98
K	0.00	0.00	0.00	0.00	0.01	0.00	0.00	0.00	0.00	0.00	0.00	0.00	0.00	0.00	0.00
Na	0.01	0.01	0.01	0.01	0.02	0.02	0.01	0.01	0.02	0.02	0.03	0.01	0.02	0.03	0.03
Cl	0.00	0.00	0.00	0.00	0.00	0.00	0.00	0.00	0.00	0.00	0.00	0.00	0.00	0.00	0.00
Total	4.00	4.00	4.00	4.00	4.00	4.00	4.00	4.00	4.00	4.00	4.00	4.00	4.00	4.00	4.00

Table 12. Electron microprobe analyses of pyroxene (continued).

Sample#	UGC-block2									
Circle#										
Point#	2	3	4	5	1	2	3	4	5	6
Analysis#										
Comment	Zone 5	Zone 5	Zone 5	Zone 5	Zone 4	Zone 4	Zone 4	Zone 4	Zone 4	Zone 4
Wt. % oxides										
SiO_2	52.01	50.92	50.84	52.37	51.38	51.21	49.95	51.20	50.63	50.60
Al_2O_3	0.63	0.03	0.12	0.93	0.64	0.53	0.27	1.05	0.17	0.15
TiO_2	0.03	0.00	0.00	0.00	0.00	0.00	0.00	0.05	0.02	0.00
Cr_2O_3	0.00	0.00	0.00	0.00	0.00	0.00	0.00	0.27	0.00	0.00
FeO	8.95	13.34	14.64	8.74	11.63	12.23	16.05	12.39	13.56	13.33
Fe_2O_3	2.62	1.97	1.87	2.25	2.57	2.53	2.27	2.35	2.02	2.40
MnO	0.95	2.87	2.04	0.85	0.78	1.01	2.23	0.68	2.34	2.34
MgO	10.91	7.42	7.08	11.16	9.28	8.75	5.68	8.34	7.33	7.32
CaO	24.56	24.32	24.23	24.30	23.98	24.17	23.64	23.51	24.31	24.44
K_2O	0.02	0.02	0.03	0.01	0.02	0.04	0.03	0.02	0.02	0.01
Na_2O	0.29	0.04	0.08	0.42	0.36	0.28	0.20	0.68	0.08	0.09
Cl										
Total	100.96	100.94	100.92	101.04	100.64	100.76	100.31	100.55	100.47	100.69
Cation (based on 6 oxygens and 4 cations using the method of Droop, 1987)										
Si	1.96	1.97	1.97	1.96	1.96	1.96	1.97	1.96	1.97	1.97
Al	0.03	0.00	0.01	0.04	0.03	0.02	0.01	0.05	0.01	0.01
Ti	0.00	0.00	0.00	0.00	0.00	0.00	0.00	0.00	0.00	0.00
Cr	0.00	0.00	0.00	0.00	0.00	0.00	0.00	0.01	0.00	0.00
Fe^{2+}	0.28	0.43	0.48	0.27	0.37	0.39	0.53	0.40	0.44	0.43
Fe^{3+}	0.07	0.06	0.05	0.06	0.07	0.07	0.07	0.07	0.06	0.07
Mn	0.03	0.09	0.07	0.03	0.03	0.03	0.07	0.02	0.08	0.08
Mg	0.61	0.43	0.41	0.62	0.53	0.50	0.33	0.48	0.42	0.42
Ca	0.99	1.01	1.01	0.98	0.98	0.99	1.00	0.97	1.01	1.02
K	0.00	0.00	0.00	0.00	0.00	0.00	0.00	0.00	0.00	0.00
Na	0.02	0.00	0.01	0.03	0.03	0.02	0.01	0.05	0.01	0.01
Cl	0.00	0.00	0.00	0.00	0.00	0.00	0.00	0.00	0.00	0.00
Total	4.00	4.00	4.00	4.00	4.00	4.00	4.00	4.00	4.00	4.00

Table 13. Electron microprobe analyses of vesuvianite.

Sample#	E:7.5			
Wt. % oxides				
SiO_2	36.23	36.27	35.85	36.04
TiO_2	0.03	0.02	0.00	0.02
Al_2O_3	17.38	17.42	17.50	17.43
Cr_2O_3	0.02	0.00	0.01	0.00
FeO	2.54	2.42	2.50	2.59
MnO	0.09	0.10	0.07	0.10
MgO	2.61	2.64	2.59	2.57
CaO	36.87	36.71	37.00	36.89
Na_2O	0.02	0.02	0.00	0.01
K_2O	0.00	0.00	0.00	0.01
Total	95.77	95.61	95.52	95.66
Cations*				
Si	17.69	17.74	17.55	17.62
Ti	0.01	0.01	0.00	0.01
Al	10.00	10.04	10.10	10.05
Cr	0.01	0.00	0.01	0.00
Fe	1.04	0.99	1.02	1.06
Mn	0.04	0.04	0.03	0.04
Mg	1.90	1.93	1.89	1.88
Ca	19.30	19.24	19.40	19.33
Na	0.02	0.01	0.00	0.01
K	0.00	0.00	0.00	0.00
H	13.78	14.32	14.62	14.16

* Based on 50 cations with all Fe as Fe^{2+}

Table 14. Electron microprobe analyses of zoisite.

Sample#	JMH-24						JMH-25								
Circle#	9	9	9	9	9	9	1	1	1	1	1	1	1	1	1
Point#															
Analysis#	215	216	217	218	219	220	148	149	150	151	152	153	154	155	156
Comment	dark	dark	dark	dark	dark	dark									
Wt. % oxides															
SiO_2	39.62	39.47	39.80	39.60	39.61	39.54	39.15	39.38	38.96	38.74	39.25	39.25	39.47	39.23	39.36
TiO_2	0.06	0.03	0.04	0.04	0.04	0.03	0.03	0.01	0.01	0.05	0.02	0.08	0.04	0.03	0.05
Al_2O_3	32.66	32.66	32.65	32.45	32.58	32.50	31.49	31.02	30.07	30.64	31.62	31.67	31.35	32.14	31.75
Cr_2O_3	0.00	0.00	0.03	0.00	0.01	0.00	0.00	0.00	0.00	0.01	0.01	0.00	0.00	0.00	0.00
FeO	0.27	0.18	0.28	0.28	0.24	0.30	1.89	2.48	3.50	2.36	1.62	1.76	2.22	1.37	1.87
MnO	0.03	0.04	0.02	0.02	0.03	0.05	0.02	0.05	0.14	0.04	0.06	0.05	0.06	0.05	0.04
MgO	0.01	0.00	0.01	0.01	0.02	0.00	0.00	0.00	0.03	0.02	0.05	0.01	0.04	0.01	0.04
CaO	23.50	23.82	23.74	23.63	23.93	23.64	24.36	23.94	23.83	23.83	25.03	23.85	24.44	24.24	24.56
Na_2O	0.00	0.00	0.00	0.00	0.00	0.01	0.00	0.02	0.01	0.01	0.01	0.07	0.02	0.00	0.02
K_2O	0.02	0.02	0.02	0.04	0.01	0.01	0.02	0.03	0.02	0.02	0.01	0.02	0.00	0.03	0.03
Total	96.18	96.21	96.59	96.06	96.47	96.09	96.97	96.92	96.56	95.71	97.67	96.76	97.64	97.10	97.71
Cations (based on 12.5 oxygens)															
Si	3.04	3.04	3.05	3.05	3.04	3.04	3.01	3.03	3.02	3.02	3.00	3.02	3.02	3.01	3.00
Ti	0.00	0.00	0.00	0.00	0.00	0.00	0.00	0.00	0.00	0.00	0.00	0.00	0.00	0.00	0.00
Al	2.96	2.96	2.95	2.95	2.95	2.95	2.86	2.81	2.75	2.82	2.85	2.87	2.82	2.90	2.86
Cr	0.00	0.00	0.00	0.00	0.00	0.00	0.00	0.00	0.00	0.00	0.00	0.00	0.00	0.00	0.00
Fe^{+3}	0.02	0.01	0.02	0.02	0.02	0.02	0.12	0.16	0.23	0.15	0.10	0.11	0.14	0.09	0.12
Mn^{+3}	0.00	0.00	0.00	0.00	0.00	0.00	0.00	0.00	0.01	0.00	0.00	0.00	0.00	0.00	0.00
Mg	0.00	0.00	0.00	0.00	0.00	0.00	0.00	0.00	0.00	0.00	0.01	0.00	0.00	0.00	0.00
Ca	1.94	1.96	1.95	1.95	1.97	1.95	2.01	1.97	1.98	1.99	2.05	1.97	2.00	1.99	2.01
Na	0.00	0.00	0.00	0.00	0.00	0.00	0.00	0.00	0.00	0.00	0.00	0.01	0.00	0.00	0.00
K	0.00	0.00	0.00	0.00	0.00	0.00	0.00	0.00	0.00	0.00	0.00	0.00	0.00	0.00	0.00

Table 14. Electron microprobe analyses of zoisite (continued).

Sample#	JMH-25														
Circle#	1	2	2	2	2	2	2	2	2	2	2	2	2	2	2
Point#															
Analysis#	157	158	159	160	161	162	163	164	165	166	167	168	169	170	171
Comment															
Wt. % oxides															
SiO_2	39.31	39.15	39.16	39.20	39.40	39.21	39.34	39.27	39.36	39.35	39.16	39.46	39.34	39.32	39.40
TiO_2	0.02	0.04	0.04	0.02	0.09	0.05	0.04	0.03	0.03	0.01	0.00	0.08	0.18	0.17	0.10
Al_2O_3	31.49	31.15	30.28	30.76	31.49	30.35	30.38	30.93	31.00	31.18	31.03	31.39	30.48	31.14	31.07
Cr_2O_3	0.00	0.00	0.00	0.00	0.00	0.00	0.01	0.00	0.02	0.00	0.00	0.00	0.00	0.00	0.00
FeO	1.89	2.72	3.46	2.90	1.86	3.68	3.25	2.57	2.25	2.21	2.24	2.20	3.14	2.13	2.33
MnO	0.09	0.11	0.06	0.23	0.05	0.16	0.06	0.04	0.01	0.03	0.03	0.03	0.07	0.04	0.00
MgO	0.02	0.02	0.02	0.07	0.01	0.05	0.04	0.00	0.00	0.02	0.01	0.01	0.03	0.01	0.00
CaO	23.69	24.08	24.30	23.60	23.75	23.99	24.48	23.97	23.94	24.75	23.70	24.49	24.11	24.19	24.23
Na_2O	0.02	0.00	0.03	0.01	0.01	0.02	0.00	0.01	0.01	0.00	0.00	0.00	0.00	0.00	0.00
K_2O	0.03	0.03	0.01	0.02	0.02	0.01	0.02	0.02	0.01	0.03	0.01	0.02	0.02	0.02	0.00
Total	96.56	97.29	97.37	96.79	96.69	97.52	97.62	96.83	96.63	97.57	96.18	97.68	97.38	97.02	97.14
Cations (based on 12.5 oxygens)															
Si	3.03	3.01	3.01	3.02	3.03	3.01	3.02	3.03	3.03	3.01	3.03	3.01	3.02	3.02	3.03
Ti	0.00	0.00	0.00	0.00	0.00	0.00	0.00	0.00	0.00	0.00	0.00	0.00	0.01	0.01	0.01
Al	2.86	2.82	2.75	2.80	2.86	2.75	2.75	2.81	2.82	2.81	2.83	2.83	2.76	2.82	2.81
Cr	0.00	0.00	0.00	0.00	0.00	0.00	0.00	0.00	0.00	0.00	0.00	0.00	0.00	0.00	0.00
Fe^{+3}	0.12	0.17	0.22	0.19	0.12	0.24	0.21	0.17	0.15	0.14	0.14	0.14	0.20	0.14	0.15
Mn^{+3}	0.01	0.01	0.00	0.01	0.00	0.01	0.00	0.00	0.00	0.00	0.00	0.00	0.00	0.00	0.00
Mg	0.00	0.00	0.00	0.01	0.00	0.01	0.00	0.00	0.00	0.00	0.00	0.00	0.00	0.00	0.00
Ca	1.96	1.98	2.00	1.95	1.96	1.97	2.01	1.98	1.98	2.03	1.97	2.00	1.98	1.99	1.99
Na	0.00	0.00	0.00	0.00	0.00	0.00	0.00	0.00	0.00	0.00	0.00	0.00	0.00	0.00	0.00
K	0.00	0.00	0.00	0.00	0.00	0.00	0.00	0.00	0.00	0.00	0.00	0.00	0.00	0.00	0.00

Table 14. Electron microprobe analyses of zoisite (continued).

Sample#	JMH-25														
Circle#	2	2	1	1	1	1	1	1	1	1	2	2	2	2	2
Point#			3	4	3	4	5	6	7	8	1	2	3	4	5
Analysis#	172	173	244	245	313	314	315	316	317	318	319	320	321	322	323
Comment															
Wt. % oxides															
SiO_2	39.64	38.99	39.10	38.82	37.02	36.85	36.61	37.56	37.92	37.92	38.11	37.76	37.40	37.06	36.51
TiO_2	0.39	0.07	0.01	0.00	0.07	0.06	0.05	0.05	0.00	0.03	0.04	0.00	0.01	0.03	0.00
Al_2O_3	30.97	30.13	31.79	30.01	31.41	31.08	31.28	30.85	31.09	31.23	31.90	31.37	31.01	31.65	31.32
Cr_2O_3	0.03	0.03	0.00	0.00	0.00	0.00	0.01	0.00	0.02	0.00	0.00	0.00	0.00	0.00	0.00
FeO	2.02	3.73	1.75	3.47	1.95	2.37	2.31	2.51	2.18	2.67	1.97	2.81	2.89	2.00	2.54
MnO	0.05	0.06	0.00	0.06	0.02	0.04	0.05	0.03	0.03	0.05	0.05	0.01	0.17	0.01	0.01
MgO	0.02	0.03	0.02	0.02	0.03	0.03	0.03	0.02	0.02	0.02	0.00	0.02	0.01	0.05	0.01
CaO	23.97	24.15	25.19	24.31	23.79	23.98	24.17	23.92	23.84	23.62	23.77	23.77	23.54	24.23	24.20
Na_2O	0.01	0.00	0.00	0.01	0.01	0.02	0.00	0.02	0.00	0.02	0.00	0.01	0.00	0.03	0.01
K_2O	0.02	0.02	0.02	0.04	0.01	0.02	0.02	0.02	0.02	0.04	0.02	0.03	0.03	0.02	0.02
Total	97.11	97.21	97.88	96.73	94.32	94.47	94.52	94.98	95.12	95.59	95.87	95.76	95.05	95.06	94.63
Cations (based on 12.5 oxygens)															
Si	3.04	3.01	2.99	3.01	2.93	2.92	2.90	2.96	2.98	2.96	2.96	2.95	2.94	2.92	2.90
Ti	0.02	0.00	0.00	0.00	0.00	0.00	0.00	0.00	0.00	0.00	0.00	0.00	0.00	0.00	0.00
Al	2.80	2.74	2.86	2.74	2.93	2.91	2.93	2.87	2.88	2.88	2.92	2.89	2.88	2.94	2.93
Cr	0.00	0.00	0.00	0.00	0.00	0.00	0.00	0.00	0.00	0.00	0.00	0.00	0.00	0.00	0.00
Fe^{+3}	0.13	0.24	0.11	0.22	0.13	0.16	0.15	0.17	0.14	0.17	0.13	0.18	0.19	0.13	0.17
Mn^{+3}	0.00	0.00	0.00	0.00	0.00	0.00	0.00	0.00	0.00	0.00	0.00	0.00	0.01	0.00	0.00
Mg	0.00	0.00	0.00	0.00	0.00	0.00	0.00	0.00	0.00	0.00	0.00	0.00	0.00	0.01	0.00
Ca	1.97	2.00	2.06	2.02	2.02	2.04	2.05	2.02	2.01	1.98	1.98	1.99	1.99	2.04	2.06
Na	0.00	0.00	0.00	0.00	0.00	0.00	0.00	0.00	0.00	0.00	0.00	0.00	0.00	0.00	0.00
K	0.00	0.00	0.00	0.00	0.00	0.00	0.00	0.00	0.00	0.00	0.00	0.00	0.00	0.00	0.00

Table 14. Electron microprobe analyses of zoisite (continued).

Sample#	JMH-25.2														
Circle#	2	2	2	2	2	2	2	2	2	3	3	3	6	6	6
Point#	1	2	3	4	5	6	7	8	9	1	2	3	1	2	3
Analysis#	324	325	326	327	328	329	330	331	332	333	334	335	336	337	338
Comment															
Wt. % oxides															
SiO_2	37.71	37.69	37.33	37.30	37.61	37.71	38.34	38.37	39.32	39.19	39.37	39.37	39.15	39.05	40.19
TiO_2	0.16	0.20	0.04	0.01	0.01	0.27	0.29	0.17	0.15	0.07	0.10	0.01	0.02	0.08	0.08
Al_2O_3	31.76	31.66	31.31	32.13	31.40	31.65	31.82	31.99	31.92	30.41	31.36	31.08	31.70	31.23	31.02
Cr_2O_3	0.00	0.01	0.00	0.00	0.00	0.00	0.03	0.00	0.00	0.00	0.00	0.00	0.00	0.04	0.00
FeO	1.67	1.68	2.59	1.69	2.37	1.72	1.77	1.63	1.67	3.44	2.18	2.57	1.91	2.32	2.08
MnO	0.02	0.05	0.01	0.03	0.08	0.04	0.06	0.02	0.03	0.06	0.02	0.01	0.17	0.05	0.08
MgO	0.02	0.02	0.02	0.01	0.03	0.03	0.03	0.02	0.02	0.06	0.03	0.01	0.03	0.02	0.03
CaO	23.75	23.68	23.81	24.07	24.00	23.73	23.69	24.29	24.72	24.31	24.59	24.40	23.84	24.00	23.21
Na_2O	0.03	0.00	0.02	0.01	0.00	0.01	0.00	0.00	0.01	0.00	0.00	0.02	0.02	0.00	0.68
K_2O	0.01	0.02	0.03	0.01	0.02	0.03	0.03	0.02	0.02	0.03	0.04	0.03	0.02	0.03	0.04
Total	95.14	95.01	95.15	95.26	95.52	95.17	96.04	96.50	97.84	97.56	97.68	97.49	96.86	96.82	97.40
Cations (based on 12.5 oxygens)															
Si	2.96	2.96	2.94	2.92	2.95	2.96	2.97	2.97	3.00	3.01	3.01	3.02	3.01	3.01	3.07
Ti	0.01	0.01	0.00	0.00	0.00	0.02	0.02	0.01	0.01	0.00	0.01	0.00	0.00	0.00	0.00
Al	2.94	2.93	2.90	2.97	2.90	2.92	2.91	2.92	2.87	2.75	2.83	2.81	2.87	2.84	2.79
Cr	0.00	0.00	0.00	0.00	0.00	0.00	0.00	0.00	0.00	0.00	0.00	0.00	0.00	0.00	0.00
Fe^{+3}	0.11	0.11	0.17	0.11	0.16	0.11	0.11	0.11	0.11	0.22	0.14	0.16	0.12	0.15	0.13
Mn^{+3}	0.00	0.00	0.00	0.00	0.01	0.00	0.00	0.00	0.00	0.00	0.00	0.00	0.01	0.00	0.01
Mg	0.00	0.00	0.00	0.00	0.00	0.00	0.00	0.00	0.00	0.01	0.00	0.00	0.00	0.00	0.00
Ca	1.99	1.99	2.01	2.02	2.01	1.99	1.97	2.01	2.02	2.00	2.01	2.00	1.96	1.98	1.90
Na	0.00	0.00	0.00	0.00	0.00	0.00	0.00	0.00	0.00	0.00	0.00	0.00	0.00	0.00	0.10
K	0.00	0.00	0.00	0.00	0.00	0.00	0.00	0.00	0.00	0.00	0.00	0.00	0.00	0.00	0.00

Table 14. Electron microprobe analyses of zoisite (continued).

Sample#	JMH-25.2				H1281-62.5										
Circle#	6	7	7	7	2	2	2	2	2	3	3	3	3	3	4
Point#	5	1	3	4	1	2	3	4	5	1	2	3	4	5	1
Analysis#	340	341	343	344	345	346	347	348	349	350	351	352	353	354	355
Comment															
Wt. % oxides															
SiO_2	39.01	38.85	39.12	39.14	38.76	39.08	38.92	40.20	39.02	38.38	38.21	38.19	38.69	38.58	38.49
TiO_2	0.03	0.00	0.02	0.00	0.00	0.02	0.00	0.00	0.00	0.03	0.01	0.03	0.00	0.00	0.07
Al_2O_3	32.10	31.58	32.93	30.69	28.96	31.06	30.92	30.44	31.28	31.12	30.26	31.66	31.26	29.85	30.91
Cr_2O_3	0.02	0.00	0.00	0.00	0.00	0.00	0.03	0.00	0.00	0.00	0.01	0.01	0.00	0.00	0.00
FeO	1.68	1.85	0.38	2.63	5.46	3.09	3.20	2.90	2.52	3.16	3.94	2.41	2.64	4.39	3.16
MnO	0.18	0.20	0.02	0.14	0.24	0.10	0.22	0.18	0.06	0.16	0.10	0.30	0.10	0.08	0.00
MgO	0.02	0.03	0.10	0.05	0.06	0.06	0.02	0.06	0.03	0.04	0.06	0.04	0.04	0.03	0.02
CaO	23.94	23.78	24.18	24.32	24.05	24.38	23.80	22.63	24.04	23.86	24.19	23.57	23.99	24.26	23.81
Na_2O	0.01	0.02	0.02	0.02	0.00	0.02	0.00	0.43	0.01	0.01	0.00	0.05	0.00	0.01	0.00
K_2O	0.03	0.04	0.02	0.03	0.01	0.03	0.02	0.21	0.03	0.03	0.02	0.01	0.03	0.00	0.01
Total	97.02	96.35	96.78	97.01	97.54	97.85	97.15	97.04	96.99	96.78	96.80	96.27	96.74	97.20	96.47
Cations (based on 12.5 oxygens)															
Si	2.99	3.00	3.00	3.02	3.00	2.99	3.00	3.08	3.00	2.97	2.97	2.96	2.99	2.98	2.98
Ti	0.00	0.00	0.00	0.00	0.00	0.00	0.00	0.00	0.00	0.00	0.00	0.00	0.00	0.00	0.00
Al	2.90	2.88	2.98	2.79	2.64	2.80	2.81	2.75	2.84	2.84	2.77	2.89	2.85	2.72	2.82
Cr	0.00	0.00	0.00	0.00	0.00	0.00	0.00	0.00	0.00	0.00	0.00	0.00	0.00	0.00	0.00
Fe^{+3}	0.11	0.12	0.02	0.17	0.35	0.20	0.21	0.19	0.16	0.20	0.26	0.16	0.17	0.28	0.20
Mn^{+3}	0.01	0.01	0.00	0.01	0.02	0.01	0.01	0.01	0.00	0.01	0.01	0.02	0.01	0.01	0.00
Mg	0.00	0.00	0.01	0.01	0.01	0.01	0.00	0.01	0.00	0.00	0.01	0.00	0.00	0.00	0.00
Ca	1.97	1.97	1.99	2.01	1.99	2.00	1.96	1.86	1.98	1.98	2.01	1.96	1.98	2.01	1.98
Na	0.00	0.00	0.00	0.00	0.00	0.00	0.00	0.06	0.00	0.00	0.00	0.01	0.00	0.00	0.00
K	0.00	0.00	0.00	0.00	0.00	0.00	0.00	0.02	0.00	0.00	0.00	0.00	0.00	0.00	0.00

Table 14. Electron microprobe analyses of zoisite (continued).

Sample#	H1281-62.5													UGC-block1	
Circle#	4	4	4	5	5	5	5	5	6	6	6	6	6		
Point#	2	3	4	1	2	3	4	5	1	2	3	4	5	1	2
Analysis#	356	357	358	359	360	361	362	363	364	365	366	367	368	459	460
Comment														matrix	matrix
Wt. % oxides															
SiO_2	38.06	39.05	38.63	39.30	38.95	38.80	38.64	38.28	38.89	38.85	38.75	38.54	38.82	38.54	38.52
TiO_2	0.01	0.00	0.00	0.00	0.00	0.02	0.00	0.00	0.00	0.01	0.00	0.01	0.00	0.12	0.05
Al_2O_3	30.72	31.33	30.25	31.72	30.71	31.06	31.63	30.13	31.60	31.51	31.63	32.01	31.69	28.45	28.98
Cr_2O_3	0.01	0.01	0.00	0.00	0.00	0.00	0.00	0.01	0.01	0.00	0.00	0.00	0.00	0.10	0.08
FeO	2.58	2.66	4.03	1.93	3.47	3.02	2.38	4.34	2.61	2.63	2.63	1.96	2.20	5.70	5.19
MnO	0.08	0.08	0.25	0.08	0.12	0.27	0.09	0.14	0.08	0.11	0.07	0.01	0.07	0.09	0.14
MgO	0.08	0.01	0.03	0.01	0.03	0.23	0.03	0.01	0.04	0.03	0.06	0.00	0.02	0.04	0.05
CaO	23.63	24.01	23.94	24.45	24.32	23.76	24.09	24.04	24.67	24.62	24.47	24.53	24.67	24.33	24.22
Na_2O	0.04	0.00	0.02	0.00	0.00	0.00	0.00	0.00	0.00	0.00	0.01	0.00	0.01	0.01	0.00
K_2O	0.05	0.01	0.03	0.02	0.02	0.06	0.02	0.02	0.02	0.01	0.03	0.03	0.02	0.06	0.08
Total	95.25	97.17	97.18	97.51	97.62	97.22	96.88	96.98	97.91	97.77	97.64	97.10	97.50	97.44	97.32
Cations (based on 12.5 oxygens)															
Si	2.99	3.00	2.98	3.01	2.99	2.98	2.98	2.97	2.97	2.97	2.97	2.97	2.98	2.99	2.99
Ti	0.00	0.00	0.00	0.00	0.00	0.00	0.00	0.00	0.00	0.00	0.00	0.00	0.00	0.01	0.00
Al	2.84	2.84	2.75	2.86	2.78	2.82	2.87	2.75	2.85	2.84	2.86	2.90	2.86	2.60	2.65
Cr	0.00	0.00	0.00	0.00	0.00	0.00	0.00	0.00	0.00	0.00	0.00	0.00	0.00	0.01	0.01
Fe^{+3}	0.17	0.17	0.26	0.12	0.22	0.19	0.15	0.28	0.17	0.17	0.17	0.13	0.14	0.37	0.34
Mn^{+3}	0.01	0.01	0.02	0.01	0.01	0.02	0.01	0.01	0.01	0.01	0.00	0.00	0.00	0.01	0.01
Mg	0.01	0.00	0.00	0.00	0.00	0.03	0.00	0.00	0.00	0.00	0.01	0.00	0.00	0.00	0.01
Ca	1.99	1.98	1.98	2.00	2.00	1.96	1.99	2.00	2.02	2.02	2.01	2.02	2.03	2.02	2.01
Na	0.01	0.00	0.00	0.00	0.00	0.00	0.00	0.00	0.00	0.00	0.00	0.00	0.00	0.00	0.00
K	0.00	0.00	0.00	0.00	0.00	0.01	0.00	0.00	0.00	0.00	0.00	0.00	0.00	0.01	0.01

Table 14. Electron microprobe analyses of zoisite (continued).

Sample#	UGC-block1											UGC-block2-zone1			
Circle#															
Point#	5	6	7	9	10	11	12	13	14	15	16	1	2	3	4
Analysis#	463	464	465	467	468	469	470	471	472	473	474	475	476	477	478
Comment	matrix	matrix	matrix	matrix	matrix	matrix	matrix	matrix	matrix	matrix	matrix				
Wt. % oxides															
SiO_2	38.45	38.27	38.34	38.79	38.50	38.36	38.72	38.55	38.85	38.62	38.57	38.52	38.71	38.68	38.45
TiO_2	0.07	0.06	0.07	0.02	0.07	0.04	0.10	0.04	0.07	0.03	0.01	0.05	0.17	0.08	0.04
Al_2O_3	29.18	28.99	28.14	27.96	28.82	29.49	28.84	29.23	29.98	29.66	29.43	29.15	29.87	30.01	28.56
Cr_2O_3	0.07	0.03	0.11	0.06	0.06	0.10	0.22	0.00	0.00	0.00	0.00	0.03	0.02	0.01	0.00
FeO	4.65	4.97	6.12	6.02	5.22	4.44	4.82	4.77	3.84	4.07	4.46	5.03	4.13	4.21	5.87
MnO	0.08	0.13	0.21	0.32	0.24	0.20	0.23	0.05	0.00	0.02	0.10	0.16	0.05	0.15	0.50
MgO	0.05	0.03	0.04	0.05	0.09	0.04	0.04	0.09	0.00	0.03	0.00	0.00	0.04	0.01	0.09
CaO	23.98	24.05	24.35	23.47	24.05	23.87	24.11	23.56	24.22	23.37	23.55	23.98	24.60	24.39	23.94
Na_2O	0.01	0.01	0.02	0.20	0.01	0.01	0.04	0.05	0.00	0.00	0.01	0.01	0.00	0.00	0.00
K_2O	0.03	0.06	0.02	0.06	0.09	0.02	0.02	0.03	0.04	0.02	0.01	0.02	0.03	0.10	0.03
Total	96.56	96.61	97.42	96.95	97.16	96.57	97.14	96.36	97.00	95.81	96.13	96.94	97.61	97.64	97.48
Cations (based on 12.5 oxygens)															
Si	3.00	2.99	2.98	3.02	2.99	2.99	3.00	3.01	3.00	3.02	3.01	2.99	2.98	2.98	2.98
Ti	0.00	0.00	0.00	0.00	0.00	0.00	0.01	0.00	0.00	0.00	0.00	0.00	0.01	0.00	0.00
Al	2.68	2.67	2.58	2.57	2.64	2.71	2.64	2.69	2.73	2.73	2.71	2.67	2.71	2.73	2.61
Cr	0.00	0.00	0.01	0.00	0.00	0.01	0.01	0.00	0.00	0.00	0.00	0.00	0.00	0.00	0.00
Fe^{+3}	0.30	0.32	0.40	0.39	0.34	0.29	0.31	0.31	0.25	0.27	0.29	0.33	0.27	0.27	0.38
Mn^{+3}	0.01	0.01	0.01	0.02	0.02	0.01	0.02	0.00	0.00	0.00	0.01	0.01	0.00	0.01	0.03
Mg	0.01	0.00	0.00	0.01	0.01	0.00	0.00	0.01	0.00	0.00	0.00	0.00	0.00	0.00	0.01
Ca	2.00	2.01	2.03	1.96	2.00	1.99	2.00	1.97	2.01	1.96	1.97	2.00	2.03	2.01	1.99
Na	0.00	0.00	0.00	0.03	0.00	0.00	0.01	0.01	0.00	0.00	0.00	0.00	0.00	0.00	0.00
K	0.00	0.01	0.00	0.01	0.01	0.00	0.00	0.00	0.00	0.00	0.00	0.00	0.00	0.01	0.00

Table 14. Electron microprobe analyses of zoisite (continued).

Sample#	zone1	zone 2						zone3				
Circle#												
Point#	5	1	2	3	4	5	6	1	2	3	4	5
Analysis#	479	480	481	482	483	484	485	486	487	488	489	490
Comment												
Wt. % oxides												
SiO_2	38.63	38.25	38.18	38.25	38.33	37.88	38.26	38.27	38.04	38.28	38.36	38.43
TiO_2	0.06	0.05	0.05	0.01	0.05	0.02	0.01	0.02	0.02	0.01	0.00	0.05
Al_2O_3	28.94	28.93	27.69	29.06	27.90	26.76	27.10	28.91	28.10	28.88	29.19	29.02
Cr_2O_3	0.00	0.01	0.14	0.01	0.04	0.05	0.00	0.00	0.00	0.01	0.00	0.00
FeO	5.37	5.35	6.44	4.80	6.09	7.65	7.37	5.63	6.50	5.30	4.81	5.17
MnO	0.03	0.07	0.14	0.07	0.35	0.57	0.60	0.10	0.08	0.05	0.07	0.07
MgO	0.01	0.01	0.05	0.02	0.09	0.10	0.11	0.04	0.05	0.04	0.00	0.00
CaO	23.95	24.04	23.79	24.20	23.89	23.67	23.52	24.00	24.34	23.95	23.55	23.91
Na_2O	0.01	0.00	0.01	0.01	0.01	0.01	0.00	0.00	0.01	0.00	0.00	0.00
K_2O	0.09	0.03	0.03	0.01	0.06	0.03	0.07	0.04	0.06	0.07	0.07	0.08
Total	97.10	96.74	96.50	96.44	96.80	96.74	97.04	97.01	97.21	96.60	96.06	96.73
Cations (based on 12.5 oxygens)												
Si	3.00	2.98	2.99	2.99	2.99	2.98	2.99	2.98	2.97	2.99	3.00	2.99
Ti	0.00	0.00	0.00	0.00	0.00	0.00	0.00	0.00	0.00	0.00	0.00	0.00
Al	2.65	2.66	2.56	2.68	2.57	2.48	2.50	2.65	2.58	2.66	2.69	2.66
Cr	0.00	0.00	0.01	0.00	0.00	0.00	0.00	0.00	0.00	0.00	0.00	0.00
Fe^{+3}	0.35	0.35	0.42	0.31	0.40	0.50	0.48	0.37	0.42	0.35	0.31	0.34
Mn^{+3}	0.00	0.00	0.01	0.00	0.02	0.04	0.04	0.01	0.01	0.00	0.00	0.00
Mg	0.00	0.00	0.01	0.00	0.01	0.01	0.01	0.00	0.01	0.00	0.00	0.00
Ca	1.99	2.01	2.00	2.03	2.00	1.99	1.97	2.00	2.03	2.00	1.97	2.00
Na	0.00	0.00	0.00	0.00	0.00	0.00	0.00	0.00	0.00	0.00	0.00	0.00
K	0.01	0.00	0.00	0.00	0.01	0.00	0.01	0.00	0.01	0.01	0.01	0.01

APPENDIX III

GEOCHEMICAL ANALYSES OF SERPENTINITES FROM DIAMOND DRILL HOLE 1281.

Table I. Chemical Analyses of Serpentinites from Diamond Drill Hole 1281

Sample		1281-01	1281-02	1281-04	1281-05
Lithologies		o.z. SH	s.z. S	o.z. SH	s.z. S
Depth interval (in feet)		592' - 608'8"	608'8" - 609'	612'3" - 613'8"	613'8" - 615'
Wt. %	D.l. (ppm)				
SiO_2	60	38.35	37.21	39.99	37.51
TiO_2	35	0.020	0.004	0.008	0.006
Al_2O_3	120	0.50	0.42	0.51	0.38
Fe_2O_3	30	7.48	7.11	4.15	6.32
MnO	30	0.103	0.088	0.095	0.092
MgO	95	39.99	38.69	40.18	40.00
CaO	15	0.05	0.02	< D.L.	0.01
Na_2O	75	0.02	0.10	< D.L.	0.11
K_2O	25	0.01	0.01	0.01	0.01
P_2O_5	35	0.007	0.006	0.005	0.007
Co (ppm)	10	116	112	104	110
Cr_2O_3 (ppm)	15	4319	3587	4184	3982
Cu (ppm)	2	21	22	17	32
Ni (ppm)	3	2497	2459	2800	2380
Zn (ppm)	2	70	68	68	71
L.O.I.	100	13.16	15.64	14.17	15.22
Total		100.39	99.92	99.83	100.32
ppm					
Mo	1	0.20	< D.L.	2.70	0.50
Nb	1	1.3	1.5	1.2	1.2
Pb	1	0.2	3.1	0.1	1.2
Rb	1	0.7	0.9	0.9	1.0
Sr	1	3.7	8.3	4.6	9.1
Th	1	< D.L.	< D.L.	< D.L.	< D.L.
U	1	0.1	0.1	< D.L.	< D.L.
Y	1	0.8	1.0	0.8	1.0
Zr	1	0.2	0.8	1.1	0.7
As	1	2.6	3.0	2.9	3.2
Sb	1	0.2	2.5	3.2	8.4
S	100	N.A.	40	N.A.	31

All analyses by X-ray fluorescence except for S which was analyzed using a LECO induction furnace and ALPHA sulfur titrator. L.O.I.: loss on ignition.

<D.L.: below detection limit, N.A.: not analysed, s.z. SH: sheared serpentinized harzburgite, o.z. SH: ore-zone serpentinized harzburgite, SH: barren serpentinized harzburgite.

Table I. Chemical Analyses of Serpentinites (Continued).

Sample	1281-06	1281-07	1281-08	1281-09	1281-10
Lithologies	o.z. SH	o.z. SH	o.z. SH	o.z. SH	o.z. SH
Depth interval	615' - 618'	618' - 623'	623' - 641'	641' - 680'	680' - 710'
Wt. %					
SiO_2	38.62	36.92	38.17	37.72	38.17
TiO_2	0.007	0.004	0.004	0.006	0.005
Al_2O_3	0.40	0.26	0.37	0.31	0.37
Fe_2O_3	5.09	6.43	7.71	6.70	6.83
MnO	0.097	0.108	0.114	0.101	0.090
MgO	40.49	40.90	40.31	40.56	39.98
CaO	< D.L.	< D.L.	< D.L.	< D.L.	< D.L.
Na_2O	< D.L.	< D.L.	< D.L.	< D.L.	< D.L.
K_2O	0.01	0.01	0.01	0.01	0.01
P_2O_5	0.006	0.005	0.005	0.005	0.006
Co (ppm)	106	127	105	123	109
Cr_2O_3 (ppm)	4281	3897	3487	4218	3653
Cu (ppm)	26	19	19	67	20
Ni (ppm)	2694	2527	2436	2622	2420
Zn (ppm)	69	65	64	72	65
L.O.I.	14.44	14.56	12.85	14.00	13.94
Total	99.83	99.82	100.10	100.09	99.99
ppm					
Mo	1.10	0.10	< D.L.	0.50	0.70
Nb	1.0	1.1	1.3	1.5	1.3
Pb	< D.L.	< D.L.	< D.L.	0.5	< D.L.
Rb	0.7	0.8	0.8	1.0	0.8
Sr	5.8	5.6	4.0	4.7	5.5
Th	< D.L.	< D.L.	< D.L.	< D.L.	< D.L.
U	< D.L.	0.1	0.4	0.4	0.2
Y	1.0	1.0	1.3	1.0	1.1
Zr	0.9	0.8	0.5	0.7	0.4
As	3.1	3.4	3.1	3.8	3.4
Sb	4.7	4.4	4.2	5.8	4.3
S	9	< D.L.	18	18	22

All analyses by X-ray fluorescence except for S which was analyzed using a LECO induction furnace and ALPHA sulfur titrator. L.O.I.: loss on ignition.

<D.L.: below detection limit, N.A.: not analysed, s.z. SH: sheared serpentinized harzburgite, o.z. SH: ore-zone serpentinized harzburgite, SH: barren serpentinized harzburgite.

Table I. Chemical Analyses of Serpentinites (Continued).

Sample	1281-12	1281-13	1281-14	1281-15	1281-18
Lithologies	o.z. SH	o.z. SH	o.z. SH	s.z. SH	s.z. SH
Depth interval	720' - 740'	740' - 749'	749' - 772'6"	772'6" - 780'	800' - 822'
Wt. %					
SiO_2	37.68	39.96	38.86	36.42	38.97
TiO_2	0.006	0.005	0.005	0.007	0.007
Al_2O_3	0.40	0.21	0.22	0.18	0.36
Fe_2O_3	6.24	4.24	6.09	8.08	6.60
MnO	0.107	0.093	0.098	0.083	0.077
MgO	40.81	41.09	40.32	40.19	39.72
CaO	< D.L.	< D.L.	< D.L.	< D.L.	< D.L.
Na_2O	0.04	< D.L.	0.01	< D.L.	0.06
K_2O	0.01	0.01	0.01	0.01	0.01
P_2O_5	0.007	0.006	0.006	0.006	0.007
Co (ppm)	112	104	118	132	115
Cr_2O_3 (ppm)	4523	3902	3833	4437	4284
Cu (ppm)	37	37	15	25	20
Ni (ppm)	2586	2722	2594	2637	2712
Zn (ppm)	74	62	61	63	64
L.O.I.	14.37	13.83	13.83	14.47	13.72
Total	100.40	100.07	100.11	100.12	100.25
ppm					
Mo	0.60	2.10	< D.L.	< D.L.	0.20
Nb	1.5	1.1	1.2	1.4	1.3
Pb	< D.L.	< D.L.	< D.L.	0.5	< D.L.
Rb	0.7	0.7	0.9	0.7	1.0
Sr	4.8	4.2	4.9	6.8	7.0
Th	< D.L.	< D.L.	< D.L.	< D.L.	< D.L.
U	0.0	< D.L.	0.2	0.5	0.2
Y	1.0	1.0	1.1	1.4	1.3
Zr	0.9	1.2	0.8	0.6	0.8
As	2.7	2.6	2.8	1.4	2.4
Sb	4.5	4.7	6.5	4.8	5.6
S	N.A.	N.A.	N.A.	27	N.A.

All analyses by X-ray fluorescence except for S which was analyzed using a LECO induction furnace and ALPHA sulfur titrator. L.O.I.: loss on ignition.

<D.L.: below detection limit, N.A.: not analysed, s.z. SH: sheared serpentinized harzburgite, o.z. SH: ore-zone serpentinized harzburgite, SH: barren serpentinized harzburgite.

Table I. Chemical Analyses of Serpentinites (Continued).

Sample	1281-20	1281-25	1281-29	1281-30
Lithologies	s.z. S	s.z. S	s.z. S	SH
Depth interval	831' - 839'4"	843'4" - 849'	863'5" - 865'5"	865'5" -867'
Wt. %				
SiO_2	39.31	41.51	40.09	37.62
TiO_2	0.010	0.011	0.007	0.007
Al_2O_3	0.62	0.32	0.29	0.41
Fe_2O_3	6.85	5.09	5.27	9.65
MnO	0.083	0.067	0.061	0.071
MgO	39.48	39.18	40.01	38.45
CaO	< D.L.	0.04	0.01	0.01
Na_2O	0.01	< D.L.	< D.L.	0.01
K_2O	0.02	0.01	0.01	0.01
P_2O_5	0.008	0.009	0.008	0.008
Co (ppm)	113	123	122	112
Cr_2O_3 (ppm)	4002	4428	3686	3898
Cu (ppm)	50	18	18	19
Ni (ppm)	2533	2536	2494	2544
Zn (ppm)	76	71	60	65
L.O.I.	13.38	13.04	13.53	13.24
Total	100.45	99.95	99.90	100.15
ppm				
Mo	< D.L.	1.20	1.00	0.40
Nb	1.4	0.9	0.7	1.2
Pb	< D.L.	0.1	< D.L.	0.5
Rb	0.9	0.7	0.7	1.1
Sr	6.6	10.7	5.0	6.8
Th	< D.L.	< D.L.	< D.L.	1.1
U	0.2	< D.L.	< D.L.	0.9
Y	1.2	1.4	1.5	1.4
Zr	1.5	0.7	0.8	0.3
As	3.0	0.7	3.0	3.6
Sb	4.0	2.9	1.1	< D.L.
S	18	N.A.	N.A.	N.A.

All analyses by X-ray fluorescence except for S which was analyzed using a LECO induction furnace and ALPHA sulfur titrator. L.O.I.: loss on ignition.
<D.L.: below detection limit, N.A.: not analysed, s.z. SH: sheared serpentinized harzburgite, o.z. SH: ore-zone serpentinized harzburgite, SH: barren serpentinized harzburgite.

Table I. Chemical Analyses of Serpentinites (Continued).

Sample	1281-33	1281-36
Lithologies	SH	SH
Depth interval	875'6" - 892'	893'3" - 896'11"
Wt. %		
SiO_2	39.06	38.77
TiO_2	0.005	0.010
Al_2O_3	0.44	0.45
Fe_2O_3	7.17	8.56
MnO	0.069	0.079
MgO	38.93	38.12
CaO	0.01	0.03
Na_2O	< D.L.	< D.L.
K_2O	0.01	0.02
P_2O_5	0.007	0.010
Co (ppm)	111	113
Cr_2O_3 (ppm)	3656	4216
Cu (ppm)	15	18
Ni (ppm)	2461	2408
Zn (ppm)	66	71
L.O.I.	13.31	12.98
Total	99.59	99.67
ppm		
Mo	0.40	0.10
Nb	1.0	1.5
Pb	0.5	1.0
Rb	0.8	1.2
Sr	5.9	8.4
Th	0.7	0.8
U	1.3	1.4
Y	1.4	1.7
Zr	0.8	1.0
As	1.1	3.2
Sb	0.9	1.8
S	N.A.	4

All analyses by X-ray fluorescence except for S which was analyzed using a LECO induction furnace and ALPHA sulfur titrator. L.O.I.: loss on ignition.
<D.L.: below detection limit, N.A.: not analysed, s.z. SH: sheared serpentinized harzburgite, o.z. SH: ore-zone serpentinized harzburgite, SH: barren serpentinized harzburgite.

APPENDIX IV

FLUID INCLUSION DATA.

Key to symbols

T: temperature

h: homogenization

V-L: vapour to liquid

Crit: critical

fr: freezing

e: first ice melting

m: melting

CLA: clathrate

TOT: total

d?: dissolution?

nb: nucleation of bubble

Table 1. Fluid inclusion data for rodingitized diorite.

Sample#	Chip#	Inclusion #	Origin	Type	Length (μm)	Host	$T_h^{V\text{-}L,Cnl}$	T_{fr}^{ICE}	T_{fr}^{CLA}	T_e	T_m^{ICE}	T_m^{CLA}	T_h^{TOT}
Flt B:1	1	6	P	2b		Gr		-53			-4.2		375
		8	P	2b		Gr							393
		10a	P	2b		Di		-49			-4.2		283
		x	P	2b		Gr		-53		-36 to -32		5	
	2	1a	P	2b		Di		-51			-4.8	5.3	325
		1b	P	2b		Di		-53		-33.5		5.4	326
		1c	P	2b		Di							325
		1d	P	2b		Di							315
		5	P	2b		Gr							310
	3	8	P	2b		Di							277
	4	2	P	2b		Di							310
		3a	P	2b		Di							300
		4a	P	2b		Di							295
		4b	P	2b		Di							300
Flt B:2	1	3	P	2b		Di							300
		4	P	2b		Di		-59.5				5.1	290
	2	1	P	2b		Gr							310
		2	P	2b		Gr							292
		3	P	2b		Gr							295
	7	2	P	2b		Di		-53	-41.7			8.6	293
		3	P	2b		Di		-51		-32	-12.8	8.7	
		4	P	2b		Di		-58.5					292
Flt B:4	3	Area3-1	P	2b		Di		-59	-42	-40	-12.3	8	
		Area4A-1	P	2b	45	Di	-88	-57	-43	-51.7	-12.2	8	
		7	P	2b	39.15	Di		-58		-43	-12.45	8	
		9	P	2b	8.35	Di		-58			-12.3	8	
		10	P	2b	14.15	Di		-56	-33	-36	-12	8.65	
		Area4C-1	P	2b		Di		-49	-39	-40	-6.4	9.15	

P = primary; Di = diopside; Gr = grossular

Table 2. Fluid inclusion data for rodingitized diorite.

Sample#	Chip#	Inclusion#	Origin	Type	Length (μm)	Host	$T_{d?}$	T_{nb}	$T_h^{V\text{-}L,Cnl}$	T_{fr}^{ICE}	T_{fr}^{CLA}	T_e	T_m^{ICE}	T_m^{CLA}	T_h^{TOT}
JMH-25.2B	1	1	P	2b		Gr				-50.5				1.4	404
		2	P	2b		Gr				-59			-3.7		355
		3	P	2b		Gr				-50			-5.2		323
		3a	P	2b		Gr				-59					332
	2	9	P	2b		Zo									318
	3	2	P	2b		Zo				-60.5		-31.2		2	
		2a	P	2b		Zo				-59.3		-31.6		-0.7	324
		6	P	1		Zo		-128	-118.7						
		7	P	1		Zo		-124	-116.5						
	4	1	P	2b		Gr				-58				8.4	333
		2	P	2b		Gr									313
		3	P	2b		Gr				-58				4	320
		4	P	2b		Gr									322
		5	P	2b		Gr				-58	-42.5			7.3	308.5
		8	P	1				-125.5	-118.4						
		9	P	1				-125	-119.1						
		10	P	1				-124.8	-118.2						
	5	1	P	2b		Gr				-59.9	-41.7	-31.3?		9.5	295
		2	P	2b		Gr				-59		-30?		9.3	
		4	P	2b		Zo				-53		-28.5?	-5.1	9.65	
		5	P	2b		Zo				-60.2				9.65	293
		6	P	2b		Zo				-59				9.2	286
		7	P	2b		Zo				-53				9.7	289
		8	P	2b		Zo				-53				9.1	292
	6	1	P	1		Zo		-127.6	-119.5						
		2	P	1		Zo		-125.5	-119.8						
		3	P	1		Zo			-100.1						
		4	P	1		Zo	-184.4	-126.5	-117.6						
		5	P	1		Zo			-119.9						
		6	P	1		Zo			-115.2						

P = primary; S = secondary; Gr = grossular; Di = diopside

Table 2. Fluid inclusion data for rodingitized diorite (continued).

Sample#	Chip#	Inclusion#	Origin	Type	Length (μm)	Host	$T_{d?}$	T_{nb}	$T_h^{V\text{-}L,Cnt}$	T_{fr}^{ICE}	T_{fr}^{CLA}	T_e	T_m^{ICE}	T_m^{CLA}	T_h^{TOT}
JMH-25.2B	7	1	P	2b	18.3	Zo			<-110	-57		-50.8	-11.7	9.2	
		1a	P	2b	23.3	Zo				-57.4			-11.8	9.2	
		3	P	2b	6.65	Zo				-60			-11.65	9.55	
		9	P	1		Zo			-118.1						
		10	P	1		Zo			-118.3						
		11	P	1		Zo			-115.8						
		12	P	1		Zo			-121.5						
		13	P	1		Zo			-122						
		14	P	1		Zo			-120.6						
		15	P	1		Zo			-113.5						
		17	P	1		Zo			-120.4						
		18	P	1		Zo			-118.1						
		19	P	1		Zo			-120.9						
		20	P	1		Zo			-110.8						
		21	P	1		Zo			-121.7						
	8	1	P	2b	22.5	Zo				-60				5.5	
		2	P	2b	21.7	Zo				-60.8	-48	-45	-18.8	5.5	
		3	P	2b	11.7	Zo			-88.1	-64		-56.8	-18	6.2	
		4	P	2b	9.2	Zo				-67	-46.8	<-36.2	-19.2	6.1	
		5	P	2b	18.3	Zo				-59.7		-43	-12	7.2	
		5a	P	2b	13.3	Zo								6.8	
		7	P	2b	7.5										
		8	P	2b	22.5	Zo				-57.9		<-36	-11.65	7.1	
		9	P	2b	21.7	Zo								9	
		10	P	2b		Zo				-58.8		<-37.3		8.8	
		11	P	2b		Zo				-60		-40.5	-15.8	7.75	
		13	P	2b		Zo			-92.2	-58.8		-42.3	-21.7	5.8	
		A	P	1		Zo			-120.7						

P = primary; S = secondary; Gr = grossular; Di = diopside

Table 2. Fluid inclusion data for rodingitized diorite (continued).

Sample#	Chip#	Inclusion#	Origin	Type	Length (μm)	Host	$T_{d?}$	T_{nb}	$T_h^{V\text{-}L,Cnl}$	T_{fr}^{ICE}	T_{fr}^{CLA}	T_e	T_m^{ICE}	T_m^{CLA}	T_h^{TOT}
JMH-25.2B	8	B	P	1		Zo			-122.9						
		C	P	1		Zo			-120.8						
		D	P	1		Zo			-121.2						
		E	P	1		Zo			-120.7						
JMH-25.2c	1	1	S	2b		Gr				-56	-40		-9.3	9.8	274
		2	S	2b		Gr				-53		-43	-9.5	10.1	
		4	S	2b		Gr				-55			-9.3	10.1	
		5	S	2b		Gr									275
		6	S	2b		Gr									262.5
		7	S	2b		Gr									270
		8	S	2b		Gr									267
		9	P	2b		Gr									316
		10	P	2b		Gr									317
		11	P	2b		Gr									316
		12	S	2b		Gr									274
	2	1	S	2b		Gr			-86.25	-60	-45	-47	-14.15	8.15	
		2	S	2b		Gr			-86	-58	-44	-45	-14	8.15	
		3	S	2b		Gr			-95.1	-59.7	-43.6	-46	-13.8	8.3	
		4	S	2b		Gr				-55			-13.9	8.3	
		5	S	2b		Gr			-86.4	-60	-43.5	-44	-14		
		6	S	2b		Gr			-86.25	-60		-42.5	-14.6	8.2	
		A	S	1		Gr			-117						
		B	S	1		Gr			-116.1						
JMH-25.2D	1	Area1-1	P	2b	28.3	Zo			-106	-59.8	-49.3	-45	-14.7	9.4	
		2	P	2b	10	Zo				-60	-43			8.4	
		3	P	2b	10.8	Zo				-59.8	-41.9		-17.2	8.3	
		4	P	2b	10	Zo				-61				8.4	

P = primary; S = secondary; Gr = grossular; Di = diopside

Table 2. Fluid inclusion data for rodingitized diorite (continued).

Sample#	Chip#	Inclusion#	Origin	Type	Length (μm)	Host	$T_{d?}$	T_{nb}	$T_h^{V\text{-}L,Cri}$	T_{fr}^{ICE}	T_{fr}^{CLA}	T_e	T_m^{ICE}	T_m^{CLA}	T_h^{TOT}
JMH-25.2D	1	Area1-5	P	2b	5.8	Zo				-62	-43	-46.7	-15.1	8.4	
		A	P	1		Zo			-119.4						
		B	P	1		Zo			-117.5						
		C	P	1		Zo			-118						
		D	P	1		Zo			-122.1						
		E	P	1		Zo			-115						
		Area2-1	P	2b	7.5	Zo				-62		-48	-14.8	7.8	
		2	P	2b	10.8	Zo				-60	-43		-14.5	8.6	
		3	P	2b	22.5	Zo				-61			-14.7	7.4	
		4	P	2b		Zo				-50	-43				
		Area3-1	P	2b	23.3	Zo			-110.5	-59	-42.8	-40	-14.2	9.1	
		2	P	2b	23.3	Zo				-60			-14.2	8.4	
		3	P	2b	4.17	Zo				-57					
		4	P	2b	10.83	Zo				-61	-43	-41	-14.3+-0.4	8.5	
		5	P	2b	20.83	Zo				-59.8		-42	-14.3	8.3	
		Area4-A	P	1		Zo			-116.7						
		B	P	1		Zo			-122.2						
		C	P	1		Zo			-121.6						
		D	P	1		Zo			-121.9						
		E	P	1		Zo			-121.5						
		F	P	1		Zo			-119.9						
		G	P	1		Zo			-119.3						
		1	P	2b	19.17	Zo			-113.6	-59		-46	-15.2	8.1	
		2	P	2b	16.67	Zo				-59		-48	-15.3	7.8	
		3	P	2b	11.67	Zo				-62		-53	-16.4	6.6	
		4	P	2b	6.67	Zo				-61		-51	-15.6	8	
		5	P	2b	10	Zo				-49			-5.5	7.1	
		6	P	2b		Zo				-63					

P = primary; S = secondary; Gr = grossular; Di = diopside

Table 2. Fluid inclusion data for rodingitized diorite (continued).

Sample#	Chip#	Inclusion#	Origin	Type	Length (μm)	Host	$T_{d?}$	T_{nb}	$T_h^{V-L,Cnt}$	T_{fr}^{ICE}	T_{fr}^{CLA}	T_e	T_m^{ICE}	T_m^{CLA}	T_h^{TOT}
JMH-25.2D	1	7	P	2b		Zo				-59					
		Area2-1	P	2b	23.3	Zo		-116	-95.7	-59	-49	-40	-22.4	3.7	
	2	2	P	2b	11.67	Zo						-45			
		4	P	2b	13.3	Zo				-75.5		-46			
		Area3A-1	P	2b	16.67	Zo				-66		-50	-22.4	3.8	
		2	P	2b	6.67	Zo				-70			-22.2+-0.3	3.9	
		3	P	2b	5.83	Zo				-69			-22.1	3.8	
		4	P	2b	5.83	Zo				-69		-48	-22	3.8	
		Area3B-1	P	2b	10.83	Zo				-72.5		-54	-23.5	2.2	
		2	P	2b	20	Zo				-64			-21.5	3.2	
		3	P	2b	8.3	Zo				-64			-23.2	3.1	
		4	P	2b	5	Zo				-73				3	
		5	P	2b	4.2	Zo				-75				3.1	
		6	P	2b	10.85	Zo				-68	-45		-23.2	2.8	
		Area4-2	P	2b		Zo				-49			-11.4	6.7	
		3	P	2b		Zo			-93.2	-75		-53.5	-23.8	-0.2	
	4	1	S	2b		Zo				-50	-40		-6.85	8.15	
		2	S	2b		Zo				-50	-39.5		-6.95	8.25	239.2
		3	S	2b		Zo				-49.5	-39.7		-7+-1	9	
		4	S	2b		Zo				-51	-40		-7	8	236.5
		5	S	2b		Zo				-51	-40		-7+-0.5	8	225
		6	S	2b		Zo									238.5
		7	S	2b		Zo									236
		8	S	2b		Zo									241.2
		9	S	2b		Zo									222
		10	S	2b		Zo									237.5
		11	S	2b		Zo									236.5

P = primary; S = secondary; Gr = grossular; Di = diopside

Table 3. Fluid inclusion data for rodingitized granite.

Sample#	Chip#	Inclusion#	Origin	Type	Length (μm)	Host	$T_{d?}$	T_{nb}	$T_h^{V\text{-}L,Crit}$	T_{fr}^{ICE}	T_{fr}^{CLA}	T_e	T_m^{HH}	T_m^{ICE}	T_m^{CLA}	T_h^{TOT}
JMH-333.2	1	10	P	2a		Di										354
	2	10	P	2a		Di										345
		8	P	2a		Di										335
	3	A-8	P	2a		Di										331
		6	P	2a		Di										342.5
		11	P	2a		Di										346
		7	P	2a		Di										358
		B1-2	P	2a		Di										325
		5	P	2a		Di										338
		6	P	2a		Di										372
		B2,3-6	P	2a		Di										342
		4	P	2a		Di										341
		3	P	2a		Di										351
		8	P	2a		Di										385
		9	P	2a		Di										
		B4-3	P	2a		Di										331
		2	P	2a		Di										341
	4	1-1	P	2a	46.67	Gr	-196.5	-100	-97.7	-87		-72	-4.6	-27.25	-3.9	
		2	P	2a	22.67	Gr			-98.6	-87		-70	5.8	-24.4	-5.4	
		3	P	2a		Gr			-99	-87		<-55			-4.3	
		1a	P	2a		Gr	-196.6		-95	-85		-50.4		-24.5	<-4.9	
		6	P	2a		Di				-87		-47		-24.6		
		8	P	2a		Di				-87		-47				
		16	P	2a		Di				-85.4		-47.5		-24.7	-6.8	
		18	P	2a		Di				-70		-56	8.2	-24.55	-7.1	
		19	P	2a		Di						-49		-24.5	-6.4	
		2-1	P	2a		Di				-83		-45	3.4	-24	3.3	
		2	P	2a		Di				-70		-44		-24.1		
		3	P	2a		Di				-70		-42				
	5	1	P	2a	36	Di			-89 (crit??)	-86		-56	10.3	-23.8	-6.1	

P = primary; S = secondary; Gr = grossular; Di = diopside

Table 3. Fluid inclusion data for rodingitized granite (continued).

Sample#	Chip#	Inclusion#	Origin	Type	Length (μm)	Host	$T_{d?}$	T_{nb}	$T_h^{V\text{-}L,Cnt}$	T_{fr}^{ICE}	T_{fr}^{CLA}	T_e	T_m^{HH}	T_m^{ICE}	T_m^{CLA}	T_h^{TOT}
JMH-333.2	5	11	P	2a		Di										287.5
		13	P	2a		Di										348.5
		14	P	2a												338
		15	P	2a												336
	6	1	P	2a	26.67	Gr	-183		-90.3	-81		-52		-23.8	-5.3	
		2	P	2a	34.67	Gr			-91.8							
		5	P	2a	22	Gr			-92.1							
		1a	P	2a	143.3	Gr			-101.9				20.8			
		6	P	2a	20	Gr			-100.6							
		7	P	2a		Di				-65		-51.7	10.5	-24.3	-6.3	
		7b	P	2a		Di				-69		-50.5		-24.2	-6	
		9	P	2a		Di				-66.9		-49.8				
	7	1	P	2a		Gr				-88.9		-52.4	1.8	-24.2		
		2	P	2a		Gr			-99.5	-85.6	-51	-57	1.75	-24.2	-3.8	
		3	P	2a		Gr			-90.4	-65		-61		-23.65	-3.2	
		4	P	2a		Gr			-96.8			-73.6	16.5	-24.9	-3.9	
		5	P	2a		Gr						-57	10.2			339
		6	P	2a		Di										
		7	P	2a		Gr						-53.3	10.8	-24.4	-6.2	
		9	P	2a		Gr						-53	10.9	-24.3		
		10	P	2a		Gr						-53.6	8.3	-24.2		
		11	P	2a		Gr						-53.4	10.9	-24.35		330
		13	P	2a		Gr										332
		14	P	2a		Gr										
		15	P	2a		Gr										319
		16	S	2a		Gr										251
	A	4	P	2a		Gr										350
		5	P	2a		Di										352
		6	P	2a		Di										349.5
		7	P	2a		Gr										337.5

P = primary; S = secondary; Gr = grossular; Di = diopside

Table 3. Fluid inclusion data for rodingitized granite (continued).

Sample#	Chip#	Inclusion#	Origin	Type	Length (μm)	Host	$T_{d?}$	T_{nb}	$T_h^{V\text{-}L,Crit}$	T_{fr}^{ICE}	T_{fr}^{CLA}	T_e	T_m^{HH}	T_m^{ICE}	T_m^{CLA}	T_h^{TOT}
JMH-333.2	B	1	P	2a		Di										343.5
		2	P	2a		Di										351.2
		3	P	2a		Di										347
		6	P	2a		Di										342
		7	P	2a		Gr										336
		8	P	2a		Gr										371
		9	P	2a		Di										382
		10	P	2a		Di										338
	C	1	P	2a		Gr										337.5
		2	P	2a		Gr										336
		3	P	2a		Gr										334
		4	P	2a		Gr										348
		5	P	2a		Gr										336
		6	P	2a		Gr										362
		7	P	2a		Gr										342.5
		8	P	2a		Gr										342.5
		9	P	2a		Gr										308
		10	P	2a		Gr										344
		11	S	2a		Gr										215
		12	P	2a		Gr										338
	D	1	P	2a		Di										337.5
		4	P	2a		Gr										381
		7	P	2a		Gr										333
		8	P	2a		Gr										344.5
		9	P	2a		Gr										337.5
		10	P	2a		Gr										363
		11	P	2a		Gr										346
		12	P	2a		Gr										350
		13	P	2a		Gr										341
		14	P	2a		Gr										337.5

P = primary; S = secondary; Gr = grossular; Di = diopside

Table 3. Fluid inclusion data for rodingitized granite (continued).

Sample#	Chip#	Inclusion#	Origin	Type	Length (μm)	Host	$T_{d?}$	T_{nb}	$T_h^{V\text{-}L,Crit}$	T_{fr}^{ICE}	T_{fr}^{CLA}	T_e	T_m^{HH}	T_m^{ICE}	T_m^{CLA}	T_h^{TOT}
JMH-333.2	D	15	P	2a		Di										365
		16	P	2a		Gr										337.5
	E	1	P	2a		Gr										334
		2	P	2a		Gr										342
		3	P	2a		Gr										346
		3a	P	2a		Gr										343
		4	P	2a		Gr										336
		6	P	2a		Gr										342.5
		7	P	2a		Gr										337.5
		7a	P	2a		Gr										355
		8	P	2a		Gr										347
		9	P	2a		Gr										349
		10	P	2a		Gr										344
		11	P	2a		Gr										344
		12	P	2a		Gr										346.5
		13	P	2a		Gr										352.5

P = primary; S = secondary; Gr = grossular; Di = diopside

Table 4. Fluid inclusion data for rodingitized slate.

Sample#	Chip#	Inclusion#	Origin	Type	Length (μm)	Host	T_{nb}	$T_h^{V\text{-}L,Crit}$	T_{fr}^{ICE}	T_{fr}^{CLA}	T_e	T_m^{HH}	T_m^{ICE}	T_m^{CLA}	T_h^{TOT}
UG-C	1		P	1		Di		-88.7							
			P	1		Di		-115.6							
			P	1		Di		-110.2							
			P	1		DI		-103.2							
	3	area3-1	P	2b		Di			-49	-39	-39		-5.5	8.5	
		area1-1	P	2a		Di			-67		-52.6		-22.8	-1.8	
		2	P	2b		Di			-68.6		-51.6	-14.3	-23.6	0.7	
		3	P	2b		Di			-56.4				-11	11.8	
		4	P	2		Di			-74.8		-52		-23.5		
		5	P	2b		Di			-70.4		-52		-23.7	0.6	
		6	P	2a		Di		-86	-72.6		-53.8		-23.8	-3.2	
		area2-7	P	2b		Di	-116	-103 (crit)	-46	-40	-41		-4.7	7.7	
		7a	P	2		Di									316
		8	P	2a		Di			-73.5		-48		-24.1	-3.1	
		9	P	2b		Di			-68	-56	-46		-23.4	0.2	
		10	P	2a		Di		-87	-82		-52.6	-6.5	-23.7	-4.6	
		11a	P	2		Di			-70						
		11b	P	2		Di			-66						
		11c	P	2		Di			-68		-52		-24		269
		12	P	2b		Di			-69				-23.4	0.7	
		13	P	2b		Di			-70				-24.2	0.7	
	4	1	P	2a		Di			-88		-53.3	6.7	-24.1	-6	
		5	P	2		Di			-76		-50.3				
		6	P	2		Di			-75		<-49				
		7	P	2b		Di		-85.1 (crit)			-52.8	-4.1	-21.75	1.1	
UG-C.4	1a	1	P	2a		Gr		-85.3	-77		-57.2	-5.6	-24.9	-5.4	
		2	P	2a	10	Gr		-92.3	-80		-53.3	-5.4	-24.3	-5.1	
		3	P	2a	21.67	Gr		-87	-79		-54		-24.1	-5	
		4a	P	2a	23.75	Gr			-76				-24.3	-5.4	

P = primary; S = secondary; Gr = grossular; Di = diopside

Table 4. Fluid inclusion data for rodingitized slate (continued).

Sample#	Chip#	Inclusion#	Origin	Type	Length (μm)	Host	T_{nb}	$T_h^{V\text{-}L,Crit}$	T_{fr}^{ICE}	T_{fr}^{CLA}	T_e	T_m^{HH}	T_m^{ICE}	T_m^{CLA}	T_h^{TOT}
UG-C.4	1a	4b	P	2a	22.3	Gr			-76				-24.3	-5.4	
		5	P	2a		Gr		-91.2	-79		-55	-6	-23.9	-5.2	
		6	P	2a		Gr		-87.6	-78		-54		-24.6	-3.9	
		7	P	2a		Gr			-79.7		-55			-5.3	
		8	P	2a		Gr		-84.8	-79		-53	-5.6	-24.4	-4.9	
		9	P	2a		Gr			-80		-52			-5.1	
		10	P	2a		Gr		-84.5	-80		-56		-23.8	-5.2	
		11	P	2a		Gr			-80		-52		-24.1	-5.2	
		12	P	2a		Gr			-80		-52		-23.9	-5.2	
	1b	2a-1	P	2		Gr			-80		-38		-25		
		2a-2	P	2a	7.92	Gr			-80				-25	-5.8	300
		2a-3	P	2		Gr									322
		2a-5	P	2		Gr									318
		2b-1	P	2a	10	Gr			-86		-45		-24.6	-6.1	
		2b-2	P	2a	3.33	Gr			-82				-24.6	-6	322.5
		2b-3	P	2		Gr									317.5
		2b-4	P	2		Gr									317.5
		2b-5	P	2		Gr									317.5
		2b-6	P	2		Gr									317.5
		2b-7	P	2		Gr									313
		2b-8	P	2		Gr									315
		3a-1	P	2a	16.67	Gr		-88.9	-81		-56		-25.2	-5.5	
		3a-2	P	2a	9.17	Gr		-88.7 (crit)	-83		-54.1		-25.4	-5.4	
		3a-3	P	2a	8.33	Gr			-81		-55		-25.6	-6.4	
		3a-5	P	2		Gr									344
		3a-6	P	2		Gr									342
		3a-9	P	2		Gr									317
		3b-1	P	2b		Di		-89 (crit)	-54.5				-16.5	6.6	
		3b-2	P	2		Di			-48						

P = primary; S = secondary; Gr = grossular; Di = diopside

Table 4. Fluid inclusion data for rodingitized slate (continued).

Sample#	Chip#	Inclusion#	Origin	Type	Length (μm)	Host	T_{nb}	$T_h^{V\text{-}L,Crit}$	T_{fr}^{ICE}	T_{fr}^{CLA}	T_e	T_m^{HH}	T_m^{ICE}	T_m^{CLA}	T_h^{TOT}
UG-C.4	1b	4-1	P	2a		Gr			-84		-67	-4.1	-25.2	-5.85	
		4-2	P	2a		Gr		-88 (crit)	-82		-76	-2	-24.8	-3.9	
		4-4	P	2		Gr									342
		4-5	P	2		Gr									329
		5-2	P	2		Gr									340
	1c	1	P	2b		Gr		-101.1	-66		-49		-24	0.3	
		2	S	2b		Di			-58		-45		-9.3	9.2	252
		3	P	2a		Di		-101.5	-75		-49		-24.4	-2.8	
		5	P	2b		Di			-68		-51		-23.8	4.2	
		6	P	2b		Gr			-64	-49	-44		-19.7	6.5	
		13	P	2		Di									331
	5a	2	P	2		Di									300
		4	P	2		Di									317
		5	P	2		Di									298
		6	P	2		Di									303
	5b	1	P	2		Di									290
		2	P	2		Di									312
		4	P	2		Di									300
		8	P	2		Di									340
		9	P	2		Di									324
		10	P	2		Di									320
	6	2	P	2		Di									261
		7	S	2		Di									230
		23a	S	2		Di									237

P = primary; S = secondary; Gr = grossular; Di = diopside

Table 5. Fluid inclusion data for rodingitized slate.

Sample#	Chip#	Inclusion #	Origin	Type	Host	$T_h^{V\text{-}L,Crit}$	T_{fr}^{ICE}	T_{fr}^{CLA}	T_e	T_m^{ICE}	T_m^{CLA}
JMH-301.1	1	Area1-1	P	2b	Di					-7.5	11.3
		2	P	2b	Di					-3	-0.15
		3	P	2b	Di		-49	-35			
		4	P	2b	Di					-22.8	2.35
	2	1	P	2b	Di		-46.5	-38	-36	-3.9	6.2
		2	P	2b	Di		-47			-3.8	
		3	P	2b	Di		-47			-3.8	8
		4	P	2b	Di		-49	-35.5		-4.35	13.2
		5	P	1	Di	-120.3					
		6	P	1	Di	-99.4					
		7	P	1	Di	-105.1					
		8	P	1	Di	-101.2					
		9	P	1	Di	-119.5					
		10	P	1	Di	-115.5					
		11	P	2b	Di		-72		-63	-19.2	2.5
		12	P	2b	Di		-48				4.25

P = primary; Di = diopside

Table 6. Fluid inclusion data from vesuvianite-rich "veins".

Sample#	Chip#	Inclusion#	Origin	Type	Length (μm)	Host	$T_h^{V\text{-}L,Crit}$	T_{fr}^{ICE}	T_{fr}^{CLA}	T_e	T_m^{ICE}	T_m^{CLA}	T_h^{TOT}
GOR-1	1	1-1	P	2c		Vsv		-45	-39	-39.8	-4.7	10.8	
		2-1	P	2c		Vsv		-48.6	-41	-42	-4.7	>9.4	
		4-1	P	2c		Vsv		-52	-47.5	-39.7	-4.7	10.4	
		A	P	1		Vsv	-90						
		A'	P	1		Vsv	-90						
	2	1-C	P	2c	28	Vsv		-42		-35.1	-5	4.8	
		B	P	2c	14.67	Vsv		-46		-36.9	-5.1		
		B1	P	2c		Vsv		-46.9			-5.3		
		A	P	2c	22	Vsv		-45		-37.9	-4.8		
		2-A	P	2c	12	Vsv		-47.4		-37.4	-4.6		
		B	P	2c	11.33	Vsv		-48			-4.5		
		3-A	P	2c	75.33	Vsv		-45		<-30.6	-4.8		
		B	P	2c	21.33	Vsv		-45		-35.2	-5.3		
		C	P	2c		Vsv		-45	-41.8		-5.2		
		D	P	2c		Vsv				-34.8		8.4	
	3		P	2c		Vsv							
GOR-2	1	2	P	2c		Di							157
		5a	P	2c		Di							180-200
		5b	P	2c		Di							180-200
		6	P	2c		Di							185-200
MIL-1	1	2-1	P	2c		Vsv		-45			-4.5		
		3-a	P	2c		Vsv					-5.7		
		3-1	P	2c		Vsv							181
		3-2	P	2c		Vsv							189
		3-4	P	2c		Vsv							184
		3-5	P	2c		Vsv							192
		3-6	P	2c		Vsv							195
		3-7	P	2c		Vsv							203
		3-8	P	2c		Vsv							185
		3-9	P	2c		Vsv							196

P = primary; Vsv = vesuvianite

Table 6. Fluid inclusion data from vesuvianite-rich "veins" (continued).

Sample#	Chip#	Inclusion#	Origin	Type	Length (μm)	Host	$T_h^{V\text{-}L,Cnt}$	T_{fr}^{ICE}	T_{fr}^{CLA}	T_e	T_m^{ICE}	T_m^{CLA}	T_h^{TOT}
MIL-1	1	3-10	P	2c		Vsv							180
		3-11	P	2c		Vsv							187
		3-12	P	2c		Vsv							200
		3-13	P	2c		Vsv							195
		4-1	P	2c		Vsv		-45		-37	-4.2		
		4-2	P	2c		Vsv		-45					
		4-3	P	2c		Vsv		-45					

P = primary; Vsv = vesuvianite